GEM-BEARING GRANITIC PEGMATITES IN MALAWI: THEIR MINERALOGY, GEOCHEMISTRY, AGE, AND FLUID COMPOSITIONAL VARIATIONS

PhD (SCIENCE) GEOLOGY THESIS

By

CHARLES FRIENDERSON KANKUZI

THESIS SUBMITTED TO FACULTY OF SCIENCE IN FULFILLMENT OF REQUIREMENTS FOR THE DEGREE OF DOCTOR OF PHILOSOPHY (SCIENCE) IN GEOLOGY AT RHODES UNIVERSITY, RSA.

January 2019

GEM-BEARING GRANITIC PEGMATITES IN MALAWI: THEIR MINERALOGY, GEOCHEMISTRY, AGE, AND FLUID COMPOSITIONAL VARIATIONS

PhD (SCIENCE) GEOLOGY THESIS

By

CHARLES FRIENDERSON KANKUZI

THESIS SUBMITTED TO FACULTY OF SCIENCE IN FULFILLMENT OF REQUIREMENTS FOR THE DEGREE OF DOCTOR OF PHILOSOPHY (SCIENCE) IN GEOLOGY AT RHODES UNIVERSITY, RSA.

January 2019

Declaration

I, ***Charles Frienderson Kankuzi***, hereby declare that the content of this submitted for the degree of PhD (Science) in Geology at Rhodes University, apart from the help recognised, is my own, unaided work and has never been formally been submitted to another University for a previous degree. I and Steffen **Büttner,** my supervisor, have together requested a two year embargo.

Acknowledgements

This work has benefited greatly from my association with **Prof. Steffen Büttner** and **Dr. Yong Yao** whose constructive criticism and suggestions have considerably improved this thesis in matter of substance as well as in format.

I am very grateful for the generous effort on their part, but any errors are of course mine. I sincerely appreciate their pieces of advice and practical suggestions that were of great help when I was writing my thesis.

I wish to thank those that provided funding for making it possible for me to attend Rhodes University to read for the Doctor of Philosophy (Science) in Geology.

My sincere thanks to Dr Johannes Glodny (GFZ, Potsdam) who assisted with analyses of Rb-Sr isochrons and Prof. Dirk Frei (Stellenbosch/UWC) who helped with the analysis of U and Pb isotopes of zircon. Prof Axel Hofmann, (University of Johannesburg) is thanked for guidance in Raman spectroscopy.

I also thank Angela, Tumeni and Tamani, my dear wife, son and daughter respectively, for their acceptance of my resolve to accomplish this project, and above all for their loyal support, remarkable patience, empathy, constant encouragement and understanding during the time I dealt with the more absorbing aspects of this thesis. I sincerely acknowledge that without their total commitment this thesis would have failed.

To Ashley Goddard, Vuyokazi, John Hepple, Andrea King, Thulani, Chris, Willie and Slyvia Erasmus, Ps Andrew Gouws, Amon, Claris and Kunaishe Magadza, Wadi Banda, Bambo Chipalapaseni, Lloyd Mughogho and Hastings Kasongo, I shall never thank you enough for your support during my stay studies.

This thesis has greatly benefited from the critical reviews by three anonymous external examiners.

Finally, I thank God Almighty for my dear mother Namayuni and all those who made many unselfish sacrifices, which helped me to get an education that has made all the difference.

Abstract

The gem bearing granitic pegmatites from different pegmatite fields across Malawi intrude all important geological entities from the Palaeoproterozoic in the north, the Mesoproterozoic in central Malawi and the Pan-African basement in the south. U/Pb zircon and Rb/Sr mineral isochron ages indicate pegmatite emplacement from the Palaeoproterozoic to Pan-African and Mesozoic time. Most pegmatites are related to the Pan-African cycle; no Mesoproterozoic pegmatites were observed in this study. Within the Pan-African pegmatite groups there are two important subgroups. Some pegmatites show Sr isotopic compositions that indicate mantle components contributing to the parental granites from which the pegmatites evolved. Others show higher Sr initials, indicating crustal granites as primary pegmatite sources or significant crustal contamination. Only for few pegmatites, such as the Palaeoproterozoic and Ordovician gem tourmaline pegmatites in the Chitipa and Dowa Districts, the granitic source is evident from their field context. For all others the granitic origin is interpreted by mineralogical and geochemical evidence.

All analysed pegmatites belong to either the Rare Element Class or the Miarolitic Class, but they vary in their degree of fractionation. The more evolved pegmatites are more enriched in incompatible elements such as Be, Li, B, and Ta, which resulted in the formation of gem minerals such as beryl, aquamarine, tourmaline and topaz, which may or may not be associated with tantalite. The Rare Element pegmatites can be further subdivided into the REL-Li subclass, beryl type, beryl-columbite subtype, and in the complex type and elbaite subtype. The Miarolitic pegmatites include Mi-Li subclass and beryl-topaz type.

Fluid inclusion studies (heating-cooling stage, Raman spectroscopy) identified a variety of fluid compositions that were present at different times and different places, indicating a variety of fluid sources. They range from aqueous-saline to CO_2–rich carbonic fluids (CO_2 +C_3H_8+ N_2), or aqueous-carbonic fluids (H_2O-CO_2-CH_4 and H_2O-CO_2-H_2-H_2S-CH_4). The dominant solutes and species for the pegmatites show genetic variations over time and orogen (Paleo-/Meso-/Neoproterozoic). Uniform homogenisation temperatures and salinities in individual samples indicate that the gem-bearing pegmatites contained homogeneous fluids at the time of their capturing in quartz. Based on fluid inclusion data, the estimated trapping conditions of inclusions in quartz for all studied pegmatites except for one pegmatite suggest low pressures between 0.9 to 2.6 kb at temperatures of 400-600 °C. The other pegmatite formed at slightly higher pressures of 2.2 to 3.6 kb. However, the pressure range for all the pegmatites is in agreement with the known liquidus conditions of Rare-Element pegmatite crystallisation. The shallow crustal emplacement level (3.4-9.8 km) and the greater depth (8.3 to 13.6 km) favoured the formation of gemstones.

Key words: granitic pegmatite, geochemistry, rare elements, fluid inclusions, Malawi.

Contents

Chapter Outline

List of Figures

List of Tables

List of Abbreviations

IMF	International Monetary Fund
LCT	Lithium Caesium Tantalite
NYF	Niobium Yttrium Fluorine
GEUS	Geological Survey of Denmark and Greenland
GEMMAP	Geological Mapping of Malawi Project
Tm_i	Initial melting temperature
T_n	Nucleation temperature
T_e	Eutectic melting
Tm_{ice}	Total melting temperature of ice
Tm_{cla}	Clathrate melting
T_h	Homogenisation temperature
Sr_i	Strontium initial ratio

1 INTRODUCTION

1.1. INTRODUCTION TO THE STUDY AREA

This study attempts to provide a first overview on the composition, distribution, and economic resource potential of gemstone bearing pegmatites in Malawi. Malawi is located in southern central Africa (Figure 1.1). This study investigates pegmatites from most parts of Malawi and from most geological episodes in which pegmatites may have formed throughout Malawi‟s geological history. Malawi lies at the junction of the Palaeoproterozoic (c. 2300-1800 Ma; Lenoir et al., 1994) Ubendian Belt (Figure 1.2) that is restricted to the northern part of the country, the Mesoproterozoic Irumide Belt (c. 1350-950 Ma; Daly, 1986), that in places overprints the Ubendian rocks, and the Neoproterozoic (Pan-African) Mozambique Belt (c. 900-450 Ma; Shackleton, 1996). The Irumide Belt is restricted to the northern and central parts. Pan-African overprints are seen in all parts of Malawi. The Mozambique mobile belt *sensu stricto* transects the southern part of Malawi from southwest to northeast (Figure 1.3).

Since Palaeoproterozoic times, younger orogenic phases may have reworked the pre-existing basement in places where the belts overlap. This polyphase and complex geological evolution created conditions suitable for pegmatite generation in numerous episodes of the geological history. Mesozoic and Cenozoic tectonic and magmatic processes related to the development of the East-African Rift form the youngest and still on-going episode that has the potential to generate pegmatites in the region. Chapter 3 describes the geological history of Malawi in more detail. The map in Figure 1.3 shows the administrative districts in Malawi, highlighting those where samples for this study were taken and to which reference is made in the text.

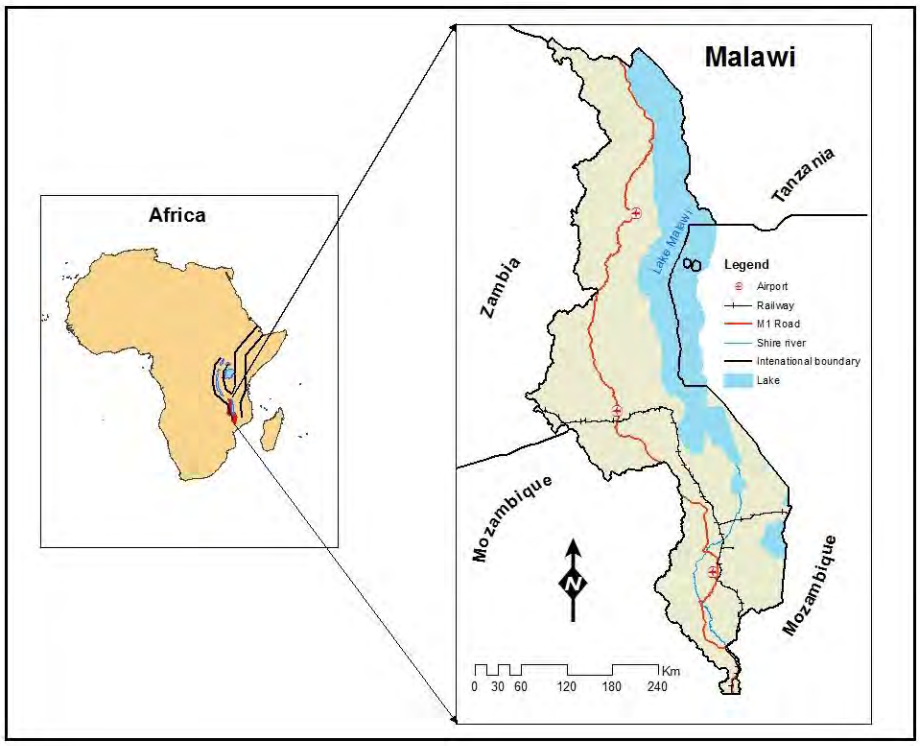

Figure 1.1: Location map showing Malawi in relation to Africa.

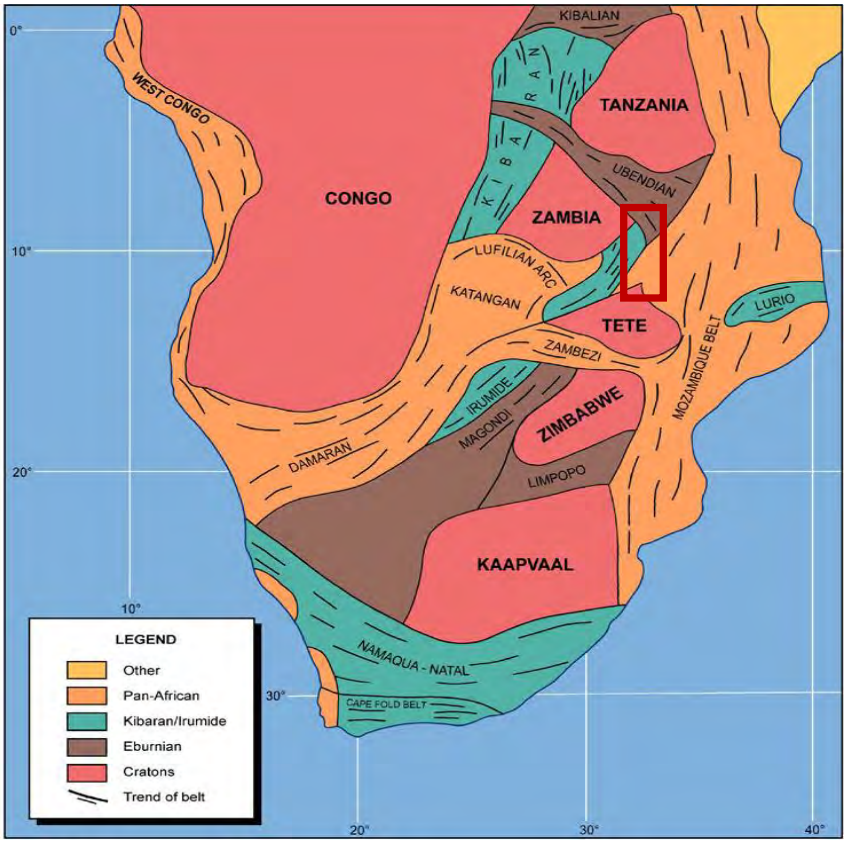

Figure 1.2: Mobile belts of central and southern Africa (modified after Hanson, 2003). The study area is highlighted.

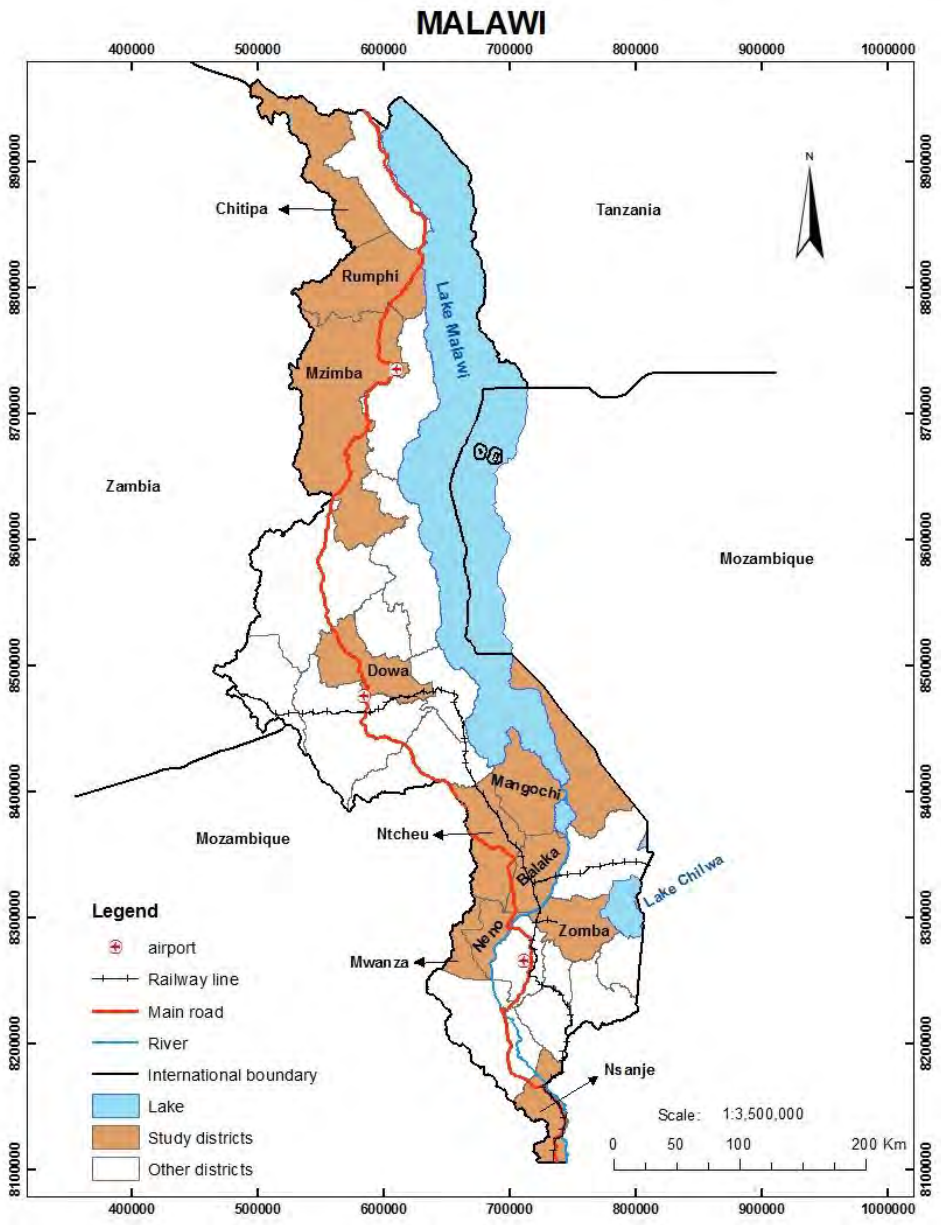

Figure 1.3: Location map of Malawi, highlighting districts where samples for this study were taken. The detailed map with sample locations and geological descriptions are shown in Figure 3.9 in Section 3.4.1.

1.2 GEOLOGICAL BACKGROUND

Globally, pegmatites are exploited to produce industrial, gemmological and technological materials (Pezzotta and Laurs, 2011; Glover et al., 2012; London and Kontak, 2012; Simmons et al., 2012). The economically most important commodities include Rare Earth Elements (REE) and gemstones. Pegmatites form and are emplaced at various depths, and form in particular geologic settings (Landes, 1935; Varlamoff, 1972; Shigley and Kampf, 1984), generally in areas with exposed igneous terrains, and in regional metamorphic rocks that have sufficiently exceeded temperatures required for partial melting (Jahns, 1955; Schneiderhohn, 1961; Cërny, 1982). In Africa, the Pan-African belts separating the Proterozoic and Archean West African, Congo and Kalahari cratons (Kennedy, 1964) are rich in pegmatites in general, and in gem mineralised pegmatites in particular.

The study area, Malawi, lies at the junction of Ubendian (c. 2300-1800 Ma), Irumide (c. 1350-950 Ma) and Mozambique (900-450 Ma) mobile belts, which were variably affected and reactivated by Ubendian, Kibaran, Irumide, and Pan-African orogenies (Ray, 1974; Ring et al., 1997). Furthermore, Malawi lies within the area of intersection and overlap of two sutures, the East African Orogen and Kuunga orogen, associated with Gondwana assembly (Meert et al., 1997; Meert, 2001; Grantham et al., 2013). These belts differ from each other not only in age but also in lithology and structural style (Foster et al., 2001). In addition, the correlation of units in different parts of individual belts is hampered by the lack of detailed mapping understanding the orogenic evolution (Schluter, 2006). Particularly the Pan-African Mozambique Belt is poorly understood and beyond the general agreement that it formed by collision of East and West Gondwana, the details of its crustal evolution are controversially discussed (e.g., Shackleton, 1994; Wilson et al., 1997; Kröner et al., 2001; Encyclopaedia of Geology, 2004; Jacobs et al., 2006; Grantham et al., 2013).

However, the widespread polyphase medium-grade metamorphism, folding, shearing and thrusting in the orogenic belts of Malawi, and the predominantly metasedimentary crustal composition provide favourable conditions for the formation of mineralised pegmatites. Even though pegmatites represent only a small portion of the Earth‟s crust, they may be locally abundant rock types (Shigley and Kampf, 1984). The study of pegmatites has provided insights into the chemical evolution of melts from magmatic to hydrothermal conditions and into the associated fractionation processes (Cërny 1991a, 1991b; London 1990, 1996, 2005). Smerekanics and Dudas (1999) point out that fluid inclusions in pegmatites record the history of late magmatic fluids. This study will show that pegmatites in Malawi formed in several time periods since the Palaeoproterozoic. It is the nature, formation and evolution of these pegmatites

that is the main concern of this study, rather than their individual relationships to the regional tectonometamorphic events to which they are related in time.

1.3 PEGMATITE ORIGIN: OVERVIEW

Even though pegmatites are important rock types due to their high concentration of incompatible elements and rare mineral phases (London, 2008), the discussion still revolves around their origin, whether they form by anatexis of sedimentary and metamorphic basement rocks (Simmons et al., 2003; London, 2008, Wise 2009), or from last vestiges of a silicate melt (Simmons et al., 2003; London, 2008), or from volatiles released by a crystallizing magma (Taylor et al., 1979; London, 2008). The complexity of geological processes that may produce pegmatites requires detailed petrogenetic investigations of each individual pegmatite field. These may include stable and radiogenic isotope studies, fluid inclusion studies, major and trace elemental analysis and the investigations that provide the understanding of the evolution of host source rocks (Dyar et al., 1999; London, 2008). Even though numerous studies have been conducted on geologically or economically important pegmatites globally, (Cërny, 1991a, 1991b; Baldwin, 1993; Keller et al., 1999; London, 2008), pegmatite petrogenesis is not yet entirely understood (London, 2008; Simmons and Webber, 2008) due to the distinctiveness of each pegmatite system (Simmons et al., 2003; London, 2008; Wise, 2009).

Pegmatites that form in association with miarolitic cavities in plutonic rocks evidently formed from residual melt that accumulated during fractional crystallization (Cameron et al., 1949: Jahns and Burnham, 1969). This may or may not involve constitutional zone refining (CZR) (London and Morgan, 2012), a process which produces a higher final concentration of incompatible components in small volumes of rock than fractional crystallisation. However, much of the hydrothermal and magmatic processes that enrich REE in pegmatites still remains unclear (Salvi and Williams-Jones, 2005; Chakhmouradian and Zaitsev, 2012). Chapter 2 will present a detailed description of the nature, classification, variation and origin of pegmatites.

1.4 PEGMATITES IN MALAWI

Pegmatites in Malawi are poorly researched and hence not well understood, which partly is related to previous government policy that emphasised agrarian production rather than the exploration of Malawi‟s mineral wealth. Similar problems exist also in other parts of Africa (Cairncross, 2004). Apart from some published work on a few known pegmatite-hosted gemstone deposits, such as those in western Mzimba (Holt, 1965; Gaskell 1973) and in Malosa (Petersen and Grossman, 1991; Cook and Ericksson, 2002), most of the gemstone bearing

pegmatites have not been mapped or sampled in a systematic, scientific manner as yet (MGDS, 2006). Accordingly, relatively little is known about the occurrence and distribution of economically relevant pegmatites, their relationship to the Ubendian, Irumide or Mozambique/Pan-African orogenic episodes or to the recent crustal rifting. There is also little information on the fluid evolution of pegmatitic melts, the spatial and relative temporal relationships of different pegmatite fields, the absolute timing of pegmatite emplacement, and their regional geological setting.

1.5 MOTIVATION FOR PEGMATITE RESEARCH IN MALAWI AND KEY OBJECTIVES OF THE STUDY

Since pegmatites are globally exploited, it is imperative to understand the processes that generate the economically important pegmatites in Malawi. The fundamental relevant data are provided by studying their fluid evolution and the timing of their emplacement. There is relatively little information available about pegmatites in Malawi, where mining activities are spearheaded by small-scale miners using indigenous knowledge and „trial and error" method for prospecting (IMF, 2005). This first overview study of mineralised pegmatites will enhance the understanding of these deposits and therefore is of economic significance to the country. Increasing mining of newly discovered gem-bearing pegmatites will help to uplift the socio-economic status of the rural population in Malawi, which is ranked the poorest country in the world (World Bank, 2017).

Globally, the majority of large gem-producing pegmatites are formed in Gondwana during the latest stages of the Pan-African orogenic event (870-550 Ma; Simmons et al., 2012). Recently, major gem bearing pegmatites have been reported from Mozambique, Tanzania, Zambia, Madagascar, and Kenya (Simmons et al., 2012), and these deposits appear to be similar to each other in their geological setting and age. For instance, pegmatites in the granulite-facies basement in the Ubendian and Usagaran Belts of Tanzania host rubies, sapphires and emerald, and these belts extend to northern Malawi (McConnel, 1950; Sutton et al., 1954; Smirmov et al., 1973; Harris, 1981). Furthermore, the metamorphic rocks of the eastern part of the Irumide orogenic belt in Zambia host granitic pegmatite swarms (Foster, 1965; Daly, 1986; Klerkx et al., 1998) that in Lundazi contain different varieties of beryl (Carranza et al., 2005). Also this belt extends into northern Malawi. Another example is the occurrence of Alto Ligonha pegmatites (Neiva, 2013), formed in the Mozambique Belt during the collision of East and West Gondwana around c. 600-550 Ma, with late-tectonic extension and plutonism occurring in northeast Mozambique at c. 520-515 Ma (Ueda et al., 2012). Additionally, a wide variety of gemstone

deposits are densely scattered along the Mozambique Belt through the neighbouring countries of Mozambique, Tanzania and Zambia, yielding spectacular occurrences of gemstones such as sapphires, rubies, emerald, tourmaline as well as beryl varieties (Malisa and Muhongo, 1990; Muhongo et al., 1999; Simonet et al., 2000; Simmons et al., 2012). Despite this abundance of gemstone-mineralised pegmatites in the Mozambique Belt of the neighbouring countries, the Pan-African of Malawi has not received much attention in related mineral exploration and research.

Accordingly, there is untapped potential for the discovery of and research in mineralised pegmatites in all major belts from the Palaeoproterozoic to the Pan-African and rifting related episodes in Malawi. This includes rare minerals, gemstones and industrial minerals. More specifically, potential pegmatite occurrences could be located in, or associated with, the mobile belts, the Neoproterozoic North Nyasa Alkaline Province of central and northern Malawi dated at 710-750 Ma (Eby et al., 1998), late Pan-African alkaline ring complexes from southern Malawi (Bloomfield, 1965), Karoo Stormberg basaltic volcanic rocks of southern Malawi (Habgood, 1963), and intrusive rocks of upper Jurassic to lower Cretaceous age known as Chilwa Alkaline Province (Eby et al., 2004), which is related to the East-African Rift.

This overview study provides a first nation-wide assessment of granitic pegmatites from all these major units. Intrinsically, the in-depth-analysis of each pegmatite field is beyond the scope of this project, but it nevertheless provides a first comparative investigation of age, mineralisation, composition, classification, and fluid composition of pegmatites across Malawi. It provides the first description of deposits known only from artisanal mining and of other deposits that were newly discovered during this research. Some of these newly discovered sites seem to have significant potential for occurrence of high quality gemstones.

Compositional characteristics of feldspar and micas provide valuable information on the geochemical evolution of pegmatites. Their trace element content indicates economic potential, and accordingly, this study uses trace element geochemistry of mica to constrain physico-chemical parameters that are relevant in that regard. There is also a strong link between rare element bearing pegmatites, gemstones and specific chemical environments in which the pegmatite melt evolved (Cërny, 1991a), and such environments can be monitored using the elemental compositions of main pegmatitic phases. This study examines the major, minor and trace elements concentrations of mica in order to decipher the nature and changes in the geochemical environment in which the analysed pegmatites formed.

Fluid inclusions in quartz are used to understand the most important aspects of the fluid evolution of the pegmatite systems. Furthermore, an understanding of fluid trapping conditions, and spatial distribution of different fluid inclusion populations is used to establish paragenetic successions relative to mineral formation.

The age of the pegmatites has been determined using the Rb-Sr isotope system (muscovite-alkali feldspar-plagioclase-biotite mineral isochrones) and U-Pb dating of pegmatitic zircon. This helps to associate pegmatite emplacement with the major orogenic episodes that have formed pegmatites in Malawi, and with specific stages of these major episodes. Therefore, this study will put respective pegmatite occurrences in a regional framework by determining their emplacement age, textural relationships and geochemical trends. The knowledge gained is required for understanding the genesis of gem-bearing pegmatites and the regional variability of gemstone forming processes.

According to the research motivation outlined above, the key scientific objectives of this thesis are to:

1) Characterise the mineralogy, geochemistry and fluid properties of pegmatites and possible variation of their different types.
2) Classify the pegmatites
3) Determine the evolution, composition and volatile content of the fluids and the pegmatites.
4) Identify the mineralisation process.
5) Approximate the temperature conditions of pegmatite crystallisation within the limitations of fluid inclusion analysis.
6) Constrain the timing of pegmatite emplacement.

2. CLASSIFICATION AND ORIGIN OF PEGMATITES

2.1 CHARACTERISTICS AND ECONOMIC SIGNIFICANCE OF PEGMATITES

This chapter presents a detailed description of the nature, classification, distribution, variation and origin of pegmatites. Pegmatites are holocrystalline rocks typically composed of igneous rock-forming minerals that are, in part, very coarse-grained, although some are extremely varied in grain size (Jahns, 1955; Simmons, 2007; London, 2008; London and Kontak, 2012). The pegmatites may be either mafic, ultramafic, alkaline, carbonatitic or granitic, depending on their chemical and mineralogical composition (Shigley and Kampf, 1984; London, 2008). They are often associated with dykes and veins of aplite, a fine-grained equivalent of pegmatites (Cairncross, 2004). However, the term pegmatite is specifically used for granitic pegmatites (London and Kontak, 2012), even though it may be applied to any rock of igneous or metamorphic (anatectic) origin that contains large crystals. Granitic pegmatites resemble ordinary granites, and are composed essentially of quartz, alkali feldspar, and may or may not contain plagioclase, tourmaline, white mica and garnet. They crystallise from volatile-rich melts with varying enrichments of lithophile rare elements, despite their differences in geochemical characteristics, structural features and paragenesis (London, 2008). More mafic varieties contain pyroxene, olivine, and plagioclase (Sinclaire, 1996), with variations in mineralogy, texture and structure (Cameron et al., 1949). Due to their significant economic importance, this study mainly focuses on the granitic pegmatites.

Granitic pegmatites can be distinguished from granites by their coarse grain size of the dominant phases, extremely variable grain size across the mineral assemblage, pegmatitic textures (i.e. random crystal orientation), chemical heterogeneity and chemical fractionation within the pegmatites (London, 1992). The size of individual crystals may range from centimetres to metres, while grain size of major minerals commonly increases from the margin to the centre of dykes. Common textures include comb structure, layered structure, graphic texture, radial crystal habit and, less commonly, skeletal crystal habit (Simmons, 2007; London, 2008; London and Kontak, 2012).

Regarding their chemical heterogeneity, pegmatites may be either unzoned, zoned, or complex. Individual crystals, if solid solutions, may be internally zoned. The compositions of such phases may vary within individual pegmatite zones. They may also be part of a continuum of a compositionally zoned field of pegmatites (London, 2008). This means that pegmatites that are unzoned have homogenous bulk composition, whereas complex and zoned ones have multiple systematically defined zones of heterogeneous composition (London, 1992; Wise, 2009).

Heterogeneity and the large grain size of pegmatites cause significant challenges to accurate whole rock chemical analysis.

In terms of chemical fractionation, most pegmatites are enriched in large ion lithophile (LIL), rare earth (REE) and high field strength (HFS) elements, such as Li, Rb, Cs, Be, Ga, Mn, Nb, Ta, Zr, Hf, Sn, Ta, B, P, F and volatiles, particularly H_2O (London, 1992; Sinclair, 1996; Wise, 2009; Simmons et al., 2012). Fractionation of the elements within a pegmatite occurs as the melt crystallises, resulting in enriched core and core margins compared to border zones (London, 1992). In some pegmatites fields the elements are fractionated amongst different pegmatites, whereby distal pegmatites in a cogenetic group that surrounds parent granite become enriched compared to proximal pegmatites (London, 1992). The enrichment in rare elements allows the crystallisation of some exotic minerals, mined for technological applications, such as production of lithium-batteries and lubricants, and the electronics industry (Cërny, 1991a, 1991b; Ercit, 2005; London 2008; Glover et al., 2012; London and Kontak 2012). Gem minerals are mostly found in the core or core margin of zoned pegmatites, and in miarolitic cavities that form as final products of crystallisation (Simmons et al., 2003, London, 2008). Such miaroles are typically located near the centres of pegmatites or in reaction zones between pegmatites and ultramafic host rocks (Simmons et al., 2012).

Pegmatites are also mined as a source of industrial minerals such as alkali feldspar and quartz for ceramic and glass industries, while mica is used for paints and cosmetics. This is due to both the concentration of mineralisation in large, very pure crystals, and their accommodation to concurrent extraction of several ores such as tantalite and pollucite (Cërny, 1991a; Linnen et al., 2012; London and Kontak 2012). Last not least, pegmatites are also an important source for gemstones such as beryl, aquamarine, tourmaline, emerald and topaz.

2.2 NOMENCLATURE RELATED TO THE SPATIAL DISTRIBUTION OF PEGMATITES

Pegmatite groups can be categorised depending on their spatial relationship with the pluton source as interior, marginal or exterior. Interior pegmatites lie within the granitic body, and are the least fractionated and mineralogically and structurally the least complex of all the pegmatites. Marginal pegmatites occur within or at the margin of a granitic pluton and are relatively more complex than interior pegmatites. Exterior pegmatites are hosted in the country rock outside the granitic body.

Usually pegmatite groups associated with a granitic source pluton consist of cogenetic bodies that may occupy less than one but up to hundreds of square kilometres within the pluton and the host rock. The swarms are distributed systematically around the less fractionated granite, and form less evolved pegmatite close to the granitic source, becoming more evolved in more distal settings (Cërny et al., 1981; 1991b; Ercit, 2005; London, 2008).

Regional zoning refers to the spatial distribution of pegmatites in relation to an associated pluton. This is influenced by composition and structure of the surrounding host rock. The number and size of associated exterior pegmatites decreases as the fractionation and mineralogical complexity increases. This zonation is due to the presence of more fractionated melts that have greater amounts of volatiles and are hence less viscous. According to Cërny (1991a), fluid-rich melts maintain their liquid state at lower temperatures; hence they travel to greater distances from their source pluton (Cërny, 1991a, 1991b). Furthermore, it has been noted that in syn- to late-orogenic magmatic suites, the metamorphic grade of the host rocks into which the pegmatites have intruded commonly restricts the emplacement of the pegmatite group in terms of their number and distance from the pluton, since hotter host rock slows down crystallisation Cërny (1991b).

Dykes related to *pegmatite swarms* share a geological or structural environment and are associated with a single tectono-magmatic event. Accordingly all bodies of pegmatite swarms are genetically related to each other and share a similar age (Cërny, 1991b; Simmons, 2007; London, 2008).

A *pegmatite belt* comprises all swarms or fields related to a particular geologic structure (e.g. tectono-metamorphic entity). A pegmatite belt may contain different classes of pegmatites that may have formed under different tectono-magmatic conditions, but which are related to the history of the hosting geological structure (Cërny, 1991b; London, 2008). On the other hand, a *pegmatite province* refers to all swarms and belts in a particular region consisting of a number of pegmatite classes that may have formed at different stages of crustal evolution, and hence might not be genetically related (Cërny, 1991b; London, 2008).

2.3 CLASSIFICATION OF PEGMATITES

Several systems have been proposed for the classification of pegmatites, such as according to their similarities with, or differences from, common plutonic rocks (Ginsburg et al., 1979). Some of them have been tailored to pegmatite varieties in specific regions (see Simmons et al., 2003, and Simmons et al., 2005 for further detail). Generally, granitic pegmatite classification is influenced by the depth-zone classification of granitic rocks, classifying pegmatites according to

their depth of emplacement, their relationship to metamorphic grade of the host rock, and their spatial and genetic relationship to granitic plutons (Cërny, 1990; 1991a; Ercit, 2005; Simmons, 2007).

The *classes* according to Ginsburg et al. (1979) are *abyssal, muscovite, rare-element,* and *miarolitic* classes, based on textural and mineralogical characteristics, the pressure and temperature of pegmatite formation and the metamorphic grade of host rocks. This classification was modified by Cërny (1991a; Table 2.1). This classification associates common minor elements of economical relevance to Ginsburg et al.‟s (1979) four classes.

On the basis of characteristic elemental enrichment, Cërny (1991a) proposed a system of three *families* of granitic pegmatites of plutonic derivation: Lithium-Caesium-Tantalum (LCT), Niobium-Yttrium-Fluorine (NYF) and mixed LCT–NYF pegmatites, which will be described in more detail below. Furthermore, Cërny (1991a) subdivided Ginsburg et al.‟s (1979) classes. The Rare-Element class was further subdivided in five sub-types: Rare-Earth, Beryl, Complex, Albite-Spodumene, and Albite (Table 2.2).

The Ginsburg et al. (1979) classification was further subdivided into subclasses, types and subtypes (Table 2.3; Cërny, 1990; 1991a; Cërny and Ercit, 2005; Cërny et al., 2012), based on trace-element signatures of pegmatites and depending on their mineral assemblages and mineral chemistry. The Rare-Element Class is subdivided into the (i) REL-REE subclass, with its Nb>Ta geochemical signature and (ii) the REL-Li subclass with Li, and rare alkali, Rb and Cs geochemical signature. Both subclasses have various subtypes depending on the dominant mineral phases (Table 2.3).

Overall, this classification system is descriptive, but specific chemical characteristics of the different classes are petrogenetically controlled. There is also some association of specific pegmatite types with specific tectonic settings. For instance, the REL-REE subclass commonly forms in extensional crustal settings, whereas REL-Li pegmatites are deemed more commonly associated with contractional orogenic settings. However, caution during classification should be taken because pegmatite classes show overlaps in definition, since some minerals appear in more than one class. The expanded Ginsburg et al. (1979) model has become widely accepted in the literature (Cërny, 1991a; Cërny and Ercit, 2005; Cërny et al, 2012).

Table 2.1: Characteristics of the four *classes* of granitic pegmatites by Ginsburg et al. (1979) with subdivision into families proposed by Cërny (1991a). LCT: Lithium-Caesium-Tantalum, NYF for Niobium-Yttrium-Fluorine.

Class	Family	Typical Minor Elements	Metamorphic Environment	Relation to Granite	Structural Features
Abyssal	—	U, Th, Zr, Nb, Ti, Y, REE, Mo poor (to moderate) mineralization	(upper amphibolite to) low- to high-P granulite facies ~4-9 kb ~700-800°C	none (segregations of anatectic leucosome)	conformable to mobilized cross-cutting veins
Muscovite	—	Li, Be, Y, REE, Ti, U, Th, Nb > Ta poor (to moderate) mineralization, micas and ceramic minerals	high-P, Barrovian amphibolite facies (kyanite-sillimanite) ~5-8 kb ~650-580°C	none (anatectic bodies) to marginal and exterior	quasi-conformable to cross-cutting
Rare - Element	LCT	Li, Rb, Cs, Be, Ga, Nb <,> Ta, Sn, Hf, B, P, F poor to abundant mineralization, gemstock industrial minerals	low-P, Abukuma amphibolite to upper greenschist facies (andalusite-sillimanite) ~2-4 kb ~650-500°C	(interior to marginal to) exterior	quasi-conformable to cross-cutting
	NYF	Y, REE, Ti, U, Th, Zr, Nb > Ta, F poor to abundant mineralization, ceramic minerals	variable	interior to marginal	interior pods, conformable to cross-cutting exterior bodies
Miarolitic	NYF	Be, Y, REE, Ti, U, Th, Zr, Nb > Ta, F poor mineralization, gemstock	shallow to sub-volcanic ~1-2 kb	interior to marginal	interior pods and cross-cutting dikes

Table 2.2: Expanded classification of pegmatites of the Rare-Element Class (Cërny, 1991a).

Pegmatite type	Pegmatite subtype	Geochemical signature	Typical minerals
RARE-EARTH	allanite-monazite	(L)REE, U, Th (P, Be, Nb > Ta)	allanite monazite
	gadolinite	Y, (H)REE, Be, Nb > Ta, F (U, Th, Ti, Zr)	gadolinite, fergusonite, euxenite, (beryl) (topaz)
BERYL	beryl-columbite	Be, Nb >< Ta (± Sn, B)	beryl columbite-tantalite
	beryl-columbite-phosphate	Be, Nb >< Ta, P (Li, F ± Sn, B)	Beryl, columbite-tantalite, triplite, triphylite
COMPLEX (rare element)	spodumene	Li, Rb, Cs, Be, Ta >< Nb (Sn, P, F ± B)	spodumene (amblygonite) beryl (lepidolite) tantalite (pollucite)
	petalite	Li, Rb, Cs, Be, Ta > Nb (Sn, Ga, P, F ± B)	petalite (amblygonite) tantalite beryl (lepidolite)
	lepidolite	F, Li, Rb, Cs, Be Ta > Nb (Sn, P ± B)	lepidolite microlite beryl topaz (pollucite)
	amblygonite	P, F, Li, Rb, Cs Be, Ta > Nb (Sn ± B)	amblygonite (lepidolite) beryl (pollucite) tantalite
ALBITE-SPODUMENE		Li (Sn, Be, Ta >< Nb ± B)	spodumene (beryl) (cassiterite) (tantalite)
ALBITE		Ta >< Nb, Be (Li ± Sn, B)	tantalite (cassiterite) beryl

Table 2.3: Principal subdivision and characteristics of Ginsburg et al.‟s (1979) five classes of granitic pegmatites (modified after Cërny and Ercit, 2005).

Class ***Subclass*** Type - Subtype	Typical minor elements	Metamorphic environment	Relation to granites
Abyssal (AB) ***AB-HREE*** ***AB-LREE*** ***AB-U***	U, Th, Zr Ti, Nb, Y, LREE: HREE poor to moderate mineralization	upper amphibolite to low- to high-P granulite facies; ~4 to 9 kbar, ~700 to 800°C	none (segregations of anatectic leucosome)
Muscovite (MS)	Ca, Ba, Sr, Fe>Mn No rare-element mineralization (micas and ceramic minerals)	high-P, Barrovian amphibolites facies (kyanite - sillimanite) 5 to 8 kbar, ~650 to 580°C	none (antectic bodies) to marginal and exterior
Muscovite– Rare-element (MSREL) ***MSREL-REE*** ***MSREL-Li***	Be, Y, REE, Ti, U, Th, Nb-Ta: muscovite, biotite, almandine-spessartine garnet, (kyanite, sillimanite) Li, Be, Nb beryl, cassiterite, columbite, lepidolite, (spodumene)	moderate to high P, (T) amphibolites facies; 3 to 7 kbar, ~650 to 520°C	interior to exterior; sometimes poorly defined
Rare-Element (REL) ***REL-REE*** Allanite-Monazite Euxinite Gadolinite ***REL-Li*** Beryl -*Beryl-columbite* *-Beryl-columbite-phosphate* Complex -*Spodumene* *-Petalite* *-Lepidolite* *-Elbaite* *-Amblygonite* Albite-Spodumene Albite	Be, Y, REE, U, Th, Nb>Ta, F Li, Rb, Cs, Be, Ga, Sn, Hf, Nb-Ta, B, P, F	variable, largely shallow and postdating regional events affecting host rocks low-P, Abukuma amphibolites (andalusite-sillimanite) to upper greenschist facies; ~2 to 4 kbar, ~650 to 450°C	Interior to marginal (rarely exterior) (interior to marginal) to exterior
Miarolitic (MI) **MI-REE** **MI-Li**	Be, Y, Nb, REE, F, Ti, U, Th, Zr Li, Be, B, F, Ta>Nb	very low P, postdating regional events that affect host rocks low-P amphibolites to greenschist, 3 to 1.5 kbar, 500 to 400°C	interior to marginal (interior to marginal) to exterior

2.4 PEGMATITE FAMILIES

LCT, NYF and Mixed Families

The three pegmatite families (LCT, NYF, Mixed) as proposed by Cërny (1991a) based on their composition, characteristics of their trace element chemistry, and the characteristics of their genetically associated granites are presented in Table 2.4.

Table 2.4: The family system of petrologic classification of granitic pegmatites of plutonic derivation (Cërny and Ercit, 2005). REL for Rare Element; MI for Miarolitic.

Family	Pegmatite subclass	Geochemical signature	Pegmatite bulk composition	Associated granites	Granite bulk composition*	Source lithologies**
LCT	REL-Li MI-Li	Li, Rb, Cs, Be, Sn, Ga, Ta>Nb, (B, P, F)	peraluminous to subaluminous	**synorogenic to late-orogenic (to anorogenic)**; largely heterogeneous	peraluminous, S, I or mixed S+I types	Undepleted upper- to middle-crust supracrustals and basement gneisses
NYF	REL -REE MI-REE	Nb>Ta, Ti Y, Sc, REE, Zr, U, Th, F	subaluminous to metaluminous (to subalkaline)	**syn-, late, post-** to **mainly anorogenic**; quasi-homogeneous	pera!uminous to subaluminous and metaluminous; A and I types	depleted middle to lower crustal granulites, or juvenile granitoids
Mixed	Cross-bred: LCT & NYF	mixed	metaluminous to moderately peraluminous	**postorogenic to anorogenic;** heterogeneous	subaluminous to slightly peraluminous	mixed protoliths or assimilation of supracrustals by NYF granites

LCT pegmatites are enriched in Cs, Rb, Li, Be, Ga, Sn, Ta>Nb, P, F, B, Mn and Hf (Table 2.4). These elements are incompatible with the main granitic phases, such as feldspars and quartz, and accordingly become progressively enriched in the residual melt, from which pegmatites form (Cërny, 1991b; Cërny and Ercit, 2005; Martin and De Vito, 2005; Martin et al., 2009). LCT pegmatites show relative enrichments in Li, Rb, Sn, Ta, and Nb (Ta < Nb); and highly variable REE patterns at very low concentrations (< 10 times chondrite: Cërny and Ercit, 2005). The per-aluminous to sub-aluminous LCT pegmatites commonly show an association with S- and I- type, or mixed S-I- type granites, the pegmatites contain spessartine garnet, muscovite and tourmaline (London, 2008). Less commonly LCT pegmatites show I-type geochemical signature.

LCT pegmatites are associated with syn-, late-, or anorogenic plutons that formed from melting of undepleted upper- to middle- crustal rocks and basement gneisses (Cërny, 1991b; Chappell and White, 1992; 2001; London, 2008; London and Kontak, 2012). LCT pegmatites are usually hosted in gneisses, schists, metapelites, metasediments, metaturbidites and metavolcanic rocks that were metamorphosed at lower amphibolites facies conditions (Cërny and Ercit, 2005).

It has been proposed that the melting of mica-rich metamorphic rocks in the pegmatite source enriches Li in the pegmatite melt, which results in the crystallisation of Li-Al-silicates such as spodumene, petalite, lepidolite, amblygonite-montebrasite or elbaite (London, 2005; 2008; Cërny et al., 2012). The melting of micas, mostly muscovite and biotite at the pegmatite source, also enriches Rare-Element pegmatites in Cs, resulting in the crystallisation of pollucite (London, 1995, 2005). Furthermore, the micas or minor quantities of ilmenite in mica schists could be the source for Ta enrichment in LCT pegmatites (London, 2008).

Within the LCT family, feldspars and micas have modal proportions according to types (Table 2.5). The beryl type contains more K-feldspar than albite and more muscovite than biotite. The complex type contains K-feldspar, albite, muscovite, and Li-rich minerals. The albite-spodumene type contains more albite than K-feldspar, and accessory muscovite and finally, the albite type contains significantly more albite than K-feldspar, muscovite and lepidolite (Cërny, 1991a).

NYF pegmatites are enriched in Y, Ti, Sc, HREE, Zr, U, Th, Nb>Ta and F (Cërny, 1991b; Cërny, 1992; London, 2008; Cërny et al., 2012; Table 2.4). NYF pegmatites show LREE contents more than 10 times the chondrite composition (Cërny and Ercit, 2005). They crystallise from relatively dry magmas (Cërny, 1991b). According to Skjerlie and Johnston (1992), fluorine accumulates in the melt by peritectic pyroxene growth during amphibole and mica melting. NYF pegmatites derive from late, post-orogenic to mainly anorogenic plutons with depleted sources, such as middle to lower crust granulites or juvenile mantle-derived granitoid rocks, with some chemical constituents from the mantle (Lenharo et al., 2003; Cërny and Ercit, 2005; Martin and De Vito. 2005; Cërny et al., 2012). An example of NYF pegmatites in Malawi are the Malosa Mountain pegmatites (Petersen and Grossman, 1994).

Mixed LCT-NYF pegmatites display characteristics of both LCT and NYF. However, they are mainly NYF pegmatites with strong LCT characteristics due to contamination from local sources (Cërny, 1991b; Martin and De Vito, 2005; Cërny et al., 2012; Table 2.4). An LCT signature results when late stage orthomagmatic fluids from NYF pegmatites cause hydrothermal reactions in sedimentary host rocks to release Li and B, that is assimilated into the NYF melt (Martin and De Vito, 2005; Cërny et al., 2012).

Cërny and Ercit (2005) modified the pegmatite classification scheme in order to show the correlation between pegmatite classes and families (Table 2.5). It suggests that the Miarolitic

Class, subdivided into MI-REE and MI-Li, forms at shallow levels in the continental crust during the late stages of collisional plate tectonic events (Cërny and Ercit 2005; Simmons et al., 2003, 2012). The gem minerals are mostly found in Miarolitic and Rare-Element classes associated with pegmatites in both LCT and NYF families. The gemstones mainly occur in interiors of zoned pegmatites or in reaction zones adjacent to the pegmatites (Simmons et al., 2012).

Table 2.5: The pegmatite classification scheme of Cërny and Ercit (2005), modified to show the correlation between pegmatite classes and families. NYF = niobium-yttrium-fluorine family; LCT = lithium-caesium-tantalum family; HREE = heavy rare earth elements; LREE = light rare earth elements.

Class	Subclass	Type	Subtype	Family
Abyssal	HREE			NYF
	LREE			
	U			NYF
	Be			LCT
Muscovite				
Muscovite - Rare Element	REE			NYF
	Li			LCT
Rare Element	REE	allanite-monazite euxenite gadolinite		NYF
	Li	beryl	beryl-columbite beryl-columbite-phosphate	
		complex	spodumene petalite lepidolite elbaite amblygonite	LCT
		albite-spodumene albite		
Miarolitic	REE	topaz-beryl gadolinite-fergusonite		NYF
	Li	beryl-topaz spodumene petalite lepidolite		LCT

The classification of pegmatites depending on their depth of emplacement is controversial since any genetic scheme that relies on one factor only, such as depth or tectonic setting, falls short of explaining a complex chemical system, in which the nature of source rocks plays a major role. Hence Martin (2007) and Martin et al. (2009) proposed a classification scheme relating pegmatite melt generation to tectonic processes. This however would be problematic to apply in

regions where the tectonic evolution and/or the relationship between the pegmatite and that evolution is poorly understood. Further evaluation of these controversies of pegmatite nomenclature however is beyond the scope of this study.

2.5 REGIONAL ZONING

Regional zonation in pegmatites refers to compositional variations within pegmatite swarms, comparing compositions close to the granitic source with compositions seen further away from that source, at increasing distance to the granite-host rock contact. This zonation may be caused by magma evolution during flow and cooling away from the source.

NYF pegmatites do not show such regional zoning resulting from magma evolution related to distance from the associated peraluminous source granites, but form local concentric zones at outcrop scale. NYF pegmatites tend to locate within or close to their parental granite (Cërny 1992; Cërny and Ercit, 2005). Attempts to distinguish NYF pegmatite groups using geochemical, or mineralogical variations have been made (Simmons et al., 2003; Wise, 2009), but are hampered by the generally uniform composition of NYF pegmatites on a regional scale.

In zoned cogenetic LCT pegmatites, the spatial sequence from the fertile granite outwards shows an increase in fractionation and volatile enrichment of the pegmatite melt, and an increase in complexity of mineralisation in individual pegmatite bodies (Cërny 1991a; Figure 2.1). The barren zone is within the pluton, but rare elements increase outwards, towards the more fractionated zone. However, not all zones from the barren through to the distal pegmatites, enriched in Li, Cs, Be, Ta and Nb, usually develop in a particular pegmatite group, but where such a zonation is present, it follows the sequence as shown in Figure 2.1.

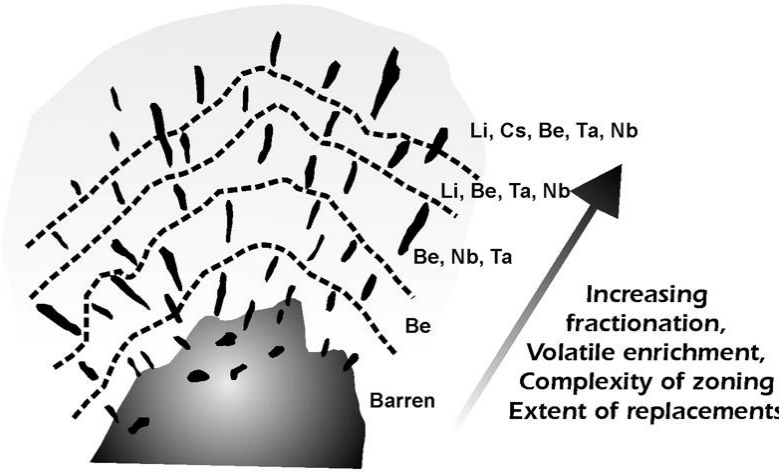

Figure 2.1: Schematic representation of regional zoning in a cogenetic granite and pegmatite group (modified from Trueman and Cërny, 1982). NYF pegmatites typically occupy the inner zone within or close to the source granite. LCT pegmatites may occur within, close to, or distal to the source. Distal LCT pegmatites typically are highly enriched in rare elements.

2.6 INTERNAL STRUCTURE AND CONCENTRIC ZONING

The internal structure of a pegmatite is defined by zones of different mineral or chemical composition that are developed locally and may form different rim and core facies, or more complex patterns consisting of several zones. According to Cameron et al. (1949), a pegmatite zone is defined by areas dominated by a specific mineral species, forming alternating shells around the centre of a pegmatite dyke (Figure 2.2). Their shape resembles the shape of the dyke, which most commonly means that pegmatite zones have plate-like geometry.

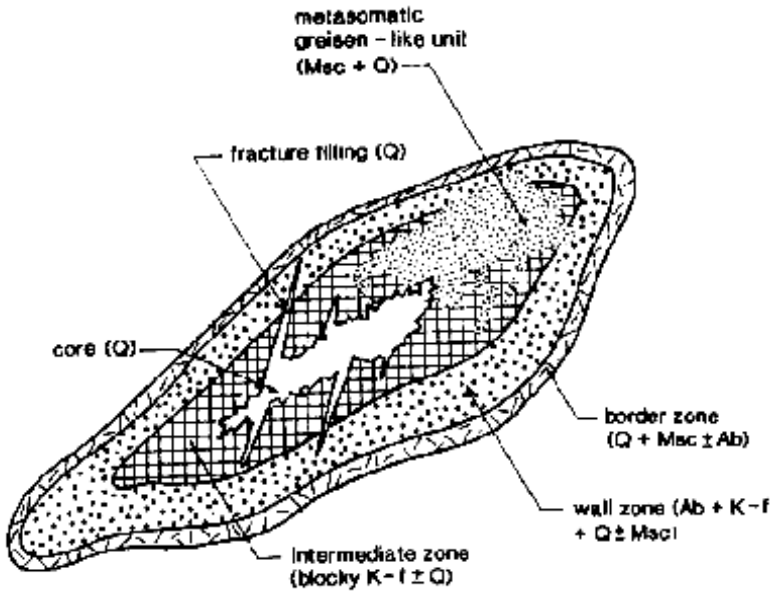

Figure 2.2: Internal structure of zoned pegmatites in schematic horizontal sections. Concentric pattern of primary zones cross-cut by fracture fillings, with a lithology-controlled, but, in part, fracture-related, metasomatic greisens-like unit with muscovite and quartz (taken from Cërny, 1991a).

Pegmatites could be zoned or unzoned. Unzoned pegmatites have homogenous texture and mineralogy but occasionally they show oriented mineral fabrics and a porphyritic texture. They are commonly found in high-grade metamorphic terrains (Simmons, 2007; London, 2008). Zoned pegmatites develop mapable shells within their bodies with distinct mineralogy, texture, grain size and crystal habit (Cameron et al., 1949; Ercit, 2005; Simmons, 2007; London, 2008). According to Cërny (1991a), the pegmatite zones may form by primary crystallization, replacement or dissolution of existing, and precipitation of secondary crystals, or the filling of secondary fractures that crosscut earlier-formed parts of the pegmatite. In Figure 2.2 the border zone has quartz, muscovite with or without albite, the wall zone has albite, K-feldspar, quartz with or without muscovite, the intermediate zone has blocky K-feldspar with or without quartz, while the central core is composed of quartz. Greisen composed of muscovite and quartz is located in both the intermediate and wall zone.

Cameron et al. (1949) and Simmons (2007) suggest that pegmatites crystallise directly from a pegmatitic melt from the outside inwards, with an increase in grain size towards the centre. Mineralogically, pegmatites become less complex and more silica-rich from the rims towards the centre of the dyke. The centre of pegmatites may consist only of quartz as a major mineral. However, Li-aluminosilicates and albite may also occur.

Zones of pegmatites are symmetrically distributed, forming the *border zone*, *wall zone*, *intermediate zone* and *core zone* (Figure 2.2). The *border zone* shows a sharp contact between aplitic to fine-grained parts of the pegmatite and the wall rock. Mineralogically, the border zone typically shows unidirectional crystal growth and occasionally a bimodal texture of crystal size distribution may be developed.

The coarse- or medium-grained *wall zone* is typically thicker than the border zone and shows gradational contacts on the outside to the wall zone and on the inside to the intermediate zone. *Intermediate zones*, though less commonly developed, vary both in thickness and mineralogy. They are characterised by sudden increase in grain size and dominance of a particular mineral species in the mineral assemblages. Furthermore, the intermediate zones tend to be more commonly present and better developed in thicker parts of pegmatites. The size of the central *core zone,* which is usually dominated by one mineral species, but may contain variable proportions of other minerals, is determined by the entire pegmatite size and the thickness of the wall and intermediate zones. Economically important mineral phases, such as tantalite and pollucite, are typically concentrated in the intermediate to core zones, which are chemically more evolved and contain the highest concentration of incompatible elements.

Rare Element pegmatites may be layered, homogenous or zoned. *Layered pegmatites* show asymmetric zonations across dykes, in which individual zones may not have a mirrored distribution on both sides of the dyke. Layered zones may occur in subhorizontal pegmatites parallel to their dyke walls. Depending on fractionation grade, mineralised vugs may be present or not. *Homogenous pegmatites* are rare. They have variable mineral assemblages, but in a given pegmatite such an assemblage is uniform and uniformly distributed. Also mineral textures do not vary significantly. *Zoned pegmatites* are more common than layered or homogenous ones. The mineral assemblage and textures show a slight variation from the margin to the core. There are also fracture fillings and late units of apparent replacement origin (Cërny 1991a; Sinclair, 1996; Cërny, 2005).

Fluids released from both zoned and homogenous pegmatites may infiltrate the host rock, where metasomatic hydrous alteration zones may contain minerals rich in mobile elements, such as tourmaline (B) and lepidolite (Li, K)/muscovite (K) (London et al., 1996; Simmons et al., 2012). Such metasomatism may also be related to greisens, which represent the most evolved residual fluids. Greisens may replace earlier pegmatite zones or parts of the host rock (auto-) metasomatically. Greisens may contain quartz, muscovite, tourmaline, fluorite, topaz, and chlorite. Tin, tungsten, beryllium and niobium mineralisation might be associated with this late-stage alteration and metasomatism (Reed, 1986). The extraction of fluids into the host also might affect the solidification of the pegmatite itself. Extraction of fluids will elevate the solidus of the melt, which may increase crystallisation rates (Simmons et al., 2003, 2012; London, 2008).

2.7 PEGMATITE TEXTURES AND GEOCHEMICAL CONDITIONS

Variations in mineral textures in pegmatites may be used as descriptive tools and in some instances may indicate the presence and location of mineralised zones. Preferential orientation and layered structures (London, 1992) may be such features. Other textures indicative for specific genetic environments are skeletal and granophyric textures (Cameron et al., 1949; Simmons, 2007; London, 2008; London and Kontak, 2012). There is some correlation between pegmatite textures and geochemical conditions (London, 2008; London and Kontak, 2012). An example of such a relationship is enrichment of rare elements with granophyric texture.

Quartz and K-feldspar graphic intergrowths result from oversaturation of SiO_2 on a skeletal growth surface of K-feldspar. Such a skeletal surface is caused by rapid growth of K-feldspar relative to the diffusion rate of potassium and aluminium through the melt. Such physical conditions are commonly met in the wall and border zone of zoned pegmatites.

Skeletal branching and radial crystal habits commonly seen in wall and border zones of pegmatites indicate rapid disequilibrium growth. These conditions are caused in these areas by increasing undercooling leading to high levels of oversaturation in specific cation species in the hydrous silicate melt. The high water content reduces the nucleation rate of new crystals but increases the diffusivity of cations. This leads to preferential attachment of cations to fast-growing crystal faces or edges, resulting in skeletal or radial crystal shapes. Such textures are commonly formed by tourmaline, quartz, muscovite or biotite, and less commonly by beryl (London 1992; 2009). It is important to note that a mineral that is able to nucleate may grow extremely quickly, and the distance between the point in the magma where its temperature is

equal to that of the solidus of the crystallising mineral and the site of nucleation determines the size of the mineral (London, 2008; Nabelek et al., 2010).

Layered structures of different grain size in pegmatites vary in size; from limited lateral extent to kilometre-scale along the pegmatite dyke (London, 1992). Aplite layering is suggested to form by a diffusion-controlled process of oscillatory nucleation along the dyke walls in undercooled melt. At the same time, heterogeneous nucleation in hydrous melt may form large crystals occupying the centre of the dyke, resulting in aplitic margins and pegmatitic dyke centres (Webber et al., 1997).

Pegmatites may show rim-core zonations containing different mineral assemblages. This variation is controlled by zones that differ in their fluid/melt ratio under conditions where these two phases have dissociated (London, 2008). Accordingly, eutectic equilibrium crystallisation produces different assemblages simultaneously but in separate parts of the dyke. This is related to variations in the solubilities of alkali metals, Al, and Si between silicate melt and the aqueous vapour. Disequilibrium fractional crystallisation of silicate melt by sequential inward crystallisation from the margins may contribute to compositional variations. Fractional crystallisation has also an impact on mineral textures. The greater tendency for oriented surface nucleation over internal nucleation correlates with the greater degree of disequilibrium between the melt and a crystalline assemblage. With increasing disequilibrium, the habits of individual crystals evolve to more graphic and skeletal shapes (London, 2008).

2.8 PETROGENETIC MODELS

The processes that form structural and lithological variations, such as zonation and layering (sections 2.5, 2.6), are related to two important petrogenetic processes, that will be discussed in more detail in the following. Two genetic models have dominated in the recent literature. These are (i) the *Jahns and Burnham model* (1969), according to which pegmatitic magmas evolve by buoyant separation of an aqueous fluid from a silicate melt, redistributing geochemical components in the system (Cërny, 1991b; London, 2005; Simmons, 2007; Alfonso and Malgarejo, 2008; London and Morgan, 2012; Thomas et al., 2012) and (ii) the *London model*, which describes the magma and dyke evolution by fractional crystallisation of a flux-bearing magma of granitic composition inward from the dyke margins to the centre (London et al., 1988). A third model combines elements of the original Jahns and Burnham and the London models (Morgan and London, 1999; London and Morgan 2012).

Jahns and Burnham (1969) presented a model for the formation and emplacement of pegmatites that has withstood many challenges (London, 2008). It has remained widely accepted but has undergone some modifications. According to Jahns and Burnham (1969), pegmatites crystallize largely *in situ.* Metasomatism of adjacent country rocks may or may not take place. Jahns and Burnham (1969) postulate that there is formation of internal zoning due to fractional crystallisation from the walls inward. Accordingly, their model does not apply to unzoned pegmatites. The fundamental assumption of the Jahns and Burnham model is that a segregated aqueous fluid interacts with magmatic melt in a closed system, causing textures and compositional variations in the pegmatites. In contrast, London‟s (2008) model assumes the fluid to be dissolved in the melt.

The Jahns and Burnham model predicts three stages of pegmatite crystallisation. The first stage involves crystallisation of anhydrous solid phases with phaneritic textures from a hydrous silicate melt. At this stage, crystallisation progresses as temperature decreases, resulting in the silicate melt being enriched in volatiles, especially H_2O. The second stage involves oversaturation of volatiles in the silicate melt and consequently the exsolution of aqueous fluid, followed by crystallisation of fine-grained aplite and sodium-bearing minerals from the silicate melt. At the same time, very large mineral phases precipitate from the coexisting segregated aqueous fluid. At this stage all silicate melt becomes consumed. The third stage involves alteration of solid phases resulting from interaction between the aqueous fluid and solid crystals. This is followed by crystallisation of pocket minerals and late-stage minerals from the aqueous phase. At this stage, fluids might infiltrate the host rock and the pre-existing solid pegmatite, leading to metasomatic alteration (Jahns and Burnham, 1969; Jahns, 1982, Burnham and Nekvasil, 1986). Incompatible elements from the lower parts of the parent plutonic magma remain in the melt and are transported upwards, fractionating increasingly into the aqueous fluid. Rare minerals, such as petalite, columbite and lepidolite precipitate from these enriched fluids.

The **London model** considers alkali and sodic feldspars, quartz and minor muscovite or biotite in a granitic system to be the first minerals to crystallize in the parent granite. These minerals incorporate the bulk of Si, Al, K, Na, O and some of the H_2O contained in the parent magma. This process results in incompatible elements, such as Cl, Li, Cs, Be, P, to become enriched in the residual melt from which pegmatitic magma may form. Pegmatitic melt is also rich in Si, K, Na, and Rb that is not incorporated in solids in the parent granite. This also applies to H_2O, because at the crystallisation temperature of the plutonic magma only few hydrous phases are stable.

The leading factor for a pegmatite to crystallise then is an increase in volatiles and fluxing components such as H_2O, F, B and P, which lower the viscosity, melting and crystallisation temperatures (London et al., 1988; London, 1990; 1992; 1997; London and Morgan, 2012). Low viscosity and low melting temperatures will enhance miscibility among otherwise less soluble constituents (Sowerby and Keppler, 2002). Meanwhile, the melt is also enriched in rare earth elements (Cameron et al., 1949; Simmons, 2007), which are not well compatible with common phases in the parent granite. Swanson and Fenn (1992) observed that flux components lower the viscosity of the melt, which promotes rapid growth and large crystals in pegmatites. Fluxes also increase the solubility of water in the melt. Furthermore, the fluxes drive the melt toward a more alkaline composition (London, 2008). From the H_2O supersaturated pegmatite, fluids may infiltrate the host rock forming metasomatic halos.

Experimental work and simulations of the thermal environment in which pegmatites may form, carried out by London et al. (1989) and London (2008), support that the undercooling of pegmatitic melt significantly below the liquidus leading to a zonation of mineral assemblages similar to that observed in natural pegmatites (section 2.6). This confirms findings on pressure and temperature of crystallisation that revealed that the temperatures recorded by mineral assemblages, fluid inclusions, and calibrated solid solutions, commonly point to temperatures of pegmatite crystallisation well below the solidus temperatures of hydrous granitic melts, which are in the range of 650 ^{o}C – 700 ^{o}C. The studies pointed to crystallisation temperatures of flux-rich pegmatites ranging between 350 ^{o}C - 630 ^{o}C (London, 1990; 1992; 1997; London and Morgan, 2012, Cërny et al., 2012) and that silicate melt may persist at temperatures as low as 262 ^{o}C (London, 2005).

The **Morgan and London (1999) model** attempts to explain the genesis of pegmatites using some aspects of both the Jahns and Burnham model and the London model. It proposes the formation of a flux-enriched boundary layer of silicate liquid adjacent to the crystal-melt interface. When during pegmatite crystallisation a particular flux, such as B, is removed from the melt as it becomes incorporated in a crystallising phase, the solidus temperature of the remaining melt increases accordingly. This increases the degree of undercooling and promotes rapid crystal growth (Simmons, 2007; Nabelek et al., 2010). Additionally, the melt becomes supersaturated in incompatible elements, and perhaps in such flux element species that are not extracted into solids. When the nuclei and crystals eventually form, a boundary layer enriched in elements that are not contained in the growing phase is generated by rapid crystallisation from the undercooled

melt (Morgan and London, 1999; Simmons, 2007; London 2008; Nabelek et al., 2010). This may inhibit or slow down further crystallisation.

As crystallisation progresses, **Constitutional Zone-Refining** (CZR) occurs, in which the boundary layer changes in volume to become further enriched in fluxes and trace elements in relation to the bulk melt composition (London, 2008, 2014). Incompatible elements in the melt of the boundary layer form complexes with fluxes, reducing the viscosity in this layer, hence increasing the purity, homogeneity and size of the crystallising phase due to transfer of more solute mass per unit volume of fluid necessary for large silicate crystal growth (Morgan and London, 1999; London, 2005; London 2008, London and Morgan, 2012). In the outer pegmatite zone undercooling is more intense, which leads to more intense temporary crystal growth inhibition. This results in anisotropic fabrics, graphic textures and fine-grained alkali feldspars, quartz and accessory minerals. However, in the inner zones, undercooling is less intense and all crystal faces can develop producing progressively coarse-grained and blocky inner zones, such as the albite-lepidolite zone and the quartz core, due to flux concentration that in return reduces the nucleation rate (London, 2009; London and Morgan, 2012; London, 2014).

Various studies (Thomas et al., 2006; 2009; 2011; 2012; Thomas and Davidson, 2012) challenge the three models described in this section. These studies propose the presence of two immiscible pegmatitic melts in pegmatites, one of which is peraluminous and the other is peralkaline. This segregation of melts is caused by local variations in the dissolved H_2O content, fluxes, and the heterogeneous distribution of melt modifiers, such as Ca^{2+} and Na^{+}. Depending on their physical and chemical characteristics these melts might interact to some variable extent, and accordingly will produce compositional and textural variations in different zones, layers or domains within the pegmatite. In consequence, Thomas et al. (2012) and Thomas and Davidson (2012) argue that compared to the effects of melt-melt immiscibility, the importance of the solidus boundary layer, the CZR processes, and the role of liquidus undercooling as major petrogenetic processes are overestimated.

3. REGIONAL GEOLOGY AND BRIEF GEOLOGY OF MALAWI

3.1 UBENDIAN BELT - GEOLOGICAL SETTING

The Palaeoproterozoic Ubendian Belt of East and Central Africa trends NW-SE for over 600 km from eastern Congo (DRC) via south-western Tanzania to northern Malawi (Figure 3.1). The Ubendian Belt is up to 600 km long and 200 km wide and separates the Archean Congo and Tanzania cratons to its north from mainly Mesoproterozoic belts (Kibaran, Irumide) in the south, including northern Malawi (Muhongo et al., 2002). The Ubendian orogeny involved terrane accretion that was followed by NE directed collision between Congo and Tanzania Craton. The Irumide Belt is described further in section 3.2. In the north, the Ubendian is overlain unconformably by Mesoproterozoic rocks of the Kibaran Supergroup and by the Neoproterozoic rocks of Bukoban Supergroup of western Tanzania. The Ubendian Belt then merges with the NE-SW trending Palaeoproterozoic Usagaran Belt (Lenoir et al, 1994a; GEUS, 1999; Figure 3.1). Further east, the Palaeoproterozoic Ubendian/Usagaran Belts are cut off by the Pan-African Mozambique Belt.

The commonly intensely deformed metamorphic rocks of the Ubendian are of sedimentary and igneous origin, and the metamorphism took place in the amphibolite to granulite facies. The Ubendian Belt is subdivided into blocks and units (Figure 3.2) according to rock type and metamorphic grade, and on the basis of lithological and structural features. It has distinct structural terranes trending NW – SE, separated by long deep-seated ductile shear zones with dextral strike–slip displacement that suggests a single evolution pattern for all the terranes (Sutton et al., 1954). Of the eight Ubendian lithotectonic terranes (UNESCO, 1983; Daly et al., 1985), three are significant to the current study. One is Katuma (Mbozi) terrane (Figure 3.2), dominated by gneiss, migmatites, quartzites, and in places granulite and metabasite. Linear fabric elements trend commonly NW-SW. The second is Ufipa terrane, dominated by granitic gneiss, with NE-SW trending fabrics. The third, the Nyika terrane, is dominated by cordierite-bearing granulites. The main fabrics trend E-W (Daly 1988; Figure 3.2).

Overall, the Ubendian Belt and its various sub-units have NW and NNW-trending fabrics associated with amphibolite facies metamorphic rocks (Figure 3.2). Accordingly, the Mbozi and Nyika terrains‟ NE–SW, E–W fabrics are at high angle to the general NW–SE terrane trends (UNESCO, 1983; Daly, 1988). Abundant mylonites along the contact zones separate differently trending terranes. This implies that the structural history recorded within the different blocks or terranes predates their arrangement as a coherent NW-SE trending belt. Furthermore, the

stretching lineation in the interior of the Ufipa terrane, present in amphibolite facies rocks, is related to dextral strike – slip displacement. In terrane boundaries, retrograded amphibolite facies rocks show greenschist facies mylonites with sinistral strike – slip movement, which may be associated with the juxtaposition of the various terranes in the Ubendian Belt (Boven et al., 1999).

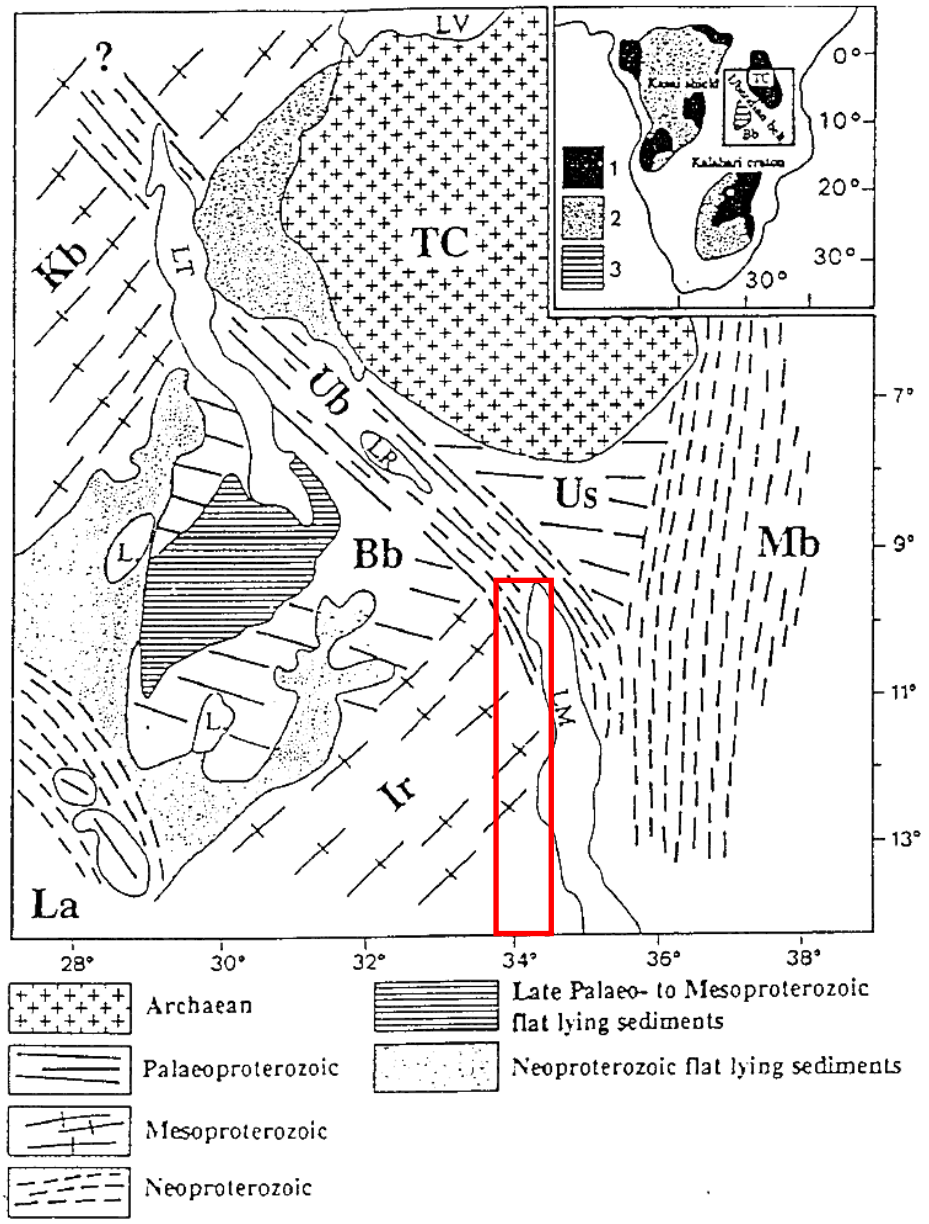

Figure 3.1: Major Precambrian geotectonic units and structural trends in eastern and central Africa (modified after Cahen and Snelling 1966; Andersen and Unrug, 1984). TC = Archean Tanzania Craton, UB = Ubendian Belt, US = Usagaran Belt, Bb = Bangweulu Block, Kb, Kibaran Belt, Ir = Irumide Belt, MB = Mozambique Belt, LA = Lufilian Arc., LT = Lake Tanganyika, LV = Lake Victoria, LR = Lake Rukwa, LM = Lake Malawi, L = other lakes, In the insert shows main cratonic areas; 1 = Archean; 2 = Stable since 1750 Ma including possible hidden Archean; 3 = Bangweulu block, stable since 1750 Ma but post-Archean (modified after Lenoir et al., 1994).The study area in Malawi is outlined in red (its southern part is not covered on the map).

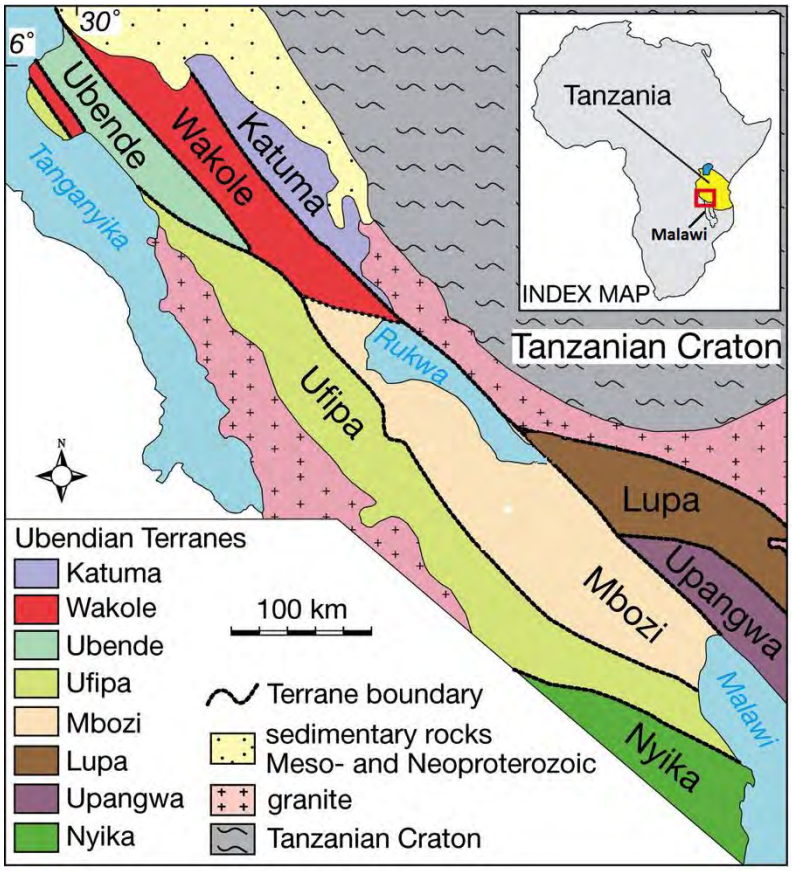

Figure 3.2: Sketch map of the Ubendian terranes in western Tanzania and northern Malawi as indicated in the insert index map. Samples for the current study were taken in the Nyika and Ufipa terranes (modified after Daly, 1988).

Boven et al. (1999) determined peak P–T conditions in Ubendian rocks of about 720 ^{o}C and 17 kb for an eclogite, indicating subduction-related metamorphism. However, metapelitic blastomylonites in shear zones show lower P – T conditions of 5 – 10 kb and 550–600 ^{o}C (Boven et al., 1999). This has been interpreted as an indication of intense retrogression of the exhumed Ubendian rocks within the shear zones (GEUS, 1999).

Intrusive rocks, or their metamorphic equivalents, in the Ubendian Belt include eclogites amphibolites, peridotites, gabbro-norites, carbonatites and granites. However, granites are dominant. In the southern part of the Ubendian Belt, late Palaeoproterozoic granites intrude volcanic rocks that overlie Ubendian gneisses (UNESCO, 1983). Neoproterozoic granites and syenites are found in ductile-brittle shear zones in this part of the belt (Theunissen et al., 1992; Lenoir et al., 1994). Pegmatites post-date all kinematic and metamorphic events related to the Palaeoproterozoic orogenic events. This particularly applies to the samples taken for this study.

Currently, the Palaeoproterozoic Ubendian Belt is regarded as a product of the collision between the Archean Tanzania and Congo cratons (Lenoir et al., 1994; Boven et al., 1999) that took place

at about 2100 – 2025 Ma (Lenoir et al., 1994) and formed the E-W trending granulites and eclogites (GEUS, 1999). The lithotectonic blocks or terranes making the Ubendian Belt were accreted or juxtaposed adjacent to the Archean Tanzania Craton about 200 m.y. later, at about 1860 Ma (Lenoir et al., 1994), resulting in the development of the persistent penetrative NW – trending shear fabrics that characterise the tectonic trend of the Ubendian (Figure 3.2). The final tectonic event of the Ubendian Orogeny occurred at 1840 Ma (Kazimoto et al., 2015). The formation of the Karoo extensional faults and the associated sediments, and the Cenozoic western arm of the East African Rift reactivated late Palaeoproterozoic NW-SE shear zones and accordingly the younger fault zones follow inherited structural trends (GEUS, 1999).

In the Ubendian Belt, abundant pegmatites of different types occur in synorogenic granites, migmatites and in metamorphic rocks. As economically relevant commodities they contain mica (muscovite), beryl, green tourmaline, emerald, feldspar (GEUS, 1999), monazite-columbite-tantalite, Ta (-Nb-Sn) (Melcher et al., 2015), allanite, uraninite, phlogopite and vermiculite. For this study, pegmatites from the Ubendian Belt containing gem-quality tourmaline and beryl were collected and analysed.

3.2 IRUMIDE BELT - GEOLOGICAL SETTING

3.2.1 Irumide Belt s.s.

The Irumide Belt is regarded as a NE-SW trending 350 km wide foreland fold and thrust belt (Figure 3.3) that formed as a result of NW-SE-directed crustal shortening (Petters, 1991). The Irumide Belt extends from the Choma-Kalomo Block of southern Zambia, where it is cut by the Zambezi Belt, to the Zambia – Tanzania – Malawi border in the northeast. Here it terminates against northwest trending shear zones (Lenoir et al., 1994; Daly, 1986; Theunissen et al., 1996; Klerk et al., 1998). Katanga Supergroup unconformably overlies Muva Supergroup that was deposited c. 1880 Ma in the northwest of the belt (Daly and Unrug, 1982; De Waele and Fitzsimons, 2004). The Katanga Supergroup is commonly in-folded and even imbricated with the underlying Muva basement sequences that consist mostly of granitic gneisses and migmatites. The extensive folding and shearing of the basement and Muva Supergroup rocks in central and eastern Zambia occurred from 1350 Ma to 1100 Ma, largely synchronous with the Kibaran Orogeny. The contact between the Muva Supergroup and the pre-Muva basement is tectonised.

Granitoid magmatism in the Irumide Belt occurred in two episodes, the first ranging from late Palaeoproterozoic to early Mesoproterozoic, and the second from late Mesoproterozoic to early

Neoproterozoic. The older granites were emplaced between 1660 to 1550 Ma (De Waele et al., 2003a). The younger episode is represented by, for example, the Choma-Kalomo Block granite, emplaced between 1345 and 1200 Ma (Figure 3.3) east of the Luangwa Valley. Charnockitic granites were emplaced in the basement below the Muva Supergroup at about 1100 Ma (De Waele et al., 2003a). The granitoids have bulk-rock geochemical signatures and highly negative $E_{Nd}(t)$ values suggesting that they formed by recycling of older continental crust (De Waele et al., 2003a).

The Irumide Belt contains prominent faults with a NE trending set that is offset by an NW trending set. However, minor faults trend north and east in some areas. Fold interference patterns and local fracture cleavage formed contemporaneous with the northwest trending faults (Harding, 1982). In general, the Irumide Belt displays north-westerly trending folds and lineations. The tectonic vergence resulted from the Irumide deformation events that took place from 1350 – 1100 Ma, where by the Mesoproterozoic metamorphic rocks were thrusted onto Palaeoproterozoic rocks of the Bangweulu Block (Johns et al., 1989). Away from the thrust zone, the Palaeoproterozoic basement was unaffected by the Mesoproterozoic tectonics. According to Mapani (1999), polyphase deformation in the belt was coeval with formation of the sub-assemblages cordierite-andalusite and sillimanite-K-feldspar in metapelite. This indicates that the prevailing metamorphic conditions in the Mesoproterozoic were relatively low-pressure-high-temperature. Moreover, the metamorphic grade changes from place to place across strike within the belt.

In Lundazi and Nyimba areas in Eastern Zambia, intrusive suites include gabbros, enderbites, charnockites, granites and pegmatites (Hickman, 1975). The pegmatites intruded into gneisses, schists and granulites. However, some igneous rocks underwent folding and developed foliation concordant with their metamorphic host rocks. Such metagranites commonly are exposed in antiformal structures. A series of micro-granites outcrop parallel to north-east trending anticlinal axial traces (Hickman, 1975). There was syntectonic emplacement of the granites and granitic pegmatites with the formation of Lukusuzi antiform trending NNE (Hickman, 1975, John et al., 1989). Late pegmatites in the Lundazi area however are ~485 Ma (Thatcher, 1974) and hence are not related to the formation of the Irumide belt.

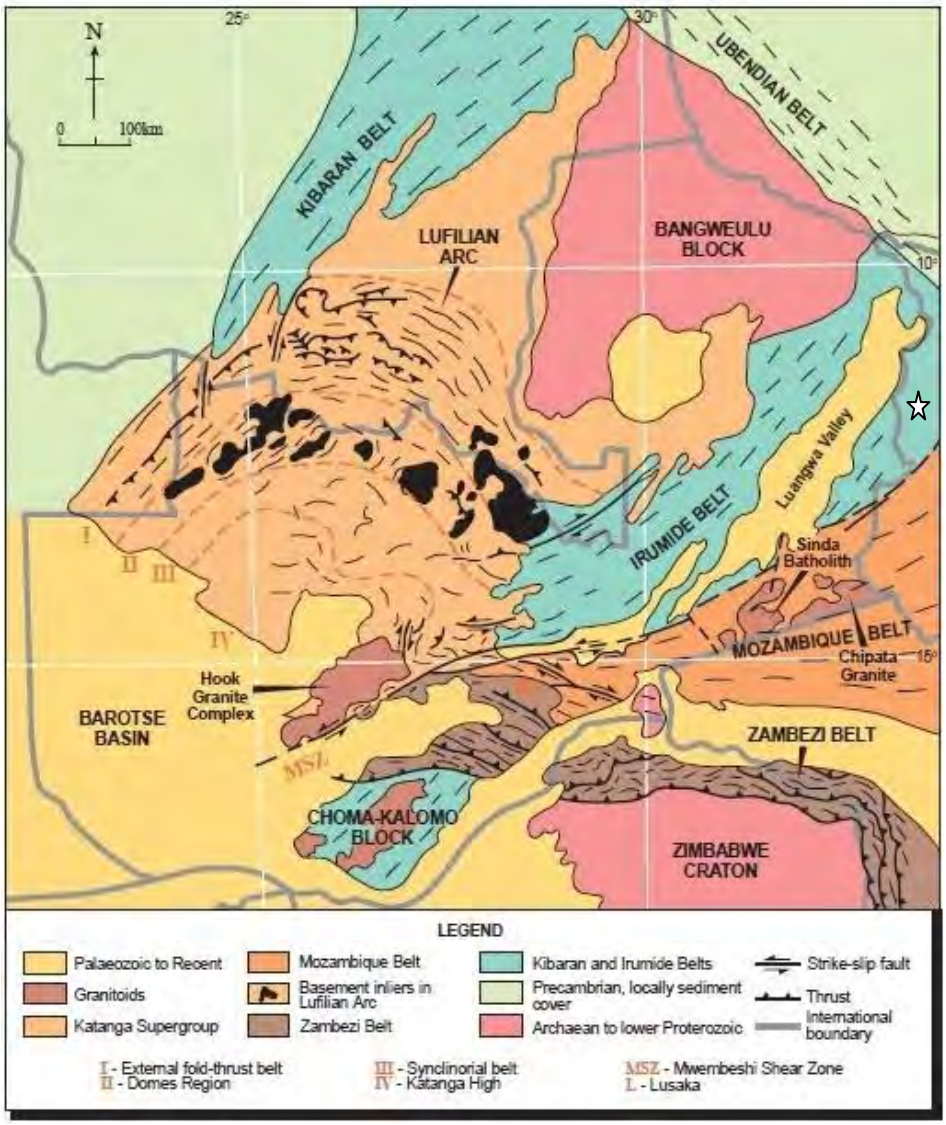

Figure 3.3: Tectonic Map of Zambia (modified after Porada, 1989). The study area in Malawi is located to the eastern part Luangwa Valley, on the map represented by a star symbol.

3.2.2 Southern Irumide Belt- Tete Chipata Belt

The Southern Irumide Belt (Johnson et al., 2005), also referred to as the Tete Chipata Belt (Westerhof et al., 2008) in SE Zambia and Mozambique, consists of Mesoproterozoic basement that has been extensively reworked under upper-amphibolite facies conditions during the Pan-African orogeny. Such a reworking is insignificant or absent in the Irumide Belt *s. str.* (Figure 3.3). This Southern Irumide Belt (Figure 3.4) matters to this study because this region covers an area in Central Malawi where DHD pegmatite samples were collected from, even though locally the area is known to belong to the Mozambique Belt.

The Southern Irumide Belt is composed of a series of distinct terranes of various ages and tectonic settings. The terranes include the Luangwa, Nyimba, Petauke-Sinda, the Chipata,

Chiwore-Rufunsu, the Fingoe and the Luia Terranes. The Luangwa Terrane contains polydeformed metasediments and dioritic gneisses; the Nyimba Terrane is marble- and calc-silicate-dominated; the Petauke-Sinda Terrane contains calc-alkaline plutonic rocks whereas the Chipata Terrane shows retrogressed mafic and felsic granulites of supracrustal origin (Mapani et al., 2004). Furthermore, the Chewore-Rufunsu Terrane has supracrustal to mid-crustal rocks (Johnson et al., 2006b, 2007). The Fingoe Terrane contains volcano-sedimentary rocks and granitoids, and the Luia Terrane shows partly retrogressed granulites and gneisses, and it is intruded by a bimodal igneous suite composed of charnockites and gabbro-anorthosites (Westerhof et al., 2008).

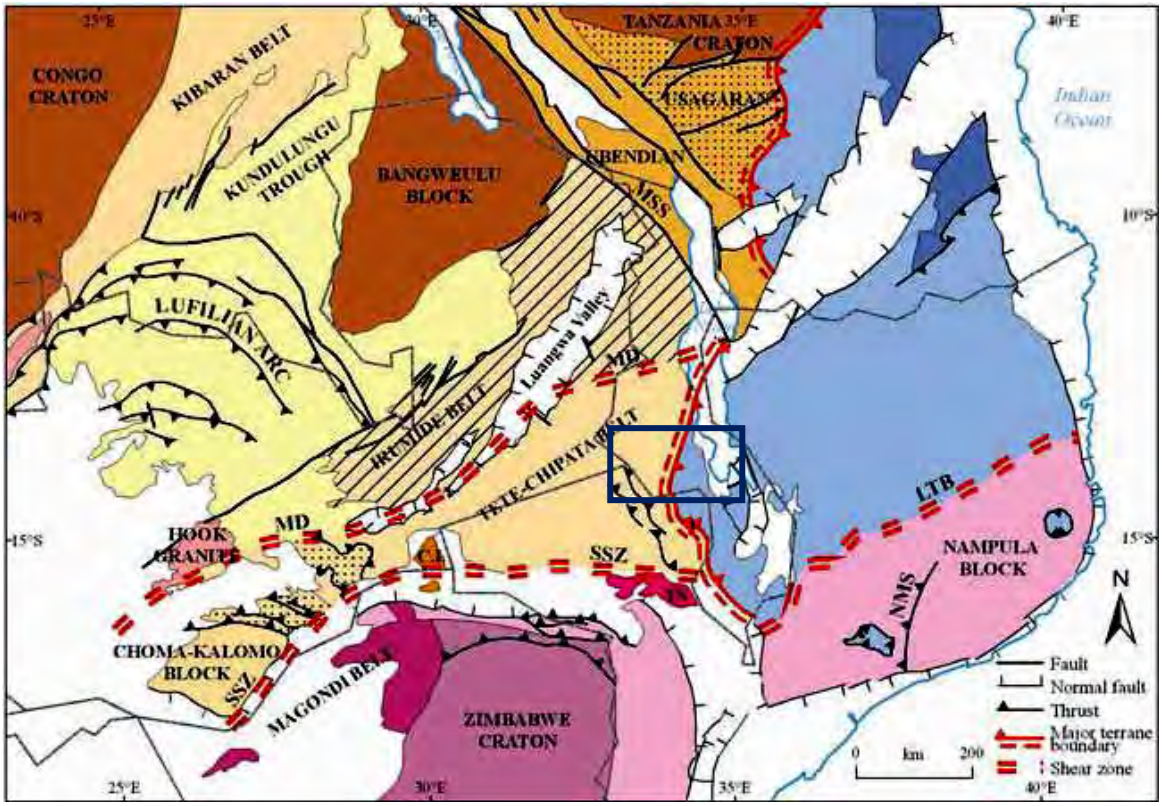

Figure 3.4: Simplified geological map of the Tete-Chipata Belt and the Zambezi-Lufilian segment of the Damara-Lufilian –Zambezi Belt (modified afterVrana et al., 2004). Key: MSS = Mughesse Shear Zone, MD = Mwembeshi Dislocations, SSZ = Sanagoe Shear Zone, CI = Chewore Inliers, TS = Tete Suite, NMS = Nanama Megashear, LTB = Lurio Thrust Belt. The dotted section in the southwestern part of the Tete-Chipata-Belt corresponds to Neoproterozoic (post-Rodinia, early Pan-African) metasediments (mainly pelites and carbonates) with minor metavolcanics, tectonically overyling Mesoproterozoic Mpande Gneiss (Westerhof et al., 2008). The light blue colour represents Mozambique Belt. Some samples for this study were collected from an area represented by the inserted blue rectangle, expanded in Figure 3.5.

During the Meso- to Neoproterozoic Mozambique cycle between 1100 - 850 Ma a large layered gabbro-anorthosite massif near Tete formed at 1025±79 Ma (Evans et al., 1999). Single zircon

magmatic emplacement ages range between ~1046 and 1004 Ma for granitic gneisses and charnockites north of Tete and at Lake Cabora Bassa (Kröner et al., 2000b; Kröner, 2001).

Intrusive granitic suites of Pan-African age, which could be coeval with pegmatites investigated in the current study, are located in an area outlined in Figure 3.4. According to early literature, Cahen and Snelling (1966), the Mozambique cycle gives Pan-African K-Ar or Rb-Sr cooling ages of ~650 to 490 Ma. However, low volume post-tectonic magmatism occurred between 510-470 Ma in the Tete-Chipata Belt (Johnson et al., 2005; De Waele et al., 2008). Located to the western part of the study area, one of the intrusive suites is the syn- to post-tectonic Sinda granite near Petauke, dated at 489±42 Ma (Haslam et al., 1986), intrusive into gneisses and earlier granites (Figure 3.5). The Sinda granite is similar in geological setting to the Lake Malawi Granitic Province, a suite of late- and post-tectonic granites outcropping around the southern half of Lake Malawi (Haslam et al., 1986). The Cape Maclear granite was emplaced at 443±30 Ma, the Cape Maclear syenite at 449±42 Ma and the Senga Bay granite at 489±14 Ma (Haslam et al., 1983). The Sinda granite has an initial $^{87}Sr/^{86}Sr$ ratio of 0.7101 ± 0.0008, and a MSWD 15.3 (Haslam et al., 1986). The Sr initial suggests an origin of magma from moderately evolved crustal rocks. However, the initial Sr isotope ratio is rather higher in the Sinda granite than in the Lake Malawi Granite Province (Haslam et al., 1986).

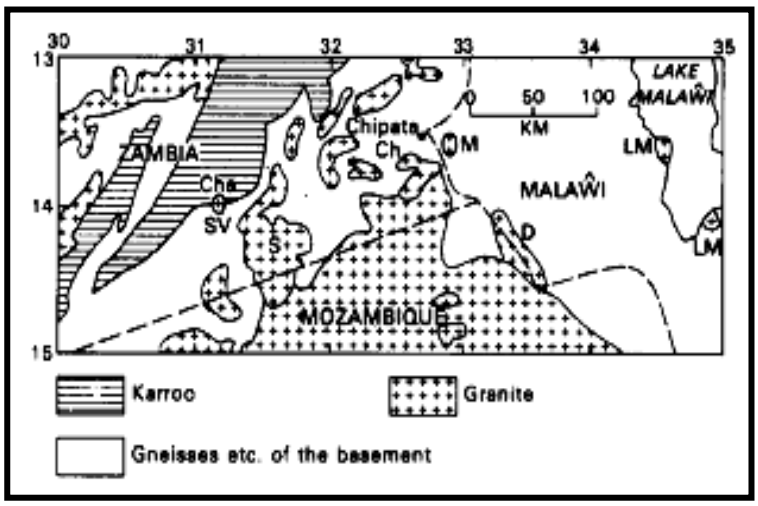

Figure 3.5: Simplified geological map of south-eastern Zambia and parts of Malawi and Mozambique. The position of this map is shown in Figure 3.4. Cha = Chapalapata granite, Ch = Chipata granite, D = Dzalanyama granite, LM = granites of Lake Malawi Granitic Province, M = Mchinji hypersthene granite, S = Sinda batholiths, SV = area of Sesare volcanic (taken from Haslam et al., 1986).

Pegmatite-related gemstone deposits bearing gemstones such as tourmaline, beryl and sapphire occur in both the Irumide Belt s.s. and the Southern Irumides / Tete-Chipata Belt, indicating the economic potential of the belt as a whole (Zgambo, 1995). These pegmatite-related gemstone

deposits can be generally subdivided into three broad groups. (i) Pegmatitic gemstones that crystallise together with the main pegmatitic phases from melts or fluids; (ii) metasomatic gemstones that crystallise within the contact zone between a pegmatite and a host mafic rock; and (iii) those that crystallise in miarolitic cavities from late-pegmatitic fluids (Simmons et al., 2012). All three groups exist in the Irumide Belt. Remarkably, the dated pegmatite occurrences in the Irumide s.s. and Tete Chipata Belt within Malawi appear to be all of Pan-African age.

An example of gem-bearing pegmatite occurrence is in Lundazi and Nyimba areas in eastern Zambia, the pegmatites are widespread (Harding, 1982; Patney, 1988; Zgambo, 1995). Some pegmatites bear gem quality aquamarine. These pegmatites have complex mineralogy, cavities, rare minerals, and are compositionally zoned (Nash, 1962). The most abundant minerals are quartz, muscovite and alkali feldspar with accessory tourmaline, beryl, apatite, chrysoberyl, cassiterite, topaz, citrin, amethyst and spessartine (Gallagher, 1959). Beryl is mostly associated with the inner pegmatite zone, particularly that adjacent to the quartz core.

3.3 PAN-AFRICAN BELTS

Pan-African belts in East Africa developed in a series of orogenic cycles over a long time period (950-450 Ma) with diverse orogenic styles, ranging from major continental collision events through the closure of small oceanic tracts to major accretionary belts of consisting of island arcs and micro-continents (Lenoir et al., 1994; Daly, 1986; Shackleton, 1996; Muhongo, 1999; Foster et al., 2001; Grantham et al., 2013). The Pan-African Orogeny reactivated pre-existing structures such as the transcurrent belt of the Mugesse Shear Zone in northern Malawi (Appel et al., 1998). Pan-African granitoid intrusions occurred between 710 and 550 Ma whereas thermal peak of Pan-African granulite metamorphism has been dated at 571-549 Ma (Kröner et al., 2001).

However, south of Lichinga in Mozambique, predominant Pan-African metamorphic ages vary between 569±9 and 527±8 Ma (Bingen et al., 2009). The high-grade metamorphic peak in that region has been dated at 550-575 Ma (Kröner et al., 1997). However, deformation and prograde and retrograde metamorphism occurred between 700 and 350 Ma, overprinting high-grade rocks associated with the major orogenic events (Ring et al., 2002; Sommer et al., 2003).

In southern Africa, the Pan-African belt system includes from east to west the Mozambique Belt, the Malawi Mosaic, the Lurio Belt, Lufilian Arc, and Zambezi Belt in Zambia and Zimbabwe, and the Damara Belt in Namibia and Botswana (Foster et al., 2001; Goscombe and Gray, 2003). In the Zambezi Belt in north-eastern Zimbabwe, the Meso- to Neoproterozoic Lomagundi and

Piriwiri Groups are unconformably overlain by the Makuti Group that formed at 825±55 Ma, which is correlated across the Zambezi River with the Katanga Supergroup (Broderick, 1976). The sequence in the Makuti Group metamorphosed during the Katangan episode and the metamorphic grade increases south-westwards from greenschist to granulite facies. These continental belts appear to constitute inland branches of the Mozambique Belt, following the east coast of Africa, and the West Congo-Gariep-Malmesbury Belt on the west and south coast (Hunter, 1981). Key events of the Pan-African Orogeny are summarised in Table 3.1.

Table 3.1: Key events of the Pan-African Orogeny (taken from Foster et al., 2001).

AGE	KEY EVENT
870 m.y.	Rifting leading to passive margin development, ophiolites occur within the northern part of the belt and were emplaced during early phases of deformation.
820-830 m.y.	Commencement of contractional tectonism in the north-central sector of the Mozambique Belt (Kenya to Tanzania).
750-650 m.y.	Collisional orogenesis
715-645 m.y.	Granulite-facies metamorphism
640-550 m.y.	Major transpression resulting in further crustal shortening and lateral tectonic escape during the final stages of continent-continent collision
538 m.y.	Possible thrust-emplacement of Neoproterozoic sedimentary rocks in northern Mozambique and Tanzania
500 m.y.	Scattered post-kinematic plutonism

3.3.1 Mozambique Belt (East Africa Orogen), Kuunga Orogen and Lurio Belt

Of particular interest for the current study is the Mozambique Belt, also known as East Africa Orogen, forming an N-S trending polycyclic Neoproterozoic belt that is widely regarded as the major tectonic boundary between East and West Gondwana (Shackleton, 1994; Wilson et al., 1997; Kröner et al., 2001; Encyclopaedia of Geology 2004; Jacobs et al., 2006). Two models regarding the formation of Gondwana are relevant in this discussion. Firstly, the East African Orogen, formed during the collision of the India, Madagascar, Sri Lanka, the East Antarctic Craton and Kalahari Craton with the Congo Craton and Arabian Nubian Shield. This took place between 800-650 Ma (Meert and van der Voo, 1997). The East African Orogen stretches from the Arabian Peninsula through trough East Africa and Madagascar into the East Antarctic Craton (inset in Figure 3.7; Stern, 1994). Secondly, a later the Kuunga Orogen, which trends east-west along the boundary of the Congo-Tanzania and Kalahari Cratons, through southern Malawi and neighbouring Mozambique, into the northern part of the East Antarctic Craton. The Kuunga

Orogen formed during the collision between South Gondwana (i.e., the Kalahari Craton, Australia and Antarctica) with North Gondwana at ~580-530 Ma (Meert and van der Voo, 1997; Möller et al., 2000; Meert, 2003; Grantham et al., 2013). The Kuunga Orogeny was associated with granulite facies metamorphism in East Gondwana (Meert and van der Voo, 1997). The final assembly of Gondwana occurred at 550 Ma (Meert et al., 1995; Appel et al., 1998; Grantham et al., 2008, 2013).

Characteristic for the Mozambique Belt / East African Orogen is the medium- to high-grade metamorphism that took place over a longer time period between ~700 and 600 Ma (Foster et al., 2001). The geological record includes a cycle of events from subsidence with deposition, uplift, folding, metamorphism and plutonism (Pinna, 1995) with major thermotectonic events in Mesoproterozoic and in Pan-African times (Stern, 1994; Wilson et al., 1997). Hence, the Pan-African event is the last stage of a polyphase evolution, which results in complex geological patterns within the Mozambique Belt.

Generally, the main Neoproterozoic collision-related tectono-thermal event in greater part of Mozambique Belt occurred at ~630 Ma. In Tanzania, the Pan-African metamorphism of the Mozambique Belt is variable with segments that show amphibolite to greenschist facies metamorphism, granulite facies metamorphism, amphibolites facies metamorphism, pyroxene granulites, and almandine-amphibolite facies metamorphism. The belt is dominated by foliated hornblende-biotite-gneisses, pyroxene granulites and migmatites. According to Kröner (2001), the peak metamorphism occurred at ~620 Ma in the southern part and at ~620 – 640 Ma in the northeast and east. The Pan-African granulites show an anticlockwise P-T evolution reaching the thermal peak at 820 °C and 13.2 kb followed by the pressure peak at 700 °C and 8 kb (Appel et al., 1998; Muhongo et al., 1999; Sommer et al., 2003). Nd and Pb isotope systematics suggest derivation of many of the Pan-African rocks from juvenile material (Möller et al., 2000; Maboko and Nakamura, 2001), recognised as deformed granitoids with enfolded schists, quartzites, marbles and amphibolites (Pinna, 1995). The granites and pegmatites in the Mozambique Belt are usually post-kinematic (Foster et al., 2001).

Generally, in East Africa, the Mozambique Belt represents subduction that might have caused the thermal resetting of the Irumide-Kibaran-Lurian sequences of areas of Zambia, Malawi and Mozambique (Shackleton, 1987). However, the tectonic and metamorphic patterns along the several thousand kilometres of the belt along strike are unlikely to have followed a uniform

evolution. A summary of simplified event sequences for the Pan-African Mozambique Belt in Tanzania is presented in Figure 3.6.

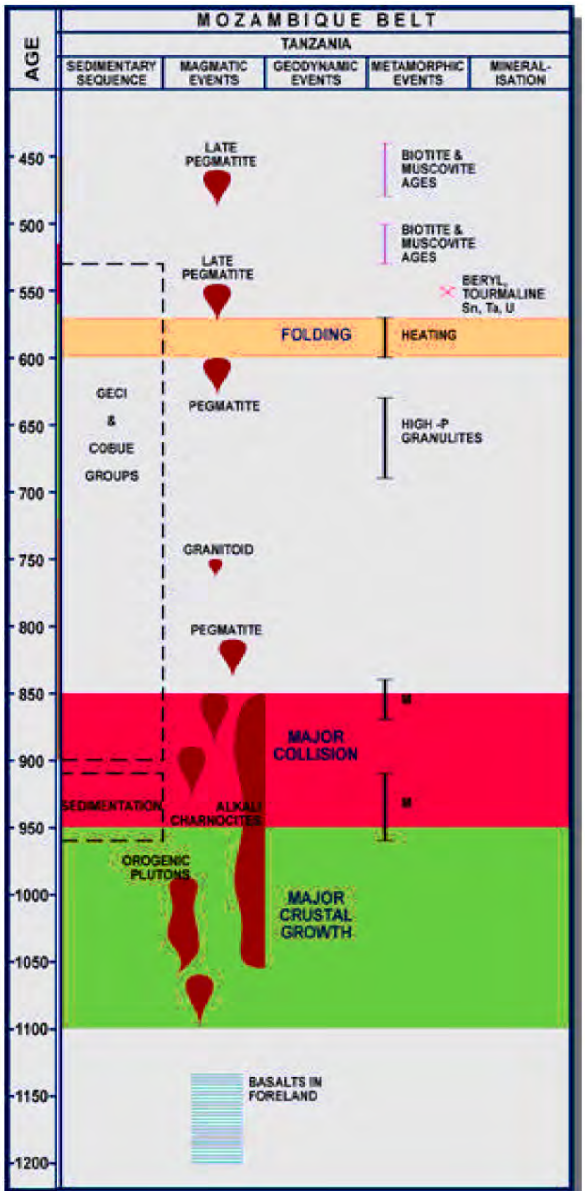

Figure 3.6: An example of simplified event sequences for the Pan-African Mozambique Belt in Tanzania (modified from Foster et al., 2001).

In NE Zimbabwe, the ENE trending Lurio Belt may have formed by collision of the Lurio Craton and the Niassa Craton (Andreoli, 1990). An island arc that now forms part of the Lurio Belt in south Malawi is part of this collision zone. In this zone Neoproterozoic mafic granulites of the Ocua Complex are associated with a melange of rocks of unknown protolith age (Bingen et al., 2009).

The tectonically-bounded Mesoproterozoic terranes of Unango, Marrupa, Nampula, Ocua and Xixano Complexes, all of which form part of the Pan-African basement in Mozambique, were accreted and juxtaposed during the polyphase Pan-African collision in Neoproterozoic to

Cambrian time (Bingen et al., 2009; Grantham et al., 2008, 2013). The Mesoproterozoic basement of the Unango and Marrupa Complexes show Kuungan high-grade metamorphism at ~550 Ma representing peak crustal thickening during Kuungan Orogeny in NE Mozambique (Fritz et al., 2013). The amalgamation of the tectonically-bounded Mesoproterozoic terranes was followed by the intrusion of late- to post tectonic K-granites between 530 and 495 Ma (Macey et al., 2007, 2010; Jacobs et al., 2008a; Ueda et al., 2012; Grantham et al., 2013; Figure 3.7). However, late magmatism occurred between 750 Ma and 800 Ma in the Unango and Marrupa Complexes (Bingen et al., 2009) whereas post-tectonic magmatism occurred in Unango Complex between 550-480 Ma (Bingen et al 2009).

Protolith ages and ages for the metamorphic overprints of the various blocks in the Mozambique Pan-African belts are under debate. Earlier geochronological studies in the blocks within the belt proposed Kibaran high-grade metamorphism (Sacchi et al., 1984; Pinna et al., 1993). However, a combined SHRIMP and evaporation age of a 614±6 Ma metamorphic zircon indicated Pan-African high-temperature metamorphism (Kröner et al., 1996; Jamal et al., 1999; Kröner, 2001).

The Nampula Block in southern part of Mozambique Belt forms a large part of the Pan-African basement in central Mozambique and extends to the south Malawi border (Figure 3.7). It consists of 1150-1070 Ma orthogneisses and metasedimentary rocks with high-grade metamorphism around 1090-1070 Ma (Macey et al., 2010; Macey et al., 2013). The Namuno Block (Grantham et al., 2008) in northern Mozambique consists of similar latest Mesoproterozoic to early Neo Proterozoic crustal gneisses with protolith ages of 1060-940 Ma (Bingen et al., 2009; Grantham et al., 2013). The youngest ages may date the metamorphic overprint. The Meso- to early Neoproterozoic basement rocks are tectonically intercalated with slices of high grade metamorphic mafic rocks (Viola et al., 2008; Bingen et al., 2009) that show high-grade metamorphism and deformation dated at 615-540 Ma. At this time or later, contractional tectonics formed a stack of west-verging Pan-African and Mesoproterozoic nappe slices.

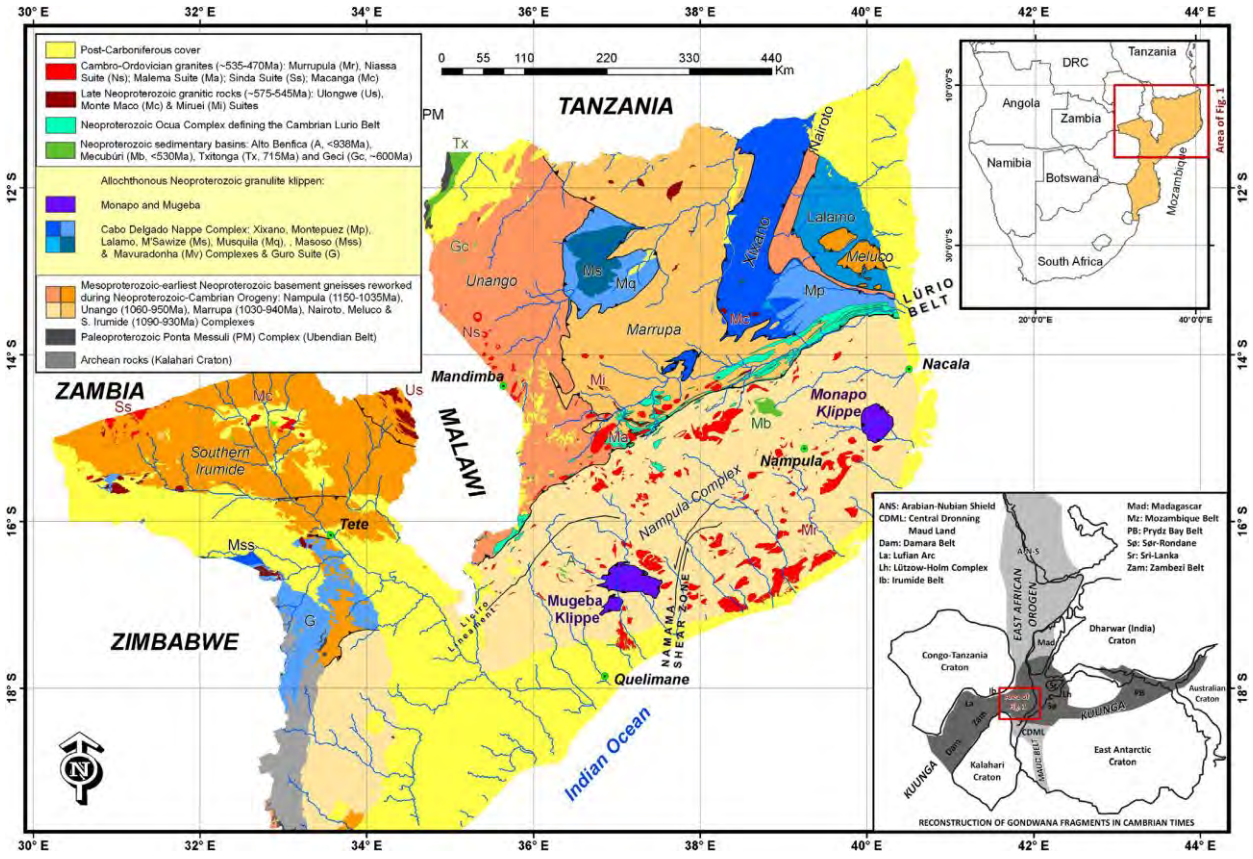

Figure 3.7: Geological map of NE Mozambique with insets showing geographical and orogenic contexts in East Africa and Gondwana, taken from Macey et al. (2013). These maps are based on previous literature (Meert, 2003; Norconsult, 2007a, b; Macey et al., 2007; Grantham et al., 2007).

The igneous activity in the Lurio-Nampula Belts in Mozambique and in southern Malawi is documented by late-Mesoproterozoic calc-alkaline granitoids and granitoid gneisses (Pinna et al., 1993; Kröner et al. 1997, 2001; Jamal et al., 1999; Jamal & De Wit, 2004). The granitoids have emplacement ages between ~1148 and ~1009 Ma. No inherited Archean or Palaeoproterozoic zircons are reported, but they show both positive and mildly negative εNd(t) values, which has been interpreted as indicating a mature island-arc-type source and tectonic setting (Kröner et al., 2001; Jamal and De Wit 2004). Furthermore, these rocks do not provide any evidence of Mesoproterozoic high-grade or high-pressure metamorphism that might be linked with continental collision. However, they may record a strong Pan-African tectono-metamorphic overprint (Kröner, 2001). The amphibolite facies overprint and voluminous post-tectonic magmatism occurred between 550-490 Ma in the Nampula Complex (Bingen et al., 2009; Macey et al., 2010).

Syn-, late- and post-tectonic Pan-African granites are a potential source of pegmatites in central and northern Mozambique. Syn-tectonic granites commonly are converted into gneisses. Dykes,

sheets and small granite bodies, and sub-circular to elliptical ring complexes, are spatially associated with the western part of the Lurio Belt. However, several large plutons and associated dyke swarms of Jurassic syenite and nepheline syenite, associated with the southern part of the East African Rift, occur in the western part Merrupa, Unango and Nampula Complex (Bingen et al., 2009).

The Mozambique Belt in southern Malawi is predominated by strongly foliated quartz-biotite-plagioclase±hornblende±microcline gneiss of tonalitic, trondhjemitic, or granodioritic composition and undoubtedly of igneous origin (Andreoli, 1984; Kröner et al., 2001). The calc-alkaline granitic orthogneisses with crystallisation ages of ~1040 – 929 Ma have Nd isotopic signatures compatible with their formation as juvenile melts in a supra-subduction zone, continental-margin-arc setting. Neoproterozoic arc magmatism that occurred between ~775 – 555 Ma is represented by juvenile calc-alkaline granitoids emplaced into the older continental-margin arc granitoids (Kröner, 2001).

The high-grade rocks of southern Malawi were considered to represent a section of the Pan-African Mozambique Belt (Holmes, 1951; Clifford, 1974; Kröner, 1977; Cahen et al., 1984). However, due to reinterpretation using Rb-Sr whole-rock and U-Pb multigrain zircon ages (Andreoli, 1981; 1984) it has been revealed that they belong to Kibaran orogenic belt, which may be correlated to similar ages in northern Mozambique and southern Tanzania (Pinna et al., 1993; Unrug, 1992; 1996; Kröner, 2001) or to granitoid magmatism in the central Zambezi Belt between ~1028 and ~680 Ma (Dirks et al., 2000). The high-grade gneiss assemblage reached the thermal peak of metamorphic conditions at 900±70 ^{o}C and 9.5±1.5 kb between ~571 and ~549 Ma (Andreoli, 1981; 1984; Kröner et al., 2001; Figure 3.8 and Table 3.2). This means that the high-grade granitoid gneisses with protolith ages of 1040-555 Ma were plastically deformed together with supracrustal rocks, and the peak of granulite facies metamorphism was reached at ~570-550 Ma.

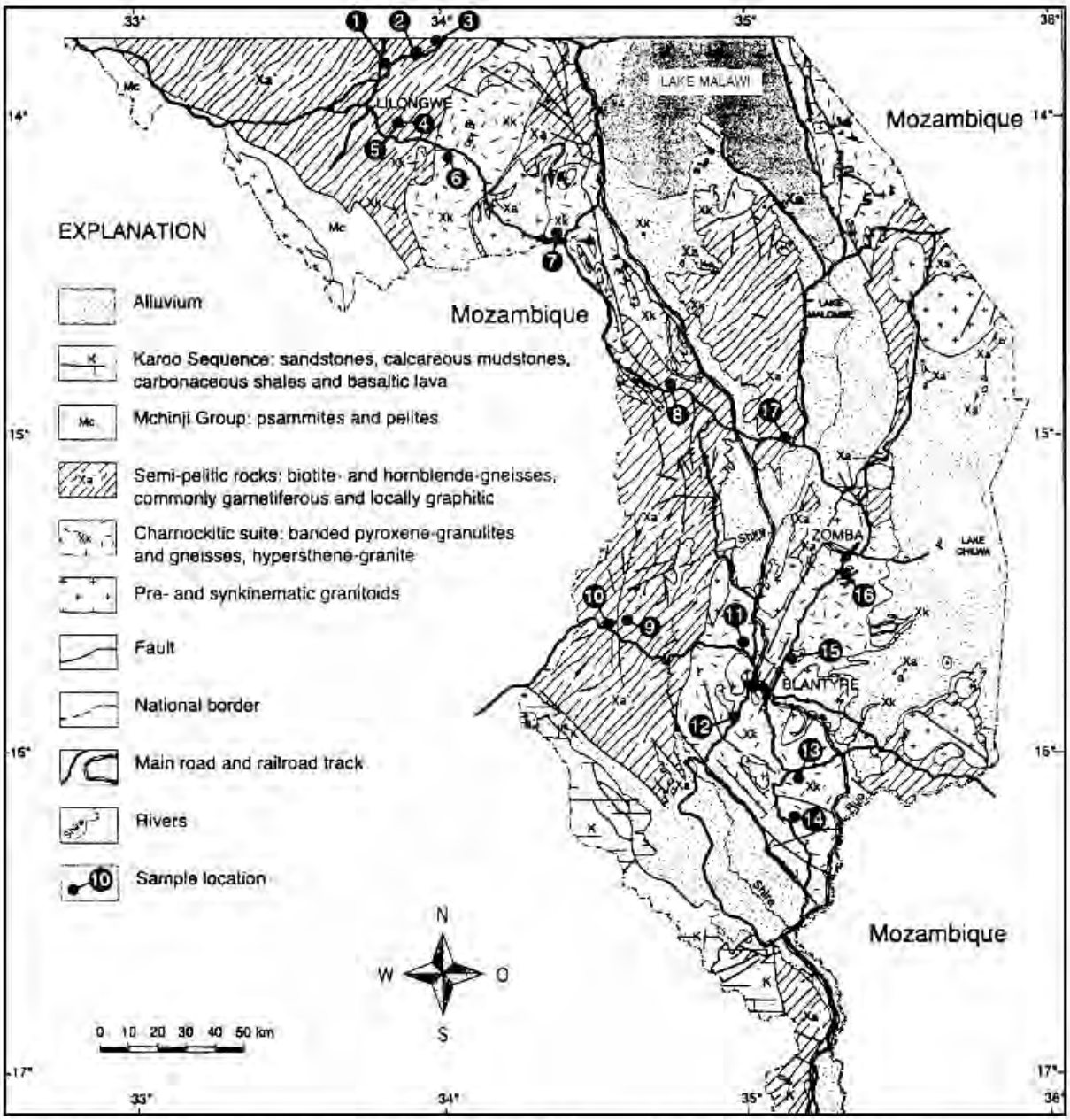

Figure 3.8: Simplified geological map of southern Malawi with areas sampled by Kröner et al. (2001), within orthogneisses, charnockites and metapelites (taken from Kröner et al., 2001).

Table 3.2: Summary of zircon ages for the Mozambique Belt of southern Malawi (taken from Kröner et al., 2001).

# in **Fig. 3.8**	**Rock type**	**Zircon age (Ma)**	**Dating Method**	**Nd model age (Ga)**	**Interpretation**
1	leucocratic granite	602.7 ±1.0	Evaporation	1.5	emplacement age
2	garnet-rich granulite	644.9 ± 0.9	Evaporation	1.0	emplacement age
3	trondhejemitic gneiss	582.9 ± 1.0	Evaporation	1.4	emplacement age
4	leucocratic granite	577.5 ± 1.0	Evaporation	1.4	emplacement age
6	charnockitic gneiss	590.5 ± 1.0	Evaporation	1.2	emplacement age
7	charnockitic gneiss	928.9 ± 1.8	Evaporation	1.8	emplacement age
8	migmatic paragneiss	576 ± 11	SHRIMP		age of melt patches
	same sample	576.7 ± 1.0	Evaporation		age of melt patches
	same sample	572 ± 9	SHRIMP		peak of metam
	same sample	575.0 ± 1.0	Evaporation		peak of metam
9	granodioritic gneiss	1012.5±0.8	Evaporation	1.2	emplacement age
10	migmatitic granite gneiss	998.9 ± 0.8	Evaporation		emplacement age
12	garnetiferous metapelite	547 ± 10	VT		peak of metam
	same sample	549.2 ± 1.0	Evaporation		peak of metam
13a	trondhjemitic gneiss	571 ± 9	SHRIMP	1.3	emplacement age
13b	same sample	576.1 ± 1.0	Evaporation		emplacement age
13c	same sample	564 ± 4	SHRIMP		Peak of metam
14	migmat granodior gneiss	1040.6±0.7		1.2	emplacement age
15	enderbitic gneiss	554.7 ± 1.0		1.2	emplacement age
16	granite gneiss	664 ± 27	SHRIMP	1.3	emplacement age
	same sample	667.5 ± 0.9	Evaporation		emplacement age
17	retrograded granulite	710.5 ± 0.9	Evaporation	1.5	emplacement age

Key: Evaporation – single grain evaporation; VT – single grain vapour transfer.

3.3.2 Economic Potential of Pegmatites in the Pan-African Basement of East Africa

In the Pan-African Belt of East Africa, gemstones are among the major economic minerals, and overwhelmingly their formation is associated with the emplacement of pegmatites. Gemstone species include tourmaline, ruby, emerald, beryl, red spinel and garnet (BRGM, 2004).

In Kenya, aquamarine bearing pegmatites are associated with two major shear zones, but their origin is yet to be established. In the Mangare area, ruby and red spinel formed as a result of metasomatic interactions between fluids, carbonatised ultramafic bodies and pegmatites. Ruby dominates within the veins, whereas red spinel forms as an accessory mineral. These gemstones, such as rubies in Mangare area, are systematically associated to carbonatised ultramafic rocks (Key and Ochieng, 1991; Simonet et al, 2000).

In Tanzania, a large variety of gemstones are found in the association of Pan-African pegmatites. These include epidote-clinozoisite group/tanzanite, corundum group minerals producing ruby

and sapphire, garnet group members such as rhodolite, almandine, and pyrope; green tourmaline; beryl and emerald, chrysoberyl (alexandrite), and aquamarine (BRGM, 2004). There are also mica-bearing pegmatites of the Uluguru Mountain, Mikese area, Mahenge Mountain in Morogoro District. Some spectacular spessartine is produced in Tanga. Furthermore, other pegmatite deposits produce industry minerals such as alkali feldspar, quartz and mica.

In Mozambique, there are more than 100 known rare-metal pegmatites in the Alto Ligonha Province (Lächelt, 2004). Some concentrically zoned, complex type, lepidolite-subtype granitic pegmatites are located at Namivo, in Alto Ligonha district (Neiva, 2013). Some of the Namivo pegmatites contain green and bluish green beryl in the outer zone, and pink beryl in the inner and core zones. In Nampula, Tete, and Zambezia, pegmatites bear tourmaline, topaz, spessartine, beryl (aquamarine), spodumene (kunzite), and rose quartz. Rare–Element granitic pegmatites are reported from the Mutala area (Knorring et al., 1973; Lächelt, 2004), Marropino, Morrua, and Muiane in the Alto Ligonha district, and the Zambezia Province (Lächelt, 2004). The Li-Be-Ta-Nb bearing pegmatites show regional zonation. The northern zone contains Be, Nb and Li mineral assemblages, and the southern zone hosts beryl and columbite-tantalite deposits (Hutchinson and Claus, 1956). In the Mozambique Belt of eastern Zambia there are gem- and Sn-bearing pegmatites. The gemstones include tourmaline, beryl and spessartine (Patney and Tether 1988).

3.4 BRIEF GEOLOGY AND STRUCTURE OF MALAWI

The geological subdivisions of structural or lithological entities in Malawi is rooted in the thinking of the 1960/70s, which is simplistic and not always well compatible with the modern interpretation of the geological evolution of East Africa. Moreover, even the modern interpretations of the regional geology of Malawi differ according to different authors who do not always agree on the spatial distribution of rocks of the Palaeoproterozoic Ubendian Belt, Mesoproterozoic orogenic belt and Neoproterozoic Mozambique Belt (cf. Fagereng, 2013; Karmakar and Schenk, 2016). However, the situation is about to improve due to the GEMMAP project, which is in progress and aims at remapping the geology of the entire country, funded by the World Bank and the European Union (World Bank, 2015). The old subdivisions for the rocks are pre–Karoo, Karoo and post- Karoo.

3.4.1 Pre- Karoo

The Pre-Karoo rocks cover much of the country and range in ages from Palaeoproterozoic to early Palaeozoic. The crystalline rocks of Precambrian to early Palaeozoic age are referred to as

Basement Complex (Carter and Bennet, 1973) as used in traditional literature in Malawi. The Pre-Karoo rocks have been affected by three major phases of deformation and metamorphism namely the Ubendian, Irumide and the Pan-African. The south-eastern end of the Palaeoproterozoic Ubendian Belt crosses through northernmost Malawi producing structures such as Mugesse Shear Zone (Ray, 1974). The belt borders at rocks formed or overprinted during the Mesoproterozoic to Neoproterozoic Irumide orogenic phase. The Irumide Belt continues westwards into Zambia. The Neoproterozoic Pan-African orogeny, regionally known as the Mozambique Orogeny, affected the pre-existing basement and also produced juvenile crust (Carter and Bennet, 1973; Kröner, 2001). Pre-Karoo crystalline rocks comprise gneisses, granulites and schists of the Basement Complex with associated mafic, ultramafic, syenites and granite rocks (Bloomfield, 1968). The Pre-Karoo crystalline rocks are subdivided into northern and southern subprovinces, distinguished on lithological, structural and metamorphic criteria (Figure 3.9, Table 3.3). They are juxtaposed along the Chimaliro Fault, which forms the southern boundary of the high-grade rocks of the Champhira Dome in the southwest of northern Malawi (Cannon et al., 1969). This dome comprises of migmatites and gneisses. It contains assemblages of the biotite-cordierite-almandine subfacies of the granulite facies. The gneisses represent a sequence of arkosic sediments that have been metamorphosed to sillimanite-cordierite gneisses whereas the migmatites were derived from more argillaceous and potassic sediments.

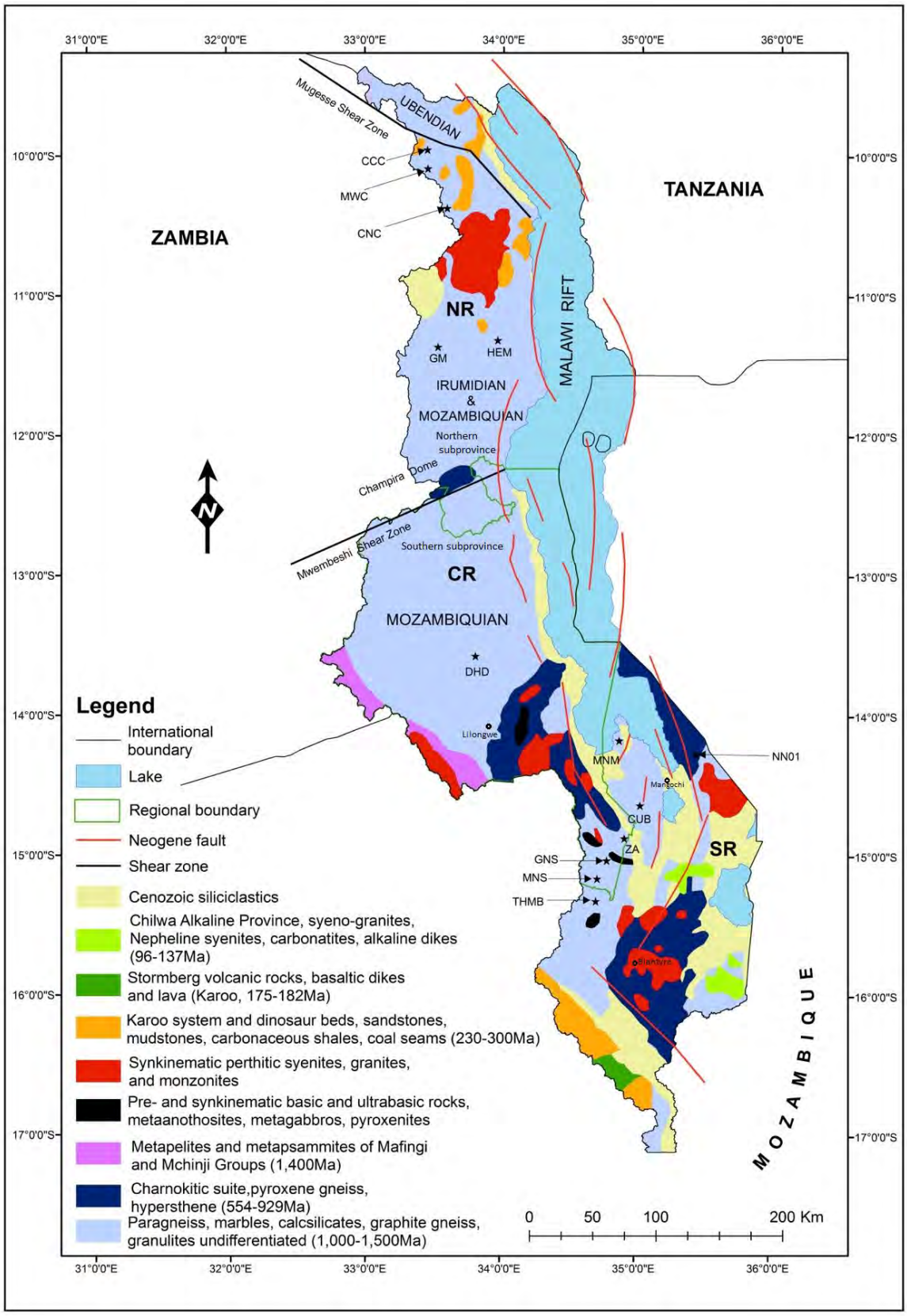

Figure 3.9: Overview map of geological units of Malawi, highlighting areas where samples for this study were taken. The northern and southern subprovinces according to geology are separated by the Champhira Dome and the dextral Mwembeshi shear zone. NR: Northern Region; CR; Central Region; SR: Southern Region of the Malawi political map (modified after Carter and Bennet, 1973; Dill, 2007). Star symbols show sampling areas together with sample codes for the current study.

Table 3.3: Lithological, structural and metamorphic differences between the northern and southern subprovinces of Malawi (taken from Thatcher, 1973).

Northern subprovince	**Southern subprovince**
Granulites rare. Where present, massive or weakly foliated	Banded gneisses and granulites widespread.
Marbles absent, calc-silicate gneisses rare	Marbles and calc-silicate gneiss common in both medium-grade gneisses and charnokitic rocks
Graphite rare	Graphite widespread in both medium-grade gneisses and charnokitic rocks
Kyanite rare	Kyanite common in pelites
Cordierite gneiss widespread	Cordierite rare
Perthite syenite and perthite gneiss absent	Large perthite complexes occur in association with perthite gneiss
Meta-anorthosite absent	Meta-anorthosite (at Linthipe) occur in association with charnokitic rocks
Main metamorphic event at about 2000 Ma	Amphibolite-facies metamorphism 718±25 Ma; granulite facies metamorphism 1126±29 Ma.

The ***northern subprovince***, which is almost entirely in the northern region of Malawi, lies at the junction of the Ubendian, Irumide and Mozambique orogenic belts. The Ubendian deformation (pre-1800 Ma) produced the dominant south-easterly structural trend into which syntectonic granites were emplaced. In places, the Palaeoproterozoic structural trend was overprinted by Mesoproterozoic deformation related to the Irumide orogenic phase (1100 Ma), resulting in some weak north trending structures (Carter and Bennet, 1973).

The intrusion of the Songwe Syenite Complex (~655 Ma) post-dated the formation of its Palaeoproterozoic host rocks by more than one billion years, and is associated with the initial Pan-African/Mozambique deformation. The amphibolite facies rocks were subjected to ESE directed compression between 580-500 Ma in northern Malawi (Ring et al., 2002) This Pan-African deformation caused a realignment of Irumide structures. Folds are geometrically controlled by the pre-existing Ubendian structural trend. The Mozambique folding was also associated with movement along several shear zones, such as the sinistral Mugesse shear zone, which forms a tectonic junction between the Songwe and the Chambo gneisses (Carter and Bennet, 1973).

Northern Malawi includes two main groups of rocks, the Jembia River Granulites to the south and the Misuku Gneisses to the extreme north. Both units are believed to have been part of the same stratigraphic unit that were metamorphosed and deformed in slightly different environment. This is supported by the presence of a distinct ferruginous quartzite in both units (Fitches, 1971).

The Misuku Gneisses are divided into two distinct units, the Chambo and the Songwe Gneisses. The Chambo Gneisses form the southern group while the Songwe Gneisses are represented along the Malawi-Tanzania borders where they form a southeast trending group of micaceous and amphibolites gneisses and schists. The predominant rock types of this group are semi-pelite schists and magmatic gneisses that are composed of quartz, muscovite, biotite, oligoclase and epidote, which grade locally into granitic gneisses with a high proportion of microcline perthite. Most of these rocks appear to belong to the epidote-amphibolite and amphibolites facies of the Barrovian metamorphism, and parts were metamorphosed under conditions intermediate between sillimanite-muscovite and sillimanite–almandine-orthoclase sub-facies (Thatcher and Bennet, 1973).

The cordierite-sillimanite bearing Jemba River Granulites form a distinct unit to the south of the Misuku Gneisses. In the Mafingi Hills region, there is a sharp junction between the Jembia River Granulites and the Misuku gneisses and it is thought to be a tectonic break (Fitches, 1971). The main structural trend within the Jembia River Granulites is SE to ESE. A brief summary of the metamorphic history of northern Malawi showing the stable minerals and metamorphic conditions is presented in Table 3.4.

Table 3.4: Metamorphic history northern region.

Region	**Stable minerals**	**Metamorphic conditions**	**Sources**
Karonga/Chitipa	Cordierite-sillimanite-andesine/oligoclase-mica-garnet-microcline-perthite (in metapelites) hypersthene-hornblende-labradorite-diopside-zoisite (in metabasites).	Granulite facies	Fitches (1970), Ring (1993)
Karonga Chitipa *Basement* *Mafingi Group*	Sillimanite-almandine-biotite Corona structures in dolerites Epidote-chloritoid-garnet-biotite-chlorite-kyanite	Upper amphibolites facies Lower amphibolites facies (500-600 ^{o}C) Upper amphibolites to granulite facies	Ray (1974), Ring (1993) Thatcher (1974), Ring (1993)
Nyika/Rumphi	Cordierite-sillimanite-almandine-biotite, local migmatisation	Upper amphibolites to granulite facies	Thatcher (1974)
Nyika/Rumphi	Cordierite-sillimanite-biotite-almandine, Locally kyanite-biotite, hypersthene in granulites	Upper amphibolites to granulite facies	Thatcher (1974), Ring (1993)
Karonga/Chitipa and Nyika/Rumphi	Garnet-biotite-chlorite-muscovite-oligoclase/andesine subsequent retrogression of these minerals to chlorite-sericite-epidote-quartz assemblages	Upper greenschist facies	Ray (1974), Thatcher (1974), Ring (1993)
Kasungu/Mzimba *Champhira dome*	Almandine-sillimanite-biotite, local anatexis	Granulite facies (700-800 ^{o}C, 5-7 kb)	Haslam et al. (1980)
Kasungu/Mzimba *Champhira dome* *Surrounding gneiss*	Cordierite-almandine-biotite (675 ^{o}C, 5 kb) Sillimanite-garnet-biotite to the south kyanite replaces sillimanite	Upper amphibolites facies Amphibolite facies	Haslam et al. (1980), Peters (1975)
Kasungu/Mzimba	Sillimanite-andalusite-garnet-biotite-staurolite Late staurolite overgrowths	Amphibolite facies	Peters (1975)

The ***southern subprovince*** is dominated by gneisses and schists with predominantly amphibolite facies mineral assemblages, which in large areas to the north and south of Blantyre, around

Dedza, east of Lilongwe and along the Mozambique border north-west of Mangochi, are underlain by banded two pyroxene granulites and gneisses (Figure 3.9). The majority of the rocks in the area are considered to be metamorphosed sediments; however, some orthogneisses are recognized. These orthogneisses are: Linthipe meta-anorthosite and minor basic and ultrabasic intrusions; the Dzalanyama granite and small bodies of nepheline syenite; the Dedza Perthitic complex and the Lake Malawi Granite Province. The subprovince can be subdivided into two regions, Central Malawi and Southern Malawi.

Central Malawi consists of graphitic gneisses interbanded with fine–grained feldspathic gneisses, thick beds of crystalline limestone and kyanite schists. The paragneisses of central Malawi can be divided into five lithostratigraphic units, namely Mchinji Quartzite Group, Bua Gneiss Formation, Ntchisi Schist Formation, Katengeza Marble Formation, and Shire Highlands Metavolcanic Formation (Carter and Bennet, 1973).

In southern Malawi, high-grade metamorphism and magmatism occurred between 605-550 Ma (Kröner et al., 2001). The region is mostly covered by medium- to high-grade paragneisses and granulites of the Basement Complex, which are mainly semi-pelitic rocks with a few psammitic and pelitic horizons. The area mainly comprises of graphitic gneisses, gneisses, schists, granites, syenites and crystalline limestone series similar to those in Central Malawi (Bloomfield 1968). Dominant in the area is a suite of banded, agmatitic or migmatitic granulites that extend into Central Malawi to the southeast and east of Dedza. Many of these rocks have compositions comparable with basalts, andesite, dacite and rhyolite. These have been interpreted as metavolcanic rocks and related sediments such as greywacke.

3.4.2 The Karoo System

Karoo sedimentary rocks in Malawi are part of the large-scale Karoo system which also passes through Zambia, Tanzania and Mozambique and which can be extended to South Africa and beyond. The Karoo sediments uncomformably overlie the crystalline gneisses and associated igneous bodies of Palaeo- to Neoproterozoic age. They crop out in Karonga and Chitipa districts in the north and Chikhwawa and Nsanje districts in the south of Malawi. The Karoo Igneous Province is represented by dolerite dyke swarms.

In the northern part of Malawi the Karoo System strata are present in a number of basins and down-faulted troughs. The rocks are assigned to the Dwyka, Ecca and lower Beaufort Groups (Permo-Triassic age). The rocks consist of basal beds that occur mainly as conglomerates and sandstones; carbonaceous shales and coal seams. The Karoo succession in the north is completed

by development of thick mudstones, marls and grits that are also of the lower Beaufort Group age (Bloomfield, 1957; Cooper and Habgood, 1959).

In the south, the Karoo differs from that in the north in that deposition is believed to have commenced later and continued longer. As a result, the sedimentary phases of Stormberg Group are overlain more widely by mudstones, sandstones and thin coal seams assigned to the upper Ecca Group. These rocks are succeeded by thick development of grits, sandstones and shales. The shales grade into calcareous sandstones, marls and siltstones. All these rocks are referred to the Beaufort Group. Grits and arkoses constitute the lower part of Stormberg Group succession. These give way upwards to sandstones which become increasingly red in colour and are followed by red sandy marls and interbedded mudstones. The deposition of the Stormberg Group sediments was brought to a close by faulting and the onset of a major episode of volcanism (Bloomfield, 1958; Habgood, 1963). However, there is no relationship between the Karoo in Malawi and the pegmatites in this study.

3.4.3 Post Karoo

Following the deposition of the Karoo Supergroup sediments and the Karoo-related volcanism and dyke formation, the region was affected by tectonics and magmatism related to the development of the East-African Rift. This evolution began in the Upper Jurassic (Bloomfield, 1965) and has continued to the present time. It has formed the Upper Jurassic and Lower Cretaceous Chilwa Alkaline Province. Intrusive rocks of this suite occur widely throughout southern Malawi and form a distinctive feature of the local geology (Figure 3.10). The origin of the alkaline and carbonatitic magmas and alkali metasomatism in Malawi is related to crustal extension and mantle upwelling, generating a substantial heat influx into the lithosphere (Eby et al., 1995). Anorogenic plutons related to this process are associated with granitic pegmatites in which Nb is more abundant than over Ta, and which show an enrichment in Ti, Y, REE, Zr, Th, U, Sc and F hence are of NYF type (Wise, 1999).

The rocks of the Chilwa Alkaline Province (130-105 Ma) consist of syeno-granitic and nepheline syenite plutons, volcanic vents in filled with carbonatite, agglomerate and feldspathic breccia, and a varied suite of alkaline dyke rocks such as microfoyaites, a swarm of solvbergites, lamprophyres, and phonolites. These rocks form two main belts, one between Mulanje Mountain and Lake Chilwa and the other within the Malawi Rift Valley to the west and southwest of Lake Malombe (Platt and Woolley, 1986; Woolley and Jones, 1987).

In the Malawi Rift Valley System, the most prominent zone of faulting has an overall N-S trend that follows the western boundary of Lake Malawi and extends southwards along the western side of the country. The faults down-throw to the east. In the southern part of the country this system is changing to NW-SE trend.

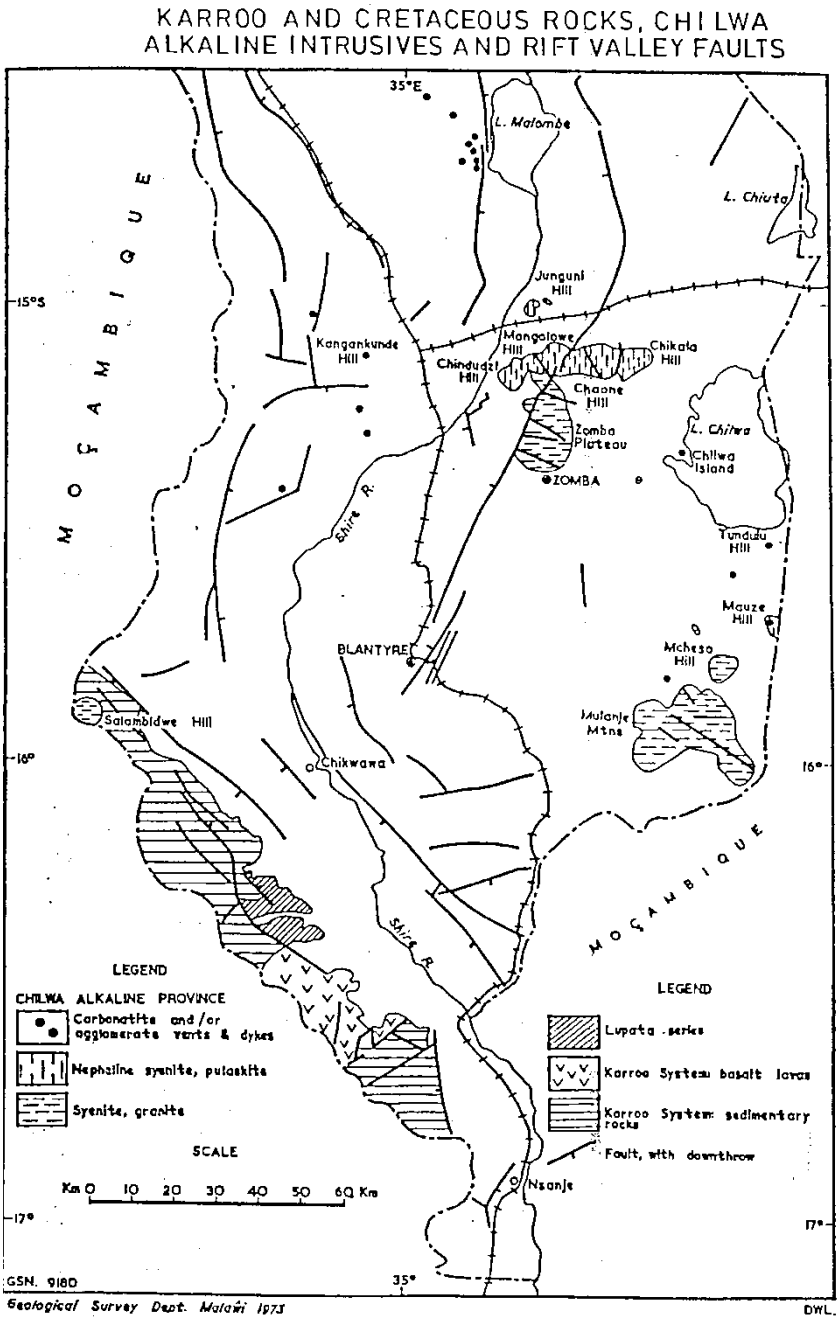

Figure 3.10: Chilwa Alkaline Province (CAP) (after Carter and Bennet, 1973)

An example of a syeno-granitic pluton in the Chilwa Alkaline Province is the Zomba-Malosa Mountain that forms a large pluton in the northern part of the province. The pluton is composed of a central plug, an inner ring, an outer ring and the roof pendant of gneiss. Furthermore, the central plug is composed of aegerine–hornblende-augite-perthosite, the inner ring contains small rounded phenocrysts of feldspar, either orthoclase or microperthite, the outer ring consists of a low narrow ridge of alkali granite, and finally the roof pendant gneiss consists of biotite, and

hornblende gneisses which are occasionally garnetiferous. The Mount Malosa area has some alkaline granite found both in the central plug and the outer ring. A varied suite of intrusions occur that includes narrow dykes of microgranite and microsyenite, quartz veins and syenitic and granitic pegmatites (Bloomfield, 1965; Carter and Bennet, 1973; Woolley and Jones, 1987). Petersen and Grossman (1994) identified the following minerals from some of the miarolitic pegmatites of the area: aegerine, arfvedsonite, barylite, caysichite (Y), epididymite, fergusonite (Y), goethite, hingganite (Y) and (Yb), parisite (Ce), smoky quartz, eudialyte, Ce-rich pyrochlore, and niobophyllite - astrophyllite among others. Jonsson and Hogdahl (1999) undertook further mineralogical research on fergusonite and epididymyte. The granitic pegmatites of Mount Malosa produce renowned semi-precious minerals (Petersen and Grossman, 1994; Cairncross, 2004).

Sedimentary rocks of Upper Jurassic and Cretaceous age crop out in the northern part of Malawi and near the Mozambique border to the southwest of Blantyre. In the north, the beds consist of friable sandstones, sandy marls and clays. The beds rest unconformably on the Basement Complex and locally on the Karoo formations. They are confined to elongated rifts that are parallel to the lakeshore and the Malawi Rift Valley and wedges of Basement Complex rocks separate them from each other. In southern Malawi, the Lupata Series comprises of sequence of pebble conglomerates, coarse sandstones, sandy shales and marls. These rocks unconformably overlie the Karoo sequence (Carter and Bennett, 1973).

Sedimentary rocks occur as lacustrine deposits in narrow belts aligned parallel to the shore of Lake Malawi in the north. They consist of a variety of clastic rocks, subdivided into Sungwa beds (grits and sandstones), Timbiri beds (clays, grits, sands and gravels) and Chiwondo beds (calcareous marls, silts, sands, shelly limestone). The sedimentary rocks are mainly buff coloured and they rest unconformably on the Dinosaur Beds and the Basement Complex. Volcanic rocks of probable Pleistocene age occur over a small area along the Tanzania border, where they overlie the Tertiary sediments (Carter and Bennet, 1973).

Various ***superficial deposits*** of Pleistocene cover large tracts of the Lake Malawi littoral, the Shire Valley and the Lilongwe, Kasungu and Mzimba Plains. Lacustrine, alluvial and colluvial deposits are particularly well developed along the shores of Lake Malawi and around Lake Malombe and Lake Chilwa. Colluvial deposits and residual soils cover extensive areas in the west of the country (Dill and Ludwig, 2008).

4. GEOLOGY AND MINERALOGY OF ANALYSED PEGMATITES

4.1 SAMPLING STRATEGY AND NOMECLATURE

This chapter describes the geology and the mineralogy of the investigated gemstone bearing pegmatites in the study areas (Figure 3.9). The mineral phases in this chapter have been identified macroscopically using hand lens and stereo-microscope. The identification process included examination of crystal systems, crystal habits, cleavage and fracture, colour and lustre. The gemstones from the different pegmatites show variation with geographic location and stratigraphic position of the host rocks. This chapter presents sample descriptions, pegmatite types and local field relationships.

Locations for the studied pegmatites were chosen depending on the geographic and litho-stratigraphic association with respect to each other and with respect to the major geological units in Malawi, and diversity of mineralogy, including types of gemstone species present. Since this study attempts to provide an overview of gem-bearing granitic pegmatites across the whole of Malawi, accessibility was another factor in sample collection. In most regions of Malawi exposure conditions are poor. Hence, in most pegmatites systematic sampling across strike and observation of structural orientations were difficult, and particularly in zoned pegmatites some zones could not be sampled.

The sample names or codes are shortened abbreviation of local areas. Samples CNC (Chinthu-Nthalire-Chitipa), CCC (Chisenga-Central-Chitipa), MWC (Matulo-Wenya-Chitipa), GM (Group Daniel Jere-Mzimba), HEM (Homero-Ekwendeni-Mzimba) and MEM (Malidade-Emcisweni-Mzimba) come from pegmatites in northern Malawi, DHD (Dzaleka-Hilo-Dowa), GNS (Gumbo-Ntonda-Senzani), MSN (Mzawira-Sikulamowa-Ntcheu) and ZA (Zamwazi-Angoni) come from central Malawi, and CUB (Chiripa-Ulongwe-Balaka), MNM (Monkey Bay-Nankhwali-Mangochi), NNO1 (Njele-Namitembo), and THMB (Thunduza-Matandani-Bayani), come from the southern region of Malawi (Figure 3.9). However, all the samples for Rb-Sr dating start with „G‟ representing geochronology as in samples GCN1, GCW1, GM1, GD1, GNS1, GNS4, GN1 and GU1. The corresponding codes for geochemical, geochronological and fluid inclusion samples have been summarised in Table 4.1, and details are presented in Appendix 1.1. All these pegmatites bear gemstones of different varieties. They are intrusive into different rock types ranging from granulites to greenschist facies rocks. The setting and local geology will be described further in the context of each pegmatite.

Table 4.1: Summarised codes for geochemical, geochronological and fluid inclusion samples used in this study. X means no sample collected for mica geochemistry or fluid inclusion studies.

CODE	SAMPLING DISTRICT	NEAREST TOWN/ VILLAGE	PART OF MALAWI	MICA GEOCHEM.	GEOCHRON.	FLINC. With underscore (_)
					Rb-Sr dating	
CNC	Chitipa	Nthalire	North	CNC	GCN1	CNC
CCC	Chitipa	Chisenga	North	CCC	GWC1	CCC
MWC	Chitipa	Wenya	North	MWC		MWC
GM	Mzimba	Kabwafu / Kafukule	North	GM	GM1	GM
MEM	Mzimba	Kabwafu / Kafukule	North			MEM
HEM	Mzimba	Luhomero	North	HEM		HEM
DHD	Dowa	Mponela/ Kamwana/ Makanjira	Central	DHD	GD1	DHD
GNS	Ntcheu	Ntonda	Central/South	GNS1-3	GNS1	GNS1
GNS	Ntcheu	Senzani	Central/South	GNS4-7	GNS4	GNS4
MSN	Ntcheu	South of Senzani	Central/South	MSN	GN1	MSNB
						MSN7
CUB	Balaka	Ulongwe	South	CUB1	GU1	CUB
					U-Pb dating	
MNM	Mangochi	Nankhwali	South	X	MNM	X
NNO	Mangochi	Chowe/ Uzuzu	South	X	NNO	X
ZA	Ntcheu	Bwanje/ Chiripa	Central/South	X	ZA	X
THMB	Ntcheu	Biliati	South	X	THMB	X

Fresh samples with overall representative mineral assemblages were collected from the accessible parts of the pegmatites for geochemical, fluid inclusion and geochronological analyses in order to assess the geological factors responsible for the variations in gemstone content in the pegmatites, their possible regional mineral distribution, pegmatite sources, and their age. A common limiting factor for determining representative characteristics of pegmatites is their large grain size, and this problem also applies to the current study. Moreover, it was not possible to collect samples for pegmatites that monitor zonation in individual dykes due to the poor or limited exposure which hampered sampling on a spatial basis. Such information could be of much relevance in establishing whether elemental enrichments are spatially related to the pegmatites. This would be an aim of a more detailed study on the evolution of individual pegmatite fields.

Mica for trace elemental analysis was not collected in close proximity to or within miarolitic cavities, because their rare/trace element concentrations are untypically high. Clear quartz samples were collected for purposes of fluid inclusion studies from all studied pegmatites. Furthermore, samples for Rb-Sr dating were collected from LCT pegmatites. Samples for U-Pb zircon were collected from NYF pegmatites. Detailed geochronological, geochemical and fluid inclusion data are provided in Chapter 6, 7 and 8 respectively.

4.2 PALAEOPROTEROZOIC PEGMATITES

4.2.1 CNC Pegmatites

The Palaeoproterozoic of Malawi is exposed in the Chitipa district in northern Malawi (Figure 1.3). The Chitipa area stretches from Mkoma in the NNW to Gamba in the SSE (Figure 4.1) and includes Nyika National Park and the towns of Nthalire and Wenya. The Palaeoproterozoic is dominated by granulitic rocks bearing cordierite, garnet, spinel and K-feldspar (Thatcher, 1974; Figure 4.1; Section 3.1). Garnet-cordierite granulite shows peak P-T conditions of 750 – 850 ^{o}C at low pressure of 5 - 5.5 kb (Ring et al., 1997). Gneiss reached greenschist to amphibolite facies P-T conditions. At least some of the rocks mapped as amphibolite-facies rocks are retrogressed and were previously subjected to granulite facies metamorphism. Intrusive rocks include granite, syenite, pegmatite and veins. Sedimentary rocks overly parts of the metamorphic basement (Figure 4.1). The pegmatites samples in this region were labelled “CNC” (for Chinthu-Nthalire-Chitipa). The sample localities are within the southern part of the Palaeoproterozoic Ubendian Belt in the northern region of Malawi (Figures 3.9 and 4.1). They mainly produce a variety of gem quality tourmalines.

4.2.2 Geological Setting of CNC Pegmatites

Individual bodies range from 15 m to 30 m in width, and some of these pegmatites can be tracked over 1.5 km along their NW-SE strike. The pegmatites were emplaced into banded cordierite gneiss that shows a foliation developed parallel or sub-parallel to the banding. The pegmatites have conformable to cross-cutting relationships with the banding and the foliation. No deformation was observed in the pegmatites at macroscopic or microscopic scale. The contact between the pegmatite and host rock is sharp.

The hosting cordierite gneiss has homogenous texture and mineralogy. It is composed of quartz, oligoclase-andesine, microcline and microperthite, cordierite, biotite, sillimanite, garnet, iron oxide, spinel and zircon (Thatcher, 1974). The gneiss has a gradational contact with the porphyritic Nyika granite, which was dated as 1930±30 Ma (Dodson et al., 1975). The granite

itself is not shown on that map but is located where Nyika National Park is indicated on Figure 4.1. It was emplaced at 12-14 km depths, corresponding to 3.4-3.9 kb, postdating the regional granulite facies metamorphism (Ring et al., 1997). The mineralogical composition of the granite is quartz, plagioclase, K-feldspar, biotite, muscovite, epidote and rare hornblende with accessory zircon, sphene, apatite and opaque phases (Ring et al., 1997). Leucogranite dykes present within the granite are composed of quartz, plagioclase, K-feldspar, muscovite, tourmaline with accessory zircon and apatite.

4.2.3 Mineralogy of CNC Pegmatites

Internal zonation of different mineral assemblages of the pegmatites was not always clearly visible in the field due to exposure conditions (Figure 4.2a), but has been observed in some places. The main mineral assemblage is composed of quartz, K-feldspar, mica, tourmaline, albite, and tantalite, whereas garnet, apatite, ilmenite and sphene are accessory minerals. Quartz has graphic intergrowth with K-feldspar, and tourmaline shows highly oriented comb structure.

Along the contact with the host rock schorl is dominant. The tourmaline colour varies from black in the wall zone to gem quality yellowish green to yellowish varieties in the inner zones. Some tourmalines reach up to 10 cm in length, often occurring in radiating aggregates. Coarse-grained feldspar mostly occupies the inner parts of intermediate zones. Their outer parts comprise intergrowths of quartz, feldspar, and muscovite. Muscovite occurs in medium- to coarse-grained aggregates, and is present in all observed pegmatite zones. However, the coarse–grained muscovite is most prevalent in the intermediate zone (Figure 4.2b). In places, quartz varies from clear to light purple colour (Figure 4.2c-d). Schorl varies in size between 1 cm and 1.5 cm (Figure 4.2e). Occasionally, miarolitic cavities contain quartz, mica, and most gem-quality tourmaline. The observed cavities vary in shape and size from 8 cm to 22 cm. Gem tourmaline varies from yellowish green to yellowish in colour (Figure 4.2e-i), suggesting Mn^{2+}-Ti^{4+} rich compositions. Quartz veins accompanying the pegmatites bear amethyst that varies in colour from light to deep purple.

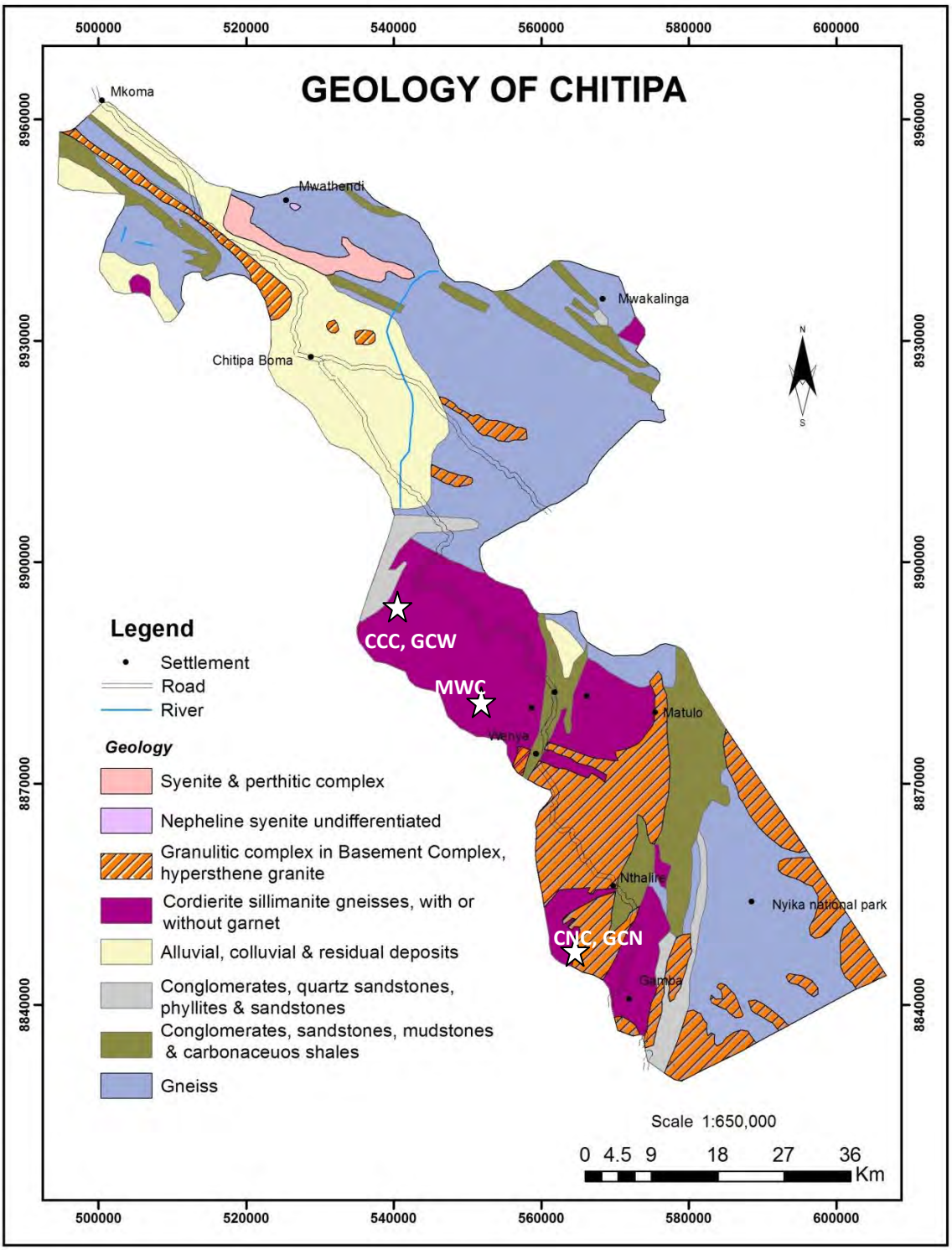

Figure 4.1: Generalised geological map of the Chitipa district in northern Malawi, showing locations for samples CNC and GCN1 (GCN1 - for age dating), CCC and GCW1 (GCW1 – for age dating), and MWC (modified after Ray, 1975). Refer to Figures 1.3 and 3.9 for the geographic and geological context of the Chitipa area.

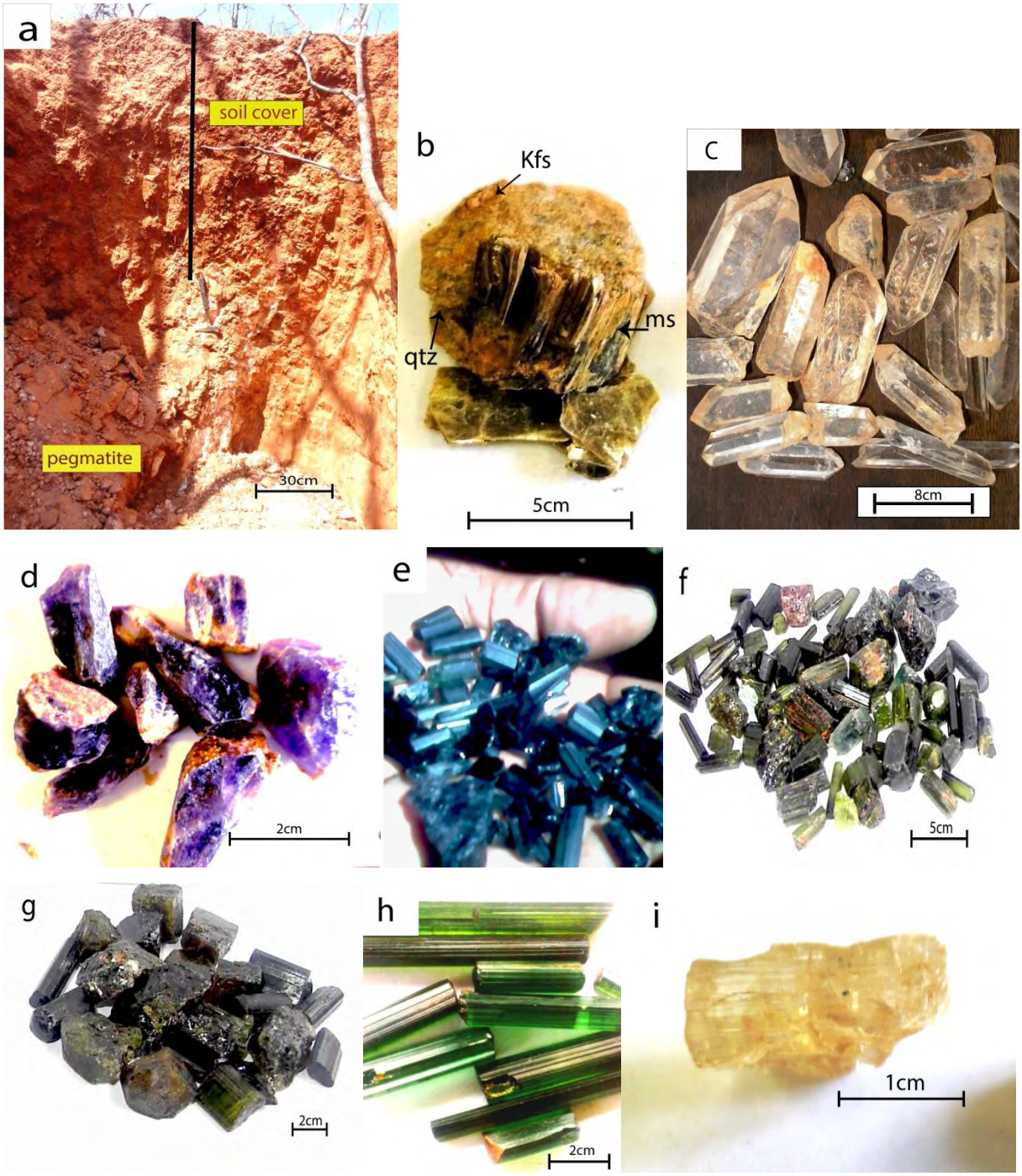

Figure 4.2: Palaeoproterozoic pegmatites and minerals; (a) Regolith obscures most of the pegmatites; (b) CNC1A sample from a zone within CNC pegmatites showing muscovite (ms), quartz (qtz), K-feldspar (Kfs), tourmaline (tur). The texture has intergrown coarse-grained crystals; (c) euhedral clear quartz (qtz) crystals; (d) amethyst; (e) schorl from the intermediate zone; (f-i) a variety of gem quality tourmalines (tur) from yellowish green to yellow: the sizes for (f) range from 3-5 cm, for (g) from 1.5 - 2 cm, for (h) between 2-8 cm, and the size for (i) is 2 cm.

4.3 PAN-AFRICAN PEGMATITES

4.3.1 CCC, MWC, GM and HEM Pegmatites

CCC, MWC, GM and HEM pegmatites occur in northern Malawi in Mesoproterozoic rocks that show a significant Pan-African overprint (Figure 3.9). The CCC and MWC pegmatites occur in the northern Chitipa district (Figure 4.1), whereas GM and HEM pegmatites occur to the southern part of Chitipa in Mzimba area that stretches from the border with Zambia to the west to the border with Nkhata Bay in the east (Figures 1.3 and 4.3). It includes Vwaza and Kabwafu trading centres. The basement is dominated by gneiss that reached greenschist to amphibolite facies (Peters, 1975; Section 3.1). Intrusive rocks include granite, syenite, pegmatite and veins. The CCC, MWC, GM and HEM pegmatites mainly produce a variety of gem quality beryl, aquamarine, tourmaline, topaz, and garnet.

4.3.2 Geological Setting of CCC, MWC, GM and HEM Pegmatites

Due to quartz resistance to weathering, some pegmatites form chains of ridges in the area near Wenya, Nthalire, and Gamba (Figure 4.1). Individual CCC, GCW and MWC pegmatite bodies are several metres thick and can be tracked over 700 m in the field. However, most of the pegmatites are obscured by regolith. The pegmatite dykes show conformable to cross-cutting relationships with the banding and foliation in the host rock, along sharp contacts. No deformation was observed in the pegmatites. The hosting cordierite gneisses have homogenous texture and mineralogy. They are composed of cordierite, quartz, microcline, perthite, oligoclase-andesine, sillimanite, biotite, garnet, accessory magnetite, and rare green spinel.

The GM and HEM pegmatites were sampled south of Chitipa in the Mzimba district (Figure 1.3 and 3.9). GM is located to the east of Kabwafu whereas HEM is located northwest of Nkhata Bay (Section 3.4.1; Figure 4.3). The pegmatites and quartz veins intruded the basement gneisses. However, most of the pegmatites are obscured by regolith. The exposed pegmatites bodies are usually 3 m to 25 m wide and some can be tracked over 100 m along their NE strike. Their dip angle is almost vertical.

The GM pegmatites are associated with sporadic MEM quartz veins. GM1, GM3, and GM5 pegmatites were emplaced into sillimanite-biotite gneiss, mica schist, and sillimanite gneiss respectively. The gneiss into which GM pegmatites intrude shows a well-developed banding with a parallel or sub-parallel foliation striking E-W. The contact between the pegmatites and host rock is sharp. The GM1 and GM3 are quasi-conformable to cross-cutting and discordant to

the layering and foliation of their host rocks, whereas the GM5 pegmatite is conformable and has cross-cutting relationships to the hosting gneiss. The pegmatites appear macroscopically undeformed.

The sillimanite gneiss is composed of quartz, sillimanite, orthoclase or microcline, biotite, garnet and iron oxides while the mica schist is composed of biotite, quartz, muscovite, orthoclase or microcline, oligoclase, accessory apatite, zircon, iron oxide and in some places sphene and garnet. The texture of the sillimanite gneiss ranges from compact granular to banded, whereas the mica schists have either medium-grained biotite and/or muscovite flakes forming a penetrative foliation (Gaskell, 1973).

The GM pegmatites appear to be similar to late pegmatites that formed in greenschist facies rocks in the adjacent Lundazi district of Zambia, where minerals such as betafite, columbite and uraninite have been found (Thatcher, 1974). It is envisaged that the pegmatites in Lundazi formed at 4 kb (Chikambwe, 2002) and 430 – 650 ^{o}C (Graziani et al., 1983). This pressure corresponds to a depth of about 15 km.

Where HEM pegmatites are located to the northwest of Nkhata Bay (Figure 4.3), there are other igneous rocks of late Precambrian to early Palaeozoic age, intrusive in the Basement Complex gneisses. The igneous complex includes hypersthene granite and syenite, with allanite and sphene as characteristic accessories. The rocks show occasional epidotisation (Hopkins, 1973). There are also other dyke-like bodies of granite and aplite that are characterised by quartz, orthoclase or microcline, with minor perthitic exsolution. Some pegmatite dykes are associated with clear quartz veins.

In general, HEM group pegmatites comprising HEM2, HEM3 and HEM4 pegmatites, have cross-cutting relationships to the country gneiss. The gneiss shows compact granular texture (Gaskell, 1973). Sharp contacts exist between the pegmatites and host gneiss.

The HEM2 pegmatite was emplaced into augen gneiss composed of K-feldspar, biotite, quartz, sericite with occasional chlorite and epidote. The HEM3 pegmatite was emplaced into calc-silicate gneiss that also contains patches of low-grade metamorphic schists. The gneiss is composed of diopside, sphene, grossularite, quartz, epidote and plagioclase while the schists are composed of epidote, albite, muscovite, quartz, garnet, tourmaline and titanite (Hopkins, 1973).

HEM4 pegmatite was emplaced into biotite-garnet gneiss composed of quartz, biotite, epidote, with occasional chlorite.

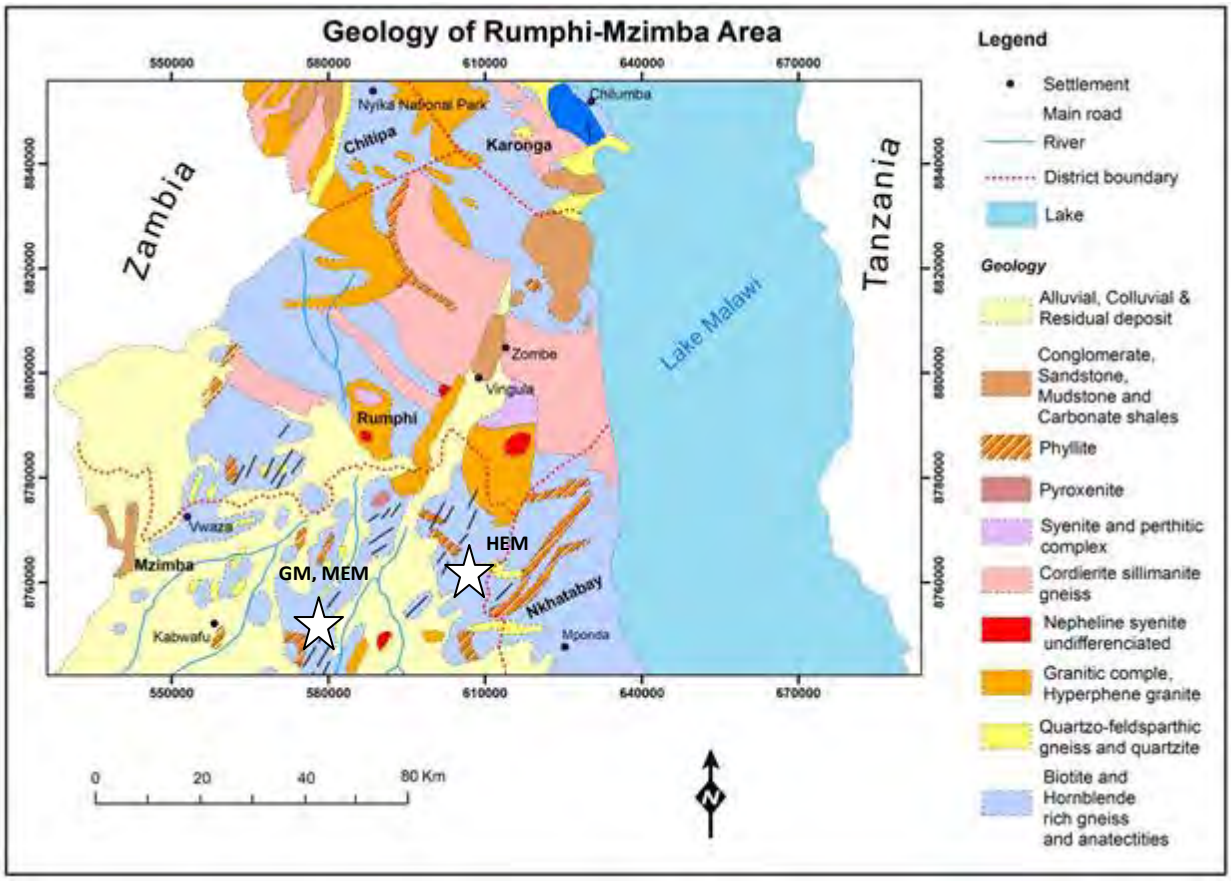

Figure 4.3: Geological map of Rumphi – Mzimba area showing location for GM pegmatites and associated MEM veins east of Kabwafu and location for HEM pegmatites northwest of Nkhata Bay (modified after Gaskell, 1973). This map shows the southern part of the northern region in Figure 3.9.

4.3.3 Mineralogy of CCC, MWC, GM and HEM Pegmatites

CCC pegmatites are poorly exposed and the description of their internal features may be incomplete (Figure 4.1). The accessible zones show essentially uniform features. In the exposed zone, the main mineral assemblage is composed of varying amounts of muscovite, K-feldspar, clear quartz, beryl, plagioclase, tourmaline, and occasional garnet and tantalite. Muscovite, that is light grey in colour, has two texturally distinctive varieties. The beryl has deep bluish colour. The general grain size increases gradually inwards from the wall zone to the monomineralic core. The intermediate zone has intergrown minerals showing coarse-grained texture (Figure 4.4a, b). Gems are mostly located around the border of the core zone. Tourmaline colours range from black along the sharp contact with the host rock, where it dominates, to dark greenish in the intermediate zone. Gem beryl is bluish (Figure 4.4 c, d) suggesting Fe^{2+} rich compositions of

aquamarine. Gem tourmaline has greenish colour (Figure 4.4e, f) suggesting Fe^{2+}- Ti^{4+} rich compositions of elbaite end-members.

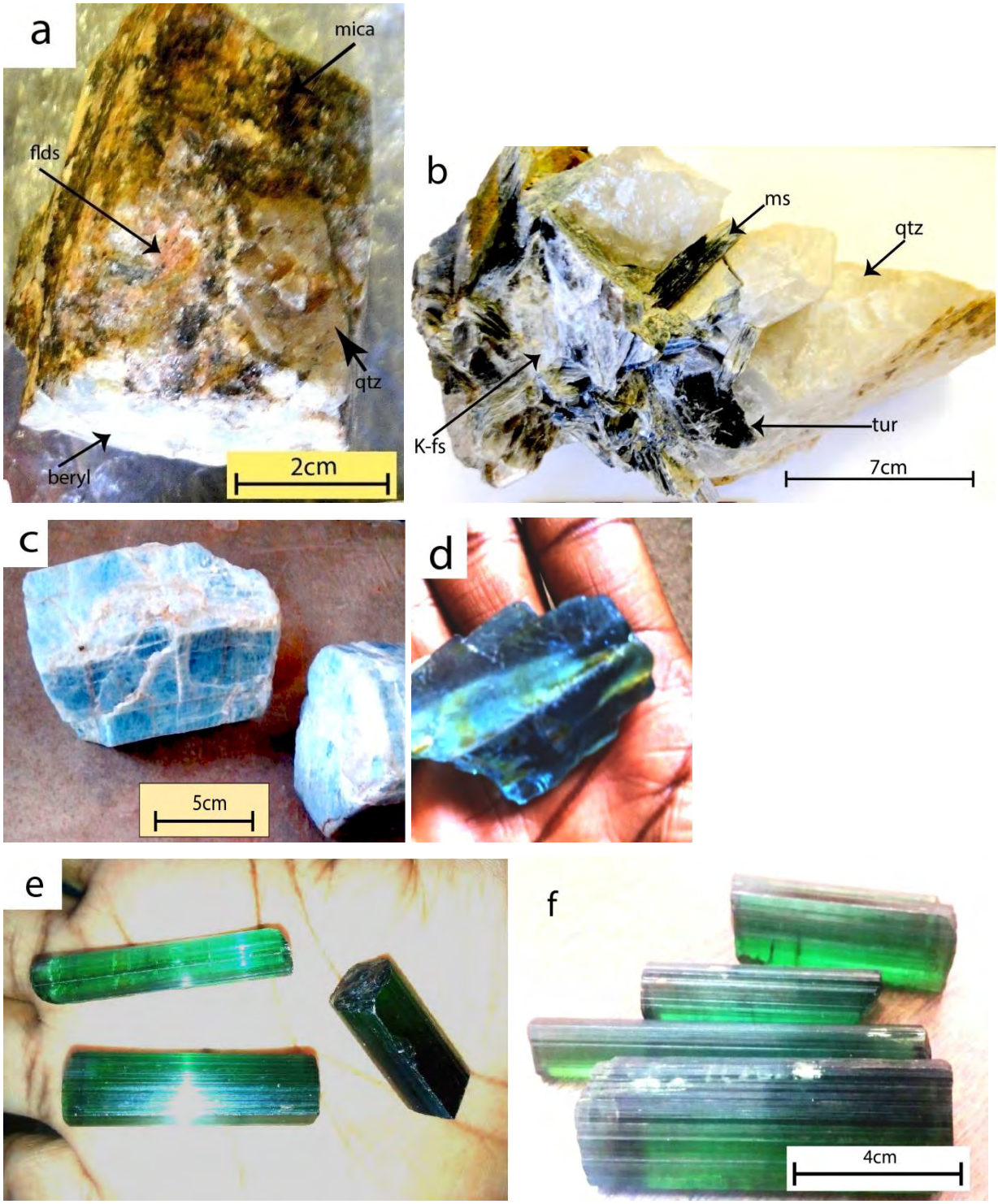

Figure 4.4: Minerals from Pan-African pegmatites from Chisenga, Chitipa; (a) intergrowth of quartz (qtz), feldspar (Kfs), muscovite (ms) and beryl from CCC1B pegmatite; (b) intergrowth of coarse grained light grey muscovite (ms), feldspar (Kfs), quartz (qtz), tourmaline (tur) from GCW1; (c, d) beryl has deep bluish colour; (e, f) gem tourmalines (tur) are greenish in colour.

Similar to the CCC pegmatites, most of the MWC pegmatites are not fully exposed, but from their exposed parts compositional zonation is evident. The MWC pegmatites are composed of muscovite, K-feldspar, quartz, beryl, tourmaline and occasional tantalite. The grain size increases from fine to medium in the wall zone to the massive quartz core. The samples in the intermediate zone generally display coarse-grained texture (Figure 4.5a). Quartz has graphic intergrowth with coarse-grained alkali feldspar. Gem beryl is bluish (Figure 4.4c, d) suggesting Fe^{2+} rich compositions of aquamarine. Gem tourmaline has greenish colour (Figure 4.4e, f) suggesting Fe^{2+}- Ti^{4+} rich compositions of elbaite end-members.

MWC zoned pegmatites are mainly composed of muscovite, K-feldspar, quartz, beryl, tourmalines and occasional tantalite. Schorl is dominant along the sharp pegmatite contact to the host rock. The schorl is associated with muscovite, quartz, feldspar, prismatic beryl and occasional red garnet. Quartz has graphic intergrowth with other coarse-grained phases such as K-feldspar and tourmaline (Figure 4.5a). From the wall zone to the core zone, tourmaline colours range from black to dark greenish respectively. Gem tourmaline (Figure 4.5b), usually occurs within pockets that border the quartz core. Light bluish aquamarine occurs with striations on the prism plane as a growth feature (Figure 4.5c). This is in contrast to the occurrence of dark bluish aquamarine in CCC pegmatites. Muscovite is light greyish in colour, and it shows two texturally distinctive varieties with preferred orientation. Clear topaz is mostly associated with pegmatites that do not bear beryl (Figure 4.5d). Occasionally, gem red garnets are present (Figure 4.5e).

The HEM pegmatites, located to the NW of Nkhata Bay (Figure 4.3; Section 3.4.1 and Figure 3.9 for geographical context), are lenticular in shape. They range from 3 m to 45 m wide but their extent is often obscured by alluvial, colluvial and regolith deposits. The pegmatites have prominent NE-NNW strike and show steep to vertical dip angles (Figure 4.6a). Typically, the HEM pegmatites contain epidote, feldspar, beryl, quartz, schorl, muscovite or biotite, with or without tantalite and or garnet. The larger pegmatites show some compositional zoning, consisting of zones containing fine to medium grained quartz, schorl, muscovite and garnet in the marginal zone, coarse grained beryl, blocky plagioclase, „book" muscovite in the intermediate zone. Schorl showing striations dominate in the sharp contacts of HEM pegmatites with the host rock. Rough beryl crystals range in width from a few centimetres to approximately one metre as shown (Figure 4.6b). Euhedral clear quartz is associated with clear green epidote in the core (Figure 4.6c). In particular, HEM2A and HEM3B pegmatite have greyish muscovite and bear both plagioclase and K-feldspar whereas HEM4B bears greyish to black biotite but

does not have K-feldspar. Occasional tantalite was observed in HEM3B pegmatite. Schorl, but no gem tourmaline is present (Figure 4.6d). However, gem aquamarine is present and usually shows light blue colour (Figure 4.6e).

Figure 4.5: Minerals from Pan-African pegmatites from Wenya, Chitipa; (a) an intergrowth of coarse-grained quartz (qtz) with alkali feldspar (K-fs) and tourmaline (tur) from MWC pegmatites; (b) gem tourmaline (tur) showing dark greenish colour, suggesting elbaite end-member; (c) aquamarine is light bluish in colour; (d) clear topaz is mostly associated with pegmatites that do not bear beryl; (e) red garnet is occasionally present.

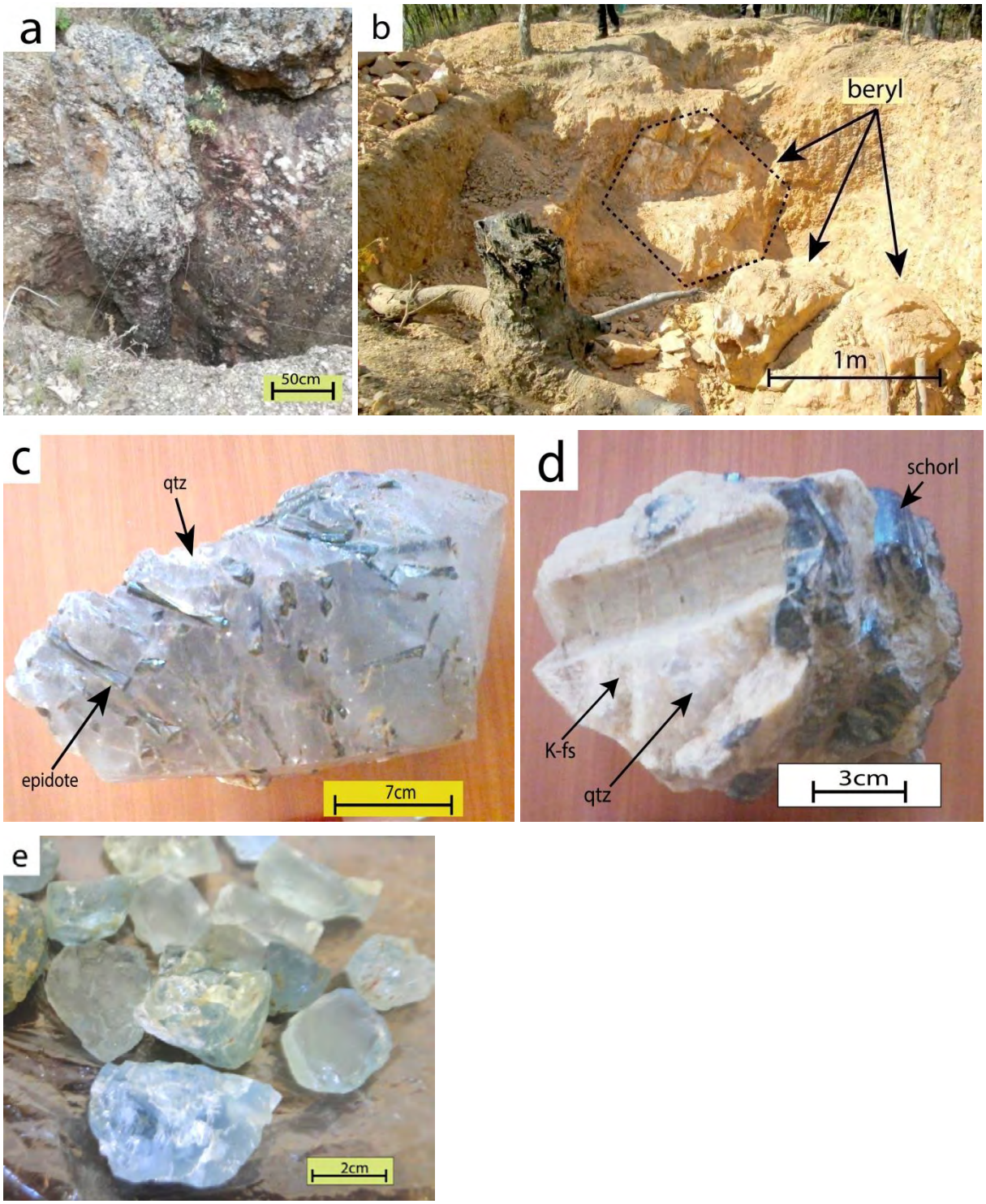

Figure 4.6: Pegmatite exposures and some minerals from Luhomero in Mzimba, northern region Malawi (Figures 3.9 and 4.3); (a) steeply dipping pegmatite; (b) > 1m-sized beryl crystals wide in HEM pegmatite; (c) green epidote inclusions in clear quartz crystal indicating pegmatitic growth; (d) K-feldspar (K-fs), clear quartz (qtz) and schorl with striations, (e) beryl is usually light blue in colour suggesting Fe^{2+} -rich composition (aquamarine).

The GM pegmatites located in the eastern part of Kabwafu (Figure 3.9 and 4.3) show sharp contacts between the zoned pegmatites and hosting gneiss (Figure 4.7a). They have occasional columnar schorl crystals in the bordering wall-rock, a wall zone of fine- to medium-grained

feldspar, white mica and quartz, an intermediate zone with radiating coarse-grain mica growth in intergrown masses, large pink microperthite crystals, and massive monomineralic quartz cores. Miarolitic cavities containing gems are usually found along the margin of the core zone.

The general mineral composition of GM pegmatites is plagioclase, greyish to pale brownish or pale greenish muscovite, K-feldspar, quartz, tourmaline, beryl, with occasional tantalite and monazite, sphene and garnet (Figure 4.7b-d, Figure 4.8a). In particular, tantalite occurs in GM3 and GM5 pegmatites but not in GM1, which is the only pegmatite bearing sphene. No gem tourmalines were observed in the pegmatites except the presence of schorl. Gem beryl is light blue to light yellowish in colour (Figure 4.8b-d) suggesting Fe^{2+} or Fe^{3+} rich compositions respectively. Occasionally, some of the pegmatites bear gem quality garnets (Figure 4.8e). The associated MEM quartz veins occasionally bear light to deep purple amethyst (Figure 4.8f).

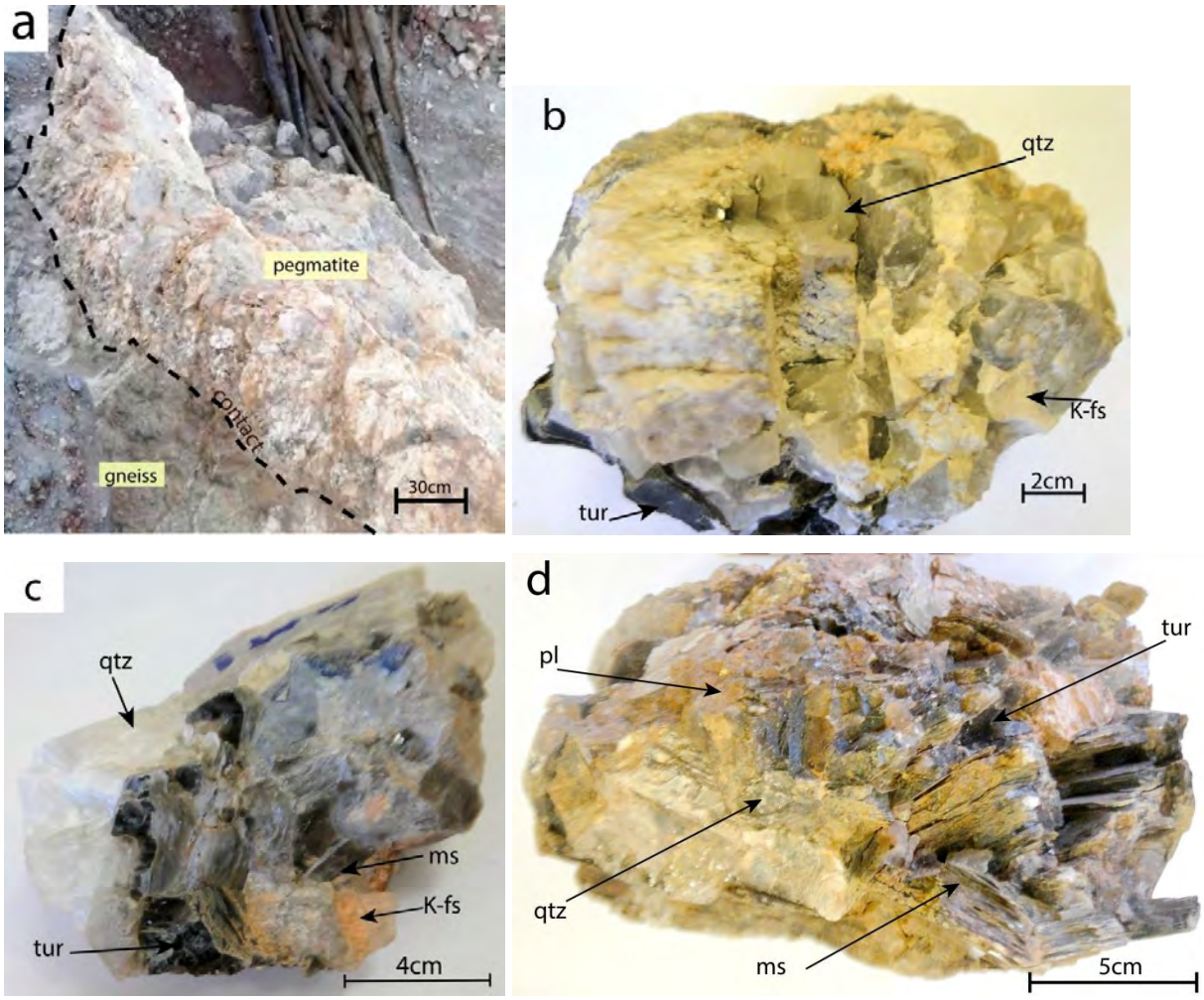

Figure 4.7: Pegmatite and some minerals from Kafukule, Mzimba; (a) Sharp contact of GM pegmatite with host rock; (b) coarse- grained quartz, tourmaline (tur) and K-feldspar (K-fs) from part of the intermediate zone of GM1 pegmatite; (c) coarse-grained muscovite (ms), K-feldspar (K-fs), plagioclase (pl) and quartz (qtz) from intermediate zone of the GM3 pegmatite; (d) Plagioclase (pl), muscovite (ms), K-feldspar K-fs), quartz (qtz) and tourmaline (tur) from the intermediate zone of GM5 pegmatites.

Figure 4.8: Some minerals from Kafukule, Mzimba; (a) Tantalite from the pegmatites; (b-d) Aquamarine ranging from light blue to deep blue to light yellow colour; (e) Gem garnets from the pegmatites; (f) Light to deep purple amethyst from associated quartz veins (MEM1B).

4.3.4 DHD Pegmatites

DHD pegmatites occur within the Pan-African Belt of the Dowa area in the central region of Malawi (Figure 3.9). The Dowa area stretches from Kabanga in the north-northwest to Chamvu in the east and from Mzingwa in the southwest to Gamadzi in the east (Figure 4.9). It includes Mponela, Kayanza, Kamwana, Makanjira and Msungwi. The basement (Figure 3.9) is dominated by gneiss (Walter, 1972; Figure 3.4 and 3.8, Section 3.2.2). The biotite and hornblende-gneisses are commonly garnetiferous and locally graphitic (Kröner et al., 2001). Intrusive rocks include granite, syenite and pegmatites. Lateritic, red-brown sand clay and sandy soil cover parts of the metamorphic basement (Figure 4.9).

DHD pegmatites sampled in this study occur to the southwest of Mponela and Kamwana and to the northeast of Makanjira. The pegmatites mainly produce a variety of gem quality tourmalines.

4.3.5 Geological Setting of DHD Pegmatites

Leucocratic and biotite granites, foliated syenite and pegmatite bodies intruded into the basement gneiss. The leucocratic granites were emplaced at 602.7±0.1 Ma and 577.5±1.0 Ma (Kröner, 2001). The biotite granite with its associated greisen bands, xenoliths of amphibolites and leucocratic banded gneiss, and veins of leucogranite, is part of the Lake Malawi Granite Complex, emplaced in the upper Ordovician to lower Silurian (Snelling, 1963). Furthermore, the biotite granite, locally grading into quartz syenite, was emplaced at 489±14 Ma. This granite magma is of deep crustal origin, with perhaps some moderate contamination (Haslam et al., 1986).

Mica-bearing and tourmaline-bearing pegmatites occur in the area. The mica-bearing pegmatites with NE-SW strike do not have tourmaline. They are unzoned, and form discordant, vertically dipping dykes. They show evidence of deformation, such as foliation and recrystallisation. These pegmatites do not form part of this study because they do not bear gemstones.

The tourmaline-bearing pegmatites, DHD1A, DHD1B, DHD1C and DHD1E, have compositional zonation (Section 4.3.6). They strike NW to SE. The DHD1B and DHD1C pegmatites were emplaced into sillimanite biotite gneiss of the basement complex (Figure 4.9). The sillimanite–biotite gneiss is composed of quartz, plagioclase, microcline, biotite, sillimanite, garnet with occasional pyrite; it has granoblastic texture (Walter, 1972). Individual bodies of these zoned pegmatites range from 10 m to 25 m in width. Poor exposure disallows to determine their extent along strike. The pegmatites have either conformable or cross-cutting relationships with the main structures in the host rocks. The contacts are sharp. No deformation is evident in the pegmatites. The DHD1A and DHD1E pegmatites show similar features and contact relationships to their host rocks like DHD1B and DHD1C, but were emplaced into granoblastic biotite gneiss and graphitic biotite-muscovite gneiss (Figure 4.9). The biotite gneiss is composed of quartz, K-feldspar, plagioclase, biotite, garnet, sphene and apatite. The graphitic biotite-muscovite gneiss contains mica, quartz, feldspar, graphite, plagioclase and sphene (Walter, 1972).

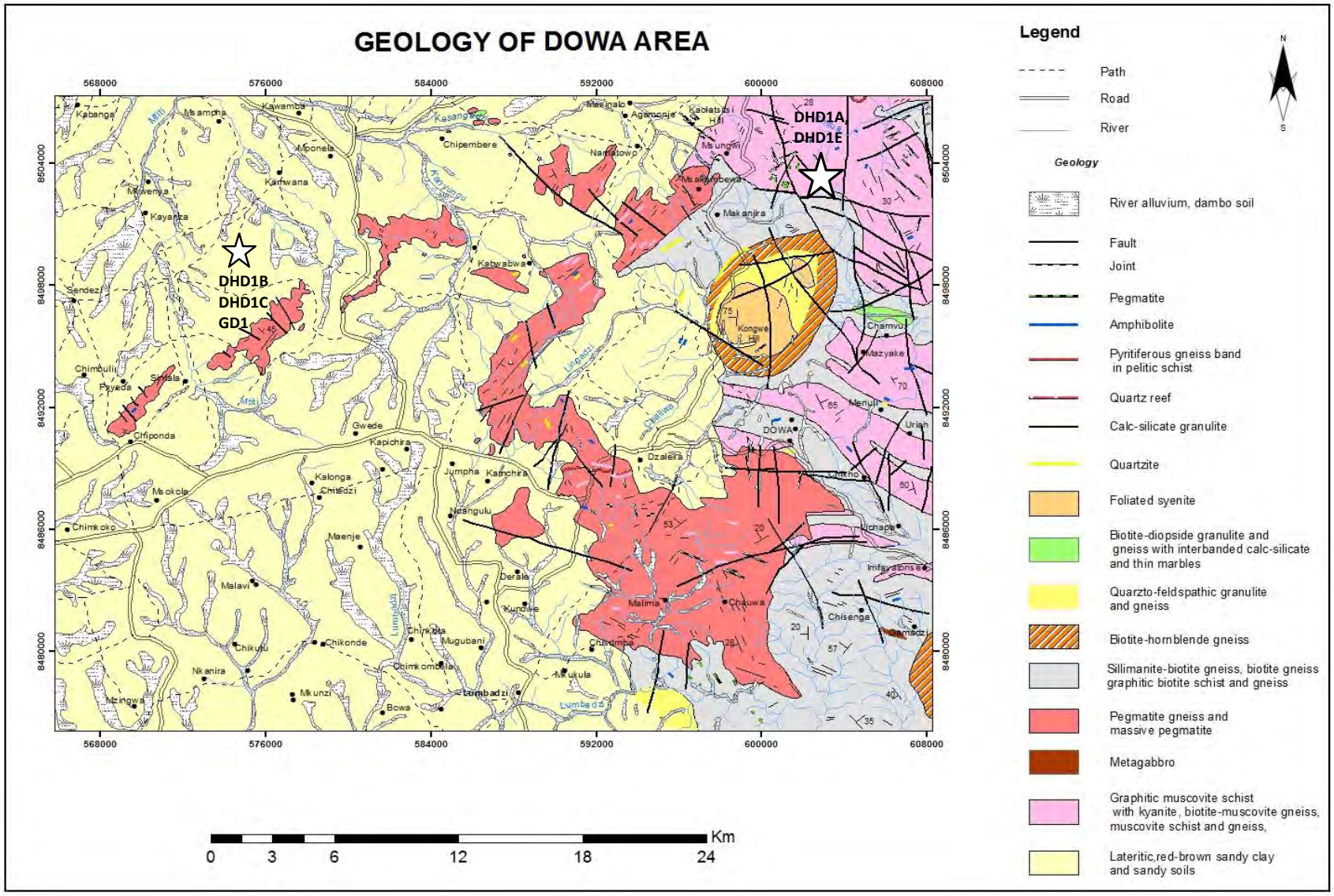

Figure 4.9: Geological map of Dowa Area (modified after Walter, 1972). Sample locations are represented by stars. Geographical context for DHD pegmatites in central Malawi is shown in Figure 3.9.

4.3.6 Mineralogy of DHD Pegmatites

Generally, the phases show grain size variation from fine- to medium- and coarse-grained from the finer-grained wall zone to the medium to coarse-grained core zone. The DHD pegmatites show a systematic distribution of minerals from the wall zone to the core zone, with a slight variation in mineralogy and texture. Principally, the mineralogy of these pegmatites is dominated by felsic minerals, and they mainly comprise of quartz, plagioclase, mica and tourmaline, with or without garnet. Sphene is also common except in DHD1B, which has apatite instead. Occasional tantalite occurs in DHD1B and DHD1C pegmatites. Along the sharp contacts between the zoned DHD pegmatites and the host rocks (Figure 4.10a), disseminated 1-2 cm columnar crystals of tourmaline are common. They occur intergrown with mica plates. The outer zone is mainly composed of feldspar, tourmaline and muscovite whereas the intermediate zone has weathered feldspar, light to deep greenish tourmaline, muscovite and quartz. Where alkali feldspar is present, it is coarse-grained (Figure 4.10b). Notably, K-feldspar has a low concentration in DHD1C pegmatite. K-feldspar shows Carlsbad twinning, while plagioclase, which is the most abundant feldspar in this study area, shows simple twinning. All the DHD pegmatites bear muscovite except for DHD1E pegmatite that bears sporadic biotite (Figure 4.10c, d). In DHD1A pegmatite some quartz show sugary texture and grain sizes from 0.5 to 1cm (Figure 4.10e). The intermediate zone also carries cavities (Figure 4.10f, Figure 4.11a, b) that usually contain euhedral quartz crystals, tourmaline, occasional clay and greyish to brownish mica. Some tourmaline occurs as inclusions in clear quartz crystals (Figure 4.11c). Coarse-grained muscovite is presented in Figure 4.11d. Sporadic muscovite occurs in the quartz-rich core. Gem tourmalines from the intermediate zone and from the miarolitic cavities close to the boundary with the central core, have a colour variation from pale green to deep green (Figure 4.11e, f, Figure 4.12a). However, gem tourmalines in the cavities reach up to 9 cm. Notably pegmatites from an area adjacent to the northern part of Dowa, bear multi-coloured tourmalines with colour range from light purple to light green (Figure 4.12b).

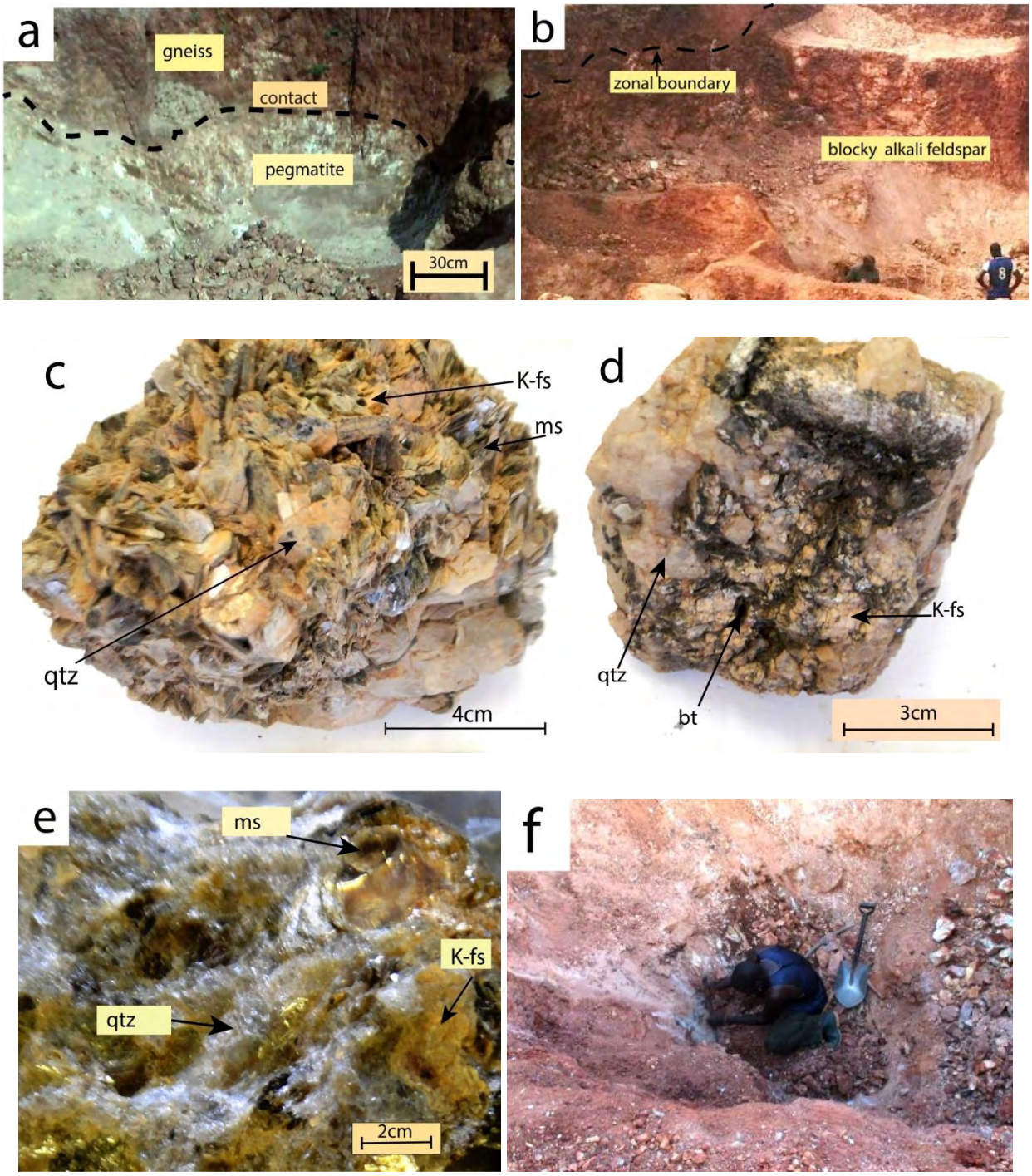

Figure 4.10: Emplacement of Pan-African pegmatites and their associated minerals from Dowa, central Malawi; (a) Sharp contact with host gneiss; (b) blocky feldspar (K-fs) in intermediate zone; (c) normal rosettas and clusters of muscovite (ms), quartz (qtz) and K-feldspar (K-fs) from the intermediate zone of DHD1C pegmatite; (d) DHD1E pegmatite medium- to coarse-grained texture; (e) quartz (qtz) showing sugary texture; (f) tourmaline (tur) extraction from pocket.

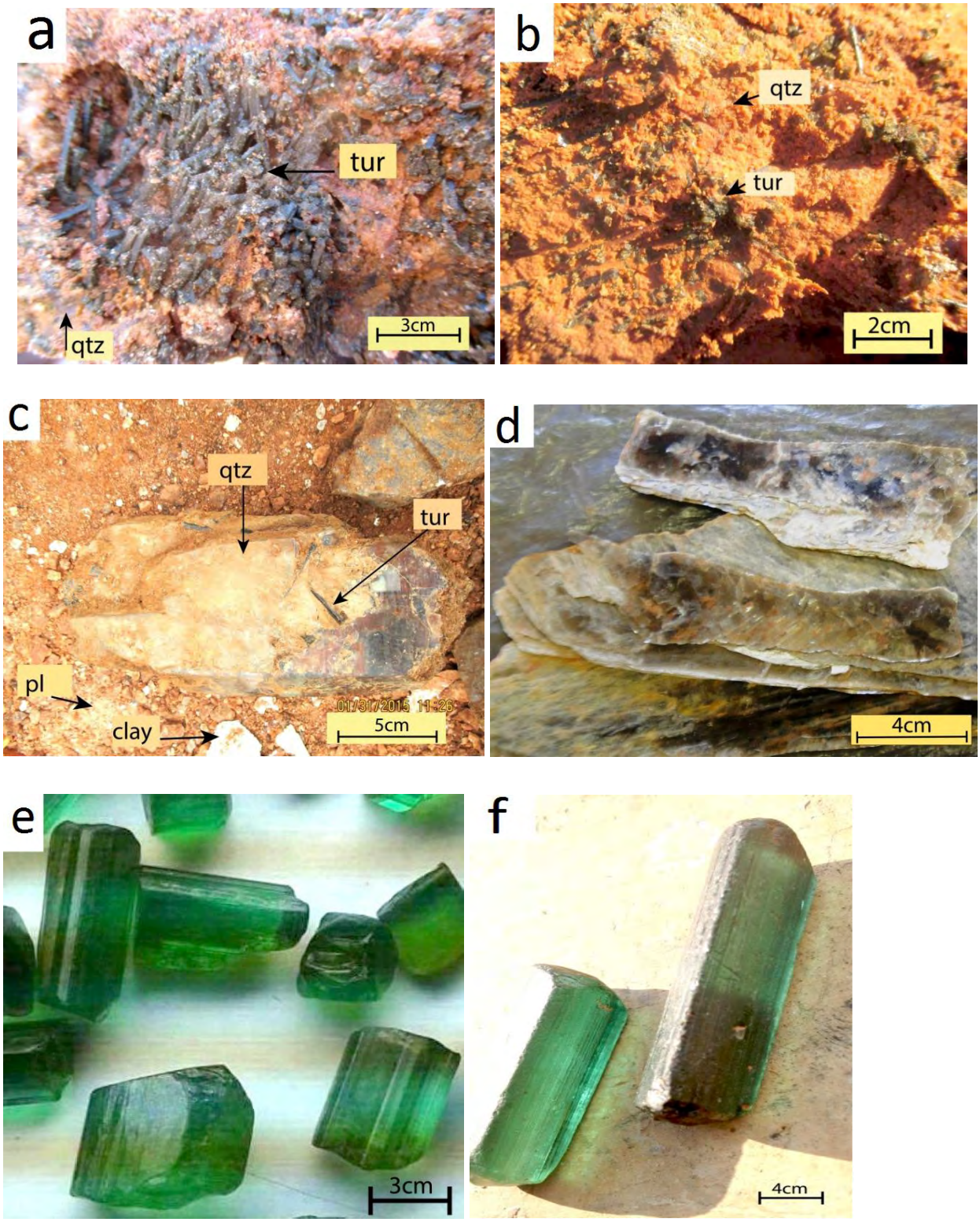

Figure 4.11: Pan-African pegmatites and their associated minerals from Dowa, central Malawi; (a) tourmaline (tur) in a pocket; (b) tourmaline-quartz (tur-qtz) intergrowth in intermediate zone close to the core zone; (c) quartz (qtz) with tourmaline and pocket clay; (d) coarse- grained muscovite (ms); (e-f) green tourmaline (tur) from the pegmatites located SW of Mponela and Kamwana (Figure 4.9), the green colour could be due to Fe^{2+}.

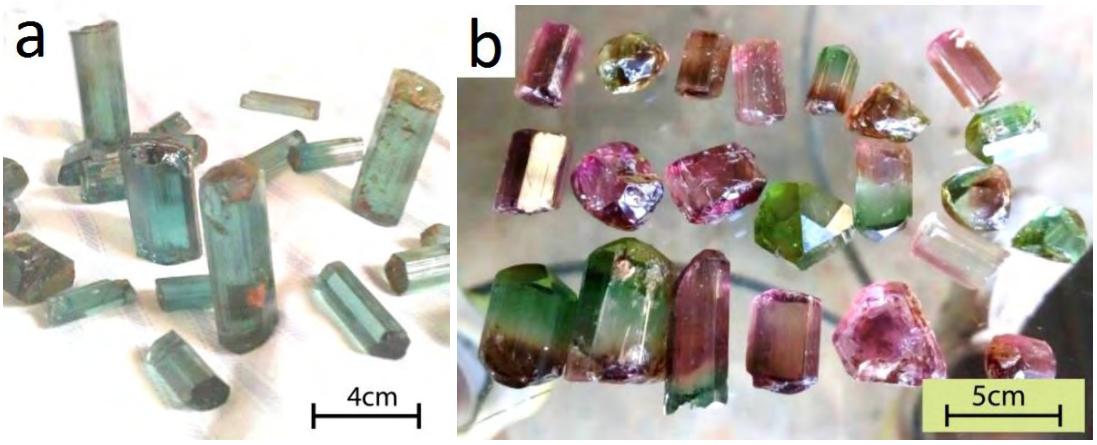

Figure 4. 12: Emplacement of Pan-African pegmatites and their associated minerals from Dowa, central Malawi; (a) light blue tourmaline (tur) from cavities taken from pegmatites SW of Mponela and Kamwana (Figure 4.9); (b) multi-coloured tourmalines (tur) found in adjacent area to the northern part of the study area in Dowa. The purple colour could be from traces of Mn^{3+}.

4.3.7 GNS, MNS and CUB Pegmatites

GNS, MNS and CUB pegmatites occur within the Pan-African Belt in central and southern Malawi (Figure 3.9). The Ntcheu-Balaka area stretches from Chingo in the NW to Zamimba in the NE and from Bayani in the SW to Mitoche in the E (Figure 4.13). It includes Ntonda and Senzani. The basement complex to the western part (Figure 3.9) is dominated by gneiss, whereas to the NE part from Zamimba to the eastern boundary on the study map, granulites predominate (Walshaw, 1965; Figure 3.9; Section 3.4.1). The biotite and hornblende-gneisses are commonly garnetiferous and locally graphitic (Kröner et al., 2001). GNS and MNS pegmatites intrude into gneiss to the west part of Zamimba, whereas CUB pegmatites intrude into granulite and gneiss east of Zamimba. GNS and MNS pegmatites mainly produce a variety of gem-quality tourmalines, sunstone and in places garnet, whereas CUB pegmatites produce gem-quality amethyst. The GNS and MNS pegmatites shall be presented separately from CUB pegmatites in the subsequent sections.

4.3.8 Geological Setting of GNS, MSN and CUB Pegmatites

The GSN pegmatite bodies comprise GNS1, GNS3, GNS4, GNS6 and GNS7 pegmatites. They range from 8m to 30m in width, but most of them are obscured by overburden. The pegmatites are hosted in gneiss, and the contact between the pegmatites and host rock is sharp. GNS1 and GNS3 pegmatites were emplaced into granular banded garnet-hornblende-diopside gneiss (Walshaw, 1965). The pegmatites are concordant or change from concordant to discordant to the foliation in the host rocks. According to Walshaw (1965), the gneiss is composed of hornblende,

biotite, epidote, quartz, oligoclase, accessory ilmenite, sphene, zircon and garnet. It also shows patches of intense tourmalinisation close to the pegmatite.

GNS4, GNS6 and GNS7 pegmatites were emplaced into hornblende-biotite-gneiss. The pegmatites have conformable to cross-cutting relationships with their host rocks. The gneiss is fine- to medium-grained, and is mainly composed of quartz, biotite, hornblende, and feldspar with accessory ilmenite, zircon and sphene, but abundant microcline or microperthite occurs in the western part of the current study area (Walshaw, 1965).

MSN and GN1 pegmatite bodies are approximately 7m to 20m wide, but often not well exposed. MSN1B, MSNB2, MSN3A, MSN3D, MSN7 and GN1 pegmatites were emplaced into hornblende-biotite gneiss. MSN7 was used for fluid inclusion studies. GN1 was dated using the Rb-Sr isotope system. The MSN and GN1 pegmatites have discordant and cross-cutting relationships to the hosting gneiss, and the contacts are sharp. No deformation is evident in the pegmatites, except minor brittle or ductile overprints along dyke margins of pegmatites GNS1 and MSN1B.

Furthermore, to the north-eastern part of Balaka, the CUB pegmatites intrude the granulite and biotite garnet gneiss of the basement complex (Bloomfield and Garson, 1965). The CUB pegmatite group comprises of CUB1A, CUB1B, CUB2B, CUB3B, CUB4B and GU1 pegmatites. GU1 was used for Rb-Sr dating. Individual CUB pegmatite bodies are approximately 4m to 15m wide; however, their lateral extent is largely obscured by residual deposits and colluvium which limit access to their structural details. CUB pegmatites have conformable to cross-cutting relationships to the biotite garnet gneisses along sharp contacts.

The biotite garnet gneiss is fine- to medium- grained, with a granular texture. Occasionally, host rocks are strongly foliated and strongly contorted into folds (Walshaw, 1965). Rose quartz veins occur in places. The hosting granulites mainly comprise of plagioclase, hypersthene, pyroxene, with accessory apatite, zircon, calcite and occasional pink garnet, while biotite-garnet gneiss is composed of quartz, feldspar, biotite, hornblende, diopside and garnet (Walshaw, 1965).

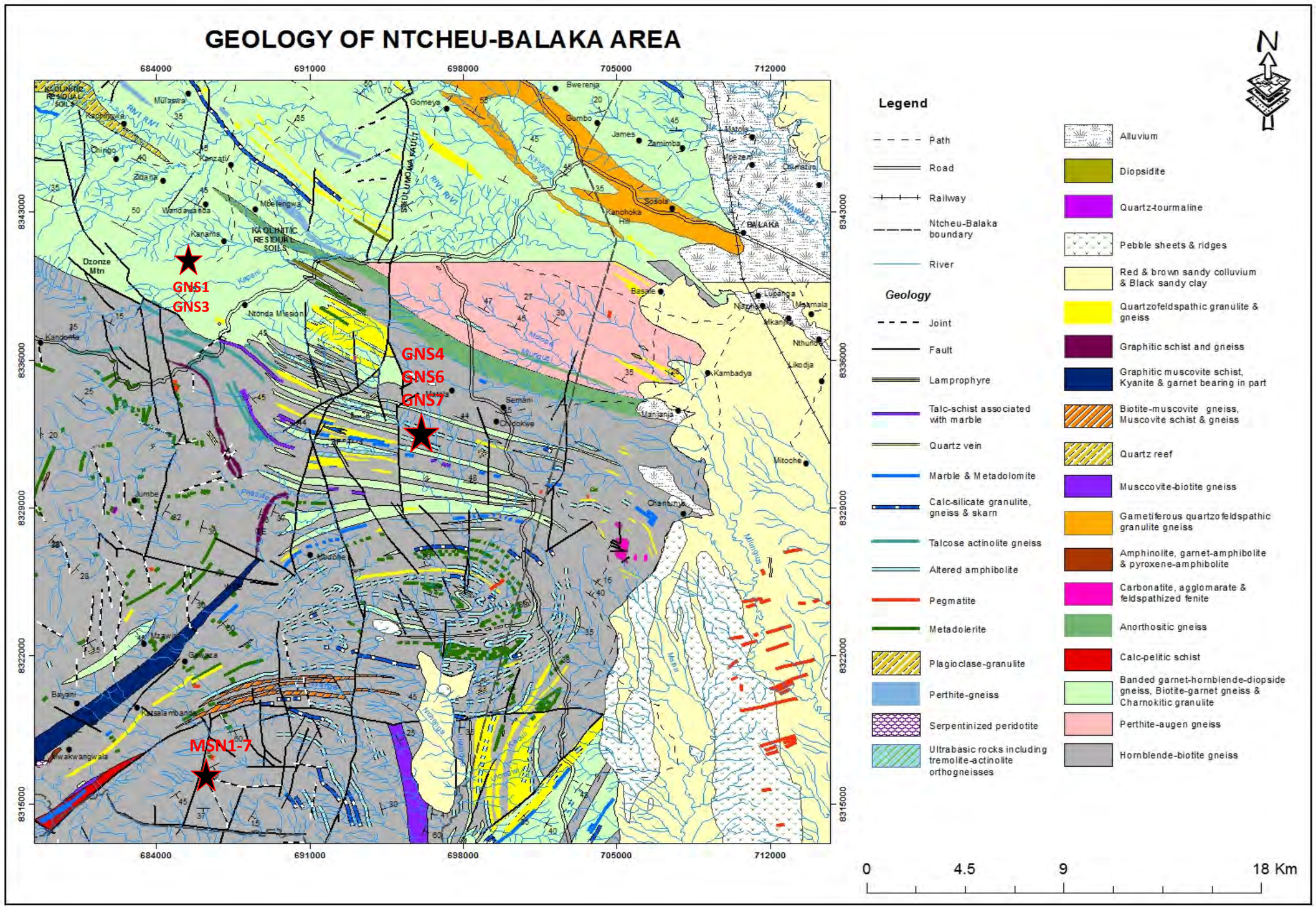

Figure 4. 13: Geological map of Ntcheu-Balaka area in southern Malawi (modified after Walshaw, 1965). Sample locations are represented by stars. Refer Figure 3.9 for the geographical context of this area.

4.3.9 Mineralogy of GNS, MSN and CUB Pegmatites

In most GNS and MSN pegmatites, the internal zonation of intermediate and core zone is obscured by soil cover. However, schorl is dominant along the sharp contacts with the host rock (Figure 4.14a). The grain size varies from fine- to medium- to coarse-grained from the wall zone to the quartz core. Some of the zoned pegmatites occasionally show miarolitic cavities that carry euhedral quartz, tourmaline and muscovite. Gem tourmaline is greenish in colour. Overall, mineralogically and texturally, the pegmatites are similar to each other, but with slight variations. This shall be discussed further in Chapter 9 after considering their mica geochemistry in Chapter 7. The schorl is present as isolated crystals or in clusters with random or radial crystal orientations (Figure 4.14b-e).

All GNS pegmatites show quartz, plagioclase, alkali feldspar, tourmaline and muscovite, garnet, monazite and sphene. Tantalite occurs in the GNS1 pegmatite, which has greenish muscovite, often intergrown with tourmaline. This seems to be in agreement with an observation made by Carter and Bennett (1973) of presence of tapiolite, a Fe-Ta oxide, in some pegmatites. Muscovite is found in all the zones (Figure 4.14e-f); in some samples there are two texturally distinct varieties of muscovite. In GNS3 pegmatite, muscovite is pale greenish to medium brown, whereas in GNS4 pegmatite it is light brown. The muscovite is light to pale greenish in GNS6 pegmatite but greenish to amber in GNS7 pegmatite. Blocky feldspar dominates the intermediate zone (Figure 4.15a, b). Tourmaline has light to dark green colours (Figure 4.15c).

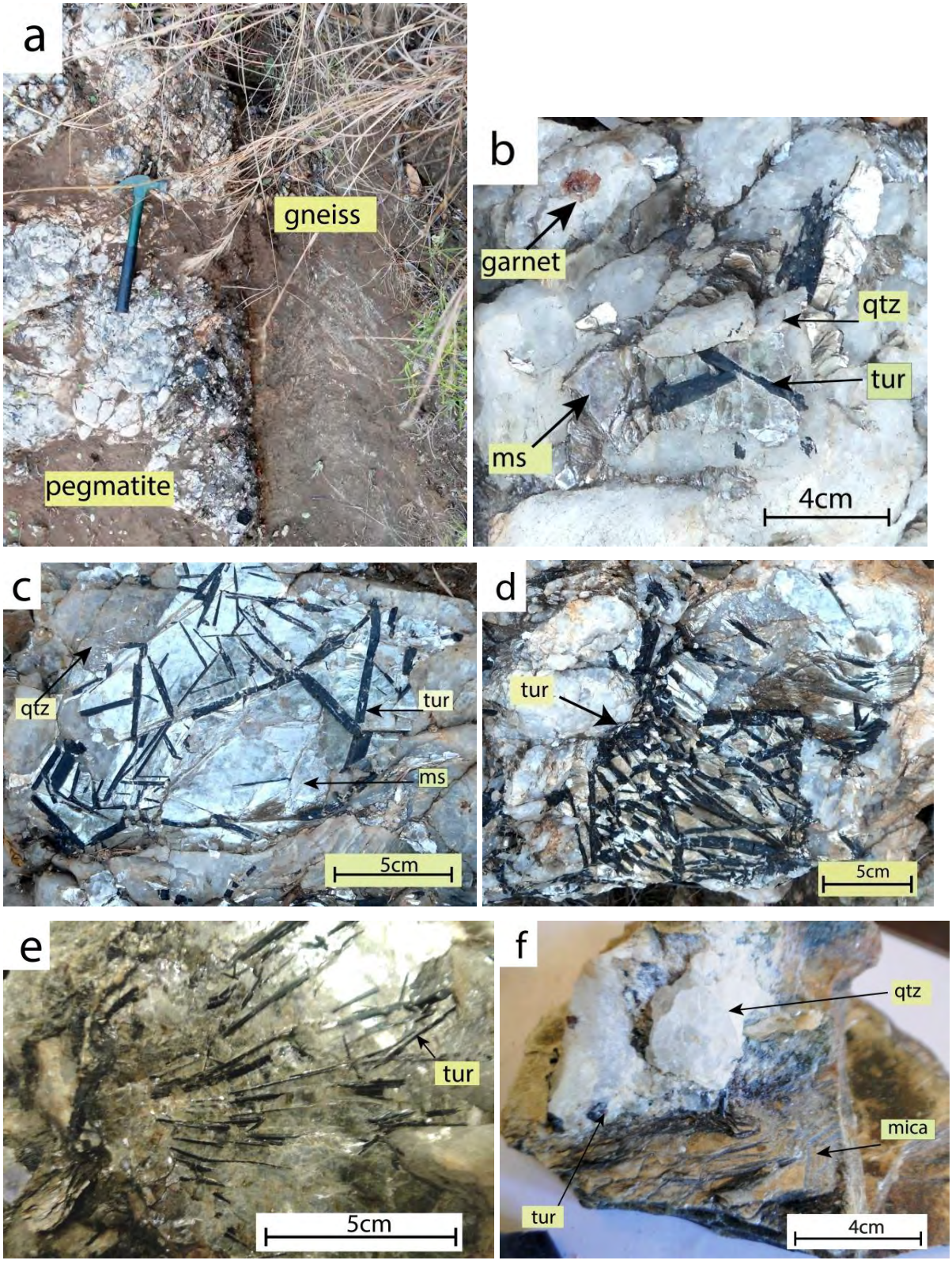

Figure 4. 14: Pan-African pegmatites and their associated minerals from Ntcheu, central Malawi; (a) Sharp contact between GNS1 pegmatite and host rock; (b) Coarse-grained quartz (qtz), black tourmaline (tur), muscovite (ms) and red garnet in pegmatite; (c) random orientation of tourmalines (tur) in GNS4 pegmatite; (d) comb texture displayed by tourmaline (tur) in a pegmatite; (e) radiating tourmaline (tur) crystals up to 5 cm from GNS1 pegmatite; (f) intergrowth of coarse-grained muscovite (ms), tourmaline (tur) and quartz (qtz).

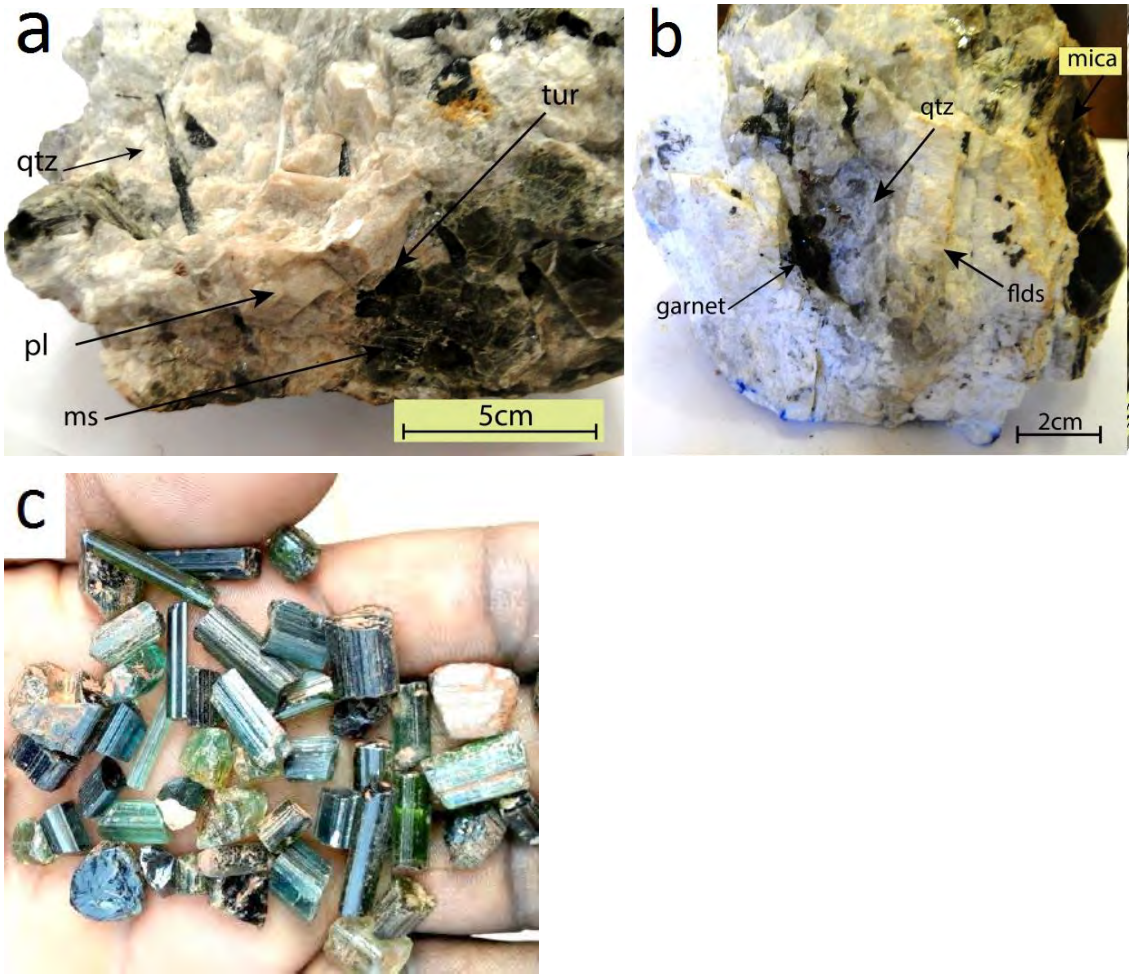

Figure 4. 15: Pan-African pegmatite and their associated minerals from Ntcheu, central Malawi; (a) intergrowth of quartz (qtz), muscovite (ms), plagioclase (pl) and tourmaline (tur) in GNS3 pegmatite; (b) intergrowth of alkali feldspar (K-fs), quartz (qtz), muscovite (ms) and garnet from GNS6 pegmatite; (c) light to dark green tourmaline (tur) suggesting Fe^{2+} rich compositions.

All MSN pegmatites show quartz, plagioclase (oligoclase), alkali feldspar, tourmaline and muscovite (Figure 4.16a-d). The MSN pegmatites show a variation in the distribution of garnet, sphene and monazite with none of the phases observed macroscopically in MSNB2 pegmatite. In MSN1B pegmatite muscovite varies from light grey to greenish. It is light brownish in MSNB2 pegmatite, light greyish in MSN3A and MSN3D pegmatites whereas in GN1 pegmatite it is greenish. GN1 pegmatite was used for age dating. Unlike in GNS pegmatites, tourmaline does not show radial crystal growth but random distribution and orientation. The gem tourmaline in MSN pegmatites is greenish whereas garnet is pinkish to light reddish in colour (Figure 4.16e, f). Gem oligoclase (sunstone) occurs in veinlets in the pegmatites.

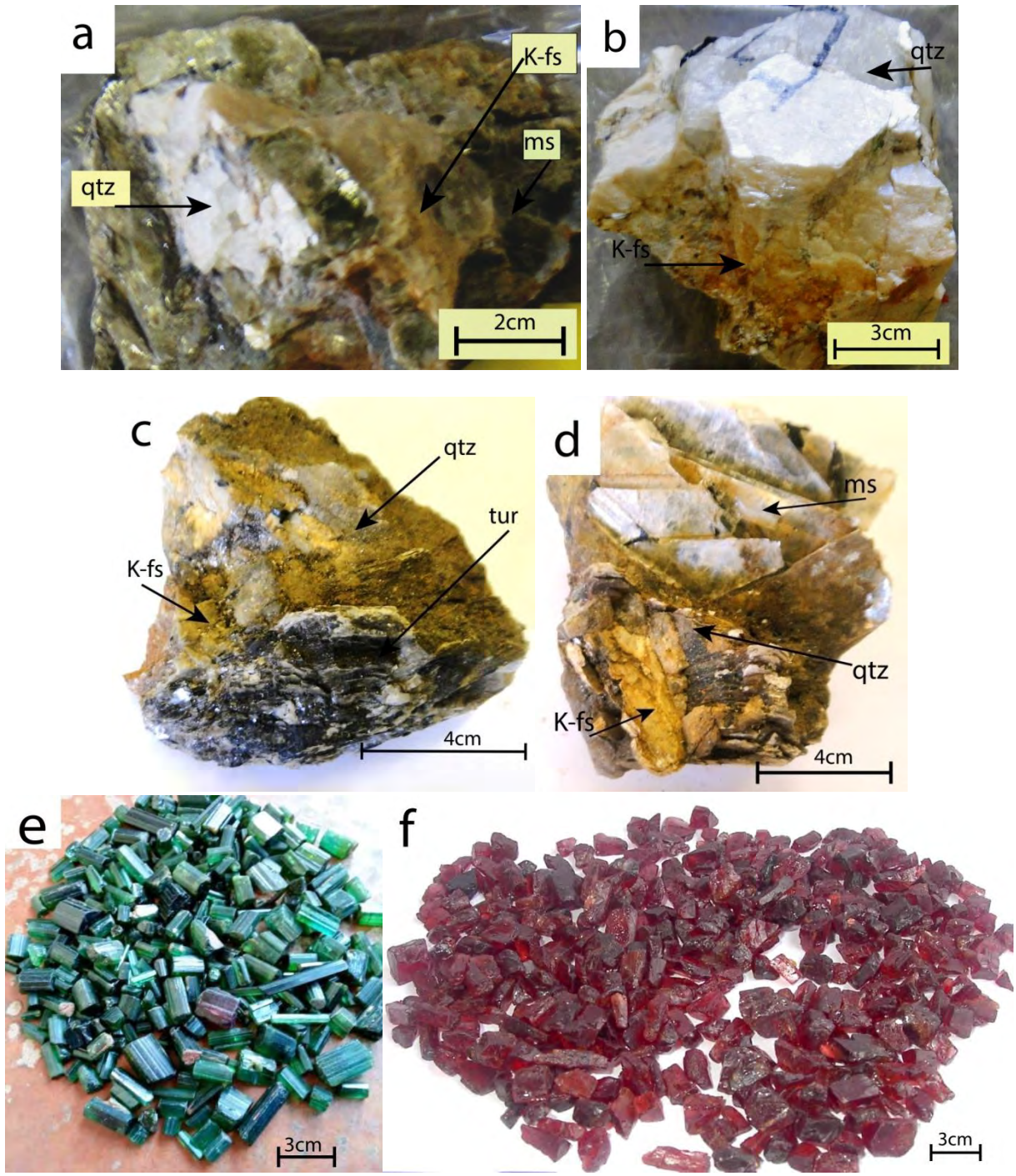

Figure 4. 16: Photographs of coarse grained mineral phases from MSN pegmatites from Ntcheu, central Malawi; (a) muscovite (ms), tourmaline (tur) and quartz (qtz) from MSN1B pegmatite; (b) quartz (qtz), K-feldspar (K-fs) from MSN2B pegmatite; (c) muscovite (ms), feldspar (K-fs), schorl and quartz (qtz) from MSN3A pegmatite; (d) muscovite (ms), K-feldspar (K-fs) and tourmaline (tur) from GN1 pegmatite; (e) green gem tourmaline (tur) from MSN pegmatite; (f) pinkish to reddish gem garnet from MSN pegmatite.

The CUB pegmatites show sharp contacts to their host rock without alteration zones. Generally, the mineralogy consists predominantly of biotite, K-feldspar, quartz, plagioclase and accessory garnet, ilmenite and monazite. GU1 pegmatite, used for age dating, is composed mainly of K-

feldspar, plagioclase and biotite (Figure 4.17a). Quartz in the pegmatites shows amethyst colours of different intensities, from light to deep purple. The growth ranges from early growth stage 1 to late growth stage 4 (Figure 4.17b-e). CUB4B is from stage 1, CUB3B from stage 2, CUB2B from stage 3, while CUB1B is from stage 4. Occasionally, the amethyst is twinned and has double terminations. The biotite varies from brownish to blackish in colour from stage 1 to stage 4 respectively. The feldspar has dark grey to pinkish colour. Some pegmatites contain epidote (Figure 4.17f).

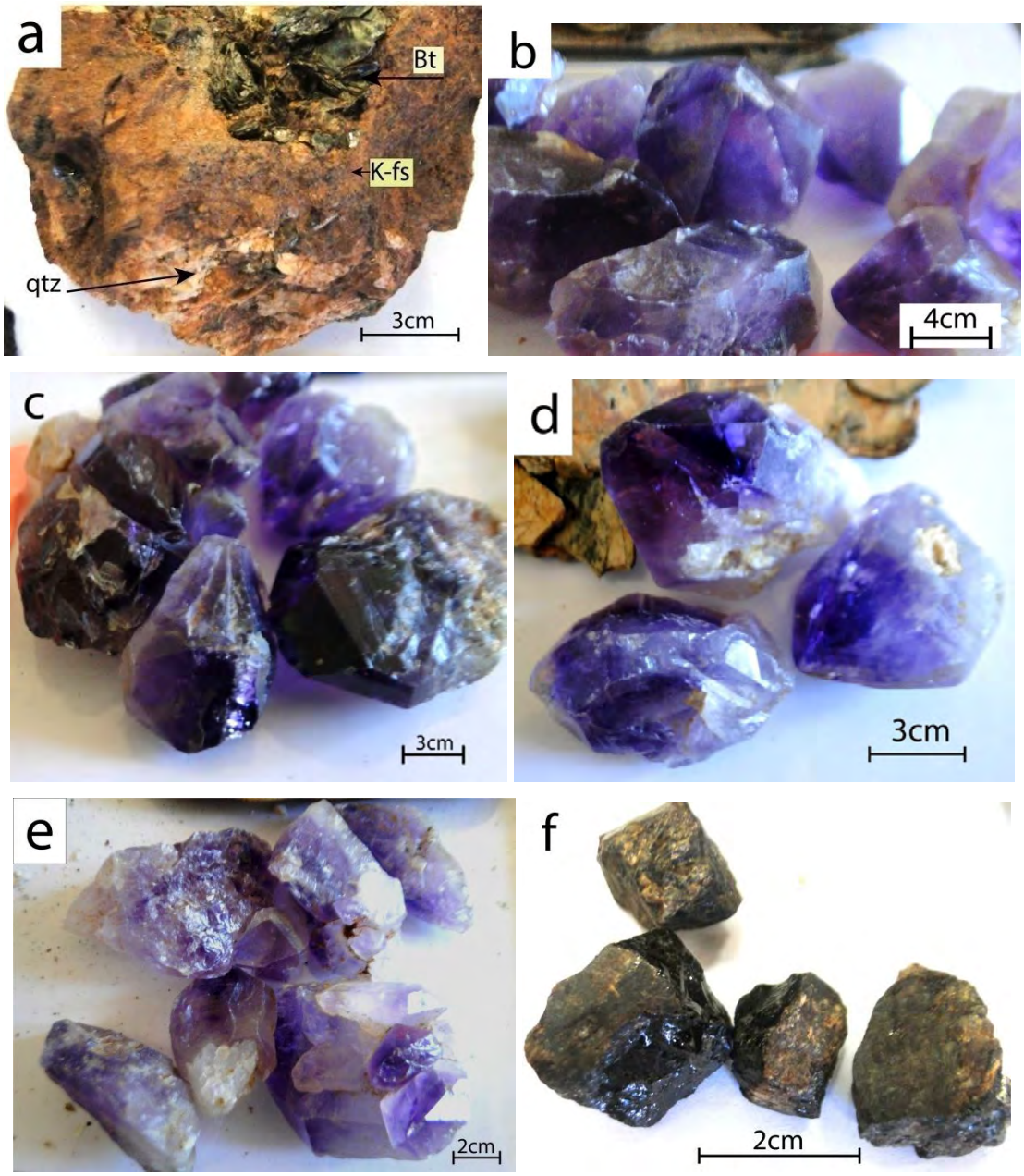

Figure 4. 17: Minerals from amethyst bearing pegmatites in Balaka, south Malawi; (a)) sample GU1 with mica, quartz (qtz), and feldspar (K-fs) used for dating; (b) CUB1A dark amethyst from pegmatite core zone (stage 4); (c) CUB2A lighter amethyst close to the core (stage 3); (d) CUB3A lighter amethyst (stage 2); (e) CUB4A clear quartz to very light amethyst (stage1); (f) epidote.

4.3.10 MNM, NNO and THMB Pegmatites

MNM, NNO, and THMB pegmatites occur in the Pan-African Belt in southern Malawi (Figure 3.9). MNM and NNO pegmatites occur in Mangochi area that stretches from Mwachikumba in the NW to Mangochi Hills in the SE (Figure 4.18) and includes Uzuzu and Cape Maclear. The basement complex is predominated by a banded two-pyroxene granulites and gneisses (King and Dawson 1976; Figure 3.9; Section 3.4.1). MNM pegmatites occur south of Cape Maclear, whereas NNO pegmatites occur north of Uzuzu (Figure 4.18).

The THMB pegmatites were emplaced into hornblende biotite gneiss, but host rocks and pegmatites are often covered by regolith. These pegmatites bear gem tourmaline. Pegmatite ages were obtained using U-Pb dating on zircons (see Chapter 6). The pegmatite occurrences are presented in detail in section 4.3.8.

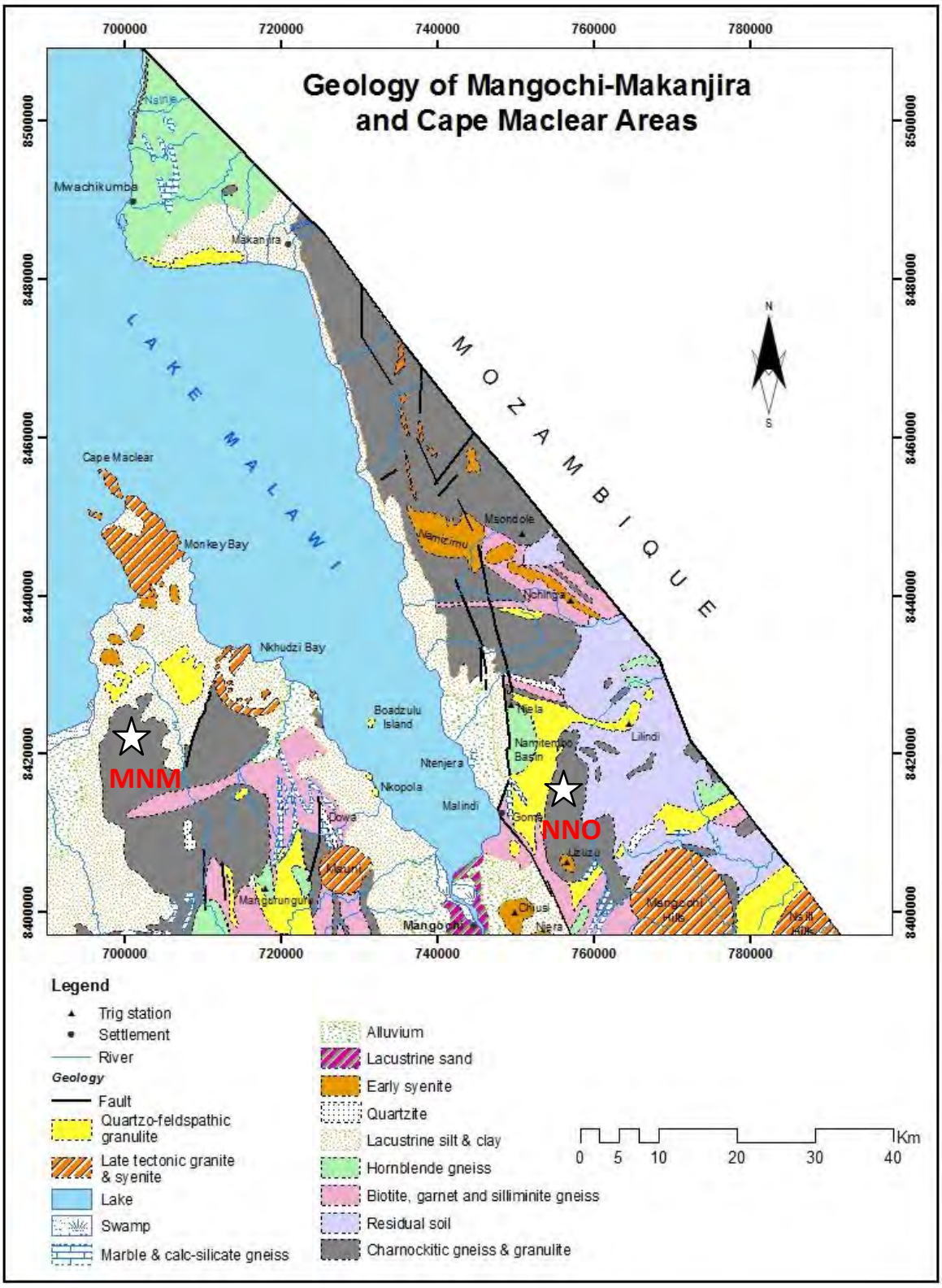

Figure 4. 18: Map of geology of Mangochi–Makanjira–Cape Maclear areas (modified after King and Dawson, 1976). The sampled pegmatites are represented by star symbols.

4.3.11 Geological Setting of MNM, NNO and THMB Pegmatites

The *MNM pegmatites* located south of Cape Maclear and *NNO pegmatites* from north of Uzuzu range in width from 8 m to 20 m, as far as exposure conditions allow measurements. The pegmatites were emplaced into medium- to high-grade gneiss and granulite or, in some areas, migmatitic garnet-biotite-gneiss. Migmatised zones may grade into patches that resemble feldspathic pegmatite, completely obliterating the gneissic banding. Biotite granite and biotite-hornblende-quartz syenite are intrusive into this basement. Quartz-feldspar pegmatite and aplitic veins with pegmatite cores occur within the biotite-granite and in its contact zone with the basement gneisses. Furthermore, King and Dawson (1968), reported a swarm of microgranite and microsyenite dykes, microdiorites and microtonalites in this area.

The MNM and NNO pegmatites analysed in this study intruded either concordant or discordant to the foliation in the basement gneisses, and are sub-vertical in orientation. They have a NNW strike and are undeformed. Their contacts with the host rock are not fully exposed. The gneiss and granulite have granoblastic texture. According to Dawson and Kirkpatrick (1976), the granulites contain hypersthene, diopside, garnet, hornblende, biotite, plagioclase, orthoclase, apatite, spinel and quartz. The garnet-biotite gneiss is composed of garnet, biotite, quartz, oligoclase, titano-magnetite with accessory zircon and apatite.

In the Cretaceous to Jurassic the area was affected by East African Rift tectonics and magmatism. Prominent are the intrusion of the Chilwa Alkaline dykes and Rift Valley faulting (Walshaw, 1965).

The *THMB pegmatites* range from 3 m to 15 m in width. Younger cover mostly obscures their outcrop. The pegmatites have conformable to cross-cutting relationships with gneissosity in their host. The pegmatites do not show any sign of deformation. The contact between the pegmatites and host rock gneisses is sharp. The gneiss has a granoblastic texture and is composed of hornblende, biotite, epidote, clinozoisite, oligoclase, microcline, quartz, accessory sphene, zircon and titanomagnetite (Bloomfield and Garson, 1965).

4.3.12 Mineralogy of MNM, NNO and THMB Pegmatites

The *MNM1D pegmatites* show gradual grain size decrease towards the host rock. The pegmatites are essentially composed of intergrown coarse-grained K-feldspar, biotite, zircon, quartz and accessory phases of sphene and monazite. Biotite shows iron staining. Zircon reaches up

approximately 30 mm in size and is generally euhedral. It is elongated, prismatic with bipyramidal terminations, and it has well-defined faces (Figure 4.19). Gem zircon is purple in colour.

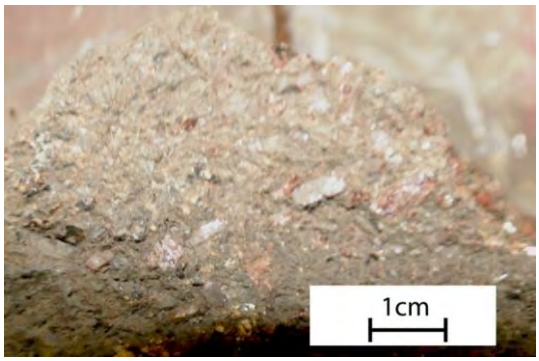

Figure 4. 19: Euhedral zircon in MNM pegmatite sample from Nankhwali in Mangochi.

The *NNO1 pegmatites* also seem to show gradual grain size decrease towards the host rock. No full section through NNO1 pegmatite is exposed. They are composed of large crystals of K-feldspar, tourmaline, quartz, fairly abundant books of muscovite, and the accessory phases garnet, zircon and ilmenite. Some of the phases are shown in Figure 4.20a. The zircon is generally euhedral, prismatic with bi-pyramidal terminations, and it has well defined faces (Figure 4.20b). Gem tourmaline, brown in colour occurs in these pegmatites.

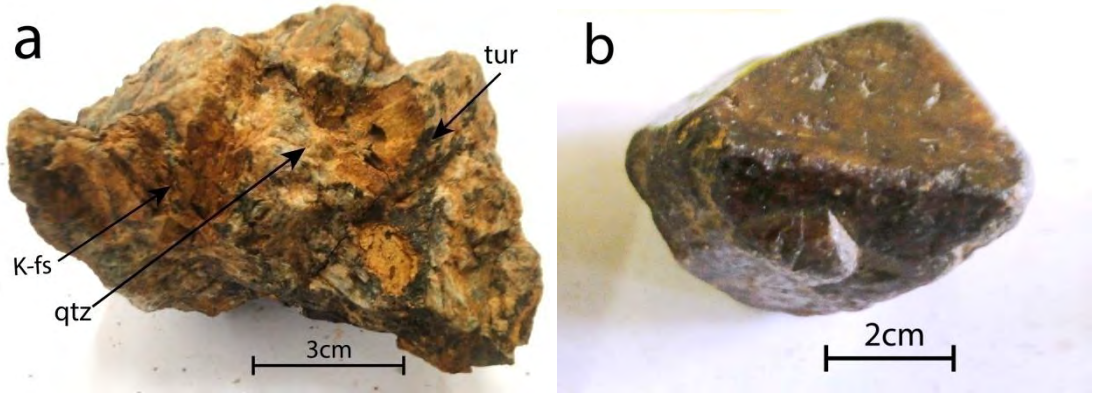

Figure 4. 20: Samples from NNO pegmatites. (a) Tourmaline (tur), K-feldspar (K-fs), muscovite (ms) and quartz (qtz); (b) zircon

The *THMB pegmatites* are mainly composed of intergrown coarse-grained K-feldspar, apatite, amphibole, zircon, quartz, biotite and ilmenite. Zircon reaches up approximately 3.5 cm in size and is generally euhedral (Figure 4.21). It is prismatic with bi-pyramidal terminations, and it has well defined faces. The texture reveals a graphic intergrowth of coarse-grained minerals. The pegmatites produce light brownish to light pinkish gem quality zircons.

Figure 4.21: Zircon from THMB pegmatite.

4.4 MESOZOIC PEGMATITES

4.4.1 ZA Pegmatites

These pegmatites are related to early East-African Rift magmatism (see Chapter 6; Section 6.4). ZA pegmatites are exposed along the streams cutting Bwanje Valley close to the border of central and southern Malawi in the Chilwa Alkaline Province (Figure 3.9, Figure 3.10, and Section 3.4.2). The ZA pegmatites are over a hundred kilometres away to the northwest of the well-known Malosa pegmatites that produce world-class spectacular mineral specimens (Figure 4.22a, b). The ZA pegmatites bear gem zircons and other quality mineral specimens.

4.4.2 Geological Setting of ZA Pegmatites in Bwanje Valley

ZA pegmatites are poorly exposed. They are undeformed and were emplaced into biotite gneiss and quartzo-feldspathic granulite (Walshaw, 1965). They have discordant cross-cutting relationships to the host gneiss, and the contact is sharp. The host rocks are fine- to medium-grained and show granular texture. According to Walshaw (1965), the quartzo-feldspathic granulite is mainly composed of quartz, feldspar, biotite hornblende and diopside, but the rocks grade laterally into syenite gneiss with very little quartz.

4.4.3 Mineralogy of ZA Pegmatites in Bwanje Valley

The ZA pegmatites show gradual grain size decrease towards the host rock, but there is no alteration along the contact. The pegmatites show similar mineralogy to Malosa pegmatites (Figure 4.22a-b; Kankuzi, 2009). The ZA pegmatites mainly comprise of intergrown coarse-grained microcline, aegerine, quartz, biotite and zircon (Figure 4.22c). Zircon is euhedral and prismatic, and it has light brownish colour (Figure 4.22d).

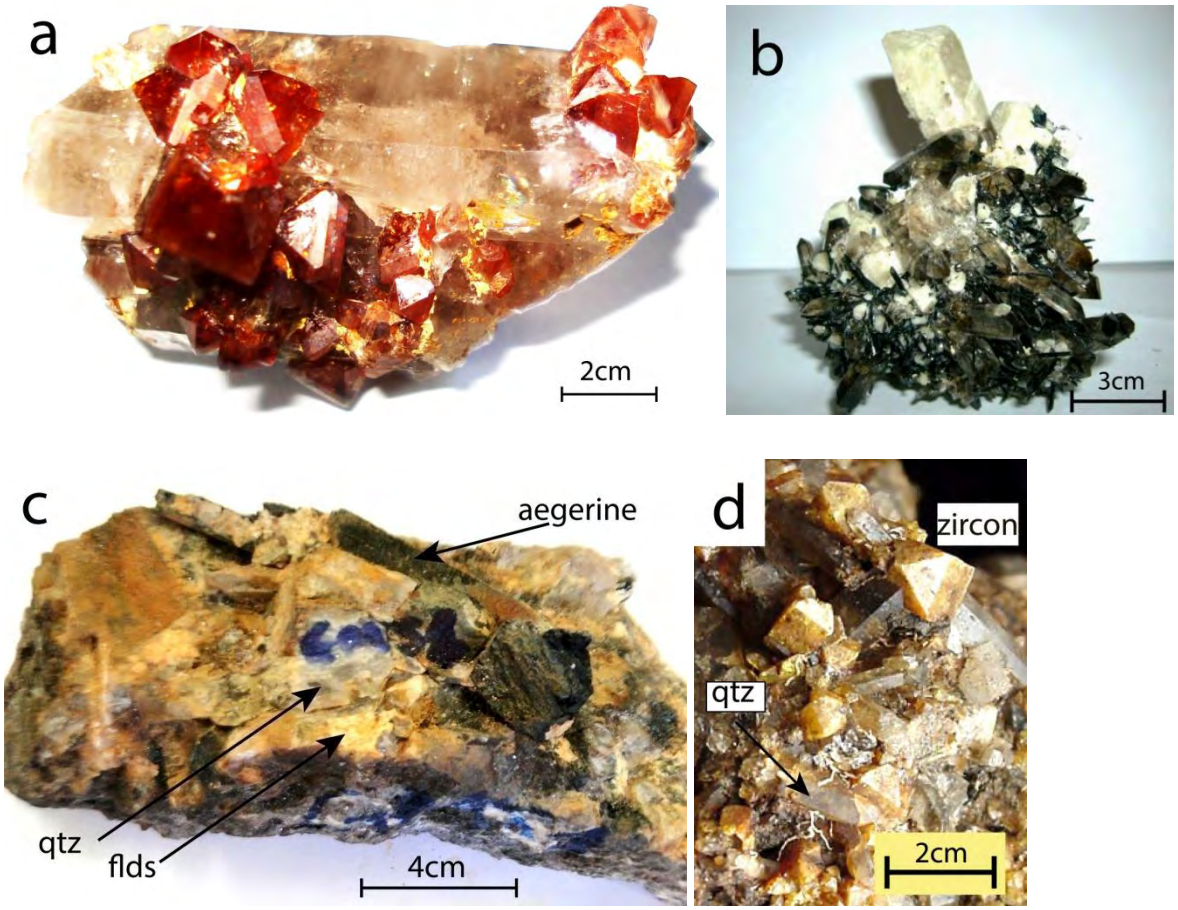

Figure 4.22: The Malosa and Bwanje pegmatites; (a) Red zircon on coarse-grained quartz (qtz); (b) Intergrowth of quartz (qtz), aegerine and microcline crystals. Both (a) and (b) are from Malosa pegmatites (Kankuzi, 2009); (c) coarse- grained quartz (qtz), aegerine and microcline; (d) brownish zircon and quartz (qtz) crystals. Both (c) and (d) are from ZA pegmatites in Bwanje Valley in Ntcheu.

5. METHODOLOGY

5.1 INTRODUCTION

This chapter describes the methods used to achieve the objectives set in Chapter 2. This chapter deals with methods for Rb-Sr mineral isochron (Thermo Scientific TRITON thermal ionisation mass spectrometer) and U-Pb zircon dating (LA-SF-ICP-MS), mica geochemistry (EPMA, LA-ICP-MS), fluid inclusion microthermometry and Raman spectroscopy.

5.2 ANALYTICAL METHODS - GEOCHRONOLOGY

5.2.1 Rubidium-strontium

For mineral separation, small, hand specimen-sized samples were crushed down to the average grain size of the main mineral phases. Crushed samples were rinsed twice with distilled water and once with analytical grade ethanol. From the crushed samples, mineral separation of muscovitic white mica, biotite, K-feldspar and/or plagioclase was done by handpicking under a binocular microscope. Mineral separates typically consisted of one or two individual fragments of pegmatitic macrocrystals. Characteristic sizes were ~15 to 20 mg for biotite and white mica, and ~30 mg for feldspar. After careful handpicking, mica fragments were ground in ethanol in a polished agate mortar and sieved, to obtain inclusion-free separates.

Rb and Sr concentrations were determined by isotope dilution using a set of mixed ^{87}Rb-^{84}Sr spikes. Sample digestion was done in a mixture of concentrated HF and conc. HNO_3 (5:1) in Savillex PFA vials for 36 h at ~90 °C. After evaporation, the residues of this dissolution step were re-dissolved in 6N HCl for 12 h, and re-evaporated to dryness. For mass spectrometric analyses, Sr was isolated and recovered from the solutes by ion exchange using Dowex AG-50 cation exchange resin with 2.5N HCl as the mobile phase.

Isotopic data were generated at GFZ Potsdam using a Thermo Scientific TRITON thermal ionisation mass spectrometer. Sr isotopic composition was measured in dynamic multi-collection mode. Rb isotope dilution analysis was done in static multi-collection mode. The value obtained for ^{87}Sr/^{86}Sr in the NIST SRM 987 isotopic standard during the period of analytical work was 0.710255 ± 0.000005 ($2\sigma_m$, n = 23). Total procedural blanks were consistently below 0.15 ng for both Rb and Sr. Because of generally low blank-to-sample ratios and highly variable blank values, no blank correction was applied. For age calculation, standard uncertainties (cf. Kullerud 1991) of ± 0.005% for ^{87}Sr/^{86}Sr and of ± 1.5% (2σ) for ^{87}Rb/^{86}Sr ratios (as derived from replicate analyses of spiked white mica samples) were assigned to the results, provided that individual analytical uncertainties were smaller than these values. Otherwise, individual analytical

uncertainties were used. Handling of mineral separates and analytical procedures are described in more detail in Glodny et al. (2008). Uncertainties of isotope and age data are quoted at 2σ throughout this work. The program ISOPLOT/ EX 3.71 (Ludwig, 2009) was used to calculate regression lines and ages, in combination with the ^{87}Rb decay constant as recommended by Villa et al. (2015). The Rb-Sr analytical data are shown in chapter 6, Table 6.1.

5.2.2 Uranium-lead

Four bulk samples were collected from pegmatites for U-Pb zircon analysis. All samples consisted of fresh rocks that were crushed in order to separate the minerals. Zircon crystals were separated from the bulk samples using conventional heavy liquid and magnetic separation methods. Clear and transparent zircon grains, free of alteration, inclusions or possible inherited cores, were handpicked under the binocular microscope. The crystal size is large (~5-30 mm), indicating pegmatitic zircon growth. The samples were mounted on section and ground and polished to 60 microns thickness. Mounts were cleaned in different steps with ethanol and deionised water to remove surface lead contamination before introduction into the sample cell. Cathodoluminescence imagery was produced using a Gatan Mini-CL detector attached to the JEOL JXA-8230 Superprobe electron microprobe with 4WD spectrometers at Rhodes University. CL images were taken on polished and carbon coated samples. CL analysis was done to assess the presence or absence of metamict, altered or inherited domains. This analysis also helped in the selection of homogenous parts for LA-SF-ICP-MS age determinations. Carbon coating was done in order to reduce charging of the samples. The imaging was done at 15 kV acceleration potential. All zircon U-Pb age data were obtained by Laser Ablation - Single collector - magnetic sectorfield - Inductively Coupled Plasma - Mass spectrometry (LA-SF-ICP-MS) employing a Thermo Finnigan Element2 mass spectrometer coupled to an ASI Resolution SE-M50 excimer laser ablation system at the Central Analytical Facility at Stellenbosch University in South Africa (Figure 5.1) under supervision and guidance of Prof Dirk Frei.

All age data were obtained by single spot analyses with a spot diameter of 25 μm and a crater depth of approximately 10–15 μm. Zircon analysis were carried out *in-situ* in approximately 100 microns thin petrographic sections. Zircon consumption was limited to less than 2% of a typical crystal. For each analysis, pre-ablation warm up involved 3 cleaning shots followed by 15 seconds background collection, then ablation duration of 15 seconds and wash out delay of 15 seconds.

Figure 5. 1: Equipment used to analyse U-Pb isotopes: ThermoFinnigan Element2 Laser Ablation - Single collector - magnetic sectorfield - Inductively Coupled Plasma - Mass spectrometer (LA-SF-ICP-MS) at the Central Analytical Laboratory at Stellenbosch University in South Africa.

For quality control, the 91500 (Wiedenbeck et al., 1995), Plešovice (Sláma et al., 2008) and M127 (Nasdala et al., 2008; Mattinson, 2010) zircon reference materials were analysed as unknowns, and the results were consistently in excellent agreement with the published ID-TIMS ages. In this analysis, U and Pb concentrations and Th/U ratios are calculated relative to GJ-1 reference zircon (Jackson et al., 2004). $^{207}Pb/^{235}U^{b}$ and $^{207}Pb/^{238}U^{b}$ data shown in Table 6.2 are corrected for background noise and within-run Pb/U fractionation, and are normalised to the reference zircon GJ-1 (ID-TIMS values/measured value). Rho is the error correlation defined as the quotient of the propagated errors of the $^{206}Pb/^{238}U$ and the $^{207}/^{235}U$ ratio. $2\sigma^{d}$ is the quadratic addition of within-run errors (2SD) and daily reproducibility of GJ-1 (2-SD). $^{207}Pb/^{206}Pb$ value is corrected for mass-bias by normalising to GJ-1 reference zircon (~0.6 per atomic mass unit) and common Pb using the model Pb composition by Stacey and Kramers (1975). Frei and Gerdes (2009) describe in detail the methods used for data analysis and processing. Full analytical details and the results for all quality control materials analysed are reported in Appendix 1.2.

Concordia diagrams (Figure 6.10-13) were constructed using decay constants to determine the theoretical isotopic composition of a sample over a given amount of time, assuming closed system behaviour (Dickin, 1995). The governing equations used to calculate the concordia diagrams are outlined in Steps 1-2 (Smith and Farquhar, 1989). Steps 3 and 4 are also used to calculate the concordia. Substitution of various *t* values into the equations results into equation 5.

$$\left(\frac{^{206}Pb}{^{204}Pb}\right)_t = \left(\frac{^{206}Pb}{^{204}Pb}\right)_0 + \left(\frac{^{238}U}{^{204}Pb}\right)_t \left(e^{\lambda_{238}t} - 1\right) \quad (1)$$

$$\left(\frac{^{207}Pb}{^{204}Pb}\right)_t = \left(\frac{^{207}Pb}{^{204}Pb}\right)_0 + \left(\frac{^{235}U}{^{204}Pb}\right)_t \left(e^{\lambda_{235}t} - 1\right) \quad (2)$$

$$\left(\frac{^{206}Pb}{^{238}U}\right) = \frac{\left(\frac{^{206}Pb}{^{204}Pb}\right)_t - \left(\frac{^{206}Pb}{^{204}Pb}\right)_0}{\left(\frac{^{238}U}{^{204}Pb}\right)_t} = \left(e^{\lambda_{238}t} - 1\right) \quad (3)$$

$$\left(\frac{^{207}Pb}{^{235}U}\right) = \frac{\left(\frac{^{207}Pb}{^{204}Pb}\right)_t - \left(\frac{^{207}Pb}{^{204}Pb}\right)_0}{\left(\frac{^{235}U}{^{204}Pb}\right)_t} = \left(e^{\lambda_{235}t} - 1\right) \quad (4)$$

$$\left(\frac{^{207}Pb}{^{235}U}\right) = \frac{\left(\frac{^{207}Pb}{^{206}Pb}\right)}{\left(\frac{^{238}U}{^{206}Pb} * \frac{1}{137.88}\right)} \quad (5)$$

The diagrams were generated using the Isoplot/Ex 3.0 software (Ludwig, 2003). Data points plotting above the concordia line represent U loss from the zircon through leaching, possibly due to chemical weathering (Faure, 1997). Consequently, U-Pb ages obtained from such zircons are inaccurate and produce apparent ages older than the true zircon age. Data points below the concordia are interpreted as zircon that has either gained U or lost Pb (Faure, 1997). Pb loss pulls data points downwards, to positions below the concordia curve and towards the origin of the diagram.

In order to determine the most likely age from a cluster of data within same error margin, a line that is the equivalent of weighted average of $^{207}Pb/^{206}Pb$ ages is fit through the diagram origin and the cluster of data. The upper intercept of the line with the concordia curve may yield the most likely age of the zircon with a mean square of weighted deviates (MSWD). Upper intercept ages obtained from discordant U-Pb zircon data are reported for completeness but only concordant zircon ages have been used for geological interpretation. Representative numerical results for analyses are given in Table 6.3 to Table 6-6.

5.3 ANALYTICAL METHODS - MICA GEOCHEMISTRY

5.3.1 Introduction

Single mica crystals may vary in composition, reflecting compositional changes in the pegmatitic melt or fluid during mica growth and progressive pegmatite crystallisation. Their physical properties, chemical composition, and their paragenetic relationships can be used to

interpret the degree of melt evolution and the conditions of crystallisation of pegmatite bodies. Trace elements contents may indicate the economic potential of pegmatites. Such analysis allows to monitor fractionation trends and to determine whether the pegmatites can be related to each other by a common fractionation path.

Some element species in white mica, such as Li, are important for analysing pegmatite petrogenesis and for classification purposes. The K/Rb ratios of micas, together with Li, F, Cs, Sn, Ba and Zn contents are commonly used as petrogenetic indicators of the degree of pegmatite evolution. In general, micas show the same evolutionary trends as feldspars, with progressively increasing Li, Rb, Cs and F contents, and a decrease in Ba, with decreasing K/Rb ratio. Analysis of major, trace, and rare earth elements in mica from pegmatites from different locations was carried out in order to understand the genesis of the pegmatites.

5.3.2 Major, Minor and Trace Element Geochemistry

Sample surfaces of all separated mica crystals were cleaned to remove contaminations caused by sample handling or processing. The samples were then mounted on standard thin section slides and polished, carbon coated, and analysed under cathode-luminescence using a Gatan Mini-CL detector attached to the JEOL JXA-8230 Superprobe electron microprobe at Rhodes University (Figure 5.2), in order to establish whether different mica species or endmembers are associated in the same crystal. The BSE images indicated lack of compositional zoning in these studied micas associated with gemstone bearing granitic pegmatites.

Figure 5. 2: JEOL electron microprobe at Rhodes University that was used for major and minor element analysis for mica and CL analysis.

Uniform BSE signal intensity seen across the entire crystals suggests homogenous major elemental composition in the sampled micas. Therefore, the samples were mounted with their (0001) faces vertical in round blocks, embedded in synthetic resin, and polished (Figure 5.3).

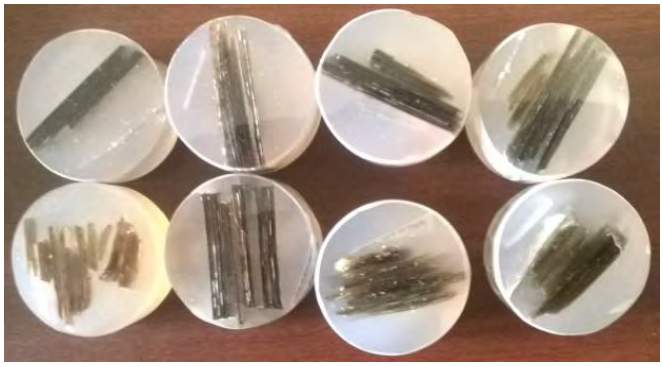

Figure 5. 3: Mica samples mounted in resin.

Major element EPMA data acquisition was then performed on the JEOL JXA-8230 Superprobe at Rhodes University, Department of Geology. The instrument is fitted with four WD spectrometers and standard size spectrometer crystals (LIF, TAP, PET) for major elemental analysis and large crystals (LIFL, TAPL, PETL) for minor and trace element analysis. The acceleration voltage was 15kV and the probe current 10 nA, counting time 10 sec on peak and 5 sec on background, a slightly defocused beam of 20 μm spot size in order to minimise rapid beam damage to the specimen, and to prevent loss of volatile components such as potassium. However, Ba, Cs and Sr had counting time of 30 sec on peak and 15 sec on each background in order to lower the detection limit. The calibration standards and crystals used for measuring the characteristic X-rays were Plag-An65_SPI, TAP for Si; Almandine_SPI, TAP for Al; Cr_Diopside_SPI, PETJ for Ca; MgF_2, TAP for F; Periclase_SPI, TAP for Mg; Biotite_SPI, LIF for Fe; Rb_2PtCl_6, TAP for Rb; Biotite _SPI, PETL for K; Rhodonite_SPI, LIFL for Mn; Chromite_SPI, PETL for Cr; Pollucite_SPI, PETL for Cs; Plag-An65_SPI, TAPL for Na; Tugtupitel, PETL for C; Rutile_SPI, PETL for Ti and SrTiO3, PETL for Sr. The average detection limits were: KαSi – 141 ppm); KαAl – 112 ppm; KαCa – 125 ppm KαMg – 74 ppm, KαFe – 637 ppm; LαRb – 95 ppm; KαK – 62 ppm; KαMn – 318 ppm; KαCr – 108 ppm; LαCs – 91 ppm; KαNa – 583 ppm; KαCl – 86 ppm; KαTi – 120 ppm, and LαSr – 146 ppm. The ZAF matrix correction method was employed for quantification.

The in situ spot chemical analyses of trace elements and REE analyses of micas were carried out using Laser Ablation Inductively-Coupled Mass Spectrometry (LA-ICP-MS) done at the Central Analytical Facility (CAF) at Stellenbosch University in South Africa. The LA-ICP-MS system used at CAF consists of an excimer laser system emitting at 193 nm (Resonetics Resolution S155 utelising a coherent CompexPro 100 laser source) coupled to an Agilent 7700 quadrupole ICP-MS (Figure 5.4). The trace element data have been obtained by single spot analysis using a 67 μm beam diameter in the same spots or close to the spots on the crystals as the microprobe analyses.

Figure 5. 4: Equipment used to analyse trace elements and REE: a Resolution 193 nm Excimer laser ablation system connected to an Agilent ICP-MS at the Central Analytical Laboratory (CAF) at Stellenbosch University in South Africa.

Ablation was performed using a double-helix ablation cell (Laurin Technic, Canberra, Australia) in helium (300 ml/min) that was mixed in a conical ablation cup into argon sample gas (950 ml/min) and N_2 (1.6 ml/min) and transferred in Nylon 10 tubing to the mass spectrometer. The isotope used for internal standardisation was ^{29}Si and NIST SRM 610 standard reference glass (values from Pearce et al., 1997) was used as external calibration standard. In a typical analytical sequence, one standard was used as external calibration standard. In atypical analytical sequence, one standard was used, followed by 10 to 15 unknowns, then one standard, and so on. For each analysis an ablation time of 20 s was applied. Background was measured for 20 s prior to ablation. Data acquisition was performed by peak hopping measuring 1 sample per peak. Reduction of time-resolved data and concentration calculations were subsequently performed off-line using the GLITTER software package for Laser Ablation Microprobe. Regular analysis of the NIST SRM 612 standard reference glasses were perfomed for quality control and the results are consistently within 2s of the average values reported by Pearce et al (1997). Overall, 42 elements were measured and the minimum detection limit for most of the elements is in the lower ppb to mid ppt range. In summary the limits for trace elements ranged from 0.00021 ppm (Li) to 0.4 ppm (U), and for REE the limits ranged from 0.0002 ppm (Tm) to 0.002 (Yb, Nd).

Calculated abundances of trace elements and rare earth elements (REE) were normalised to upper continental crust (UCC) using values in ppm reported by Taylor and McLennan (1995) as follows: Li - 20; Be - 3; B - 15; Sc - 13.6; Ti - 3000; V - 107; Cr - 85; Mn - 600; Co - 10; Ni - 44; Cu - 25; Zn - 71; Ga - 17; Rb - 112; Sr - 350; Y - 22; Zr - 190; Nb - 12; Mo - 1.5; Sn - 525; Cs - 4.6; Ba - 550; La - 30; Ce - 64; Pr - 7.1; Nd - 26; Sm - 4.5; Eu - 0.88; Gd - 3.8; Tb - 0.64; Dy - 3.5; Ho -0.8; Er - 2.3; Tm -0.33; Yb - 2.2; Lu - 0.32; Hf - 5.8, Ta – 2.2; W - 2; Pb - 17; Th - 10.7 and U - 2.8. However, in the UCC-normalised REE patterns (Taylor and McLennan, 1995)

the behaviour of some elements including Eu are not shown. In order to show all the REE, the patterns were also normalised to chondrite values reported by Nakamura, 1974) and they have also been plotted.

5.4 ANALYTICAL METHODS - FLUID INCLUSIONS

5.4.1 Basic Principles

Fluid inclusions are small quantities of fluid that are trapped in mostly small cavities within minerals (Van den Kerkhof, 1988). Composition of the fluids may include gas, gas bearing liquid, water, vapour, brines of varying salinity, or supercritical fluid (Roedder, 1984; Bodnar, 2003a). The fluid may carry minor amounts of one or more solid phases. Fluid inclusion studies help to characterise the composition of fluid that participated in the crystallisation of host minerals, and to determine the pressure and temperature (P-T) during inclusion entrapment.

Three types of fluid inclusions based on their origin are primary, pseudosecondary and secondary. Primary fluid inclusions are trapped ***during*** crystal growth within a free fluid phase. Pseudosecondary inclusions form when fluid is trapped ***along*** cracks that develop within the mineral ***during*** crystal growth. Secondary inclusions are trapped ***along*** healed fractures ***after*** the mineral has crystallised (Roedder, 1984; Bodnar, 2003a). According to Roedder (1984), the primary inclusions may occur in three-dimensional groups or as isolated inclusions along a growth zone or a twin plane. Pseudosecondary inclusions occur along trails that end abruptly against grain boundaries, or along growth zones. Secondary inclusions occur in trails or clusters that continue into neighbouring grains.

Meaningful fluid inclusion analysis depends on that no mass, volume or chemical composition has changed since fluid entrapment. The density of a fluid is correlated with fluid composition and P-T of entrapment. Accordingly, the fluid density can be determined and used as a tool to obtain information on the pressure and temperature at which the fluid was trapped as an inclusion. The line of constant fluid density on a P-T diagram is termed an isochore. Fluids of different compositions will have isochores with different slopes in P-T space.

Among many rock-forming minerals that contain fluid inclusions, quartz becomes ideal for fluid inclusion studies because it does not react chemically with trapped fluids, it is not prone to fluid inclusion leakage because it does not have a mineral cleavage, it is common in most crustal rocks, and it also contains abundant fluid inclusions. However, care must be taken because

quartz may undergo recrystallisation or other plastic deformation over a wide range of pressure and temperature conditions, with possible impact on the integrity of fluid inclusions.

Microthermometry and Raman micro-spectroscopy techniques are mostly used in fluid inclusion studies in order to gather information that helps to determine the fluid composition and the P-T conditions during the entrapment of fluids. This study used both techniques extensively.

5.4.2 Sample Selection and Preparation

15 samples were selected from various pegmatite samples from various locations for fluid inclusion studies. Two samples came from CNC pegmatites, one sample each from CCC and MWC pegmatites, three samples from GM pegmatites, two from HEM pegmatites, one sample from DHD, two samples each from GNS and MNS pegmatites and one sample from CUB pegmatites. In all samples, quartz was selected for the analysis. Doubly polished wafers were prepared at 150 microns thickness in Geology Laboratory at Rhodes University. Optical transmitted light microscopy of fluid inclusions was done on a petrographic microscope. All samples of fluid inclusions populations were photographed using a DeltaPixInvenio digital camera.

5.4.3 Analytical Techniques

Cathodoluminescence and fluid inclusion petrography

Cathodoluminescence (CL) reveals primary and secondary textures of minerals. The primary structures include growth zonation while secondary structures include healed micro-cracks. The CL signal intensity relies on the type of chemical bond, lattice defects and impurity elements. CL images were taken on polished and carbon coated samples at Rhodes University. This technique was used on quartz as a host mineral in order to help identify the chronology of the fluid inclusion assemblages.

Different techniques were used to establish the textural relationship between fluid inclusions and the host mineral quartz. The inclusions were carefully selected based on fluid inclusion population, type, and occurrence. Classification of the fluids involved petrographic description of the phases, examination of relative phase volumes, inclusion size and morphology and their relative age to each other.

Microthermometric measurements were conducted on selected fluid inclusions. It involves freezing and heating of inclusions while observing phase changes using a petrographic

microscope. The phase changes and the temperature at which phase changes occur are recorded. These temperatures are interpreted in terms of fluid composition, density, estimation of phase proportions and homogenisation.

In this study, microthermometric measurements were performed using a calibrated LINKAM TMH 600 heating and freezing stage, together with a TMS93 temperature controller and programmer and a liquid nitrogen pump (LNP93/) cooling system mounted on Nikon Eclipse E600 transmitted-light microscope, with objective lenses of 4x to 100x magnification (Figure 5.5). This was fitted with a DeltaPixInvenio digital camera and supported by DeltaPixInSight software. All equipment used in microthermometry is based at Rhodes University.

Synthetic fluid inclusion wafers on a G7 sample holder were used to calibrate the heating and cooling stage by setting the melting point and homogenisation standards for T < 0 ^{o}C and T > 25 ^{o}C. The wafer then was heated from above 25 ^{o}C to 125 ^{o}C at a fixed rate of 10 ^{o}C per minute. Afterwards, the rate of heating above 125 ^{o}C was set to 5 ^{o}C per minute heating to 450 ^{o}C. 5 ^{o}C per minute was then set as the cooling rate from 25 ^{o}C to 0 ^{o}C. Below 0 °C down to -100 °C the cooling rate was 2 ^{o}C per minute.

Figure 5.5: Equipment for microthermometric measurements: a calibrated LINKAM TMH 600 heating and freezing stage, together with a TMS93 temperature controller and programmer and a liquid nitrogen pump (LNP93/) cooling system mounted on Nikon Eclipse E600 transmitted-light microscope with objective lenses of 4x to 100x magnification. A DeltaPixInvenio Camera is fitted to the microscope. The equipment is housed at Rhodes University, Geology Department R.S.A.

The documented measurements are nucleation temperature T_n, initial melting temperature (T_{mi}), eutectic melting (T_e), total melting temperature of ice (Tm_{ice}), clathrate melting (Tm_{cla}) and

homogenisation temperature (T_h). According to Van den Kerkhof (1988), a combination of homogenisation and final melting temperature can produce an estimate of fluid composition and molar volume.

In order to identify the chemical compounds in individual fluid inclusions, microthermometry was used in combination with ***Raman microspectroscopy*** techniques on the same samples. It involves Raman scattering of monochromatic light, usually from a laser source on to a sample, which then produces a Raman spectrum. This is useful for assessing molecular motion and fingerprinting chemical species. The technique can be used to study solid, liquid and gaseous samples. It is very effective in fluid inclusion studies because of its high spatial resolution and its non-destructive procedure.

The samples in this study were analysed using a Raman Spectrometer fitted to confocal optics and a motorised stage at the University of Johannesburg, South Africa (Figure 5.6). WITec Project 2.10.3 (2012), CrystalSleuth Application (Laetsch and Downs, 2006) and Raman Tool Set software (Candeloro, 2013) were used for analysing the Raman data. Prof. Axel Hofmann assisted with instrument calibration and data collection.

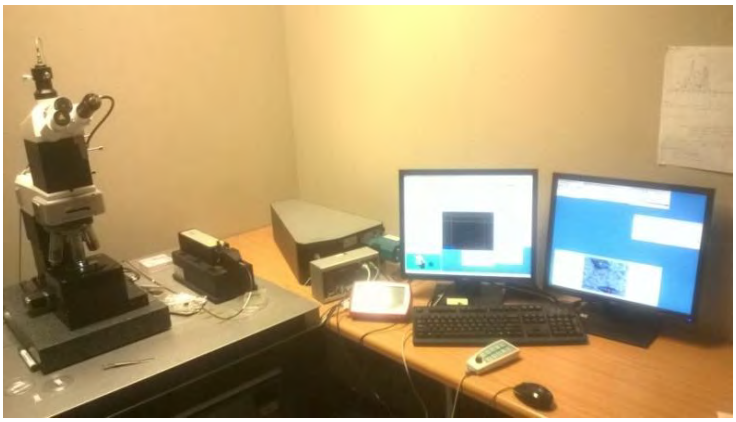

Figure 5.6: Fluid composition determination was done by Raman Spectrometer fitted with confocal optics and motorised stage at the University of Johannesburg, South Africa.

The fluid inclusions in this study belong to different fluid systems, including the H_2O – NaCl system, H_2O-CO_2-NaCl system, H_2O-CO_2-CH_4 system, and CO-CH_4-N_2 system. Therefore, several software programmes were used to calculate compositions, bulk fluid densities and salinities. Since concentration of species is related to amount of substance contained in a fluid, averages of results obtained by Raman analysis were used to determine the relative composition of the phases. The data collected are useful for pressure and temperature estimates for pegmatite formation. The various software packages and equations of state were used depending on the system under investigation (Table 8.17). The ISOC program (Bakker, 2003), with its built-in

capability to automatically select relevant equations of state depending upon fluid composition, was used to calculate corresponding isochores for hypothetical bulk compositions obtained from the other software. The ISOC program has an option for selection of a predefined fluid system or a manually selected system. In this software, input of relative composition of non-aqueous phases must always be equal to 1.

6. GEOCHRONOLOGY

6.1 INTRODUCTION

In Chapter 4 the sampled pegmatites have been described according to their association with crustal entities that have formed or underwent tectono-metamorphic overprints in Palaeoproterozoic to Mesozoic time. This chapter presents geochronological data that specify the emplacement age of specific pegmatites or pegmatites groups. The crystallisation ages of eight pegmatite samples have been dated using Rb-Sr mineral isochrons. Four further samples contain pegmatitic zircon that has been dated using the U-Pb isotope system. The analytical methods have been described in the previous Chapter 5.

6.2 RESULTS OF Rb - Sr GEOCHRONOLOGY

The numerical results for eight analysed pegmatites are shown in Table 6.1. Figures 6.1 to 6.8 show the isochron spectra. Where spatial relationships to other dated rocks in the respective sampling areas were available, the initial $^{87}Sr/^{86}Sr$ ratios of these different pegmatites were used to evaluate possible genetic relationships. Furthermore, the $^{87}Sr/^{86}Sr$ ratios are used as a tracer to establish magma evolution and provenance, assuming mantle-derived rocks having Sr_i ~0.700-0.706, whereas Sr_i ~0.705-0.800 suggest crustal sources of, or their contribution to, magma generation and evolution (White, 2015). The pegmatites discussed in this study are derivatives of granitoid magmas that are likely to have segregated from these magmas in the crust. From these magmas they are likely to inherit the Sr isotope signature, resulting in low values where the pegmatite derived from a granitoid magma with a high mantle source component. High Sr initials point to a crustal granite source of the pegmatite, and crustal contamination during magma rise may increase the Sr initial ratios further (Faure, 1997).

All eight dated pegmatites have produced multi-mineral isochrons with low MSWD values, not exceeding 3.3. This is interpreted as an indication of isotopic equilibrium between the analysed phases. The analytical uncertainties are smaller than 1.1% (2σ). In the following, the age results are presented in a geographical order from north to south (Figure 3.9 shows the sample locations).

Table 6.1: Rb/Sr analytical data for K-feldspar, muscovite, plagioclase and biotite from different pegmatites in this study. The samples are ordered geographically from north to south.

Sample	Material	Rb [ppm]	Sr [ppm]	$^{87}Rb/^{86}Sr$	$^{87}Sr/^{86}Sr$	$^{87}Sr/^{86}Sr$ $2\sigma_m$ [%]
pegmatite						
GCN-1 (1859 ± 20 Ma, MSWD = 0.07, Sr_i = 0.716 ± 0.024)						
	K-feldspar	819	54.8	48.7	1.997740	0.0014
	muscovite 2	1436	14.4	1119	30.12447	0.0011
	muscovite 1	1407	14.5	1012	27.39492	0.0013
pegmatite						
GCW-1 (498.4 ±5.2 Ma; MSWD = 1.7, Sr_i = 0.790177 ± 0.000053)						
	muscovite 2	1400	7.13	941	7.412003	0.0010
	muscovite1	1375	7.73	797	6.320319	0.0020
	plagioclase	13.4	137	0.286	0.792172	0.0021
pegmatite						
GM-1 (485.1 ±4.8 Ma; MSWD = 1.03, Sr_i = 0.7762 ± 0.0012)						
	muscovite 2	835	5.15	690	5.496292	0.0010
	muscovite 1	874	4.87	797	6.182156	0.0009
	K-feldspar	163	22.8	21.2	0.919024	0.0033
	plagioclase	53.8	16.5	9.54	0.841344	0.0080
pegmatite						
GD-1 (489.0 ±5.1 Ma; MSWD = 0.41, Sr_i = 0.7405 ± 0.0048)						
	K-feldspar	235	18.3	38.1	1.001654	0.0023
	muscovite 2	984	2.66	3850	27.22056	0.0017
	muscovite 1	974	2.64	3751	26.37325	0.0020
pegmatite						
GNS-1 (555.4 ±4.7 Ma; MSWD = 2.0, Sr_i = 0.706067 ± 0.000035)						
	muscovite 1	471	8.24	189	2.158278	0.0013
	muscovite 2	297	16.7	53.5	1.124887	0.0041
	K-feldspar	377	161	6.82	0.759585	0.0011
	plagioclase	1.41	273	0.0150	0.706183	0.0020
pegmatite						
GNS-4 (552.4 ±6.0 Ma; MSWD = 0.14, Sr_i = 0.70558 ± 0.00062)						
	muscovite 1	380	12.3	96.4	1.454274	0.0021
	feldspar*	297	204	4.22	0.738285	0.0016
	muscovite 2	442	14.6	94.0	1.432295	0.0011
pegmatite						
GU-1 (520.4 ±5.5 Ma; MSWD = 3.3, Sr_i = 0.718733 ± 0.000059)						
	K-feldspar	835	142	17.3	0.843494	0.0014
	plagioclase	21.2	171	0.358	0.721346	0.0017
	biotite	488	7.34	224	2.364989	0.0010
pegmatite						
GN-1 (459.6 ±5.2 Ma; MSWD = 0.03, Sr_i = 0.7893 ± 0.0099)						
	K-feldspar	1300	49.8	79.9	1.304030	0.0011
	muscovite 2	1524	7.17	1010	7.291396	0.0012
	muscovite 1	1609	6.34	1380	9.687070	0.0040

*"Feldspar" refers to a phase that could not be unequivocally identified during hand picking. This phase might be plagioclase, K-feldspar, perthitic or anti-perthitic feldspar, or ternary feldspar.

Tourmaline-bearing pegmatites from Nthalire–Chitipa: sample GCN-1

The tourmaline-bearing pegmatite GCN-1 is hosted in cordierite gneiss that formed during the Ubendian orogeny. Two muscovite varieties of different grain size (muscovite 1 and 2) - feldspar define a Rb-Sr mineral isochron (Figure 6.1) with a slope corresponding to a weighted mean age of 1859±20 Ma. This is the only Palaeoproterozoic pegmatite dated in this study. The MSWD of 0.07 is small. The initial $^{87}Sr/^{86}Sr$ ratio of 0.716 ± 0.024 (Table 6.1) suggests a crustal signature, but within the analytical uncertainty (0.692-0.740) also mantle sources or components contributing to the pegmatitic melt may be possible. This large uncertainty is related to high Rb/Sr ratio of 48.7 in K-feldspar, to which an analytical uncertainty of ±1.5% applies (i.e. Rb/Sr ~ 48.0 to 49.5). Calculating the initial Sr ratio for a rock of Palaeoproterozoic age using this possible range in Rb/Sr creates the unusually large error in Sr_i for this sample. The Palaeoproterozoic age of sample GCN-1 correlates well to regional plutonism at around 1860 Ma in neighbouring NE Zambia (De Waele et al., 2006).

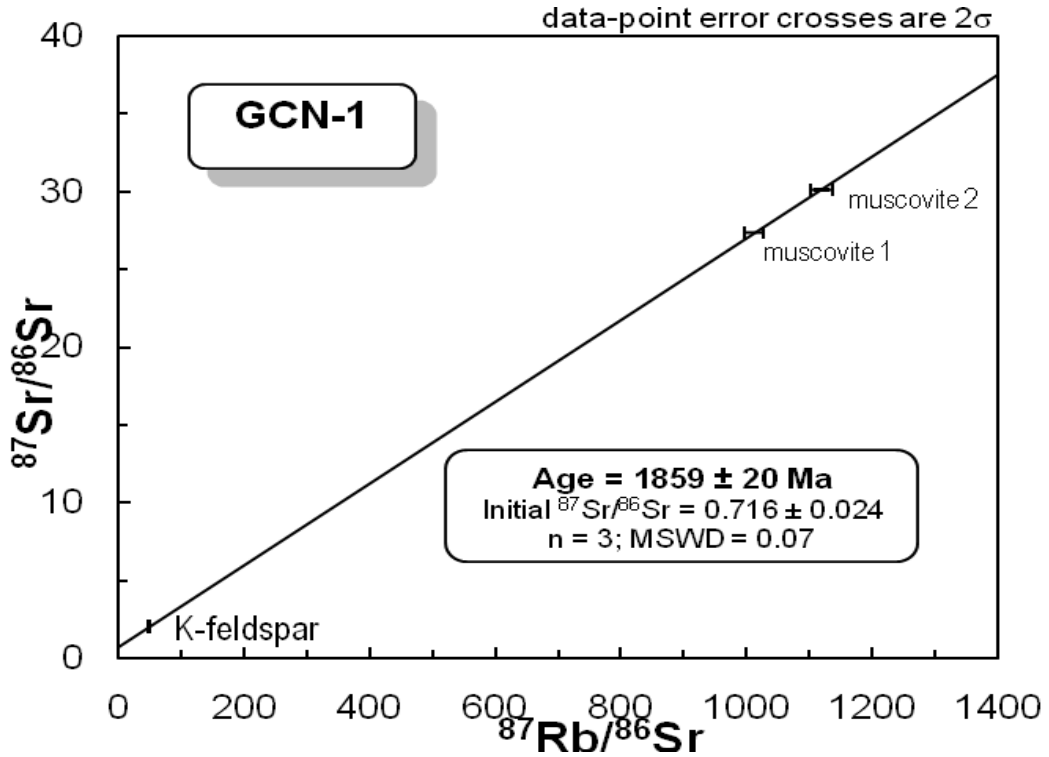

Figure 6.1: Rb-Sr isochron plot for muscovite and K-feldspar from tourmaline bearing pegmatite, GCN-1 from Nthalire, Chitipa.

Beryl and tourmaline-bearing pegmatites of Chisenga and Wenya in Chitipa: GCW1

The beryl and tourmaline bearing pegmatite GCW1 is hosted in cordierite sillimanite gneiss. However, the Rb-Sr isochron defined by plagioclase and two texturally distinct varieties of

muscovite yields a late-Pan-African age of 498±5.2 Ma (MSWD: 1.7; Figure 6.2). The initial $^{87}Sr/^{86}Sr$ ratio of 0.790177 ± 0.000053 falls well in the range of values considered for rocks derived from the crust. Further interaction with crustal material during rise of the magma may have increased the Sr initial.

The Pan-African age of GCW1 indicates the presence of a crustal magma source nearby that is much younger than the orogenic episodes that have formed the hosting gneisses and metapelites.

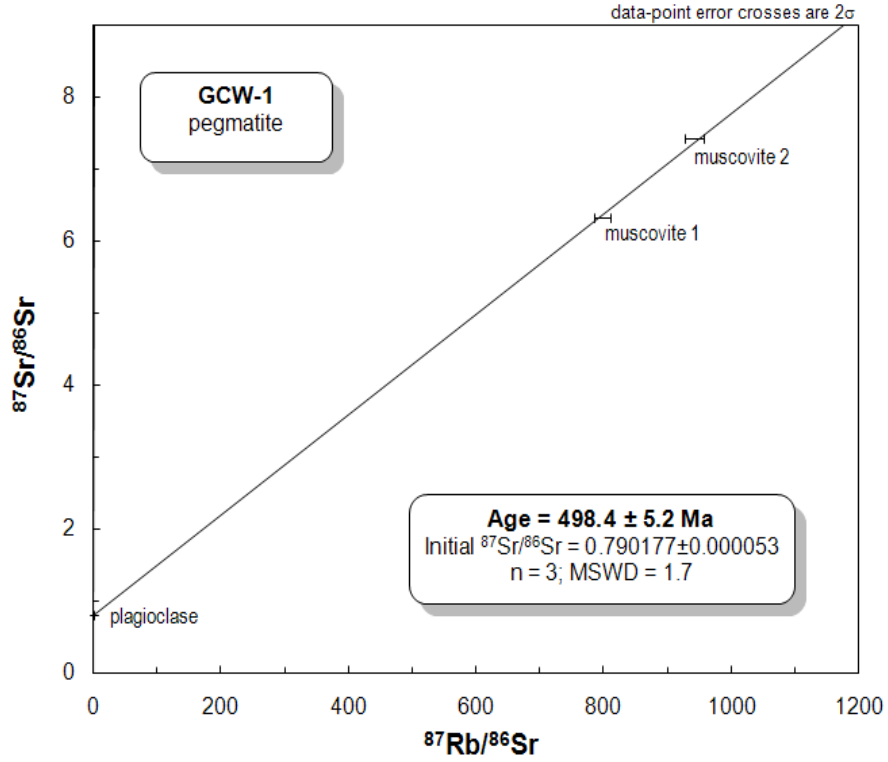

Figure 6.2: Rb-Sr isochron diagram for muscovite and plagioclase from beryl and tourmaline bearing pegmatites, GCW-1 from Chisenga-Wenya in Chitipa.

Aquamarine-bearing pegmatites of Kafukule and Luhomero–Mzimba: sample GM1

Two muscovite varieties, K-feldspar and plagioclase from the aquamarine-bearing pegmatite GM1 yield a mineral isochron of 485.1±4.8 Ma. This pegmatite is about 15 m.y. younger than the GCW1 pegmatite, which comes from similar kind of Mesoproterozoic host rock, but was sampled 120 km further north. Within their analytical uncertainties, GM1 and GCW1 do not overlap. MSWD of GCW1 is small 1.03 (Figure 6.3). The initial $^{87}Sr/^{86}Sr$ ratio of 0.7762 ± 0.0012 may suggest significant crustal contamination during the rise of the magma.

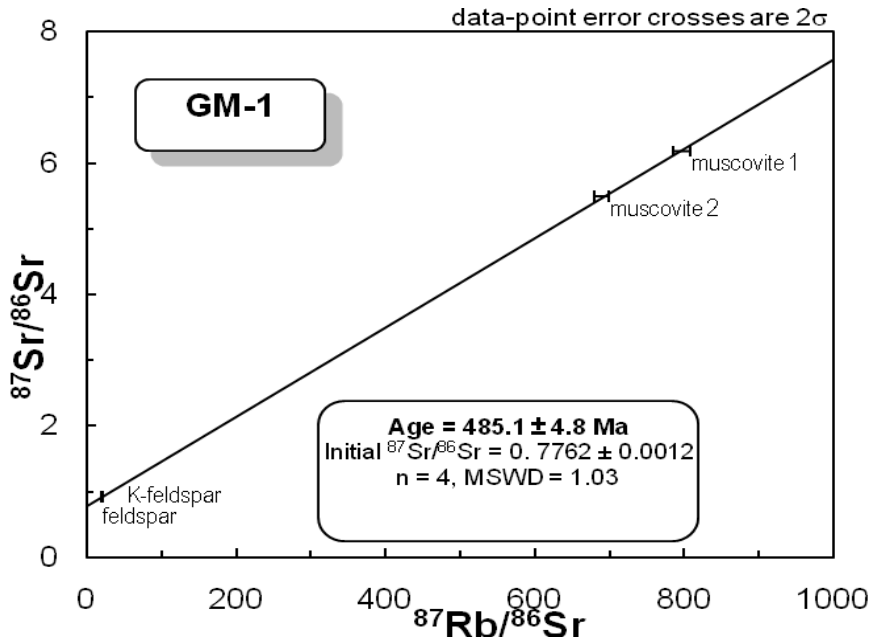

Figure 6.3: Rb-Sr isochron diagram for muscovite, K-feldspar and plagioclase from aquamarine-bearing pegmatite, GM-1, from Kafukule in Mzimba.

Tourmaline-bearing pegmatites of Dowa: sample GD-1

This sample comes from a pegmatite emplaced into gneiss of the Basement Complex south-west of Mponela town in Dowa (Figure 4.9), which formed in Mesoproterozoic time. Muscovite 1/2 and plagioclase yield a weighted mean age of 489.0±5.1 Ma for GD-1 (MSWD of 0.41; Figure 6.4), overlapping with the younger sample GM-1 and the older GCW1. The initial $^{87}Sr/^{86}Sr$ ratio of sample GD-1 is with 0.7405 smaller than both, but still falls well into the range of values suggesting an origin of magma from a moderately evolved crustal source.

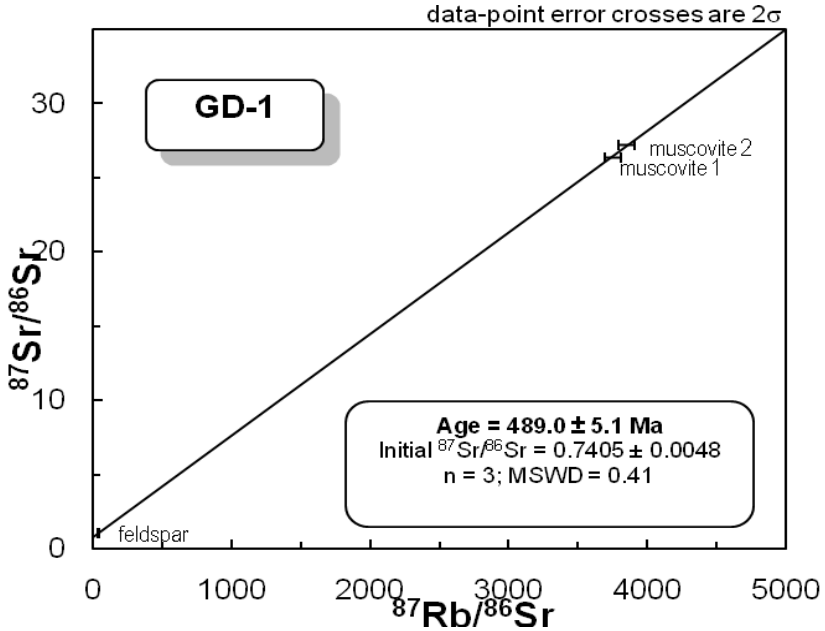

Figure 6.4: Rb-Sr isochron diagram for muscovite and plagioclase from tourmaline-bearing pegmatite, GD-1 from Dowa.

Tourmaline-bearing pegmatite from Ntcheu: sample GNS-1

GNS-1, a tourmaline-bearing pegmatite from Ntcheu hosted in Mesoproterozoic hornblende-biotite-gneiss, consists of two muscovite fractions, K-feldspar and plagioclase. The mineral isochron yields a Rb-Sr isochron age of 555.4±4.7 Ma (Figure 6.5). This is more than 50 m.y. older than the Pan-African pegmatites from central and north Malawi (GD-1, GM1 and GCW1). The initial $^{87}Sr/^{86}Sr$ ratio of 0.706067 ± 0.000035 for the GNS-1 pegmatite is significantly lower than seen in pegmatites further north, and suggests Neoproterozoic juvenile mantle sources of the pegmatite‟s granitic parent magma. In Figure 6.5, the two muscovite fractions plot apart from each other, suggesting that these two muscovite species formed at different stages of melt fractionation. However, both fractions are well in agreement with the isotope ratios obtained from the plagioclase and K-feldspar, indicating isotopic equilibrium between all mica and feldspar phases.

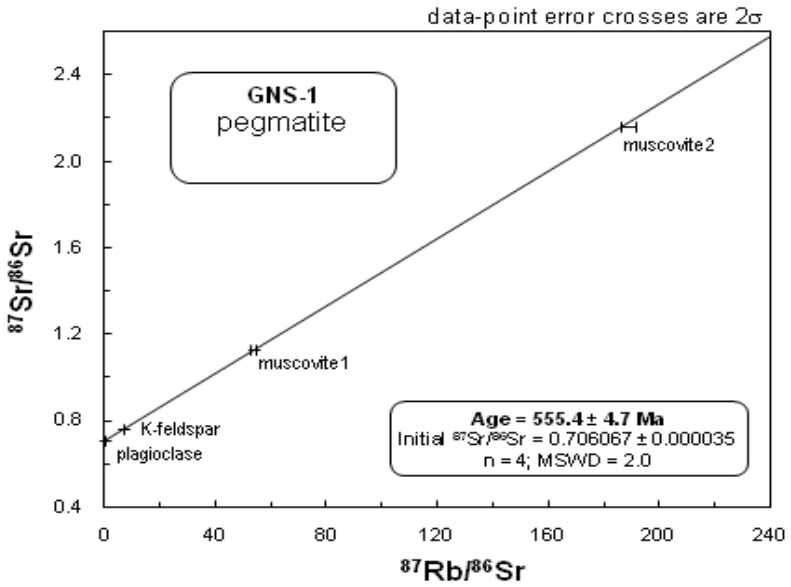

Figure 6.5: Rb-Sr isochron diagram for muscovite, K-feldspar and plagioclase from tourmaline-bearing pegmatite, GNS-1 from Ntcheu.

Tourmaline-bearing pegmatite of Ntcheu: sample GNS-4

GNS-4 is a tourmaline-bearing pegmatite from Ntcheu district. It is hosted in Mesoproterozoic banded garnet-hornblende-diopside gneiss. Muscovite fractions and plagioclase yield a three-point isochron age of 552.4±6.0 Ma (Figure 6.6). Within the analytical uncertainty, GNS-4 is indistinguishable from GNS-1, which was sampled from a similar geological environment 12 km to the east. Also in their strontium initials the samples are similar. Like in GNS-1, the initial $^{87}Sr/^{86}Sr$ ratio of 0.70558 ± 0.00062 suggests juvenile mantle components forming the parent granite magma.

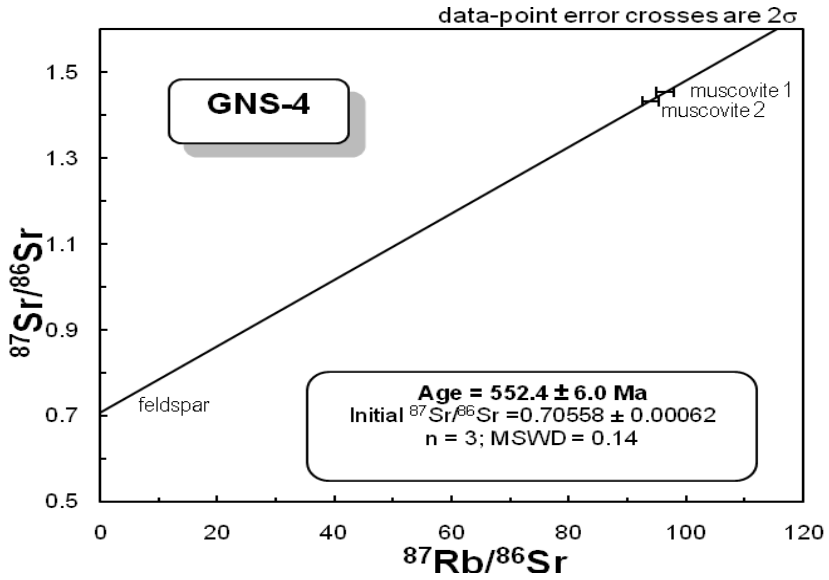

Figure 6.6: Rb-Sr isochron diagram for muscovite and plagioclase from tourmaline-bearing pegmatite, GNS-4 from Ntcheu.

Tourmaline and sunstone-bearing pegmatite from Ntcheu: sample GN-1

GN-1 is also from the Ntcheu district, but located south of both GNS1 and GNS4 (Figure 4.14, Figure 4.15). GN-1, as a part of MSN pegmatite group (Section 4.3.8) is hosted in Mesoproterozoic hornblende-biotite gneiss, and it contains gem-quality tourmaline and sunstone. GN-1 is significantly younger than GNS-1 and GNS-4. A muscovite 1/2 and K-feldspar isochron of 459.6±5.2 Ma indicates an almost 100 m.y. younger emplacement age (Figure 6.7) than seen in the Pan-African pegmatites discussed above. As indicated by its high initial $^{87}Sr/^{86}Sr$ ratio of 0.7893 ± 0.0099, this pegmatite melt formed from crustal granite magma.

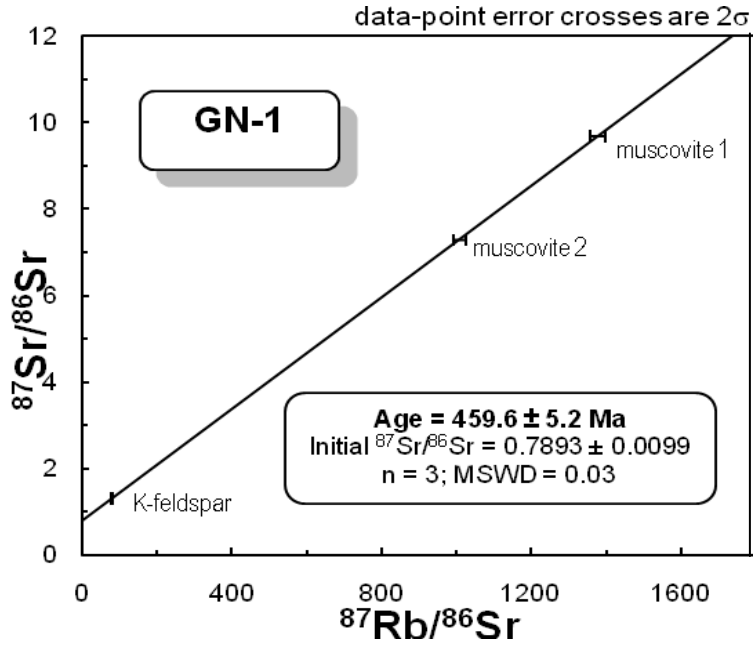

Figure 6.7: Rb-Sr isochron diagram for muscovite and K-feldspar from tourmaline and sunstone-bearing pegmatites, GN-1 from Ntcheu.

Amethyst-bearing pegmatite from Balaka: sample GU-1

GU-1 sample is from a CUB amethyst-bearing pegmatite from the Balaka district (Section 4.3.8). The pegmatites are hosted in Mesoproterozoic granulite and biotite garnet gneiss of the Basement Complex that shows a significant Pan-African overprint. The pegmatites bear gem amethyst of varying colour from light to deep purple. The pegmatite age of 520.4±5.5 Ma, obtained from a three-point isochron of K-feldspar, plagioclase and biotite (Figure 6.8), is in good agreement with the tectono-metamorphic episode that overprinted the host rock. The age lies between those of the <500 Ma pegmatites (samples GM-1, GM-4, GD-1 and GM1; Table 6.1) and the ~550 Ma pegmatites (GNS-1, GNS-4) that show crustal magma sources. GU-1 also shows a crustal magma source indicated by its $^{87}Sr/^{86}Sr$ ratio of 0.718733 ± 0.000059.

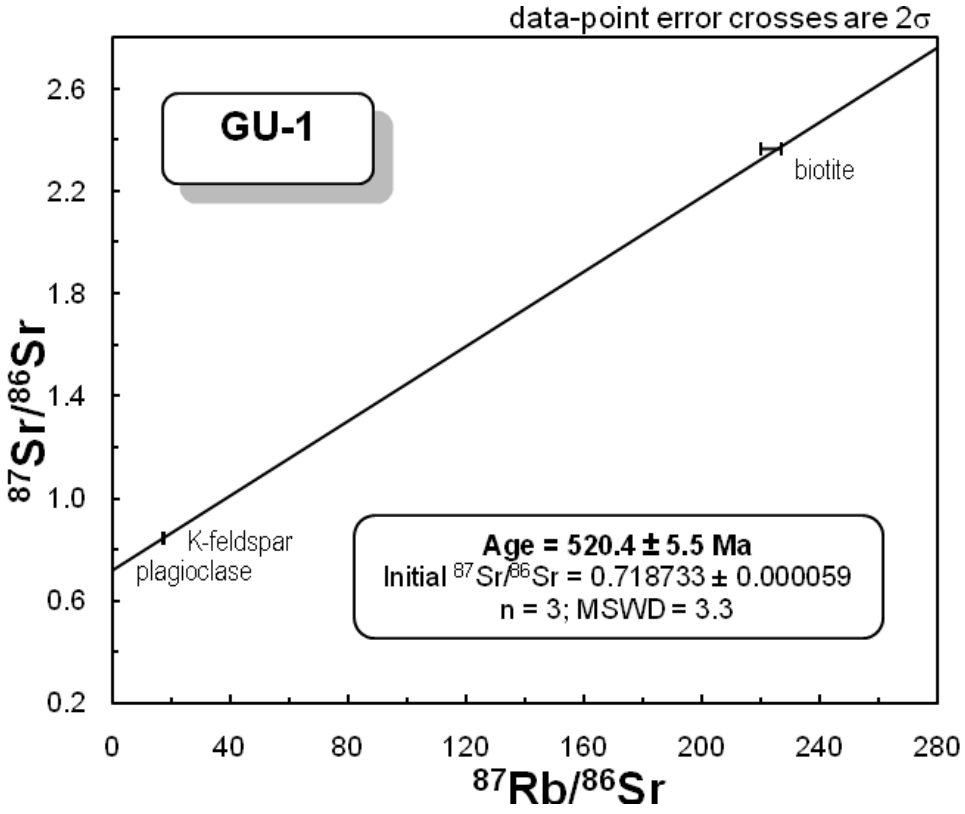

Figure 6.8: Rb-Sr isochron diagram from biotite, K-feldspar and plagioclase from amethyst bearing pegmatites, CUB - sample GU1 from Balaka.

6.3 U-Pb GEOCHRONOLOGY

Four pegmatites, one from Neno, two from Mangochi, and one from Bwanje-Ntcheu (Figure 3.9) contain large pegmatitic zircon and have been dated using the U-Pb isotope system. A summary of the U-Pb zircon ages is presented in Table 6.2; detailed geochronological data are presented in Tables 6.3-6.6. Cathodoluminescence imagery of zircon from the pegmatites shows strong concentric zonation and some with oscillatory zones (Figure 6.9A). Zircon imagery shows distribution of some sampled spots in analysis mode for the four pegmatites (Figure 6.9B, C).

Concordia diagrams for the dated samples show the geochronological results graphically (Figures 6.10 to 6.13).

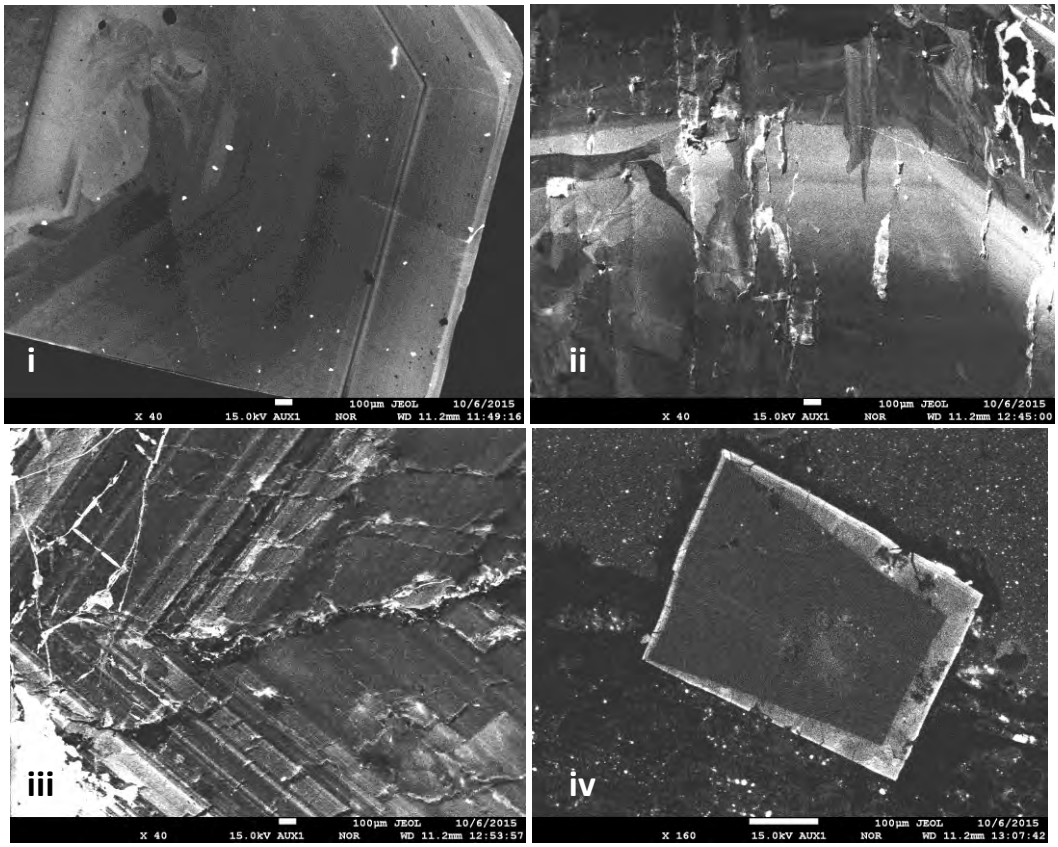

Figure 6.9A: Representative cathodo-luminescence (CL) images of analysed zircon grains used for U-Pb analyses; (i) MNM1D shows internal concentric growth zonation; (ii) NNO1 shows oscillatory zoning; (iii) THMB shows concentric zoning; (iv) ZA shows oscillatory zoning.

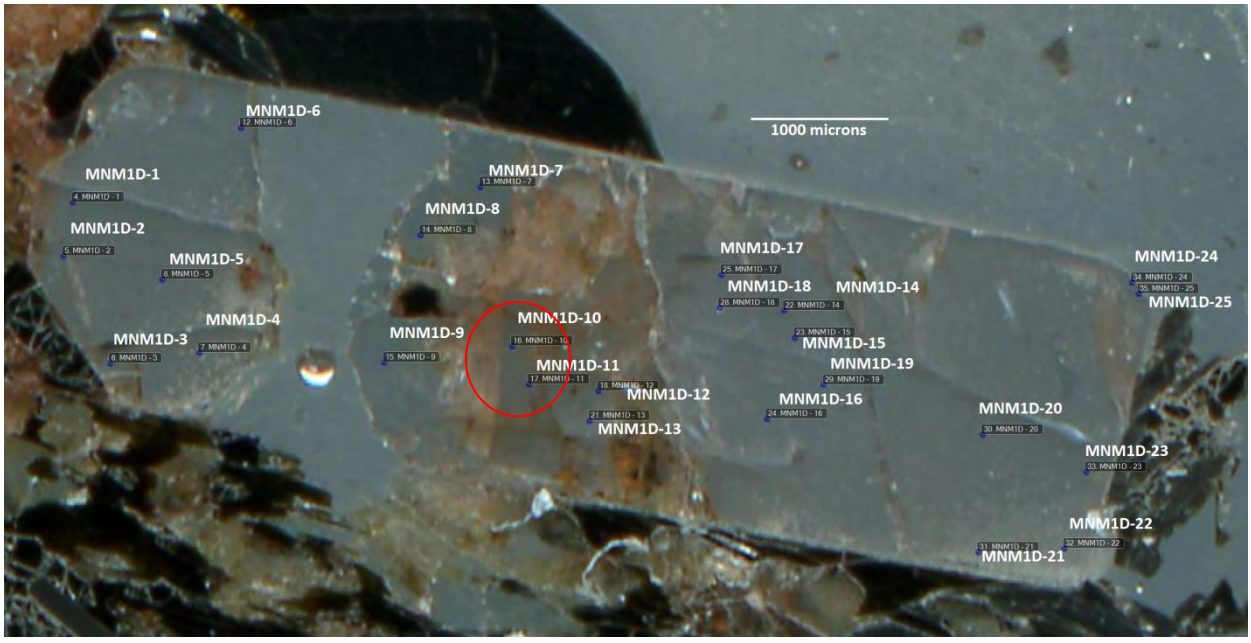

Figure 6.9B: Euhedral zircon image showing some laser-ablation pits for MNM1D. The red circle encloses two points that suggest an inherited core; more details are given in the text.

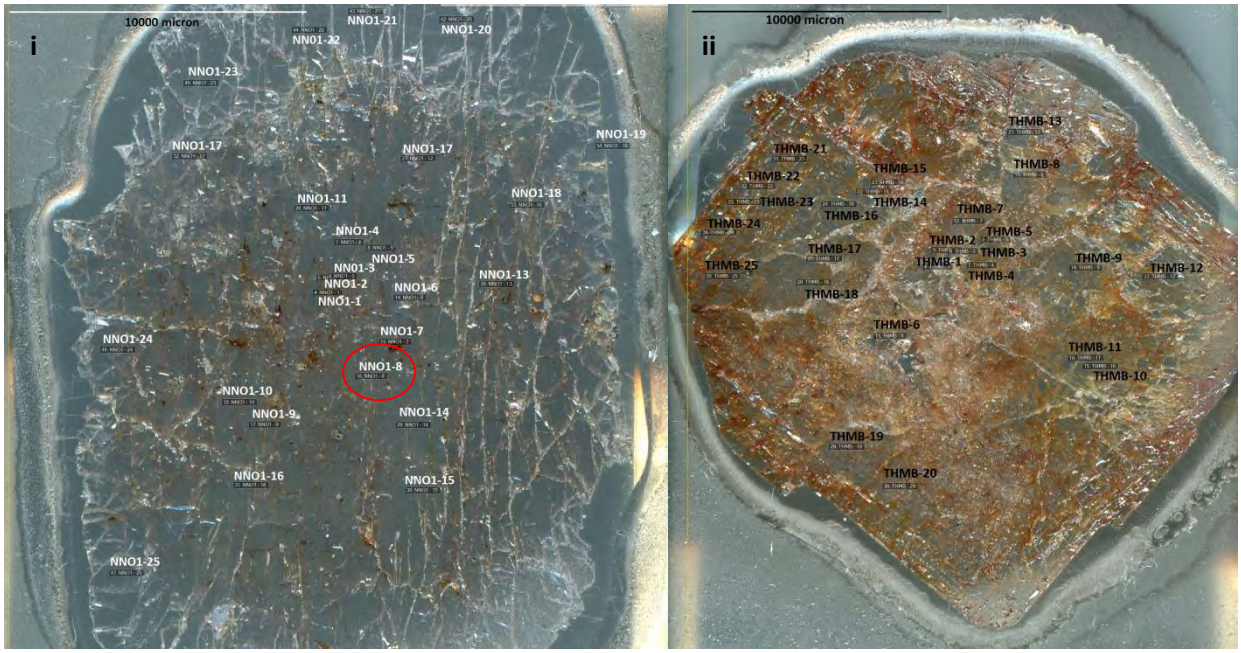

Figure 6.9C: Zircon imagery in analysis mode for; (i) NNO1, red ellipse shows a laser-ablation pit that gave a Th/U ratio >1 (ii) THMB.

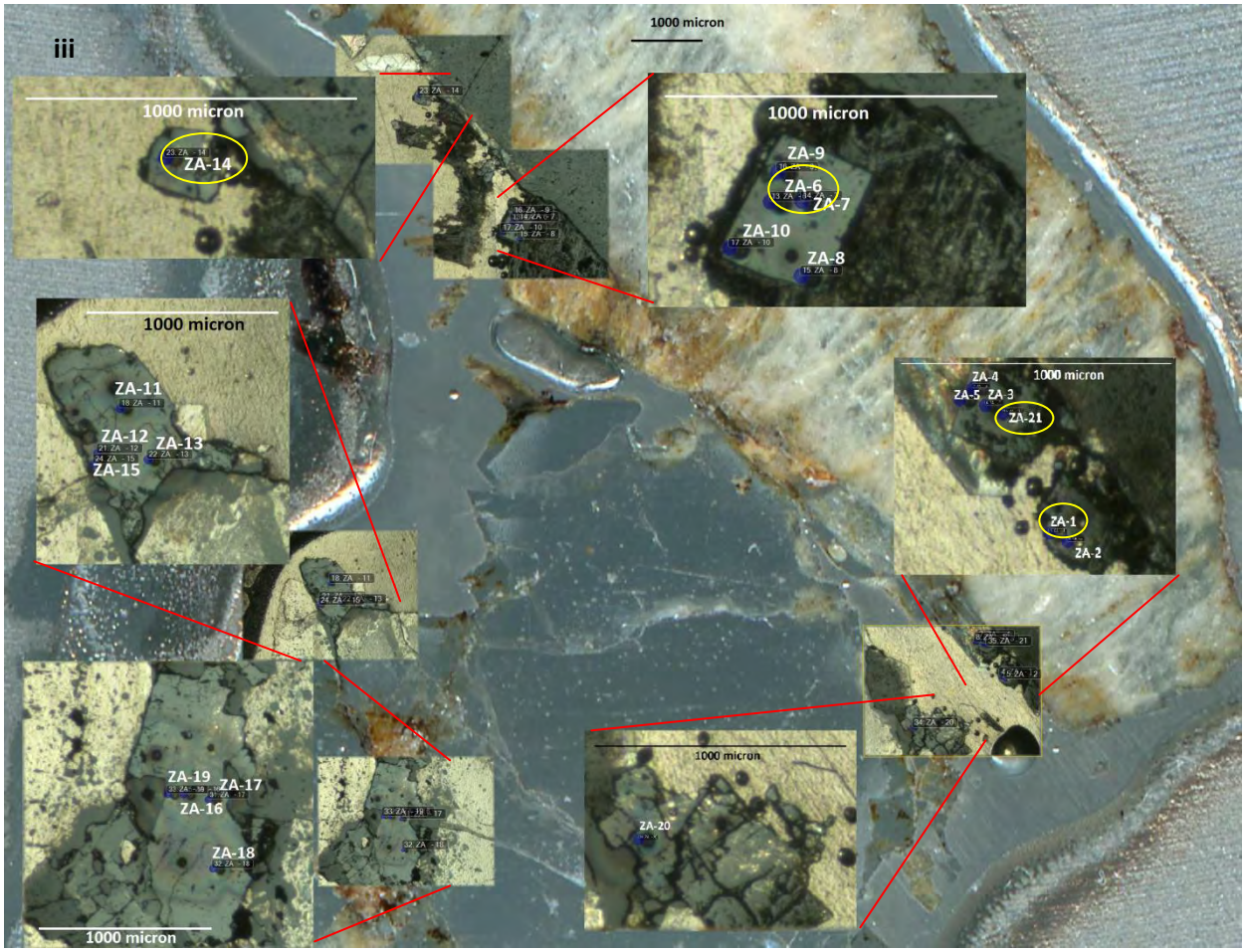

Figure 6.9C (cont.): Zircon imagery in analysis mode for (iii) ZA showing zircons that were analysed. Inserts are enlarged areas, where yellow ellipses represent spots in zircon cores that yielded high Meso- or Palaeoproterozoic ages (see text).

Table 6.2: U-Pb analytical data summary for zircon sample MNM1D, NNO1, THMB and ZA.

SAMPLE	CONCODIA AGE	MSWD		UPPER INTERCEPT	MSWD
MNM1D	597±19 Ma	0.22		597±19 Ma	0.016
NNO1	725±15 Ma	0.24		724±15 Ma	0.23
THMB	731±3 Ma	0.71		725±11 Ma	0.35
ZA	120.3±0.7 Ma	0.64		120.8±0.8 Ma	1.4

Sample MNM1D Nankhwali - Mangochi

The sample MNM1D is from a pegmatite emplaced into Mesoproterozoic gneiss from Nankhwali area, south of Cape Maclear in Mangochi. Zircon reaches up to 30 mm in size and is generally euhedral. In places, irregularly shaped cores may indicate either inherited material or may be related to resorption processes in the early growth stage of pegmatitic zircon. However, such domains are overgrown by thick zircon rims with oscillatory patterns that indicate magmatic growth (Figure 6.9Ai). Such a magmatic zone was analysed for U and Pb isotopes (Figure 6.9B).

The analysed areas contain between 19 and 153 ppm uranium (Table 6.3) with a mean Th/U ratio of 0.2. This is in agreement with igneous origin (Belousova et al., 2002). Thirty seven analyses, each 25 microns in diameter, yielded (near-) concordant (90% - 102%) analyses, from which a concordant age of 594±3 Ma with MSWD of 0.22 was calculated (Figure 6.10A). This age is interpreted as the emplacement age of MNM1D. The concordant age within the uncertainty is indistinguishable from the upper intercept of the discordant data (Figure 6.10B). The $^{207}Pb/^{206}Pb$ ages range from 585 to 625 Ma (Table 6.3). The calculated weighted mean $^{207}Pb/^{206}Pb$ age of these data is 600±5 Ma. This excludes two ages that are significantly older U-Pb and Pb-Pb ages (732-753 Ma). These data were obtained from the core of the zircon (Figure 6.9B) and may represent an inherited zircon from a growth event older than 700 Ma.

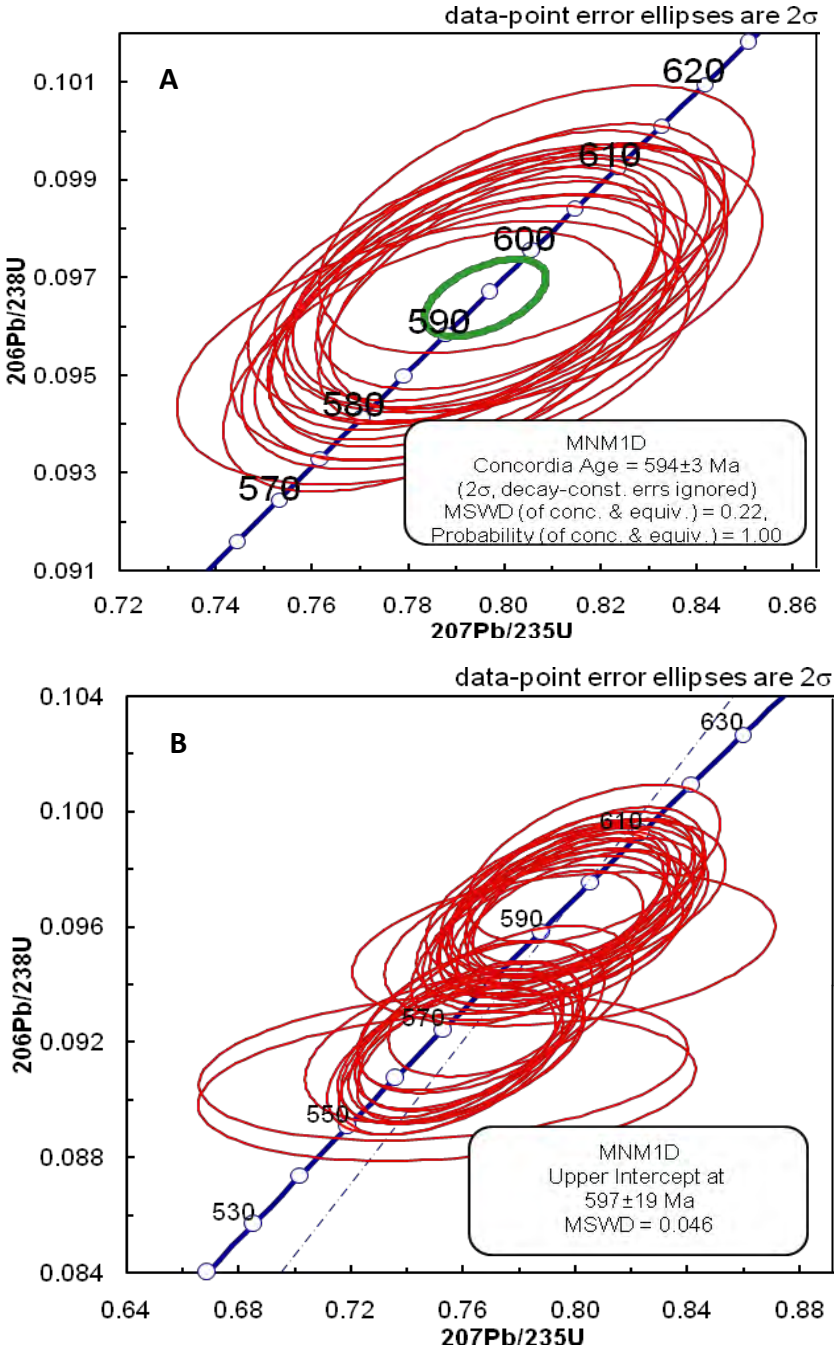

Figure 6.10: U-Pb concordia diagrams from zircon from sample MNM1D, from Nankhwali in Mangochi; **(**A) U-Pb concordia diagram shows the emplacement age of 594±3 Ma; (B) This sample shows an upper intercept of discordant ages at 597±19 Ma.

Table 6.3: Zircon U-Pb isotopic data for sample MNM1D from Nankhwali, Mangochi.

MNM1D																				
						RATIOS								AGES [Ma]						Conc.
Sample	Analysis	U [ppm][a]	Pb [ppm][a]	Th/U[a]		$^{207}Pb/^{235}U$[b]	2 σ[d]	$^{206}Pb/^{238}U$[b]	2 σ[d]	rho[c]	$^{207}Pb/^{206}Pb$[e]	2 σ[d]		$^{207}Pb/^{235}U$	2 σ	$^{206}Pb/^{238}U$	2 σ	$^{207}Pb/^{206}Pb$	2 σ	%
MNM1D	D-1	25	2	0.17		0.803	0.041	0.0970	0.0022	0.44	0.0601	0.0028		598	31	597	14	606	100	98
MNM1D	D-2	25	2	0.18		0.803	0.035	0.0974	0.0022	0.53	0.0598	0.0022		599	26	599	14	597	79	100
MNM1D	D-3	24	2	0.17		0.803	0.035	0.0970	0.0022	0.53	0.0600	0.0022		599	26	597	14	605	79	99
MNM1D	D-4	28	3	0.17		0.799	0.036	0.0970	0.0022	0.50	0.0597	0.0023		596	27	597	14	593	84	101
MNM1D	D-5	26	2	0.17		0.792	0.033	0.0966	0.0022	0.54	0.0595	0.0021		592	25	594	14	585	77	102
MNM1D	D-6	28	3	0.19		0.754	0.032	0.0913	0.0021	0.54	0.0599	0.0021		571	24	563	13	600	76	94
MNM1D	D-7	24	2	0.15		0.777	0.035	0.0934	0.0021	0.50	0.0603	0.0024		584	27	576	13	615	85	94
MNM1D	D-8	29	3	0.18		0.758	0.031	0.0920	0.0021	0.55	0.0598	0.0021		573	24	567	13	595	75	95
MNM1D	D-9	29	3	0.20		0.791	0.033	0.0964	0.0022	0.55	0.0595	0.0021		592	25	593	14	587	76	101
MNM1D	D-10	150	18	0.52		1.069	0.039	0.1205	0.0026	0.61	0.0643	0.0018		738	27	733	16	753	60	97
MNM1D	D-11	153	18	0.50		1.060	0.040	0.1203	0.0026	0.58	0.0639	0.0020		734	28	732	16	739	66	99
MNM1D	D-12	59	6	0.34		0.800	0.035	0.0960	0.0021	0.51	0.0604	0.0022		597	26	591	13	619	80	96
MNM1D	D-13	28	3	0.17		0.756	0.032	0.0917	0.0021	0.54	0.0598	0.0021		572	24	566	13	595	78	95
MNM1D	D-14	29	3	0.15		0.753	0.071	0.0911	0.0021	0.24	0.0599	0.0055		570	54	562	13	601	199	94
MNM1D	D-15	21	2	0.15		0.767	0.036	0.0929	0.0022	0.50	0.0599	0.0024		578	27	572	13	599	88	96
MNM1D	D-16	25	2	0.16		0.753	0.034	0.0914	0.0021	0.50	0.0598	0.0024		570	26	564	13	597	85	94
MNM1D	D-17	54	5	0.21		0.797	0.029	0.0967	0.0022	0.60	0.0598	0.0018		595	22	595	13	597	64	100
MNM1D	D-18	27	3	0.14		0.761	0.033	0.0922	0.0021	0.53	0.0599	0.0022		575	25	569	13	599	79	95
MNM1D	D-19	19	2	0.14		0.754	0.072	0.0905	0.0021	0.24	0.0605	0.0056		571	55	558	13	620	201	90
MNM1D	D-20	29	3	0.18		0.761	0.031	0.0918	0.0021	0.55	0.0601	0.0021		574	24	566	13	608	75	93
MNM1D	D-21	30	3	0.18		0.763	0.032	0.0922	0.0021	0.53	0.0600	0.0022		576	25	568	13	604	78	94
MNM1D	D-22	27	2	0.18		0.753	0.041	0.0918	0.0021	0.42	0.0595	0.0029		570	31	566	13	587	106	97
MNM1D	D-23	27	3	0.18		0.759	0.036	0.0917	0.0021	0.49	0.0600	0.0025		573	27	566	13	604	89	94
MNM1D	D-24	23	2	0.18		0.801	0.037	0.0963	0.0022	0.50	0.0603	0.0024		598	28	593	14	616	87	96
MNM1D	D-25	23	2	0.18		0.764	0.034	0.0929	0.0021	0.51	0.0596	0.0023		576	26	573	13	591	84	97
MNM1D	D-26	27	3	0.18		0.805	0.034	0.0970	0.0022	0.55	0.0602	0.0021		600	25	597	14	611	76	98
MNM1D	D-27	25	2	0.19		0.796	0.062	0.0952	0.0022	0.30	0.0606	0.0045		594	46	586	13	625	159	94
MNM1D	D-28	26	2	0.19		0.790	0.036	0.0958	0.0022	0.50	0.0598	0.0024		591	27	590	14	596	86	99
MNM1D	D-29	22	2	0.16		0.794	0.035	0.0963	0.0022	0.52	0.0598	0.0022		593	26	592	14	597	81	99
MNM1D	D-30	25	2	0.16		0.807	0.037	0.0982	0.0022	0.50	0.0596	0.0024		601	27	604	14	588	86	103
MNM1D	D-31	22	2	0.16		0.793	0.040	0.0960	0.0022	0.45	0.0599	0.0027		593	30	591	14	600	98	98
MNM1D	D-32	23	2	0.17		0.796	0.034	0.0967	0.0022	0.54	0.0597	0.0022		595	25	595	14	592	78	100
MNM1D	D-33	25	2	0.17		0.783	0.034	0.0953	0.0022	0.53	0.0596	0.0022		587	25	587	13	589	79	100
MNM1D	D-34	24	2	0.19		0.785	0.043	0.0955	0.0022	0.42	0.0597	0.0030		588	33	588	14	591	109	99
MNM1D	D-35	23	2	0.18		0.799	0.035	0.0972	0.0023	0.53	0.0596	0.0022		596	26	598	14	589	81	102
MNM1D	D-36	25	2	0.19		0.796	0.041	0.0968	0.0022	0.45	0.0597	0.0027		595	30	596	14	592	99	101
MNM1D	D-37	23	2	0.17		0.792	0.036	0.0960	0.0022	0.51	0.0599	0.0023		592	27	591	14	599	85	99

[a]U and Pb concentrations and Th/U ratios are calculated relative to GJ-1 reference zircon

[b]Corrected for background and within-run Pb/U fractionation and normalised to reference zircon GJ-1 (ID-TIMS values/measured value); $^{207}Pb/^{235}U$ calculated using $(^{207}Pb/^{206}Pb)/(^{238}U/^{206}Pb * 1/137.88)$

[c]Rho is the error correlation defined as the quotient of the propagated errors of the $^{206}Pb/^{238}U$ and the $^{207}/^{235}U$ ratio

[d]Quadratic addition of within-run errors (2 SD) and daily reproducibility of GJ-1 (2 SD)

[e]Corrected for mass-bias by normalising to GJ-1 reference zircon (~0.6 per atomic mass unit) and common Pb using the model Pb composition of Stacey &Kramers (1975)

Sample NNO1 Chowe - Mangochi

Sample NNO1 is from a zircon-bearing pegmatite from Chowe area, north of Uzuzu in Mangochi (Figure 4.19). The pegmatite is intrusive into Mesoproterozoic granulite (Section 4.3.8). The pegmatite is composed of K-feldspar, tourmaline, quartz, muscovite, garnet and zircon. It produces some gem tourmaline. Its zircon reaches up to 20 mm in size and is generally euhedral. CL imagery shows oscillatory patterns for NNO1 (Figure 6.9Aii). The magmatic zone analysed for U and Pb isotopes is shown in Figure 6 9Ci.

Results for an analysed euhedral zircon grain are presented in Table 6.4. The analysed areas contain between 41 and 615 ppm uranium with a mean Th/U ratio of 0.35, indicating the igneous origin of zircon (Belousova et al., 2002). Twenty three analyses yield concordant (89% - 104%) analyses. A concordant age of 726±4 Ma with MSWD of 0.24 was obtained from this data set (Figure 6.11A), which is the best estimate of the emplacement age. The $^{207}Pb/^{206}Pb$ ages range from 694 to 749 Ma. The calculated weighted mean $^{207}Pb/^{206}Pb$ age is 728±14 Ma, overlapping the concordant age. A regression line gives an upper intersection with the concordia line at 724±15 Ma with a mean square of weighted deviates (MSWD) of 0.23 (Figure 6.11B).

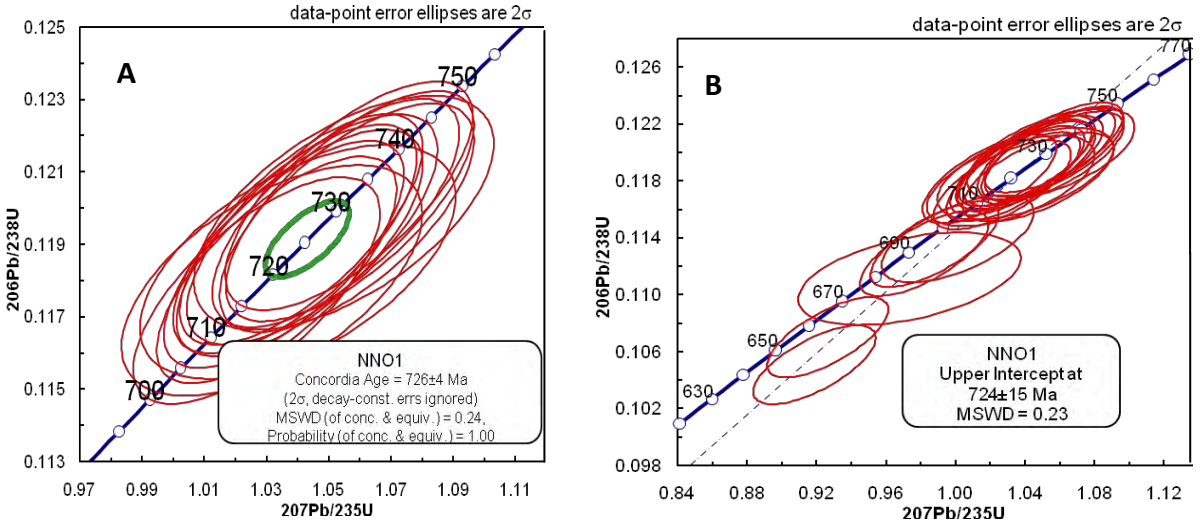

Figure 6. 11: U-Pb plots from zircon from sample NNO1 from Chowe area, north of Uzuzu in Mangochi; (A) U-Pb concordia diagram shows the emplacement age of 726±4 Ma; (B) The discordia diagram shows the upper intercept age of 724±15 Ma.

Table 6.4: Zircon U-Pb isotopic data for sample NNO1 from Chowe, Mangochi.

NNO1																				
						RATIOS								AGES [Ma]						Conc.
Sample	Analysis	U [ppm][a]	Pb [ppm][a]	Th/U meas		$^{207}Pb/^{235}U$[b]	2 σ[d]	$^{206}Pb/^{238}U$[b]	2 σ[d]	rho[c]	$^{207}Pb/^{206}Pb$[e]	2 σ[d]		$^{207}Pb/^{235}U$	2 σ	$^{206}Pb/^{238}U$	2 σ	$^{207}Pb/^{206}Pb$	2 σ	%
NNO1	O1-1	466	55	0.10		1.033	0.031	0.1183	0.0026	0.71	0.0634	0.0014		721	22	721	16	720	46	100
NNO1	O1-2	615	72	0.97		1.027	0.032	0.1177	0.0026	0.69	0.0633	0.0014		717	23	717	16	717	48	100
NNO1	O1-3	382	46	0.25		1.041	0.032	0.1194	0.0026	0.71	0.0632	0.0014		724	22	727	16	716	46	102
NNO1	O1-4	394	47	0.12		1.039	0.032	0.1192	0.0026	0.70	0.0633	0.0014		723	22	726	16	717	46	101
NNO1	O1-5	373	44	0.06		1.045	0.033	0.1194	0.0026	0.69	0.0635	0.0014		726	23	727	16	723	48	101
NNO1	O1-6	480	57	0.80		1.036	0.032	0.1187	0.0026	0.71	0.0633	0.0014		722	22	723	16	717	46	101
NNO1	O1-7	365	43	0.07		1.019	0.032	0.1182	0.0026	0.70	0.0626	0.0014		714	22	720	16	694	47	104
NNO1	O1-8	452	51	1.39		0.988	0.030	0.1136	0.0025	0.71	0.0631	0.0014		698	21	693	15	712	46	97
NNO1	O1-9	431	49	0.63		0.982	0.030	0.1129	0.0024	0.70	0.0631	0.0014		695	21	690	15	711	47	97
NNO1	O1-10	385	46	0.72		1.057	0.033	0.1201	0.0026	0.70	0.0638	0.0014		732	23	731	16	736	46	99
NNO1	O1-11	383	41	0.15		0.926	0.028	0.1070	0.0023	0.70	0.0628	0.0014		666	20	655	14	701	47	93
NNO1	O1-12	262	28	0.31		0.919	0.029	0.1051	0.0023	0.69	0.0634	0.0014		662	21	644	14	722	48	89
NNO1	O1-13	450	54	0.77		1.052	0.032	0.1199	0.0026	0.70	0.0637	0.0014		730	22	730	16	731	47	100
NNO1	O1-14	434	52	0.77		1.056	0.032	0.1203	0.0026	0.70	0.0637	0.0014		732	22	733	16	731	47	100
NNO1	O1-15	404	48	0.74		1.041	0.032	0.1190	0.0026	0.69	0.0634	0.0014		724	22	725	16	722	48	100
NNO1	O1-16	320	38	0.51		1.056	0.033	0.1197	0.0026	0.68	0.0640	0.0015		732	23	729	16	740	49	99
NNO1	O1-17	190	22	0.04		1.001	0.036	0.1139	0.0025	0.61	0.0637	0.0018		704	25	695	15	733	60	95
NNO1	O1-19	41	5	0.18		1.055	0.039	0.1199	0.0026	0.59	0.0638	0.0019		731	27	730	16	736	64	99
NNO1	O1-20	42	5	0.18		1.123	0.041	0.1221	0.0027	0.60	0.0667	0.0020		765	28	743	16	829	61	90
NNO1	O1-21	78	9	0.23		1.032	0.039	0.1180	0.0026	0.58	0.0634	0.0020		720	28	719	16	722	66	100
NNO1	O1-22	43	5	0.17		1.040	0.041	0.1185	0.0026	0.56	0.0637	0.0021		724	29	722	16	730	70	99
NNO1	O1-23	208	25	0.13		1.047	0.036	0.1183	0.0026	0.64	0.0642	0.0017		728	25	721	16	749	55	96
NNO1	O1-24	54	6	0.17		0.973	0.052	0.1111	0.0027	0.45	0.0635	0.0031		690	37	679	16	726	102	94

[a]U and Pb concentrations and Th/U ratios are calculated relative to GJ-1 reference zircon

[b]Corrected for background and within-run Pb/U fractionation and normalised to reference zircon GJ-1 (ID-TIMS values/measured value); $^{207}Pb/^{235}U$ calculated using ($^{207}Pb/^{206}Pb$)/($^{238}U/^{206}Pb$ * 1/137.88)

[c]Rho is the error correlation defined as the quotient of the propagated errors of the $^{206}Pb/^{238}U$ and the $^{207}/^{235}U$ ratio

[d]Quadratic addition of within-run errors (2 SD) and daily reproducibility of GJ-1 (2 SD)

[e]Corrected for mass-bias by normalising to GJ-1 reference zircon (~0.6 per atomic mass unit) and common Pb using the model Pb composition of Stacey &Kramers (1975)

Sample THMB - Neno

Sample THMB is from zircon-bearing pegmatite from Neno in southern Malawi (Figure 3.9). The pegmatite is intrusive in Mesoproterozoic hornblende-biotite gneiss. This pegmatite is mainly composed of coarse-grained alkali feldspar, quartz, zircon and mica. Zircon reaches up to 35 mm in size and is generally euhedral. CL imagery of the zircon reveals concentric zonation with irregularly shaped areas (Figure 6.9Aiii). The spots that were analysed for U and Pb isotopes are presented in Figure 6.9Cii.

An analysed euhedral zircon grain (see Table 6.5) contains between 120 and 1100 ppm uranium with a mean Th/U ratio of 0.5, suggesting igneous origin (Belousova et al., 2002). Twenty three analyses yielded more or less concordant (73% - 106%) analyses. A concordant age of 731±3 Ma with MSWD of 0.71 was obtained (Figure 6.12a). This age is interpreted as the emplacement age of THMB pegmatite. The $^{207}Pb/^{206}Pb$ ages ranged from 693 to 749 Ma (2σ errors). The calculated weighted mean $^{207}Pb/^{206}Pb$ age is 726±8 Ma, overlapping in the uncertainty with the concordant age. A regression line gives an upper intersection with the concordia line at 725±11 Ma with a mean square of weighted deviates (MSWD) of 0.35 (Figure 6.12B).

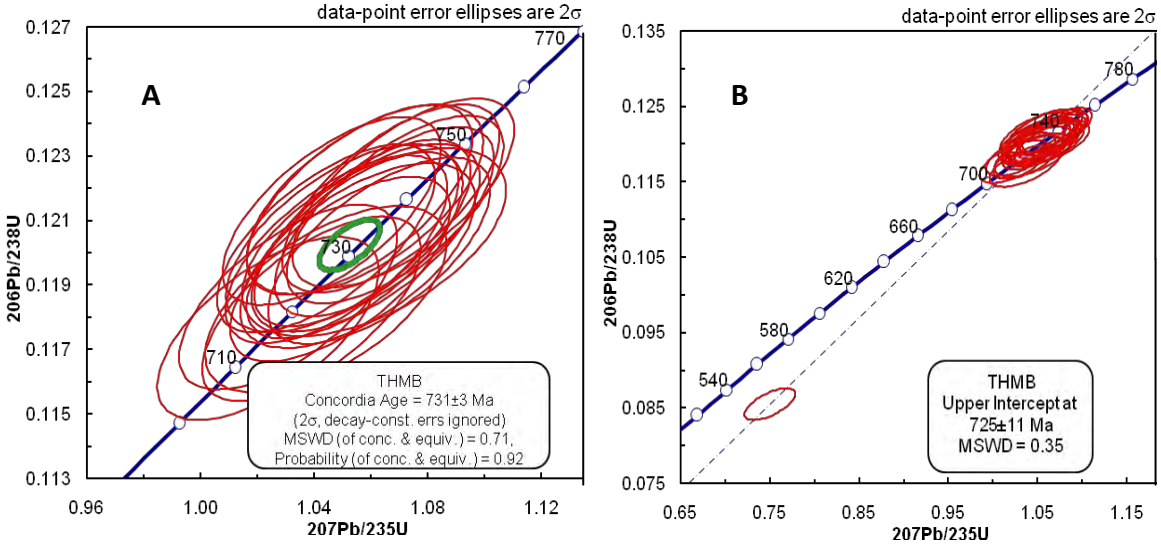

Figure 6.12: U-Pb plots from zircon grain from sample THMB from NENO southern Malawi; (A) U-Pb concordia diagram for zircon shows the emplacement age of 731±3 Ma; (B) The discordia diagram shows the upper intercept age of 725±11 Ma.

Table 6.5: Zircon U-Pb isotopic data for sample THMB from Neno.

THMB																				
						RATIOS								AGES [Ma]						Conc.
Sample	Analysis	U [ppm][a]	Pb [ppm][a]	Th/U[a]		$^{207}Pb/^{235}U$[b]	2 σ[d]	$^{206}Pb/^{238}U$[b]	2 σ[d]	rho[c]	$^{207}Pb/^{206}Pb$[e]	2 σ[d]		$^{207}Pb/^{235}U$	2 σ	$^{206}Pb/^{238}U$	2 σ	$^{207}Pb/^{206}Pb$	2 σ	%
THMB	B-1	536	46	0.28		0.750	0.023	0.0855	0.0017	0.65	0.0636	0.0015		568	18	529	11	729	50	73
THMB	B-3	446	54	0.39		1.044	0.031	0.1204	0.0024	0.66	0.0629	0.0014		726	22	733	14	704	48	104
THMB	B-4	594	72	0.88		1.065	0.031	0.1210	0.0024	0.67	0.0638	0.0014		736	22	736	15	736	46	100
THMB	B-5	835	101	0.71		1.050	0.033	0.1205	0.0024	0.62	0.0632	0.0016		729	23	733	14	716	53	102
THMB	B-6	120	14	0.20		1.044	0.035	0.1186	0.0024	0.60	0.0639	0.0017		726	24	722	14	738	56	98
THMB	B-7	790	93	0.62		1.039	0.031	0.1183	0.0023	0.65	0.0637	0.0015		723	22	721	14	732	49	98
THMB	B-8	842	102	0.84		1.058	0.034	0.1217	0.0024	0.61	0.0631	0.0016		733	24	740	15	711	54	104
THMB	B-9	897	108	0.75		1.061	0.038	0.1203	0.0024	0.55	0.0640	0.0019		734	26	732	14	740	63	99
THMB	B-10	1100	132	0.86		1.048	0.032	0.1201	0.0024	0.65	0.0633	0.0015		728	22	731	14	718	49	102
THMB	B-11	1015	123	0.89		1.056	0.032	0.1216	0.0024	0.64	0.0630	0.0015		732	22	740	15	707	50	105
THMB	B-13	752	91	0.77		1.046	0.031	0.1213	0.0024	0.65	0.0626	0.0014		727	22	738	14	693	48	106
THMB	B-14	714	85	0.48		1.031	0.031	0.1186	0.0023	0.65	0.0630	0.0015		719	22	723	14	709	49	102
THMB	B-15	800	96	0.48		1.058	0.033	0.1205	0.0024	0.64	0.0637	0.0015		733	23	733	14	732	51	100
THMB	B-16	680	83	0.43		1.071	0.032	0.1219	0.0024	0.66	0.0638	0.0014		739	22	741	15	734	47	101
THMB	B-17	739	87	0.46		1.024	0.032	0.1177	0.0023	0.63	0.0631	0.0015		716	22	717	14	712	51	101
THMB	B-18	786	92	0.46		1.036	0.033	0.1171	0.0023	0.62	0.0642	0.0016		722	23	714	14	747	52	96
THMB	B-19	724	88	0.35		1.067	0.031	0.1217	0.0024	0.67	0.0636	0.0014		737	22	740	14	728	46	102
THMB	B-20	1024	123	0.44		1.055	0.034	0.1199	0.0023	0.61	0.0638	0.0016		732	23	730	14	736	54	99
THMB	B-21	524	63	0.26		1.049	0.032	0.1195	0.0023	0.65	0.0637	0.0015		728	22	728	14	731	49	100
THMB	B-22	341	41	0.18		1.057	0.031	0.1206	0.0024	0.66	0.0636	0.0014		732	22	734	14	727	47	101
THMB	B-23	367	45	0.18		1.068	0.031	0.1213	0.0024	0.67	0.0639	0.0014		738	22	738	14	737	46	100
THMB	B-24	270	32	0.17		1.063	0.032	0.1201	0.0024	0.65	0.0642	0.0015		735	22	731	14	749	48	98
THMB	B-25	372	45	0.46		1.054	0.031	0.1202	0.0024	0.67	0.0636	0.0014		731	22	732	14	728	47	100

[a]U and Pb concentrations and Th/U ratios are calculated relative to GJ-1 reference zircon

[b]Corrected for background and within-run Pb/U fractionation and normalised to reference zircon GJ-1 (ID-TIMS values/measured value); $^{207}Pb/^{235}U$ calculated using ($^{207}Pb/^{206}Pb$)/($^{238}U/^{206}Pb$ * 1/137.88)

[c]Rho is the error correlation defined as the quotient of the propagated errors of the $^{206}Pb/^{238}U$ and the $^{207}/^{235}U$ ratio

[d]Quadratic addition of within-run errors (2 SD) and daily reproducibility of GJ-1 (2 SD)

[e]Corrected for mass-bias by normalising to GJ-1 reference zircon (~0.6 per atomic mass unit) and common Pb using the model Pb composition of Stacey &Kramers (1975)

ZA from Bwanje area in Ntcheu

The sample ZA is from a NYF pegmatite (see Chapter 7) from Bwanje area in Ntcheu. It mainly comprises of intergrown coarse-grained microcline, aegerine, quartz, biotite and gem-quality zircon. The pegmatitic zircons are generally euhedral. One of the zircons shows oscillatory zonation pattern (Figure 6.9Aiv). The spots that were analysed for U and Pb isotopes are shown in Figure 6.9Ciii. Numerical results from the euhedral zircon grains are shown in Table 6.6.

The analysed areas contain between 63 and 328 ppm uranium with a mean Th/U ratio of 45, consistent with igneous origin (Belousova et al., 2002), and suggest a late stage of crystallisation of zircon from magma. Twenty analyses yield concordant (7% - 100%) analyses. The concordant age of 120.3±0.7 Ma (MSWD 0.64) is interpreted as an Early Cretaceous emplacement of pegmatite ZA (Figure 6.13A). The $^{206}Pb/^{238}U$ ages spread from 118 to 241 Ma. However, some analyses from the cores of some zircons (Figure 6.9Ciii) yield older U-Pb data (162-241 Ma), and those ages also have older Pb-Pb ages that spread all the way into the Palaeoproterozoic (820-1654 Ma). The zircon data show no indication of Pan-African heritage. Instead, pegmatite formation may be related to the early stages of rifting (Dill, 2015), which is in agreement with the sampling site of ZA within the East-African Rift zone. Therefore, the $^{206}Pb/^{238}U$ ages used to calculate the weighted average range from 118 to 124 Ma. The weighted average $^{206}Pb/^{238}U$ age obtained is 120.8±0.8 Ma with MSWD of 1.4 (Figure 6.13B). In the uncertainty, this age is indistinguishable from the concordant age reported above.

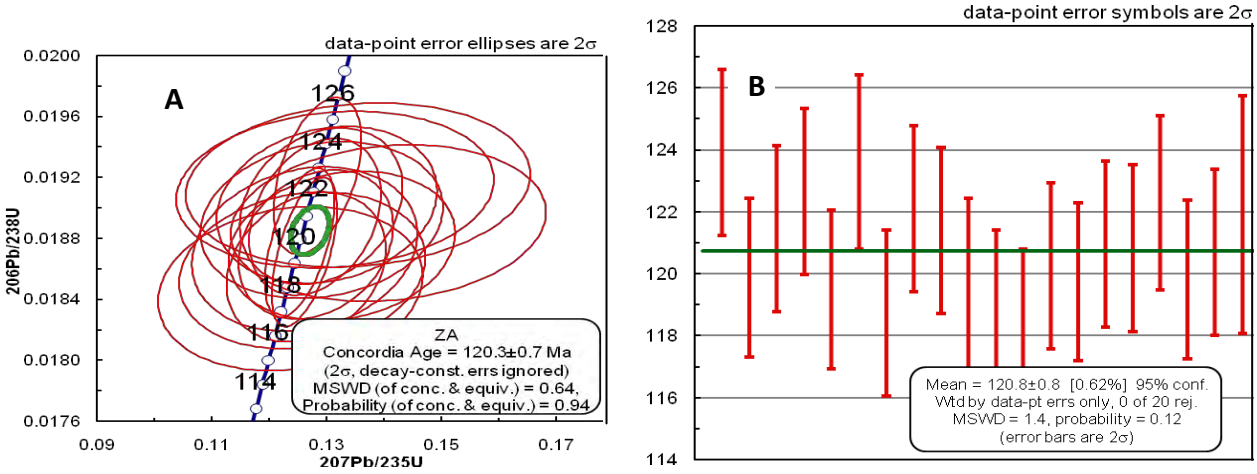

Figure 6.13: Conventional concordia plot showing U-Pb isotopic data for sample ZA from Bwanje in Ntcheu; (A) The concordia age is 120.3±0.7; (B) The mean age is 120.8±0.8 Ma. Error ellipses (A) and error boxes (B) are shown at 2σ level.

Table 6.6: Zircon U-Pb isotopic data for sample ZA from Ntcheu.

ZA																				
						RATIOS							AGES [Ma]						Conc.	
Sample	Analysis	U [ppm][a]	Pb [ppm][a]	Th [ppm]	Th/U calc	$^{207}Pb/^{235}U$[b]	2 σ[d]	$^{206}Pb/^{238}U$[b]	2 σ[d]	rho[c]	$^{207}Pb/^{206}Pb$[e]	2 σ[d]	$^{207}Pb/^{235}U$	2 σ	$^{206}Pb/^{238}U$	2 σ	$^{207}Pb/^{206}Pb$	2 σ	%	
ZA	A-2	193	4	27454	52.39	0.125	0.005	0.01877	0.00040	0.54	0.0484	0.0016	120	5	120	3	119	78	100	
ZA	A-3	117	2	26713	81.32	0.130	0.016	0.01902	0.00042	0.18	0.0496	0.0059	124	15	121	3	175	277	69	
ZA	A-4	328	6	22708	23.54	0.128	0.006	0.01921	0.00042	0.45	0.0485	0.0021	123	6	123	3	122	102	100	
ZA	A-5	711	13	10770	5.43	0.126	0.005	0.01871	0.00040	0.58	0.0489	0.0015	121	4	119	3	143	70	84	
ZA	A-8	119	2	25567	79.83	0.126	0.018	0.01859	0.00042	0.16	0.0491	0.0067	120	17	119	3	151	322	79	
ZA	A-9	118	2	26376	80.61	0.131	0.023	0.01912	0.00042	0.13	0.0499	0.0085	125	22	122	3	189	397	65	
ZA	A-10	114	2	25216	82.27	0.129	0.012	0.01901	0.00042	0.25	0.0492	0.0043	123	11	121	3	159	203	76	
ZA	A-11	80	2	5571	24.44	0.126	0.016	0.01873	0.00044	0.18	0.0489	0.0061	121	15	120	3	141	293	85	
ZA	A-12	174	3	17940	36.18	0.126	0.011	0.01861	0.00040	0.24	0.0493	0.0043	121	11	119	3	161	203	74	
ZA	A-13	63	1	6376	34.80	0.124	0.019	0.01847	0.00044	0.16	0.0486	0.0073	118	18	118	3	127	354	93	
ZA	A-15	179	3	22569	44.30	0.133	0.016	0.01875	0.00040	0.18	0.0513	0.0061	126	15	120	3	255	275	47	
ZA	A-16	195	4	17450	32.44	0.128	0.009	0.01894	0.00042	0.30	0.0490	0.0034	122	9	121	3	148	164	82	
ZA	A-17	188	4	15695	29.39	0.129	0.017	0.01892	0.00042	0.17	0.0495	0.0065	123	16	121	3	172	307	70	
ZA	A-18	68	1	3593	17.05	0.135	0.024	0.01915	0.00044	0.13	0.0513	0.0092	129	23	122	3	254	412	48	
ZA	A-19	222	4	17779	28.93	0.128	0.011	0.01876	0.00040	0.25	0.0495	0.0041	122	11	120	3	173	194	69	
ZA	A-20	136	3	13855	35.02	0.141	0.022	0.01890	0.00042	0.14	0.0540	0.0085	134	21	121	3	371	355	33	
ZA	A-1	196	4	28291	49.40	0.231	0.024	0.01941	0.00042	0.21	0.0863	0.0087	211	22	124	3	1344	195	9	
ZA	A-6	115	2	24874	71.96	0.183	0.033	0.01936	0.00044	0.13	0.0686	0.0121	171	30	124	3	886	364	14	
ZA	A-14	145	3	35467	68.17	0.172	0.023	0.01883	0.00042	0.17	0.0664	0.0087	162	21	120	3	820	273	15	
ZA	A-21	143	3	30308	71.59	0.267	0.024	0.01909	0.00060	0.35	0.1016	0.0085	241	22	122	4	1654	156	7	

[a]U and Pb concentrations and Th/U ratios are calculated relative to GJ-1 reference zircon

[b]Corrected for background and within-run Pb/U fractionation and normalised to reference zircon GJ-1 (ID-TIMS values/measured value); $^{207}Pb/^{235}U$ calculated using ($^{207}Pb/^{206}Pb$)/($^{238}U/^{206}Pb$ * 1/137.88)

[c]Rho is the error correlation defined as the quotient of the propagated errors of the $^{206}Pb/^{238}U$ and the $^{207}/^{235}U$ ratio

[d]Quadratic addition of within-run errors (2 SD) and daily reproducibility of GJ-1 (2 SD)

[e]Corrected for mass-bias by normalising to GJ-1 reference zircon (~0.6 per atomic mass unit) and common Pb using the model Pb composition of Stacey &Kramers (1975)

6.4 SYNOPSIS OF GEOCHRONOLOGICAL DATA

The age distribution of the dated pegmatites indicates their chronologic relationship with three of the four major orogenic events in central East Africa. These are the Palaeoproterozoic Ubendian and the Neoproterozoic to early Palaeozoic Pan-African orogenies, and the Mesozoic extensional tectonics related to the East-African Rift. The Mesoproterozoic Kibaran orogeny has produced large numbers of pegmatites in neighbouring countries (e.g. Tanzania, DR Congo, Burundi; Fernandez, 2007; Tack et al., 2010; Melcher et al., 2015). Although several dated pegmatites intruded basement of Mesoproterozoic protolith age, no such ages are seen in the current data set. This however may be a matter of sampling density. Ages of the pegmatites, metamorphism and magmatism in the region have been summarised in Table 6.7. The intrusive nature, sharp contacts, absence of ductile deformation of pegmatites and lack of indications for significant metasomatism (cf. Chapter 4) support pegmatite formation by magma emplacement and crystallisation, and not by anatexis or metasomatism. The ages presented above therefore indicate the ages of gemstone formation.

The oldest age in the study areas is sample GCN1 from the Nthalire pegmatites (Table 6.1; Figure 6.1), with a weighted mean age of 1859±20 Ma. Resulting from either slight Sr isotope disequilibria or analytical error, its initial $^{87}Sr/^{86}Sr$ ratio of 0.716 has a large uncertainty of ±0.024, which disallows any interpretation of specific magma source for this pegmatite. The age of the pegmatite sample does not coincide within the uncertainties with age data for the S-type Nyika granite and its associated intrusions. Dodson et al. (1975) reported an age of 1930±30 Ma based on U-Pb zircon dating for emplacement of granite and other smaller two-mica granites, after the peak of regional granulite facies metamorphism. However, the age dates from 1975 may not be analytically as robust as data produced with modern instrumentation. The Nyika granite is exposed 12 km to the east of the GCN1 pegmatite. Further Palaeoproterozoic plutonism occurred in adjacent northern Zambia around 1860 Ma, which is identical to the GCN-1 pegmatite. U-Pb SHRIMP data of granites forming part of the basement to the Muva Supergroup yielded crystallisation ages of 1868±7 and 1860±13 Ma (Brewer et al., 1979; De Waele et al., 2006). However, this area in northern Zambia is about 400 km west of the GCN1 sampling site. The emplacement of the GCN1 pegmatite may therefore be related to the widespread plutonism seen in large parts of central East Africa. Palaeoproterozoic plutonism also occurred in the Ubendian terranes in Tanzania, where granite intruded in north Upangwa terrane, north Lupa terrane and Ufipa terrane at ~1875 Ma, ~1871 Ma, and 1864 Ma respectively (Daly, 1988). These predate the final collisional event of the Ubendian Orogeny dated at 1840 Ma (Kazimoto et al., 2015).

Table 6.7: A summary of metamorphism age from literature, estimated P-T conditions for pegmatites and recorded magmatism in the region.

Studied Pegmatites	Age of metamorphism for related host rock from literature	Age Results from this study	Recorded Magmatism
GCN1	1995 Ma (Ring et al., 1997); ~1880 Ma –Katuma (Daly, 1988)	1859±20 Ma (Rb-Sr)	1875 Ma – Upangwa, 1871 Ma - north Lupa, 1864 Ma – Ufipa (Daly, 1988); 1868±7 Ma, 1860±13 Ma (Brewer et al., 1979; De Waele, 2006)
THMB	Peak of granulite facies metamorphism at ~570-550 Ma. (Andreoli, 1981; 1984; Kröner et al., 2001).	731±3 Ma (U-Pb)	Lithospheric heating, extension, rift related magmatic events and break up of Rodinia at about 735-720 Ma (Unrug, 1998); emplacement of alkaline plutons at 726 Ma in southern Malawi (Ashwal et al., 2016), and Meponda that is 100 km to the north of the study area in Mozambique, emplaced at 755±115 Ma (Lulin et al., 1985)
NNO1	650-600 Ma (Meert and van der Voo 1997).	725±15 Ma (U-Pb)	Lithospheric heating, extension, rift related magmatic events and break up of Rodinia at about 735-720 Ma (Unrug, 1998)
MNM1D	650-600 Ma (Meert and van der Voo 1997).	597±19 Ma (U-Pb)	Collision of East and West Gondwana (Unrug, 1998) Plutonism in late stages of East African orogen at 650-600 Ma (Meert and van der Voo 1997).
GCW1	580-550 Ma (Ring et al., 2002); 569-527 Ma – Lichinga, (Bingen et al., 2009)	498.4±5.2 Ma (Rb-Sr)	Lithospheric 550-480 Ma delamination in Mozambique, Madagascar (Fritz et al., 2013); Cambro – Ordovician granites at 535-470 Ma (Macey et al., 2007 and Grantham et al. 2007).
GM1	580-550 Ma (Ring et al., 2002)	485.1±4.8 Ma (Rb-Sr)	550-480 Ma extension (Fritz et al., 2013), Late to post tectonism plutonism at 517-493 Ma; Cambro – Ordovician granites at 535-470 Ma (Macey et al., 2007 and Grantham et al. 2007)
GD1	1080-1050 Ma, Zambia (Johnson et al. 2005; De Waele et al., 2008)	489.0±5.1 Ma.(Rb-Sr)	550-480 Ma extension (Fritz et al., 2013); Late to post tectonism plutonism at 510-470 Ma (Zambia; Johnson et al. 2005; De Waele et al., 2008); Cambro – Ordovician granites at 535-470 Ma (Macey et al., 2007 and Grantham et al. 2007)
GNS1; GNS4	950 Ma; 550-520 Ma (Unango-Mozambique; Bingen et al., 2009). 571-549 Ma (Kröner et al., 2001)	555.4±4.7 Ma; 552.4±6.0 Ma; (Rb-Sr)	East African orogen 560-550 Ma (Möller et al., 2000; Meert, 2003); 605-550 Ma magmatism (Kröner et al., 2001); late Neoproterozoic granitic rocks at 575-545 Ma – NE Mozambique (Macey et al., 2007 and Grantham et al. 2007); 550-480 Ma post-tectonic magmatism (Unango-Mozambique; Bingen et al., 2009).
GN1	571-549 Ma (Kröner et al., 2001)	459.6±5.2 Ma (Rb-Sr)	Waning stages of Pan-African cycle, 605-550 Ma magmatism (Kröner et al., 2001); 550-480 Ma post-tectonic magmatism (Unango-Mozambique; Bingen et al., 2009); Cambro – Ordovician granites at 535-470 Ma (Macey et al., 2007 and Grantham et al., 2007)
GU1	571-549 Ma (Andreoli 1981; Kröner et al., 2001)	520±5.5 Ma (Rb-Sr)	520-515 Ma Kuunga tectonic extension and plutonism 605-550 Ma magmatism (Kröner et al., 2001); 550-480 Ma post-tectonic magmatism (Unango-Mozambique; Bingen et al., 2009); Cambro – Ordovician granites at 535-470 Ma (Macey et al., 2007 and Grantham et al., 2007).
ZA	Not determined	120.3±0.7 Ma (U-Pb)	Magmatism in Chilwa Alkaline Province

Pan-African pegmatites

The term Pan-African is here used in a broad sense, because the pegmatites dated in this study include intrusions that spread over 270 m.y., from ~730 to ~460 Ma. The oldest pegmatites in this group can be related to the initiation of the Pan-African Wilson cycle during Rodinia break-up, whereas the younger ages may be related to extension due to lithospheric delamination that affected Mozambique and Madagascar at ~550-480 Ma (Fritz et al., 2013). Some of the younger ages can be related to granites typical of the Kuunga Orogeny, caused by the collision of North Gondwana and South Gondwana (Grantham et al., 2013). However, the youngest pegmatites, of Ordovician age, postdate by some measure what is generally considered the end of the Pan-African cycle (Kennedy, 1964).

The zircons of pegmatite sample THMB and NNO1 from the Neoproterozoic basement in the Neno and Mangochi districts yield concordant ages of 731±3 Ma and 725±4 Ma respectively. These ages coincide within the emplacement of alkaline plutons; Thambani at 726 Ma to the southern part of Neno in southern Malawi (Ashwal et al., 2016), and Meponda, which is 100 km to the north of the study area in Mozambique, emplaced at 755±115 Ma (Lulin et al., 1985). This time period marks the breakup of Rodinia (Unrug, 1998). Accordingly, the magma generation and emplacement of the THMB and NNO1 pegmatites most likely are related to lithospheric heating, extension, rifting and breakup of Rodinia at about 720-735 Ma.

The zircon of pegmatite sample MNM1D from the Neoproterozoic basement in the Nankhwali – Mangochi district yield the concordant age of 594±3 Ma. This age coincides with the collision of East and West Gondwana (Unrug, 1998), mainly the last stages of formation of the East African Orogen. However, this study could not establish large-scale geological features formed at that time in the vicinity of the sampling sites.

The Rb/Sr mineral isochrons from the Neoproterozoic pegmatites from the Ntcheu district (Sample GNS1, GNS4, Table 6.1, Figure 6.5 and 6.6) yield ages of 555±4.7 Ma and 552.4±6 Ma, which postdate the main collision of East and West Gondwana (Unrug, 1998). These ages could fit well with ages for East African Orogeny that involved the west-directed collision between Tanzania/Congo and India cratons (Meert, 2003). Their Sr_i of 0.706067 and 0.70558 indicate that the parent granite magma, likely emplaced in the crust, might have formed from sources with a significant mantle component. Within error limits, the Sr_i ratios of GNS1 and GNS4 are indistinguishable, which, together with their near-identical age, suggests that they formed from the same source, or from sources of the same age and with similar Sr isotopic signatures. Furthermore, the pegmatites seem to be spatially related, since they are separated by

only about 15 km. They also have similar mineral compositions with slight modal variations, and they both bear gem-quality tourmalines. Sharp pegmatite contacts suggest magma intrusions into solid host rocks (Section 4.3.8). However, large plutonic rocks in the region that may be potential pegmatite sources have not been identified.

The Rb/Sr isochron for the Cambrian Balaka pegmatite yields an emplacement age of 520.4±5.5 Ma (Sample GU1, Table 6.2, Figure 6.8), and this pegmatite, with a Sr_i of 0.718733, derived from crustal magma sources. The age of the GU1 pegmatite coincides with late Pan-African Kuunga orogen plutonism in NE Mozambique at 520 – 515 Ma (Bingen et al., 2009), following the collision of N and S Gondwana (~580-540 Ma; Grantham et al., 2013). A possible metamorphic overprint of the pegmatite will be discussed in the context of fluid inclusion data in Chapter 9.

The isochrons from the Chisenga and Wenya pegmatites (Sample GCW1, Table 6.1, and Figure 6.2) yield concordant ages of 498±5.2 Ma, indicating emplacement at the Cambrian/Ordovician boundary, post-dating the main Pan-African orogeny. Grantham et al. (2013) describe post-collisional tectonics in Sør Rondane (Antarctica) that are correlated with the crustal evolution in northern Mozambique, and that extend from 520 to 490 Ma, overlapping with the age of GCW1. The very high Sr_i of 0.790177 suggests significant crustal contamination during rise of the pegmatitic melt. The presence of CH_4 and N_2 in fluid inclusions (Chapter 8) supports this.

The Rb/Sr isochron for the Ordovician Kafukule pegmatite yields an emplacement age of 485.1±4.8 Ma (sample GM1, Table 6.1, Figure 6.3). The Sr_i of 0.7762 ± 0.0012 suggests crustal magma sources and probably significant contamination during magma evolution. The pegmatite is similar to GD1 in age (485±4.8 Ma) and Sr_i (0.7762). Both pegmatites have identical ages to the 485 Ma Lundazi pegmatites in adjacent Zambia (Graziani et al., 1983).

The Dowa pegmatite (sample GD1, Table 6.1, Figure 6.4) was emplaced at 489±5.1 Ma. The high Sr_i of 0.7405 gives evidence for a large crustal component in the magma that formed the pegmatite. The age of the pegmatite coincides with the emplacement of the Senga Bay granite of the Lake Malawi granitic province (489±14 Ma), but the Senga Bay granite‟s Sr_i of 0.7075 suggests a significant contribution of juvenile mantle magma (White, 2015). The pegmatites could also be correlated with the Sinda Batholith in Zambia, 170 km to the west, which has been dated as 489±42 Ma, and which with a Sr_i of 0.710±0.0008 appears to be of crustal origin

(Haslam et al., 1986). The age date has been narrowed down by more recent work that proposes an age of emplacement of 502±8 Ma (Manttari, 2009), which within the uncertainty overlaps with the age of GD1 emplacement. The presence of CH_4 and H_2S in fluid inclusions in GD1 supports the presence of crustal fluids (see Chapter 8). Like all other Pan-African pegmatites investigated in this study that are ~520 Ma or younger, this pegmatite is a crustal derivative.

Pegmatite GN1 from the Ntcheu district, containing tourmaline and sunstone as gems, is the youngest of the Pan-African pegmatites with and emplacement age of 459.6±5.2 Ma. Its Sr_i of 0.7893 is almost as high as that of GCW1 (Table 6.1), and accordingly shows crustal magma sources. The tectonic context of this pegmatite is unclear, since it postdates all known significant tectonometamorphic events in the region by at least ~20-30 m.y.

Rift-related pegmatites

The 120.3±0.7 Ma ZA pegmatite from the Mesozoic Ntcheu pegmatite field is spatially, chronologically, and very likely genetically, related to the Chilwa Alkaline Province. These plutons are interpreted as an anorogenic suite (Woolley 2001) and are related to the initiation of the East African Rift (McConnell, 1972).

7. MICA GEOCHEMISTRY AND PEGMATITE CLASSIFICATION

7.1 INTRODUCTION

This chapter presents results for the geochemistry of mica in the gemstone bearing pegmatites. The analyses are for major oxides, trace and rare earth elements. The major oxides are analysed in order to evaluate any compositional variations that may indicate complex magmatic processes during mica growth. Trace elements are used to monitor fractionation processes in the pegmatites melt and provide constraints for pegmatite classification. Since trace elements show that even masses are much higher than odd masses, the data were normalised against average upper continental crust (UCC) or chondrite compositions in order to remove jaggedness that would result when original data were plotted. UCC-normalized trace elements patterns approximate the relative abundances of elements in upper continental crust whereas chondrite-normalised abundance patterns approximate the primordial relative abundances of elements in the silicate part of the earth. Rare Earth Elements (REE) are analysed in order to understand the petrogenetic conditions for pegmatite evolution. In this study, UCC-normalized trace elements and REE patterns (Taylor and McLennan, 1995) and chondrite normalised abundance patterns (Nakamura, 1974) have been presented in either spider plots or in boxplots. Where the boxplot has been used, the black bar in the box shows the median. The top and lower bars represent the greatest and lowest values excluding outliers (represented by diamond symbols) hence they show sample variability. Furthermore, the chondrite normalised REE abundance patterns (Nakamura, 1974) have been used to show the behaviour of more elements including Eu, which are not shown in the UCC-normalized REE pattern (Taylor and McLennan, 1995). An Eu anomaly can either be negative or positive. A negative anomaly means fractional crystallisation of plagioclase whose removal yields REE enriched - Eu depleted liquids whereas positive anomalies in whole rock compositions are typical for plagioclase-rich cumulates (Bowden and Whitely, 1974). All the normalised abundance patterns have been used in classification, nomenclature and petrogenesis of the pegmatites.

Since representative bulk sampling of a pegmatite is difficult due to the large size of the constituent mineral crystals, mica is commonly used as a representative proxy that monitors the evolution of pegmatitic melt. An introduction to mica geochemistry and its significance to pegmatite formation have already been given in Chapter 5. Since the chemical composition of mica depends strongly on the magma it crystallised from (Villaros et al., 2010), trace elements in muscovites have been used to understand the progress of differentiation of the pegmatite magmas and its origin. The K/Rb ratios of micas, together with Li, F, Cs, Sn, Ba and Zn contents are commonly used as petrogenetic indicators of the degree of pegmatite evolution. The

distribution of Rb, Sr, Ba, K, Pb, Ga can be used to evaluate the degree of pegmatite melt evolution (Kontak et al., 2002; Alfonso et al., 2003; Ren, 2004). The compatible elements Ba and Sr concentrate in the melt only during the early stages of magmatic differentiation, whereas incompatible elements concentrate in late residual portions of the parental melt, from which granitic pegmatites form. According to Cërny (1991a), trace elements in mica can be used to examine the degree of evolution and to classify the pegmatites, using binary element plots. The plots include the most widely used chemical indicator elements for magma evolution. The K/Rb ratio in mica (Clarke, 1992) varies with trace element concentration in different types of pegmatites and according to their degree of evolution. Furthermore, K/Rb as a fractionation index in micas decreases with the increase of the concentration of certain incompatible elements (Foord et al., 1995; Roda-Robles et al., 2006; Vieira et al., 2011). K/Rb vs. Cs in muscovite is considered to be the best indicator of pegmatite evolution (Cërny et al., 1985; Jolliff et al., 1987; Cërny, 1991a).

The samples will be presented in certain groups considering the spatial distribution, age and gemstone mineralisation. The groups are as follows: (i) Palaeoproterozoic samples CNC (Chinthu-Nthalire-Chitipa) from Chitipa; (ii) Pan-African samples CCC (Chisenga-Central-Chitipa) and MWC (Matulo-Wenya-Chitipa) from Chitipa, (iii) Pan-African samples GM (Group Daniel Jere-Mzimba), samples HEM (Homero-Ekwendeni-Mzimba) and samples MEM (Malidade-Emcisweni-Mzimba) from pegmatites from Mzimba in the northern region of Malawi; (iv) Pan-African samples DHD (Dzaleka-Hilo-Dowa) from Dowa; (v) Pan-African GNS (Gumbo-Ntonda-Senzani) from Ntcheu; (vi) Pan-African samples MSN (Mzawira-Sikulamowa-Ntcheu) from Ntcheu in central region of Malawi and (vii) Pan-African samples CUB (Chiripa-Ulongwe-Balaka) from Balaka in southern region of Malawi (Figure 3.9).

This chapter will present the geochemical data that allow classifying the pegmatites to a significant extent. However, a full classification will be presented in Chapter 9, contextualising the geochemistry presented here, the petrographic and mineralogical features (Chapter 4), the metamorphic grade of host rocks, and spatial and genetic relationship to granitic plutons, and results from fluid analysis (Chapter 8).

7.2 CHEMICAL COMPOSITION OF MICAS FROM PALAEOPROTEROZOIC AND PAN-AFRICAN PEGMATITES

Muscovitic mica has only a limited potential of major elemental variations, and BSE images of all studied micas show that the selected crystals do not show any major elemental composition that would cause variations in the BSE signal intensity (Figure 7.0 A, B). Hence the major and minor elemental composition was determined on the basis of randomly placed EPMA point analyses, which confirmed homogeneity of individual crystals. Trace elemental variations were analysed in a similar way using LA-ICP-MS.

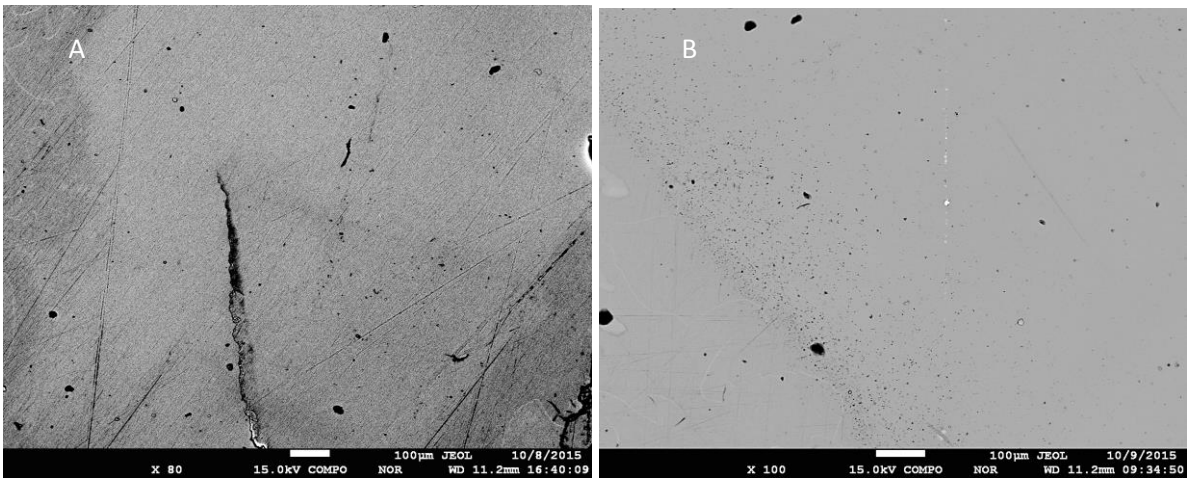

Figure 7.0: Uniform signal intensity on backscattered electron images suggests homogenous major elemental composition. Examples are micas from (A) aquamarine-bearing pegmatite sample GM3 from Kafukule, Mzimba in northern Malawi; (B) amethyst-bearing pegmatite sample CUB1B from Balaka, southern Malawi.

7.2.1 Tourmaline-bearing, and Beryl- and Tourmaline-bearing Pegmatites from Chitipa

This group includes the ***Palaeoproterozoic*** pegmatites from Nthalire and the ***Pan-African*** pegmatites from Chisenga and Wenya in Chitipa. Representative compositions are shown in Table 7.1A, B and the full data sets can be found in Appendix 2.1A and B. The Si content (6.18 – 6.21 atoms per formula unit; a.p.f.u.) is generally higher than Al (5.09 - 5.19 a.p.f.u.).

Trace elemental analysis has confirmed low concentrations of Li, which have been partly used to classify the mica as proposed by Tischendorf et al. (1997), where [Fe_{tot} + Mn +Ti - Al^{vi}] is plotted versus [Mg – Li]. The analysed white micas plot mainly in the muscovite field, with a trend range towards phengite (Figure 7.1A). According to Si versus Al_{total} diagram (Figure 7.1B), the tetrahedral occupancies of Si are 6.1 to 6.2 a.p.f.u. for muscovites from Palaeoproterozoic pegmatites, similar to the spread of 6.1 to 6.3 a.p.f.u. for the Pan-African pegmatites. These tetrahedral occupancies of Si are less than 6.5 a.p.f.u that is a minimum for

phengite. The octahedral occupancies are between 4.0 to 4.1 a.p.f.u. for the Palaeoproterozoic and 4.0 to 4.2 a.p.f.u. for the Pan-African pegmatitic micas. Calculated anion site occupancy is 4.0 a.p.f.u., and the interlayer occupancy ranges from 2.0 to 2.6 a.p.f.u. for the Pan-African, and 2.2 to 2.4 a.p.f.u. for the Palaeoproterozoic micas (Table 7.1; Appendix 2.1A).

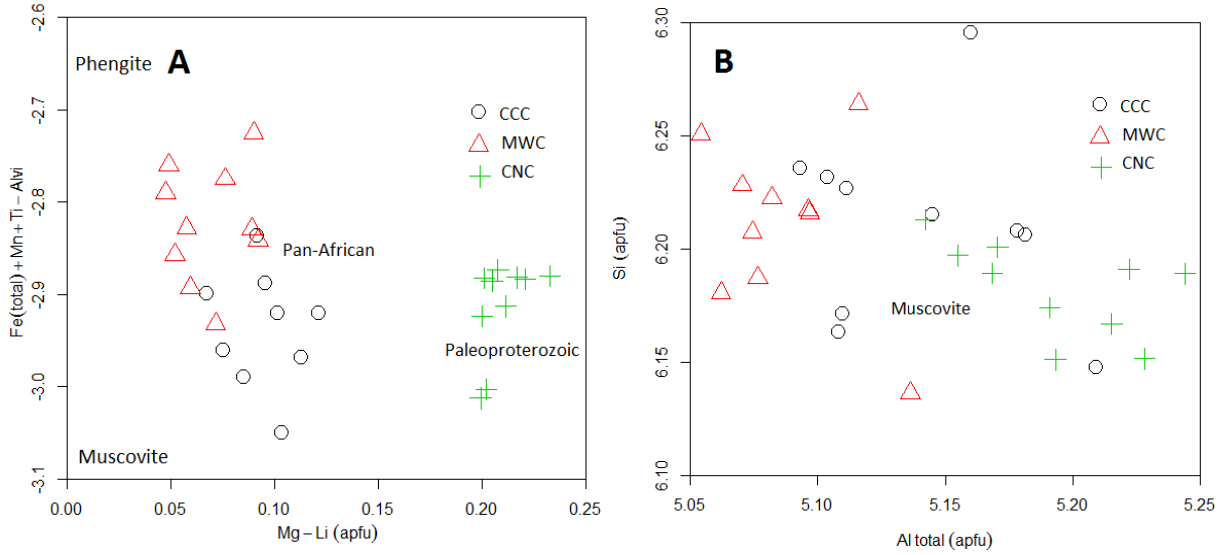

Figure 7.1: Chemical composition of mica for Palaeoproterozoic and Pan-African pegmatites from Chitipa; (A) Mica classification proposed by Tischendorf et al. (1997); (B) Classification of white mica phases in Si vs. Al diagram.

Table 7.1A: Average composition (n=10 each) for major and minor elemental data of micas from Palaeoproterozoic tourmaline-bearing pegmatite (CNC) and Pan-African beryl- and tourmaline-bearing pegmatites (CCC and MWC) from Chitipa. Full geochemical data in Appendix 2.1A.

Mineral	Ms	Ms	Ms
	Palaeoprot	Pan-African	Pan-African
Sample	CNC	CCC	MWC
SiO_2	45.61	46.18	46.52
TiO_2	0.26	0.34	0.63
Al_2O_3	32.48	32.29	32.42
FeO	3.76	3.55	3.52
MnO	0.06	0.06	0.07
MgO	1.04	0.92	1.05
CaO	0.01	0.01	0.01
Na_2O	0.58	0.64	0.65
K_2O	12.37	12.39	11.63
F	0.03	0.77	1.07
Cl	0.01	0.02	0.01
Li_2O*	0.00	0.16	0.18
H_2O*	4.42	4.10	4.05
Subtotal	100.63	101.43	101.81
O=F,Cl	0.02	0.33	0.46
Total	100.61	101.10	101.35
Site -T			
Si	6.18	6.21	6.21
Al^{iv}	1.82	1.79	1.79
∑(Si,Al)	8.00	8.00	8.00
Site-M			
Al^{vi}	3.38	3.35	3.30
Ti	0.03	0.03	0.08
Fe	0.43	0.40	0.39
Mn	0.01	0.01	0.01
Mg	0.21	0.18	0.21
Li*	0.00	0.09	0.14
∑(Al, Fe,Mg,Ti)	4.05	3.97	4.12
$\sum Al_{total}$	5.19	5.14	5.09
Site - A			
Ca	0.00	0.00	0.00
Na	0.15	0.17	0.17
K	2.14	2.16	2.07
∑(Ca,Na,K)	2.30	2.33	2.24
Site - OH			
OH*	3.98	3.67	3.55
F	0.01	0.33	0.45
Cl	0.00	0.00	0.00
∑(F,Cl,OH)	4.00	4.00	4.00
TOTAL	18.34	18.39	18.35

* Calculated.

Table 7.1B: Average analyses of trace elements of micas from Palaeoproterozoic tourmaline-bearing pegmatite (CNC) and Pan-African beryl- and tourmaline-bearing pegmatites (CCC, MWC) from Chitipa. The complete data set is presented in Appendix 2.1B. All concentrations are given in ppm.

Element	CNC1B-Mean	Max-Min	CCC Mean	Max-Min	MWC-mean	Max-Min
Li	34	[38-28]	845	[999-739]	1133	[1321-956]
Be	3	[7-2]	11	[15-9]	20	[26-16]
B	53	[67-43]	35	[45-34]	35	[41-27]
Sc	31	[57-19]	34	[39-27]	37	[45-31]
Ti	1529	[2088-1246]	2364	[2492-2075]	4260	[4907-4142]
V	31	[128-12]	42	[54-24]	15	[26-10]
Cr	1	[13-0.14]	7	[32-1]	0.3	[0.62-0.18]
Mn	257	[277-230]	503	[543-481]	761	[641-738]
Co	5	[9-4]	9	[23-3]	3	[3-2]
Ni	4	[5-3]	2	[3-2]	0.2	[0.47-0.06]
Cu	4	[34-0.04]	1	[1-0]	0.1	[0.2-0.04]
Zn	61	[128-37]	128	[133-119]	113	[113-97]
Ga	116	[140-85]	125	[129-118]	119	[124-119]
Rb	1498	[1637-1076]	1441	[1485-1350]	1674	[1744-1695]
Sr	3	[6-2]	1	[2-1]	4	[4-4]
Y	0.01	[0.009-0.07]	0	0	0.02	[0.04-0.01]
Zr	3	[30-2]	2	2	3	[3-3]
Nb	324	[441-46]	206	[222-190]	199	[210-204]
Mo	4	[5-4]	0	0	0.3	[0.35-28]
Sn	9	[13-6]	25	[29-21]	16	[17.38-14.05]
Cs	34	[99-24]	16	[17-15]	23	[24.59-20.53]
Ba	112	[335-61]	131	[154-99]	96	[143-79]
Hf	0.43	[0.55-0.27]	0	0	0.3	[0.34-0.22]
Ta	16	[18-12]	13	[14-12]	21	[23-22]
W	76	[89-59]	26	[29-24]	34	[49-32]
Pb	4	[9-3]	4	[6-3]	4	[5.22-3.81]
Th	0.001	[0.003-0.0034]	0	0	0.001	[0.008-0.002]
U	0.021	[0.026-0.015]	0	0	0.011	[0.017-.001]

Palaeoproterozoic pegmatite

In the Palaeoproterozoic pegmatite (sample CNC1B; Table 7.1B; Appendix 2.1B), the micas generally show low concentrations of trace elements, but with higher concentrations in Rb (1076-1637 ppm), Ta (12-18 ppm), Nb (46-441 ppm), Ti (1246-2088 ppm) and less Ba (61-335 ppm). Li and Be are low while Ga has a wider concentration range (85-140 ppm). Boron (43-67 ppm) shows higher concentration than Be (2-7 ppm). A high Cu value in a single analysis is probably caused by a micro-inclusion of a Cu mineral (sulphide).

In the spider diagram (Figure 7.2A) comparing the mica/UCC composition (upper continental crust; Taylor and McLennan, 1995), Rb and Ti are strongly enriched, Ba, Cs and Nb are moderately enriched, Ta, Sr and Zr are slightly enriched, whereas P and Hf are slightly depleted, Th, U and Y are strongly depleted.

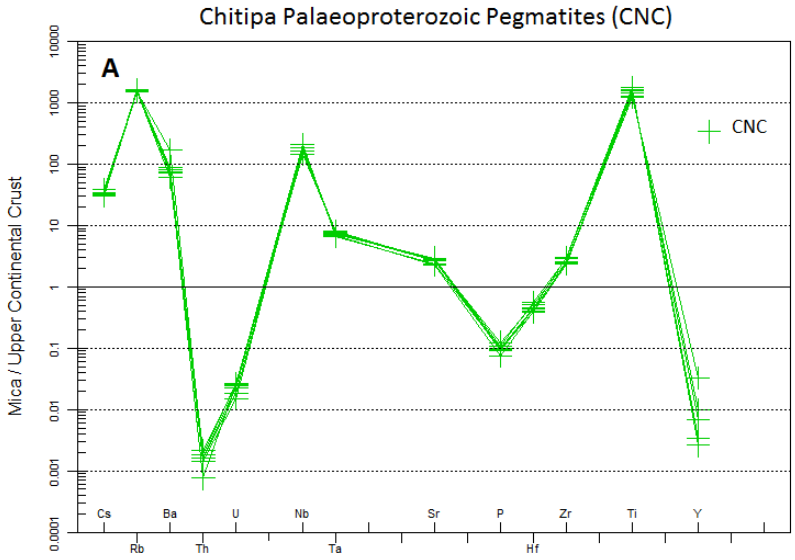

Figure 7.2A: Normalised relative abundance patterns of trace elements (Taylor and McLennan, 1995) for muscovite from Palaeoproterozoic pegmatites from Nthalire, Chitipa (sample CNC).

The UCC-normalised diagram for REE (Figure 7.2B, Appendix 2.1C) shows that all REE are moderately depleted, except Tb and Tm, which are strongly depleted. This suggests that the pegmatite-forming residual melts are rich in rare–element cations, Nb, Ta and Ti and also in Rb, Cs and Ba. The high B content is in agreement with abundant tourmaline in the Palaeoproterozoic pegmatites.

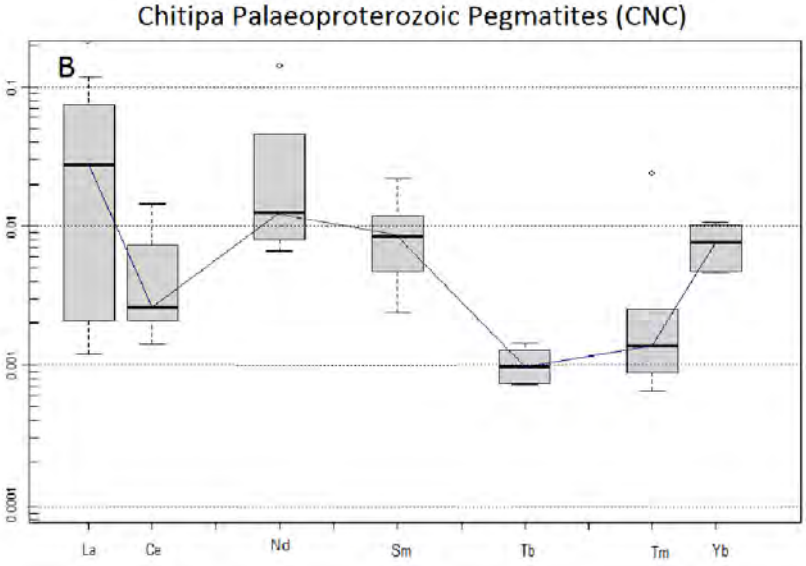

Figure 7.2B: Boxplot of UCC-normalised relative abundance pattern of REE (Taylor and McLennan, 1995) for muscovite from Palaeoproterozoic tourmaline-bearing pegmatites from Nthalire, Chitipa. The diamond symbols represent outliers.

7.2.2 Pan-African Pegmatites from Chisenga (CCC) and Wenya (MWC), Chitipa.

The trace element and REE analytical results for mica from the Pan-African pegmatites from Chitipa are presented in Table 7.1B, Appendix 2.1B. The muscovite in CCC (Table 7.1B, Appendix 2.1B) generally shows low concentrations of trace elements, but with fairly abundant in Rb (1350-1485 ppm), Ta (12-14 ppm), Nb (190-222 ppm), Ti (2075-12492 ppm) and less abundant Ba (99-154 ppm). Li concentrations are high (739-999 ppm), whereas Ga (118-129 ppm), B (34-45 ppm) and Be (9-15 ppm) show lower concentrations.

In MWC muscovites (Table 7.1B, Appendix 2.1B) trace elements have generally low concentrations but with enrichment pattern similar to CCC muscovite. They show high Rb (1695-1744 ppm), Ti (4142-4907 ppm), but less Nb (210-240 ppm), Ta (22-23 ppm) and Ba (79-143 ppm). Li (956-1321 ppm) and Ga (119-124 ppm) are fairly abundant and minor B (27-41 ppm) and Be (16-26 ppm) are present.

The binary diagrams (Figure 7.3A, D-G) show a general decrease in the K/Rb ratio in the muscovite with increasing Rb, Be, Cs, Li, Nb and Ta in the Pan-African pegmatites. A reversed general, but not strongly developed trend is seen for Ti and Be. Ba and K/Rb are not correlated. In the muscovites from Chisenga (CCC) and Wenya (MWC), the K/Rb ratio correlates negatively with Ti (Figure 7.3H). Lithium concentrations generally increase in the muscovites from Chisenga (CCC) to Wenya (MWC) as shown in Table 7.1B and Appendix 2.1B.

According to Cërny (1982b), a plot of K/Ba versus Ba (Figure 7.3J) can identify the extent of fractionation, where the steeper the gradient in Ba, the less fractionated the pegmatites are. The data show that MWC pegmatites, with a steep gradient, are more highly fractionated than CCC pegmatites.

Since Ga behaves geochemically similar to Al, a plot of Al/Ga against Ga (Figure 7.3K) shows a systematic correlation with increasing Ga contents from Wenya (MWC) towards Chisenga (CCC) pegmatites.

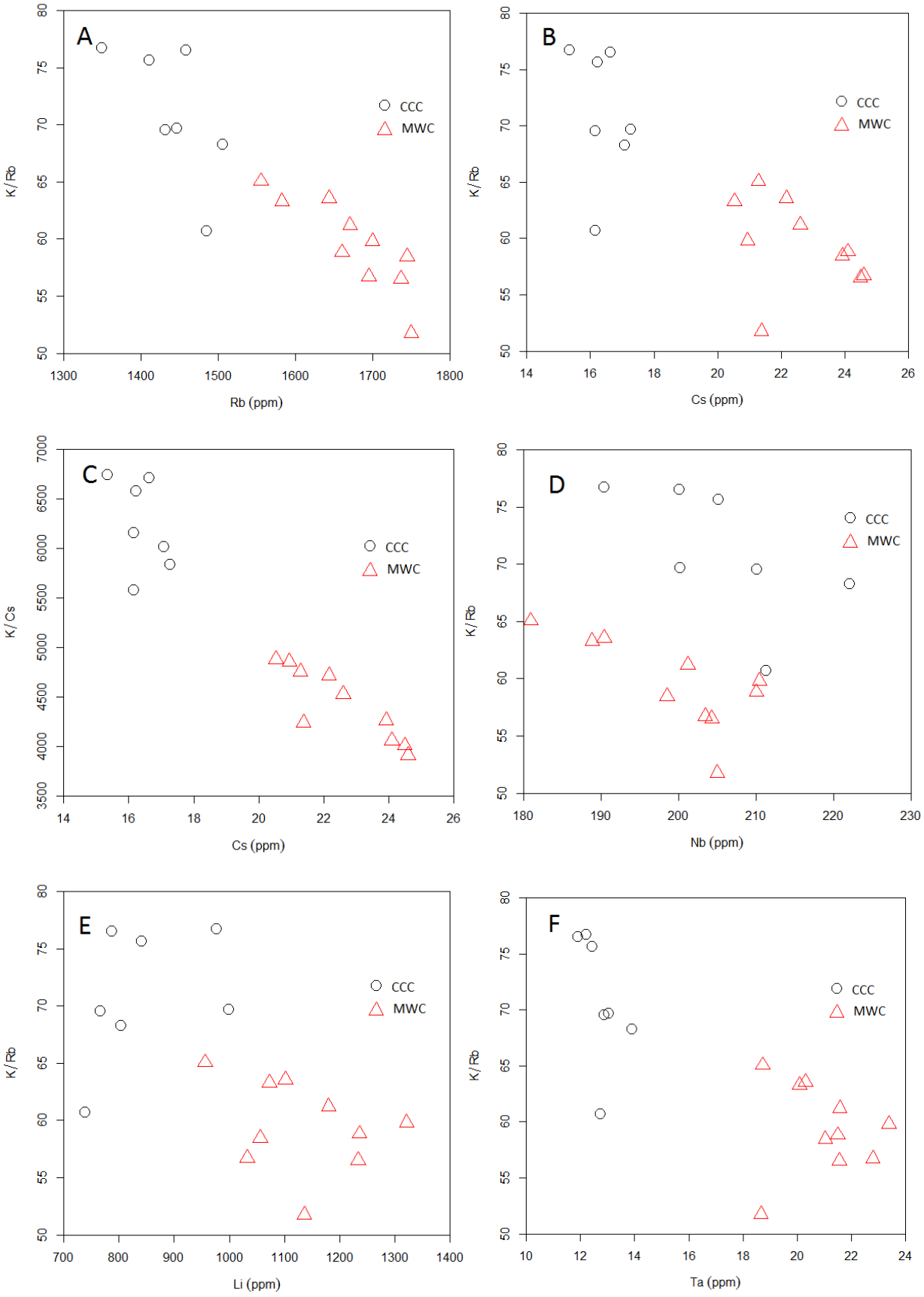

Figure 7.3A-F: Binary plots of selected compatible and incompatible element ratios in micas illustrate fractionation of CCC and MWC Pan-African pegmatites.

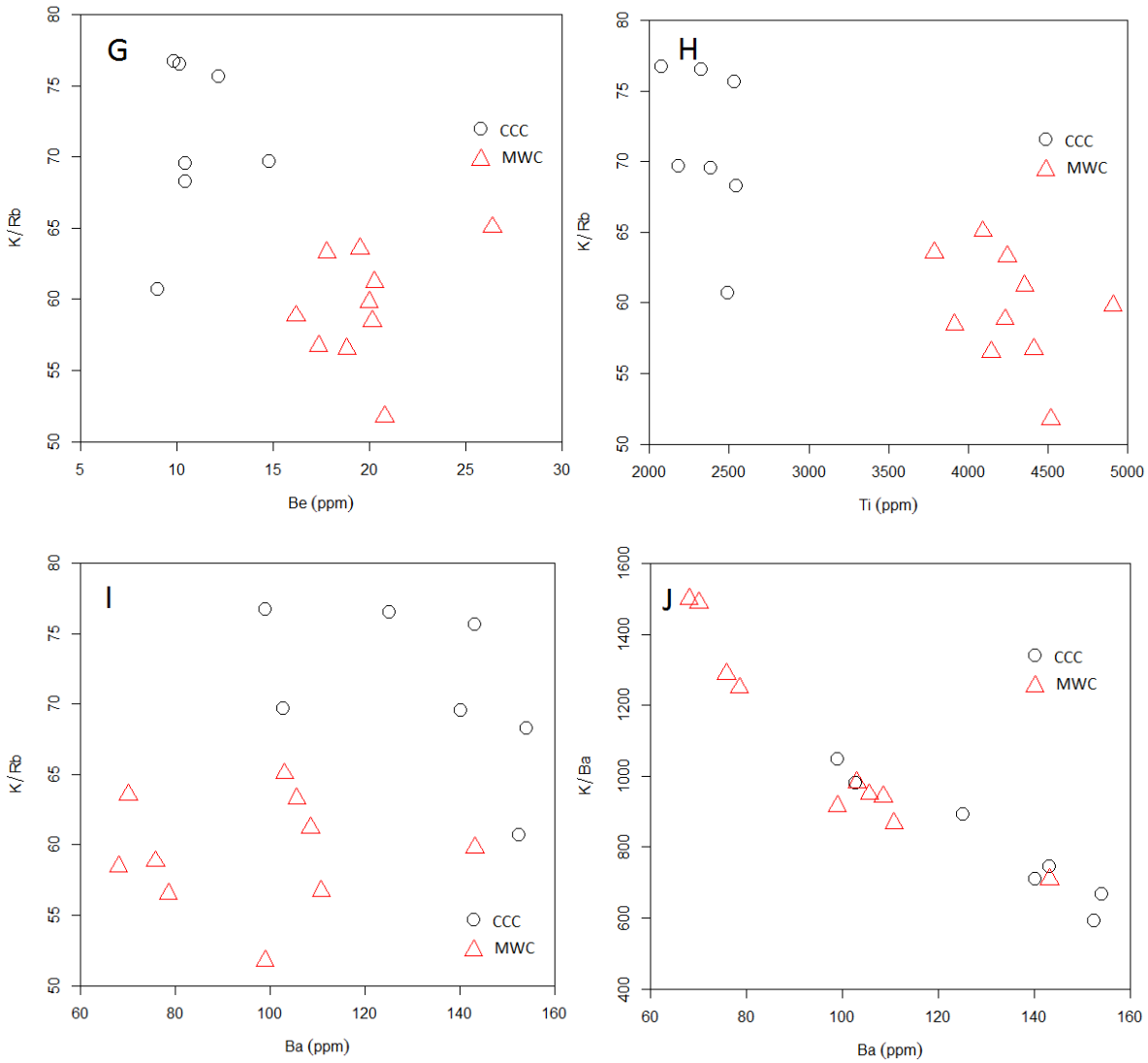

Figure 7.3G-J: Binary plots of selected compatible and incompatible element ratios in micas illustrating fractionation of CCC and MWC Pan-African pegmatites.

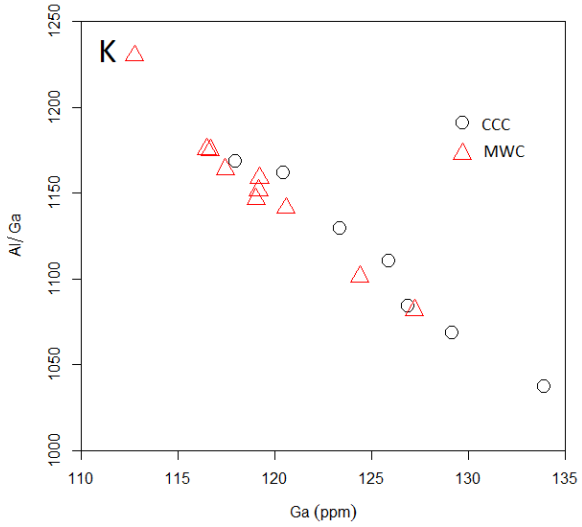

Figure 7.3K: Binary plots of elements (Al/Ga vs. Ga) in micas from CCC and MWC pegmatite field.

The spider diagram for the samples CCC and MWC pegmatites from Wenya and Chisenga shows uniform patterns (Figure 7.3L). Rb and Ti are strongly (2000-5000 x) enriched, Nb, Ta, Cs and Ba are moderately (7-200 x) enriched, Sr and Zr are slightly enriched (1.5-5 x) and Hf, P and Zr are slightly depleted (~0.1 to 0.4 x UCC), and Th, U and Y are strongly depleted. Wenya samples show slightly higher Ta enrichment and more Sr enrichment compared to Chisenga samples.

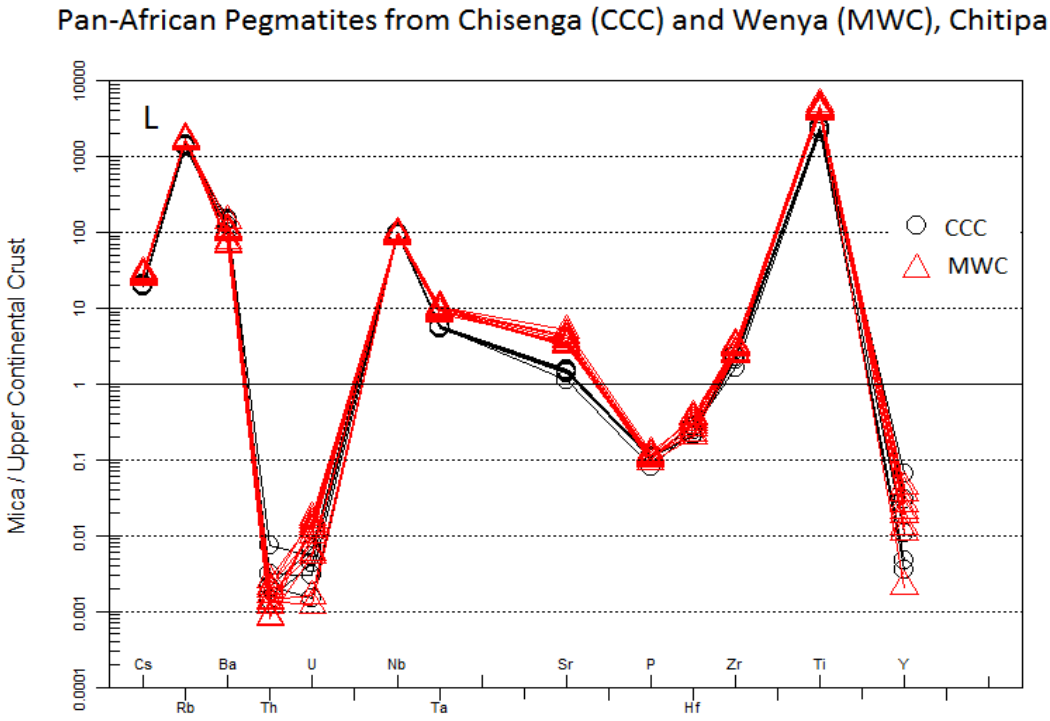

Figure 7.3L: UCC-normalised abundance patterns of trace elements for muscovite from Pan-African pegmatites from Chisenga (CCC) and Wenya (MWC) in Chitipa, northern Malawi after Taylor and McLennan (1995).

In UCC-normalized REE pattern (Taylor and McLennan, (1995); Figure 7.3M, Appendix 2.1C), the Pan-African Chisenga (CCC) and Wenya (MWC) pegmatites show the strongest (0.0007 x UCC) depletion seen in Tm and Tb.

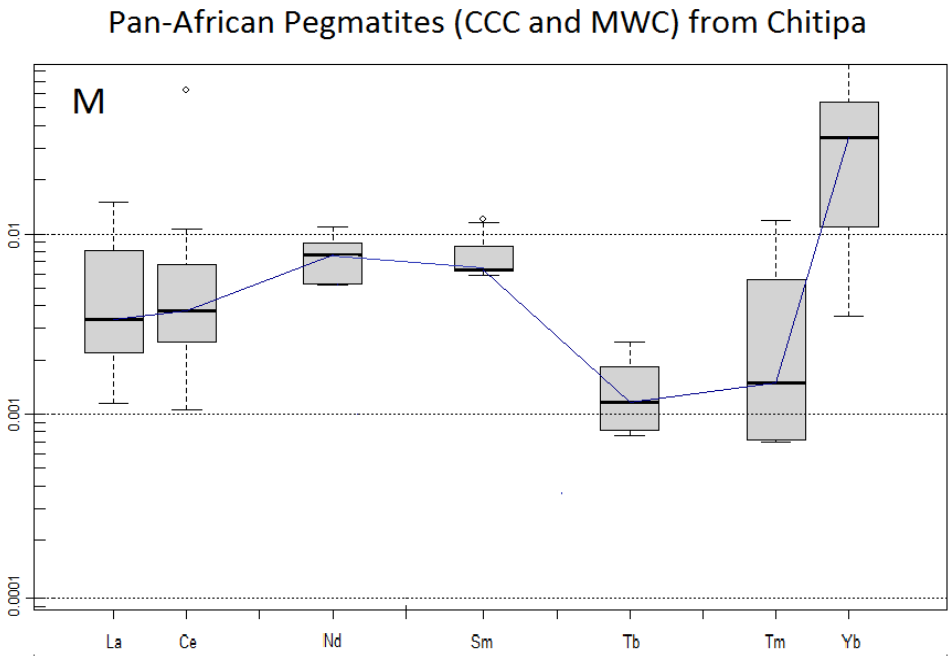

Figure 7.3M: Boxplot of UCC-normalised relative abundance pattern of REE (Taylor and McLennan, 1995) in muscovite from Pan-African beryl and tourmaline-bearing pegmatites from Chisenga and Wenya in Chitipa. The diamond symbols represent outliers.

7.2.3 Pan-African Pegmatites from Luhomero (HEM) and Kafukule (GM) in Mzimba

The chemical compositional variations for the Pan-African pegmatites are shown in Table 7.2A-B, and in Appendix 2.2A-B. The micas are peraluminous, indicated by their Al saturation index values of greater than 1. However, in the biotite Mg is higher than Al. According to mica classification proposed by Tischendorf et al. (1997), in which [Fe_{tot} + Mn +Ti - Al^{vi}] is plotted versus [Mg – Li], the analysed white micas plot mainly in the muscovite field (Figure 7.4A). According to Si versus Al_{total} diagram (Figure 7.4B), the muscovites have Si of 6.1 to 6.33 a.p.f.u. In comparison to the muscovite (CCC, MWC) from Chitipa (Figure 7.1B), the entire set of muscovite analyses plots below phengite (Si = 6.5) and close to muscovite in the muscovite celadonite series (Figure 7.4C). Phlogopite has a uniform composition with Al^{iv} between 2.55 and 2.58 a.p.f.u., indicating a large eastonitic mica component; its X_{Mg} is 0.94-0.95 (Figure 7.4D).

According to the Forster (1960) diagrams showing Li - R_{2+} - R_{3+}: Li - R_{3+} (Al^{vi}+Ti) - R_{2+} (Fe+Mn+Mg), the mica compositions show Al-rich muscovite to lithian muscovite, and an Al-poor, high-Mg phlogopite cluster (Figure 7.4E).

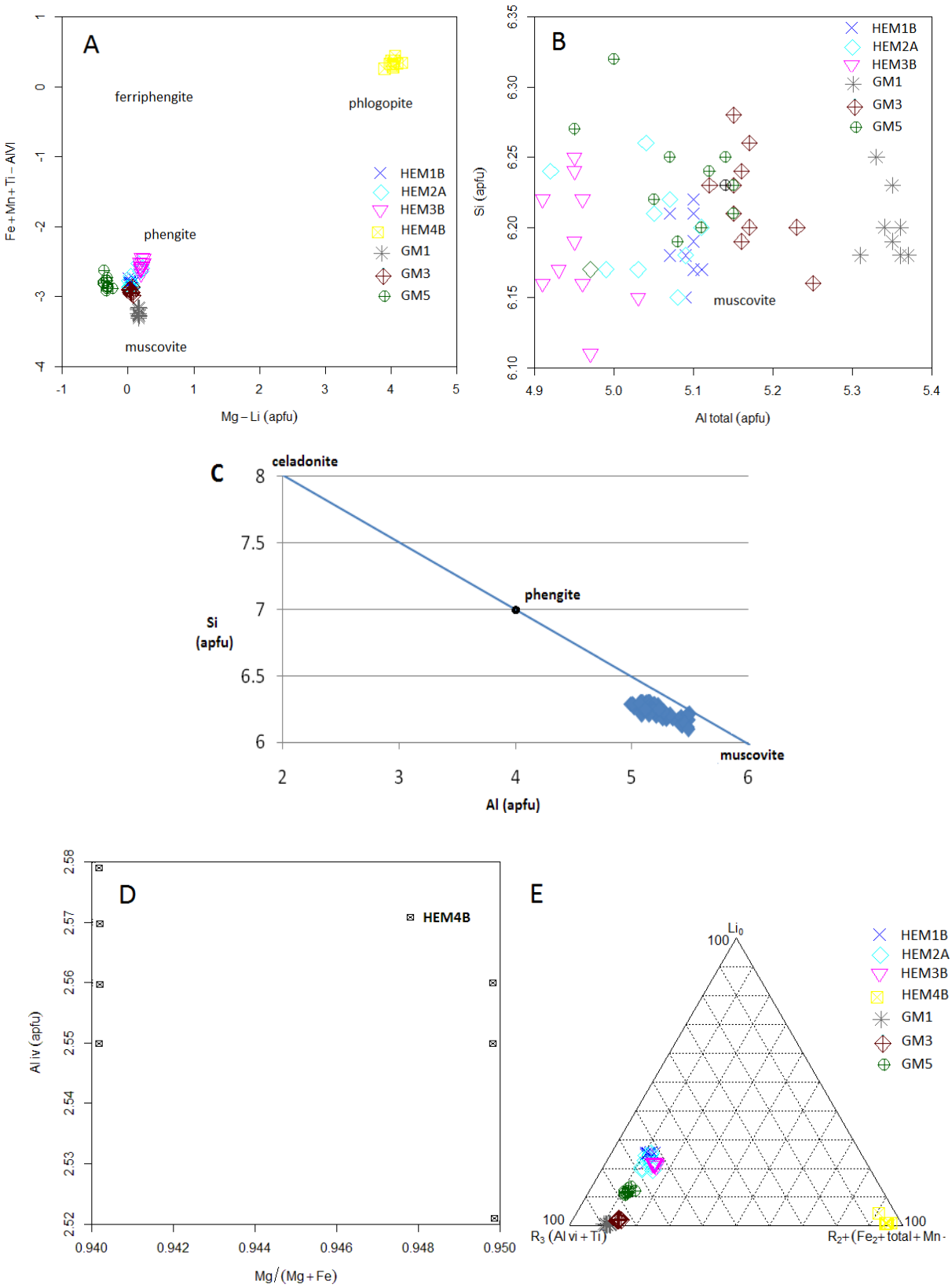

Figure 7.4: Chemical composition of mica from Pan-African pegmatites; (A) Mica classification after Tischendorf et al. (1997); (B) Muscovite classification (Si vs. Al_{total}) for HEM and GM; (C) Muscovite classification for CCC, MWC, HEM and GM; (D) Classification of biotite in Al^{iv} vs. Mg/(Mg+Fe) diagram; (E) Mica classification according to Forster (1960): Li_0 vs. R_3+(Al^{vi}+Ti) vs. R_2+(Fe+Mn+Mg).

Table 7.2A: Average mica (Ms, Bt) compositions (n=10 each) for major elements in micas from Pan-African aquamarine-bearing pegmatites from Kafukule (GM) and Luhomero (HEM) in Mzimba. Full data set in Appendix 2.2A.

	Ms	Ms	Ms	Ms	Ms	Ms	Bt
Sample	GM1	GM3	GM5	HEM1B	HEM2A	HEM3B	HEM4B
SiO_2	46.2	45.61	45.93	46.11	45.76	45.64	38.70
TiO_2	0.16	0.24	0.06	0.70	0.80	1.10	1.30
Al_2O_3	33.71	32.18	31.80	31.91	31.68	31.06	16.07
FeO	2.58	3.71	3.75	3.56	3.69	4.05	2.59
MnO	0.01	0.10	0.67	0.08	0.09	0.08	0.06
MgO	0.8	0.60	0.00	1.00	1.10	1.21	23.32
CaO	0.01	0.01	0.01	0.00	0.01	0.01	0.01
Na_2O	0.70	0.61	0.52	0.63	0.62	0.42	0.18
K_2O	11.81	12.36	12.98	12.52	12.62	13.01	12.75
Rb_2O	0.00	0.13	0.30	0.00	0.00	0.00	0.00
Cs_2O	0.00	0.01	0.01	0.00	0.00	0.00	0.00
F	0.20	0.69	2.13	1.10	0.98	0.57	1.40
Cl	0.01	0.00	0.01	0.01	0.01	0.00	0.02
Cr_2O_3	0.00	0.02	0.02	0.02	0.01	0.01	0.01
Li_2O*	0.00	0.14	0.59	0.31	0.23	0.10	1.55
H_2O*	4.37	4.07	3.42	3.91	3.96	4.16	3.60
Subtotal	100.58	100.48	102.29	101.86	101.55	101.44	101.55
O=F,Cl	0.09	0.29	0.90	0.52	0.41	0.24	0.59
Total	100.49	100.19	101.39	101.34	100.74	101.20	100.96
Si	6.20	6.22	6.24	6.18	6.20	6.19	5.44
Al^{iv}	1.80	1.78	1.76	1.82	1.80	1.81	2.56
∑(Si,Al)	8.00	8.00	8.00	8.00	8.00	8.00	8.00
Al^{vi}	3.54	3.39	3.32	3.28	3.23	3.14	0.11
Ti	0.02	0.02	0.01	0.07	0.08	0.11	0.14
Cr	0.00	0.00	0.00	0.00	0.00	0.00	0.00
Fe	0.29	0.42	0.43	0.40	0.42	0.47	0.30
Mn	0.00	0.01	0.08	0.01	0.01	0.01	0.01
Mg	0.16	0.12	0.00	0.20	0.22	0.26	4.91
Li*	0.00	0.08	0.32	0.17	0.12	0.06	0.88
∑(Al, Fe,Mg,Ti)	4.01	3.96	3.76	3.94	3.96	3.99	5.47
$\sum Al_{total}$	5.34	5.17	5.09	5.09	5.04	4.95	2.67
Ca	0.00	0.00	0.00	0.00	0.00	0.00	0.00
Na	0.18	0.16	0.14	0.16	0.16	0.12	0.05
K	2.02	2.15	2.26	2.16	2.18	2.27	2.29
Rb	0.00	0.01	0.03	0.00	0.00	0.00	0.00
∑(Ca,Na,K)	2.21	2.31	2.40	2.33	2.35	2.39	2.34
OH*	3.91	3.7	3.09	3.48	3.58	3.75	3.37
F	0.09	0.3	0.91	0.52	0.42	0.25	0.62
Cl	0.00	0.00	0.00	0.00	0.00	0.00	0.01
∑(F,Cl,OH)	4.00	4.00	4.00	4.00	4.00	4.00	4.00
TOTAL	18.22	18.37	18.59	18.44	18.44	18.45	20.69

* Calculated.

Table 7.2B: Average composition (Ms, Bt) for trace element data for micas from Pan-African aquamarine-bearing pegmatites from Kafukule (GM) and Luhomero (HEM) in Mzimba district. Full data set in Appendix 2.2B. All concentrations are given in ppm.

Type	Ms		Ms		Ms		Ms		Ms		Ms		Bt	
Element	GM1	Max-Min	GM3	Max-Min	GM5	Max-Min	HEM1B	Max-Min	HEM2A	Max-Min	HEM3B	Max-Min	HEM4B	Max-Min
Li	232	[839-122]	834	[1016-739]	5170	[5967-4561]	1284	[1366-1126]	1126	[1339-960]	1103	[1124-1049]	49	[50-45]
Be	9	[22-3]	24	[28-18]	26	[30-21]	19	[23-16]	21	[25-18]	22	[26-19]	0	0
B	35	[45-28]	65	[75-51]	84	[105-67]	26	[30-20]	51	[78-23]	82	[94-72]	61	[66-55]
Sc	20	[23-3]	3	[4-3]	0.5	[0.7-0.5]	30	[42-21]	50	[88-24]	87	[93-79]	2	[2-1]
Ti	1075	[1573-557]	1571	[1680-1461]	444	[468-402]	3674	[4574-3076]	4503	[5565-3212]	5610	[5956-5218]	6684	[6713-6505]
V	11	[16-8]	17	[20-15]	0	0	10	[24-3]	89	[185-5]	178	[190-165]	125	[126-123]
Cr	8	[45-1]	0	0	0	0	0	0	0.3	[1-0.1]	0	0	65	[71-64]
Mn	270	[641-231]	697	[877-589]	6071	[7112-5347]	719	[879-609]	629	[768-401]	616	[732-523]	569	[570-541]
Co	289	[2869-1]	2	[3-2]	0	0	13	[24-3]	9	[40-3]	4	[5-3]	10	[17-4]
Ni	2	[5-1]	0.4	[2.1-1]	0	0	0	0	2	[8-0.07]	3	[4-2]	4	[5-4]
Cu	138	[1377-0.03]	0	0	0	0	0.4	[1-0.1]	1	[2-0.6]	0	0	1	[1-1]
Zn	80	[148-19]	181	[367-89]	2597	[3165-2116]	106	[120-83]	98	[130-62]	107	[120-94]	155	[172-122]
Ga	97	[139-40]	134	[141-125]	160	[164-155]	118	[121-115]	104	[122-84]	97	[101-94]	61	[64-57]
Rb	762	[3473-338]	3313	[3574-2993]	7026	[7919-6328]	1692	[1861-1525]	1484	[1702-1178]	1312	[1401-1232]	548	[542-531]
Sr	3	[4-3.4]	0	0	0	0	3	[4-2]	4	[5-2]	5	[5-5]	6	[6-5]
Y	0	0	0	0	0	0	0	0	0	0	0	0	0	0
Zr	2	[3-2]	2	[4-2]	1	[1-1]	3	[4-0.2]	3	[4-1]	2	[2-2]	18	[18-17]
Nb	71	[451-48]	444	[485-410]	191	[200-172]	194	[206-180]	144	[198-86]	93	[100-85]	46	[46-46]
Mo	0	0	0	0	0	0	0	0	0	0	0	0	0	0
Sn	37	[129-11]	11	[11-10]	8	[8-7]	14	[17-12]	16	[20-12]	19	[21-17]	3	[3-3]
Cs	10	[105-8]	99	[113-90]	267	[324-225]	23	[26-19]	125	[273-19]	234	[251-213]	38	[38-37
Ba	36	[42-4]	4	[5-3]	1	[0.6-0.4]	63	[122-29]	256	[610-38]	554	[626-505]	1272	[1305-1317]
Hf	0	0	0	0	0	0	0	0	0	0	0	0	0	0
Ta	5	[56-3]	57	[65-48]	39	[46-35]	21	[23-19]	49	[106-20]	62	[72-58]	3	[3-3]
W	18	[21-8]	20	[23-17]	8	[9-6]	34	[36-30]	26	[36-18]	18	[20-17]	0	0
Pb	6	[7-3]	3	[3-2]	2	[3-2]	4	[7-3]	5	[6-4]	5	[5-4]	3	[3-3]
Th	0	0	0.02	[3-0.005]	0	0	0	0	0	0	0	0	0	0
U	0	0	0	0	0	0	0	0	0	0	0	0	0	0

The trace element and REE analytical results for the Pan-African pegmatites from Mzimba are presented in Table 7.2B and Appendix 2.2B.

The muscovites in GM (GM1, GM3, GM5; Table 7.2B, Appendix 2.2B) are similar to the trace element patterns in CCC and MWC muscovites. They show variable but often high Rb (338-7919 ppm) and Li (122-5967 ppm), variable Nb (48-485 ppm), Ti (402-1680 ppm) and low Ta (3-65 ppm), Ba (0.4-42 ppm), Ga (40-164 ppm) B (28-105 ppm) and Be (3-30 ppm).

The muscovites in HEM (HEM1B, HEM2A, HEM3B; Table 7.2B, Appendix 2.2B) also show generally low concentrations of trace elements, but with patterns similar to GM, CCC and MWC muscovite. The HEM muscovites contain moderate contents of Rb (1178-1861 ppm) and Li (960-1366 ppm), high Ti (3076-5956 ppm), an variable but mostly low amounts of Ta (19-106 ppm), Nb (85-206 ppm), Ba (29-626 ppm), Ga (84-122 ppm), B (20-94 ppm) and Be (16-26 ppm).

In HEM4B (Table 7.2B, Appendix 2.2B), the biotites show lower trace element concentrations except in Ti and Ba compared to the HEM muscovites. However, they also show generally low concentrations of trace elements, with a variation pattern similar to the HEM muscovites. The biotites show some Rb (531-542 ppm), high Ti (6505-6713 ppm) and abundant Ba (1305-1317 ppm). Ga (57-64 ppm), B (53-66 ppm), Li (45-50 ppm), Nb (46 ppm) concentrations are low. Minor Ta (3 ppm) is present; Be is below detection limit.

The binary plots of K/Rb, K/Ba versus elements such as Li, Cs, Ba, Ga (Section 7.1) in Figure 7.5A-F and Figure 7.6A can be used to estimate the extent of fractionation of compatible and incompatible elements and hence the extent of melt evolution in which the micas have grown (see Section 7.1). The diagrams show a decrease in the K/Rb ratio in the muscovite with increasing Rb, Be, Cs, Li, Nb and Ta in the Pan-African pegmatites. A reversed general trend is seen for Ti and Ba. However, some of these trends are unsystematic. In the muscovites from Kafukule (GM) and Luhomero (HEM) in Mzimba, the K/Rb ratio shows positive correlation with Ba and Ti (Figure 7.6B-C). Lithium concentrations generally increase in the muscovites from Luhomero (HEM2A-3B) to Kafukule (GM); however lithium has less concentrations in biotite (HEM4B) from Mzimba as shown in Table 7.2B. In Chitipa, lithium concentrations increase in the muscovites from Chisenga (CCC) to Wenya (MWC), as shown in Table 7.1B and Appendix 2.1B. The lithium concentrations in these particular areas of

study are over 1.5 wt%, which is typical for early formed muscovite (Cërny et al., 1985). This suggests that an enrichment of Li and Cs led to the precipitation of Li-muscovite.

The positive correlations of Ba, Ti and the negative ones of Rb, Cs and Li vs. K/Rb indicate fractionation trends that suggest that GM3 and GM5 pegmatites formed in the most evolved pegmatitic melts. Accordingly, they plot at the right bottom end of negative correlation trends. HEM4B plots at the upper left end of negative correlation trends (and top right for positive ones), indicating growth in the least evolved melts.

According to Cërny (1982b), a plot of K/Ba versus Ba (Figure 7.6D), can identify pegmatites which develop a relative primitive geochemical fractionation character, where the steeper the gradient in Ba, the less the fractionated the pegmatites are; the result shows that pegmatites HEM2A, 3B, 4B are more fractionated than GM1 and HEM1B pegmatites.

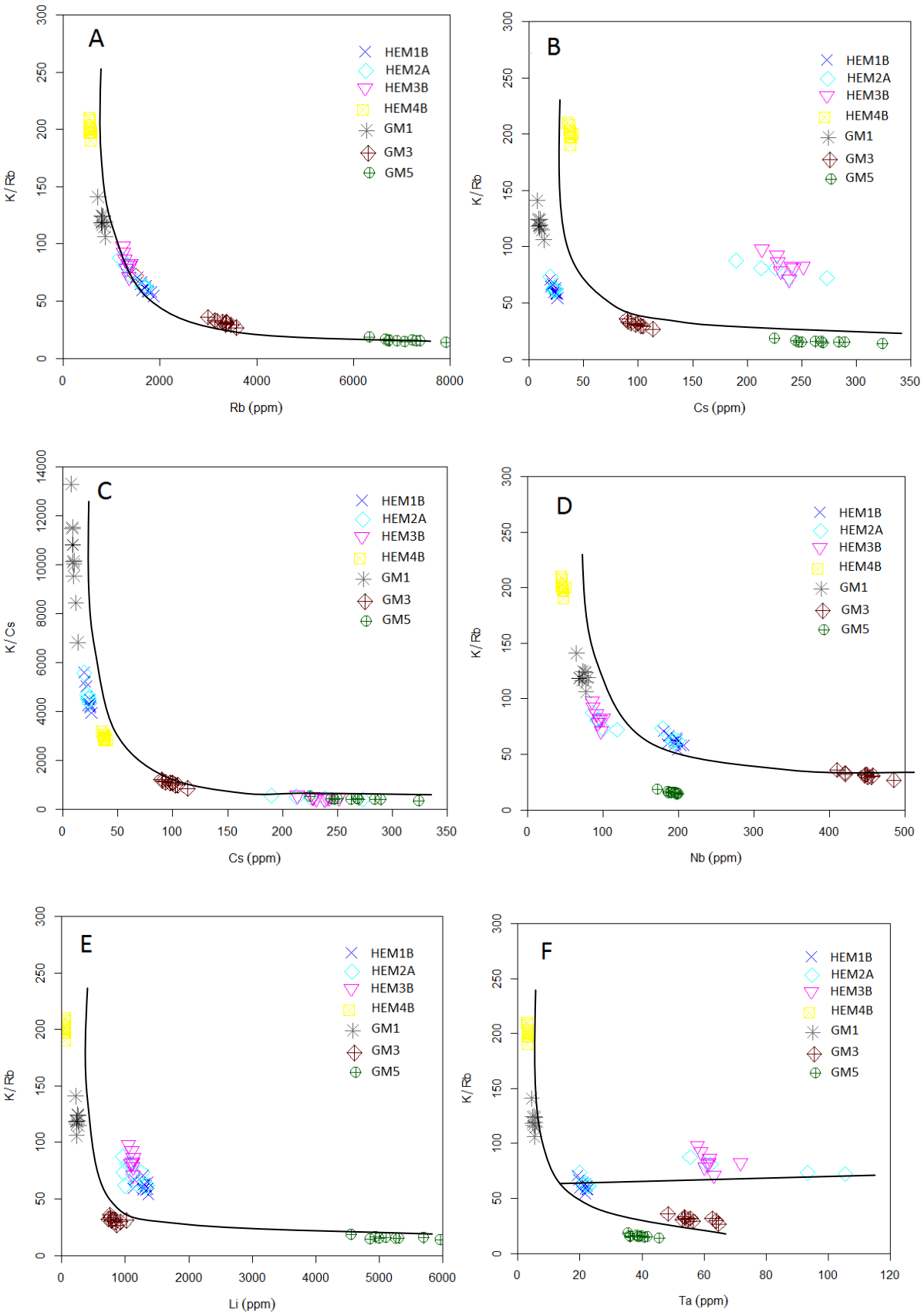

Figure 7.5: Binary plots of selected compatible and incompatible element ratios from micas illustrate fractionation of GM and HEM Pan-African pegmatites.

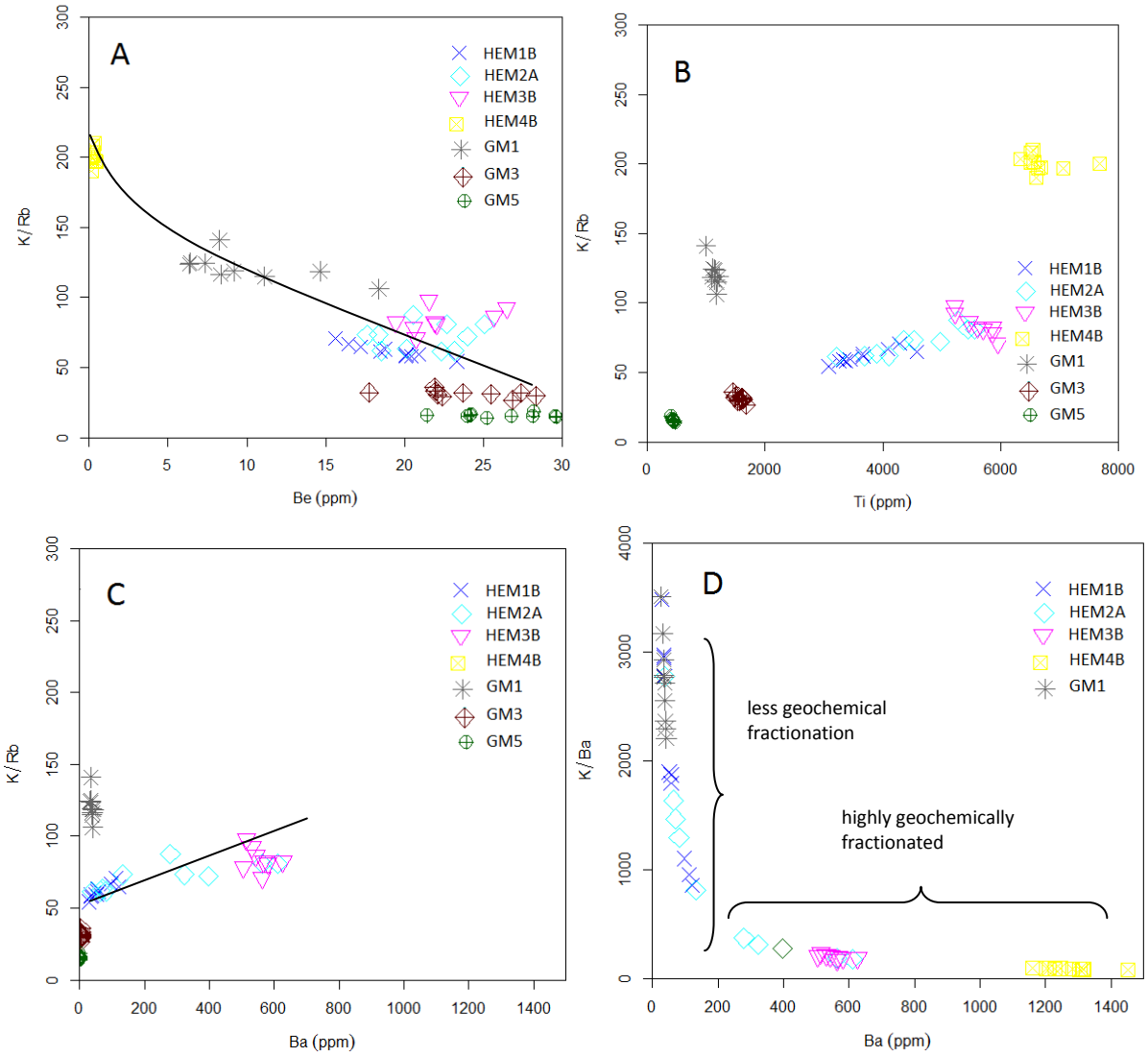

Figure 7.6: Binary plots of selected compatible and incompatible element ratios from micas illustrating fractionation of GM and HEM Pan-African pegmatites.

In the Al/Ga versus Ga diagram (Figure 7.7A), all white micas show a coherent fractionation trend with samples HEM2A, HEM3B and GM1 showing mica grown from least and sample GM5 from most fractionated melt. Biotite from sample HEM4B (yellow symbols) shows lower Ga contents and plots off the white mica trend. The K/Rb ratio against Al/Ga (Figure 7.7B) shows a positive correlation, with GM3 and GM5 plotting at the lower left position, indicating growth from highly evolved melt. At the opposite end of the trend GM1 shows element ratios suggesting growth from less evolved pegmatitic melt. Also in this diagram biotites from HEM4B plot off the muscovite trend.

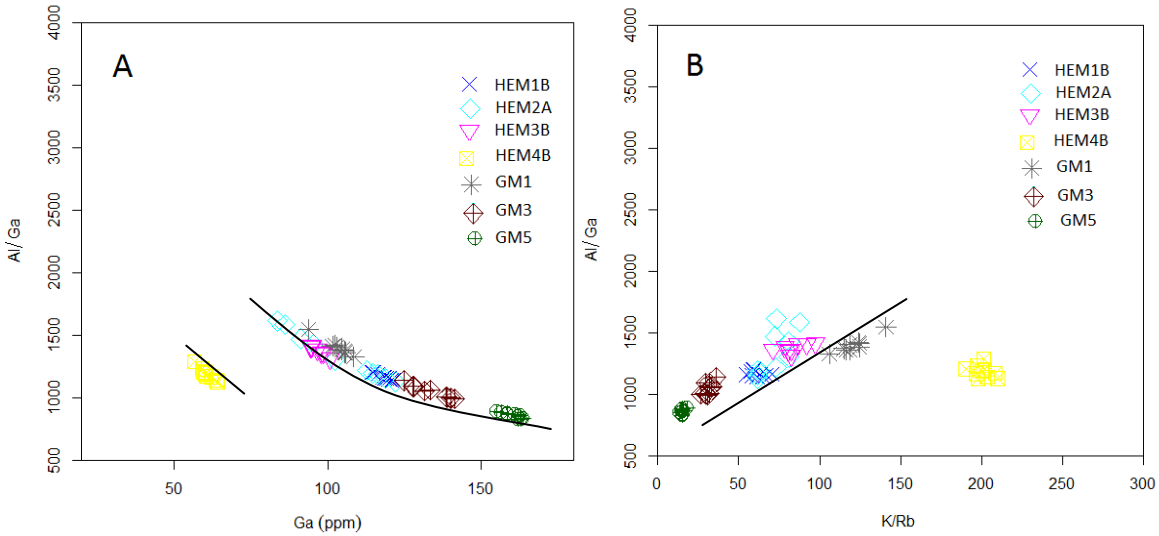

Figure 7.7: Binary diagrams of selected compatible and incompatible elements in micas from GM, HEM pegmatite field illustrating fractionation; (A) Al/Ga vs. Ga; and (B) Al/Ga vs. K/Rb.

The spider diagrams for Kafukule (GM) pegmatites (Figure 7.8A) and HEM pegmatites from Luhomero (Figure 7.8B) show similar patterns like the pegmatites from further north in Malawi (see previous sections) with strongly or moderately enriched Cs, Rb, Nb, Ta, and Ti, and strongly or moderately depleted U, Th, P, and Y. Ba, Hf and Zr are either slightly enriched or depleted compared to UCC. A significant difference between GM and HEM samples is that Sr is mildly depleted in GM3 and GM5, but not in GM1. GM1 and all HEM samples show slightly enriched Sr contents. Also Ba in HEM samples is more strongly enriched than in GM samples. Figure 7.8C shows all trace element patterns from HEM and GM samples in comparison.

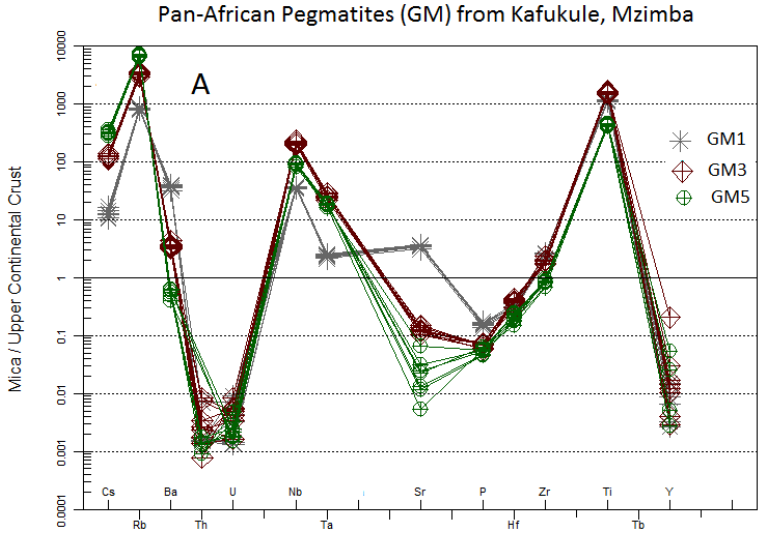

Figure 7.8A: UCC-Normalised abundance patterns of trace elements in muscovite from Pan-African pegmatites (GM) from Kafukule, after Taylor and McLennan (1995).

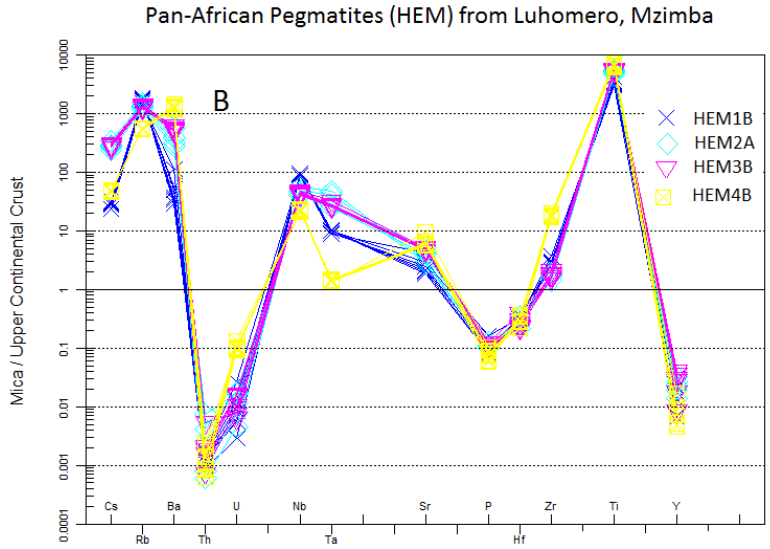

Figure 7.8B: UCC-normalised abundance patterns of trace elements in biotite (HEM4B; yellow symbols) and muscovite (all other symbols) from Pan-African pegmatites from Luhomero in Mzimba, after Taylor and McLennan (1995).

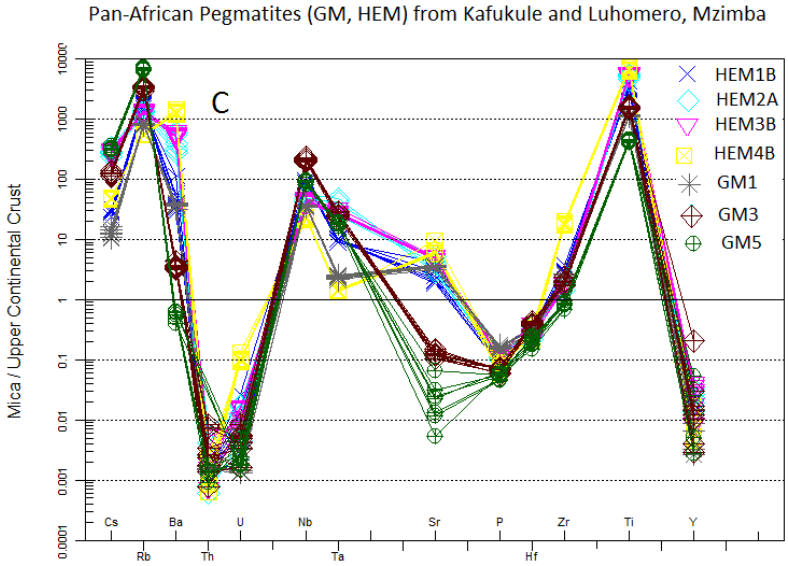

Figure 7.8C: UCC-normalised abundance patterns of trace elements in biotite (HEM4B; yellow symbols) and muscovite (all other symbols) from Pan-African pegmatites from Kafukule and Luhomero in northern Malawi, after Taylor and McLennan (1995).

Figure 7.8D adds CCC, MWC and CNC pegmatites discussed in Section 7.2.1 and Section 7.2.2 to the samples shown in Figure 7.8C. These samples show similar patterns like the HEM samples, but with lower Ba contents. The Ba contents plot between HEM and GM samples. Also the Sr variations are evident.

In UCC-normalized REE patterns (Figure 7.8E, F, Appendix 2.2C) the Pan-African HEM and GM pegmatites generally show depleted REE. A comparison of distributions reveals that Tm and Yb have more depleted ratios in GM than in HEM.

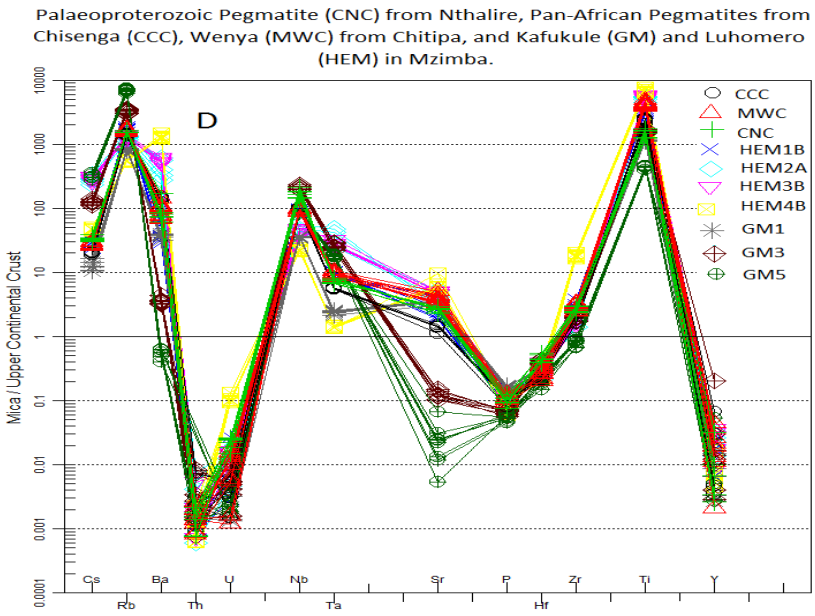

Figure 7.8D: UCC-normalised abundance patterns of trace elements in muscovite and biotite from Palaeoproterozoic pegmatites (CNC) and Pan-African pegmatites (CCC, MWC, GM, HEM) from northern Malawi, after Taylor and McLennan (1995).

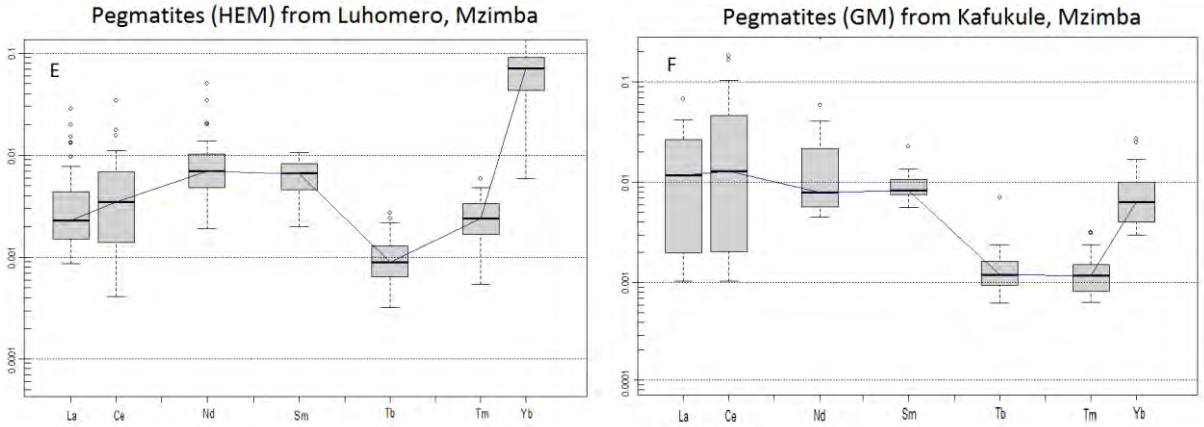

Figure 7.8E-F: Boxplots of UCC-normalised abundance pattern of REE for mica from Pan-African pegmatite, after Taylor and McLennan (1995). The diamond symbols represent outliers; (E) Aquamarine-bearing (HEM) Luhomero pegmatites, Mzimba; (F) Beryl-bearing (GM) Kafukule pegmatite, Mzimba.

A preliminary interpretation of the observed patterns needs to consider the variable but uniform enrichment in incompatible elements such as Rb, Cs, and Nb, and a variable either mild enrichment or depletion in compatible elements such as Ba, P, and Sr. These patterns correlate with rare-element enrichment of incompatible elements in the evolving pegmatite melt through fractionation processes. In pegmatite melt, partitioning of rare elements into pegmatitic solid and volatile phases will show the highest enrichment of incompatible elements in more evolved pegmatites. These processes suggest progressive differentiation of

felsic magmas. However, the most enriched Ti contents from the Chitipa and Mzimba pegmatites (CCC, MWC); suggest that some magmas in the north Malawi (Chitipa) were generally less evolved than those to the south at Luhomero and Kafukule (Mzimba).

Using the geochemical data, the Palaeoproterozoic gem tourmaline bearing pegmatites (CNC), show enrichment of Rb, Ti, Nb>Ta, U, Hf and B, although some are only slightly enriched (Table 7.1B, Appendix 2.1B, Figure 7.2A). According to pegmatite classification scheme of Ginsburg et al. (1979), and Cërny (1991a; Chapter 2, Section 2.3, Table 1.1), these Palaeoproterozoic pegmatites belong to the Rare Element Class and mixed NYF - LCT family which may show low to abundant mineralisations. However, according to classification by Cërny and Ercit (2005), the CNC pegmatites show mixed geochemical signature of both LCT and NYF families, which could be due to contamination from local sources (Cërny, 1991b; Martin and De Vito, 2005; Cërny et al., 2012; Table 2.4). More information regarding classification of these pegmatites will be discussed in Chapter 9.

The Pan-African gem beryl- and tourmaline-bearing pegmatites (CCC, MWC) show enrichment in Rb, Cs, Li, Be, Ga, Nb>Ta and B (Table 7.1B, Appendix 2.1B, Figure 7.3L). According to the pegmatite classification scheme of Ginsburg et al. (1979) and Cërny 1991a (Chapter 2, Section 2.3, Table 2.1), these pegmatites belong to the Rare Element Class and LCT family. According to subdivisions of Ginsburg et al.‟s (1979) classes by Cërny (1991a, Chapter 2, Section 2.3, Table 2.2), the LCT pegmatites belong to Beryl type, Beryl-columbite subtype, even though columbite was not observed. Furthermore, according to further subdivisions of the Ginsburg et al.‟s (1979) classification into subclasses, types and subtypes (Table 2.3; Cërny, 1990; 1991a; Cërny and Ercit, 2005; Cërny et al., 2012), the CCC and MWC pegmatites belong to Rare Element class, in the REL-Li subclass, Beryl type, Beryl-columbite subtype, and in the Complex type, Elbaite subtype, and in the Miarolitic Class, Mi-Li subclass, beryl-topaz type. This is based on trace-element signatures of pegmatites and their mineral assemblages which in this case include Li-muscovite, tantalum beryl and topaz.

The Pan-African Ordovician gem beryl- and aquamarine-bearing pegmatites (GM, HEM) show trace element patterns similar to the CCC and MWC in Chitipa (northern Malawi), but they are not mineralised in gem tourmaline and topaz (Table 7.2B, Appendix 2.2B, Figure 7.8D). According to the pegmatite classification scheme of Ginsburg et al. (1979) and Cërny 1991a (Chapter 2, Section 2.3, Table 2.1), these pegmatites belong to the Rare Element Class and LCT family. According to subdivisions of Ginsburg et al.‟s (1979) classes by Cërny

(1991a, Chapter 2, Section 2.3, Table 2.2), the LCT pegmatites belong to Beryl type, Beryl - columbite subtype even though columbite was not observed. Furthermore, according to further subdivisions of the Ginsburg et al.‟s (1979) classification into subclasses, types and subtypes (Table 2.3; Cërny, 1990; 1991a; Cërny and Ercit, 2005; Cërny et al., 2012), the GM and HEM pegmatites belong to Rare Element class, in the REL-Li subclass, Beryl type, Beryl-columbite subtype, and in the Miarolitic Class, Mi-Li subclass, beryl-topaz type, even though topaz was not observed. The pegmatites have not yet been related to known plutons. More information regarding classification of these pegmatites will be discussed in Chapter 9. In this chapter a table presents an overview of the classification of the pegmatites analysed in this study.

7.2.4 Tourmaline-bearing Pegmatites from Dowa

The chemical compositional variations in mica from the Pan-African pegmatites (DHD) from Dowa are shown in Table 7.3A-B and in Appendix 2.3A-B. The muscovites are peraluminous, indicated by their A.S.I. that is greater than 1 (Table 7.3A). According to Tischendorf et al.‟s (1997) mica classification (Figure 7.9A), the analysed white micas show two narrow clusters between the muscovite and phengite endmembers, and a third cluster of biotite near the phlogopite endmembers. The cluster plotting on the bottom includes analyses from the sample DHD1A. Samples DHD1B and DHD1C plot in the cluster above. The phlogopite cluster contains analyses from sample DHD1E.

In the classification using Si versus Al_{total} (Figure 7.9B), the Si contents for the mica solid solutions range from 6.08 to 6.25 a.p.f.u. and the Al contents range from 5.2 to 5.6 a.p.f.u. (Figure 7.9B). Hence, the compositional variability is not large amongst the white micas. The analyses form scatters with groupings of sample DHD1C at low, samples DHD1B at middle (~5.3), and sample DHD1A at high Al values. The analyses plot in the muscovite – celadonite series (Figure 7.9C).

The classification diagram used for the phlogopitic mica (Deer et al., 1966) shows the mica compositions at Si 5.51 to 5.62 a.p.f.u. and is low in Fe with X_{Fe} ratios between 0.074 to 0.096 (Figure 7.10D). The phlogopite has Al^{iv} between 1.76 and 2.47 a.p.f.u. The octahedral site occupancies range from 3.92 to 4.1 a.p.f.u. for muscovite, while they range from 5.75 to 5.9 a.p.f.u. for biotite (Table 7.3A, sample DHD1E). Calculated anion site occupancy ranges

from 3.9 to 4.0 a.p.f.u. for both muscovite and biotite. The interlayer occupancy ranges from 2.13 to 2.55 a.p.f.u. for muscovite while biotite has 2.2 to 2.54 a.p.f.u.

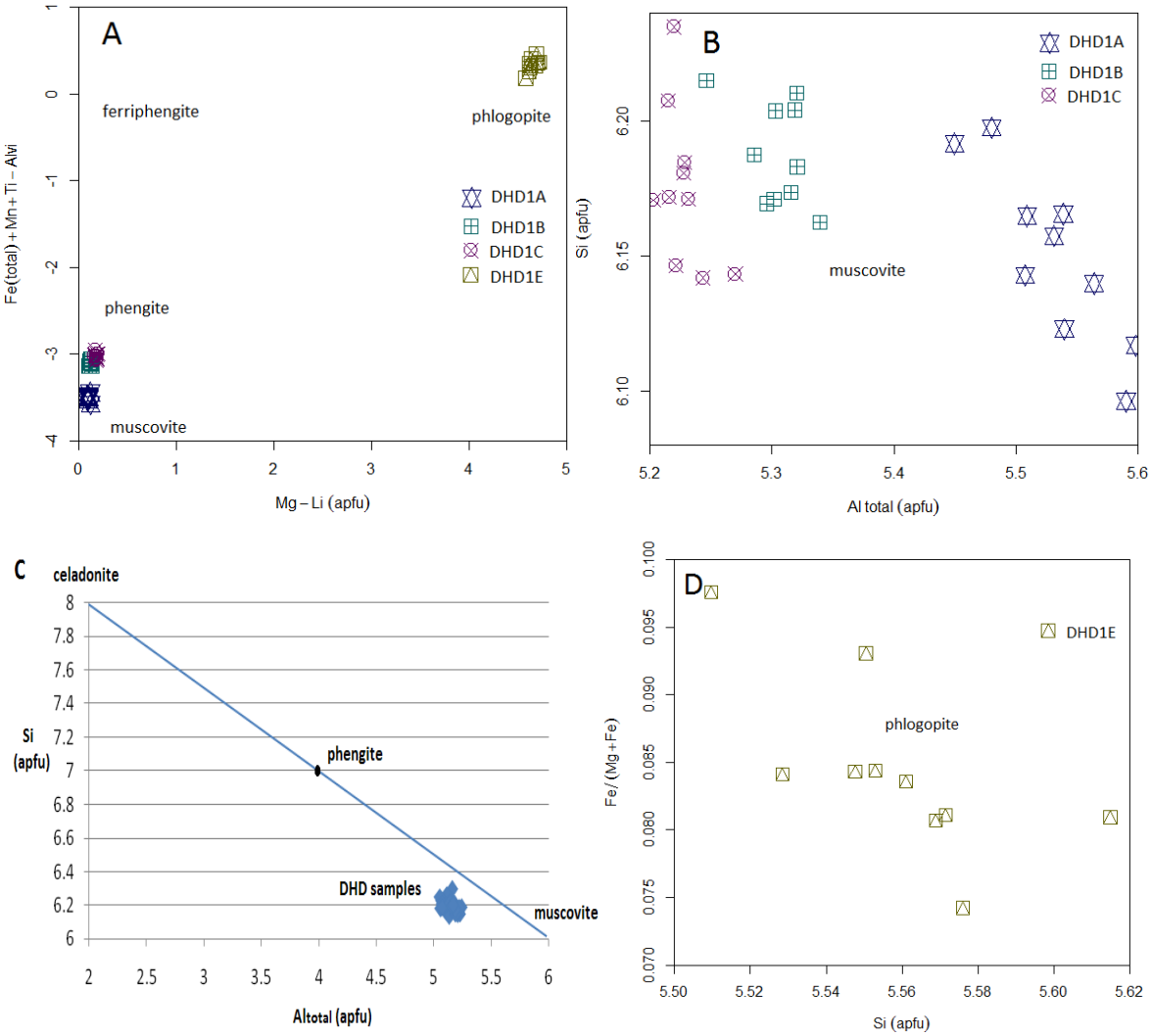

Figure 7. 9: Chemical composition of mica from the Pan-African pegmatites from Dowa; (A) Mica classification proposed by Tischendorf et al. (1997); (B) Classification of white mica phases in diagram Si vs. Al; (C) DHD mica samples in the muscovite celadonite series; (D) Classification of biotite according to Deer et al. (1966).

Table 7. 3A: Average composition (n=10 each) for major oxides in micas from Pan-African Dowa pegmatites (DHD) in central Malawi. For the full data set see Appendix 2.3A.

Type	Ms	Ms	Ms	Bt
Sample	DHD1A	DHD1B	DHD1C	DHD1E
SiO_2	46.50	45.82	46.55	38.81
TiO_2	0.21	0.07	0.22	1.34
Al_2O_3	35.43	33.32	33.24	16.01
FeO	1.32	3.30	3.17	3.71
MnO	0.01	0.08	0.06	0.05
MgO	0.50	0.67	0.92	22.53
CaO	0.02	0.02	0.01	0.01
Na_2O	0.86	0.70	0.69	0.23
K_2O	11.90	11.97	12.20	12.73
Rb_2O	0.00	0.08	0.20	1.15
F	0.09	0.34	0.00	0.05
Cl	0.01	0.03	0.02	0.01
Cr_2O_3	0.01	0.03	0.01	0.28
H_2O*	4.49	4.27	4.42	3.63
Subtotal	101.34	100.68	101.62	100.55
O=F,Cl	0.04	0.15	0.09	0.50
Total	101.30	100.53	101.43	100.05
Si	6.15	6.19	6.18	5.56
Al^{iv}	1.85	1.81	1.82	2.44
∑(Si,Al)	8.00	8.00	8.00	8.00
Al^{vi}	3.68	3.49	3.40	0.26
Ti	0.02	0.01	0.02	0.14
Cr	0.00	0.00	0.00	0.00
Fe	0.15	0.37	0.35	0.44
Mn	0.00	0.01	0.01	0.01
Mg	0.10	0.13	0.18	4.81
Li*	0.00	0.02	0.00	0.16
∑(Al, Fe,Mg,Ti)	3.95	4.01	3.96	5.66
$\sum Al_{total}$	5.53	5.30	5.23	2.70
Ca	0.00	0.00	0.00	0.00
Na	0.22	0.18	0.18	0.06
K	2.01	2.06	2.26	2.33
Rb	0.00	0.01	0.00	0.00
∑(Ca,Na,K)	2.23	2.25	2.44	2.39
OH*	3.96	3.85	3.91	3.47
F	0.04	0.14	0.09	0.52
Cl	0.00	0.01	0.00	0.01
∑(F,Cl,OH)	4.00	4.00	4.00	4.00
TOTAL	18.18	18.29	18.41	20.22

* Calculated.

Table 7.3B: Average analysis (n=10 each) for trace elements for Ms and Bt from Pan-African pegmatites (DHD) from Dowa in central Malawi. All concentrations are given in ppm. For the full data set see Appendix 2.3B.

Type	Ms		Ms		Ms		Bt	
Element	DHD1A	Max-Min	DHD1B	Max-Min	DHD1C	Max-Min	DHD1E	max-min
Li	110	[385-40]	994	[1063-921]	387	[436-352]	73	[76-70]
Be	16	[19-14]	22	[24-19]	14	[18-12]	0	0
B	101	[135-32]	64	[74-55]	63	[69-58]	48	[52-42]
Sc	11	[14-18]	1	1	12	[13-11]	1	[2-1]
Ti	1518	[1840-1241]	498	[534-469]	1579	[1657-1461]	7058	[7453-6671]
V	11	[40-2]	11	[12-10]	41	[47-37]	118	[121-111]
Cr	0.2	[1-0.1]	0.3	[1-0.2]	0	0	78	[82-76]
Mn	88	[318-39]	609	[867-535]	322	[440-193]	554	[578-533]
Co	2	[5-2]	3	[6-1]	2	[2-1]	12	[35-8]
Ni	2	[2-0.1]	0	0	0	0	8	[9-8]
Cu	0	0	1	1	0	0	3	[9-1]
Zn	42	[44-33]	211	[270-185]	39	[46-23]	198	[241-160]
Ga	91	[103-81]	135	[143-130]	83	[86-78]	64	[68-61]
Rb	440	[1063-266]	2844	[3056-2748]	1048	[1093-998]	543	[563-522]
Sr	27	[40-1]	0	0	1	1	9	[10-0]
Y	0	0	0	0	0	0	0	0
Zr	2	[3-1]	1	[2-1]	3	[3-2]	16	[17-15]
Nb	38	[85-25]	178	[183-172]	85	[88-80]	50	[52-47]
Mo	0	0	0	0	0	0	0	0
Sn	29	[37-12]	59	[64-56]	13	[14-11]	3	[4-3]
Cs	7	[19-3]	48	[54-43]	19	[21-18]	39	[41-37]
Ba	990	[1533-5]	1	[2-0]	5	[6-4]	1422	[1507-1350]
Hf	0	0	0	0	0	0	0	0
Ta	4	[9-2]	14	[15-14]	9	[9-7]	3	[3-3]
W	33	[38-30]	19	[20-18]	34	[36-27]	0	0
Pb	23	[30-3]	3	[3-2]	3	[4-3]	3	[3-3]
Th	0	0	0	0	0	0	0	0
U	0	0	0	0	0	0	0	0

In the Pan-African DHD pegmatites (Table 7.3B, Appendix 2.3B, samples DHD1A, DHD1B, DHD1C) the muscovites generally show low concentrations of trace elements with variably low to high Rb (266-3056 ppm) and Ti (469-1840 ppm), Li (40-1063 ppm), and Ba (1-1533 ppm). Ta (2-15 ppm), Nb (25-183 ppm), Ga (78-143 ppm), B (32-135 ppm) and Be (12-24 ppm) are variably low in abundance. Biotites in sample DHD1E (Table 7.3B, Appendix 2.3B) show trace element patterns similar to the DHD muscovites but have higher concentrations in Ti (6671-7453 ppm) and Ba (1350-1507 ppm). The biotites show abundant Rb (522-563

ppm), and minor Li (70-76 ppm), Nb (47-52 ppm), Ga (61-68 ppm), B (42-52 ppm) and Ta (3 ppm). Be is below detection limit.

In muscovite from DHD1A to DHD1B, the K/Rb ratio decreases with increasing Rb, Cs, Nb, and Ta (Figure 7.10A-E), following similar trends as seen in CCC, MWC, GM and HEM (Sections 7.2.2 and 7.2.3). In a similar way like shown for these samples, these diagrams in Figure 7.10A-E show that micas in sample DHD1A formed from the least evolved and in sample DHD1B from the most evolved melt. In Figure 7.10C the biotites plot away from the white mica trends because of their higher Cs contents.

Plotted against Ti the white micas show that white micas show no Ti variation with variable K/Rb. Biotites plot in a separate cluster (Figure 7.11A). The diagram of K/Rb ratio with Ba shows a positive correlation with two white mica clusters (Figure 7.11B). Biotite from sample DHD1E forms a separate cluster at moderate K/Rb and high Ba contents. The Al/Ga against Ga diagram shows a strong negative correlation (Figure 7.12A) with the highest Ga concentrations of 130-143 ppm in DHD1B followed by DHD1A; DHD1C and DHD1E contain less Ga (61-86 ppm).

Since the decreasing K/Rb ratio with increasing concentration of the incompatible elements Rb, Ta, and Nb suggests increasing magma fractionation, micas in samples DHD1B and DHD1C formed in more evolved environments than micas samples DHD1A and DHD1E. The same is indicated by an increase of Ti and Ba concentrations in the less evolved (DHD1A, DHD1E) than in the more evolved (DHD1B and DHD1C). Furthermore, K/Rb against Al/Ga also shows more evolved DHD1B to less evolved DHD1A (Figure 7.12B).

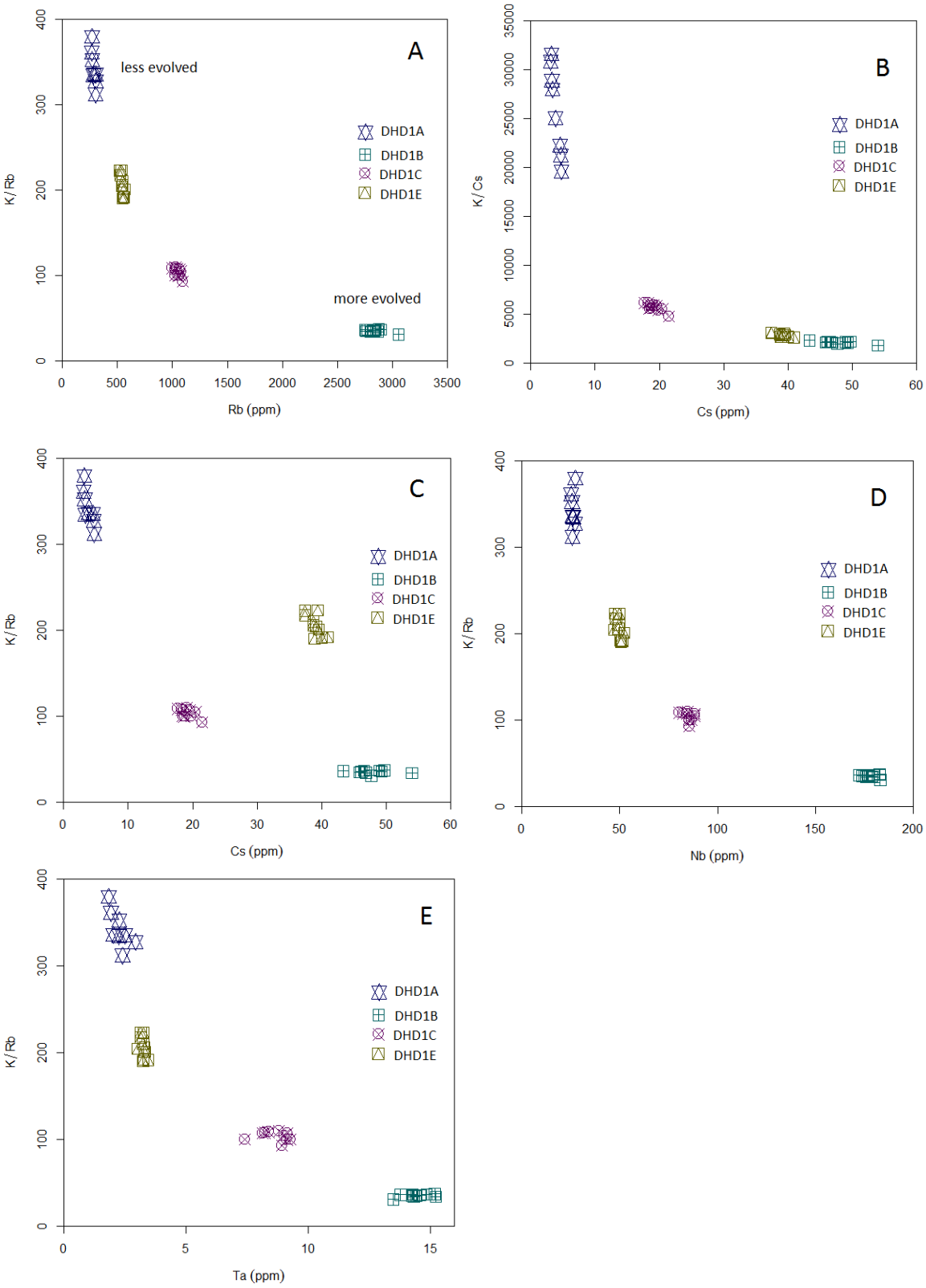

Figure 7.10A-E: Binary plots of selected compatible and incompatible elements in micas illustrating fractionation trends of DHD pegmatites.

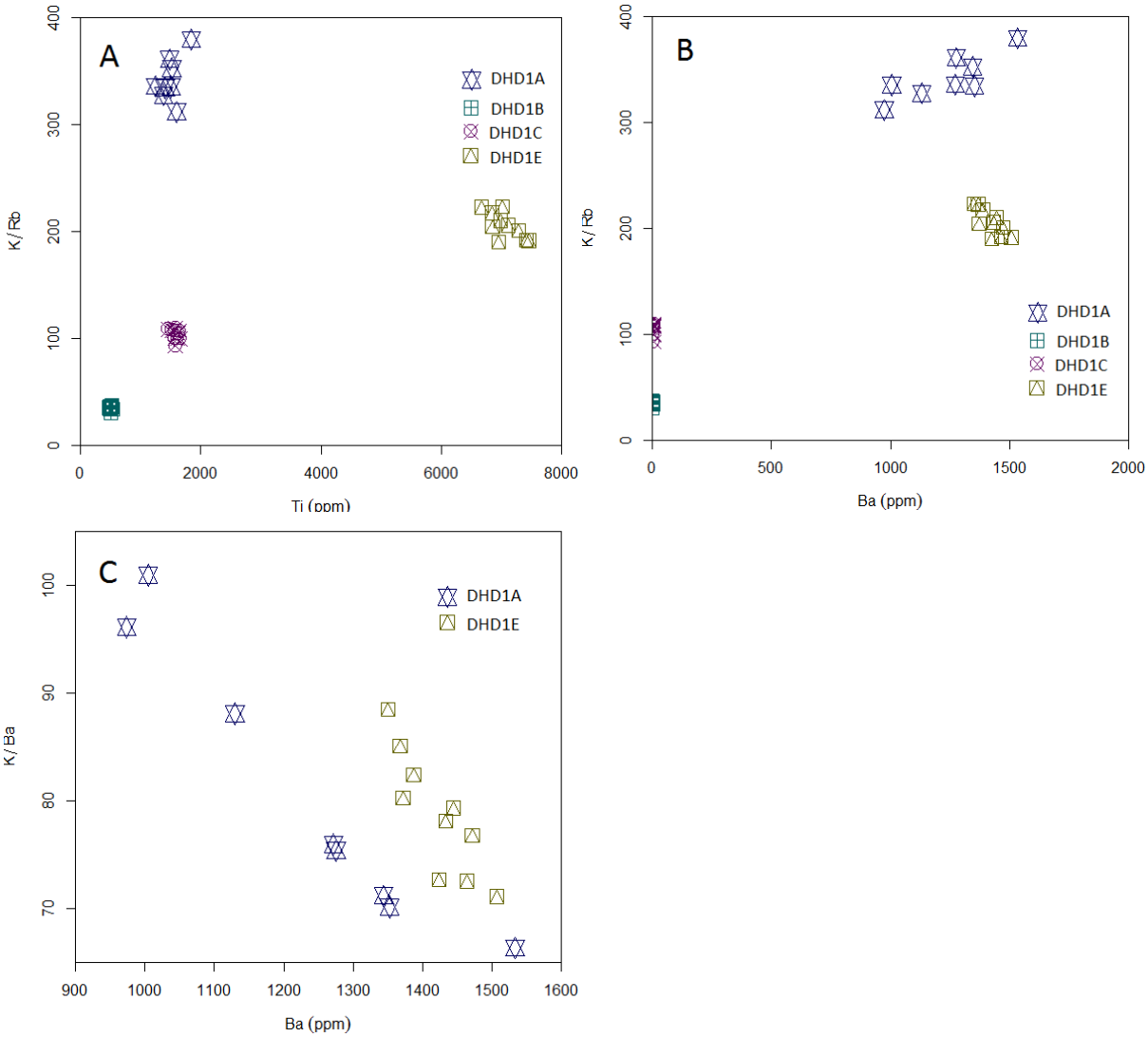

Figure 7. 11A-C: Binary plots of selected compatible and incompatible element ratios from micas illustrating fractionation trends of DHD pegmatites.

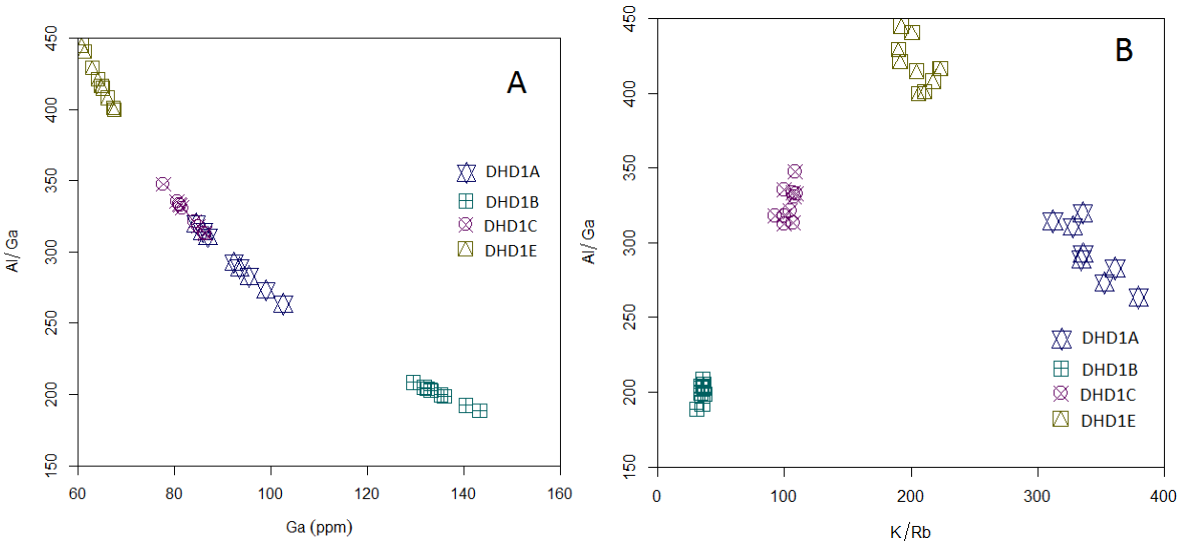

Figure 7. 12A-B: Binary plots of selected compatible and incompatible element ratios from micas illustrating fractionation of DHD pegmatites.

In UCC-normalised abundances of trace elements (Figure 7.13) show the familiar pattern seen also in other pegmatites. Rb and Ti are strongly enriched (200-8000 x UCC). Nb (~10-100 x UCC) is moderately enriched, similar to Cs (20-80 x) in DHDIB, DHD1C and DHD1E. Cs is only slightly (4-7 x) enriched in DHD1A. Ba contents vary between strongly (1000-2000 x) enriched and mildly (~4 x) enriched or slightly (0.2-0.9 x) depleted. Ta content ranges shows neutral to slight (~6 x) enrichment. Sr is variably either moderately (9-40 x) enriched or slightly to moderately (0.02-0.9 x) depleted different samples. Zr ranges from neutral to moderate enrichment (1-11 x). Th, U, P, Hf and Y are variably depleted, with strong depletion in Th, U and Y.

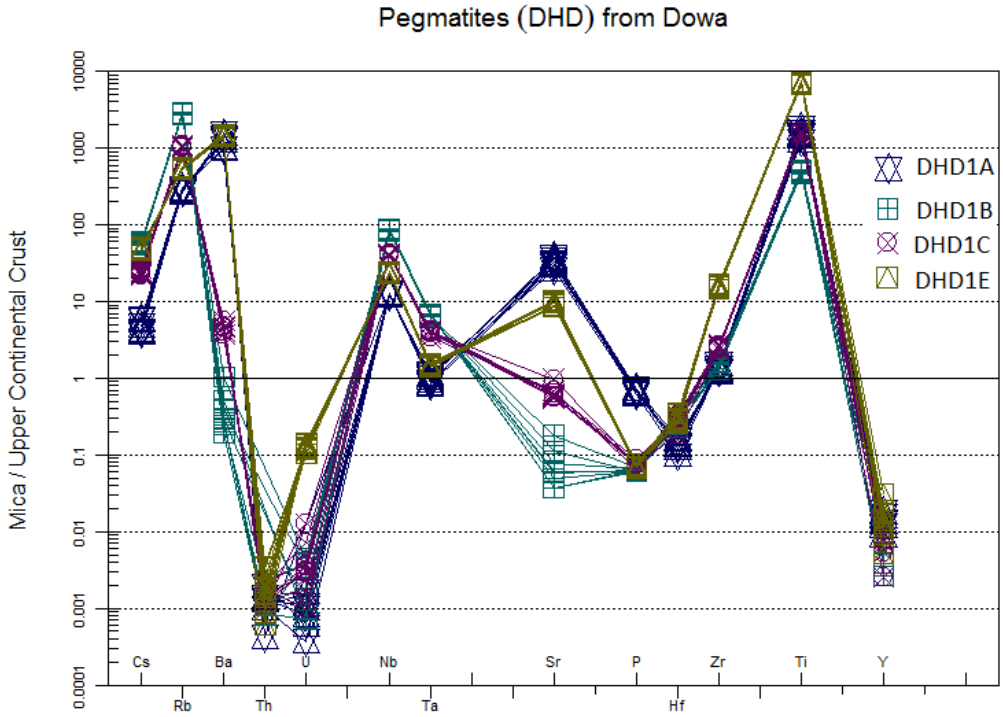

Figure 7. 13: UCC-normalised abundance trace elements patterns for muscovite (DHD1A, DHD1B, DHD1C) and biotite (DHD1E) from DHD pegmatites, after Taylor and McLennan (1995).

The normalised REE patterns (Figure 7.14, Appendix 2.3C) in the Dowa pegmatite (DHD) micas are similar to those in CCC, MWC, GM and HEM pegmatites from Chitipa and Mzimba (Sections 7.2.2 and 7.2.3). They show depleted REE throughout, with more depletion in Tb and Tm.

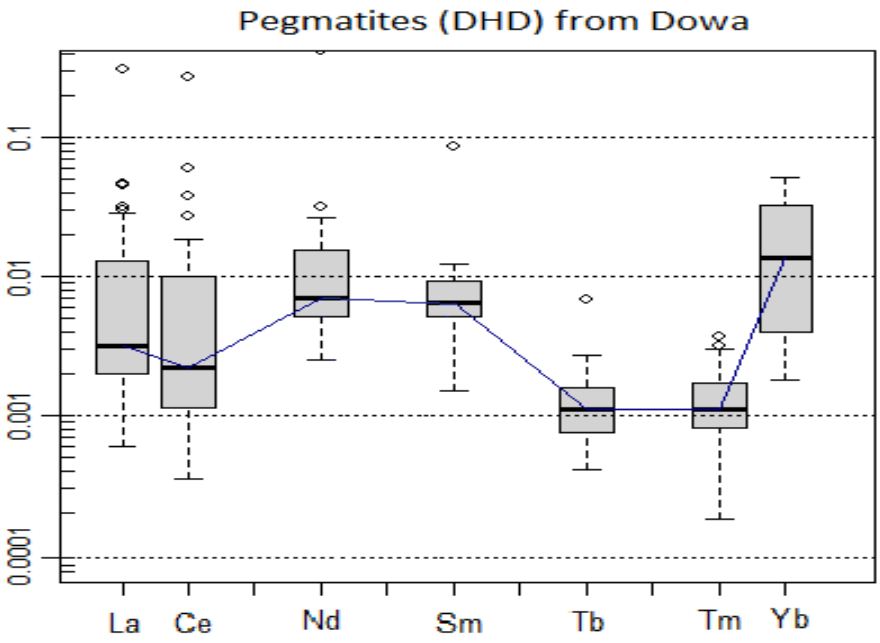

Figure 7. 14: Boxplot of UCC-normalised REE pattern for mica from Dowa pegmatites, after Taylor and McLennan (1995). The diamond symbols represent outliers

A preliminary interpretation is that the K/Rb value monitors pegmatite melt evolution, with a decrease from the least evolved DHD1A, with highest Ba, to DHD1E and moderately evolved DHD1C, then to the most evolved DHD1B (Figure 7.10A-E) with its highest enrichment in Rb and Li (Table 7.3B, Appendix 2.3B). Rb, Cs, Nb, and Ta reveal different magnitude of differentiation and evolution amongst DHD pegmatites (Figure 7.10C). The concentration patterns (Figure 7.13) where incompatible trace elements such as Rb, Cs and Nb and Ta show higher concentration whereas compatible trace elements such as Ba, P and Sr show less concentrations correlate with rare-element enrichment of incompatible elements in the evolving pegmatite melt through fractionation processes. In pegmatite melt, partitioning of rare elements into pegmatitic solid and volatile phases will show the highest enrichment of incompatible elements in more evolved pegmatites. This means that the samples with higher concentration of incompatible elements in mica formed from the more evolved melt whereas those that show more compatible elements formed from less evolved melt. These results are similar to the findings in Luhomero and Chitipa (Sections 7.2.2 and 7.2.3) where these patterns suggest progressive differentiation of felsic magmas.

According to Al/Ga against Ga (Figure 7.12A) the more evolved pegmatites have higher Ga, which can be related to the abundance of muscovite, tourmaline, biotite and albite in the pegmatite assemblage (Chapter 4, Section 4.3.6, and Appendix 1.1).

The Sr concentration varies according to the abundance of K-feldspar and muscovite in the pegmatites since Sr exhibits greater affinity for K-feldspar than for muscovite (Alfonso et al., 2003). Hence, in pegmatites that are rich in K-feldspar the Sr contents in muscovite will be lower than in low-K-feldspar pegmatites.

Fe concentrations in the highly evolved DHD1B and DHD1C pegmatites (Table 7.3B, Appendix 2.3B) would be consistent with the formation of Nb-Ta-Fe oxides, which are, however, not observed. On the other hand, the depleted Hf and elevated Zr may be correlated with the occasional presence of garnet in the pegmatites (Figure 7.13, Appendix 1.1). A higher concentration of B in the white micas promoted tourmaline formation in the pegmatites.

The observed negative Ce anomaly in the UCC-normalised pattern (Figure 7.14) indicates oxidising conditions during mineralisation (Akagi and Masuda, 1998). Taylor et al. (1986) advanced a view that a weak negative Ce signature and strong positive Eu signature denotes low degrees of fractionation. Regarding the oxidation state, Rudnick and Gao (2003) observed that during melt formation element transportation is promoted, and solubility of metals in melt is affected by the oxidation state within the magma. Therefore the gemstones formed from granitic melts with low degrees of differentiation during an oxidation period.

Using the geochemical data, the gem tourmaline bearing pegmatites (DHD), show enrichment of Rb, Cs, Li, Be, Ga and Nb<>Ta (Table 3B; Figure 7.13). According to the classification by Ginsburg et al. (1979) and Cërny (1991a; Chapter 2, Section 2.3, Table 2.1), these pegmatites belong to the Rare Element Class and LCT family which has gemstock. According to subdivisions of the Ginsburg et al."s (1979) classification into subclasses, types and subtypes (Table 2.3; Cërny, 1990; 1991a; Cërny and Ercit, 2005; Cërny et al., 2012), based on trace-element signatures of pegmatites and depending on their mineral assemblages, which in this case include tourmaline, the DHD pegmatites belong to Rare Element class, in the REL-Li subclass, Complex type, Elbaite subtype. The pegmatites can be related to the Senga Bay granite according to their age and provenance (Chapter 6, Section 6.2). More information regarding classification of these pegmatites will be discussed in Chapter 9.

7.2.5 Tourmaline- and Sunstone-bearing Pegmatites (GNS, MSN) from Ntcheu and Amethyst-Bearing Pegmatites (CUB) from Balaka

The mica compositions from the Pan-African pegmatites from Ntcheu and Balaka area are shown in Table 7.4A and B and in supplementary tables in Appendix 2.4A and, B. White

micas from GNS and MSN pegmatites have Si contents of 6.1 to 6.3 and Al from 5.0 to 5.5 a.p.f.u. Biotite from *amethyst-bearing* CUB pegmatites has Si of 5.39 to 5.8 a.p.f.u. and Al from 2.6 to 2.8 a.p.f.u. According to mica classification proposed by Tischendorf et al. (1997; Figure 7.15A) the analysed white micas mainly cluster in the muscovite field. The mica in samples CUB1B, CUB2B, CUB3B and CUB4B are biotites and accordingly cluster in the biotite field. In the Si vs. Al_{total} diagram (Figure 7.15B) most samples form an elongate cluster with a negative correlation trend. Only sample MNS3D is separated from that cluster at higher Si and lower Al values. In the muscovites-celadonite diagram all white micas plot close to the muscovite endmembers up to about half way to the phengite position (Figure 7.15C).

In the X_{Fe}-Si diagram, the biotites show a scatter between phlogopite and eastonitic endmembers (Figure 7.15D). The compositional variability is however small (X_{Fe} for most analyses between 0.07 and 0.09; Si between 5.38 and 5.53 a.p.f.u.). The biotite has Al^{iv} between 2.42 and 2.61 a.p.f.u (Figure 7.15E). Calculated anion site occupancy is 4 a.p.f.u. for all the muscovite and phlogopite. The interlayer occupancy ranges from 2.0 to 2.6 a.p.f.u for GNS muscovite, 1.12 to 2.5 a.p.f.u. for MSN muscovite and 2.0 to 2.5 a.p.f.u. for CUB biotite.

Tourmaline-bearing Pegmatites (GNS) from Ntcheu: Trace Elements and REE

The muscovites in GNS pegmatites (samples GNS1, GNS3, GNS6, GNS7; Table 7.4B, Appendix 2.4B) show generally low concentrations of trace elements, but with relative abundances similar to DHD muscovite. The GNS muscovites show moderate Rb (283-585 ppm), and Ti (429-1856 ppm), Ba ranges from 229-5820 ppm, some Nb (41-131 ppm), Ga (134-284 ppm) and B (86-509 ppm) are present. Li (4-20 ppm), Ta (1-11 ppm) and Be (2-11 ppm) are low.

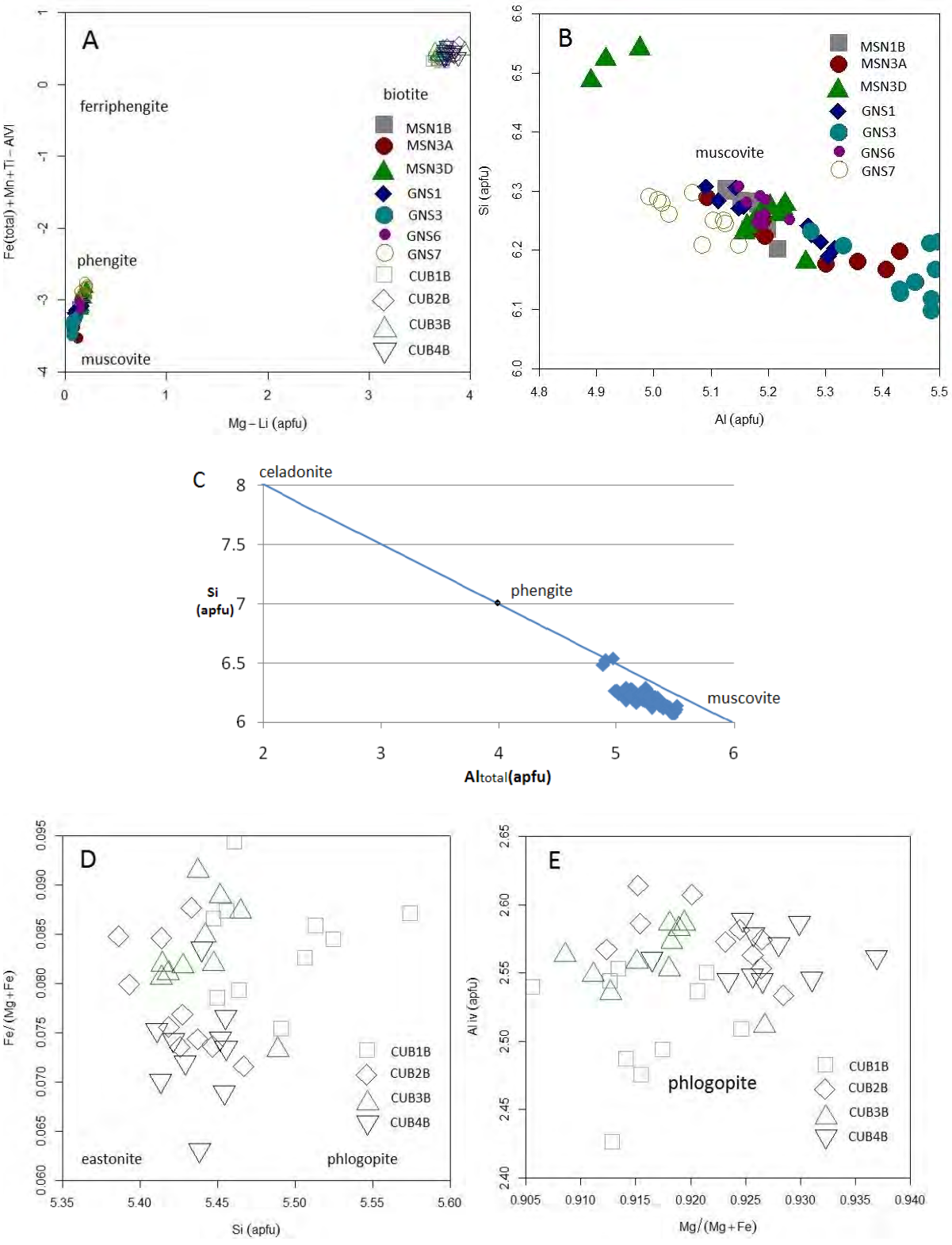

Figure 7. 15: Chemical composition of micas from the Pan-African pegmatites from Ntcheu and Balaka; (A) Mica classification proposed by Tischendorf et al. (1997); (B) Classification of white mica phases in diagram Si vs. Al; (C) Classification of white mica showing the analyses in the muscovite-celadonite series; (D) Classification of biotite according to Deer et al. (1966) and (E) according to Deer et al. (1992).

Table 7. 4A: Average mica (Ms, Bt) analyses (n=10 each) for major elements in micas for Ntcheu (GNS, MSN) and Balaka (CUB) pegmatites. Supplementary geochemical data in Appendix 2.4A.

	Ms	Ms	Ms	Ms
Sample	GNS1	GNS3	GNS6	GNS7
SiO_2	46.09	46.36	46.58	46.19
TiO_2	0.11	0.06	0.04	0.19
Al_2O_3	32.3	34.29	32.69	32.24
FeO	3.01	1.99	3.47	3.87
MnO	0.05	0.08	0.07	0.03
MgO	0.68	0.39	0.77	0.98
CaO	0.01	0.01	0.01	0.02
Na_2O	0.50	0.39	0.50	0.42
K_2O	12.76	13.12	12.33	13.44
F	0.05	0.06	0.08	0.05
Cl	0.00	0.00	0.01	0.00
Cr_2O_3	0.00	0.01	0.00	0.00
H_2O*	4.40	4.48	4.42	4.40
Subtotal	100.22	101.23	100.96	101.83
O=F,Cl	0.02	0.02	0.04	0.02
Total	100.20	101.21	100.91	101.81
Si	6.25	6.17	6.27	6.26
Al^{iv}	1.75	1.83	1.73	1.74
∑(Si,Al)	8.00	8.00	8.00	8.00
Al^{vi}	3.46	3.60	3.45	3.33
Ti	0.01	0.01	0.00	0.02
Cr	0.00	0.00	0.00	0.00
Fe	0.34	0.22	0.39	0.44
Mn	0.01	0.01	0.01	0.00
Mg	0.14	0.08	0.15	0.20
∑(Al, Fe,Mg,Ti)	3.95	3.91	4.00	3.98
$\sum Al_{total}$	5.21	5.44	5.19	5.07
Ca	0.00	0.00	0.00	0.00
Na	0.13	0.10	0.13	0.11
K	2.21	2.28	2.12	2.29
∑(Ca,Na,K)	2.34	2.38	2.25	2.4
OH*	3.98	3.98	3.96	3.98
F	0.02	0.02	0.03	0.02
Cl	0.00	0.00	0.00	0.00
∑(F,Cl,OH)	4.00	4.00	4.00	4.00
TOTAL	18.30	18.30	18.26	18.39

	Ms	Ms	Ms
Sample	MSN1B	MSN3A	MSN3D
SiO_2	46.46	46.39	46.67
TiO_2	0.04	0.07	0.03
Al_2O_3	33.99	33.31	32.96
FeO	3.41	2.87	3.42
MnO	0.09	0.03	0.06
MgO	0.79	0.68	0.80
CaO	0.01	0.02	0.02
Na_2O	0.43	0.42	0.54
K_2O	12.68	12.99	12.69
F	0.05	0.03	0.07
Cl	0.01	0.01	0.01
Cr_2O_3	0.02	0.01	0.01
H_2O*	4.49	4.51	4.46
Subtotal	101.49	101.32	101.26
O=F,Cl	0.02	0.01	0.03
Total	101.47	101.31	101.23
Si	6.26	6.24	6.25
Al^{iv}	1.74	1.76	1.75
∑(Si,Al)	8.00	8.00	8.00
Al^{vi}	3.43	3.53	3.45
Ti	0.00	0.01	0.00
Cr	0.00	0.00	0.00
Fe	0.38	0.32	0.38
Mn	0.01	0.00	0.01
Mg	0.16	0.13	0.16
∑(Al, Fe,Mg,Ti)	3.98	3.99	4.00
$\sum Al_{total}$	5.17	5.29	5.20
Ca	0.00	0.00	0.00
Na	0.11	0.11	0.14
K	2.21	2.11	2.13
∑(Ca,Na,K)	2.32	2.22	2.27
OH*	3.98	3.99	3.97
F	0.02	0.01	0.03
Cl	0.00	0.00	0.00
∑(F,Cl,OH)	4.00	4.00	4.00
TOTAL	18.31	18.22	18.28

	Bt	Bt	Bt	Bt
Sample	CUB1B	CUB2B	CUB3B	CUB4B
SiO_2	38.97	38.80	38.58	38.63
TiO_2	1.52	1.68	1.51	1.64
Al_2O_3	16.61	16.44	16.34	16.42
FeO	3.62	3.30	3.62	3.20
MnO	0.02	0.04	0.04	0.06
MgO	22.07	22.48	22.91	22.75
CaO	0.06	0.01	0.04	0.01
Na_2O	0.38	0.32	0.34	0.21
K_2O	10.92	11.47	11.43	11.75
F	1.15	1.33	1.23	1.33
Cl	0.09	0.02	0.06	0.03
Cr_2O_3	0.02	0.02	0.03	0.02
Li_2O*	1.63	1.63	1.79	1.70
H_2O*	3.69	3.67	3.76	3.68
Subt	100.74	101.21	101.69	101.47
O=F,Cl	0.50	0.57	0.53	0.57
Total	100.24	100.64	101.16	100.90
Si	5.49	5.42	5.44	5.44
Al^{iv}	2.51	2.58	2.56	2.56
∑(Si,Al)	8.00	8.00	8.00	8.00
Al^{vi}	0.24	0.12	0.15	0.13
Ti	0.16	0.18	0.16	0.17
Cr	0.00	0.00	0.00	0.00
Fe	0.43	0.40	0.43	0.37
Mn	0.00	0.00	0.01	0.01
Mg	4.63	4.70	4.72	4.73
Li*	0.92	0.91	0.99	0.95
∑(Al, Fe,Mg,Ti)	5.46	5.40	5.46	5.40
$\sum Al_{total}$	2.76	2.70	2.71	2.69
Ca	0.01	0.00	0.01	0.00
Na	0.11	0.09	0.09	0.06
K	1.96	2.29	2.05	2.25
∑(Ca,Na,K)	2.08	2.37	2.15	2.31
OH*	3.47	3.41	3.45	3.40
F	0.51	0.59	0.53	0.59
Cl	0.02	0.01	0.01	0.01
∑(F,Cl,OH)	4.00	4.00	4.00	4.00
TOTAL	20.47	20.69	20.61	20.68

Table 7. 4B: Average analysis (n=10 each) for trace elements in micas for Ntcheu (GNS, MSN) and Balaka (CUB) pegmatites. Supplementary geochemical data in Appendix 2.4B. All concentrations are given in ppm.

Mineral	Ms		Ms		Ms		Ms		Ms		Ms		Ms	
Element	GNS1	Max-Min	GNS3	Max-Min	GNS6	Max-Min	GNS7	Max-Min	MSN1B	Max-Min	MSN3A	Max-Min	MSN3D	Max-Min
Li	11	[15-4]	6	[7-4]	12	[14-9]	16	[20-10]	14	[15-13]	8	[16-6]	19	[24-12]
Be	3	[5-2]	9	[11-7]	3	[5-2}	5	[6-4]	4	[6-2]	4	[4-2]	4	[6-2]
B	222	[317-144]	459	[509-409]	222	[296-176}	114	[137-86]	214	[239-187]	356	[464-273]	1599	7712-529]
Sc	17	[24-7]	21	[37-11]	10	[15-7]	63	[81-42]	9	[10-9]	14	[29-7]	10	[10-9]
Ti	816	[1096-487]	615	[876-457]	483	[579-429]	1564	[1856-1294]	460	[472-436]	606	[916-335]	448	[452-444]
V	36	[78-2]	16	[31-9]	3	[7-2]	47	[61-33]	3	[3-2]	30	[64-7]	3	[4-2]
Cr	0.2	[1-0.1]	1	[2-0.1]	0	0	0.1	[1-0.1]	0	0	0.4	[2-0.1]	0.3	[2-0.1]
Mn	356	[473-284]	323	[376-268]	357	[414-316]	219	[299-145]	347	[385-264]	160	[213-104]	325	[374-283]
Co	1	[2-1]	9	[58-1]	10	[29-1]	3	[4-2]	7	[22-2]	3	[7-1]	2	[2-2]
Ni	0	0	0	0	0	0	2	[2-1]	0	0	0.2	[1-0.1]	0	0
Cu	0	0	1	[5-0.03]	1	[3-0]	0.4	[1-0.1]	0.7	[2-0.1]	0.3	[1-0.2]	0.4	[1-0.1]
Zn	60	[79-47]	30	[36-22]	51	[60-45]	56	[68-48]	62	[73-51]	43	[59-21]	68	[70-66]
Ga	191	[234-134]	155	[166-144]	208	[225-174]	259	[284-237]	223	[234-206]	163	[197-115]	230	[239-215]
Rb	407	[585-295]	547	[576-506]	324	[371-298]	315	[350-283]	325	[338-309]	487	[529-441]	312	[329-301]
Sr	12	[17-4]	8	[9-7]	14	[17-11]	17	[19-13]	14	[15-14]	13	[18-6]	14	[15-14]
Y	0	0	0	0	0	[1-0]	0	0	0	0	0	0	0	0
Zr	1	[2-1]	1	1	1	1	1	[2-1]	1	[1-1]	1	[1-1]	1	[1-1]
Nb	79	[130-41]	108	[131-96]	52	[60-48]	55	[60-50]	54	[55-51]	92	[118-67]	53	[55-52]
Mo	0	0	0	0	0	0	0.5	[1-0.5]	0	0	0	0	0	0
Sn	4	[5-2]	5	[8-4]	2	[3-2]	8	[10-6]	2	[2-2]	3	[5-2]	2	[2-2]
Cs	18	[49-9]	32	[43-25]	13	[31-10]	11	[15-9]	10	[11-10]	33	[52-23]	10	[11-10]
Ba	2729	[4740-229]	744	[944-585]	3686	[4485-2339]	5201	[5820-4416]	4048	[4236-3864]	1902	[3513-447]	3834	[4002-3695]
Hf	0.3	[0.5-0.2]	0	0	0	0	0	0	0.2	[1.3-0.2]	0.3	[1-0.2]	0	0
Ta	2	[5-1]	5	[11-3]	1	[3-1]	1	2	1	[1-1]	5	[20-3]	1	[1-1]
W	33	[45-20]	7	[9-5]	38	[42-32]	56	[60-51]	39	[42-36]	20	[26-15]	38	[40-37]
Pb	16	[24-12]	25	[28-21]	14	[17-12]	14	[16-11]	14	[15-13]	25	[29-20]	14	[16-13]
Th	0	0	0	0	0	0	0	0	0	<0.0090	0	0	0	0
U	0	0	0	0	0	0	0	0	0	0	0	0	0	0

Table 7. 4B (continued): Average analysis (n=10 each) for trace elements in micas for Balaka pegmatites (CUB). Supplementary data in Appendix 2.4B. All concentrations are given in ppm.

Mineral	Bt		Bt		Bt		Bt	
Element	CUB1B	Max-Min	CUB2B	Max-Min	CUB3B	Max-Min	CUB4B	Max-Min
Li	97	[152-69]	56	[63-43]	63	[81-52]	92	[108-81]
Be	0.2	[1-0.03]	0	0	0	[1-0]	0	0
B	142	[211-90]	57	[55-41]	64	[90-47]	86	[106-69]
Sc	2	[2-2]	1	1	2	[2-1]	2	[2-1]
Ti	8525	[8798-8213]	9800	[9353-8530]	7869	[8286-7533]	7943	[8513-7550]
V	73	[77-70]	77	[73-68]	73	[76-70]	75	[80-71]
Cr	60	[65-58]	69	[69-58]	56	[61-54]	57	[62-54]
Mn	291	[307-270]	307	[288-265]	281	[296-269]	274	[289-259]
Co	14	[15-13]	15	[14-13]	20	[60-14]	17	[27-15]
Ni	72	[75-69]	77	[72-67]	68	[72-65]	71	[74-69]
Cu	0.3	[1-0.1]	4	[37-0.1]	2	[19-0.03]	2	[4-1]
Zn	191	[219-177]	222	[210-194]	199	[211-183]	198	[218-172]
Ga	58	[63-54]	63	[61-55]	54	[59-50]	54	[58-51]
Rb	509	[536-499]	576	[544-515]	522	[554-412]	576	[615-537]
Sr	12	[14-6]	15	[15-13]	13	[14-12]	13	[15-11]
Y	1	[7-0.01]	0	0	1.5	[19-0.03]	1	[4-0-1.03]
Zr	14	[19-3]	20	[34-14]	18	[20-17]	16	[18-13]
Nb	48	[49-46]	50	[48-43]	51	[52-49]	52	[56-50]
Mo	0	0	0	0	0	0	0	0
Sn	2	[2-1]	2	2	2	[3-2]	2	[3-2]
Cs	25	[27-24]	27	[26-24]	25	[27-21]	27	[29-26]
Ba	1200	[1255-1129]	1432	[1381-1239]	1108	[1184-887]	1155	[1234-1040]
Hf	0	0	0	0	0	0	0	0
Ta	3	[3-2]	3	[3-2]	3	[3-2]	3	[3-2]
W	0	0	0	0	0	0	0	0
Pb	2	[2-1]	2	2	2	2	3	[4-2]
Th	0	0	0	0	0	0	0	0
U	0	0	0	0	0	0	0	0

The binary diagrams (Figure 7.16A-E) show a systematic decrease in the K/Rb ratio in the muscovite with increasing Rb, Cs, Nb and Ta in the Pan-African GNS pegmatites, following similar fractionation trends as seen in the DHD (Section 7.2.4). Even though incompatible element concentrations are very low in GNS pegmatites, they increase from GNS7 to GNS1 muscovites. Cs concentrations are low (10-43 ppm); however in GNS muscovites, GNS3 has highest concentration (25-43 ppm), followed by GNS1 (9-10 ppm; Figure 7.16B). Li concentrations are also low, ranging from 4-20 ppm (Figure 7.16F), and so are Be concentrations (2-11 ppm; Figure 7.17A). In the GNS muscovite, Ti is lowest in GNS6 and GNS3 whereas GNS7 has the highest concentration followed by GNS1; however none exceeds 1800 ppm (Figure 7.17B).

The K/Rb ratio correlates positively with Ba in GNS1-GNS7 (Figure 7.17C). A diagram of K/Ba versus Ba (Figure 7.17D) shows that GNS1, GNS6 and GNS7 muscovites are more fractionated than GNS3 muscovites.

The Al/Ga against Ga diagram shows highest Ga concentrations in GNS7 muscovites of 250-280 ppm whereas GNS1, GNS3, GNS6 have ~140-235 ppm (Figure 7.17E). The K/Rb against Al/Ga diagram (Figure 7.17F) shows that Ga increases with the less evolved pegmatites. Since the decreasing K/Rb ratio with increasing concentration of the incompatible elements Rb, Ta, Nb, suggests increasing magma fractionation, in the GNS pegmatites, samples GNS3 and GNS6 formed in more evolved melts than samples GNS1 and GNS7. Accordingly, the samples that formed in more evolved melt plot at the right bottom end of negative correlation trends. Samples that plot to the upper left end of negative correlation trends or to the right for positive trends indicate growth in least evolved melts.

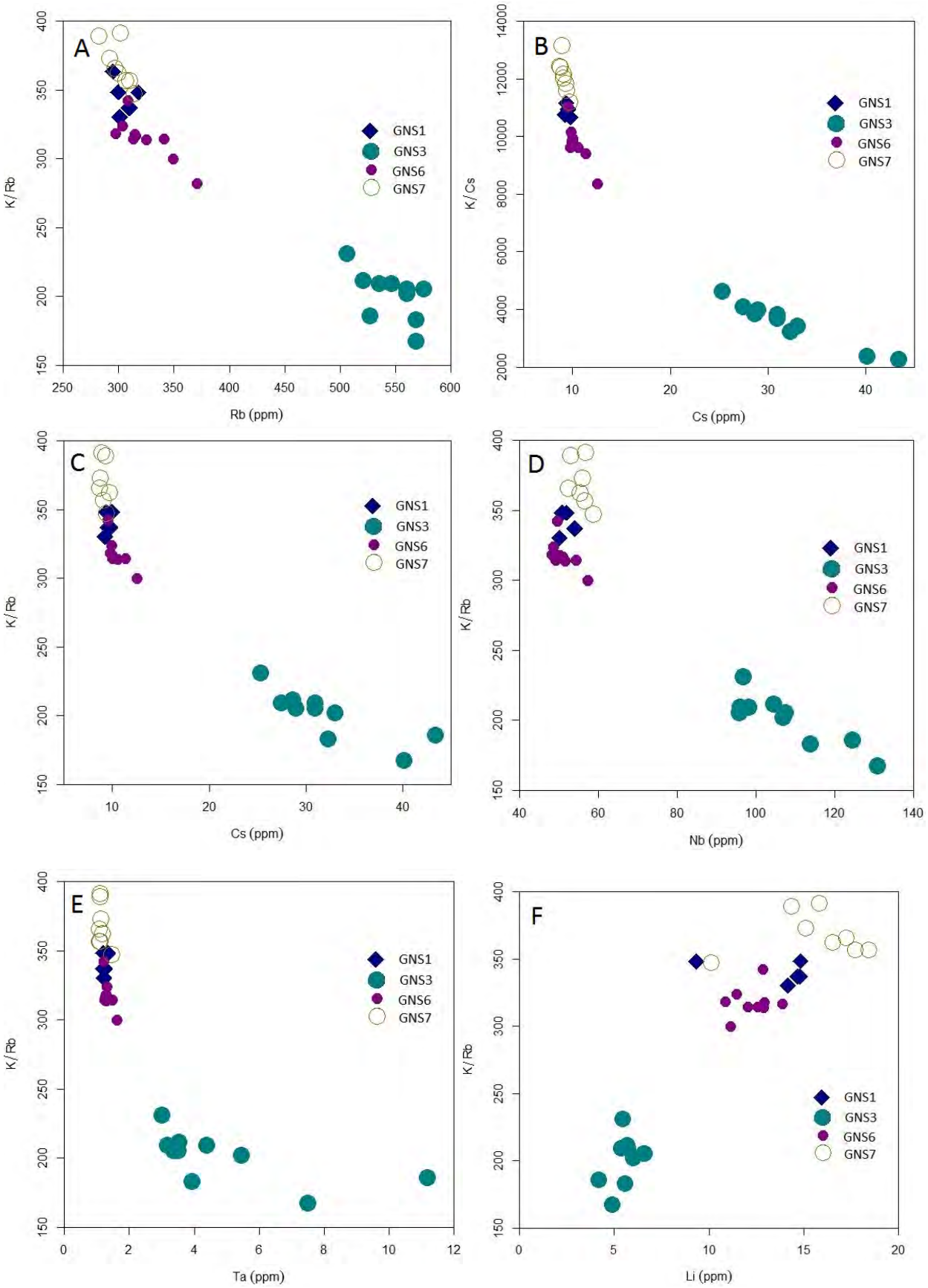

Figure 7.16A-F: Binary plots of selected compatible and incompatible element ratios in micas illustrating fractionation of pegmatites.

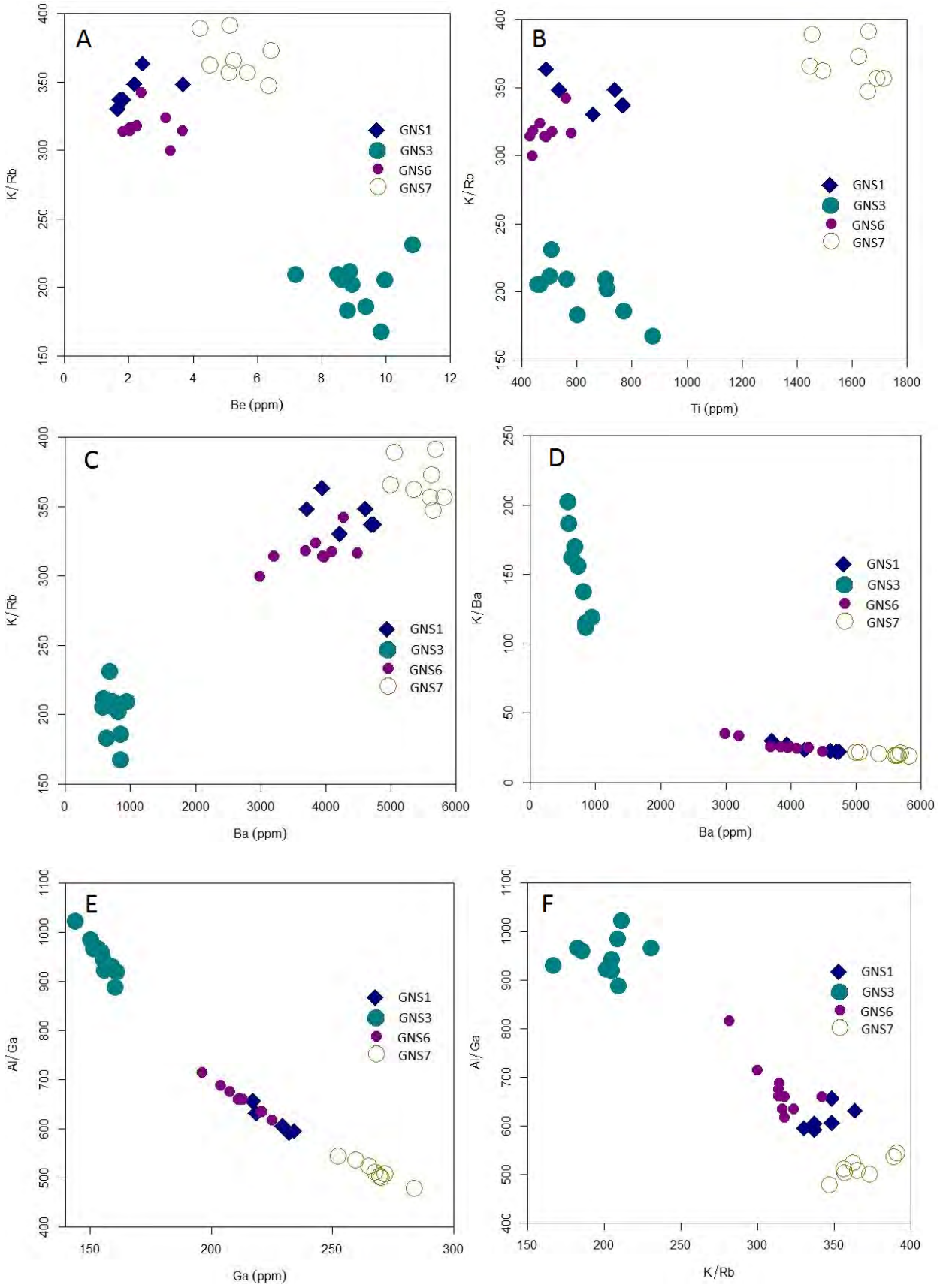

Figure 7. 17A-F: Binary plots of selected compatible and incompatible element ratios in micas illustrating fractionation of pegmatites.

In the UCC-normalised abundances of trace elements in mica samples from GNS pegmatites (Figure 7.18), all muscovite from the Neoproterozoic GNS pegmatites show familiar patterns with strongly enriched Rb, Ba and Ti, less enriched Cs and Nb, whereby in some sample Nb is depleted. Sr is always enriched but does not exceed 20 x UCC. P, Hf and Zr are close to UCC, either slightly enriched or depleted. Y is slightly to moderately, and U and Th, as in all analysed pegmatites, strongly depleted. Remarkable are the high Ba (300-6000 x UCC) and the uniformly enriched Sr. Both are compatible elements which only in early stages of differentiation are abundant in pegmatitic melt.

Generally, all muscovite samples from GNS pegmatites show that Rb, Nb, Ba, Sr, Ti increase as Ta decrease. However, small variations occur within the strongly enriched Rb, Ba, Ti (200-7000 x UCC) and moderately enriched Cs and Nb (10-80 x UCC). Th, U and Y (0.0003-0.06 x) are moderately to strongly depleted.

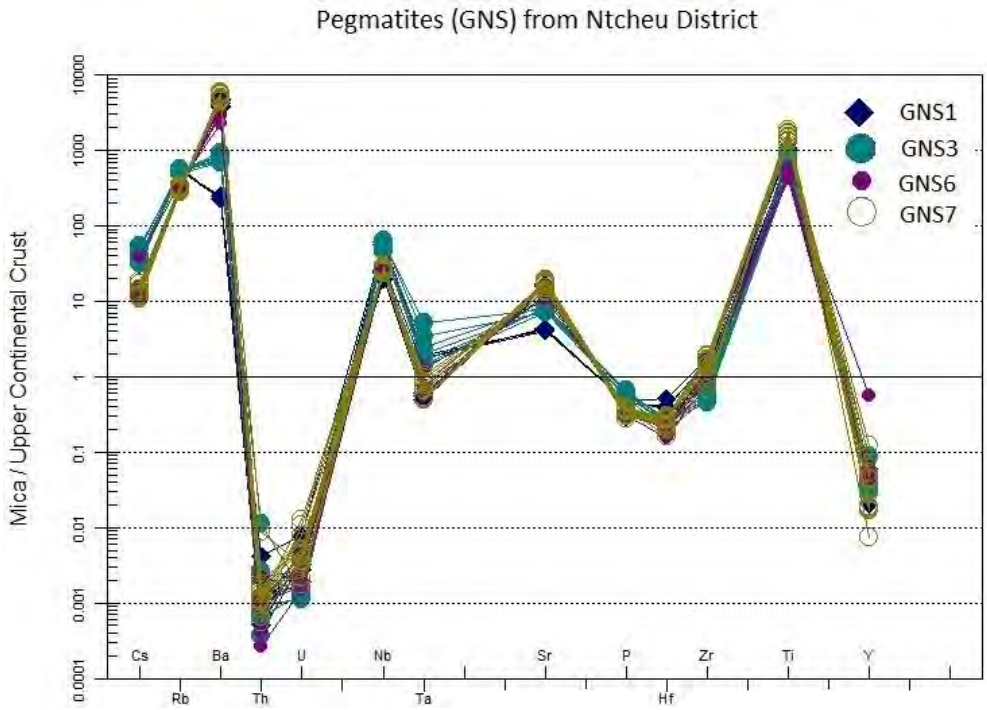

Figure 7.18: UCC-normalised abundance patterns (Taylor and McLennan, 1995) of trace elements in muscovite from tourmaline-bearing pegmatites (GNS) from Ntcheu District.

UCC-normalised REE patterns in the muscovites from the Pan-African GNS pegmatites (Figure 7.19, Appendix 2.4C) from Ntcheu generally show depleted REE, with most depletion in Ce , moderate depletion in Sm and Tb and least depletion in Tm and Yb. This trend differs from those for CCC, MWC, GM and HEM pegmatites, which show more depletion in Tb and Tm (Figure 7.2B, Figure 7.3M, Figure 7.8E-F, Figure 7.14).

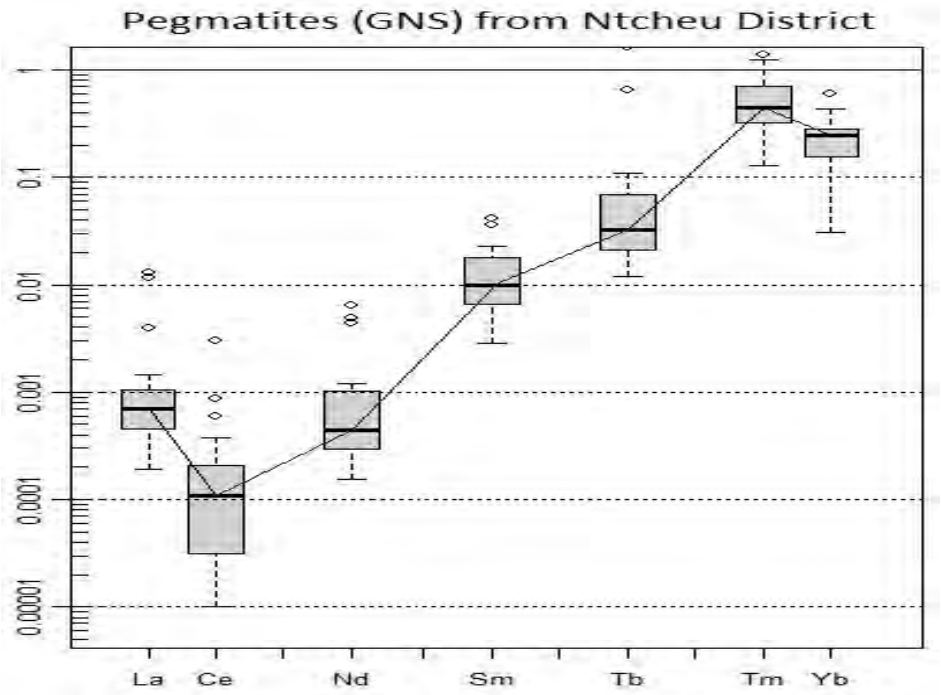

Figure 7.19: Boxplot of UCC-normalised abundance patterns of REE (Taylor and McLennan, 1995) for muscovite from *gem tourmaline-bearing* pegmatites from Ntcheu. The diamond symbols represent outliers.

Tourmaline- and Sunstone-Bearing Pegmatites (MSN) from Ntcheu

The muscovites in MSN (MSN1B, MSN3A, MSN3D; Table 7.4B, Appendix 2.4B) show generally low concentrations of trace elements, but with a relative abundances similar to GNS and DHD muscovite. Ba concentrations are high, varying from 447 ppm to 4236 ppm, and also B may be higher than usually seen (187-7712 ppm). Ti (335-916 ppm), Rb (301-529 ppm) and Ga (115-239 ppm) are fairly abundant. Nb (51-118 ppm) and Li (6-24 ppm), Be (2-6 ppm) and Ta (1-5 ppm) are variably low.

The binary diagrams (Figure 7.20A-E) show the typical evolution trends in the K/Rb ratio against Rb, Cs, Nb and Ta, with negative correlations, as seen in DHD (Section 7.2.4) and other pegmatites. Even though incompatible element concentrations are very low in the pegmatites, they increase from MSN1B to MSN3D and MSN3A muscovites. Cs has low concentrations (10-52 ppm); however, MSN3A muscovites (23-52 ppm) show the highest Cs concentration amongst MSN muscovites (Figure 7.20B-C). Li concentrations are low, ranging from 6-24 ppm in MSN muscovites, and micas from the three samples show positively correlated cluster positions (Figure 7.20F). Be and Ti do not show a systematic or clear correlation with K/Rb (Figures 7.21A, B). Be concentrations are also very low (2-6 ppm; Figure 7.21A).

The K/Rb ratio diagrams for the MSN muscovites show that MSN3A micas formed in more fractionated melt than MSN3D and MSN1B muscovites. In comparison between the GNS and MSN pegmatites, the GNS muscovites formed generally from more fractionated melt than the MSN muscovites.

The Al/Ga vs. Ga diagram shows highest Ga concentrations of 160-240 ppm in MSN pegmatites (Figure 7.21E). MSN3A forms a well spread-out fractionation trend that is continued by MSN1B and MSN3D clusters. The K/Rb against Al/Ga diagram (Figure 7.21F) shows how Ga decreases towards more evolved pegmatites (i.e. MSN3A). Since the decreasing K/Rb ratio with increasing concentration of the incompatible elements Rb, Ta, and Nb suggests increasing magma fractionation, in the MSN pegmatites, sample MNS3A formed in more evolved melts than samples MSN1B and MSN3D.

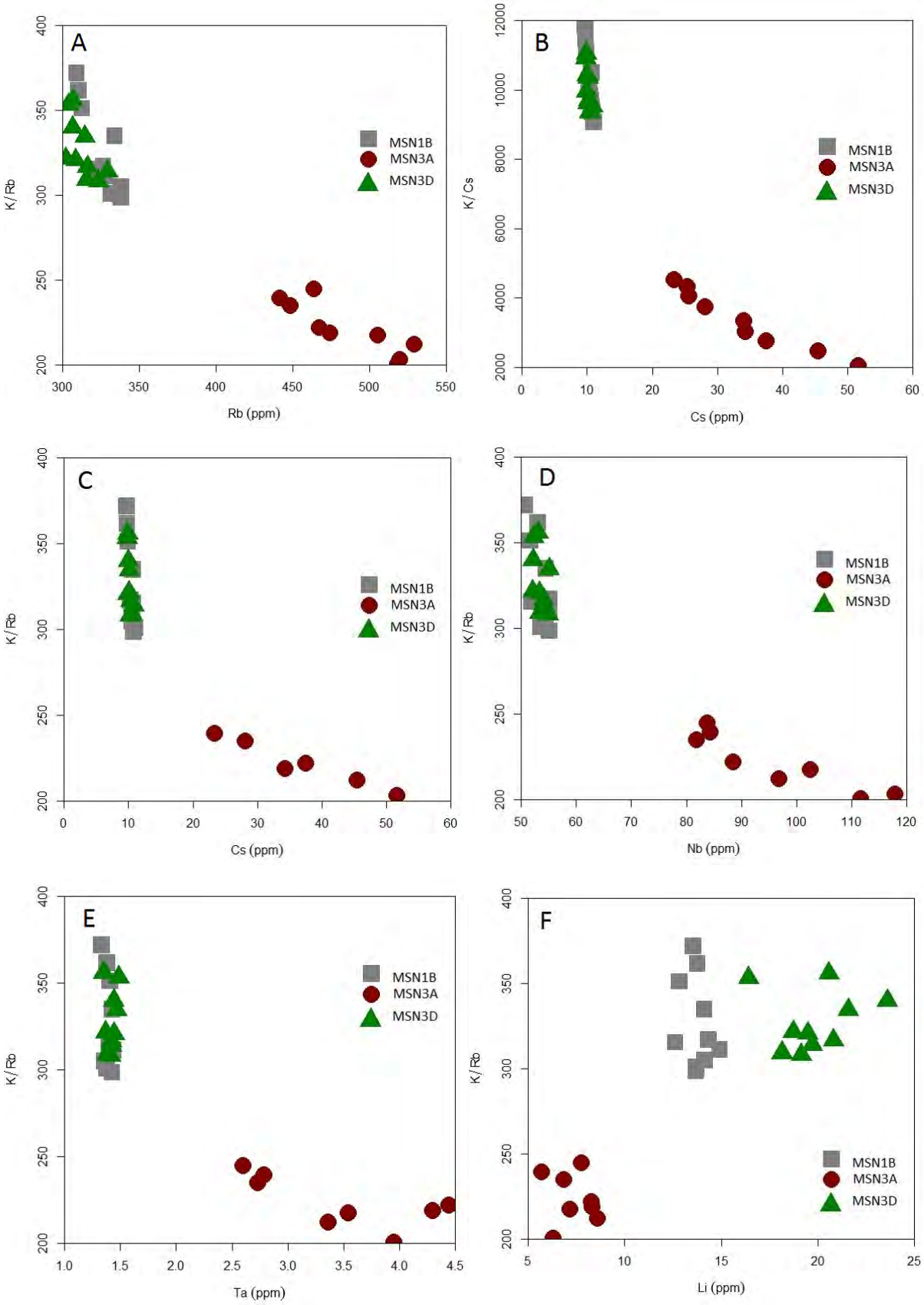

Figure 7.20A-F: Binary plots of selected compatible and incompatible element ratios in micas illustrating fractionation of pegmatites.

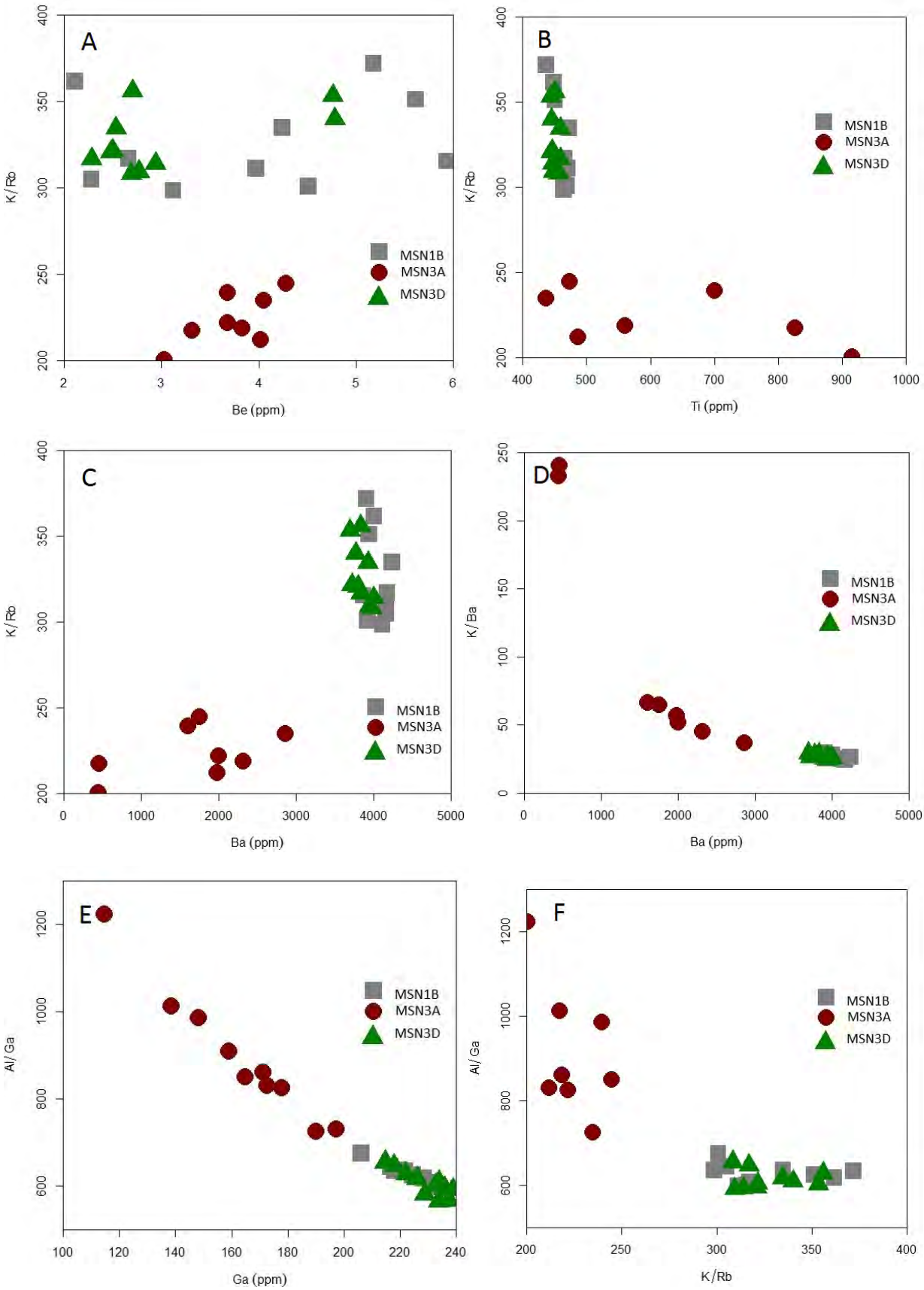

Figure 7.21A-F: Binary plots of selected compatible and incompatible element ratios in micas illustrating fractionation of pegmatites.

In the UCC-normalised abundances of trace elements in mica for samples from MSN pegmatites (Figure 7.22A) are very similar to the GNS pegmatites discussed in the previous section, apart perhaps from some minor differences in Ba and Ta (Figure 7.22B). All muscovites from Ordovician MSN pegmatites show a strongly enriched Rb, Nb, Ba and Ti (300-4000 x UCC), with the strongest Rb enrichment in MSN3A and the least enrichment in MSN3D. Cs (10-80 x), Nb (20-70 x) have moderate enrichment. Ba has moderate to highest (400-4000 x UCC) enrichment with sample MSN1B showing the highest concentrations. Also Ti (300-1000 x) shows strong enrichment. Ta varies from moderately (2 x UCC) enriched in sample MSN3A to slightly (0.6 x) depleted in sample MSN3D. Sr (9-20 x) is consistently UCC enriched. Hf (0.2-0.3 x UCC) and P (0.3-0.8 x) are slightly depleted. Zr varies from slightly (2 x) enriched to slightly (0.5 x) depleted in sample MSN3A. Th, U (0.0003-0.009 x) are, as commonly seen, strongly depleted whereas Y is moderately (0.01-0.1 x) depleted.

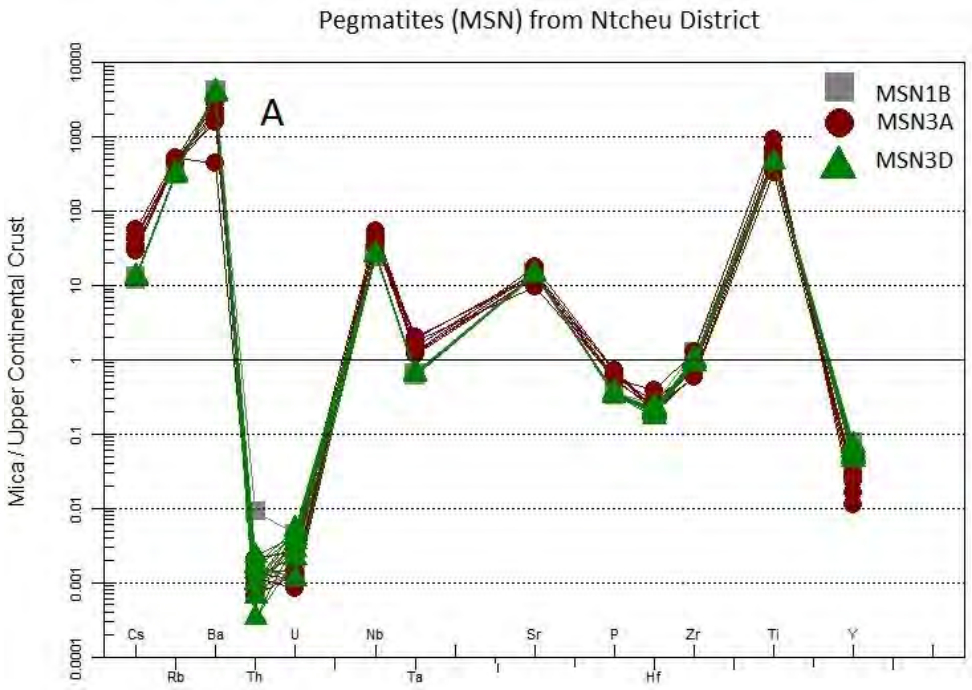

Figure 7.22A: UCC-normalised abundance patterns of trace elements (Taylor and McLennan, 1995) for muscovite from tourmaline- and sunstone-bearing pegmatites (MSN) from Ntcheu District.

Figure 7.22B adds GNS and MSN pegmatites that show similar patterns to each other but with higher Ba (6000 x UCC) and Ti (2000 x UCC) concentration than Nb (~70 x UCC) and Ta (~2 x UCC. This pattern shows higher Ba content than Rb whereas the patterns for CNC, CCC, MWC, GM, HEM and DHD show lower Ba contents than Rb (Section 7.2.3, Figure 7.8D, Section 7.2.4, Figure 7.13).

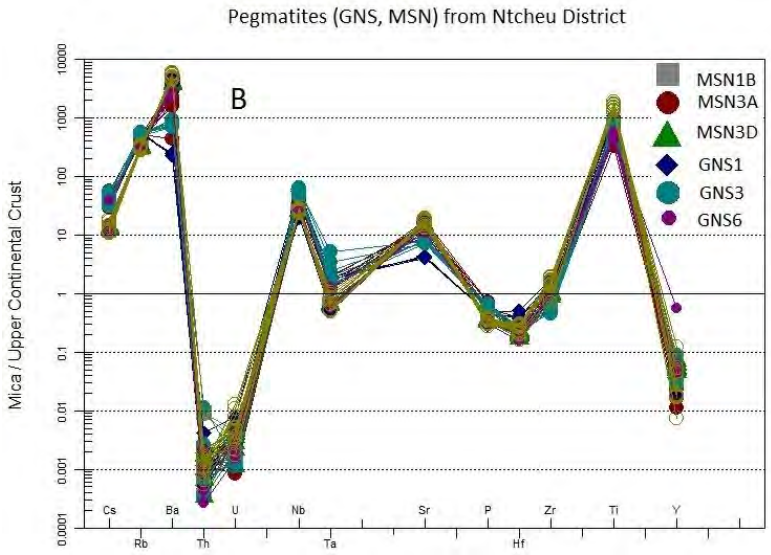

Figure 7. 22B: UCC-normalised abundance patterns of trace elements (Taylor and McLennan, 1995) in muscovite from tourmaline- and sunstone-bearing pegmatites (GNS and MSN) from Ntcheu District.

Normalised REE pattern in the muscovites from the Pan-African MSN pegmatites from Ntcheu show depleted REE with the strongest depletion in Ce (Figure 7.23, Appendix 2.4). This pattern is similar to that for GNS pegmatites (Figure 7.19).

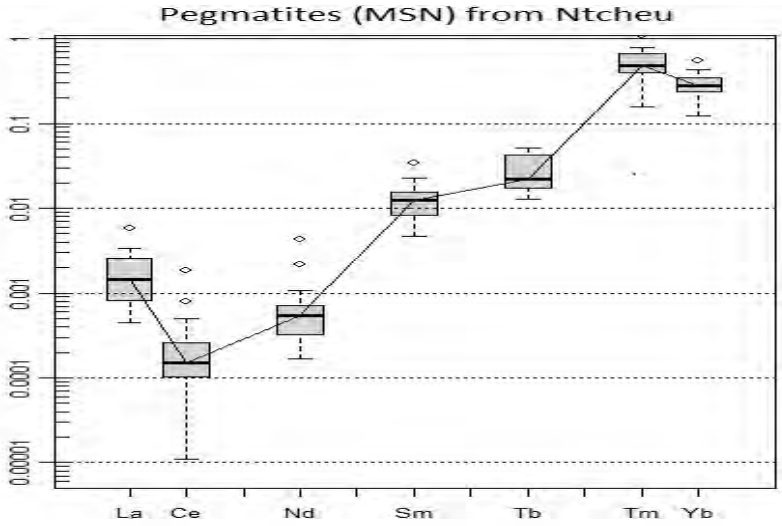

Figure 7. 23: Boxplot of UCC-normalised abundance patterns of REE (Taylor and McLennan, 1995) for muscovite from *gem tourmaline- and sunstone-bearing* pegmatites (MSN) from Ntcheu. The diamond symbols represent outliers.

Amethyst-bearing Pegmatites (CUB) from Balaka

Biotite from the Cambrian amethyst-bearing pegmatites (CUB) from Balaka (Table 7.4B, Appendix 2.4B) shows trace elements concentrations with moderate Rb (412-615 ppm), very high Ti (7533-9353 ppm), and abundant Ba (887-1381 ppm). B (41-211 ppm), Li (43-152 ppm), Ga (51-63 ppm), Nb (43-56 ppm), Ta (2-3 ppm) are much less abundant or low. Be contents are below detection limit.

Rb contents are lowest in CUB1B and highest in CUB4B, but the K/Rb ratio does not correlate with Rb and varies unsystematically between ~170 and 220 (Figure 7.24A). The diagrams for Nb, Li, Ta, Ti and Ba show similar scattering, but in general, analyses from individual pegmatites form more or less coherent clusters (Figure 7.24B-D, and Figure 7.25A-B). Overall the concentrations in these elements and in the K/Rb ratios are not highly variable. Lithium has higher concentrations in CUB phlogopites than seen in the muscovites from GNS and MSN muscovites in Ntcheu district (Figure 7.16F; Figure 7.20F; Figure 7.24C). However, the lithium concentrations in CUB phlogopites are much lower compared to high lithium concentrations in the more evolved GM pegmatites (Section 7.2.3, Figure 7.5E).

The K/Ba ratio correlates negatively with Ba in the CUB phlogopites (Figure 7.25C). Al/Ga vs. Ga (Figure 7.25D), and K/Rb against Al/Ga diagrams (Figure 7.25E) show that Ga increases from CUB4B, CUB2B, CUB3B to CUB1B (Table 7.4B).

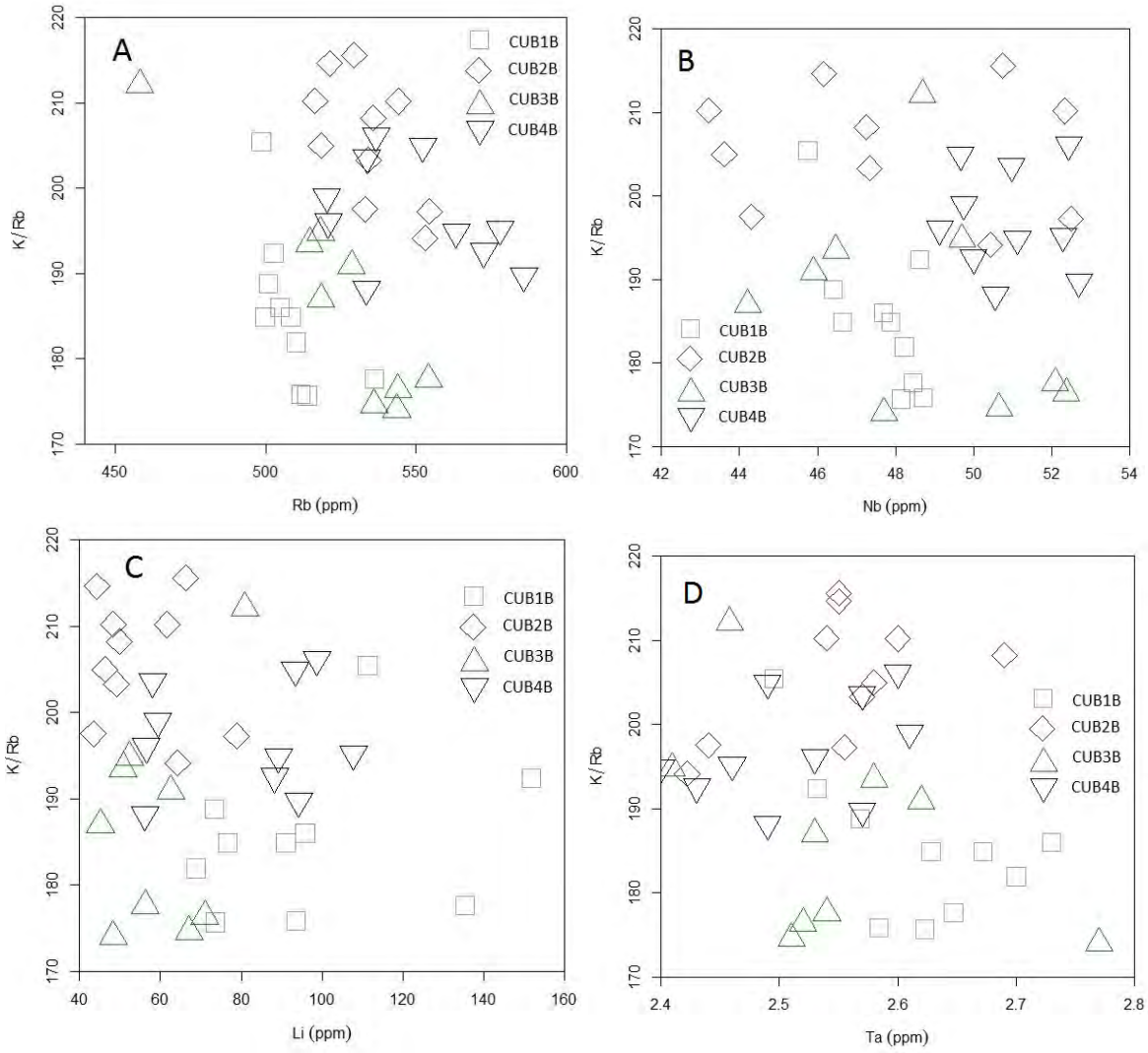

Figure 7. 24A-D: Binary plots of selected compatible and incompatible element ratios in micas from biotites illustrating fractionation of CUB pegmatites.

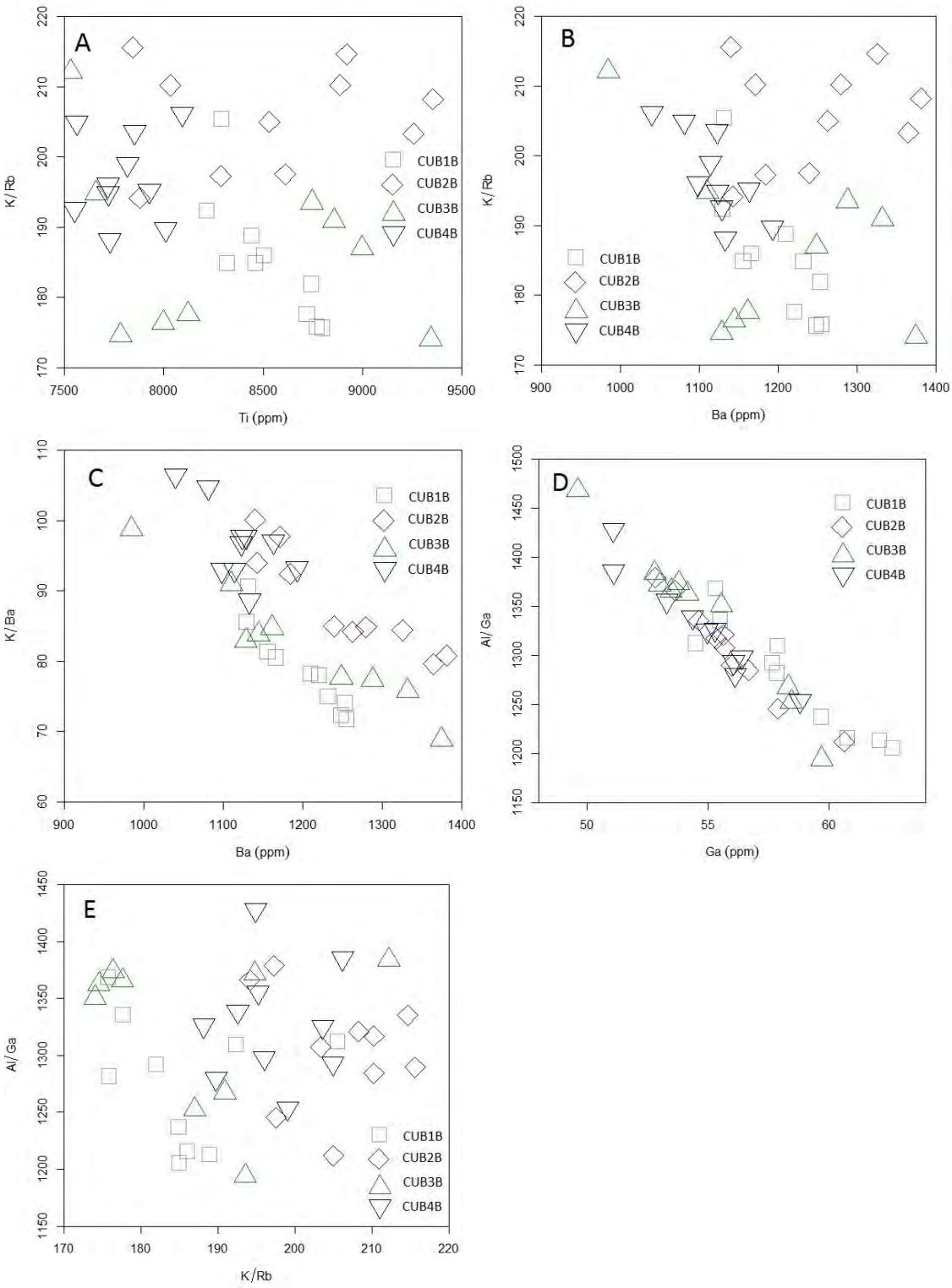

Figure 7. 25A-E: Binary plots of selected compatible and incompatible element ratios in biotites illustrating fractionation of CUB pegmatites.

In the spider diagram for the samples CUB from Cambrian amethyst-bearing pegmatites from Balaka (Figure 7.26), biotite shows a fairly uniform pattern with some similarity to muscovite patterns seen elsewhere. Rb, Ba (700-1500 x UCC) and particularly Ti (7000 x UCC) are strongly enriched. Less enriched are Cs, Nb, Sr and Zr (~10-30 x UCC). Ta is neutral. P (0.03-

0.1 x) and Hf (0.2-0.3 x) are slightly depleted. Thorium is highly depleted (0.008-0.0002 x) whereas U is much less depleted than in other micas (0.2-0.02 x). Y is highly variable ranging from slightly (10 x) enriched in sample CUB3B to moderately (0.01 x) depleted in sample CUB2B.

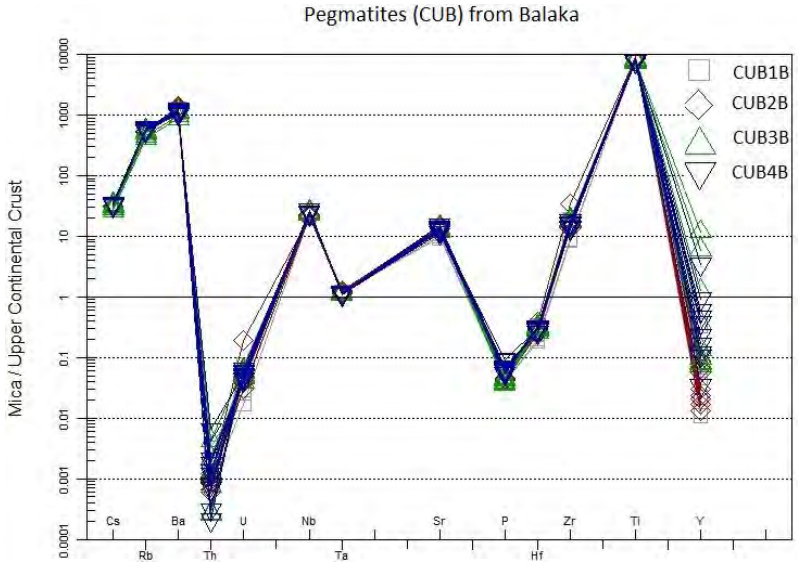

Figure 7. 26: UCC-normalised abundance patterns of trace elements (Taylor and McLennan, 1995) for biotite from amethyst-bearing pegmatites from Balaka.

Normalised REE patterns in the biotites from the Pan-African CUB pegmatites from Balaka show a pattern with depleted REE (Figure 7.27, Appendix 2.4C). The biotites show more depleted LREE, less depleted MREE and comparatively enriched HREE. Yb is weakly depleted. The strongest depletion is seen in Ce (0.0002 x UCC).

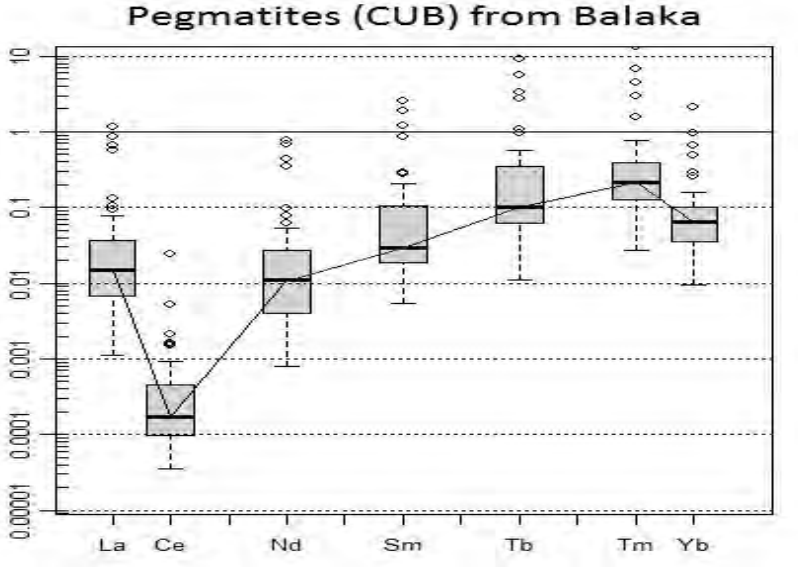

Figure 7.27: Boxplot of UCC-normalised abundance patterns of REE in mica from amethyst-bearing pegmatites from Balaka, after Taylor and McLennan (1995) The diamond symbols represent outliers.

In the following the REE data of all analysed micas are briefly discussed normalised to chondrite (Nakamura, 1974, Appendix 2.1D, 2.2D, 2.3D and 2.4D). Generally, the chondrite-normalised abundance patterns of REE (Figures 7.28A-F; Figure 7.29A) show that REEs vary from slightly enriched to strongly depleted. Mica from the Palaeoproterozoic pegmatite (Figure 7.28A), show Ce strongly depleted; Pr and Eu are above neutral or slightly enriched, and Tm (20 x) and Lu (4 x) are slightly enriched. REE show minor depletion except Tm, which is 10x enriched.

The micas from the Pan-African (CCC, MWC, GM and HEM) pegmatites from Chitipa and Mzimba (Sections 7.2.2 and 7.2.3, Figure 7.28B-D), the Pan-African (DHD) pegmatites from Dowa (Figure 7.28E) and the Pan-African Neoproterozoic GNS and Ordovician MSN pegmatites from Ntcheu (Figure 7.28F) generally show similar normalised REE patterns. They show variably depleted LREE, less depleted MREE and enriched HREE. However, the biotites from the Pan-African Cambrian (CUB) pegmatites from Balaka (Figure 7.29A, Appendix 2.4D) show a flattened pattern with slightly enriched LREE and HREE, and less depleted MREE. In all the pegmatites, Ce is the most depleted in the LREE whereas Eu is slightly enriched in the less depleted MREE.

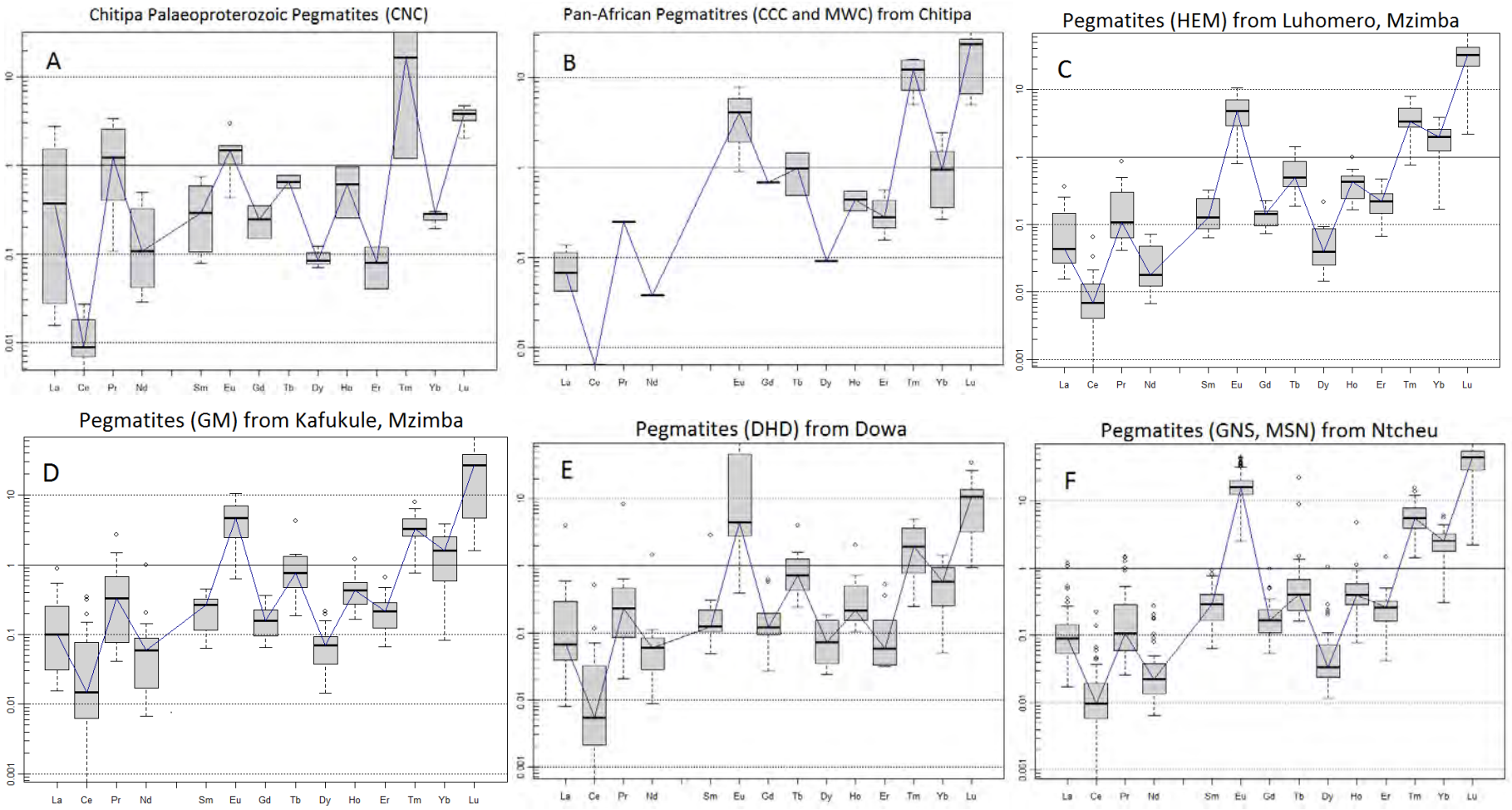

Figure 7. 28: Boxplots of chondrite normalised abundance patterns of REE (Nakamura, 1974) for mica from Palaeoproterozoic and Pan-African pegmatites. The black bar in the box shows the median. The top and lower bars represent the greatest and lowest values excluding outliers represented by diamond symbols. (A) Palaeoproterozoic tourmaline-bearing pegmatites from Nthalire, Chitipa; (B) Beryl- and tourmaline-bearing (CCC, MWC) pegmatites, Chisenga and Wenya pegmatites, Chitipa; (C) Aquamarine-bearing (HEM) Luhomero pegmatites, Mzimba; (D) Beryl-bearing (GM) Kafukule pegmatite, Mzimba; (E) Tourmaline-bearing (DHD) pegmatites from Dowa; (F) Tourmaline- and sunstone-bearing (GNS and MSN) pegmatites from Ntcheu.

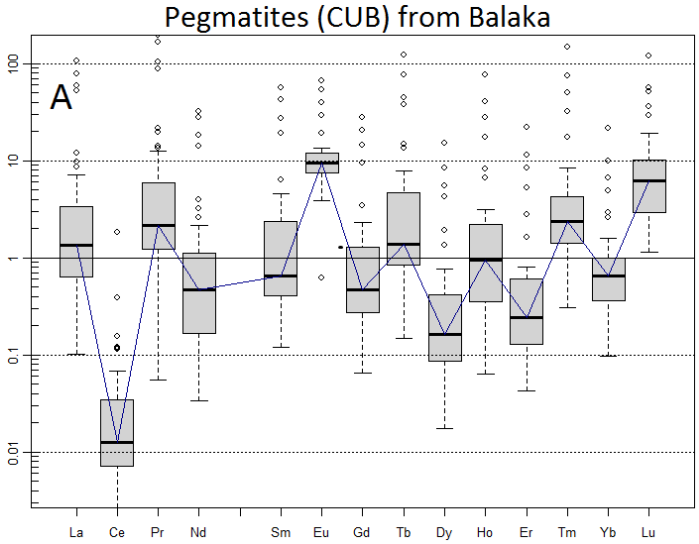

Figure 7. 29: Boxplot of chondrite-normalised abundance patterns of REE (Nakamura, 1974) for biotite from amethyst-bearing pegmatites from Balaka. The diamond symbols represent outliers.

According to the pegmatite classification scheme of Ginsburg et al. (1979) and Cërny (1991a; Section 2.3, Table 2.1), these GSN and MSN pegmatites belong to the Rare Element Class and LCT family which shows low to abundant mineralisation. According to subdivisions of the Ginsburg et al.‟s (1979) classification into subclasses, types and subtypes (Table 2.3; Cërny, 1990; 1991a; Cërny and Ercit, 2005; Cërny et al., 2012), the LCT pegmatites belong to REL-Li subclass, Complex type and Elbaite subtype. According to Cërny and Ercit (2005; Table 2.4) the GNS and MSN pegmatites belong to Rare Element class, in the REL-Li subclass, and in the Miarolitic Class, Mi-Li subclass. Furthermore, according to the pegmatite classification scheme of Ginsburg et al., (1979) and Cërny 1991a (Chapter 2, Section 2.3, Table 2.1), these CUB pegmatites belong to the Rare element Class and LCT family bearing gemstock. According to Cërny and Ercit, 2005 (Table 2.4), the amethyst bearing (CUB) pegmatites belong to Rare Element class, in the REL-Li subclass, and also in the Miarolitic Class, Mi-Li subclass. These pegmatites like the GSN and MSN pegmatites have not yet been related to known plutons. More information regarding classification of these pegmatites will be discussed in Chapter 9.

7.3 SYNOPSIS OF GEOCHEMICAL DATA

The trace element variations shown in this chapter show fractionation trends for all pegmatite fields. These fractionation trends indicate the geochemical evolution of parental magma from which the pegmatites were derived (Taylor and McLennan, 1985). The more evolved pegmatites (e.g. GM) have highest abundance of rare elements, Be, Li, Rb, Ta and Nb, and depletion of Ba and Sr suggesting progressive differentiation of felsic magmas. However, the Neoproterozoic gem tourmaline-bearing pegmatites (GNS), and the Ordovician gem tourmaline- and sunstone-

bearing pegmatites (MSN) in Ntcheu (Section 4.3.9, Appendix 1.1), show highest enrichments in Rb, Ba, Cs, Nb, Ti, moderate enrichment in Sr and moderate enrichment to depletion in Ta (Section 7.2.5). Since a pegmatitic melt is already an evolved melt from a crystallising granite, these results correlate with rare-element enrichment through fractionation processes where partitioning of rare elements into pegmatitic solid and volatile phases show lowest enrichment of incompatible elements in less evolved pegmatites. Hence the GNS and MSN pegmatites show low differentiation of felsic magmas (Section 7.2.5), even though Ba is highly compatible in micas (Icenhover and London, 1996).

The element patterns in the Cambrian amethyst-bearing pegmatites (CUB) from Balaka vary unsystematically but with individual pegmatites forming more or less coherent clusters (Table 7.4B, Appendix 2.4B; Figure 7.24A-D; Figure 7.25B). This implies normal differentiation of the moderately fractionated pegmatites where the feldspar and mica incorporate the bulk of alkali metals. Decreasing Sr contents and increasing Y contents confirm the fractionation processes (Belousova et al., 2002).

The REE concentrations in the micas are generally low and all REE patterns normalised to upper continental crust (UCC) show depletion. The micas from the Palaeoproterozoic (CNC) pegmatites, the Pan-African (CCC, MWC, GM and HEM) pegmatites from Chitipa and Mzimba, and the Pan African (DHD) pegmatites from Dowa show moderately depleted REE. However, the Neoproterozoic (GNS) and Ordovician (MSN) pegmatites from Ntcheu, and the Pan-African Cambrian (CUB) pegmatites from Balaka show more depleted LREE than HREE (Figure 7.19, Figure 7.23, Figure 7.27).

REE patterns normalised to chondrite (Nakamura 1974; Figure 7.28A-F) show more enriched HREE than LREE. The micas from the Pan-African (CCC, MWC, GM, HEM and DHD) pegmatites from Chitipa and Mzimba and the Neoproterozoic GNS and Ordovician MSN pegmatites from Ntcheu generally show depleted LREE, less depleted MREE and enriched HREE (Figure 7.28B-D, Figure 7.28F). A strong LREE depletion suggests that the pegmatites are generally highly fractionated (Belousova et al., 2002). Variable depletion in MREE and HREE, as seen in pegmatites CCC, MWC, HEM and DHD (Figure 7.28A-F) suggests variably evolved pegmatitic magma (e.g. plagioclase fractionation, Wang et al., 1989) in the pegmatites. DHD pegmatites, which show stronger MREE depletion, formed from less evolved magma than CCC and MWC, where MREE and HREE are more enriched. Furthermore, the Pan-African

Cambrian CUB pegmatites from Balaka (Figure 7.29A) show a flattened pattern with slightly enriched LREE, less depleted MREE and slightly enriched HREE. However, all the chondrite-normalised REE patterns show strong positive Eu and negative Ce anomalies (Figure 7.28), which are indicative for the redox environment in which fractional crystallisation took place (see further discussion in Chapter 9).

Van Orman et al. (2001) observed that more enriched MREE and HREE indicate a low-temperature partitioning, because diffusion rates in melt are faster for MREE than for LREE. This shows that the pegmatites formed from residual melts enriched in incompatible components, volatiles, fluxes and rare elements. Cameron et al. (1949) and Simmons (2007) observed that the residual melts may be enriched in rare earth elements that are not well compatible with common phases in the parent granite. The fluxes and volatiles lower the crystallisation temperature thereby decreasing the nucleation rates, melt polymerization and viscosity, and increasing diffusion rates and solubility hence being critical to the development of large crystals (Swanson and Fenn, 1992; Simmons and Webber, 2008). These large crystals may be gemstones, nucleating in the rare element rich melts. The less depleted MREE for CUB pegmatites may imply a magma evolution from an early to late stage (e.g., plagioclase fractionation, Wang et al., 1989). It is known that divalent Eu substitutes for alkali elements and Ca in plagioclase. Therefore the source for the positive Eu anomaly observed in MREE-depleted patterns in analysed micas from Dowa (DHD) and Ntcheu (GNS; Figure 7.14 and 7.19) means the melt did not produce plagioclase before micas formed as such the Eu was available in the residual melt and was incorporated in the muscovite.

The observed negative Ce signatures (Figure 7.28A-F, Figure 7.29A) indicate oxidising conditions during mineralisation (Akagi and Masuda, 1998). Taylor et al. (1986) advanced a view that a weak negative Ce signature and strong positive Eu signature denotes low degrees of fractionation. Regarding the oxidation state, Rudnick and Gao (2003) observed that during melt formation element transportation is promoted, and solubility of metals in melt is affected by the oxidation state within the magma. This means that gemstone mineralisation formed from granitic melts through fractionation during oxidation periods. However, the observed variation in enrichment and depletion of Sr in micas (e.g. Figure 7.8D) is likely not related to oxidation state, but to its greater affinity for K-feldspar than for muscovite (Alfonso et al., 2003).

The high quality gem phases are found where mica is enriched in incompatible elements. This applies particularly to the aquamarine- and beryl-, and also lithian muscovite-bearing Ordovician GM3 and GM5 pegmatites in Mzimba (Section 4.3.3, Appendix 1.1), in which mica is particularly enriched in beryllium and lithium (Section 7.2.3). Other examples are the aquamarine- and beryl-, and also lithian muscovite-, and tourmaline-bearing CCC and MWC pegmatites in Chitipa (Section 4.3.3, Appendix 1.1), in which the mica is particularly enriched in beryllium, lithium and boron (Section 7.2.2). A higher concentration of B in the white micas promoted internal zoning of the pegmatite and tourmaline formation (Section 7.2.2, Table 7.3B).

The mica from the gem tourmaline- and sunstone-bearing pegmatites show particular depletion of beryllium and lithium (Section 7 2.5), hence being less evolved. This is in agreement with the observation that the GNS and MSN pegmatites in Ntcheu do not show beryl mineralisation, in contrast to the GM pegmatites in Mzimba. Furthermore, the gem tourmaline found in the pegmatites from Ntcheu (Section 4.3.9) is of lower quality compared to that from Chitipa (Section 4.3.3). This is because the CCC and MWC pegmatites are most fractionated, and hence provide conditions favourable for high quality gemstone formation. The most fractionated pegmatites, such as CCC and MWC, show beryl and in places tantalite in addition to tourmaline. In less evolved pegmatites such as DHD, GNS and MSN pegmatites, beryl is absent.

The Ti content in all the analysed micas suggests variations of felsic magmas. The high Ti content indicates that the melt is derived from the crust (Rudnick and Gao (2003). Nevertheless, Ti enrichment or depletion does not influence the beryl and tourmaline potential, because abundant beryl and tourmaline are equally observed in pegmatite with high- or low-Ti mica.

The micas in the gem bearing pegmatites show depletion of U and Th (Figure 7.8D, Figure 7.13, Figure 7.22B, Figure 7.26). The concentrations of high field strength elements (HFS) such as U and Th are controlled by the compositions of the magma source and the evolution of the melts. Depletion of U and Th in the gem bearing pegmatites may have resulted from the lack of reducing conditions to retain the U and Th (De Vivo et al., 1984). This is in agreement with the observation of oxidising conditions as shown by positive Eu anomalies.

The compatible element Sr concentrates in the melt only during the early stages of magmatic differentiation in residual portions of the parental melt from which granitic pegmatites form. The Sr concentration varies according to the abundance of K-feldspar and muscovite in the

pegmatites since Sr exhibits greater affinity for K-feldspar than for muscovite (Icenhover, J.P. and London, D. 1995; Alfonso et al., 2003). Hence, in pegmatites that are rich in K-feldspar the Sr contents in muscovite will be lower than in low-K-feldspar pegmatites.

The variable abundance of Ga in the GNS, MSN, CUB pegmatites (Figure 7.12A, Figure 7.17E, Figure 7.21E, Figure 7.25D-E) can be related to variable abundance of high-Al phases such as muscovite, tourmaline, biotite, albite, K-feldspar and quartz in the pegmatite assemblage (Section 4.3.6 and 4.3.9, Appendix 1.1). Where few other high-Al phases have formed prior to muscovite, Ga will be enriched in mica.

All pegmatites analysed in this study formed from residual melts through fractional crystallisation, the dominant process that enriched the pegmatitic melt in rare elements. The studied pegmatites are classified by their chemical characteristics (Section 7.2.1- to 7.2.5). LCT family pegmatites show Ta> Nb and highly variable REE patterns at very low concentrations (< 10 times chondrite) whereas. NYF family pegmatites show LREE > 10 times chondrite (Section 2.4, Cërny and Ercit, 2005). Furthermore, mixed type are NYF pegmatites with strong LCT characteristics due to contamination from local sources. The results show that all pegmatites are Rare-Element Class, which is in agreement with the favourable conditions for formation of the gemstones. The Palaeoproterozoic CNC pegmatites belong to the mixed NYF-LCT family. All those associated with the main Pan-African contractional, collisional, or latest Pan-African (post-contractional) episodes between ~550 and 480 Ma belong to the LCT family. The early Pan-African MNM, NNO1 and THMB pegmatites, and also the Mesozoic ZA pegmatite, all related to episodes of crustal extension or rifting, contain zircon, which defines them as NYF pegmatites.

8. FLUID INCLUSION STUDIES

8.1 INTRODUCTION

This chapter describes fluid inclusion types and phase transitions, and geochemical characteristics of the inclusions according to their relative age, fluid variations and estimated P-T conditions of entrapment. All studied fluid inclusions are hosted in quartz. An introduction to the general principles and their application of fluid inclusion and Raman microspectroscopy data in igneous petrology and analytical methods has been given in Chapter 5.

8.2 CATHODOLUMINESCENCE AND FLUID INCLUSION TYPES

This study uses the diagnostic criteria for classification of fluid inclusions as primary or secondary inclusions as proposed by Roedder (1984), and as described in section 5.4.1. Since cathodoluminescence (CL) reveals primary and secondary textures of minerals, CL imaging of quartz was used in the identification of primary, pseudosecondary and secondary fluid inclusions (Figure 8.1). The fluid inclusions were targeted in order to understand the phase changes for the original magmatic fluids. These primary inclusions occur in three-dimensional groups or as isolated inclusions along a growth zone, while the pseudosecondary inclusions occur along trails ending abruptly against grain boundaries, or along growth zones.

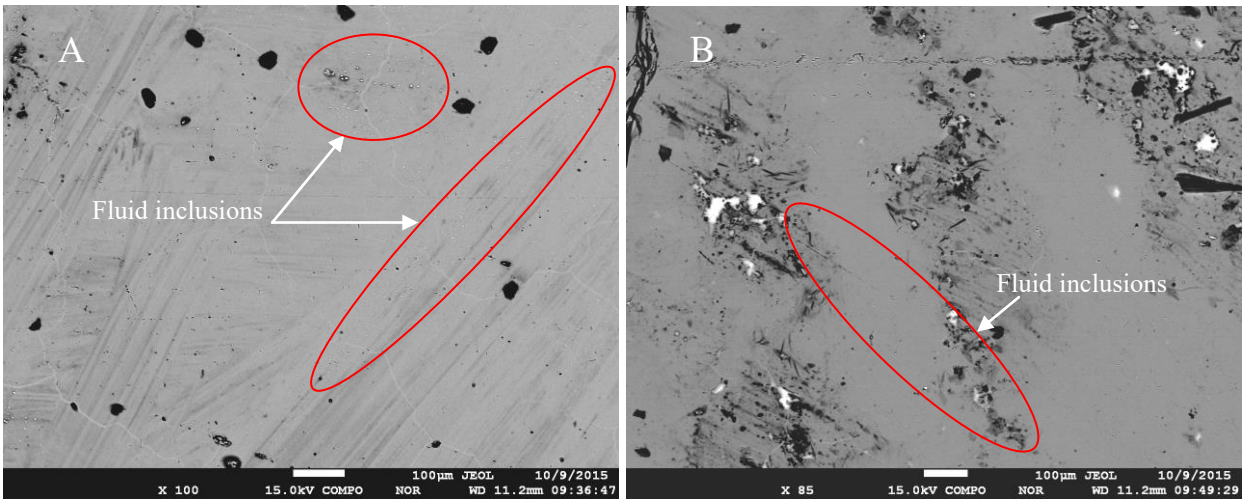

Figure 8.1A-B: CL images of some of the quartz wafers prepared for fluid inclusion studies show primary and pseudosecondary inclusions within the red ovals; (A) sample GM5 from beryl bearing pegmatite from Kafukule, (B) sample DHD1C from gem tourmaline-bearing pegmatite.

Based on microscopic observations, microthermometric measurements and Raman spectroscopy, five types of fluid inclusions (Type 1-5) were identified. A summary of the results is given in Table 8.1.

8.2.1 Type 1 Fluid Inclusions

Type 1 fluid inclusions are primary and aqueo-carbonic in composition. Hence they contain both H_2O and CO_2 in either liquid or gas form (Table 8.1). They always contain an opaque solid phase. The subhedral inclusions range in size from 4 μm to 26 μm and they occur in clusters. In sub-type 1a, inclusions have halite crystal present, indicating salinities in excess of 26.3 wt% NaCl equivalent (Bodnar, 1994). The halite daughter mineral failed to dissolve on heating due to decrepitation, confirming high fluid salinity. In sub-type 1b, inclusions have saline aqueous solution. However, the composition of the CO_2 phase varies from being pure in Type 1a to containing a component of either H_2S or N_2 or CH_4 in Type 1b. The specific details will be discussed in each pegmatite field.

8.2.2 Type 2 Fluid Inclusions

Type 2 fluid inclusions are also primary and of aqueo-carbonic composition. Hence they contain both saline aqueous solution and CO_2 in either liquid or gas form (Table 8.1). They do not contain an opaque phase. Sub-type 2a are subhedral inclusions, ranging in size from 21 μm to 29 μm and occurring in trails, contain a CO_2 vapour phase that occurs together with H_2, H_2S, and CH_4. The sub-type 2b inclusions, ranging in size from 8 μm to 16 μm and occurring in clusters, contain H_2, CH_4 and N_2 gas bubbles. Sub-type 2b is CO_2-free.

8.2.3 Type 3 Fluid Inclusions

Type 3 primary fluid inclusions are also aqueo-carbonic in composition range in size from 11 μm to 46 μm. They contain saline H_2O and CO_2 phases. Sub-type 3a contains both saline aqueous solution and pure CO_2 phases whereas sub-type 3b has a CO_2 phase with CH_4 (Table 8.1). Neither subtype contains an opaque phase. The subhedral inclusions of subtype 3a occur in clusters while those in subtype 3b occur in trails.

8.2.4 Type 4 Fluid Inclusions

Type 4 inclusions are predominantly CO_2 inclusions that show gas and liquid components. Their sizes range from 5 μm to 20 μm. The subhedral inclusions occur in trails. These primary inclusions have a sub-type 4a that contains pure CO_2. Sub-type 4b contains CH_4 and N_2 phases that are dissolved in liquid CO_2 (Table 8.1). No opaque phases were observed.

8.2.5 Type 5 Fluid Inclusions

Subhedral saline aqueous fluid inclusions of Type 5 occur in clusters. These primary inclusions range in size from 8 μm to 11 μm. Inclusions undersaturated in NaCl define sub-type 5a, whereas NaCl oversaturated ones of sub-type 5b contain halite crystals (Table 8.1) that indicate that the salinity exceeds 26.3 wt% NaCl equivalent (Bodnar, 1994).

Table 8. 1: Summary of the fluid inclusion data for Type 1 to Type 5 hosted in quartz from all gem-bearing pegmatites in this study.

SAMPLE	FLUID TYPE	COMPOSITIONAL PHASES (size range) mean size (µm)	T_e Avg.	T_e Range	St. dev .avg. T_e	T_h Avg.	T_h Range	St .dev. avg. T_h	T_{mice} Avg.	T_{mice} Range	St. dev. avg. T_{mice}	Salinity Avg.	Salinity Range	St. dev. avg. salinity
CNC1B_1	Type 5	H_2O - NaCl (8.4-10.5) 9.7	-22.23	(-21.1 - -23.2)	0.7	160	(157 - 164)	1.98	-1.6	(-1.2 - -1.9)	0.17	2.7--->26.3 wt% equi	(2.07 - >26.3wt%)	0.27
CNC1B2_1	Type 1	H_2O-CO_2-NaCl - Opaque (10.14 -15.9) 12.5	-24.9	(-23.2 - -24.5)	0.44	333	(324 - 342)	5.57	-4.1	(-2.2 - -4.9)	0.9	6.5->26.3 wt% equi.	(3.75 - >26.3 wt%)	1.38
CCC1B_1	Type 2b	H_2O-CO_2- CH_4 (C_3H_8) NaCl (14.25-16.4) 15.3	-18.9	(-18.2 - -19.5)	0.37	270	(267 - 278)	4.6	-8.8	(-8.2 - -9.9)	0.41	12.8	(12.8 - 13.99)	0.45
MWC_1	Type 2b	H_2O-CO_2- CH_4 (C_3H_8)-NaCl (8.29-13.93) 11.6	-19.9	(-19.5 - -20.4)	0.22	261	(252 - 270)	4.7	-7.2	(-6.7 - -7.9)	0.31	10.9	(10.24 -11.73)	0.37
GM3_1	Type 1	H_2O-CO2- CH4-NaCl - opaque (18.24-25.94) 23.5	-77.2	(-76.5 - -77.6)	0.27	277	(267 - 292)	5.57	6.1	(5.6 - 6.7)	0.29	>26.3 % wt equi	-	-
GM5_1	Type 3a	H_2O-CO_2-NaCl (38.46-46.17) 39.1	no data	-	-	270	(260 - 286)	7.08	-2.7	(-2.2 - -3.3)	0.34	4.5	(3.75 - 5.48)	0.55
MEM1B_1	Type 1b	H_2O-CO_2-N_2-NaCl-Opaque ($NaSO_4$-Thenardite, $SrSO_4$-Celestine - Sulphates (16.35-18.62) 17.9	-21	(-20.5 - -21.4)	0.28	247	(246 - 252)	4.16	-4.3	(-4.3 - -4.6)	0.2	7	(6.53 - 7.4)	0.3
HEM1A_1	Type 3a	H_2O-CO_2-NaCl (9.68-14.25) 12.6	-24.2	(-23.6 - -24.7)	0.34	327	(317 - 337)	5.81	-3.2	(-2.7 - -3.8)	0.36	5.4	(4.55 - 6.24)	0.56
HEM2C_1	Type 1a	H_2O-CO_2-NaCl-Opaque ($Na_2Ca(CO_3)2.5H_2O$)-Gaylussite-Hydrated Carbonate (4.62-6.37) 5.7	-14.2	(-13.7 - -14.6)	0.33	379	(370 - 390)	5.43	-1.1	(-0.4 - -1.8)	0.39	2->26.3 % wt. equi	(1.1 - >26.3 wt%)	0.6
MNS7g_1	Type 3a	H_2O-CO_2-NaCl (16.5-20.72) 18.6	-19.01	(-18.6 - -19.4)	0.21	175	(168 - 183)	4.21	-0.9	(-0.5 - -1.2)	0.19	1.6	(0.91 - 2.1)	0.3
MNSB2_1	Type 1b	H_2O-CO_2-H_2S_NaCl -Opaque (8.47-11.59) 10.3	-25.9	(-25.2 - -26.2)	0.23	250	(243 - 256)	3.14	-3.2	(-3.9 - -2.4)	0.37	5.3	(4.07-6.38)	0.58
GNS1_1	Type 3b	H_2O-CO_2-CH_4-NaCl (11.38-15.42) 13.2	-20.5	(-20 - -21.1)	0.34	295	(285 - 305)	5.32	-1.2	(-0.8 - -1.8)	0.38	2	(1.43 - 3)	0.63
GNS4_2_1	Type 4a	CO_2 (5.27-10.44) 8.04	-47.02	(-46.2 - -47.3)	0.2	27	(26.2 - 28.4)	0.5	-	-	-	-	-	-
CUB1A_2_1	Type 4b	CO_2-CH_4-N_2 (17.02-20.31) 18.8	-57.6	(-57.6 - -56.3)	0.27	160	(152 - 167)	4	-1.2	(-0.8 - -1.4)	0.2	low salinity	-	-
DHD1C_1	Type 2a	H_2O-CO_2-H_2-CH_4-H_2S-NaCl (21-29) 26	-74.1	(-73.4 - -74.7)	0.34	220	(220 - 229)	4.3	-3.3	(-2.6 - -3.7)	0.3	5.5	(4.39 - 6.24)	0.5

8.3 FLUID INCLUSIONS FROM THE PALAEOPROTEROZOIC TOURMALINE-BEARING PEGMATITES

Quartz samples from the Palaeoproterozoic (CNC) pegmatites of Nthalire, Chitipa show Type 1a and Type 5 fluid inclusions, identified using microthermometric and Raman microspectroscopic analyses. These are presented in the following sections.

8.3.1 Type 1 Fluid Inclusions

These primary and aqueo-carbonic fluid inclusions range in size from 10 μm to 16 μm (Table 8.1; Figure 8.2A). The CO_2 phase occupies about 35% of the bulk composition. It shows melting temperature of between -56.8 and -56.3 ^oC, suggesting a pure CO_2 composition (Table 8.2). This is also supported by the Raman spectrum, which also shows the presence of some optically-hidden H_2O in CO_2-rich fluid in the vapour phase (Figure 8.2B). The mean clathrate melting temperature is 8.9 ^oC and the carbonic phase homogenises to the liquid phase at a mean temperature of 23.2 ^oC. In the aqueous phase, the T_e values range from -24.5 to -23.2 ^oC, indicating dominance of Na(±K)Cl as the main solutes. The melting temperatures range from -2.2 ^oC to -4.9 ^oC; with a mean salinity of 6.5 wt% NaCl equiv. for Type 1b. Total homogenisation occurs between 324 ^oC and 342 ^oC with mean of 333 ^oC. Given the limited temperature and salinity variation in Type 1b, $T_h{}^oC$ plotted against salinity suggests a homogeneous fluid (Figure 8.3B). The opaque phase is unidentified.

In these pegmatites subhedral secondary fluid inclusions were also identified. They range in size from 7 μm to 10 μm containing H_2O-CO_2-NaCl (halite)-opaque (Figure 8.4A, B). Raman microspectroscopy revealed that opaque phase is covellite (CuS). However, FI studies in this thesis aim at understanding the genesis of the pegmatites, not their later hydrothermal overprints and modification. Therefore these secondary inclusions have not been evaluated further.

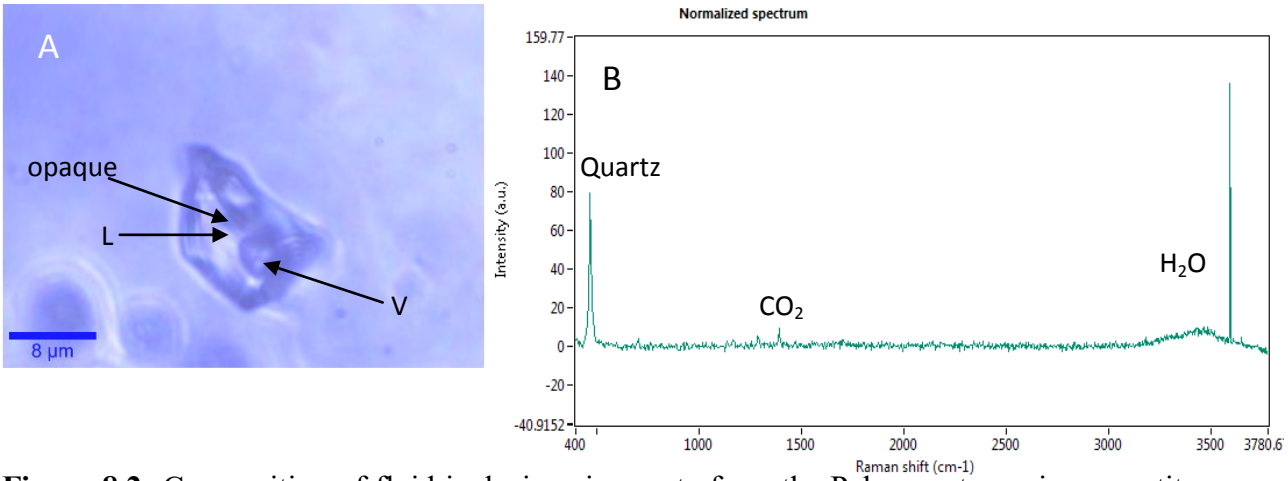

Figure 8.2: Composition of fluid inclusions in quartz from the Palaeoproterozoic pegmatite; (A) Type 1b primary fluid inclusion shows vapour, liquid and a solid phase; (B) Optically-hidden H_2O in CO_2-rich fluid expressed as broad H_2O+NaCl feature from 3200 – 3780 cm^{-1} shown in a normalised Raman spectrum.

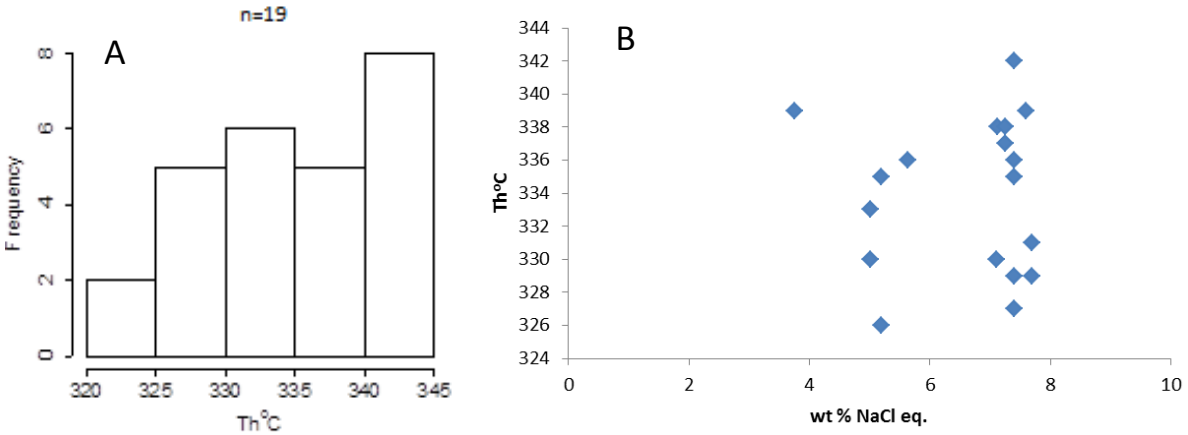

Figure 8.3: Total homogenisation temperatures and salinity of fluid inclusions in quartz from Palaeoproterozoic pegmatite; (A) Histogram showing the distribution of T_h°C values for Type 1b fluid inclusion with mean of 333°C; (B) T_h°C versus salinity diagram for sample Type 1b CNC1B2_1 shows homogenous fluid.

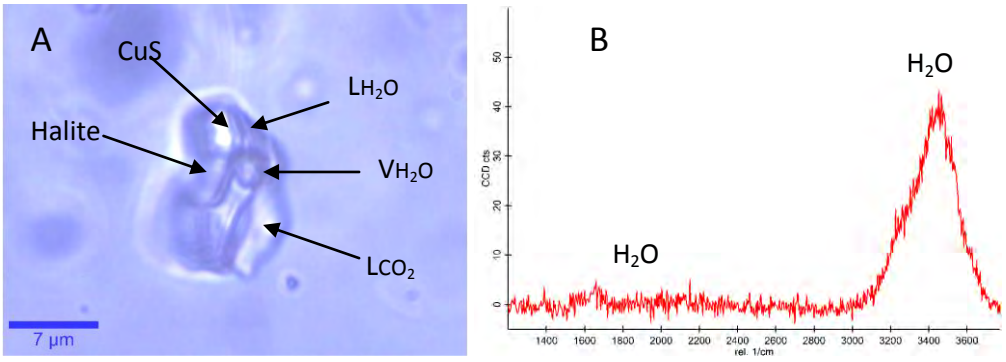

Figure 8.4: Composition of secondary fluid inclusion in quartz from the Palaeoproterozoic pegmatite, sample CNC1B2_1; (A) Secondary fluid inclusion with an opaque identified by Raman spectroscopy as CuS; (B) Spectrum of the liquid phase shows the composition of the fluid inclusion as saline H_2O.

Table 8. 2: Microthermometric characteristics for Type 1b fluid inclusions in quartz for Palaeoproterozoic tourmaline-bearing pegmatites from Nthalire, Chitipa. All results for temperature are in ^{o}C.

Inclusion	Flinc Type	Size (µm)	Prop. CO_2	Prop. H_2O	Composition	TfH_2O	$TfCO_2$	$TmCO_2$	Tm i	Tm ice	Tm cl	$ThCO_2$	Mode of Homog.	Th Total	Mode of Homog.	Bulk (g/cc)	Salinity (wt %)
CNC1B2_1	1b	14.5	25.0	75.0	H_2O-CO_2-NaCl + opaque	-32.20	-96.4	-56.6	-23.2	-3	8.7	23.1	L+V→L	330	L+V→L	0.74	5.0
2	1b	13.8	24.2	75.8	H_2O-CO_2-NaCl + opaque	-30.60	-96.7	-56.4	-25.1	-2.2	9.3	21.9	L+V→L	339	L+V→L	0.75	3.8
3	1b	12.01	40.0	60.0	H_2O-CO_2-NaCl + opaque	-36.80	-96.2	-56.6	-24.7	-4.6	9.4	23.6	L+V→L	329	L+V→L	0.73	7.4
4	1b	13.4	23.0	77.0	H_2O-CO_2-NaCl + opaque	-29.40	-95.9	-56.7	-24.8	-3.1	9	22.5	L+V→L	335	L+V→L	0.75	5.2
5	1b	14.5	25.0	75.0	H_2O-CO_2-NaCl + opaque	-32.90	-96	-56.7	-25.3	-2.7	8.6	22.8	L+V→L	338	L+V→L	0.74	4.1
6	1b	10.47	38.5	61.5	H_2O-CO_2-NaCl + opaque	-33.70	-96.1	-56.6	-24.6	-4.7	9.5	23.4	L+V→L	339	L+V→L	0.73	7.6
7	1b	15.9	26.0	74.0	H_2O-CO_2-NaCl + opaque	-28.70	-96.7	-56.7	-24.9	-3.1	9.3	23.1	L+V→L	326	L+V→L	0.74	5.2
8	1b	11.52	39.5	60.5	H_2O-CO_2-NaCl + opaque	-36.60	-95.5	-56.5	-25.4	-4.5	9.7	22.8	L+V→L	337	L+V→L	0.74	7.3
9	1b	15	26.5	73.5	H_2O-CO_2-NaCl + opaque	-30.30	-96.6	-56.4	-25.2	-3	9.1	22.4	L+V→L	333	L+V→L	0.75	5.0
10	1b	12.25	40.3	59.8	H_2O-CO_2-NaCl + opaque	-34.90	-95.8	-56.5	-25	-4.6	8.6	23.7	L+V→L	336	L+V→L	0.73	7.4
11	1b	11.6	39.1	59.9	H_2O-CO_2-NaCl + opaque	-36.00	-96.3	-56.6	-25.2	-4.8	9.5	24.6	L+V→L	331	L+V→L	0.72	7.7
12	1b	11.36	39.4	60.6	H_2O-CO_2-NaCl + opaque	-35.30	-95.9	-56.4	-25	-4.6	9.1	24.1	L+V→L	335	L+V→L	0.72	7.4
13	1b	12.31	40.3	59.7	H_2O-CO_2-NaCl + opaque	-37.10	-95.4	-56.6	-24.8	-4.4	8.8	24	L+V→L	330	L+V→L	0.73	7.1
14	1b	12.32	40.3	59.7	H_2O-CO_2-NaCl + opaque	-36.80	-96.9	-56.7	-24.9	-4.6	8.3	22.3	L+V→L	327	L+V→L	0.75	7.4
15	1b	12.8	25.0	75.0	H_2O-CO_2-NaCl + opaque	-31.60	-95.7	-56.3	-24.7	-3.4	7.2	23.6	L+V→L	336	L+V→L	0.73	5.6
16	1b	11.42	39.4	60.6	H_2O-CO_2-NaCl + opaque	-36.20	-95.7	-56.6	-25.4	-4.8	9.9	22.7	L+V→L	329	L+V→L	0.74	7.7
17	1b	10.14	38.1	61.9	H_2O-CO_2-NaCl + opaque	-36.60	-95.7	-56.6	-25.3	-4.4	9.5	23.5	L+V→L	338	L+V→L	0.73	7.1
18	1b	12.33	40.7	59.4	H_2O-CO_2-NaCl + opaque	-34.80	-96.9	-56.7	-24.7	-4.6	8.3	22.3	L+V→L	342	L+V→L	0.75	7.4
19	1b	11.51	40.0	60.0	H_2O-CO_2-NaCl + opaque	-36.60	-95.5	-56.5	-25.4	-4.5	9.1	21.3	L+V→L	338	L+V→L	0.76	7.3
Mean		12.5	34.7	65.2		-33.9	-96.2	-56.6	-24.9	-4.0	8.9	23.2		333		0.7	6.5

8.3.2 Type 5a Fluid Inclusions

The subhedral aqueous inclusions have melting temperature that ranges from -23.2 °C to -21.1 °C showing occurrence of saline H_2O, which is confirmed by Raman spectroscopy (Figure 8.5A, Table 8.3). This agrees with the stable eutectic temperature at -21.2 °C for the H_2O – NaCl system. The mean ice melting temperature is -1.6 °C corresponding to an average salinity of 2.7 wt% NaCl equivalent. These high density aqueous inclusions homogenise to liquid at mean temperature of 160.6 °C (Figure 8.5B). Th plotted against salinity may suggest homogeneous fluid (Figure 8.5C).

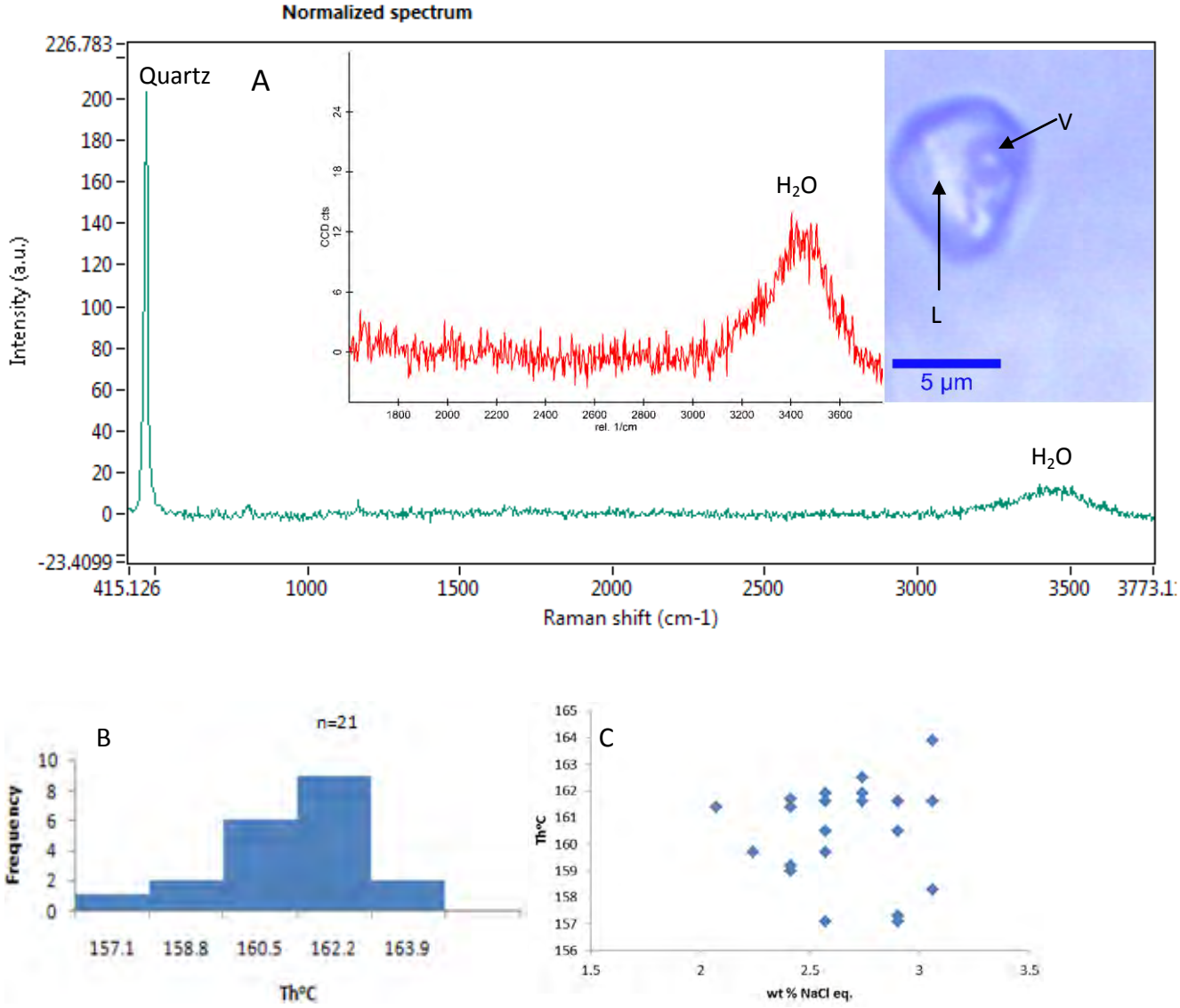

Figure 8.5: Composition and homogenisation temperatures of Type 5a fluid inclusions in quartz from the Palaeoproterozoic pegmatite, sample CNC1B_1; (A) H_2O expressed as broad H_2O+NaCl feature from 3200 – 3773cm^{-1} shown in a normalised Raman spectrum, inserted Type 5a primary fluid inclusion photomicrograph shows liquid and vapour; (B) Histogram showing T_h°C values for Type 5a fluid inclusion with a mean of 160.6 °C; (C) T_h°C versus salinity indicates homogeneous fluid.

Table 8. 3: Fluid inclusion analyses for Type 5a fluid inclusions in quartz for Palaeoproterozoic tourmaline-bearing pegmatites from Nthalire, Chitipa. All analytical results for temperature are in ^{o}C.

Inclusion	Flinc Type	Size (µm)	Prop. V	Prop. L	Composition	TfH_2O	Tm i	Tm ice	Th H_2O	Mode of Homog.	Bulk (g/cc)	Salinity (wt %)
CNC1B_1	5a	10.2	18.2	81.8	H_2O-NaCl	-47.8	-22.1	-1.6	162.5	L+V→L	0.91	2.7
2	5a	8.4	18.6	81.4	H_2O-NaCl	-46.4	-21.5	-1.4	159.2	L+V→L	0.91	2.4
3	5a	9.6	18.1	81.9	H_2O-NaCl	-47.2	-22.2	-1.8	163.9	L+V→L	0.9	3.1
4	5a	9.8	18.4	81.6	H_2O-NaCl	-46.7	-22.4	-1.2	161.4	L+V→L	0.91	2.1
5	5a	10	18.1	81.9	H_2O-NaCl	-47.1	-23	-1.7	157.1	L+V→L	0.91	2.9
6	5a	9.7	18	82.0	H_2O-NaCl	-47.7	-22.6	-1.6	161.9	L+V→L	0.91	2.7
7	5a	8.4	18.4	81.6	H_2O-NaCl	-46.9	-21.2	-1.4	159	L+V→L	0.91	2.4
8	5a	10.5	18.5	81.5	H_2O-NaCl	-47.3	-23.1	-1.5	160.5	L+V→L	0.91	2.6
9	5a	10	18.1	81.9	H_2O-NaCl	-48	-22.5	-1.7	161.6	L+V→L	0.91	2.9
10	5a	10	18.7	81.3	H_2O-NaCl	-46.4	-21.4	-1.8	158.3	L+V→L	0.91	3.1
11	5a	10.1	18.3	81.7	H_2O-NaCl	-47.5	-22.7	-1.4	161.7	L+V→L	0.91	2.4
12	5a	8.6	18.2	81.8	H_2O-NaCl	-47.1	-21.3	-1.5	159.7	L+V→L	0.91	2.6
13	5a	9.9	18.4	81.6	H_2O-NaCl	-47.3	-23.2	-1.7	160.5	L+V→L	0.91	2.9
14	5a	10	18.6	81.4	H_2O-NaCl	-47.1	-23.1	-1.5	157.1	L+V→L	0.91	2.6
15	5a	10	18.1	81.9	H_2O-NaCl	-48	-22.5	-1.6	161.6	L+V→L	0.91	2.7
16	5a	9.8	18.2	81.8	H_2O-NaCl	-47.7	-22.3	-1.5	161.9	L+V→L	0.91	2.6
17	5a	8.6	18.9	81.1	H_2O-NaCl	-47.1	-21.7	-1.3	159.7	L+V→L	0.91	2.2
18	5a	10.2	18.2	81.8	H_2O-NaCl	-47.8	-22.9	-1.8	161.6	L+V→L	0.91	3.1
19	5a	10	18.2	81.8	H_2O-NaCl	-46.4	-21.1	-1.7	157.3	L+V→L	0.91	2.9
20	5a	9.8	18.5	81.5	H_2O-NaCl	-46.7	-22.4	-1.4	161.4	L+V→L	0.91	2.4
21	5a	10	18.8	81.2	H_2O-NaCl	-48	-22.8	-1.5	161.6	L+V→L	0.91	2.6
Mean		9.7	18.3	81.7		-47.2	-22.3	-1.6	160.6		0.9	2.7

8.4 FLUID INCLUSIONS FROM THE PAN-AFRICAN GEM-BEARING PEGMATITES

8.4.1 Fluid Inclusions from Gem Tourmaline- and Beryl-bearing Pegmatites from Chisenga, Chitipa

The CCC pegmatites from Chisenga contain Type 2b aqueo-carbonic fluid inclusions that occur as clusters (Table 8.1). The subhedral inclusions range in size from 14 µm to 16 µm. Microthemometric analysis show that the CO_2 phase melt temperatures range from -56.7 ^{o}C to -57.6 ^{o}C with an average of -57.2 ^{o}C. The phases H_2, C_3H_8, and N_2 were identified by Raman analysis. A spectrum for C_3H_8 is shown in Figure 8.6. The mean clathrate melting temperature is 6 ^{o}C and the carbonic phase homogenises to a liquid at a mean of 28.4 ^{o}C. The mean ice melting temperature is -8.8 ^{o}C. The melting temperature of the aqueous phase of the inclusions ranges from -19.5 to -18.2 ^{o}C. This is close to the stable eutectic temperature for the H_2O-NaCl system for -21.2 ^{o}C and it shows the dominance of Na cations in the aqueous solutions. Total homogenisation occurred over a small temperature range from 260 ^{o}C to 274 ^{o}C with a mean of 270 ^{o}C (Figure 8.7A). The density is 0.7g/cc, corresponding to a mean salinity of 12.8 wt% NaCl equivalent (Table 8.4). A plot of T_h^{o}C against salinity shows data point scattering in a relatively narrow range, suggesting a more or less homogenous fluid (Figure 8.7B).

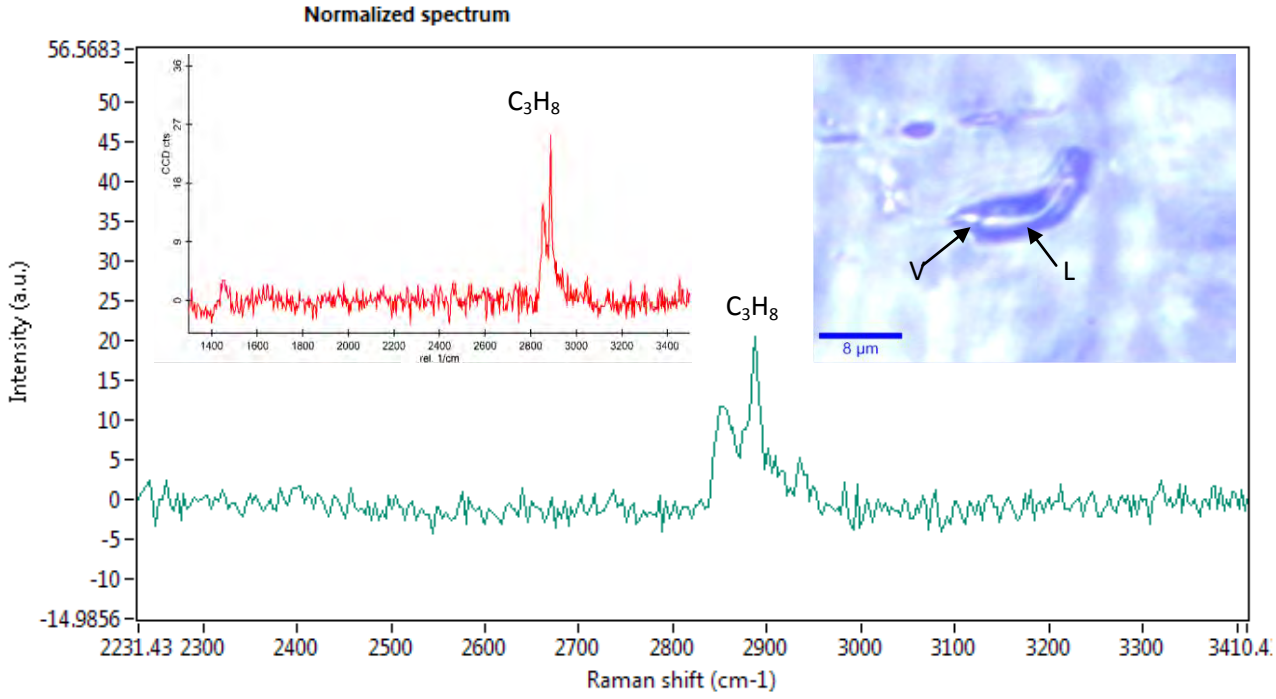

Figure 8.6: C_3H_8 expressed in a normalised Raman spectrum for sample CCC1B; inserted photomicrograph of Type 2b primary fluid inclusion in quartz shows liquid and vapour.

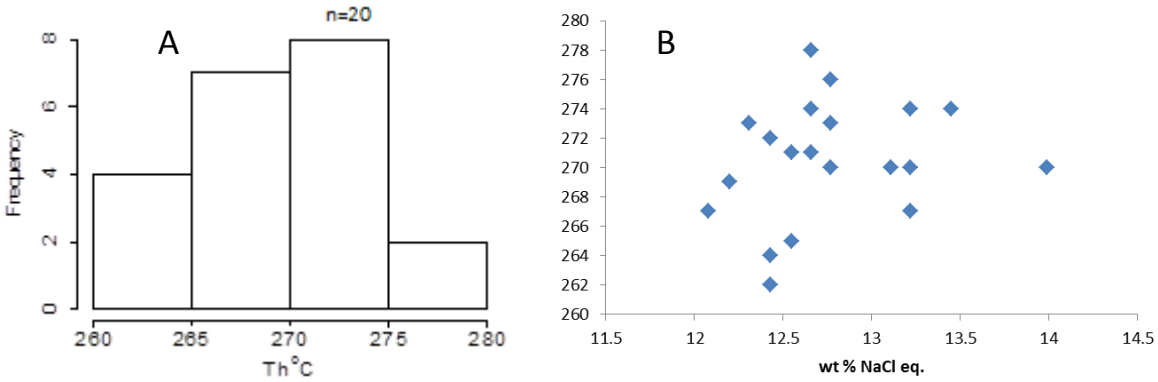

Figure 8.7: Total homogenisation temperatures of fluid inclusions in quartz from the Pan-African tourmaline- and beryl-bearing pegmatite from Chisenga, Chitipa, sample CCC1B; **(**A) Histogram showing the distribution of T_h ^oC values for Type 2b fluid inclusion with mean of 270^oC; (B) $T_h{}^oC$ versus salinity suggests a homogenous fluid (Figure 8.1C).

Table 8. 4: Fluid inclusion analyses for Type 2b fluid inclusions in quartz for Pan-African tourmaline- and beryl-bearing pegmatites from Chisenga, Chitipa. All results for temperature are in ^{o}C.

Inclusion	Flinc Type	Size (µm)	Prop. v	Prop. L	Composition	TfH_2O	T_n CH_4	TfCO_2	$T_n CO_2$	TmCO_2	Tn H_2O	Tm i	Tm ice	Tm cl	ThCO_2	Mode of Homog.	Th Total	Mode of homog	Bulk (g/cc)	Salinity (wt %)
CCC1B_1	2b	15.27	31.5	68.5	H_2O-CO_2-H_2-CH_4(C_3H_8)-N_2	-34.7	-95.2	-95.9	-121	-57.2	-16.2	-19	-8.2	6.2	29.2	L+V→L	267	L+V→L	0.68	12.1
2	2b	16.13	34.8	65.2	H_2O-CO_2-H_2-CH_4(C_3H_8)-N_2	-34.5	-94.5	-96.3	-120.9	-56.9	-16.9	-18.7	-9.9	5.9	28.9	L+V→L	270	L+V→L	0.69	14.0
3	2b	15.24	36.1	63.9	H_2O-CO_2-H_2-CH_4(C_3H_8)-N_2	-34.1	-94.7	-96.1	-121.3	-56.7	-16.5	-18.5	-8.7	6.1	28.4	L+V→L	274	L+V→L	0.69	12.7
4	2b	15.16	25.3	74.7	H_2O-CO_2-H_2-CH_4(C_3H_8)-N_2	-33.9	-94.9	-96.2	-122.1	-57.5	-15.8	-18.9	-8.5	6.3	29	L+V→L	272	L+V→L	0.69	12.4
5	2b	15.12	22.4	77.6	H_2O-CO_2-H_2-CH_4(C_3H_8)-N_2	-34.5	-95	-96.3	-121.9	-56.7	-16.5	-18.3	-9.2	6	28.7	L+V→L	270	L+V→L	0.69	13.2
6	2b	14.43	27.8	72.2	H_2O-CO_2-H_2-CH_4(C_3H_8)-N_2	-34.3	-94.3	-95.8	-119.6	-57	-16.1	-19.5	-8.8	5.8	29.1	L+V→L	273	L+V→L	0.68	12.8
7	2b	15.24	32.4	67.6	H_2O-CO_2-H_2-CH_4(C_3H_8)-N_2	-34.7	-94.7	-96.4	-121.5	-57.4	-16.3	-18.8	-8.5	6.1	29	L+V→L	262	L+V→L	0.69	12.4
8	2b	16.12	23.6	76.4	H_2O-CO_2-H_2-CH_4(C_3H_8)-N_2	-34	-94.9	-96.1	-120.7	-57.1	-16.6	-18.3	-8.7	5.9	29.2	L+V→L	271	L+V→L	0.69	12.7
9	2b	14.25	24.6	75.4	H_2O-CO_2-H_2-CH_4(C_3H_8)-N_2	-34.9	-94.4	-96.5	-121.4	-57.4	-16.8	-19	-8.4	5.7	28.5	L+V→L	273	L+V→L	0.69	12.3
10	2b	16.1	33.3	66.8	H_2O-CO_2-H_2-CH_4(C_3H_8)-N_2	-33.6	-94.6	-96.2	-120.3	-57.6	-15.7	-18.9	-9.2	6.3	28.9	L+V→L	267	L+V→L	0.68	13.2
11	2b	14.68	27.7	72.3	H_2O-CO_2-H_2-CH_4(C_3H_8)-N_2	-34.2	-95.3	-95.9	-121.6	-57.3	-16.6	-18.6	-8.6	5.9	29.1	L+V→L	265	L+V→L	0.68	12.6
12	2b	15.09	37.0	63.1	H_2O-CO_2-H_2-CH_4(C_3H_8)-N_2	-34.8	-94.5	-96.4	-120.8	-56.8	-16.7	-19.3	-8.3	6.2	28.7	L+V→L	269	L+V→L	0.68	12.2
13	2b	14.53	26.2	73.8	H_2O-CO_2-H_2-CH_4(C_3H_8)-N_2	-34.2	-94.6	-95.9	-119.9	-56.9	-16.2	-19.4	-8.8	5.9	27.3	L+V→L	276	L+V→L	0.69	12.8
14	2b	15.31	33.8	66.2	H_2O-CO_2-H_2-CH_4(C_3H_8)-N_2	-33.7	-94.9	-96.2	-121.2	-57.7	-16.6	-18.6	-9.1	6.2	26.9	L+V→L	270	L+V→L	0.69	13.1
15	2b	15.27	32.7	67.3	H_2O-CO_2-H_2-CH_4(C_3H_8)-N_2	-34.6	-94.2	-96.3	-121.5	-57.2	-16.2	-18.9	-8.5	6.3	28.6	L+V→L	264	L+V→L	0.68	12.4
16	2b	16.4	33.5	66.5	H_2O-CO_2-H_2-CH_4(C_3H_8)-N_2	-32.6	-94.5	-96	-120.7	-57	-15.9	-18.9	-8.7	6.1	27.3	L+V→L	278	L+V→L	0.69	12.7
17	2b	15.3	36.8	63.3	H_2O-CO_2-H_2-CH_4(C_3H_8)-N_2	-34.5	-94.5	-96.4	-120.7	-57.2	-16.8	-18.7	-9.4	6.1	28.4	L+V→L	274	L+V→L	0.69	13.5
18	2b	15.37	31.3	68.7	H_2O-CO_2-H_2-CH_4(C_3H_8)-N_2	-34.7	-94.2	-95.7	-121.2	-56.8	-16.3	-18.2	-9.2	5.9	28.6	L+V→L	274	L+V→L	0.69	13.2
19	2b	15.1	22.6	77.4	H_2O-CO_2-H_2-CH_4(C_3H_8)-N_2	-34.2	-94.7	-96.5	-121.6	-57.3	-16.5	-19	-8.6	6.2	27.1	L+V→L	271	L+V→L	0.69	12.6
20	2b	15.29	25.6	74.4	H_2O-CO_2-H_2-CH_4(C_3H_8)-N_2	-33.9	-94.8	-95.7	-121.5	-57.5	-15.7	-18.9	-8.8	5.7	26.8	L+V→L	270	L+V→L	0.69	12.8
Mean		15.3	29.6	70.4		-34.3	-94.7	-96.1	-121.0	-57.2	-16.3	-18.9	-8.8	6.0	28.4		270.0		0.7	12.8

8.4.2 Fluid Inclusions from Gem Tourmaline- and Beryl-bearing Pegmatites from Wenya, Chitipa

Like the aqueo-carbonic fluid inclusions CCC pegmatites from Chisenga, the MWC pegmatites from Wenya contain Type 2b inclusions. These are subhedral in shape (Figure 8.8A). They occur in clusters with a size range of individual inclusions of 8 µm to 14 µm. Their CO_2 phase shows melting temperatures from -56.9 to -57.9 ^oC with an average of -57.5 ^oC, indicating the presence of vapour phases other than CO_2 (Table 8.5). Raman analysis shows the presence of H_2, C_3H_8, and N_2. A propane (C_3H_8) spectrum is shown in Figure 8.8B. The mean clathrate melting temperature is 7 ^oC while the CO_2 liquid and gas phases homogenise to a liquid phase at a mean temperature of 28.2 ^oC. The mean ice melting temperature is -7.2 ^oC. The melting temperature of the aqueous phase ranges from -20.4 to -19.5 ^oC, indicating that H_2O dominates the system. Total homogenisation temperature ranges from 252 to 270 ^oC with a mean temperature at 261 ^oC (Figure 8.8C). The density is 0.6 g/cc while the mean salinity is 10.9 wt% NaCl equiv. $T_h{}^oC$ versus salinity shows homogenous fluid (Figure 8.8D).

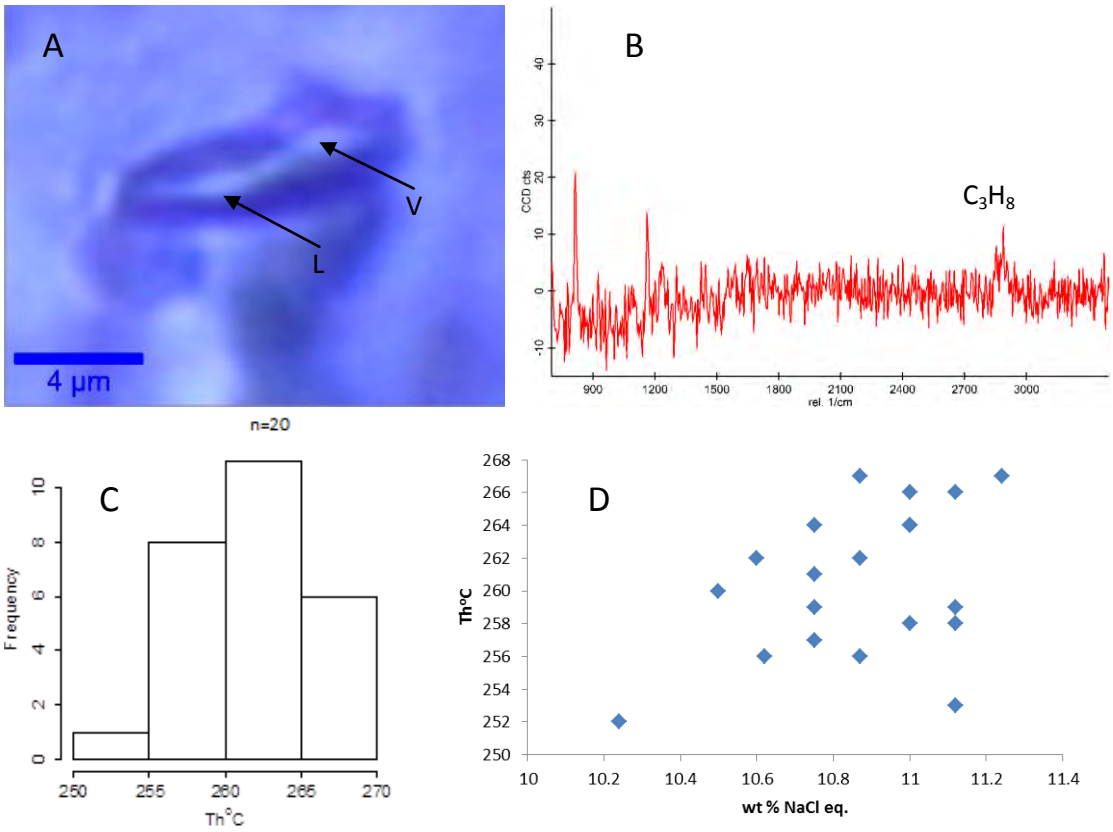

Figure 8.8: Composition, homogenisation and salinity of fluid inclusions in quartz from the Pan-African tourmaline- and beryl-bearing pegmatite from Wenya, Chitipa; (A) Type 2b primary fluid inclusion photomicrograph shows liquid and vapour (B) C_3H_8 shown in a Raman spectrum; (C) Distribution of Th ^oC values for Type 2b fluid inclusion with mean of 261^oC; (D) $T_h{}^oC$ versus salinity shows homogenous fluid.

Table 8. 5: Fluid inclusion analyses for Type 2b fluid inclusions in quartz for Pan-African tourmaline- and beryl-bearing pegmatites from Wenya, Chitipa. All results for temperature are in ^{o}C.

Inclusion	Flinc Type	Size (µm)	Prop. V	Prop. L	Composition	TfH_2O	$Tn\ CH_4$	TfCO2	$TnCO_2$	$TmCO_2$	$Tn\ H_2O$	Tm i	Tm ice	Tm cl	$ThCO_2$	Mode of Homog.	Th Total	Mode of Homog.	Bulk (g/cc)	Salinity (wt %)
MWC_1	2b	10.31	35.2	64.9	H_2O-CO_2-H_2-CH_4(C_3H_8)-N_2	-34.6	-94.9	-95.8	-118.3	-57.5	-19.1	-19.9	-7.3	7.2	28.9	L+V→L	264	L+V→L	0.63	11
2	2b	10.47	32.4	67.7	H_2O-CO_2-H_2-CH_4(C_3H_8)-N_2	-35.1	-95.4	-95.7	-121.4	-57.9	-19.3	-20.1	-7.3	7	27.9	L+V→L	266	L+V→L	0.63	11
3	2b	13.62	40.7	59.3	H_2O-CO_2-H_2-CH_4(C_3H_8)-N_2	-34.9	-94.8	-96.1	-121	-57.9	-18.9	-19.7	-7	6.6	28.1	L+V→L	262	L+V→L	0.63	10.6
4	2b	12.74	38.1	61.9	H_2O-CO_2-H_2-CH_4(C_3H_8)-N_2	-34.5	-95.7	-95.9	-119.6	-57.7	-19.3	-20.1	-7.1	6.8	28.5	L+V→L	259	L+V→L	0.63	10.8
5	2b	8.29	35.9	64.1	H_2O-CO_2-H_2-CH_4(C_3H_8)-N_2	-35.3	-95.3	-95.7	-121.5	-57.6	-19.3	-19.9	-7.3	7.1	28.4	L+V→L	264	L+V→L	0.63	11
6	2b	11.53	31.8	68.2	H_2O-CO_2-H_2-CH_4(C_3H_8)-N_2	-35.1	-94.6	-97.2	-119.4	-57	-19.4	-20	-7.1	7	28.6	L+V→L	261	L+V→L	0.63	10.8
7	2b	9.41	35.6	64.4	H_2O-CO_2-H_2-CH_4(C_3H_8)-N_2	-34.7	-95.4	-95.6	-121.1	-57.8	-19.3	-19.9	-7.4	7.2	28.9	L+V→L	259	L+V→L	0.63	11.1
8	2b	10.37	42.6	57.4	H_2O-CO_2-H_2-CH_4(C_3H_8)-N_2	-34.5	-95.1	-98.3	-120.7	-57.6	-18.5	-19.7	-7.2	6.8	28.2	L+V→L	262	L+V→L	0.63	10.9
9	2b	13.5	36.4	63.6	H_2O-CO_2-H_2-CH_4(C_3H_8)-N_2	-35	-95.3	-96.1	-119.2	-57.2	-19.1	-19.8	-7.1	6.9	27.7	L+V→L	257	L+V→L	0.63	10.8
10	2b	10.27	34.4	65.7	H_2O-CO_2-H_2-CH_4(C_3H_8)-N_2	-35.8	-95.2	-98.7	-121.3	-57.4	-19.9	-20.1	-7.4	7.3	28.5	L+V→L	258	L+V→L	0.63	11.1
11	2b	8.39	31.9	68.1	H_2O-CO_2-H_2-CH_4(C_3H_8)-N_2	-35.2	-95.1	-95.6	-121.8	-57.6	-19.7	-19.9	-7.2	7.6	28.3	L+V→L	267	L+V→L	0.63	10.9
12	2b	13.54	39.7	60.3	H_2O-CO_2-H_2-CH_4(C_3H_8)-N_2	-34.6	-94.7	-96.3	-121.4	-56.9	-18.3	-19.6	-7.4	6.9	28.2	L+V→L	253	L+V→L	0.63	11.1
13	2b	13.71	37.5	62.5	H_2O-CO_2-H_2-CH_4(C_3H_8)-N_2	-34.1	-95.2	-95.5	-120.9	-57	-18.8	-19.9	-6.9	6.3	28.5	L+V→L	270	L+V→L	0.63	10.5
14	2b	10.46	36.2	63.8	H_2O-CO_2-H_2-CH_4(C_3H_8)-N_2	-35.9	-95	-96.1	-121.2	-57.7	-19.6	-19.5	-7	9.9	27.8	L+V→L	256	L+V→L	0.63	10.6
15	2b	11	43.1	56.9	H_2O-CO_2-H_2-CH_4(C_3H_8)-N_2	-34.3	-95.2	-95.8	-120.7	-57.8	-19.4	-19.8	-7.3	7.1	28.5	L+V→L	258	L+V→L	0.63	11
16	2b	11.9	34.5	65.6	H_2O-CO_2-H_2-CH_4(C_3H_8)-N_2	-34.6	-94.7	-95.7	-118.5	-57.4	-19.3	-19.8	-7.4	6.7	28.2	L+V→L	266	L+V→L	0.63	11.1
17	2b	12.63	37.7	62.3	H_2O-CO_2-H_2-CH_4(C_3H_8)-N_2	-34.7	-95.2	-95.7	-119.3	-57.2	-19.7	-20.2	-6.7	6.9	27.4	L+V→L	252	L+V→L	0.63	10.2
18	2b	10.41	33.8	66.2	H_2O-CO_2-H_2-CH_4(C_3H_8)-N_2	-35.3	-95.5	-97.3	-121.1	-57.6	-19.6	-19.8	-7.1	7.2	28.2	L+V→L	264	L+V→L	0.63	10.8
19	2b	10.79	40.6	59.4	H_2O-CO_2-H_2-CH_4(C_3H_8)-N_2	-34.8	-95	-95.6	-120.4	-56.9	-18.4	-20.4	-7.5	6.6	28.4	L+V→L	267	L+V→L	0.63	11.2
20	2b	12.68	38.5	61.5	H_2O-CO_2-H_2-CH_4(C_3H_8)-N_2	-35.1	-94.9	-95.6	-120.7	-57.9	-18.9	-19.6	-6.8	6.8	27.6	L+V→L	262	L+V→L	0.63	10.4
Mean		11.6	36.6	63.4		-34.8	-95.1	-96.3	-120.4	-57.5	-19.2	-19.9	-7.2	7.0	28.2		261.0		0.6	10.9

8.4.3 Fluid Inclusions from Aquamarine-Bearing Pegmatites from Kafukule

Type 1 aqueo-carbonic fluid inclusions from Kafukule (GM3) range in size from 18 µm to 26 µm (Figure 8.9A, Table 8.6). The inclusions are subhedral in shape. The carbonic phase shows melting temperature from -57.7 to -56.8 ^{o}C with an average of -57.4 ^{o}C, suggesting the presence of other vapour phases such as CH_4. Another melting event was observed within the range of -77.6 to -76.5 ^{o}C, with an average -77.2 ^{o}C. This may support the presence of a H_2O-LiCl-NaCl salt system (Huizenga, 2010). The mean clathrate melting temperature is 9 ^{o}C and the carbonic phase homogenises to a liquid at a mean of 28.3 ^{o}C. The salinity of Type 1a inclusions is not determined because decrepitation occurs before the dissolution of halite. The fluid has a mean density of 0.7 g/cc. The mean Tm_i is -40.7 ^{o}C while the temperature for total homogenisation ranges from 267 ^{o}C to 292 ^{o}C, with an average of 277 ^{o}C (Figure 8.9B).

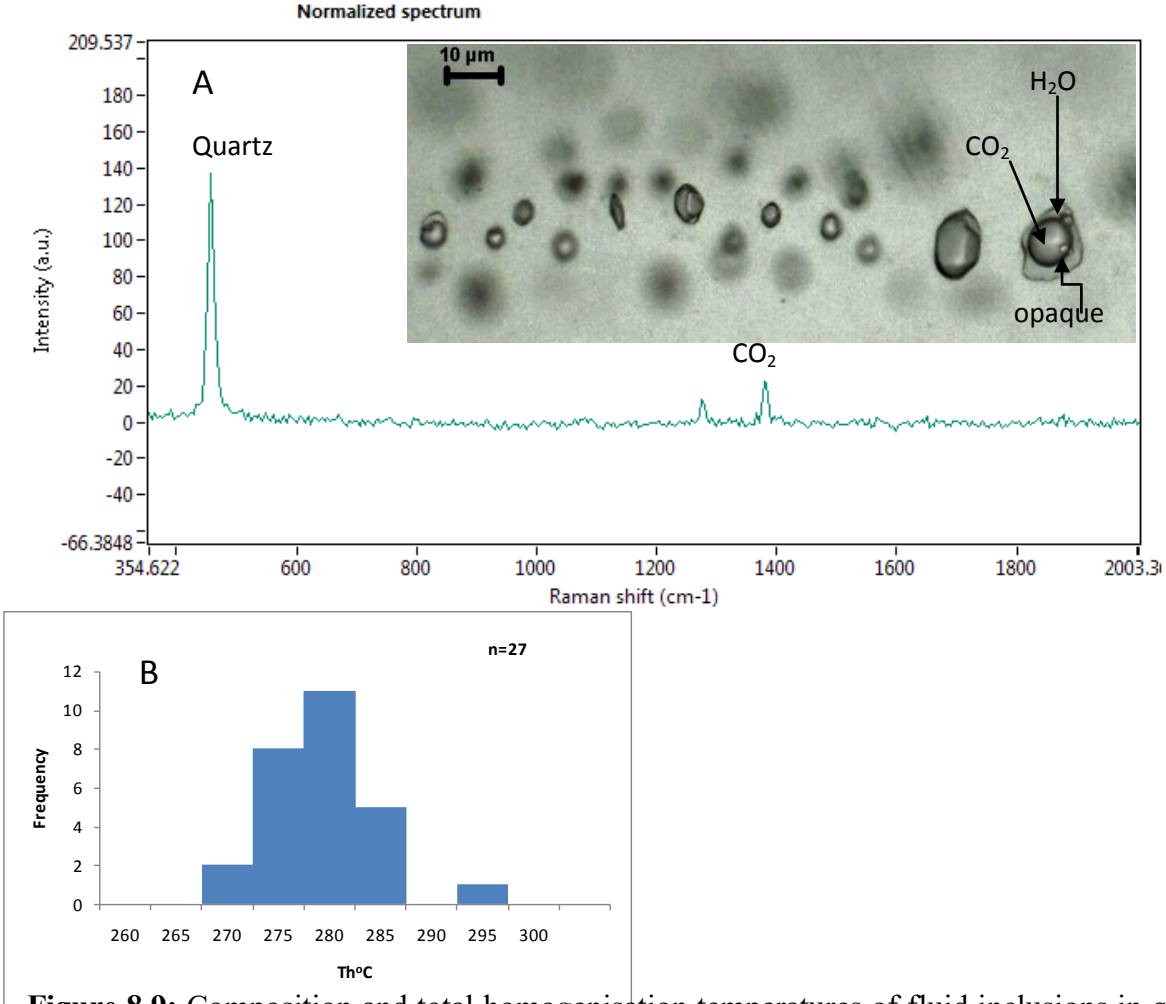

Figure 8.9: Composition and total homogenisation temperatures of fluid inclusions in quartz from Pan-African gem aquamarine-bearing pegmatites from Kafukule, sample GM3_1; (A) Normalised Raman spectrum showing CO_2; inserted Type 1b primary fluid inclusions showing liquid, vapour and opaque phase; (B) Histogram shows the distribution of T_h^{o}C values for Type 1a fluid inclusion with a mean of 277 ^{o}C.

Table 8. 6: Fluid inclusion analyses for Type 1a fluid inclusions in quartz for Pan-African gem aquamarine-bearing pegmatites from Kafukule, Mzimba. All results for temperature are in ^{o}C.

Sample	Flinc Type	Size (μm)	Prop. L	Prop. V	Composition	TfH_2O	$TfCO_2$	Te	$TmCO_2$	Tm i	Tm ice	Tm cl	$ThCO_2$	Mode of Homog.	Th Total	Mode of Homog.	Bulk (g/cc)	Salinity (wt %)
GM3_1	1a	25.31	72.6	27.4	H_2O-CO_2-CH_4-NaCl-opaque	-26.7	-91.8	-77.2	-57.6	-40.1	no data	9.1	28.2	L+V→L	285	L+V→L	0.69	
2	1a	20.54	69.1	30.9	H_2O-CO_2-CH_4-NaCl-opaque	-26.1	-91.3	-77.4	-57.7	-39.7	no data	9.3	27.8	L+V→L	292	L+V→L	0.7	
3	1a	22.07	78.5	21.5	H_2O-CO_2-CH_4-NaCl-opaque	-26.5	-91.5	-76.8	-57.6	-41.3	no data	9.1	28.6	L+V→L	278	L+V→L	0.69	
4	1a	25.94	74.9	25.1	H_2O-CO_2-CH_4-NaCl-opaque	-26.1	-92.1	-77.1	-57.7	-40.1	no data	8.7	29.1	L+V→L	276	L+V→L	0.68	
5	1a	23.55	70.1	29.9	H_2O-CO_2-CH_4-NaCl-opaque	-26.3	-90.9	-77.3	-57.5	-40.3	no data	9	28.4	L+V→L	273	L+V→L	0.69	
6	1a	21.36	65.2	34.8	H_2O-CO_2-CH_4-NaCl-opaque	-26.5	-91.7	-77	-57.5	-39.5	no data	9.4	29	L+V→L	280	L+V→L	0.69	
7	1a	24.57	77.4	22.6	H_2O-CO_2-CH_4-NaCl-opaque	-26	-91.5	-76.5	-57.6	-41.2	no data	8.8	28.3	L+V→L	276	L+V→L	0.68	
8	1a	25.71	68.2	31.8	H_2O-CO_2-CH_4-NaCl-opaque	-26.3	-91.8	-77.1	-57.7	-40.6	no data	9	27.5	L+V→L	273	L+V→L	0.69	
9	1a	20.39	74.4	25.6	H_2O-CO_2-CH_4-NaCl-opaque	-25.9	-91.6	-77.4	-57.6	-41.4	no data	9.1	28.2	L+V→L	278	L+V→L	0.69	
10	1a	25.78	71.5	28.5	H_2O-CO_2-CH_4-NaCl-opaque	-26.2	-90.7	-77.6	-57.7	-40.9	no data	9.4	27.6	L+V→L	283	L+V→L	0.69	
11	1a	24.64	79.3	20.7	H_2O-CO_2-CH_4-NaCl-opaque	-26.6	-91.4	-77.2	-57.4	-41	no data	8.8	27.4	L+V→L	272	L+V→L	0.68	
12	1a	22.75	72.1	27.9	H_2O-CO_2-CH_4-NaCl-opaque	-26.3	-92	-76.9	-57.6	-41.5	no data	9.2	28.1	L+V→L	279	L+V→L	0.68	
13	1a	24.37	73.5	26.5	H_2O-CO_2-CH_4-NaCl-opaque	-26.2	-91.3	-76.8	-56.8	-40.2	no data	8.6	28.5	L+V→L	281	L+V→L	0.69	
14	1a	25.51	76.4	23.6	H_2O-CO_2-CH_4-NaCl-opaque	-26.4	-92.1	-77.2	-57.3	-41.6	no data	8.9	29	L+V→L	275	L+V→L	0.69	
15	1a	18.24	77.1	22.9	H_2O-CO_2-CH_4-NaCl-opaque	-25.8	-91.5	-77.4	-57.5	-39.8	no data	9	28.3	L+V→L	273	L+V→L	0.68	
16	1a	25.63	78.6	21.4	H_2O-CO_2-CH_4-NaCl-opaque	-26.3	-91.2	-77.2	-57.1	-40.7	no data	9.4	29.4	L+V→L	280	L+V→L	0.69	
17	1a	22.59	69.2	30.8	H_2O-CO_2-CH_4-NaCl-opaque	-26.5	-91.6	-77.5	-56.8	-40.2	no data	8.9	28.6	L+V→L	279	L+V→L	0.69	
18	1a	21.52	71.5	28.5	H_2O-CO_2-CH_4-NaCl-opaque	-26.1	-91.2	-77	-57.5	-40.5	no data	9	27.5	L+V→L	283	L+V→L	0.69	
19	1a	23.16	76.9	23.1	H_2O-CO_2-CH_4-NaCl-opaque	-25.7	-90.9	-77.3	-57.2	-41.5	no data	9.2	28.1	L+V→L	277	L+V→L	0.69	
20	1a	24.65	72.7	27.3	H_2O-CO_2-CH_4-NaCl-opaque	-26.4	-90.7	-77.5	-57.4	-41.2	no data	9.4	28.2	L+V→L	271	L+V→L	0.69	
21	1a	23.28	72.6	27.4	H_2O-CO_2-CH_4-NaCl-opaque	-26	-91.5	-76.9	-57	-41.1	no data	9.2	28.5	L+V→L	268	L+V→L	0.68	
22	1a	23.63	69.4	30.6	H_2O-CO_2-CH_4-NaCl-opaque	-26.3	-90.6	-77.4	-56.9	-39.4	no data	8.8	27.5	L+V→L	279	L+V→L	0.69	
23	1a	24.72	75.2	24.8	H_2O-CO_2-CH_4-NaCl-opaque	-25.8	-91	-77.2	-57.3	-41.2	no data	9.3	28.4	L+V→L	267	L+V→L	0.68	
24	1a	23.7	73.3	26.7	H_2O-CO_2-CH_4-NaCl-opaque	-26.2	-91.8	-77.1	-57.6	-41.5	no data	8.6	28.9	L+V→L	271	L+V→L	0.68	
25	1a	23.41	71.6	28.4	H_2O-CO_2-CH_4-NaCl-opaque	-26.4	-90.6	-77.4	-56.9	-40.9	no data	8.7	29	L+V→L	278	L+V→L	0.69	
26	1a	22.85	74.9	25.1	H_2O-CO_2-CH_4-NaCl-opaque	-26.1	-91.4	-76.8	-57.6	-41.6	no data	8.6	28.1	L+V→L	284	L+V→L	0.69	
27	1a	24.63	70.2	29.8	H_2O-CO_2-CH_4-NaCl-opaque	-26.3	-91.5	-77.5	-56.9	-40.1	no data	9.4	28.5	L+V→L	273	L+V→L	0.69	
Mean		23.68	73.2	26.8		-26.2	-91.4	-77.2	-57.4	-40.7	no data	9.0	28.3		277.2		0.69	

8.4.4 Inclusions from Beryl and Aquamarine bearing Pegmatites from Kafukule

Subrounded primary Type 3a aqueo-carbonic fluid inclusions from the beryl - aquamarine bearing pegmatites (GM5) from Kafukule occur in trails. The inclusions show a size range from 38 µm to 46 µm with an average of 39 µm (Figure 8.10A and Table 8.7). The carbonic phase (Figure 8.10B) shows melting temperatures from -56.8 to -56.3 ^{o}C with an average of -56.5 ^{o}C. The mean clathrate melting temperature is 12.1 ^{o}C and the carbonic gas-liquid phases homogenise to a liquid phase at a mean of 30.1 ^{o}C. The mean ice melting temperature is -2.7 ^{o}C. Total homogenisation ranges from 260 to 286 ^{o}C with an average of 270 ^{o}C (Figure 8.11A). The inclusions have a density of 0.6 g/cc and a mean salinity of 4.6 wt% NaCl equivalent. A plot of $T_h{}^{o}$C against salinity shows an overall uniform fluid composition (Figure 8.11B).

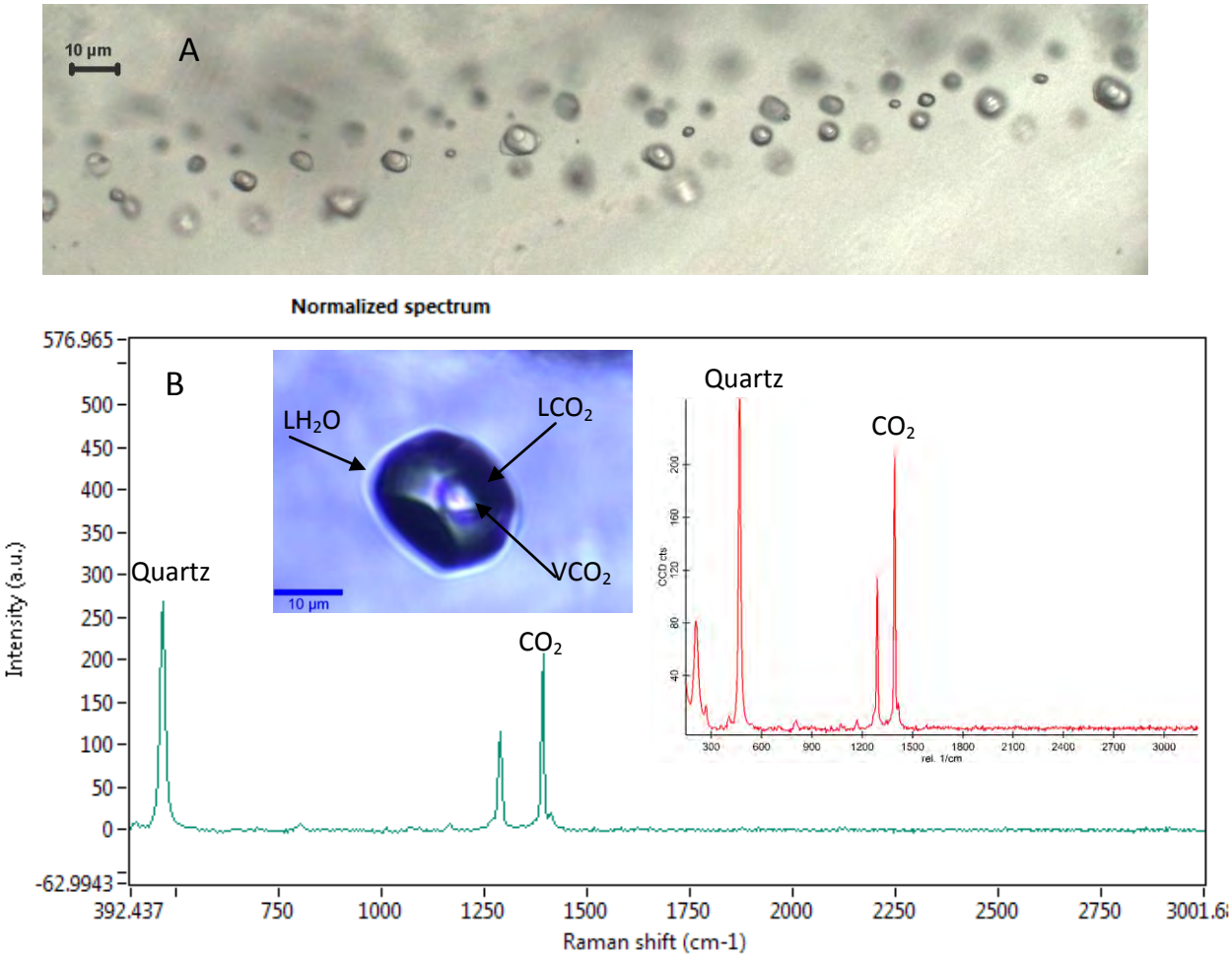

Figure 8.10: Fluid inclusion shape, composition and photomicrograph in quartz from Pan-African gem beryl-bearing pegmatites from Kafukule, sample GM5; (A) Trails of subrounded inclusions; (B) normalised Raman spectrum shows CO_2; inserted Type 3a primary fluid inclusion photomicrograph shows H_2O liquid, CO_2 liquid and CO_2 vapour.

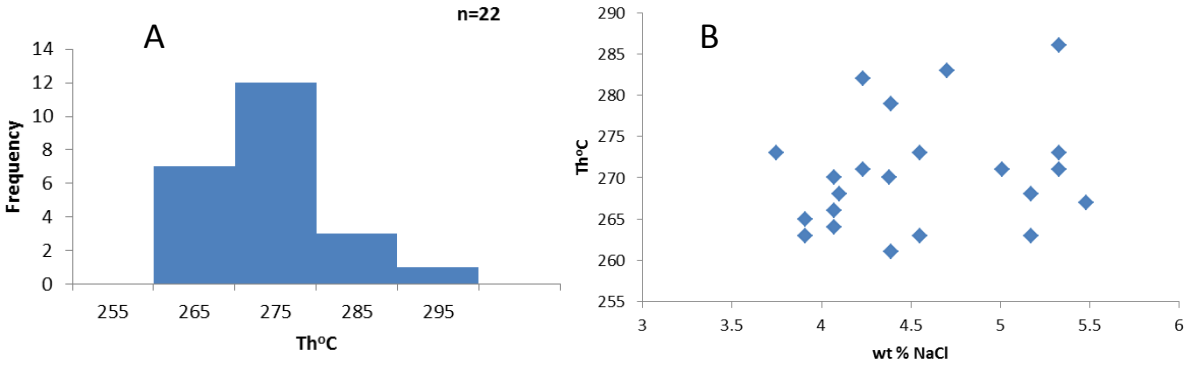

Figure 8. 11: Fluid inclusion total homogenisation temperatures in quartz from Pan-African gem beryl-bearing pegmatites from Kafukule, Mzimba; sample GM5; (A) Histogram shows the distribution of T_h°C values for Type 3a fluid inclusion with mean of 270 °C. (B) T_h°C plotted against salinity shows homogenous fluid.

Table 8. 7: Fluid inclusion analyses for Type 3a fluid inclusions in quartz for Pan-African aquamarine-bearing pegmatites (GM5) from Kafukule, Mzimba. All results for temperature are in ^{o}C.

Sample	Flinc Type	Size (μm)	Prop. V	Prop. L	Composition	TfH_2O	$TfCO_2$	$TmCO_2$	Tm i	Tm ice	Tm cl	$ThCO_2$	Mode of Homog.	Th Total	Mode of Homog.	Bulk (g/cc)	Salinity (wt %)
GM5_1	3a	38.46	14.2	85.8	H_2O-CO_2-NaCl	-26.3	-97.1	-56.4	-	-3.1	12.4	29.9	L+V→L	263	L+V→L	0.6	5.2
2	3a	40.72	17.1	82.9	H_2O-CO_2-NaCl	-26	-96.8	-56.6	-	-2.4	12.6	30.6	L+V→L	270	L+V→L	0.6	4.1
3	3a	36.25	15.9	84.1	H_2O-CO_2-NaCl	-26.3	-97.2	-56.4	-	-2.7	11.8	29.4	L+V→L	273	L+V→L	0.6	4.6
4	3a	40.08	14.6	85.4	H_2O-CO_2-NaCl	-26.5	-96.6	-56.7	-	-3.2	12.1	30.2	L+V→L	271	L+V→L	0.6	5.3
5	3a	39.51	19.3	80.7	H_2O-CO_2-NaCl	-26.5	-96.4	-56.4	-	-2.4	12	30.4	L+V→L	268	L+V→L	0.6	4.1
6	3a	36.87	13.7	86.3	H_2O-CO_2-NaCl	-26.6	-96.3	-56.6	-	-2.4	11.6	30.3	L+V→L	266	L+V→L	0.6	4.1
7	3a	40.63	19.5	80.5	H_2O-CO_2-NaCl	-26.4	-97	-56.4	-	-2.6	12.3	30.5	L+V→L	261	L+V→L	0.6	4.4
8	3a	38.95	16.8	83.2	H_2O-CO_2-NaCl	-26.2	-96.8	-56.5	-	-3.1	11.4	29.8	L+V→L	268	L+V→L	0.6	5.2
9	3a	39.4	18.4	81.6	H_2O-CO_2-NaCl	-26.6	-97.1	-56.7	-	-2.2	12	30.1	L+V→L	273	L+V→L	0.6	3.8
10	3a	37.52	17.9	82.1	H_2O-CO_2-NaCl	-26.7	-97	-56.6	-	-3	11.7	29.7	L+V→L	271	L+V→L	0.6	5.0
11	3a	46.17	15.7	84.3	H_2O-CO_2-NaCl	-26.1	-96.5	-56.5	-	-2.6	12	30	L+V→L	263	L+V→L	0.6	3.9
12	3a	36.48	17.7	82.3	H_2O-CO_2-NaCl	-26.6	-96.8	-56.4	-	-2.3	12.2	30.3	L+V→L	265	L+V→L	0.6	3.9
13	3a	41.02	15.6	84.4	H_2O-CO_2-NaCl	-26.5	-97.5	-56.7	-	-2.8	12.1	30.3	L+V→L	283	L+V→L	0.6	4.7
14	3a	38.57	17.3	82.7	H_2O-CO_2-NaCl	-26	-96.9	-56.3	-	-2.5	11.6	30.1	L+V→L	271	L+V→L	0.6	4.2
15	3a	40.5	19.5	80.5	H_2O-CO_2-NaCl	-26.6	-96.2	-56.6	-	-3.3	12	30.7	L+V→L	267	L+V→L	0.6	5.5
16	3a	37.44	16.8	83.2	H_2O-CO_2-NaCl	-26.3	-96.8	-56.3	-	-2.5	11.9	29.6	L+V→L	282	L+V→L	0.6	4.2
17	3a	39.5	15.4	84.6	H_2O-CO_2-NaCl	-25.9	-96.4	-56.6	-	-2.6	12.6	30.4	L+V→L	270	L+V→L	0.6	4.4
18	3a	38.41	18.7	81.3	H_2O-CO_2-NaCl	-26.1	-96.7	-56.7	-	-3.2	12.4	30	L+V→L	273	L+V→L	0.6	5.3
19	3a	40.16	19.1	80.9	H_2O-CO_2-NaCl	-26	-97.2	-56.6	-	-2.6	12.1	29.8	L+V→L	279	L+V→L	0.6	4.4
20	3a	39.65	14.3	85.7	H_2O-CO_2-NaCl	-26.2	-96.3	-56.6	-	-2.4	11.8	30.4	L+V→L	264	L+V→L	0.6	4.1
21	3a	36.72	13.5	86.5	H_2O-CO_2-NaCl	-26.7	-96.5	-56.8	-	-3.2	12.1	29.8	L+V→L	286	L+V→L	0.6	5.3
22	3a	39.15	19.6	80.4	H_2O-CO_2-NaCl	-26.5	-96.9	-56.5	-	-2.7	12.4	30.1	L+V→L	263	L+V→L	0.6	4.6
Mean		39.13	16.9	83.1		-26.3	-96.8	-56.5		-2.7	12.1	30.1		270.0		0.6	4.6

8.4.5 Fluid Inclusions Amethyst-bearing Veins Associated Pegmatites from Kafukule

The subhedral Type 1b aqueo-carbonic fluid inclusions in sample MEM1B from amethyst bearing veins that are associated with pegmatites from Kafukule range in size from 16 µm to 19 µm with mean of 18 µm (Table 8.8). The Raman spectrum for the aqueous phase in Figure 8.12 shows a broad H_2O peak. These inclusions contain two opaque phases; the sulphates thernadite ($NaSO_4$) and celestine ($SrSO_4$) are identified by Raman analysis. The carbonic phase is not pure CO_2. It has a melting temperature from -54.8 to -52.3 ^oC with an average of -53.7 ^oC, showing the presence of other volatiles. Raman analysis identified the presence of limited amounts of N_2 (Figure 8.13A). The mean clathrate melting temperature is 18.2 ^oC and the carbonic liquid and gas phases homogenises to a liquid at a mean of 27.3 ^oC. The mean ice melting temperature is -4.3 ^oC. Total homogenisation into the liquid state ranges between 246 ^oC to 252 ^oC, averaging at 247 ^oC (Figure 8.13B). The inclusions have a density of 0.7 g/cc and mean salinity of 7 wt% NaCl equivalent. The narrow scattering of data in the diagram of $T_h{}^oC$ against salinity suggests a relatively homogeneous fluid (Figure 8.13C).

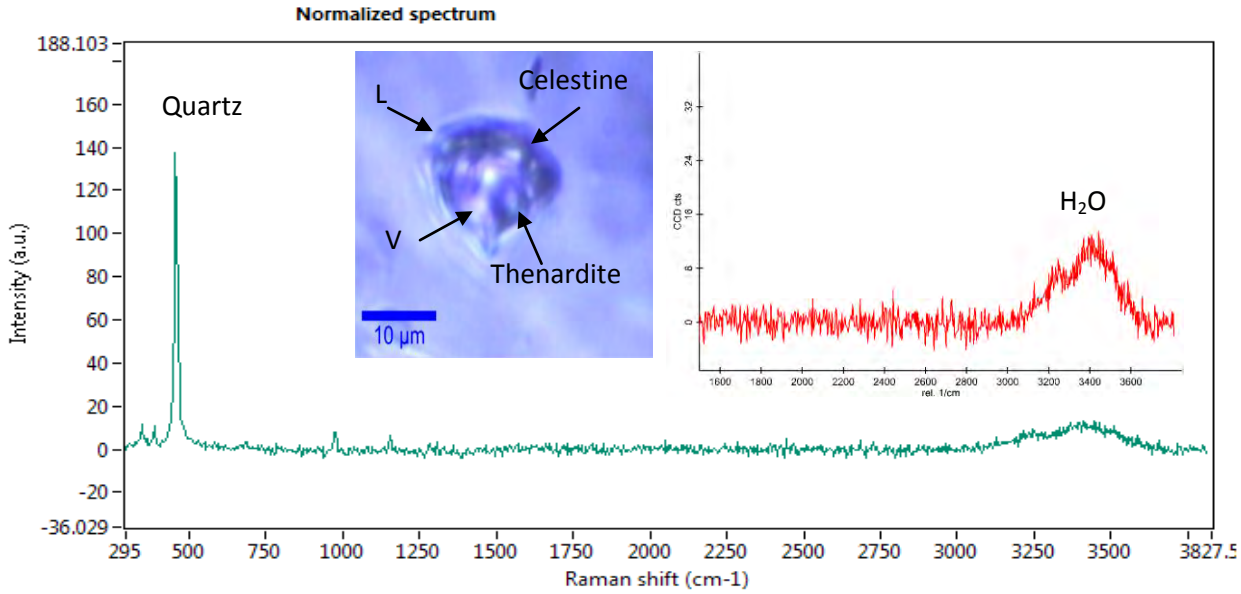

Figure 8. 12: Normalised spectrum obtained from fluid inclusions in quartz using Raman microspectroscopy shows the presence of H_2O+NaCl in fluid inclusion from amethyst-bearing veins (MEM) associated with Pan-African beryl-bearing pegmatites from Kafukule; inserted photomicrograph shows liquid phase, vapour phase and presence of solid phases: thernadite ($NaSO_4$) and celestine ($SrSO_4$), as identified by Raman spectroscopy.

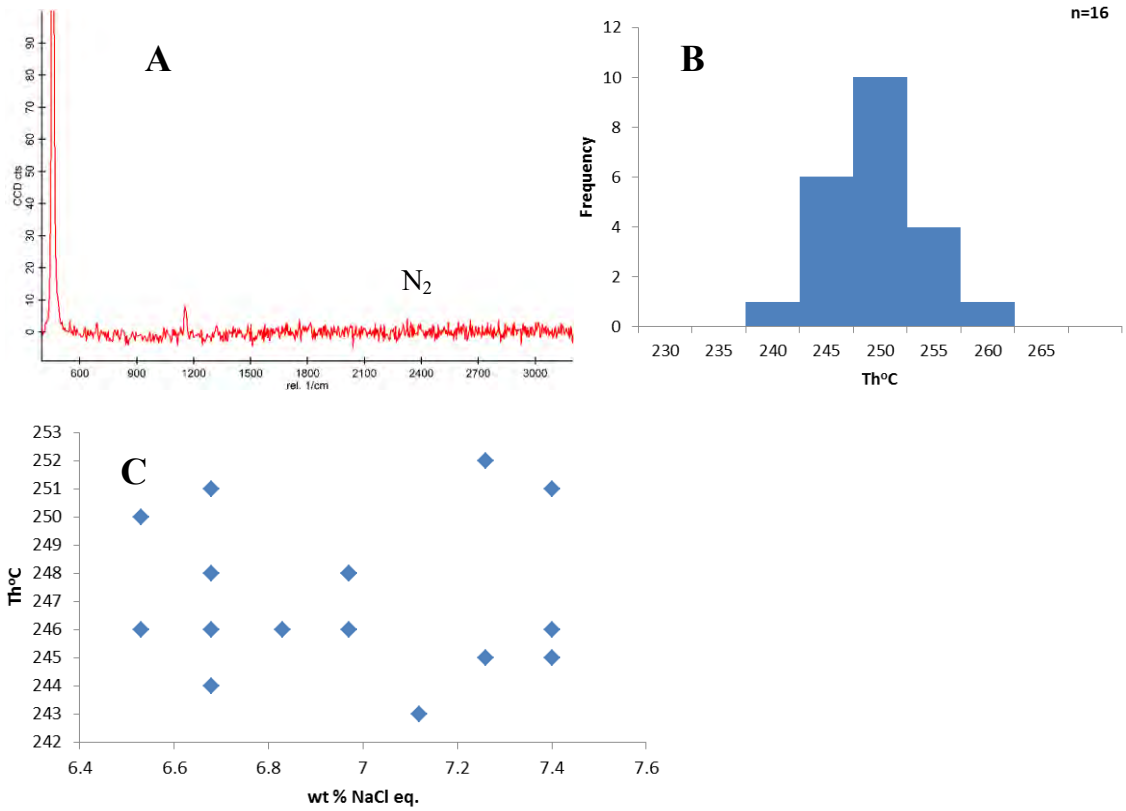

Figure 8. 13: Raman microspectroscopy, total homogenisation temperatures and salinity for amethyst bearing veins that are associated with pegmatites from Kafukule; (A) Spectrum obtained shows the presence of some N_2; (B) Histogram shows the distribution of T_h°C values for Type 1b fluid inclusion with mean of 247 °C; (C) T_h°C plotted against salinity shows a homogeneous fluid.

Table 8. 8: Fluid inclusion analyses for Type 1b fluid inclusions in quartz for amethyst-bearing veins associated with pegmatites from Kafukule, Mzimba. All results for temperature are in ^{o}C.

Sample	Flinc Type	Size	Prop. V	Prop. L	Composition	TfH_2O	TfCO_2	TmCO_2	Tm i	Tm ice	Tm cl	ThCO_2	Mode of homog.	Th Total	Mode of Homog.	Bulk (g/cc)	Salinity (wt %)
MEM1B_1	1b	18.47	14.6	85.4	H_2O-CO_2-N_2-NaCl-Opaque	-33.7	-83.4	-52.3	-21.2	-4.6	17.6	27.2	L+V→L	246	L+V→L	0.7	7.4
2	1b	18.01	11.8	88.2	H_2O-CO_2-N_2-NaCl-Opaque	-32.4	-84.1	-54.1	-21	-4.3	18.8	27.5	L+V→L	248	L+V→L	0.7	7.0
3	1b	16.95	16.4	83.6	H_2O-CO_2-N_2-NaCl-Opaque	-32.9	-83	-53.6	-20.9	-4.6	18.1	27.8	L+V→L	245	L+V→L	0.7	7.4
4	1b	18.52	13.9	86.1	H_2O-CO_2-N_2-NaCl-Opaque	-32.7	-82.8	-52.7	-21.1	-4	18.4	27.3	L+V→L	250	L+V→L	0.7	6.5
5	1b	17.98	10.5	89.5	H_2O-CO_2-N_2-NaCl-Opaque	-33.5	-83.7	-54.8	-21.4	-4.1	17.4	26.4	L+V→L	246	L+V→L	0.7	6.7
6	1b	18.42	19.1	80.9	H_2O-CO_2-N_2-NaCl-Opaque	-33.3	-83.2	-53.5	-20.7	-4.3	18.2	26.9	L+V→L	246	L+V→L	0.7	7.0
7	1b	18.56	14.7	85.3	H_2O-CO_2-N_2-NaCl-Opaque	-32.9	-83.6	-53.1	-21.2	-4.6	18.7	27.3	L+V→L	251	L+V→L	0.7	7.4
8	1b	16.73	16.9	83.1	H_2O-CO_2-N_2-NaCl-Opaque	-33	-83.1	-54.4	-21.1	-4.4	18.2	26.8	L+V→L	243	L+V→L	0.7	7.1
9	1b	18.36	15.3	84.7	H_2O-CO_2-N_2-NaCl-Opaque	-33.3	-83.3	-54.1	-21.3	-4.1	17.6	27.5	L+V→L	251	L+V→L	0.7	6.7
10	1b	17.57	18.5	81.5	H_2O-CO_2-N_2-NaCl-Opaque	-33.1	-82.9	-53.9	-20.7	-4.1	17.9	26.7	L+V→L	246	L+V→L	0.7	6.5
11	1b	18.44	20.2	79.8	H_2O-CO_2-N_2-NaCl-Opaque	-32.7	-84	-55.7	-21.4	-4.3	19	27.1	L+V→L	248	L+V→L	0.7	7.0
12	1b	16.37	13.4	86.6	H_2O-CO_2-N_2-NaCl-Opaque	-33.5	-83.9	-52.4	-20.9	-4.5	18.4	27.7	L+V→L	245	L+V→L	0.7	7.3
13	1b	16.35	13.1	86.9	H_2O-CO_2-N_2-NaCl-Opaque	-33.3	-83.5	-52.8	-20.5	-4.2	18.2	27.8	L+V→L	246	L+V→L	0.7	6.8
14	1b	18.62	15.6	84.4	H_2O-CO_2-N_2-NaCl-Opaque	-32.9	-83.3	-54.1	-20.8	-4.1	18.4	26.9	L+V→L	248	L+V→L	0.7	6.7
15	1b	18.41	19.3	80.7	H_2O-CO_2-N_2-NaCl-Opaque	-33	-84.2	-53.4	-21	-4.5	18.1	27.2	L+V→L	252	L+V→L	0.7	7.3
16	1b	17.69	18.9	81.1	H_2O-CO_2-N_2-NaCl-Opaque	-33.4	-82.8	-54	-21.2	-4.1	18.7	27	L+V→L	244	L+V→L	0.7	6.7
Mean		17.9	15.9	84.1		-33.1	-83.4	-53.7	-21.0	-4.3	18.2	27.3		247.1		0.7	7.0

8.4.6 Fluid Inclusions from Aquamarine-Bearing Pegmatites from Luhomero, Mzimba.

The type 3a fluid inclusions from the Luhomero pegmatite (HEM1A) range in size from 7 µm to 14 µm with a mean of 13 µm (Table 8.9). The Raman spectrum showing the aqueous phase is shown in Figure 8.14. The morphology of the inclusions is subhedral. The carbonic phase shows melting temperature from -56.7 to -56.1 ^{o}C with an average of -56.4 ^{o}C. The mean clathrate melting temperature is 12.2 ^{o}C and the carbonic phase homogenises to a liquid phase at an average temperature of 30 ^{o}C. The mean ice melting temperature is -3.2 ^{o}C. A histogram for total homogenisation shows a range from 317 to 337 ^{o}C with an average at 327.2 ^{o}C (Figure 8.15A). The density is 0.6g/cc while the mean salinity is 5.4 wt% NaCl equivalent. The narrow range of T_h^{o}C and salinity data shows fluid homogeneity (Figure 8.15B).

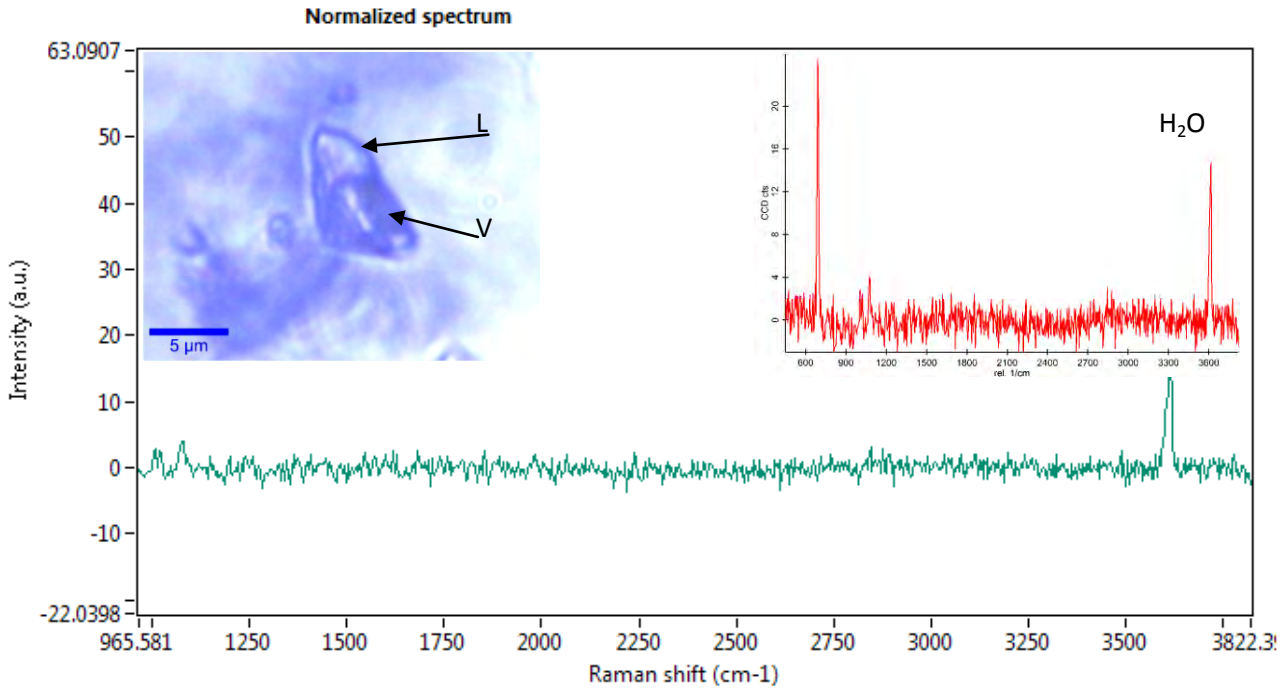

Figure 8. 14: H_2O is shown in a normalised spectrum obtained from fluid inclusions in quartz using Raman microspectroscopy for Pan-African aquamarine bearing pegmatites from Luhomero; the inserted photomicrograph shows a Type 3a FI with liquid and vapour phases.

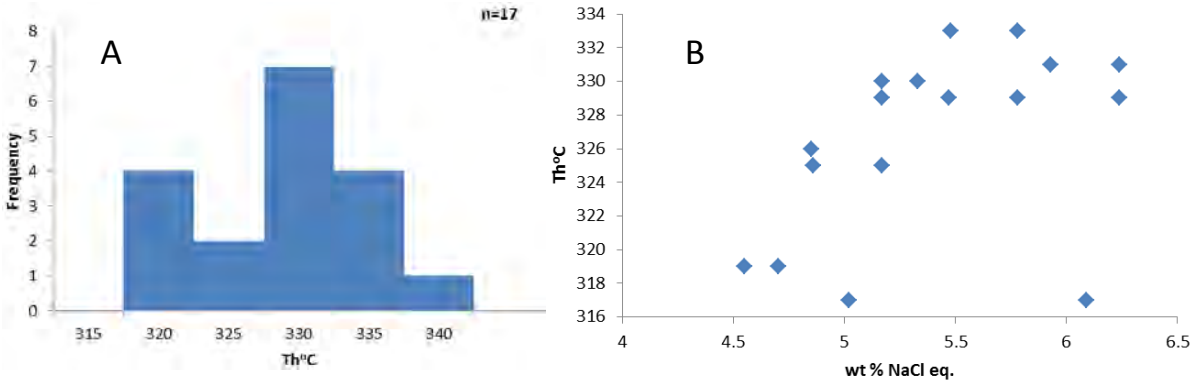

Figure 8. 15: Fluid inclusion total homogenisation temperatures in quartz from Pan- African aquamarine bearing pegmatites from Luhomero; (A) Histogram shows the distribution of T_h°C values for Type 3a fluid inclusion with mean of 327°C; (B) T_h°C plotted against salinity shows homogeneous fluid composition (Figure 8.1C).

Table 8. 9: Fluid inclusion analyses for Type 3a fluid inclusions in quartz for Pan-African aquamarine-bearing pegmatites from Luhomero, Mzimba. All temperature results are in ^{o}C.

Sample	Flinc Type	Size	Prop. CO_2	Prop. H_2O	Phases	TfH_O 2	$TfCO_2$	$TmCO_2$	Tm i	Tm ice	Tm cl	$ThCO_2$	Mode of homog.	Th Total	Mode of homog	Bulk (g/cc)	Salinity (wt %)
HEM1A_1	3a	13.15	79.7	20.3	H_O-CO_-NaCl 2 2	-26.3	-95.4	-56.4	-24.3	-3.8	12.2	30.1	L+V→L	329	L+V→L	0.6	6.2
2	3a	10.82	76.5	23.5	H_O-CO_-NaCl 2 2	-25.7	-96.1	-56.6	-24	-3.5	12.4	30.4	L+V→L	333	L+V→L	0.6	5.8
3	3a	14.01	78.2	21.8	H_O-CO_-NaCl 2 2	-25.2	-95.7	-56.6	-23.8	-2.9	12.1	30	L+V→L	325	L+V→L	0.6	4.9
4	3a	13.53	72.4	27.6	H_O-CO_-NaCl 2 2	-26.1	-96	-56.3	-24.6	-3.7	12.9	29.7	L+V→L	317	L+V→L	0.6	6.1
5	3a	12.96	76.1	23.9	H_O-CO_-NaCl 2 2	-26.3	-95.8	-56.7	-24.1	-3.1	11.7	30.1	L+V→L	330	L+V→L	0.6	5.2
6	3a	9.68	75.8	24.2	H_O-CO_-NaCl 2 2	-25.6	-96.1	-56.7	-23.9	-2.8	12.1	29.7	L+V→L	319	L+V→L	0.6	4.7
7	3a	11.42	72.7	27.3	H_O-CO_-NaCl 2 2	-25.8	-96.3	-56.1	-23.6	-3.3	12.4	30.3	L+V→L	333	L+V→L	0.6	5.5
8	3a	13.05	68.9	31.1	H_O-CO_-NaCl 2 2	-25.6	-95.9	-56.4	-24.5	-3.1	12.6	29.8	L+V→L	329	L+V→L	0.6	5.2
9	3a	12.97	74.2	25.8	H_O-CO_-NaCl 2 2	-26.6	-96.4	-56.3	-24.3	-3	11.6	30.1	L+V→L	317	L+V→L	0.6	5.0
10	3a	11.14	71.5	28.5	H_O-CO_-NaCl 2 2	-25.9	-95.6	-56.1	-24.7	-3.6	12.4	30.4	L+V→L	331	L+V→L	0.6	5.9
11	3a	13.59	70.9	29.1	H_O-CO_-NaCl 2 2	-26.1	-95.4	-56.4	-24.3	-2.9	11.3	29.8	L+V→L	326	L+V→L	0.6	4.9
12	3a	11.46	73.4	26.6	H_O-CO_-NaCl 2 2	-25.9	-96.3	-56.3	-23.7	-2.7	12.3	29.6	L+V→L	319	L+V→L	0.6	4.6
13	3a	13.68	76.1	23.9	H_O-CO_-NaCl 2 2	-26.1	-95.5	-56.7	-23.9	-3.1	12.2	30.2	L+V→L	325	L+V→L	0.6	5.2
14	3a	14.25	72.5	27.5	H_O-CO_-NaCl 2 2	-26.5	-95.8	-56.7	-24.6	-3.5	12	30.3	L+V→L	329	L+V→L	0.6	5.8
15	3a	13.62	70.4	29.6	H_O-CO_-NaCl 2 2	-26.2	-96.4	-56.1	-24.3	-3.2	11.5	29.9	L+V→L	330	L+V→L	0.6	5.3
16	3a	13.19	73.1	26.9	H_O-CO_-NaCl 2 2	-26.1	-95.7	-56.6	-23.7	-3.8	12.3	30.1	L+V→L	331	L+V→L	0.6	6.2
17	3a	12.73	69.3	30.7	H_O-CO_-NaCl 2 2	-25.8	-96.1	-56.2	-24.3	-3.3	12.6	29.7	L+V→L	329	L+V→L	0.6	5.5
Mean		12.6	73.6	26.4		-26.0	-95.9	-56.4	-24.2	-3.2	12.2	30.0		327.2		0.6	5.4

8.4.7 Fluid Inclusions from Gem Aquamarine-Bearing Pegmatites from Luhomero, Mzimba

The Type 1a aqueo-carbonic fluid inclusions analysed in quartz from the aquamarine bearing pegmatite (HEM2C) from Luhomero range in size from 5 µm to 7 µm (Table 8.1). These inclusions occur in clusters (Figure 8.16). The carbonic phase shows melting temperature of between -56.8 and -56.4 ^{o}C with an average of -56.6 ^{o}C suggesting that it is pure CO_2 (Table 8.10). The mean clathrate melting temperature is 10.3 ^{o}C and the carbonic phase homogenises to a liquid at a mean temperature of 22.2 ^{o}C. The aqueous phase (Figure 8.17A) has Tm_i values range from -14.6 ^{o}C to -13.7 ^{o}C indicating Na(±K)Cl as the abundant solutes. The total melting temperatures range from -1.8 to -0.4 ^{o}C. The density is 0.8 g/cc and the mean salinity of 2 wt% NaCl equivalent is low. The mean total homogenisation temperature is 379 ^{o}C (Figure 8.17B). The $T_h{}^{o}$C /salinity readings scatter over 20 ^{o}C but over a narrow salinity interval, which suggests a fairly uniform fluid composition (Figure 8.17C). The opaque phase has been identified as a hydrated carbonate, gaylussite ($Na_2Ca(CO_3)$ 2.5 H_2O).

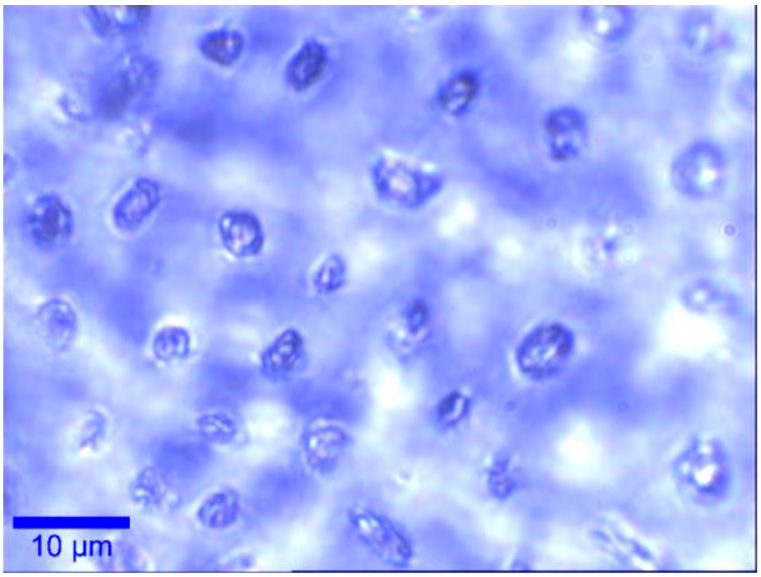

Figure 8. 16: Cluster of Type 1a inclusion in quartz from aquamarine-bearing pegmatites from Luhomero, Mzimba.

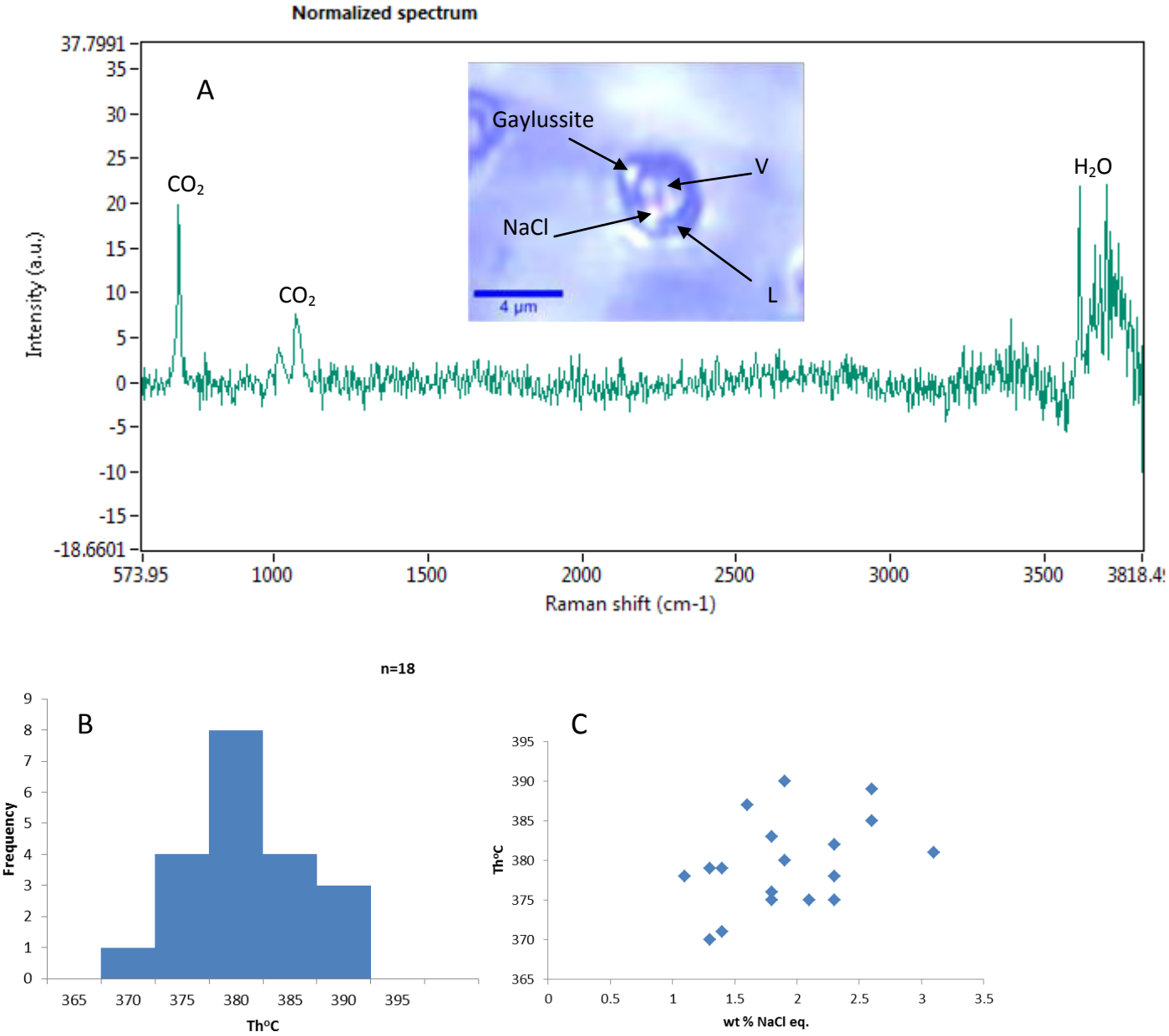

Figure 8. 17: Composition, homogenisation temperatures and salinity of fluid inclusions in quartz from aquamarine-bearing pegmatites from Luhomero, Mzimba; (A) Normalised spectrum obtained using Raman microspectroscopy shows the presence of H_2O; insert photomicrograph shows liquid, vapour and solid phases, the solid phase was identified by Raman spectrometry; (B) Histogram shows the distribution of T_h°C values for Type 1a fluid inclusion with mean of 379 °C; (C) T_h°C plotted against salinity shows some variation in homogenisation temperature in a narrow salinity range.

Table 8. 10: Fluid inclusion analyses for Type 1a fluid inclusions in quartz for Pan-African aquamarine-bearing pegmatites from Luhomero, Mzimba. All temperature results are in ^{o}C.

Sample	Flinc Type	Size (µm)	Prop. CO_2	Prop. H_2O	Composition	TfH_2O	$TfCO_2$	$TmCO_2$	Tm i	Tm ice	Tm cl	$ThCO_2$	Mode of homog.	Th Total	Mode of homog.	Bulk (g/cc)	Salinity (wt%)
HEM2C_1	1a	6.21	72.4	27.6	H_2O-CO_2-NaCl-opaque	-26.1	-97.5	-56.7	-13.7	-0.9	8.4	23.5	L+V→L	387	L+V→L	0.73	1.6
2	1a	4.74	71.3	28.7	H_2O-CO_2-NaCl-opaque	-25.9	-98.3	-56.6	-14.6	-1.8	10.1	21.6	L+V→L	381	L+V→L	0.76	3.1
3	1a	5.82	74.9	25.1	H_2O-CO_2-NaCl-opaque	-26.2	-98	-56.6	-14.2	-1.1	9.2	22.1	L+V→L	390	L+V→L	0.75	1.9
4	1a	6.09	73.3	26.7	H_2O-CO_2-NaCl-opaque	-26.4	-98.2	-56.6	-13.9	-0.8	11.1	22.5	L+V→L	379	L+V→L	0.75	1.4
5	1a	5.3	71.1	28.9	H_2O-CO_2-NaCl-opaque	-26.1	-98.4	-56.4	-14.5	-1.1	10.5	21.8	L+V→L	380	L+V→L	0.75	1.9
6	1a	5.38	69.5	30.5	H_2O-CO_2-NaCl-opaque	-26.3	-98.1	-56.8	-14.6	-0.6	9.1	22.4	L+V→L	378	L+V→L	0.75	1.1
7	1a	4.62	72.9	27.1	H_2O-CO_2-NaCl-opaque	-26.1	-97.9	-56.4	-13.8	-0.8	11.3	22.1	L+V→L	371	L+V→L	0.75	1.4
8	1a	6.14	76.1	23.9	H_2O-CO_2-NaCl-opaque	-26.2	-98.2	-56.6	-14.1	-1	10.9	21.7	L+V→L	383	L+V→L	0.75	1.8
9	1a	5.42	75.6	24.4	H_2O-CO_2-NaCl-opaque	-25.7	-97.7	-56.7	-14.6	-1.5	11.1	21.4	L+V→L	385	L+V→L	0.76	2.6
10	1a	4.93	70.8	29.2	H_2O-CO_2-NaCl-opaque	-26.1	-98.1	-56.5	-14.4	-1.3	11	22.6	L+V→L	382	L+V→L	0.74	2.3
11	1a	6.04	69.3	30.7	H_2O-CO_2-NaCl-opaque	-26.3	-98.7	-56.6	-14.2	-1	10.8	21.5	L+V→L	375	L+V→L	0.76	1.8
12	1a	6.1	74.9	25.1	H_2O-CO_2-NaCl-opaque	-26.3	-98.4	-56.7	-13.8	-0.4	11.3	22.6	L+V→L	378	L+V→L	0.74	2.3
13	1a	5.84	68.4	31.6	H_2O-CO_2-NaCl-opaque	-26.2	-98.2	-56.5	-14.5	-0.7	9.5	22.2	L+V→L	370	L+V→L	0.75	1.3
14	1a	6.36	70.8	29.2	H_2O-CO_2-NaCl-opaque	-26.4	-97.8	-56.7	-14.4	-1.5	9.3	22.7	L+V→L	389	L+V→L	0.74	2.6
15	1a	5.29	75.2	24.8	H_2O-CO_2-NaCl-opaque	-26	-98.1	-56.6	-14.6	-1.2	11	21.9	L+V→L	375	L+V→L	0.75	2.1
16	1a	4.95	73.1	26.9	H_2O-CO_2-NaCl-opaque	-26.3	-97.6	-56.8	-13.9	-0.7	11.2	22.4	L+V→L	379	L+V→L	0.75	1.3
17	1a	6.37	70.6	29.4	H_2O-CO_2-NaCl-opaque	-25.8	-87.2	-56.6	-14.6	-1	9.9	23.7	L+V→L	376	L+V→L	0.73	1.8
18	1a	6.24	76.3	23.7	H_2O-CO_2-NaCl-opaque	-26.1	-98.4	-56.5	-13.8	-1.3	10.4	21.9	L+V→L	375	L+V→L	0.75	2.3
Mean		5.7	72.0	28.0		-26.1	-97.6	-56.6	-14.2	-1.1	10.3	22.2		379		0.7	2.0

8.4.8 Fluid Inclusions from Gem Tourmaline-bearing Pegmatites from Dowa

The Type 2a aqueo-carbonic fluid inclusions from the gem tourmaline-bearing pegmatites (DHD) from Dowa are subrounded (Table 8.1) and occur in trails. The inclusions have a size range between 21 µm and 29 µm with an average of 26 µm. The carbon dioxide phase shows melting temperature from -56.3 to -55.6°C with an average of -55.9 °C, indicating the presence of another component dissolved in it (Table 8.11). Using Raman analyses other vapour phases were identified as H_2, H_2S (Figure 8.18) and C_3H_8 (Figure 8.19A). The mean clathrate melting temperature is 8.1 °C. The carbonic phases homogenise to a liquid at a mean temperature of 18.5 °C. The mean ice melting temperature is -3.3 °C and mean Tm_i is -14.1 °C. Melting was also observed ranging from -74.7 to -73.4 °C with a mean of -74.1 °C. This may suggest LiCl – NaCl in the system (Huizenga, 2010). Total homogenisation ranges from 221 to 229 °C, averaging 220 °C (Figure 8.19B). The density is 0.5 g/cc while the mean salinity is 5.5 wt% NaCl equivalent, with little variation (Figure 8.19C).

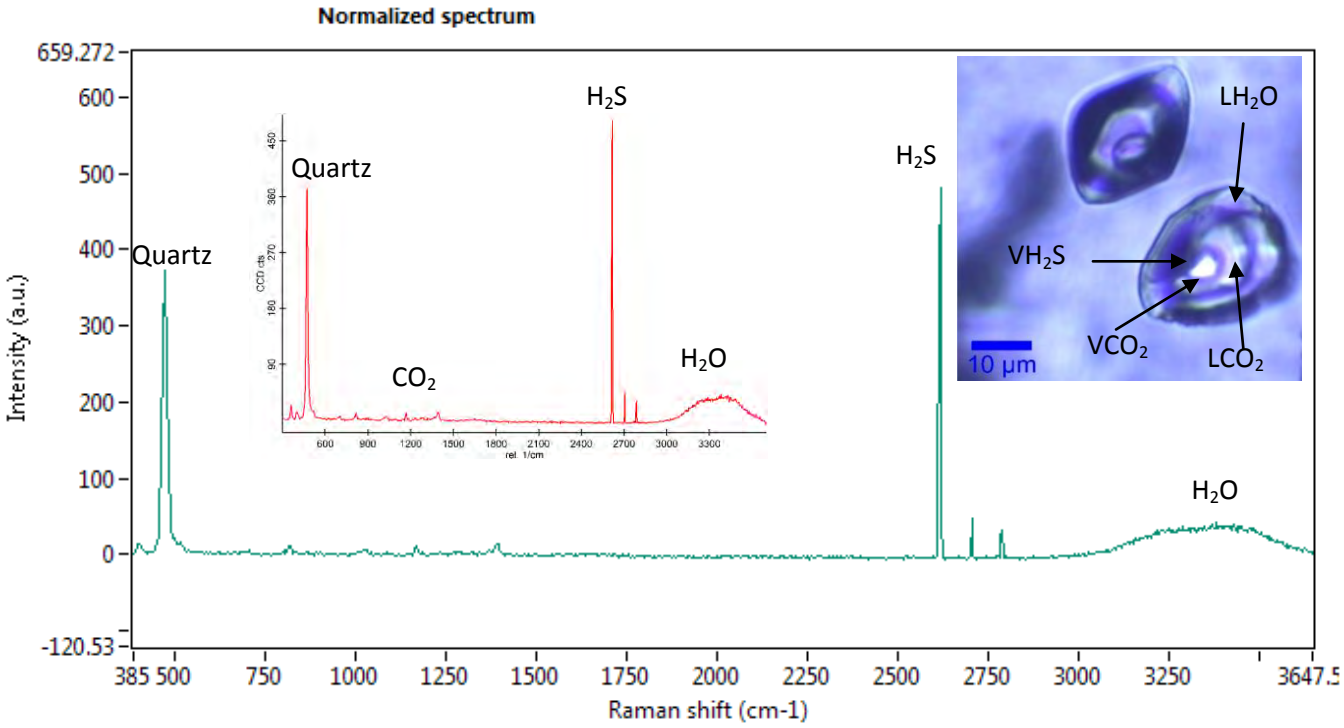

Figure 8. 18: Normalised spectrum obtained from fluid inclusions in quartz from gem tourmaline-bearing pegmatites (DHD) from Dowa using Raman microspectroscopy shows the presence of CO_2, H_2O, H_2S; insert photomicrograph shows liquid, vapour phases identified by Raman spectrometry.

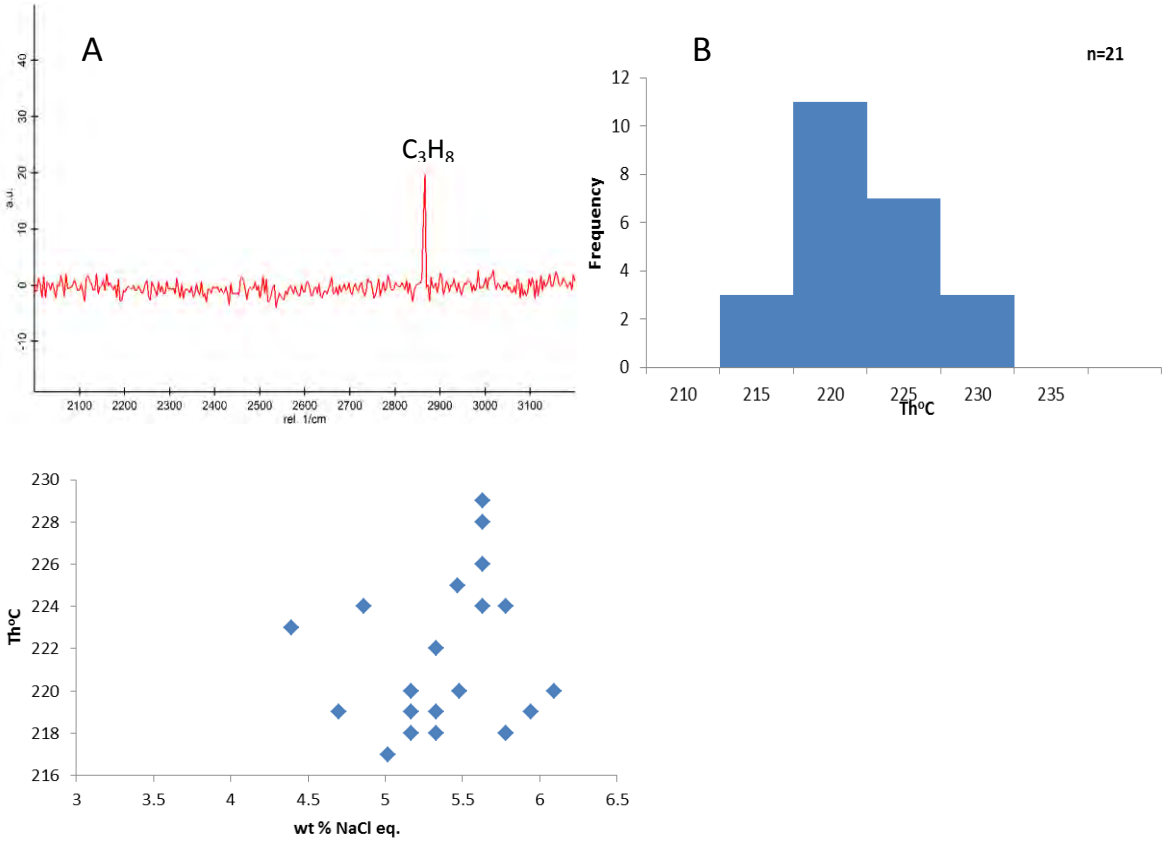

Figure 8. 19: Composition, homogenisation temperatures and salinity of fluid inclusions in quartz from gem tourmaline-bearing pegmatites (DHD) from Dowa; (A) Normalised spectrum obtained using Raman microspectroscopy shows the presence of C_3H_8; (B) Histogram showing the distribution of T_h°C values for Type 2a fluid inclusion with mean of 220 °C; (C) Narrow scattering in T_h°C vs. salinity shows fluid homogeneity.

Table 8. 11: Fluid inclusion analyses for Type 2a fluid inclusions in quartz for Pan-African tourmaline-bearing pegmatites from Dowa in Central Malawi. All results for temperature are in ^{o}C.

Sample	Flinc Type	Size	Prop. V%	Prop. L%	Composition	TfH_2O	Tn CH_4	$TfCO_2$	$TnCO_2$	Tm?	$TmCO_2$	Tn H_20	Tm i	Tm ice	Tm cl	$ThCO_2$	Th?	Mode of Homog.	Th Total	Mode of Homog.	Bulk (g/cc)	Salinity (wt %)
DHD1C_1	2a	28.43	14.9	85.1	H_2O-CO_2-H_2-CH_4-H_2S-NaCl	-25.8	-94.7	-95.9	-117.3	-73.4	-56.1	-17.3	-13.6	-3.3	7.6	18.7	34.1	L+V→L	225	L+V→L	0.5	5.5
2	2a	27.71	12.6	87.4	H_2O-CO_2-H_2-CH_4-H_2S-NaCl	-25.7	-94.9	-96.4	-118.6	-73.8	-56	-17.1	-14.1	-3.5	8	19	34.9	L+V→L	218	L+V→L	0.5	5.8
3	2a	23.58	15.8	84.2	H_2O-CO_2-H_2-CH_4-H_2S-NaCl	-25.1	-93.8	-95.5	-117.9	-74.1	-55.9	-16.8	-14.3	-3.4	7.4	18.3	35.1	L+V→L	224	L+V→L	0.5	5.6
4	2a	26.94	13.5	86.5	H_2O-CO_2-H_2-CH_4-H_2S-NaCl	-25.4	-93.4	-95.3	-117.5	-74.6	-55.7	-17.5	-14	-3.7	8.3	18.9	35.3	L+V→L	220	L+V→L	0.5	6.1
5	2a	24.2	12.2	87.8	H_2O-CO_2-H_2-CH_4-H_2S-NaCl	-25.6	-95.1	-96.4	-117.9	-74.1	-56.2	-17	-14.2	-3	8.2	18.1	35.1	L+V→L	217	L+V→L	0.5	5.0
6	2a	23.91	16.1	83.9	H_2O-CO_2-H_2-CH_4-H_2S-NaCl	-25.2	-95.3	-96.5	-118.4	-74	-55.7	-17.3	-14	-3.1	8	18.3	34.8	L+V→L	220	L+V→L	0.5	5.2
7	2a	28.54	14.6	85.4	H_2O-CO_2-H_2-CH_4-H_2S-NaCl	-24.8	-94.2	-96.1	-119	-73.9	-55.6	-17.1	-13.8	-2.9	8.1	17.8	35	L+V→L	224	L+V→L	0.5	4.9
8	2a	25.73	12.9	87.1	H_2O-CO_2-H_2-CH_4-H_2S-NaCl	-25.7	-94.6	-96.3	-118.3	-74.6	-55.7	-17.1	-14.7	-3.2	7.6	19.7	34.6	L+V→L	219	L+V→L	0.5	5.3
9	2a	26.38	15.4	84.6	H_2O-CO_2-H_2-CH_4-H_2S-NaCl	-25.8	-94.7	-96	-117.6	-74.1	-56.2	-17.6	-14.3	-3.1	8.2	17.4	35	L+V→L	218	L+V→L	0.5	5.2
10	2a	24.91	13.9	86.1	H_2O-CO_2-H_2-CH_4-H_2S-NaCl	-25.4	-93.5	-95.2	-118.4	-74	-55.5	-17.1	-14.5	-2.6	7.8	19	35.3	L+V→L	223	L+V→L	0.5	4.4
11	2a	27.41	15.7	84.3	H_2O-CO_2-H_2-CH_4-H_2S-NaCl	-25.6	-94.3	-96.5	-117.9	-73.9	-55.7	-16.8	-14.2	-3.1	8.2	17.8	34.8	L+V→L	219	L+V→L	0.5	5.2
12	2a	21.39	14.3	85.7	H_2O-CO_2-H_2-CH_4-H_2S-NaCl	-25.9	-95.8	-96.3	-118.8	-74.2	-56.2	-17.6	-13.6	-3.2	7.9	18.9	35	L+V→L	218	L+V→L	0.5	5.3
13	2a	26.5	17.1	82.9	H_2O-CO_2-H_2-CH_4-H_2S-NaCl	-25.5	-94.1	-96.1	-118.4	-73.8	-55.7	-16.7	-13.8	-3.5	7.7	18.3	34.9	L+V→L	224	L+V→L	0.5	5.8
14	2a	28.73	16.3	83.7	H_2O-CO_2-H_2-CH_4-H_2S-NaCl	-25.1	-93.6	-95.9	-118.6	-74.7	-55.6	-17.5	-14.3	-3.4	8.3	17.8	35.2	L+V→L	229	L+V→L	0.5	5.6
15	2a	25.39	14.9	85.1	H_2O-CO_2-H_2-CH_4-H_2S-NaCl	-24.6	-95.5	-95.4	-118.7	-74.1	-56.3	-17.3	-13.8	-3.6	8.1	18.7	34.8	L+V→L	219	L+V→L	0.5	5.9
16	2a	27.14	12.7	87.3	H_2O-CO_2-H_2-CH_4-H_2S-NaCl	-25.2	-94.87	-96.3	-117.5	-73.4	-55.9	-17.7	-14.4	-3.3	7.6	18.3	35.2	L+V→L	220	L+V→L	0.5	5.5
17	2a	26.58	11.8	88.2	H_2O-CO_2-H_2-CH_4-H_2S-NaCl	-25.9	-93.2	-95.5	-119.8	-73.8	-55.8	-17.3	-14.1	-3.2	8.6	18.1	34.9	L+V→L	222	L+V→L	0.5	5.3
18	2a	26.47	13.4	86.6	H_2O-CO_2-H_2-CH_4-H_2S-NaCl	-24.8	-93.7	-95.7	-118.3	-74.6	-56.2	-17.6	-14.7	-2.8	8.2	18.9	35.3	L+V→L	219	L+V→L	0.5	4.7
19	2a	24.13	17.9	82.1	H_2O-CO_2-H_2-CH_4-H_2S-NaCl	-25.1	-94.3	-96.6	-118.4	-73.9	-55.9	-17.1	-14.2	-3.4	8.1	19.7	35.2	L+V→L	226	L+V→L	0.5	5.6
20	2a	24.84	12.4	87.6	H_2O-CO_2-H_2-CH_4-H_2S-NaCl	-25.8	-93.9	-96.4	-118.6	-74.1	-55.7	-17.5	-13.8	-3.4	8.5	18.9	35.1	L+V→L	228	L+V→L	0.5	5.6
21	2a	28.62	13	87	H_2O-CO_2-H_2-CH_4-H_2S-NaCl	-24.4	-95.2	-96.3	-117.5	-73.8	-56.2	-17.6	-14.5	-3.5	8.2	18.3	35.3	L+V→L	218	L+V→L	0.5	5.8
Mean		26.0	14.1	85.9		-25.4	-94.5	-96.0	-118.3	-74.1	-55.9	-17.3	-14.1	-3.3	8.1	18.5	35.0		220		0.5	5.5

8.4.9 Fluid Inclusions from Gem Tourmaline-bearing Pegmatite from West of Senzani, Ntcheu

The Type 3b aqueo-carbonic fluid inclusions occur in trails. Their sizes range from 11 µm to 15 µm with mean at 13 µm. Their carbonic phase shows melting temperature from -57.8 to -56.7 ^{o}C with an average of -57.3 ^{o}C (Table 8.12). These microthermometric results seem to be in agreement with the presence of CH_4, C_2H_6, C_3H_8 that has been supported by Raman analysis (Figure 8.20). The mean clathrate melting temperature is 7.7 ^{o}C and the carbonic phase homogenises to a liquid phase at a mean of 28.7 ^{o}C. The mean ice melting temperature is -1.2 ^{o}C. The mean Tm_i is -20.5 ^{o}C. Total homogenisation ranges from 285 to 305 ^{o}C averaging 295 ^{o}C (Figure 8.21). The density is 0.4g/cc and the salinity is 2.0 wt%.

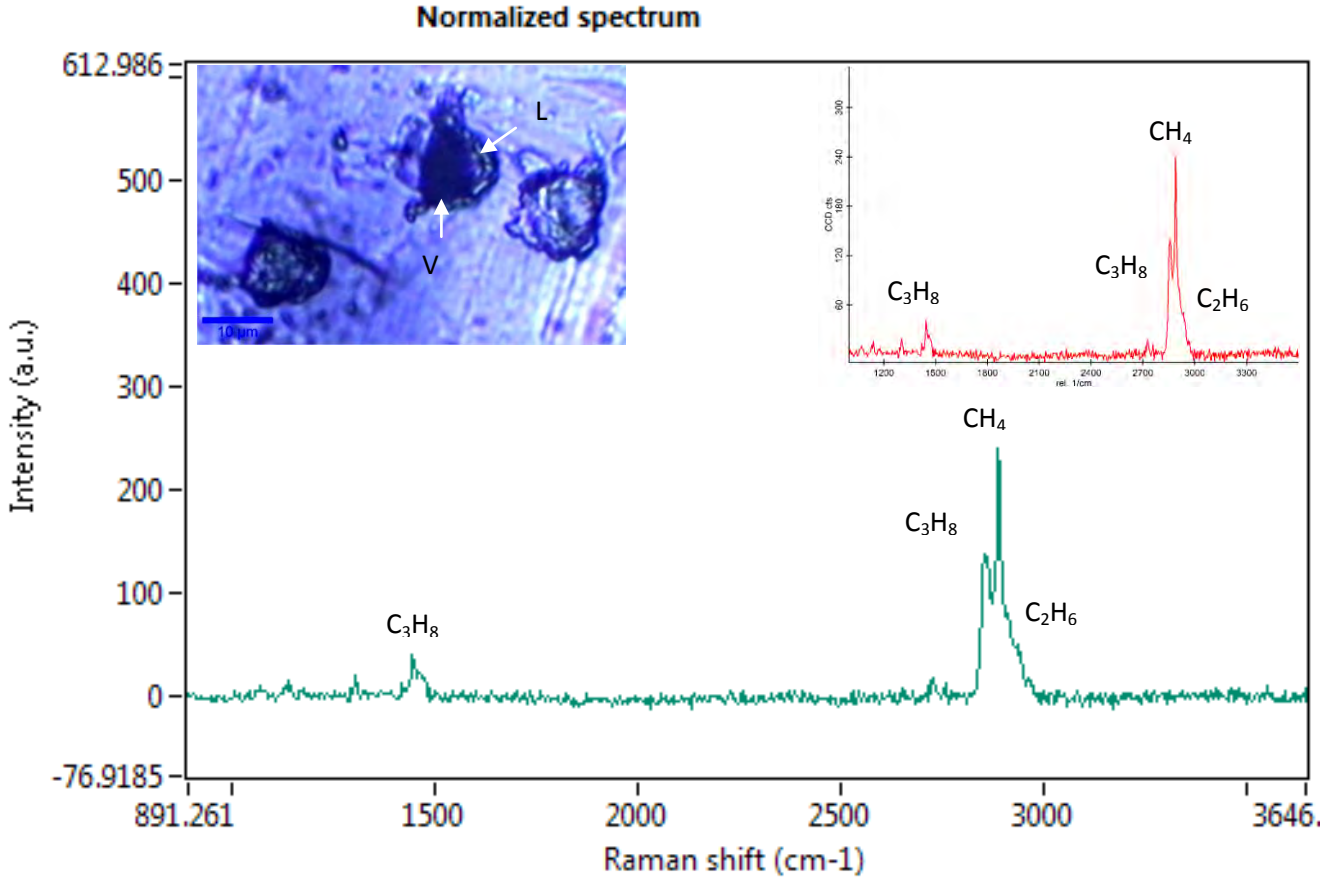

Figure 8. 20: Normalised spectrum obtained from fluid inclusion in quartz using Raman microspectroscopy shows the presence of C_2H_6, C_3H_8, CH_4; inserted photomicrograph shows liquid, vapour phases identified by Raman spectrometry.

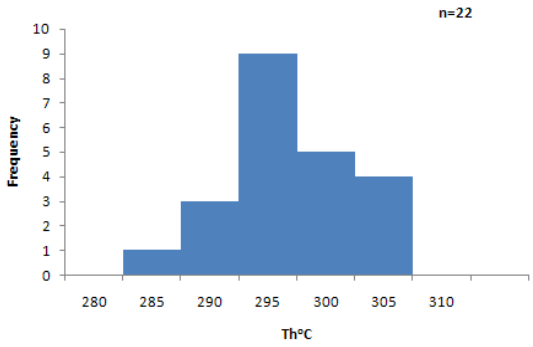

Figure 8. 21: Histogram showing the distribution of T_h values for Type 3b fluid inclusion with mean of 295 ^{o}C.

Table 8. 12: Fluid inclusion analyses for Type 3b fluid inclusions in quartz for Pan-African tourmaline-bearing pegmatites from west of Senzani, Ntcheu. All results for temperature are in ^{o}C.

Sample	Flinc Type	Size	Prop. V	Prop. L	Composition	TfH_20	Tn CH_4	$TnCO_2$	$TmCO_2$	Tm i	Tm ice	Tm cl	$ThCO_2$	Th?	Mode of homog.	Th Total	Mode of homog.	Bulk (g/cc)	Salinity (wt %)
GNS1_1	3b	14.52	65.1	34.9	H_2O-CO_2-CH_4-(NaCl-H_2-N_2)	-34.1	-91.7	-118	-57.3	-20.2	no data	7.6	28.5	34.8	L+V→L	295	L+V→L	0.36	no data
2	3b	11.86	59.7	40.3	H_2O-CO_2-CH_4-(NaCl-H_2-N_2)	-34.3	-91.9	-119	-57.8	-20.4	no data	7.9	29	34.3	L+V→L	300	L+V→L	0.36	no data
3	3b	13.47	62.4	37.6	H_2O-CO_2-CH_4-(NaCl-H_2-N_2)	-34.1	-91.5	-118	-57.7	-20	-1.7	7.3	28.8	34.5	L+V→L	293	L+V→L	0.36	2.9
4	3b	11.93	63.6	36.4	H_2O-CO_2-CH_4-(NaCl-H_2-N_2)	-34.2	-91.7	-117	-56.9	-20.7	no data	7.8	28.9	34.3	L+V→L	291	L+V→L	0.36	no data
5	3b	12.26	62.2	37.8	H_2O-CO_2-CH_4-(NaCl-H_2-N_2)	-33.9	-91.3	-118	-57.1	-21	no data	7.8	28.1	34.2	L+V→L	294	L+V→L	0.36	no data
6	3b	14.75	59.5	40.5	H_2O-CO_2-CH_4-(NaCl-H_2-N_2)	-33.7	-91.5	-118	-57.5	-20.5	-1.1	7.5	28.4	34.6	L+V→L	302	L+V→L	0.36	2.0
7	3b	11.38	64.3	35.7	H_2O-CO_2-CH_4-(NaCl-H_2-N_2)	-34.2	-91.7	-116	-57.3	-20.4	-1.5	7.3	28.4	34.8	L+V→L	290	L+V→L	0.36	2.6
8	3b	15.42	61	39	H_2O-CO_2-CH_4-(NaCl-H_2-N_2)	-34.1	-91.7	-119	-57.6	-20.3	no data	8	29	35	L+V→L	295	L+V→L	0.36	no data
9	3b	13.89	60.7	39.3	H_2O-CO_2-CH_4-(NaCl-H_2-N_2)	-34.3	-91.3	-119	-56.8	-20.2	-0.8	7.3	28.6	34.6	L+V→L	293	L+V→L	0.36	1.4
10	3b	12.04	64.9	35.1	H_2O-CO_2-CH_4-(NaCl-H_2-N_2)	-33.9	-91.9	-118	-57.6	-20.4	no data	7.9	28.8	34.5	L+V→L	297	L+V→L	0.36	no data
11	3b	14.66	63.2	36.8	H_2O-CO_2-CH_4-(NaCl-H_2-N_2)	-34.1	-91.8	-117	-57.4	-20.3	no data	8	28.5	35	L+V→L	294	L+V→L	0.36	no data
12	3b	13.35	61.5	38.5	H_2O-CO_2-CH_4-(NaCl-H_2-N_2)	-34	-91.5	-119	-57.8	-21.1	no data	7.9	28.9	34.3	L+V→L	300	L+V→L	0.36	no data
13	3b	11.75	58.6	41.4	H_2O-CO_2-CH_4-(NaCl-H_2-N_2)	-34.2	-91.7	-116	-57.5	-20.3	no data	7.8	28.7	34.2	L+V→L	304	L+V→L	0.36	no data
14	3b	14.36	62.4	37.6	H_2O-CO_2-CH_4-(NaCl-H_2-N_2)	-34	-91.4	-119	-57.1	-20.4	no data	8.1	29	34.6	L+V→L	292	L+V→L	0.36	no data
15	3b	14.49	63.6	36.4	H_2O-CO_2-CH_4-(NaCl-H_2-N_2)	-34.1	-91.9	-119	-57.4	-21	no data	7.4	28.8	34.4	L+V→L	297	L+V→L	0.36	no data
16	3b	11.72	62.8	37.2	H_2O-CO_2-CH_4-(NaCl-H_2-N_2)	-33.8	-91.7	-117	-57.4	-20.7	-1.8	7.3	28.3	34.7	L+V→L	289	L+V→L	0.36	3.1
17	3b	12.44	65.1	34.9	H_2O-CO_2-CH_4-(NaCl-H_2-N_2)	-34.2	-91.5	-116	-56.7	-20.2	no data	7.9	28.6	34.5	L+V→L	285	L+V→L	0.36	no data
18	3b	13.61	61.9	38.1	H_2O-CO_2-CH_4-(NaCl-H_2-N_2)	-34.2	-91.3	-118	-56.9	-21.1	no data	7.3	28.9	34.3	L+V→L	305	L+V→L	0.36	no data
19	3b	12.07	60.2	39.8	H_2O-CO_2-CH_4-(NaCl-H_2-N_2)	-33.6	-91.7	-117	-57.4	-21	no data	7.6	28.7	34.4	L+V→L	290	L+V→L	0.36	no data
20	3b	13.62	61.1	38.9	H_2O-CO_2-CH_4-(NaCl-H_2-N_2)	-34.2	-91.3	-119	-57.2	-20.1	-1	7.8	28.5	34.8	L+V→L	298	L+V→L	0.36	1.8
21	3b	14.29	63.7	36.3	H_2O-CO_2-CH_4-(NaCl-H_2-N_2)	-33.9	-92	-116	-57.8	-20.5	-1.5	8	28.8	34.5	L+V→L	291	L+V→L	0.36	2.6
22	3b	12.1	64.3	35.7	H_2O-CO_2-CH_4-(NaCl-H_2-N_2)	-33.7	-91.5	-118	-57.5	-20.3	no data	7.5	28.5	34.2	L+V→L	303	L+V→L	0.36	no data
Mean		13.2	62.4	37.6		34.0	91.6	-117.8	-57.4	-20.5	-1.2	7.7	28.7	34.5		295		0.4	2.0

8.4.10 Fluid Inclusions from Tourmaline-bearing Pegmatite from Senzani, Ntcheu

The Type 4a carbonic fluid inclusions from the tourmaline-bearing pegmatites (GNS4) from Ntcheu are anhedral (Figure 8.22A). The sizes range from 5 µm to 10 µm. The phase shows melting temperature of between -57.3 and -56.5 ^{o}C with an average of -57 ^{o}C (Figure 8.22B; Table 8.13). No other gas phases were observed but the microthermometric analyses suggest the limited presence of some other vapour phase in the CO_2. The carbon dioxide phases homogenise to a liquid between 26.2 and 28.4 ^{o}C with a mean of 27 ^{o}C (Figure 8.22C). The density is 0.7 g/cc.

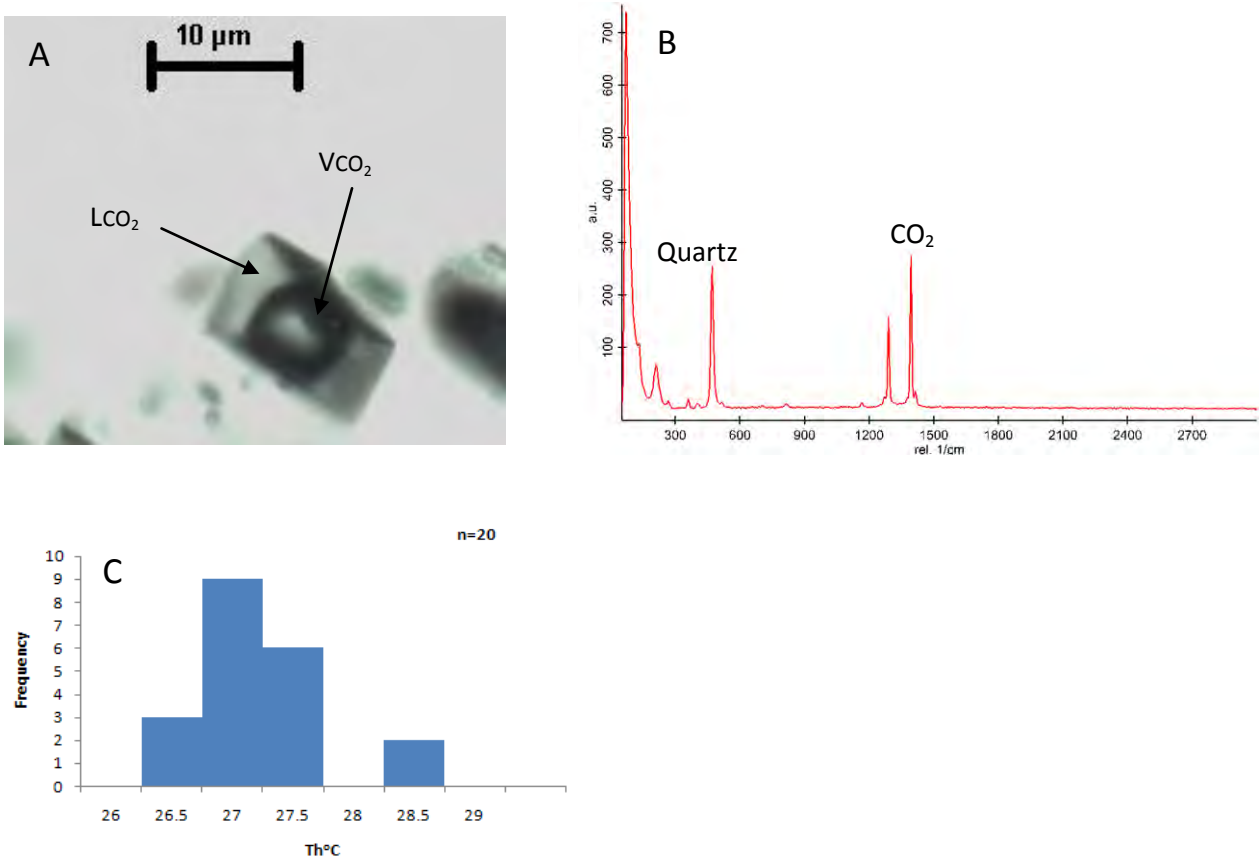

Figure 8. 22: Composition and homogenisation temperatures of fluid inclusions in quartz from Pan-African gem tourmaline-bearing pegmatite from Senzani, Ntcheu; (A) Type 4a primary fluid inclusion photomicrograph shows CO_2 liquid and vapour phase; (B) Normalised spectrum shows CO_2 obtained by Raman spectrometry; (C) Histogram showing the distribution of T_h^{o}C values for Type 4a fluid inclusion with mean of 27 ^{o}C.

Table 8. 13: Fluid inclusion analyses for Type 4a fluid inclusions in quartz for Pan-African tourmaline-bearing pegmatites from Senzani, Ntcheu. All results for temperature are in ^{o}C.

Sample	Flinc Type	Size (µm)	Prop. V	Prop. L	Composition	$TfCO_2$	$TmCO_2$	Th CO_2	Mode of Homog.	Bulk (g/cc)
GNS4_2_1	4a	8.41	30.1	69.9	CO_2	-93.2	-56.9	26.9	L+V→L	0.68
2	4a	5.27	34.7	65.3	CO_2	-93	-56.8	27.1	L+V→L	0.67
3	4a	7.62	30.7	69.3	CO_2	-93.5	-57.3	27	L+V→L	0.68
4	4a	9.93	29.5	70.5	CO_2	-92.7	-56.8	28.2	L+V→L	0.65
5	4a	10.44	31.4	68.6	CO_2	-93	-57.1	27	L+V→L	0.68
6	4a	7.11	33.9	66.1	CO_2	-93.1	-56.9	26.8	L+V→L	0.68
7	4a	8.25	28.4	71.6	CO_2	-93.1	-57.1	27.1	L+V→L	0.67
8	4a	6.29	34.2	65.8	CO_2	-92.9	-57	26.9	L+V→L	0.68
9	4a	7.56	31.9	68.1	CO_2	-93.5	-57.2	27.1	L+V→L	0.67
10	4a	7.43	29.3	70.7	CO_2	-93.1	-57.1	26.8	L+V→L	0.68
11	4a	5.31	33.6	66.4	CO_2	-92.6	-56.9	27.1	L+V→L	0.67
12	4a	10.32	32.7	67.3	CO_2	-93	-57.3	27	L+V→L	0.68
13	4a	7.12	31.5	68.5	CO_2	-92.7	-57.2	27.2	L+V→L	0.67
14	4a	9.63	31.9	68.1	CO_2	-92.5	-56.5	27	L+V→L	0.68
15	4a	8.48	29.3	70.7	CO_2	-93.1	-57.2	26.5	L+V→L	0.69
16	4a	7.24	32.1	67.9	CO_2	-92.8	-56.9	27	L+V→L	0.68
17	4a	7.97	31.7	68.3	CO_2	-93	-57.2	26.4	L+V→L	0.69
18	4a	10.4	33.2	66.8	CO_2	-93.2	-57.1	26.2	L+V→L	0.69
19	4a	7.62	29.9	70.1	CO_2	-93.4	-57	28.4	L+V→L	0.65
20	4a	8.45	31.2	68.8	CO_2	-92.6	-56.8	27.1	L+V→L	0.67
Mean		8.04	31.6	68.4		-93	-57	27		0.68

8.4.11 Fluid Inclusions in quartz from Tourmaline- and Sunstone-bearing Pegmatite from South of Senzani, Ntcheu

The Type 3a aqueo-carbonic inclusions range in size from 17 µm to 21 µm with a mean of 18.6 µm (Figure 8.23A). The carbonic phase shows melting temperatures between -56.8 and -56.4 °C with an average of 56.6 °C (Figure 8.23B; Table 8.14). The mean clathrate melting temperature is 5.3 °C and the carbonic phase homogenises to a liquid at a mean of 30.0 °C. The aqueous phase has Te values ranging from -18.6 to -19.4 °C, indicating that the dominating salt in the system is NaCl. The melting temperatures range from -1.2 to -0.5 °C. The total homogenisation ranges from 168 °C to 183 °C with mean 175 °C (Figure 8.23C). The inclusions have density of 0.6g/cc and a low salinity of 1.6 wt% NaCl equivalent. A plot of T_h°C against salinity shows fluid homogeneity (Figure 8.23D).

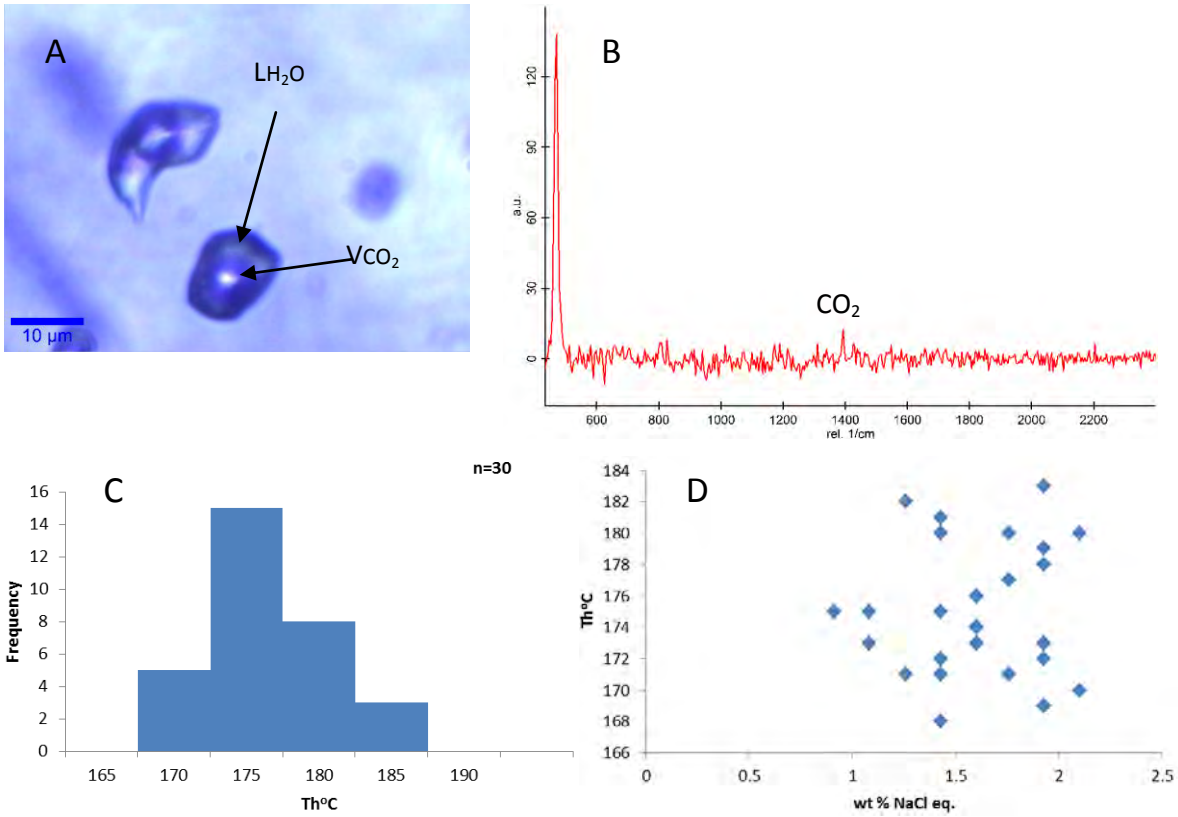

Figure 8. 23: (A) Type 3a primary fluid inclusion photomicrograph showing CO_2 liquid and vapour phase from the Pan-African gem tourmaline- and sunstone-bearing pegmatite from south of Senzani in Ntcheu; (B) Normalised spectrum showing CO_2 obtained by Raman spectrometry; (C) Histogram showing the distribution of T_h°C values for Type 3a fluid inclusion with mean of 175 °C; (D) T_h°C plotted against salinity shows homogeneous fluid composition.

Table 8. 14: Fluid inclusion analyses for Type 3a fluid inclusions in quartz for Pan-African tourmaline- and sunstone-bearing pegmatites from south of Senzani, Ntcheu. All results for temperature are in ^{o}C.

Sample	Flinc Type	Size (µm)	Prop. CO_2	Prop. H_2O	Phases	TfH_2O	$TfCO_2$	$TmCO_2$	Tm i	Tm ice	Tm cl	$ThCO_2$	Mode of Homog.	Th Total	Mode of Homog.	Bulk (g/cc)	Salinity (wt %)
MNS7g_1	3a	16.59	43.5	56.5	H_2O-CO_2-NaCl	-27.2	-97.1	-56.5	-18.6	-1.1	5.6	29.8	L+V→L	178	L+V→L	0.6	1.9
2	3a	19.27	42.1	57.9	H_2O-CO_2-NaCl	-27	-97.3	-56.8	-19.2	-0.9	5.4	30.2	L+V→L	173	L+V→L	0.58	1.6
3	3a	18.54	43.6	56.4	H_2O-CO_2-NaCl	-27.3	-96.7	-56.6	-19	-1	5.1	30.1	L+V→L	180	L+V→L	0.59	1.8
4	3a	18.35	40.2	59.8	H_2O-CO_2-NaCl	-26.8	-97.3	-56.6	-18.9	-0.8	5.4	30	L+V→L	175	L+V→L	0.59	1.4
5	3a	20.08	42.5	57.5	H_2O-CO_2-NaCl	-27.1	-97	-56.7	-19.1	-1.1	5.4	30.6	L+V→L	173	L+V→L	0.56	1.9
6	3a	17.63	40.6	59.4	H_2O-CO_2-NaCl	-26.7	-96.9	-56.8	-19.4	-0.7	5.6	30.3	L+V→L	171	L+V→L	0.58	1.3
7	3a	16.05	39.4	60.6	H_2O-CO_2-NaCl	-26.7	-97.2	-56.6	-19.2	-0.5	5.2	30.3	L+V→L	175	L+V→L	0.58	0.9
8	3a	18.41	41.7	58.3	H_2O-CO_2-NaCl	-26.6	-96.7	-56.7	-19.2	-0.9	5.1	30.1	L+V→L	176	L+V→L	0.59	1.6
9	3a	17.29	42.8	57.2	H_2O-CO_2-NaCl	-26.9	-97.1	-56.5	-19.4	-0.8	5.4	29.7	L+V→L	180	L+V→L	0.61	1.4
10	3a	20.72	41.1	58.9	H_2O-CO_2-NaCl	-26.6	-97	-56.8	-18.9	-0.6	5.2	29.9	L+V→L	175	L+V→L	0.6	1.1
11	3a	18.76	38.4	61.6	H_2O-CO_2-NaCl	-27.2	-97.2	-56.4	-19.2	-1.1	5	30.2	L+V→L	173	L+V→L	0.58	1.9
12	3a	18.63	42.4	57.6	H_2O-CO_2-NaCl	-27.4	-97.3	-56.6	-19.3	-0.8	5.3	30	L+V→L	171	L+V→L	0.59	1.4
13	3a	17.51	40.6	59.4	H_2O-CO_2-NaCl	-26.6	-97.1	-56.4	-19.1	-0.9	5.1	30.2	L+V→L	173	L+V→L	0.58	1.6
14	3a	20.64	41.3	58.7	H_2O-CO_2-NaCl	-27.2	-96.7	-56.7	-19	-1.2	5.6	30.5	L+V→L	170	L+V→L	0.57	2.1
15	3a	19.32	41.8	58.2	H_2O-CO_2-NaCl	-26.9	-97.2	-56.8	-19.1	-1.1	5.1	30.1	L+V→L	183	L+V→L	0.59	1.9
16	3a	20.68	41.3	58.7	H_2O-CO_2-NaCl	-26.7	-97.2	-56.8	-18.8	-0.8	4.8	29.5	L+V→L	168	L+V→L	0.61	1.4
17	3a	18.54	43.6	56.4	H_2O-CO_2-NaCl	-26.5	-96.8	-56.6	-19.3	-1.1	5.2	29.8	L+V→L	179	L+V→L	0.6	1.9
18	3a	18.29	41.3	58.7	H_2O-CO_2-NaCl	-27.2	-97	-56.6	-19.2	-0.7	5.5	30.1	L+V→L	182	L+V→L	0.59	1.3
19	3a	18.37	42.5	57.5	H_2O-CO_2-NaCl	-26.8	-97.3	-56.4	-19.1	-0.9	4.9	29.6	L+V→L	174	L+V→L	0.61	1.6
20	3a	19.6	41.4	58.6	H_2O-CO_2-NaCl	-27.1	-97.1	-56.7	-19	-0.6	5.6	30.1	L+V→L	173	L+V→L	0.59	1.1
21	3a	17.42	41.9	58.1	H_2O-CO_2-NaCl	-27.4	-96.9	-56.6	-18.9	-1.2	5.3	29.7	L+V→L	180	L+V→L	0.61	2.1
22	3a	19.61	40.2	59.8	H_2O-CO_2-NaCl	-26.7	-97.3	-56.7	-18.7	-0.9	5.6	30.1	L+V→L	176	L+V→L	0.59	1.6
23	3a	18.39	42.4	57.6	H_2O-CO_2-NaCl	-27	-97	-56.7	-19.2	-1.1	5.1	30.3	L+V→L	169	L+V→L	0.58	1.9
24	3a	19.57	42.9	57.1	H_2O-CO_2-NaCl	-26.6	-97.2	-56.7	-19.1	-0.8	5.4	30.2	L+V→L	172	L+V→L	0.58	1.4
25	3a	19.24	41.6	58.4	H_2O-CO_2-NaCl	-27.1	-97.1	-56.5	-18.7	-1	5.2	29.9	L+V→L	171	L+V→L	0.6	1.8
26	3a	17.97	39.5	60.5	H_2O-CO_2-NaCl	-27.4	-97.3	-56.8	-19.1	-0.9	4.8	30.1	L+V→L	174	L+V→L	0.59	1.6
27	3a	20.46	40.4	59.6	H_2O-CO_2-NaCl	-26.9	-97.2	-56.4	-19.1	-1.1	5	29.5	L+V→L	172	L+V→L	0.61	1.9
28	3a	18.4	41.1	58.9	H_2O-CO_2-NaCl	-27.2	-96.8	-56.7	-19.3	-0.8	5.3	30.3	L+V→L	181	L+V→L	0.58	1.4
29	3a	18.68	43.7	56.3	H_2O-CO_2-NaCl	-26.6	-97.3	-56.6	-18.9	-1	5.5	29.7	L+V→L	177	L+V→L	0.61	1.8
30	3a	16.42	42.8	57.2	H_2O-CO_2-NaCl	-27	-97.2	-56.8	-19.1	-1.1	5.3	30.1	L+V→L	169	L+V→L	0.59	1.9
Mean		18.6	41.7	58.3		-27.0	-97.1	-56.6	-19.1	-0.9	5.3	30.0		175		0.6	1.6

8.4.12 Fluid Inclusions from Tourmaline- and Sunstone-bearing Pegmatite from South of Senzani, Ntcheu

The Type 1b aqueo-carbonic inclusion sizes range from 9 µm to 12 µm (Figure 8.24, Table 8.15). The carbonic phase shows melting temperature from -56.7 to -55.4 ^{o}C with an average of -56 ^{o}C. The melting temperature in this phase suggests presence of gas phase which was identified as H_2S using Raman analysis (Figure 8.25A). The mean clathrate melting temperature is 9.1 ^{o}C and the carbonic phase homogenises to liquid at a mean of 21.7 ^{o}C. The initial melting of the aqueous phase ranges from -26.2 ^{o}C to -25.2 ^{o}C, indicating that the dominant salt system is NaCl - KCl. The mean ice melting temperature is -3.2 ^{o}C. Total homogenisation ranges from 243 to 256 ^{o}C, averaging at 250 ^{o}C (Figure 8.25B). The density is 0.7g/cc while the mean salinity is 5.3 wt% NaCl equivalent. T_h^{o}C - salinity bivariate plot suggests homogeneous fluid compositions (Figures 8.25C).

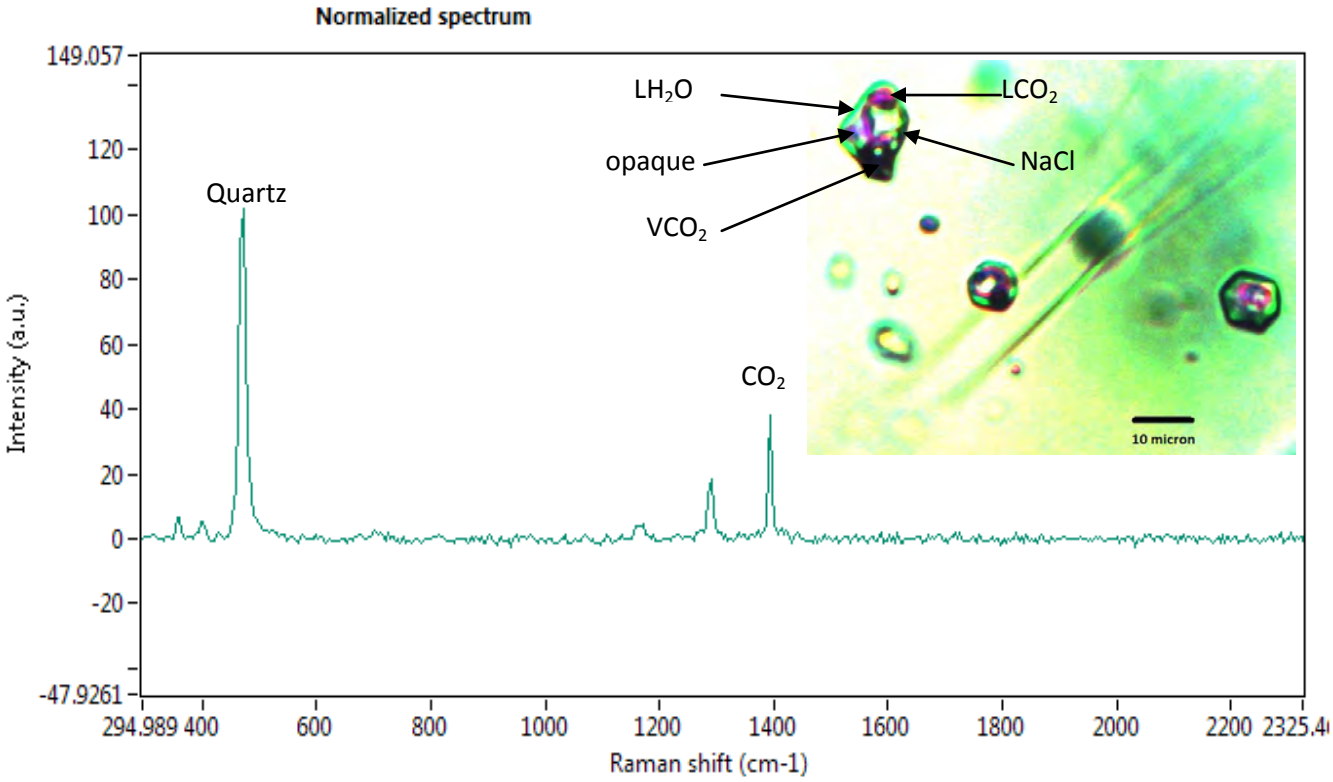

Figure 8.24: Normalised spectrum obtained from fluid inclusions in quartz using Raman microspectroscopy show the presence of CO_2; insert photomicrograph shows liquid, vapour and opaque phases.

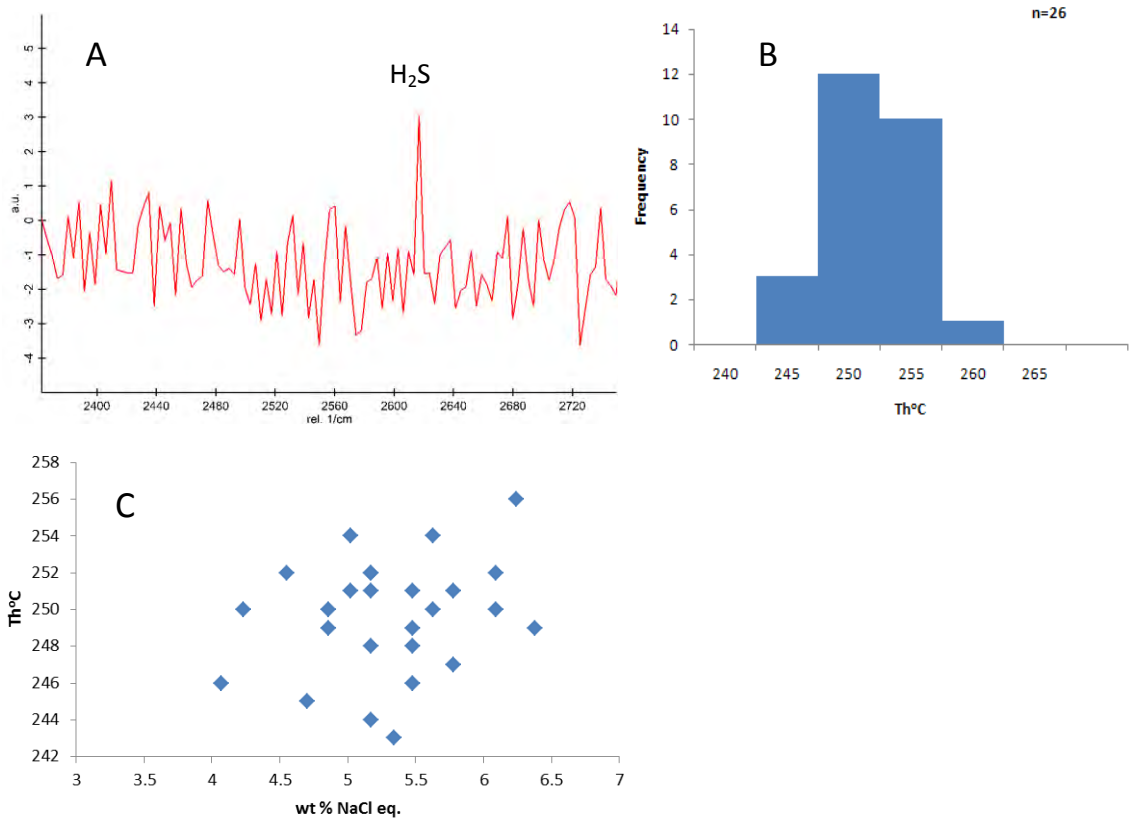

Figure 8. 25: Composition, homogenisation temperatures and salinity of fluid inclusions in quartz from tourmaline- and sunstone bearing pegmatites from south of Senzani, Ntcheu; (A) Normalised spectrum shows H_2S obtained by Raman spectrometry; (B) T_h°C values for Type 1b fluid inclusion show a mean temperature of 250 °C; (C) Narrow scattering in the T_h°C vs. salinity diagram shows the uniform composition of the MNS7g fluid.

Table 8. 15: Fluid inclusion analyses for Type 1b fluid inclusions in quartz for Pan-African tourmaline- and sunstone-bearing pegmatites from south of Senzani, Ntcheu. All results for temperature are in ^{o}C.

Sample	Flinc Type	Size (µm)	Prop V	Prop L	Composition	TfH_2O	TfCO_2	TmCO_2	Tm i	Tm ice	Tm cl	ThCO_2	Mode of homog.	Th Total	Mode of homog.	Bulk (g/cc)	Salinity (wt%)
MNSB2_1	1b	9.21	35.2	64.8	H_2O-CO_2-H_2S-NaCl-opaque	-35.3	-96.2	-56.3	-25.9	-3.1	9.2	22	L+V→L	252	L+V→L	0.68	5.2
2	1b	10.58	36.4	63.6	H_2O-CO_2-H_2S-NaCl-opaque	-35.1	-96.2	-55.8	-26	-3.7	9.3	21.4	L+V→L	250	L+V→L	0.68	6.1
3	1b	11.03	35.3	64.7	H_2O-CO_2-H_2S-NaCl-opaque	-34.8	-96	-56.1	-25.7	-3.3	9.3	21.7	L+V→L	246	L+V→L	0.68	5.5
4	1b	8.47	34.9	65.1	H_2O-CO_2-H_2S-NaCl-opaque	-35	-96.4	-55.7	-25.9	-3	9	21.5	L+V→L	254	L+V→L	0.68	5.0
5	1b	10.62	34.4	65.6	H_2O-CO_2-H_2S-NaCl-opaque	-35.2	-96.1	-56.5	-26.1	-3.1	9.1	22.1	L+V→L	251	L+V→L	0.68	5.2
6	1b	11.59	35.8	64.2	H_2O-CO_2-H_2S-NaCl-opaque	-34.9	-95.7	-55.9	-26	-3.9	9.1	21.8	L+V→L	249	L+V→L	0.68	6.4
7	1b	11.25	32.7	67.3	H_2O-CO_2-H_2S-NaCl-opaque	-34.8	-96.2	-56.7	-25.7	-3.4	9.3	21.9	L+V→L	250	L+V→L	0.68	5.6
8	1b	9.63	35	65	H_2O-CO_2-H_2S-NaCl-opaque	-34.9	-96.4	-55.4	-25.7	-3.8	8.9	21.3	L+V→L	256	L+V→L	0.68	6.2
9	1b	11.04	34.1	65.9	H_2O-CO_2-H_2S-NaCl-opaque	-35.3	-96.4	-56.2	-26	-2.4	9.4	21.8	L+V→L	246	L+V→L	0.68	4.1
10	1b	9.6	36.8	63.2	H_2O-CO_2-H_2S-NaCl-opaque	-35	-95.9	-56.0	-26	-3.3	9.1	21.6	L+V→L	251	L+V→L	0.68	5.5
11	1b	8.91	35.7	64.3	H_2O-CO_2-H_2S-NaCl-opaque	-35.2	-96.6	-55.8	-25.8	-2.9	9	21.9	L+V→L	249	L+V→L	0.68	4.9
12	1b	10.28	35.8	64.2	H_2O-CO_2-H_2S-NaCl-opaque	-35	-96.4	-56.5	-26.1	-3.4	9.3	21.4	L+V→L	254	L+V→L	0.68	5.6
13	1b	10.67	35.1	64.9	H_2O-CO_2-H_2S-NaCl-opaque	-35.2	-96.3	-55.7	-25.7	-3.1	8.8	21.6	L+V→L	248	L+V→L	0.68	5.2
14	1b	10.35	34.9	65.1	H_2O-CO_2-H_2S-NaCl-opaque	-35.1	-95.8	-56.1	-26.2	-2.7	9.3	21.5	L+V→L	252	L+V→L	0.68	4.6
15	1b	11.26	36.2	63.8	H_2O-CO_2-H_2S-NaCl-opaque	-34.9	-96.1	-55.9	-25.5	-3.3	9.1	22.4	L+V→L	249	L+V→L	0.67	5.5
16	1b	9.43	35.7	64.3	H_2O-CO_2-H_2S-NaCl-opaque	-35.3	-96.4	-55.7	-26	-3	9	20.8	L+V→L	251	L+V→L	0.68	5.0
17	1b	10.61	35.4	64.6	H_2O-CO_2-H_2S-NaCl-opaque	-34.7	-96.3	-56.3	-26.1	-3.1	9.2	21.6	L+V→L	244	L+V→L	0.68	5.2
18	1b	11.04	34.6	65.4	H_2O-CO_2-H_2S-NaCl-opaque	-35.2	-95.7	-55.7	-25.9	-3.5	9.4	22.1	L+V→L	251	L+V→L	0.67	5.8
19	1b	10.86	34.1	65.9	H_2O-CO_2-H_2S-NaCl-opaque	-35.1	-96.4	-56.1	-26.1	-2.9	9.3	22	L+V→L	250	L+V→L	0.68	4.9
20	1b	9.64	35.5	64.5	H_2O-CO_2-H_2S-NaCl-opaque	-35.3	-96	-56.4	-25.8	-3.3	8.9	21.3	L+V→L	248	L+V→L	0.68	5.5
21	1b	10.58	34.1	65.9	H_2O-CO_2-H_2S-NaCl-opaque	-35.1	-96.3	-55.8	-25.2	-3.1	9.2	20.9	L+V→L	252	L+V→L	0.68	5.2
22	1b	9.42	35.9	64.1	H_2O-CO_2-H_2S-NaCl-opaque	-34.9	-96.1	-56.0	-26	-2.8	8.6	21.5	L+V→L	245	L+V→L	0.68	4.7
23	1b	10.74	34	66	H_2O-CO_2-H_2S-NaCl-opaque	-35.4	-96.2	-55.8	-26.2	-2.5	9.4	21.3	L+V→L	250	L+V→L	0.68	4.2
24	1b	11.23	35.8	64.2	H_2O-CO_2-H_2S-NaCl-opaque	-35.2	-96.1	-56.1	-25.7	-3.2	9.2	21.9	L+V→L	243	L+V→L	0.68	5.3
25	1b	9.86	35.2	64.8	H_2O-CO_2-H_2S-NaCl-opaque	-34.8	-95.9	-55.6	-26.1	-3.7	9.1	22	L+V→L	252	L+V→L	0.68	6.1
26	1b	9.49	36.3	63.7	H_2O-CO_2-H_2S-NaCl-opaque	-35.2	-96.4	-55.9	-25.7	-3.5	9.3	21.6	L+V→L	247	L+V→L	0.68	5.8
Mean		10.3	35.2	64.8		-35.1	-96.2	-56.0	-25.9	-3.2	9.1	21.7		250		0.7	5.3

8.4.13 Fluid Inclusions from the Pan- African Amethyst-bearing Pegmatites from Balaka

The type 4b carbonic fluid inclusions range in size from 17 µm to 20 µm (Figure 8.26A; Table 8.16). The melting temperature of this phase ranges from -57.6 to -56.8 ^{o}C with a mean of -57.3 ^{o}C. This variation seems to agree with the presence of vapour phases of C_3H_8 and N_2 identified by Raman spectroscopy (Figure 8.26B). The liquid and gas carbonic phases homogenise to a liquid phase at a mean temperature of 28.5 ^{o}C. The total homogenisation temperature ranges from 154 ^{o}C to 167 ^{o}C with an average of 160 ^{o}C (Figure 8.26C). The fluid density is 0.4 g/cc.

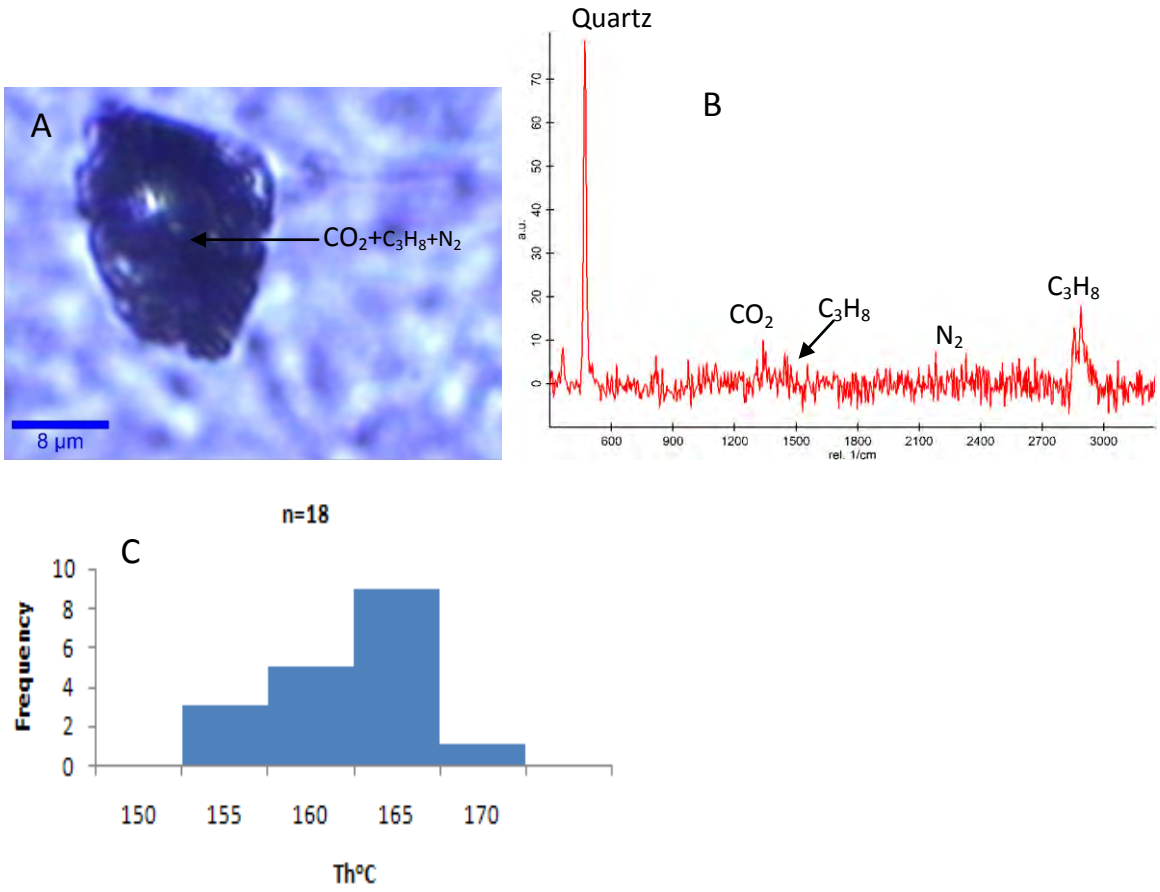

Figure 8. 26: Composition and homogenisation temperatures of fluid inclusions in quartz from Pan-African amethyst-bearing pegmatite from Balaka; (A) Type 3b primary fluid inclusion photomicrograph shows CO_2 +C_3H_8+ N_2 phase; (B) Normalised spectrum shows CO_2 +C_3H_8+ N_2 obtained by Raman spectrometry; (C) Histogram shows the distribution of T_h^{o}C values for Type 3b fluid inclusion with mean of 160 ^{o}C.

Table 8. 16: Fluid inclusion analyses for Type 4b fluid inclusions in quartz for Pan-African amethyst-bearing pegmatites from Balaka. All results for temperature are in ^{o}C.

Sample	Flinc Type	Size	Prop. V	Prop. L	Composition	$TfCO_2$	$TmCO_2$	Tm ice	Tm cl	$ThCO_2$	Mode of Homog.	Th Total	Mode of Homog.	Bulk (g/cc)
CUB1A_2_1	4b	18.62	85.2	14.8	CO_2-CH_4-N_2	-97.5	-57.3	-1.3	7.3	28.7	L+V→L	160	L+V→L	0.37
2	4b	18.44	89.1	10.9	CO_2-CH_4-N_2	-98.1	-57.5	-1.1	7.1	28.1	L+V→L	163	L+V→L	0.37
3	4b	17.63	88	12	CO_2-CH_4-N_2	-97.6	-57.4	-1.4	6.9	28.2	L+V→L	154	L+V→L	0.37
4	4b	19.02	86.3	13.7	CO_2-CH_4-N_2	-96.4	-57.2	-0.9	7.3	29	L+V→L	163	L+V→L	0.37
5	4b	18.49	85.7	14.3	CO_2-CH_4-N_2	-97.3	-57.6	-1.2	7.2	28.1	L+V→L	159	L+V→L	0.37
6	4b	20.31	91.5	8.5	CO_2-CH_4-N_2	-97.6	-57.4	-1.4	7.2	28.7	L+V→L	162	L+V→L	0.37
7	4b	19.27	87.1	12.9	CO_2-CH_4-N_2	-97.5	-56.8	-1.3	7.3	28.2	L+V→L	158	L+V→L	0.37
8	4b	18.54	88.4	11.6	CO_2-CH_4-N_2	-98.2	-57.4	-1	6.7	29.4	L+V→L	163	L+V→L	0.37
9	4b	20.16	90.6	9.4	CO_2-CH_4-N_2	-97.3	-57.6	-1.1	6.7	28.8	L+V→L	161	L+V→L	0.37
10	4b	19.84	87.3	12.7	CO_2-CH_4-N_2	-97.7	-57.6	-0.9	7.3	28.1	L+V→L	163	L+V→L	0.37
11	4b	17.68	86.9	13.1	CO_2-CH_4-N_2	-96.9	-57.4	-1.3	7.1	28.5	L+V→L	161	L+V→L	0.37
12	4b	19.41	88.7	11.3	CO_2-CH_4-N_2	-97.4	-57.5	-1.1	6.8	28.2	L+V→L	158	L+V→L	0.37
13	4b	19.36	85.9	14.1	CO_2-CH_4-N_2	-97.7	-56.9	-1.3	7.3	28.6	L+V→L	162	L+V→L	0.37
14	4b	18.52	86.5	13.5	CO_2-CH_4-N_2	-98.3	-57.6	-0.8	6.9	29.5	L+V→L	158	L+V→L	0.37
15	4b	17.08	87.1	12.9	CO_2-CH_4-N_2	-97	-57.4	-1.2	6.7	28	L+V→L	154	L+V→L	0.37
16	4b	17.59	87	13	CO_2-CH_4-N_2	-96.8	-57.2	-1.4	7.2	28.2	L+V→L	165	L+V→L	0.37
17	4b	18.45	89.2	10.8	CO_2-CH_4-N_2	-97.6	-57.6	-0.8	6.9	28.1	L+V→L	152	L+V→L	0.37
18	4b	20.08	88.4	11.6	CO_2-CH_4-N_2	-96.9	-56.8	-1.3	7.1	29.3	L+V→L	167	L+V→L	0.37
Mean		18.8	87.7	12.3		-97.4	-57.3	-1.2	7.1	28.5		160		0.37

8.5 P-T ESTIMATIONS OF FLUID ENTRAPMENT

Fluid inclusion assemblages consisting of co-genetic inclusions containing compositionally different fluids allow P-T estimations of fluid entrapment by intersections of isochores for these different fluids (Section 5.4.1, Roedder, 1984; Shepherd et al., 1985). Since the previous sections have shown that each pegmatite contains only one primary fluid species, this method cannot be applied. Instead, the isochores of the fluids are plotted in P-T space, where they form lines of steep positive slopes. A summary of programs and equations of state used for modelling of representative isochores for the established fluid inclusion types are presented in Table 8.17.

The measured homogenisation temperatures (Th) indicate only the minimum of trapping of a given fluid (Roedder, 1984; Shepherd et al., 1985). The fluid could have been trapped at any point along the isochores. Pegmatites crystallise, depending on the amount of flux elements, between 350 ^{o}C - ~630 ^{o}C (London et al., 1988; London, 1990; 1992; 1997; London and Morgan, 2012, Cërny et al., 2012), and silicate melt may persist at temperatures as low as 262 ^{o}C (London, 2005). The temperature interval between 400 ^{o}C - 600 ^{o}C along the isochores has been used to narrow down the likely pressure interval and hence the depth of emplacement. The depth has been calculated assuming a density of the crust of 2.7 g/cc.

The P-T history of the host rocks is usually not well known. Furthermore, in several cases they formed during orogenic events that are unrelated to pegmatite formation and emplacement (e.g. Pan-African pegmatites intruding Mesoproterozoic crust). Hence the information from the host rocks‟ geological history provides little or no constraint on the depth estimation of pegmatite emplacement. Other methods of temperature estimation of pegmatite formation, such as garnet-biotite thermometry and or feldspar thermometry have not been attempted here because in the volatile-rich environment of pegmatites the chemistry of these phases is susceptible to retrograde and metasomatic reaction and partial re-equilibration (Anderson, 1996).

Table 8. 17: A summary of programs and equations of state used for modelling of representative isochores for the established fluid inclusions types.

SAMPLE	COMPOSITIONAL PHASES	EQUATION OF STATE USED			
		Bakker (2003) Package FLUIDS 1.	Estimated proportions	ISOC	Estimated proportions
CNC1B_1	H_2O-NaCl	Archer (1992)	xH_2O=1	Archer (1992), Zhang & Frantz (1987)	xH_2O=1
CNC1B2_1	H_2O-CO_2-NaCl-opaque	Archer (1992)	xH_2O=0.65, xCO_2=0.35	Anderko & Pitzer (1993a); Duan et al (1995)	xH_2O=0.65, xCO_2=0.35
CCC_1	H_2O-CO_2-CH_4	Duan et al. (1992), Archer (1992)	xCO_2=0.7, CH_4=0.3	Duan et al. (1992a, 1992b)	xH_2O=0.7, xCO_2=0.2, xCH_4=0.1
MWC_1	H_2O-CO_2-CH_4	Duan et al. (1992), Archer (1992)	xCO_2=0.6, xCH_4=0.4	Duan et al. (1992a, 1992b)	xH_2O=0.6, xCO_2=0.3, xCH_4=0.1
GM3_1	H_2O-CO_2-CH_4-NaCl-opaque	Duan et al. (1992), Archer (1992)	xCO_2=0.7, xCH_4=0.3	Duan et al. (1992a, 1992b)	xH_2O=0.3, xCO_2=0.6, xCH_4=0.1
GM5_1	H_2O-CO_2-NaCl	Archer, Krugalz et al. (1996), Duan et al. 1992	xL=75, xV25	Bowers & Helgeson (1983)	xH_2O=0.7, xCO_2=0.3
MEM _1	H_2O-CO_2-N_2-NaCl-Opaque	Thiery et al. (1994a,b), Archer (1992)	xCO_2=0.9, xN_2=0.1	Bakker R.J. (1999)	xH_2O=0.6, xCO_2=0.35, xN_2=0.05
DHD1C_1	H_2O-CO_2-H_2-CH_4-H_2S-NaCl	Duan et al. (1992) , Archer (1992)	xH_2S=0.6, xCO_2=0.3, xCH_4=0.1	Duan et al. (1992, 1996)	xH_2O =0.7, xCO_2=0.05, xCH_4=0.02, xH_2S=0.23
HEM1A_1	H_2O-CO_2-NaCl	Krumgalz et al.. (1996), Archer (1992)	xH_2O =0.3, xCO_2=0.7	Anderko & Pitzer (1993a), Anderko and Pitzer (1993b), Duan (1995)	xH_2O =0.3, xCO_2=0.7
HEM 2C_1	H_2O-CO_2-NaCl-opaque	Krumgalz et al.. (1996), Archer (1992)	xH_2O =0.3, xCO_2=0.7	Anderko & Pitzer (1993a), Anderko and Pitzer (1993b), Duan (1995)	xH_2O =0.3, xCO_2=0.7
GNS1_1	H_2O-CO_2-CH_4-NaCl	Redlich & Kwong (1949), Holloway (1987)	xL=38, xV62	Bakker R.J (1999)	xH_2O=0.3, xCO_2=0.2, xCH_4=0.5
GNS4_2_1	CO_2	Bakker R.J. (2003)	CO_2=1	Span and Wagner (1996)	xCO_2=1
MNS7g_1	H_2O-CO_2-NaCl	Bakker R.J. (2003), Archer (1992)	xH_2O=0.6, xCO_2=0.4	Anderko & Pitzer (1993a), Anderko and Pitzer (1993b), Duan et al (1995)	xH_2O=0.6, xCO_2=0.4
MNSB2_1	H_2O-CO_2-H_2S-NaCl	Bowers & Helgeson (1983), Bakker R.J. (1999)	CO_2=0.7, H_2S=0.3	Bakker R.J. (1999)	CO_2=0.6, H_2O=0.3, H_2S=0.1
CUB1A_2_1	CO_2-CH_4-N_2	Thiery et al. (1994a,b)	xH_2O=0.6; xCH_4=0.25; xCO_2=0.1; xN_2=0.05	Thiery et al, (1994a,b); Soave (1972); Bakker R.J. (1999)	xCO_2=0.25, xCH_4=0.63, xN_2=0.12

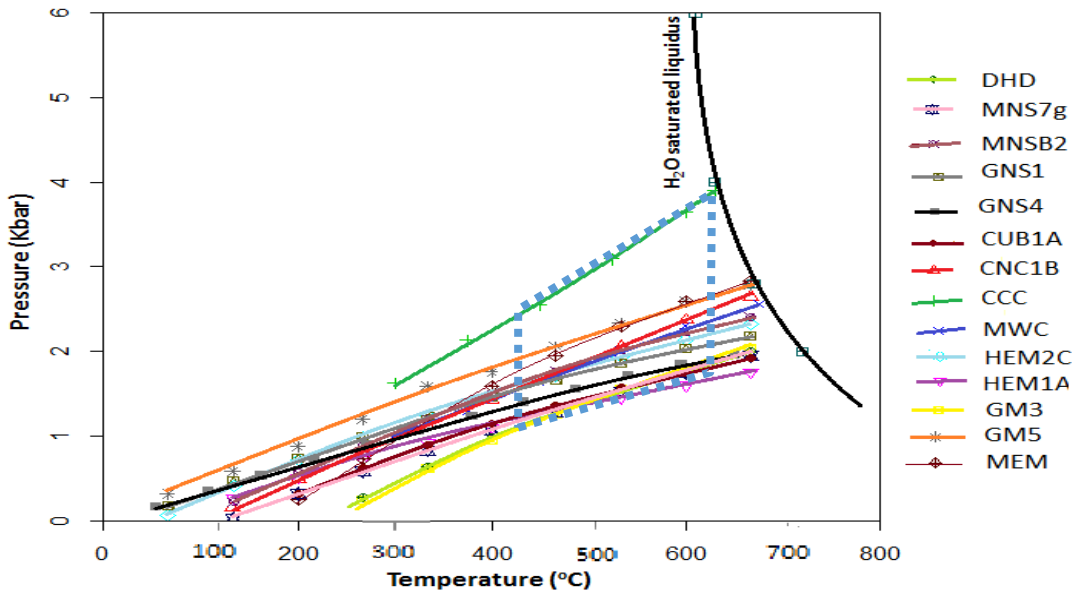

Figure 8.27: Modelled isochores for fluid inclusions in quartz from Type 1a from Palaeoproterozoic gem tourmaline-bearing pegmatites (CNC); Type 2b from pegmatites (CCC), Type 5a from MWC pegmatites, Type 1a from GM3 pegmatites; Type 3a from GM5 pegmatites; Type 1b from MEM amethyst-bearing veins occurring in close proximity with GM5 pegmatites; Type 3a from HEM1A pegmatites, Type 1a from HEM2C pegmatites; Type 2a from tourmaline-bearing (DHD1C) pegmatite; isochores from GNS1, GNS4, MSN7, MSNB2 and the amethyst-bearing (CUB) pegmatites. The P-T conditions of emplacement are estimated as 400-600 ^{o}C and c. 0.9-2.5 kb, except the CCC pegmatite (2.2-3.6 kb; dotted field).

All isochores have been plotted in Figure 8.27. Assuming pegmatite solidification at temperatures between 400 and 600 ^{o}C constrains the emplacement depths to 3.4 to 9.8 km, corresponding to 0.9 to 2.6 kb. Only the CCC pegmatites may have been emplaced at greater depth of 8.3 to 13.6 km (2.2 to 3.6 kb). For the Palaeoproterozoic gem tourmaline-bearing pegmatites (CNC), an estimated pressure of 2.5 kb at 600 ^{o}C suggests a maximum depth of formation of ~9.4 km for the Type 5 inclusion.

The likely depths of emplacement of all analysed pegmatites was the shallow and very likely brittle crust of less than 10 km, perhaps with the exception of CCC pegmatites, which might have been emplaced at 13.6 km. This shallow crustal emplacement is in good agreement with field observations that suggest pegmatite intrusion along sharp contacts into cold crust, preventing significant metasomatic interaction and promoting rapid cooling of the pegmatitic melt.

Table 8.18: Summary of estimated P-T conditions at 400 ^{o}C and 600 ^{o}C and depth of formation based on representative isochores.

SAMPLE	Kbar at 400 ^{o}C	Kbar at 600 ^{o}C	Depth range Km (400)	Depth range Km(600)	Approximate depth range Km (400-600)	Class
CNC1B_1	1.4	2.5	5.3	9.4	5.3-9.4	RE-MI
CNC1B2_1	4	8	-	-	-	RE-MI
CCC1B_1	2.2	3.6	8.3	13.6	8.3-13.6	RE
MWC_1	1.4	2.3	5.3	8.7	5.3-8.7	RE-MI
GM3_1	0.9	1.9	3.4	7.2	3.4-7.2	RE-MI
GM5_1	1.8	2.6	6.8	9.8	6.8-9.8	RE-MI
MEM1B_1	1.5	2.6	5.7	9.8	5.7-9.8	MI
HEM1A_1	1.1	1.6	4.2	6.0	4.2-6.0	RE-MI
HEM2C_1	1.4	2	5.3	7.6	5.3-7.6	RE-MI
DHD1C_1	0.9	1.8	3.4	6.8	3.4-6.8	RE-MI
MNS7g_1	1	1.8	3.8	6.8	3.8-6.8	RE-MI
MNSB2_1	1.4	2.3	5.3	8.7	5.3-8.7	RE-MI
GNS1_1	1.4	2.1	5.3	7.9	5.3-7.9	RE-MI
GNS4_2_1	1.3	1.9	4.9	7.2	4.9-7.2	RE-MI
CUB1A_2_1	1.1	1.8	4.2	6.8	4.2-6.8	RE-MI

8.6 SYNOPSIS OF FLUID INCLUSION STUDIES DATA

8.6.1 Palaeoproterozoic Pegmatites

Raman spectroscopy and microthermometric analyses of fluid inclusions from the Palaeoproterozoic pegmatites in Chitipa show low salinities in a H_2O-CO_2-NaCl system and a H_2O-NaCl system. Such fluids are commonly associated with granitic magmatic systems (Roedder, 1984; Cërny 1993b; London 1995, 1996; Sirbescu and Nabelek, 2003). The low salinity pegmatitic and hence late magmatic fluid was rich in B which led to the abundant tourmaline crystallisation. Pegmatite formation involved mainly H_2O-rich fluids. CO_2 with H_2O have been observed to occur together in granitic fluids (Roedder, 1984; Sirbescu and Nabelek 2003).

8.6.2 Pan-African Pegmatites

Fluid inclusions from the tourmaline- and beryl-bearing pegmatites from Chisenga and Wenya, Chitipa show the presence of the H_2O-CO_2-H_2-CH_4-N_2-NaCl system. The inclusions have moderate salinity. The presence of C_3H_8 and N_2 suggest interaction of magmatic fluid with metamorphic fluids during formation.

In the inclusions from the beryl-bearing pegmatites of Kafukule, Mzimba, two fluid types belong to the H_2O-CO_2-CH_4-NaCl system for GM3 and the H_2O-CO_2-NaCl system for GM5. In GM3 the first melting temperature is lower than the temperatures of the H_2O system (Potter and Brown, 1977). This may indicate the presence of a complex salt solution such as LiCl-NaCl (Huizenga, 2010). GM3 contains CH_4 which is absent in GM5. CH_4 is a compound that is typical for fluids extracted from host rocks rich in organic material and hence might indicate an interaction between the granitic/pegmatitic fluid and the mica schist host rock into which GM3 was emplaced. However, since the pegmatite is likely to have solidified in shallow and cold crust at 3.4 to 7.2 km depth, such an interaction might not have taken place at the emplacement level but rather closer to the source.

Furthermore, the inclusions in the amethyst-bearing veins (MEM) indicate the presence of that the dominant salt in solution is NaCl (Huizenga, 2010. The carbonic phase in the Type 3a fluid contains N_2 gas phase suggesting interaction of magmatic fluid with metamorphic fluids during formation. The formation of thernadite ($NaSO_4$) and celestine ($SrSO_4$) as identified by Raman analysis provided a sink for sulphur. The variation of Sr in the GM pegmatites (Chapter 7) is in agreement with the formation of $SrSO_4$. The presence of thernadite supports the presence of low salinity fluids in the GM5 pegmatites that resulted from the removal of Na which is essential for NaCl formation.

In the Luhomero area in Mzimba, the fluid inclusions belong to the H_2O-CO_2-NaCl system but according to the observed melting temperatures the carbonic phase does not show other vapour phases. The Type 3a (HEM1A) and Type 1a (HEM2C) fluid inclusions do not show interaction of magmatic fluid with metamorphic fluids during their formation.

The results from Type 2a fluid inclusions in the tourmaline-bearing pegmatites in Dowa reveal the presence of H_2O-CO_2-H_2-H_2S-CH_4-NaCl system (cf. Section 8.4.8). The source of H_2S is not obvious but its association with CH_4, which almost certainly is derived from the organic component of the host rock, may suggest that also H_2S infiltrated from outside into the pegmatitic melt. In the hosting sillimanite-biotite gneiss, sulphur is present in pyrite, which implies metasomatic pyrite breakdown and sulphur leaching processes involving the reduction of S^- and S^{2-}.

In Ntcheu the tourmaline-bearing pegmatites of Senzani (GNS4) and west of Senzani (GNS1) show two fluid systems: the H_2O-CO_2-CH_4-NaCl system and the CO_2 system. The aqueo-

carbonic system has CH_4, C_2H_6, C_3H_8 whereas the CO_2 system has no other volatile phases. The hydrated carbon compounds indicate the interaction of the pegmatitic with host rock fluids at some stage of pegmatite ascent from the parent granite to the emplacement level. During solidification the fluid pressure must have been high enough to form miarolitic cavities in which most gem-quality tourmaline formed. This is in agreement with the shallow emplacement level suggested by the position of fluid isochores in P-T space (Figure 8.27).

To the south of Senzani the tourmaline- and sunstone-bearing pegmatites contain fluids of the H_2O-CO_2-NaCl system, but with variation in the volatile components. Pure carbon dioxide in MNS7g, and H_2S vapour is present in the carbonic phase of MNSB2 fluids. As seen in other pegmatites, H_2S is likely to have infiltrated from the host rock after pyrite breakdown.

Also in the amethyst-bearing pegmatites (CUB) of Balaka the presence of C_3H_8 and N_2 vapour together with the carbonic phase suggests the interaction of magmatic and hydrothermal host rock fluids somewhere along the pathway of the pegmatite melt. The growth of gemstones however is related to the low-pressure environment of the emplacement level.

All studied pegmatites show fractionation crystallisation trends and are enriched in fluxing elements such as B, Be and Li (Chapter 7, Section 7.3). The fluxing elements significantly lower the magma solidification temperature (Cërny et al., 2012). According to the modelled isochores, the P-T conditions indicate that the gem-bearing pegmatites were formed at low pressure and moderate temperatures, conditions which have also been determined for the Lundazi pegmatites, which formed at slightly higher a pressure of 4 kb at temperatures of 430-650 ^{o}C, corresponding to an emplacement depth of 15 km (Graziani et al., 1983). Miarolitic cavities and textures indicative of strong and rapid undercooling are in agreement with shallow-crustal pegmatite emplacement into cold crust.

9. DISCUSSION: THE GENESIS OF THE GEMSTONE BEARING PEGMATITES

In two sections this chapter discusses the geochemical characteristics and classification, processes of crystallisation, evolution and differentiation of the gemstone bearing pegmatites in Malawi, implications of fluid composition variations on pegmatite genesis, the timing of pegmatite emplacement and their links to global pegmatite-forming episodes.

9.1 PEGMATITE CLASSIFICATION AND MELT SOURCES

The pegmatites analysed in this study have been classified according to the classification scheme proposed by Cërny (1991) and Ginsburg et al. (1979). The emplacement depths (cf. Section 8.5) were used as an additional criterion. The classification of analysed pegmatites is summarised in Table 9.1, which also shows further subclasses into which the pegmatites can be categorised. This table also contains information on the geochemical criteria that were used for the classification.

The results show that all pegmatites belong to the Rare-Element and Miarolitic Classes, both of which favour the formation of gemstones (Cërny, 1991a). However, according to classification by Ginsburg et al. (1979), modified after Cërny and Ercit (2005, Table 2.3), the mineral species belong to the Rare-Element, REL-Li – Elbaite and the Miarolitic, MI-REE, MI-Li Classes. The Palaeoproterozoic CNC pegmatites belong to the mixed NYF-LCT family. All those associated in time with the main Pan-African contractional, collisional, or latest Pan-African (post-contractional) episodes between ~550 and 480 Ma belong to the LCT family. The early Pan-African MNM, NNO1 and THMB pegmatites, and also the Mesozoic ZA pegmatite, all related to episodes of crustal extension or rifting, contain zircon, which defines them as NYF pegmatites.

Table 9.1: Summary of the different studied pegmatites, their ages, characteristics and classifications.

Age of studied pegmatites and gem species found.	**Ginsburg et al. (1979) Cërny (1991a) with mineralisation as part of the classification**	**Ginsburg et al.'s (1979) classification into subclasses, types and subtypes**	**Cërny and Ercit (2005)**	**Geochemical criteria**	**Approximated P-T-depth of formation temperature is estimated at 400 and 600.^{o}C**
Palaeoproterozoic CNC, variety of gem tourmaline	Rare Element Class and the NYF family shows low to abundant mineralisations		Mixed geochemical signature of both LCT and NYF families	Enrichment of Rb, Ti, Nb>Ta, U, Hf, (H)REE and B, even though some are only slightly enriched;	1.4-2.5 kb corresponding to depths of 5.3-9.4 km.
Pan-African GNS, tourmaline; Pan-African MNS, tourmaline and sunstone	Rare Element Class and LCT family shows low to abundant mineralisations	The LCT pegmatites belong to REL-Li subclass, Complex type and Elbaite subtype	Rare Element Class, in the REL-Li subclass, and in the Miarolitic Class, Mi-Li subclass	Relative enrichment of Rb, Cs, Ga, Nb, Ta, B and Hf, even though some are only slightly enriched	1.4–2.9 kb corresponding to depths of 4.9-7.9 km for GNS; 1-2.3 kb corresponding to depth of 3.8-8.7 km for MNS.
Pan-African CUB, amethyst	Rare Element Class and LCT family bearing gemstock		Rare Element Class, in the REL-Li, and in the Miarolitic Class, Mi-Li subclass.	Enrichment in Li, Cs, Ga, Nb, Ta and Hf	1.1-1.8 kb corresponding to depths of 4.2-6.8 km.
Pan-African CCC and MWC, beryl, aquamarine, tourmaline and topaz	Rare Element Class and LCT family LCT pegmatites belong to Beryl type, Beryl - columbite subtype, even though columbite was not observed		Rare Element Class: REL-Li subclass, Beryl type, Beryl- columbite subtype, and to the Complex type, Elbaite subtype. Miarolitic Class: Mi-Li subclass, beryl-topaz type.	Enrichment in Li, Rb, Cs, Be, Ga, Nb>Ta, Hf, B	2.2-3.6 kb corresponding to depths of 8.3-13.6 km for CCC; 1.4-2.3 kb corresponding to depths of 5.3-8.7 km for MWC
Pan-African GM & MEM, and HEM, GM: beryl, and or aquamarine, MEM amethyst HEM: aquamarine, and tourmaline	Rare Element Class and LCT family: Beryl type, Beryl - columbite subtype even though columbite was not observed		Rare Element Class, in the REL-Li subclass, Beryl type, Beryl-columbite subtype, and in the Miarolitic Class, Mi-Li subclass, beryl-topaz type.	Enrichment in Li, Rb, Cs, Be, Ga, Nb>Ta, Hf, B	HEM: 1.1-2 kb corresponding to depths of 4.2-7.6 km. GM & MEM: 0.9-2.6 kb corresponding to depth of 3.4-9.8 km.
Pan-African DHD tourmaline	Rare Element Class and LCT family which has gemstock		Rare Element Class, in the REL-Li subclass, Complex type, Elbaite subtype.	Enrichment of Li, Rb, Cs, Be, Ga, Nb> Ta, Hf and B	0.9-1.8 kb corresponding to a depth of 3.4-6.8 km.
Pan-African MNM, NNO1, THMB, ZA, variety of gem zircons	Rare Element Class, NYF family due to presence of zircon			Not analysed	Not determined

The pegmatites analysed in this study formed in several episodes since the Palaeoproterozoic (~1.8 Ga). Most dated pegmatites are associated with the Pan-African orogeny, and pegmatite formation is indicated for the early, main and late stages of this episode, spanning over 150 m.y. Some pegmatites are Mesozoic in age. Regionally and episodically different magma sources can be identified.

The Palaeoproterozoic 1859 Ma **CNC pegmatites** from Nthalire in Chitipa, containing a variety of gem-tourmaline, are the only pegmatite of this age and therefore are not compared to other pegmatites. Their tectonic setting is not well known but in time they correlate with widespread plutonism in East Africa (Brewer et al., 1979; De Waele et al, 2006). Their source is unclear because of a large uncertainty in their Sr initial (Sr_i 0.716±0.024; Section 6.2, Table 6.1). The Rb, Sr and Ba elemental patterns show S-type granite affinity, but their source pluton is not exposed. The pegmatites, like all others analysed in this study except CCC (13.6 km), were emplaced into shallow crust at less than 10 km.

The earliest Pan-African NYF pegmatites THMB, MNM, NNO1 and the Mesozoic ZA pegmatites, emplaced at ~ 730-597 Ma and 120 Ma, respectively, are mainly mineralised with gem zircon, except NNO1, which contains gem tourmaline. No Sr_i data are available for these pegmatites, and hence the importance of crustal or mantle sources cannot be estimated. The pegmatites are mildly alkaline and K-rich, which are characteristics of A-Type granites, which is in agreement with the rift/extensional tectonic setting that the hosting crust was exposed to at the times of THMB, NNO1 and ZA pegmatite emplacement. The earliest Pan-African pegmatites were emplaced at ~730 Ma, which corresponds to initiation of the Pan-African Wilson Cycle during the breakup of Rodinia at about 720-735 Ma (Unrug, 1998). The 597±19 Ma MNM pegmatites however fall in a time period that may correlate with early Pan-African collisions, such as the collision of the Nampula terrane with the East African Orogen in nearby northern Mozambique (Unrug, 1998; Grantham et al., 2013). The large uncertainty of the age date does not allow determining whether the pegmatites were emplaced prior, during or after collision. The lack of significant deformation of the pegmatite may suggest the latter. The Mesozoic rift related ZA pegmatites were emplaced at ~120 Ma and are very likely genetically related to an anorogenic magmatic suite (Woolley, 2001) that formed during the initiation of the East African Rift (McConnell, 1972).

The GNS pegmatites are associated with the main contractional episodes of the Pan-African orogeny, emplaced at around 555 Ma. This follows high-T low-P metamorphism (Kröner et al., 2001), likely related to the collision of the North and South Gondwana during the Kuunga Orogeny,

which occurred around c. 580-530 Ma (Unrug, 1998; Grantham et al., 2013; Macey et al., 2013). However, the pegmatites were emplaced after the regional metamorphic peak, when the host rocks had been exhumed to around 4.9-7.9 km. The source granite of these pegmatites must have formed with a significant mantle contribution, indicated by low strontium initials around 0.7055. This is in agreement with observations that many Pan-African rocks in the Mozambique Belt were derived from juvenile material (Möller et al., 2000; Maboko and Nakamura, 2001).

Most pegmatites dated in this study were emplaced in the waning stages of the Pan-African Orogeny. The earliest of this group, the amethyst-mineralised CUB pegmatites, emplaced in the Cambrian at ~520 Ma, can be correlated with regional post-collisional extension and abundant plutonism observed in nearby NE Mozambique at 520-515 Ma (Grantham et al., 2007; Macey et al., 2007; Bingen et al., 2009; Ueda et al., 2012). These younger ages correlate with the Kuunga Orogeny. However, the pegmatites have no direct relationship with an exposed granite intruding at the same time. The CUB pegmatites are derivatives of crustal melting, as indicated by their reasonably high Sr_i of 0.718733. Decompression melting of lower or midcrustal high-T rocks during post-collisional collapse or crustal relaxation might be a viable process to generate crustal granites and pegmatites at that time.

Pegmatite emplacement carried on for several tens of million years, with the GCW (498 Ma), DHD (489 Ma), GM1 (485 Ma), and GN1 (460 Ma). All of these have high Sr initials (0.776-0.790) and therefore derived from crustal material, possibly with some secondary contamination during melt flow in reactive continental crust. Their tectonic association with the Pan-African cycle is questionable, particularly for the younger Ordovician pegmatites. However, there are precedents for post-orogenic pegmatites that cannot be related to coeval plutonism, and that follow long periods of high-temperature metamorphism and granitic plutonism (Shaw et al., 2016). The Orange River Pegmatite Belt in South Africa, emplaced 10-30 m.y. after the end of exposed granitic plutonism and high-temperature metamorphism, is such an example (Thomas et al., 1994; Doggart, 2018). Remarkable is that in Malawi the crust, irrespective of several cycles of high temperature metamorphism, anatexis and magma mobility still was suitable to produce granitic melts enriched in rare elements, in absence of an obvious heat source.

Timing of Pegmatite Emplacement and Links to Global Pegmatite-Forming Episodes

A summary of data that associate the likely pressures of pegmatite emplacement and solidification and the time of their emplacement with the P-T-t data available for the respective host rocks is presented in Table 9.2. It is evident that the pegmatites were emplaced at lower pressure than the

pressure at which their host rocks equilibrated during their regional metamorphism. This places the pegmatites either on the retrograde P-T paths of the host rocks or into the context of orogenic event that postdate the orogenies that formed the host rocks. The classified pegmatites are chronologically linked to regional periods of pegmatite formation and other key events in the Pan-African Mozambique Belt in Tanzania, Mozambique and Kenya (Table 9.2).

Table 9. 2: A summary of host rock, their metamorphic grade, P-T conditions and age from literature, results of dating data, estimated P-T conditions and recorded magmatism.

Studied Pegmatites	**Intruded Host Rock, Metamorphic grade and age from Literature**	**P-T conditions of Formation and Age Results estimated at 400 - 600 ^{o}C**	**Recorded Magmatism**
CNC	cordierite gneiss (Ray, 1975); garnet-cordierite granulite peak P-T of 750-850 ^{o}C at 5-5.5 kb at 1995 Ma (Ring et al., 1997); granulite facies at ~1880 Ma –Katuma (Daly, 1988)	1.4-2.5 kb at 1859±20 Ma (Rb-Sr)	1875 Ma – Upangwa, 1871 Ma - north Lupa, 1864 Ma – Ufipa (Daly, 1988); 1868±7 Ma, 1860±13 Ma (Brewer et al., 1979; De Waele et al., 2006)
CCC, MWC	greenschist to amphibolite facies (Peters, 1975); amphibolite facies ~635 ^{o}C at 5.5 kb at 580-550 Ma (Ring et al., 2002); 569-527 Ma – Lichinga, (Bingen et al., 2009)	2.2–3.6 kb (MWC), 1.4-2.3 kb (CCC) at 498.4±5.2 Ma (Rb-Sr)	Lithospheric 550-480 Ma delamination in Mozambique, Madagascar (Fritz et al., 2013); Cambro – Ordovician granites at 535-470 Ma (Macey et al., 2007 and Grantham et al. 2007).
GM, MEM, HEM	greenschist facies rocks; gneiss, augen gneiss (Gaskell 1973); Amphibolite facies at ~635 ^{o}C at 5.5 kb at 580-550 Ma (Ring et al., 2002)	0.9–2.6 (GM and MEM), 1.1-2 kb (HEM) at 485.1±4.8 Ma (Rb-Sr)	550-480 Ma extension (Fritz et al., 2013), Late to post tectonism plutonism at 517-493 Ma; Cambro – Ordovician granites at 535-470 Ma (Macey et al., 2007 and Grantham et al., 2007)
DHD	gneiss (Walter, 1972); High temperature metamorphism at 1080-1050 Ma, Zambia (Zambia; Johnson et al., 2005; De Waele et al., 2008)	0.9-1.8 kb at 489.0±5.1 Ma.(Rb-Sr)	550-480 Ma extension (Fritz et al., 2013); Late to post tectonism plutonism at 510-470 Ma (Zambia; Johnson et al. 2005; De Waele et al., 2008); Cambro – Ordovician granites at 535-470 Ma (Macey et al., 2007 and Grantham et al., 2007)
GNS	gneiss, granulite (Walshaw, 1965); High temperature metamorphism; amphibolite to granulite overprint at 950 Ma and at 550-520 Ma (Unango-Mozambique; Bingen et al., 2009); Granulite facies 770-780 ^{o}C at 4.3-6 kb at 605-550 Ma; high grade metamorphism at 571-549 Ma (Kröner et al., 2001)	1.4-2.1 kb at 555.4±4.7 Ma; and 1.3-2.9 kb at 552.4±6.0 Ma; (Rb-Sr)	East African orogen 560-550 Ma (Möller et al., 2000; Meert, 2003); 605-550 Ma magmatism (Kröner et al., 2001); late Neoproterozoic granitic rocks at 575-545 Ma – NE Mozambique (Macey et al., 2007 and Grantham et al., 2007); 550-480 Ma post-tectonic magmatism (Unango-Mozambique; Bingen et al., 2009).
MNS	hornblende, biotite garnet gneiss (Walshaw, 1965); High temperature metamorphism; amphibolite to granulite overprint (Unango-Mozambique; Bingen et al., 2009). Granulite facies 770-780 ^{o}C at 4.3-6 kb at 605-550 Ma high grade metamorphism at 571-549 Ma (Kröner et al., 2001)	1-2.3 kb at 459.6±5.2 Ma (Rb-Sr)	Waning stages of Pan-African cycle, 605-550 Ma magmatism (Kröner et al., 2001); 550-480 Ma post-tectonic magmatism (Unango-Mozambique; Bingen et al., 2009). Cambro – Ordovician granites at 535-470 Ma (Macey et al., 2007 and Grantham et al., 2007)
CUB	granulite, biotite garnet gneiss (Bloomfield and Garson, 1965); High temperature metamorphism; amphibolite to granulite overprint (Unango-Mozambique; Bingen et al., 2009). Granulite facies 770-780 ^{o}C at 4.3-6 kb at 605-550, Ma high grade metamorphism at 571-549 Ma (Kröner et al., 2001)	1.1-1.8 kb at 520±5.5 Ma (Rb-Sr)	520-515 Ma Kuunga tectonic ext. and plutonism 605-550 Ma magmatism (Kröner et al., 2001); 550-480 Ma post-tectonic magmatism (Unango-Mozambique; Bingen et al., 2009); Cambro – Ordovician granites at 535-470 Ma (Macey et al., 2007 and Grantham et al., 2007).

In Tanzania, pegmatites were formed at ~800 Ma, granitoids at 750 Ma, other pegmatites at 650-600 Ma, late pegmatites bearing beryl, tourmaline, Sn, Ta and U at 525 Ma and late pegmatites at 450 Ma (Foster et al., 2001; cf. Section 3.3 Table 3.1; Figure 3.6). The dated emplacement episodes are further linked to major global periods of pegmatite formation. According to McCauley and Bradly (2014), granitic pegmatites have global age peaks at 1853, 988, 525 and 483 Ma, ages that broadly correspond to supercontinent assembly. Furthermore, they observed some similarity in age distribution between both LCT and NYF pegmatites at 1800, 962, 529, and 485 Ma. However, NYF pegmatites have a strong age cluster at ca. 1000 Ma, which is well known in other parts of East Africa (Rwanda, DRC, Tanzania; Tack et al., 2010, Melcher et al., 2015; Büttner et al., 2016), bearing beryl-columbite-tantalite, and gem tourmaline, among others. However, no Mesoproterozoic gem-bearing pegmatites have been analysed in this study, although the Mesoproterozoic orogenic period is prominently represented in the geology of Malawi. Possibly this is caused by the limited sample number that could be processed in this study. There is no obvious reason why the Kibaran orogeny should not have produced gem-bearing pegmatites in Malawi.

In the larger regional context, the pegmatites emplaced at the Cambrian/Ordovician boundary and the Ordovician zoned pegmatites (MWC, CCC) have some similarities with zoned Ordovician granitic pegmatites of Nampula, Tete and Zambezia in Mozambique, which bear tourmaline, topaz, spessartine, beryl (aquamarine), spodumene and rose quartz (Bingen et al., 2009; Neiva, 2013; Section 3.3.1). The Ordovician pegmatites in the Alto Ligonha Province in Mozambique bear gemstones such as green, bluish green and pink beryl (Lächelt, 2004; Melcher et al., 2008b; Neiva, 2013). However, these pegmatites are Complex type, lepidolite subtype, whereas their counterparts (CCC and MWC) in this study in Malawi belong to Beryl type, Beryl-columbite subtype; Complex type, Elbaite subtype, and fall in the Miarolitic Class, Mi-Li subclass, beryl-topaz type (Cërny, 1991a; Cërny and Ercit, 2005). The CCC and MWC pegmatites are less evolved and therefore lack spodumene and columbite mineralisation. Furthermore, the granitic pegmatites in Mozambique bear Li-Be-Ta-Nb deposits, which may be present also in Malawi, but have not been discovered as yet.

The Ordovician DHD pegmatites in Dowa have a similar age with GM and HEM in Mzimba, and granitic late pegmatites of Lundazi in adjacent Zambia (Graziani et al., 1983; Chapter 6, Section 6.4). The pegmatites in Zambia bear different varieties of beryl, tourmaline, spessartine, betafite, columbite, uraninite (Thatcher, 1974; Carranza et al., 2005), whereas the GM and HEM

pegmatites mostly bear beryl and aquamarine (Section 4.3.3). Furthermore, the DHD pegmatites in central Malawi only bear a variety of tourmalines.

In terms of estimated P-T conditions, the Lundazi pegmatites were formed at a pressure of 4 kb at temperatures of 430-650 ^{o}C, corresponding to 15 km (Graziani et al., 1983). The GM, HEM pegmatites have estimated low formation pressure of 0.9-2.6 kb at 400-600 ^{o}C, corresponding to 3.4-9.8 km depth, similar to the DHD pegmatites that were emplaced at 3.4-6.8 km. This means that the pegmatites in Lundazi, in eastern Zambia were formed deeper than the GM, HEM and DHD pegmatites. Moreover, the Lundazi pegmatites show that they are more evolved than their counterparts in Malawi, containing a more diverse rare mineral assemblage.

9.2 PEGMATITE MELT GENESIS AND EVOLUTION

Field relationships

The studied pegmatites show intrusive relationships, crosscutting or parallel to pre-existing host rock structures. There is no evidence of significant metasomatic interaction with the host rocks, or the local influx of, or interaction of pegmatitic melt with, anatectic melt that may have existed in the host rocks at some stage prior to pegmatite emplacement (Chapter 4). No pegmatite analysed in this study shows deformation, except for minor brittle overprints along dyke margins of pegmatites GNS1 and MSN1B (Section 4.3.8). This suggests that they were emplaced at times post-dating the main tectono-metamorphic events that formed their host rocks. This is in agreement with the overall shallow emplacement depth that is indicated by the results of fluid thermometry.

Fractional Crystallisation

All the analysed pegmatites show that they are generated from residual melts by fractional crystallisation, a process where a buoyant separation of an aqueous fluid from the silicate melt affects the redistribution and concentration of chemical compounds and components, which may contribute to compositional variations (Section 1.3; Section 2.8). The process involves soluble flux components such as B, P, F and volatiles to lower the crystallisation and solidification temperatures of the magma, thereby decreasing the nucleation rates, melt polymerization and viscosity, and increasing diffusion rates and solubility. These processes are critical to the development of large crystals (e.g. Swanson and Fenn, 1992; Keppler, 1993; Simmons and Webber, 2008; Nabelek et al., 2010), and the large grain sizes, reaching up to 1m for instance in pegmatites HEM, and GM show that these processes apply to the investigated pegmatites. They

involve inward progression of flux bearing granitic melt from the margins of the pegmatite body to the centre, forming textural relationships of minerals reflecting the increasing degree of pegmatite undercooling, nucleation rate and growth rate during crystallisation (London et al., 1988; Webber and Simmons, 2007; Simmons et al., 2012). The habits of individual crystals evolve to more graphic and radial shapes with increasing degree of disequilibrium between the melt and a crystalline assemblage (London, 2008). These features are prominent in pegmatites MWC, DHD and GNS1 (Sections 4.3.3; 4.3.6 and 4.3.9, Figures 4.4b, 4.9b and 4.12e), indicating the intense oversaturation and undercooling of the melt in these pegmatites.

The abundance of phases in the studied pegmatites, containing incompatible rare elements that concentrate in evolved residual melts (boron and lithium in tourmaline; beryllium in beryl; fluorine in topaz) can only crystallise after significant fractional crystallisation (London, 2008). Commonly (pegmatites DHD, GNS, MSN), miarolitic gem mineralised cavities are likely to have formed in the final stages of fractional crystallisation and pegmatitic melt evolution (Simmons et al., 2003, London, 2008).

Mineralogy

The pegmatites show a variation of mineral assemblages that are consistent with primary crystallisation from volatile-rich siliceous melt as postulated by Jahns and Burnham, (1969), Cërny, (1991a) and London, (1990). Generally, the gem-bearing pegmatites show a combination of some of the following minerals: quartz, alkali feldspar, plagioclase, muscovite, lithian muscovite, beryl, tourmaline, and topaz except for epidote that is included in the Cambrian pegmatites (CUB) from Balaka. These can be grouped into simple mineralisations that lack columbite, betafite, and high-Li phases such as spodumene of petalite. This indicates that the analysed pegmatites are less differentiated than pegmatites of similar age and setting in neighbouring Mozambique, Tanzania and Zambia, in which high-Li phases are regularly observed (Muhongo et al., 1999; Carranza et al., 2005, Neiva, 2013).

The Pan-African pegmatites emplaced at the Cambrian/Ordovician boundary are mineralised with beryl, aquamarine, tourmaline and topaz in the CCC and MWC pegmatites in Chitipa in north Malawi whereas those to the south of Chitipa have gem beryl and/or aquamarine and amethyst in the Ordovician pegmatites (GM, HEM1B-2A-3B) in Mzimba (Section 4.3.3). By contrast, Palaeoproterozoic pegmatites (CNC) in northern Malawi, late Pan-African GNS and

Ordovician DHD and MSN pegmatites in central and southern Malawi show tourmaline without beryl (Chapter 4, Appendix 1.1).

Mineralisation of both beryl and tourmaline in pegmatites (CCC, MWC and HEM1B-2A-3B beryl) is bound to the Rare Element Class and Miarolitic Class, emplaced at the Cambro-Ordovician boundary (~498-481 Ma; Appendix 1.1) in the northern region. The magma of these pegmatites shows crustal sources. The Be and B contents in pegmatitic muscovite are not strictly correlated with the presence or absence of beryl. For instance, Be concentrations in muscovite from the beryl-mineralised CCC, MWC and HEM1B-2A-3B range between 2 and 30 ppm. In other pegmatites with Be concentrations in muscovite of 0-19 ppm, such as in the Palaeoproterozoic CNC pegmatites or the Cambrian and Cambro-Ordovician HEM4B, GNS, MSN, and CUB pegmatites, beryl is absent. The boron concentration in pegmatitic muscovite varies considerably and ranges between ~40 and 200 ppm in most samples. GM has somewhat lower (26-16 ppm); in sample MSN one analysis shows 7712 ppm. Tourmaline is present in all these pegmatites except in CUB pegmatites.

This somewhat inconsistent relationship between Be and B concentrations in muscovite and the presence and absence of the phases containing these elements as major components is likely related to the timing of muscovite and beryl or tourmaline growth. Where beryl and tourmaline coexist with low Be/B muscovite, the muscovite postdates beryl or tourmaline growth and grew in a Be/B-depleted melt (e.g. pegmatite HEM4B). Moderate or highly variable Be/B contents in muscovite will be present where tourmaline and beryl crystallise concurrently or in overlapping time episodes with muscovite (pegmatites GM3, GM5 and MWC).

Geochemical Behaviour of Elements in the Pegmatitic Melts

According to the mica geochemistry from all studied pegmatites (cf. Chapter 7, Section 7.2.1 to 7.2.5, Table 7.1A-4A), the white micas have low CaO and Na_2O but high LILE content. Pegmatitic melt fractionation enriches alkali elements, leading to abundant muscovite growth in which K may be substituted particularly by Rb or Li. The observation that the trace elements trends show enrichment in Rb, Be, Cs, Ta, Nb and depletions Ba, Sr and P with increasing distance to the source pluton (e.g. Senga Bay granite, Section 6.4) correlates with increasing fractionation and volatile enrichment of the pegmatite melt (Cërny 1991a; Figure 2.1). Although the source plutons for most analysed pegmatites, such as the Palaeoproterozoic CNC pegmatites, the Pan-African Cambrian CUB and GNS pegmatites, the Cambro-Ordovician GM, HEM, DHD

and MSN pegmatites are not exposed, the observed element trends are interpreted as indicative of increasing fractionation of the pegmatitc melt and increasing distance to the hidden source granites. For instance, the most evolved pegmatites, such as GM3 and GM5 (Figure 7.8A and 7.8D), showing the highest abundance of rare elements (Be, Li, Rb, Ta, Nb), are considered to show the strongest differentiation amongst the studied pegmatites, and probably the largest distance between pegmatite location and granite source. Here we also see the highest Li content in lithian muscovite (3-4 wt% lithium oxide in GM3; Figure 7.5E). However, the differentiation and fractionation did not progress to stages where Li phases such as spodumene would have become stable.

This overall moderate fractionation of the studied pegmatites is also seen in Nb and Ta patterns in GM3, GM5, CCC and MWC pegmatites (Figure 7.8D). GM3 pegmatites have highest concentrations of Nb and Ta compared to the other pegmatites in this category, but the Nb content is significantly lower than the Ta content. This agrees with observations that Ta and Nb behave differently during crystallisation because of differences in solubility of Nb and Ta in Li-rich pegmatitic melts (Linnen, 1998). The relatively low contents of Nb, Ta and Cs, which are mineralisation indicators of pegmatite bodies (Beus, 1996), suggest a generally low or moderate degree of melt fractionation.

However, some of the Neoproterozoic gem tourmaline-bearing pegmatites (GNS), and the Ordovician gem tourmaline- and sunstone-bearing pegmatites (MSN) show high enrichments in Ba, Ti, and moderate enrichments in Sr (Section 7.25, Figure 7.18, Figure 7.22). This still correlates with rare-element enrichment through fractionation, where incompatible elements get increasingly enriched in the pegmatitic melt with increasing fractionation. However, high Ti, Ba and Sr contents (i.e. compatible elements) together with low Y contents, as seen in for instance GNS and MSN pegmatites (Figure 7.22B) suggest that fractionation was still in an early stage (e.g., Belousova et al., 2002).

Similarly, the element patterns in the Cambrian amethyst-bearing pegmatites (CUB) from Balaka vary unsystematically (Figure 7.24B-D; Figure 7.25B), implying differentiation of moderately fractionated pegmatites in which alkali feldspar and mica fractionate the bulk of alkali metals. In the gem tourmaline bearing pegmatites from Dowa (DHD; Figure 7.13) the Sr concentration varies according to occurrence of K-feldspar and muscovite, as a result of greater Sr affinity for K-feldspar than for muscovite (Alfonso et al., 2003).

Also the REE concentrations and variation patterns correlate magmatic fractionation processes during progressive differentiation of felsic magmas (London, 2008). REE patterns normalised to upper continental crust (UCC) typically show REE depletion. The micas from the Palaeoproterozoic (CNC) pegmatites, the Pan-African (CCC, MWC, GM and HEM) pegmatites from Chitipa and Mzimba, and the Pan-African (DHD) pegmatites show moderately depleted REE. The Neoproterozoic (GNS) and Ordovician (MSN) pegmatites from Ntcheu, and the Pan-African Cambrian (CUB) pegmatites from Balaka show more depleted LREE than HREE (Figure 7.19, Figure 7.23, and Figure 7.27).

The REE patterns normalised to chondrite (Nakamura 1974; Figure 7.28A-F) show more enriched HREE than LREE. The micas from the Pan-African (CCC, MWC, GM, HEM and DHD) pegmatites from Chitipa and Mzimba and the Neoproterozoic GNS and Ordovician MSN pegmatites from Ntcheu generally show depleted LREE, less depleted MREE and enriched HREE (Figure 7.28B-D, Figure 7.28F). The extent of LREE depletion correlates with the extent of pegmatite melt fractionation (Belousova et al., 2002). Variable depletion in MREE and HREE, as seen in pegmatites CCC, MWC, HEM and DHD (Figure 7.28A-F), suggests variably evolved pegmatitic magma (Wang et al., 1989). Accordingly, DHD pegmatites, which show stronger MREE depletion, formed from less evolved magma than CCC and MWC, where MREE and HREE are more enriched. Van Orman et al. (2001) observed that more enriched MREE and HREE indicate a low-temperature partitioning, because diffusion rates in melt are faster for MREE than for LREE. This shows that the pegmatites formed from residual melts enriched in incompatible components, volatiles, fluxes and rare elements.

The Pan-African Cambrian CUB pegmatites from Balaka (Figure 7.29A) show a flattened pattern with slightly enriched LREE, less depleted MREE and slightly enriched HREE, suggesting moderate fractionation. However, these data from CUB pegmatites were obtained from biotite, which may limit the comparability with other pegmatites where trace and rare earth elements were obtained from muscovite.

All the REE patterns show strong positive Eu and negative Ce anomalies (e.g. Figures 7.28A-F, Figure7.29A). Taylor et al. (1986) proposed that a weak negative Ce signature and strong positive Eu signature denotes low degrees of fractionation, which is in agreement with the interpretation of other geochemical indicators presented above. The negative Ce anomalies (Figure 7.28A-F, Figure 7.29A) indicate oxidising conditions during mineralisation (Akagi and Masuda, 1998). Furthermore, Rudnick and Gao (2003) observed that during melt formation

element transportation is promoted, and solubility of metals in melt is affected by the oxidation state within the magma. This may suggest that gemstone mineralisation in the analysed pegmatites has been promoted by periods of oxidation in the late evolution of the pegmatitic melts.

Pegmatites with white mica that is moderately enriched in rare elements, such as GM3 and GM5 (Figure 7.9B), are interpreted to have formed from the more evolved melts, in which such elements would have been more abundant. During the pegmatite melt evolution, rare elements fractionate progressively into solid and volatile phases and the residual melt eventually becomes rich in incompatible elements. Gem phases such as beryl and tourmaline form from such residual melts with abundant beryllium, lithium and boron. Fluxing components such as B lower the viscosity, melting and crystallisation temperatures (London et al., 1988; London, 1990; 1992; 1997; London and Morgan, 2012). The lowered viscosity of the melt promotes rapid growth and large crystals in pegmatites (Swanson and Fenn, 1992). Li and B contents vary in the analysed pegmatite systems. For instance, CCC pegmatites have muscovite with high Li (~845 ppm), and low B (~35 ppm; Section 7.2.1, Table 7.1B), whereas GNS3 mica has low Li (~6 ppm) and high B (~459 ppm; Section 7.2.5, Table 7.4B). If more Li is present in the system, elbaite will form and consume Li and B. If some boron remains in the system after Li is consumed (e.g. CCC pegmatite; Section 4.3.3), the boron forms schorl-dravite in the pegmatite.

There is textural evidence for an increase in degree of undercooling and nucleation rate during crystallisation that progresses from the wall to the core (Webber and Simmons, 2007, Sections 4.3.3 and 4.3.9, CCC, GNS and MSN). A variety of growth textures include comb texture (e.g. pegmatites CNC, GNS3; Chapter 4; Sections 4.2.3, and 4.3.9), radial growth (e.g. pegmatite GNS1; Section 4.3.9), graphic intergrowth (e.g. pegmatite MWC, ZA; Sections 4.3.3 and 4.4.1), and random orientation (sample MSN3A, Section 4.3.9), indicate specific thermal or thermodynamic processes related to the degree of undercooling and oversaturation of the residual melt. Thermometric estimates suggest that the pegmatites were emplaced in shallow and therefore likely cold crust. This will have increased the cooling rate further, promoting the generation of the related and indicative textural features.

In summary, the geochemical results indicate that high quality gemstones are found where mica is enriched in incompatible elements. This applies particularly to the aquamarine- and beryl-, lithian muscovite- and occasional tantalite-bearing Ordovician GM pegmatites in Mzimba and CCC and MWC pegmatites in Chitipa (Section 4.3.3, Appendix 1.1), in which mica is

particularly enriched in Be and Li (Section 7.2.2 and 7.2.3). These pegmatites are comparatively highly evolved and hence provide conditions favourable for gemstone formation. By contrast, the least evolved pegmatites do not show beryl mineralisation but only tourmaline. Accordingly there is a correlation between melt evolution, mica composition and the potential of gem mineralisation.

The distribution of gemstones within the pegmatites is variable, with some gemstones in the wall and border zones, others in intermediate zones, in border of the core zone and in miarolitic cavities. Some gem-garnet and tourmaline are observed in the wall and border zones of MWC pegmatites (Section 4.3.3), some gem tourmaline are observed in the intermediate zone and miarolitic cavities in CNC pegmatites (Section 4.2.3) whereas most gem tourmaline and beryl in the CCC pegmatites form in the border of the core zone (Sections 4.3.3).

It is likely that CZR process contributed to the crystallisation of high quality gems in these pegmatites because elements incompatible with the main pegmatitic phases become concentrated in a boundary layer melt where fluxes and rare elements may get enriched and facilitate the nucleation of rare mineral phases (London, 2008; London and Morgan 2012).

Most gem-bearing pegmatites in the study areas contain mineralised miarolitic cavities (e.g. DHD, GNS, MSN pegmatites, Sections 4.3.6 and 4.3.9), which are magmatic-hydrothermal transitional features and therefore are interpreted as the last pegmatitic features that have formed during solidification. Miarolitic cavities commonly contain the highest quality tourmalines in DHD, GNS, and MSN pegmatites. According to Simmons et al. (2012) and London (2008), miarolitic pockets develop when the saturation of volatiles in the residual melt is exceeded at the final stages of crystallisation.

Implications of Fluid Thermometry and Compositional Variations on Pegmatite Genesis

The studied fluid inclusions in quartz from micas in the pegmatites from different locations are discussed in the light of their composition, salinity and associated mineralisations. The description of each sample is provided in Chapter 8. Assuming temperatures of solidification of 400 to 600 °C emplacement depths for most pegmatites must have been between 3.4 and 9.8 km, well in the shallow brittle crust. Only CCC pegmatites show an isochore at higher pressure which, at 400-600 °C implies an emplacement depth of 8.3-13.6 km. Accordingly, all pegmatites have intruded into shallow crust, much shallower than the P_{max} of their respective host rocks.

The abundant textures of strong undercooling in many pegmatites, the sharp contacts and the lack of evidence of significant interaction between intruding pegmatite and host rocks at emplacement level is in agreement with pegmatites intruding cold, brittle and shallow crust. Hence, the P-T-d evolution that formed the metamorphic assemblages and fabrics in the host rocks predates the pegmatite emplacement, which either intruded at the end of their retrograde P-T evolution or in younger orogenic cycles. This interpretation is also consistent with the available geochronological data.

For instance, augen gneiss host rocks of pegmatite GM went through a cycle of HT-LP metamorphism in the early Kuunga orogeny, reaching 635 ^{o}C and 5.5 kbar at 580-550 Ma. Pegmatite GM was emplaced at ~ 485 Ma and at pressures of less than 3 kbar along sharp contacts. At that pressure and time the host rock likely had cooled down to sub-greenschist facies temperatures. Similarly, granulite host rocks of pegmatite MSN in Ntcheu in central region went through a cycle of HT-LP metamorphism in the early Kuunga orogeny, reaching 770-780 ^{o}C and 4.3-6 kbar at 605-550 Ma. Pegmatite MSN was emplaced at ~460 Ma and at pressures of less than 2.4 kbar along sharp contacts. Low pressure and low/moderate temperature of pegmatite emplacement are in agreement with highly differentiated melt and miarolitic features which are suitable for crystallisation of gemstones (Cërny, 1991a).

However, the granitic sources of these pegmatites indicate that at depth the crust remained hot enough over extended time periods to produce granitic magma from fertile sources. The low Sr initials in pegmatite GNS1 and GNS4 suggests that the parent granites at 555 and 552 Ma, when North and South Gondwana collided, formed with a contribution of juvenile mantle material. The younger Pan-African and Cambro-Ordovician pegmatites however formed from crustal granitic magmas (section 6.4).

Most of the analysed pegmatites show common hydrous-carbonic fluids that were present at the latest stages of pegmatite formation at the time when quartz crystallised. This is in agreement with occurrence of CO_2 and H_2O together in granitic fluids (Thomas et al., 1989, Nabelek and Ternes, 1997, Sirbescu and Nabelek, 2003; Roedder, 1984). The CO_2-bearing fluids were showing a depression of eutectic temperatures compared to pure CO_2 indicating the presence of components like CH_4, C_2H_6, C_3H_8, H_2S, and N_2 (Sections 8.3-4, Tables 8.1-16). Generally low CO_2 concentrations observed in some fluid inclusions (e.g. GM3, Section 8.4.3, Figure 8.9A) may have resulted from low solubility of CO_2 in felsic melts (Thomas et al., 2009). The main solutes in fluid systems as indicated by variable values for first melting temperature of ice for inclusions from different pegmatites show the presence of low-saline H_2O-Na(±K)Cl fluid (e.g.

Type 1a, HEM2C) to complex brine (LiCl-NaCl) in GM3 pegmatites (Section 8.4). The low salinities indicate magmatic origin (Cërny 1993b; London 1995, 1996), and the largely uniform homogenisation temperatures and salinities in each investigated sample suggest that the pegmatitic fluids were largely homogeneous. Fluid inclusions with Na and K in the system are predominant, as it can be expected from evolved granitic melts that crystallise alkali feldspar and albite. The fractionation of Na and perhaps K into albite and alkali feldspar reduced salinities dusting progressive crystallisation which is reflected in different average salinities in different samples. The Palaeoproterozoic gem tourmaline-bearing pegmatite CNC pegmatite provides an example. Aqueous fluids (H_2O-NaCl) in the sample CNC1B_(Type 5a) and aqueous carbonic fluids in sample CNCB2 (Type 1a) are both primary and come from the same pegmatite. The lower salinity in the aqueous inclusions suggests that they formed at a later stage. This correlates with a decrease from the moderate salinity (Type 1a, CNCB2_1) to low salinity (Type 5a, CNC1B_1) fluid inclusions. The low salinity pegmatitic and hence late magmatic fluid was rich in B which led to the abundant tourmaline crystallisation. The precipitation of quartz, tourmaline, K-feldspar, muscovite, albite, and tantalite removes B, Li, K, Si, Na, Al, and Ta from the melt. The extraction of Na and K during progressive crystallisation reduced the salinity in the fluid and is interpreted as a reason for the variable salinities of fluid in the CNC pegmatites.

Since the gem phases and the quartz are late formations in the pegmatite solidification the fluids captured in quartz were present during gemstone crystallisation and therefore reflect the fluid environment in which these gemstones formed. At the latest stage, such fluids were exsolved from the residual melt and concentrated in miarolitic cavities or escaped from the pegmatite bodies.

In places, the pegmatitic fluid shows compounds that suggest contamination with metamorphic fluids, such as CH_4 or larger organic molecules during formation. This contamination must have occurred closer to the source granite because at the shallow emplacement level the crust was unlikely to have shown fluid activity significant enough to contaminate the pegmatitic fluid, particularly since the contacts of the pegmatites do not show evidence of significant metasomatism and contamination. Therefore, the observed CH_4 and other C-H compounds in the low salinity fluids suggest organic material extracted from metasedimentary rocks that mixed with the pegmatitic or the primary granitic fluid. This contamination however is not likely to have taken place anywhere near the level of emplacement, which was shallow and occurred in cold crust.

The contamination of pegmatitic fluids with host rock fluids containing organic compounds show some regional and age patterns. All late Pan-African pegmatites (DHD, CCC, MWC, GM, and HEM) are located further north than earlier Pan-African pegmatites (GNS and CUB). The late Pan-African pegmatites are seen from Dowa in the central region to Chitipa in northern region. The fluids in pegmatites related to the main Pan-African Kuunga Orogeny show more intense and regular infiltration of organic compounds, whereas in the late Pan-African pegmatites only GM5 and HEM show no such contamination. However, the more evolved Cambro-Ordovician boundary pegmatites (GM3, CCC and MWC) in northern Malawi mostly show host rock fluid influx, but the Ordovician pegmatites (MSN) occurring in southern Malawi do not. The reason for this pattern is not clear, but since gemstone mineralisation is seen in all these pegmatites, the presence or absence of host rock fluid contamination is not a factor that influences gemstone formation. Gemstone formation in the studied pegmatites is primarily controlled by the extent of melt differentiation and fractional crystallisation.

10. CONCLUSIONS AND FUTURE WORK

This first overview on gem-mineralised pegmatites from Malawi presents geochemical, geochronological and fluid analysis on a selection of pegmatites that formed mainly related to the Pan-African orogenic cycle, including the Rodinia break-up, collision, late orogenic extension/collapse and post-Pan-African episodes. One sample each formed in the Palaeoproterozoic and in relation to early East African Rift tectonics in Cretaceous time. All pegmatites analysed in this study formed from residual melts that through fractional crystallisation and evolution of granitic parent magmas became enriched in rare elements.

The pegmatites are hosted in rocks that at the time of pegmatite emplacement had largely completed their metamorphic and deformation history. They were exhumed to upper crustal levels where most pegmatites were emplaced at shallow crustal depths of less than 10 km, corresponding to ~1-2.6 kb pressure. Sharp contacts and rapid cooling of the pegmatitc melt, indicated by textural and geochemical evidence, supports low host rock temperatures at the time of emplacement. Accordingly, the metasomatic exchange between pegmatites and their host rocks at the emplacement level was insignificant. In the shallow emplacement level with rapidly progressing crystallisation, miarolitic cavities could commonly form, providing sites for the crystallisation of gemstones from these most evolved melts and fluids. Other positions within the pegmatites that commonly show gemstone mineralisation are the intermediate zones and close to the boundary with the central core.

The fluid compositions, mainly low- to moderately saline hydrous and CO_2-rich fluids, are well compatible with their granitic source. They represent a late stage of crystallisation and are accordingly depleted in the major elements that have formed the main pegmatitic mineral assemblage. Minor variations in salinity monitor the late pegmatitic growth of alkali feldspar and albite, extracting alkali metals from the residual fluids, which reduced the salinity in places. Organic components, such as CH_4 or C_3H_8 are present in some pegmatites, suggesting some contribution of fluids extracted from organic-rich metasediments. Because of the limited or negligible metasomatic exchange in the emplacement level this contamination must have taken place closer to the granitic magma source.

Fractional crystallisation was the dominant process that enriched the pegmatitic melt in rare elements. The most fractionated pegmatites, such as GM, CCC and MWC, show beryl and in places tantalite in addition to tourmaline. In less evolved pegmatites beryl is absent. The

crystallisation of exotic minerals such as tourmaline (B, Li), beryl (Be) and topaz (F) that are rare in typical granitic melts means that supersaturation is reached in the pegmatitic melt. Miarolitic cavities formed as final products of crystallisation and they also provide favourable conditions for formation of gemstones.

The Rare-Element pegmatites associated with the main contractional and post-contractional Pan-African episodes show LCT compositions. Those emplaced during the Kuunga Orogeny (~550 Ma) show a significant mantle contribution to their source, whereas the post-collisional and latest Pan-African Cambro-Ordovician pegmatites are crustal derivatives.

NYF pegmatites formed during episodes that can be associated with rifting or continental breakup. These are the early Pan-African MNM, NNO1 and THMB pegmatites, and also the East African Rift-related ZA sample. No such setting can be verified for the NYF pegmatite that formed in the Palaeoproterozoic, the CNC pegmatite from northern region. The nature of the granitic source of the NYF pegmatites is unclear. The Sr initial for the CNC pegmatite is inconclusive. No Sr initials are available for the MNM, NNO1, THMB and ZA samples, but plutonism related to rifting and continental breakup very likely will show a significant mantle component.

In age, origin and mineralisation, the gem-bearing granitic pegmatites in Malawi fit well into the regional pattern seen in neighbouring Mozambique, Tanzania and Zambia, which correlate well with the main geological entities that extend from these countries into and through Malawi. However, the studied pegmatites in Malawi show comparatively low fractionation as indicated by absence of minerals associated with more evolved melts such as betafite, lepidolite, pollucite and spodumene, which are seen elsewhere in the East African region. It is not clear whether this is a regional pattern or whether such highly evolved pegmatites have not been samples in the current or previous studies. Given the very limited exploration and research activities in Malawi in the past it is obvious that this country offers economic potential disproportional to its size.

Future Work

An obvious research and exploration target on gemstone mineralised pegmatites in Malawi would be NYF pegmatites of Mesoproterozoic age, which have not been encountered in this study. There is no reason to believe that Malawi should not have mineralised pegmatites of that age, which are abundant and successfully mined in neighbouring countries.

Furthermore, the current study did not assess local and regional zonations in individual pegmatites and pegmatite fields, which may allow to target and localise unknown gem deposits, to the benefit of local artisanal mining communities. The current study provides starting points in that regard. Since this study did not provide insight into the factors that control the quality of gemstone crystals, more research needs to be conducted on the quality of gemstones from the granitic pegmatites from different parts of Malawi.

Finally, gem deposits formed by metasomatic reactions along pegmatites in suitable host rock lithologies are likely present and have been described in Mozambique and Tanzania, producing ruby and sapphire (BRGM, 2004, Malisa and Muhongo, 1990; Simonet et al., 2000). The similar geology in southern Malawi suggests an untapped potential for a variety of gemstone species to be discovered in such settings and environments.

REFERENCES

Akagi, T. & Masuda, A. (1998). A simple thermodynamic interpretation of Ce anomaly, *Geochemical Journal*, **22**: 301-314.

Alfonso, P., Melgarejo, J. C., Yusta, I. & Francisco, V.R. (2003). Geochemistry of feldspars and muscovite in granitic pegmatite from the Cap De Creus Field, Catalonia, Spain. *The Canadian Mineralogist*, **41**, pp. 103-116.

Alfonso, P. & Malgarejo, J.C. (2008). Fluid evolution in the zoned rare-element pegmatite field at Cap de Creus, Catalonia, Spain. *The Canadian Mineralogist,* **46**, 597-617.

Anderko, A. & Pitzer, K.S. (1993a). Equation-of-state representation of phase equilibria and volumetric properties of the system NaCl-H_2O above 573 K. *Geochemica et Cosmochimica Acta*, **57**, 1657-1680.

Anderko, A. & Pitzer, K.S. (1993b). Phase equilibria and volumetric properties of the system KCl-H_2O and NaCl-KCl-H_2O above 573 K: Equation of state representation. *Geochemica et Cosmochimica Acta,* **57**, 4885-4897.

Andersen, L.S., & Unrug, R., (1984). Geodynamic evolution of Bangweulu Block, north Zambia. *Precambrian Research,* **25**, 187-212.

Anderson J.L. (1996). Status of thermobarometry in granitic batholiths *In* (eds) Brown, M., Candela, P.A., Peck, D.L., Stephens, W.E., Walker, R.J. & Zen, E., The Third Hutton Symposium of Origin of Granites and Related Rocks. *Geosociety of America*, p359.

Andreoli, M.A.G. (1981). *The amphibolites to granulite facies rocks of southern Malaw*i. Unpublished PhD thesis. University of Witwatersrand. Johannesburg, South Africa, 345p.

Andreoli, M.A.G. (1984). Petrochemistry, tectonic evolution and metasomatic mineralization of Mozambique Belt granulites from S. Malawi and Tete, Mozambique. *Precambrian Research*, **25**, 161-186.

Andreoli, M.A.G. (1990). Metasomatised granulites and eclogites of the Mozambique Belt; implications for mantle devolatilisation. *In*: Hurlbutt, H.H. and Ho, S.E (Eds.). Proceedings on the conference on stable isotopes and fluid processes in mineralisation, Queensland, 1985. *Geological Department University of Western Australia Publication* No. **23**, 121-140.

Appel, P., Möller, A. & Schenk, V. (1998). High-pressure granulite facies metamorphism in the Pan-African Belt of eastern Tanzania: P-T-t evidence against granulite formation by continent collision. *Journal of Metamorphic Geology* **16**, 491-509.

Archer, D.G. (1992). Thermodynamic properties of NaCl+H_2O system. *Journal of Physical and Chemical Reference Data,* **21**, 793.

Ashwal, L.D., Patzelt, M, Schmitz, M.D., & Bulke K. (2016) Isotopic evidence for a lithospheric origin of alkaline rocks and carbonatites: an example from southern Africa. *Canadian Journal of Earth Sciences*, **53(11)**: 1216-1226.

Bakker, R.J., (1999). Optical Interpretation of microthermometrical data from fluid inclusions: Thermodynamic modelling and computer programming. Habilitation thesis, University of Heidelberg, Germany.

Bakker, R.J. (2003). Package FLUIDS 1. Computer programs for analysis of fluid inclusion data and for modelling bulk fluid properties. *Chemical Geology*, **194**, 2-23.

Baldwin, J.R. (1993). Lithium and tantalum mineralization in rare-element pegmatites from southern Africa. *Unpublished Ph.D. thesis, Univ. St. Andrews,* **314**pp.

Belousova, E.A., Griffin W.L. & O'Reilly S.Y. and Fischer N.I. (2002). Igneous zircon: trace element composition as an indicator of source rock type. Contrib. *Mineralogy Petrology,* **143**: 602-622.

Beus, A.A. (1996). Distribution of tantalum and niobium in muscovites from granitic pegmatites. *Geokhima* **10**, 1216-1220.

Bingen, B., Jacobs, J., Viola, G., Henderson, I.H.C., Skar, O., Boyd, R, Thomas, R.J., Solli, A., Key, R.M. & Daudi, E.X.F. (2009).Geochronology of the Precambrian crust in the Mozambique Belt of NE Mozambique, and implications for Gondwana assembly. *Precambrian Research*, **170**, 231-255.

Bloomfield, K. (1957). The geology of the Nkana coalfield, Karonga District, *Bulletin. of Geological Survey Nyasaland,* **8**.

Bloomfield, K. (1958), The geology of the Port Herald area. *Bulletin of Geological Survey Nyasaland*, **8**.

Bloomfield, K. (1965). Infracrustal ring – complexes of southern Malawi. – *Memoir Geological. Survey Malawi,* **4**, p.115.

Bloomfield, K. (1965). The geology of Zomba area. *Bulletin Geological Survey Malawi,* **16**, 193p.

Bloomfield, K. (1968). The pre-Karoo geology of Malawi, *Memoir, Bulletin Geological Survey,* **5.**

Bloomfield, K. and Garson, M.S. (1965). The geology of the Kirk-Range-Lisungwe Valley Area, *Bulletin Geological Survey, Malawi* **17**.

Bodnar, R.J. (2003a). Introduction to fluid inclusions. *In*: Samson, I., Anderson, A., Marshall, D. (Eds.) Fluid inclusions: analysis and interpretation. *Mineralogical Association of Canada Short Course Series Volume* 32, pp1-8.

Boven, A., Theunissen, K., Sklyarov, E., Klerkx, J., Melnikov, A., Mruma, A., & Punzalani, L. (1999). Timing of exhumation of a high-pressure mafic granulite terrane of the Palaeoproterozoic Ubende Belt (West Tanzania). *Precambrian Research,* **93**, 119-137.

Bowden, P. & Whitley, J. E., (1974). Rare earth element patterns in peralkaline and associated granites, *Lithos*, **v7**, pp15-21.

Bowers, T.S. & Helgeson, H.C. (1983). Calculation of the thermodynamic and geochemical consequences of non-ideal mixing in the system H_2O-CO_2-NaCl on phase relations in geochemical systems. Equation of state for H_2O-CO_2-NaCl fluids at high pressures and temperatures. *Geochemica et Cosmochimica Acta,* **47**, 1247-1275.

Brewer, M.S., Haslam, H.W., Derbyshire P.F.P. & Davis A.E. (1979). Rb-Sr age determination in the Bangweulu Block, Luapula Province, Zambia, vol. **79/5**. *Institute of Geological Sciences*, London.

BRGM, (2004). Geology and gemstones deposits of East Africa. Orleans.

Broderick, T.J. (1976). Explanation of the geological map of the country east of Kariba, *Short Report Geological Survey Zimbabwe,* **43**, 98pp.

Burnham, C.W. & Nekvasil, H. (1986). Equilibrium properties of granitite pegmatite magmas. *American Mineralogist*, **71**, 239-263.

Büttner, S.H., Reid, W.K., Glodny, J., Wiedenbeck, M., Chuwa, G., Moloto, T., Gucsik, A. (2016). Fluid sources in the Twangiza-Namoya Gold Belt (Democratic Republic of Congo): evidence from tourmaline and fluid compositions, and from boron and Rb-Sr isotope systematics. *Precambrian Research* 280, 161-178.

Cahen, L. & Snelling, N.J., (1966). The geochronology of Equatorial Africa. Amsterdam: North-Holland Publishing Cy., p195.

Cahen, L., Snelling, N.J., Delhal, J. & Vail, J.R. (1984). The geochronology and evolution of Africa. Clarendon Press. Oxford. U.K. p512.

Cairncross, B. (2004). Field guide to rocks and minerals of southern Africa. Cape Town: Struik.

Cameron, E.N., Jahns, R. H., McNair, A. M. & Page, L.R. (1949). Internal structure of granitic pegmatites. *Monograph 2, Economic Geology*, Urbana, IL, p115.

Candeloro, P. (2013). Raman tool set. Analyst 138, 7331-40 (package code web. address: http://ramantoolset.sourceforge.net).

Cannon, R.T., Hopkins, D.A., Thatcher, E.C., Peters, E.R., Kemp, J., Gaskell, J.L. & Ray, G.E. (1969). Polyphase deformation in the Mozambique Belt, northern Malawi. *Bulletin of Geological Society of America*, **80**, 2615-22.

Carranza, E.J.M., Woldai, T., & Chikambwe, E.M. (2005). Application of data-driven evidential belief functions to prospectivity mapping for aquamarine-bearing pegmatites, Lundazi district, Zambia. *Natural Resources Research*, **14(1)**, 47-63.

Carter, G.S. & Bennet, J.D. (1973). The geology and mineral resources of Malawi. *Bulletin Geological Survey Malawi,* **6**.

Cërny, P. (1982). (Ed.) *Granitic pegmatites in science and industry. Short Course Handbook,* Vol. **8***, Mineralogical Association of Canada.* Winnipeg.

Cërny, P. (1990). Distribution, affiliation and derivation of rare-element granitic pegmatites in the Canadian Shield, *Geologische Rundschau*, **79**, 183-226.

Cërny, P. (1991a). Rare-element granitic pegmatites. Part 1: Anatomy and Internal Evolution of Pegmatite deposits. *Geoscience Canada,* **18**, 29-46.

Cërny, P. (1991b). Rare-element granitic pegmatites. Part II: regional to global environments and petrogenesis. *Geoscience Canada,* **18**, 49-62.

Cërny, P. (1992). Geochemical and petrogenetic features of mineralisation in rare-element granitic pegmatites in the light of current research. *Applied Geochemistry,* **7**, 393-416.

Cërny, P. (1993b). Rare – element granitic pegmatites. Part II: Regional to global environments and petrogenesis, in P.A. Sheahan and M.A. Cherry (Eds.). Ore deposit models, vol. II *Geoscience Canada,* Reprint Series, **6**, 49-62.

Cërny, P. (2005). The Tanco rare-element pegmatite deposit, Manitoba: regional context, internal anatomy, and global comparison. *In* Linnen, R. and Samson, I (Eds.). Rare element geochemistry of ore deposits. *Geological Association of Canada, Short Course Handbook* **17**, 127-158.

Cërny, P. & Burt, D.M. (1984). Paragenesis, crystallochemical characteristics and geochemical evolution of micas in granites and pegmatites: *In*: Biley, S.W. (Ed.), Mica. *Mineralogical Society of America, Reviews in Mineralogy*, **13**, 257-297.

Cërny, P. & Ercit, T.S. (2005). The classification of granitic pegmatites revisited. *The Canadian Mineralogist,* **43(6),** 2005-2026.

Cërny, P., London, D. & Novak, M. (2012). Granitic pegmatites as reflections of their sources. *Elements: An International Magazine of Mineralogy, Geochemistry, and Petrology,* **8(4),** 289-294.

Cërny, P., Meintzer, R.E., & Anderson, A.J. (1985). Extreme fractionation in rare-element granitic pegmatites: selected examples of data mechanisms. *Canadian Mineralogist,* **23**, 381-421.

Cërny, P., Trueman, D.L., Ziehlke, D.V., Goad, B.E. & Paul, B.J. (1981). The Cat Lake-Winnipeg River and the Wekusko Lake pegmatite fields, Manitoba. *Manitoba Department of Energy and Mines, Mineral Resources Division, Economic Geology Report* **ER80-1**.

Chakhmouradian, A.R. & Zaitsev, A.N. (2012). Rare earth mineralisation in igneous rocks: sources and processes. *Elements: An International Magazine of Mineralogy, Geochemistry, and Petrology,* **8**, 347-353.

Chappell, B.W. and White, A.J.R. (1992). I- and S-type granites in the Lachian Fold Belt. *Transactions of the Royal Society of Edinburgh, Earth Sciences* **86**, 1-26.

Chappell, B.W. & White, A.J.R. (2001). Two contrasting granite types: 25 years later. *Australian Journal of Earth Sciences,* **48**, 489-499.

Chikambwe, E.M. (2002). GIS-based predictive mapping for aquamarine-bearing pegmatites, Lundazi area, northeast Zambia. *ITC*, Netherlands, 1-79.

Clifford, T.N. (1970). The structural framework of Africa *In* Clifford, T.N. and Gas, I.G. (1970) *African magmatism and tectonics*. Edinburgh: Oliver and Boyd, 1-26.

Clifford, T.N. (1974). Review of African granulites and related rocks. *Geological Society of America Special Paper*, **156**, 49p.

Cook, R.B. & Ericksson, S. (2002). Abstracts of the 23rd Annual Tucson Mineralogical Symposium: Minerals of Africa. *The Mineralogical Record,* **33**, 75-82.

Collins, A. & Pisarevsky, S. (2005). Amalgamating eastern Gondwana: The evolution of circum-Indian orogens. *Earth-Science Reviews*, 71, 229-270.

Cooper, W.G.G. & Habgood, F. (1959). The geology of the Livingstonia coalfield. *Bulletin of Geological Survey Nyasaland*, **11**.

Daly, M.C. (1986). Crustal shear zones and thrust belts: their geometry and continuity in Central Africa. – *Phil.-Transactions Royal Society of London*, **A317**, p.111-128.

Daly, M.C. (1988). Crustal shear zones in central Africa. A kinematic approach to Proterozoic tectonics. *Episodes,* **11**, 5-11.

Daly, M.C. & Unrug, R. (1982). The Muva Supergroup, northern Zambia. *Transactions of the Geological Society of South Africa,* **85**, 155-165.

Daly, M.C., Klerkx, J. & Nanyaro, J.T. (1985). Early Proterozoic exotic terranes and strike-slip accretion in the Ubendian Belt of southwest Tanzania. *Abstract Volume. Terra Cognita,* **5**, 257.

Dawson, A.L. & Kirkpatrick, I.M. (1968). The geology of the Cape Maclear Peninsula and Lower Bwanje Valley. *Bulletin of Geological Survey Malawi,* **28**.

De Vivo, B., Ippolito, F., Calpadi, G. and Simpson, P.R. (1984). Uranium geochemistry, mineralogy, geology, exploration and resources. Springer. https://doi.org/10.1007/978-94-099-6060-2.

De Waele, B. & Fitzsimons, I.C.W. (2004). The age and detrital fingerprint of the Muva Supergroup of Zambia: molasse deposition to the southwest of the Ubendian Belt. *Abstracts, Geoscience Africa*, Johannesburg, 162-163.

De Waele, B., Johnson, S.P. & Pisarevsky, S.A. (2008). Palaeoproterozoic to Neoproterozoic growth and evolution of the western Congo Craton: Its role in the Rodinia puzzle. *Precambrian Research*, **160**, 127-141.

De Waele, B., Nemchin, A.A. & Kampunzu, A.B. (2003a). The Bangweulu Block of northern Zambia: where is the pre-Ubendian crust? *Abstracts, Assembly and Breakup of Rodinia, South China Field Symposium,* Hanzhou, 19-21.

De Waele, B., Kampunzu, A.B., Mapani B.S.E & Tembo F. (2006). The Mesoproterozoic Irumide Belt of Zambia. *Journal of African Earth Sciences,* **46**: 36-70.

Deer, W.A., Howie, R.A. & Zussman, J. (1966). An Introduction to the rock forming minerals, United Kingdom; Pearson Prentice Hall, 1966.

Deer, W.A., Howi, R.A. & Zussman, J. (1992). An Introduction to the rock forming minerals, United Kingdom; Pearson Prentice Hall, 1992.

Dickin, A.P, (1995). Radiogenic isotope geology. Cambridge University Press, Cambridge 490 pp.

Dill, H.G. (2007). A review of mineral resources in Malawi: with special reference to aluminum variation in mineral deposits. *Journal of Africa Earth Sciences*, **47**: 153-173.

Dill, H.G. (2015). Pegmatites and aplites: sources for energy, ore and industrial minerals –I. Meggener Rohstofftage "*Minerals for the World*," 17th-19 September, Lennestadt-Meggen, BDG Berufsverband Deutscher Geowissenschaftler and Traktor-Technik GMbH & Co. KG and Sachtleben Bergbau Verwaltungs – GMbH, Germany.

Dill, H.G. & Ludwig, R.R. (2008). Geomorphological – sedimentological studies of landform types and modern placer deposits in the savanna (southern Malawi). *Ore Geology Reviews,* **33**, 3-4, 411-34.

Dirks, P.H.G.M., Kröner, A., Jelsma, H.A., Maneya, C., & Jamal, D.L. (2000). Pb-Pb zircon ages and tectonic framework for Zambezi Belt, Zimbabwe. *Journal of African Earth Sciences*, **30**, 4A, 23-24.

Dodson, M.H., Cavanagh, B.J., Thatcher, E.C. & Aftalion, M. (1975). Age limits of for the Ubendian metamorphic episode in northern Malawi. *Geological Magazine,***112**, 403-410.

Doggart, S.W. (2018). Geochronology and isotopic characterisation of LCT pegmatites from the Orange River Pegmatite Province. MSc thesis, Stellenbosch University, 236 pp.

Duan Z., Moller N. & Weare J.H. (1992a). An equation of state for CH_4-CO_2-H_2O system; I. Pure systems from 0-1000 ^oC and 0 to 8000 bar. *Geochemica et Cosmochimica Acta,* **56**, 2605-2617.

Duan, Z., Moller, N. & Weare, J.H. (1992b). An equation of state for CH_4-CO_2-H_2O system; II. Mixtures from 50-1000^oC and 0 to 1000 bars. *Geochemica et Cosmochimica Acta,* **56**, 2619-2631.

Duan, Z., Moller N. & Weare, J.H. (1995). Equation of state for NaCl-H_2O-CO_2 system: Prediction of phase equilibria and volumetric properties. *Geochemica et Cosmochimica Acta,* **59**, 2869-2882.

Duan, Z., Moller, N. & Weare, J.H. (1996). A general equation of state for supercritical fluid mixtures and molecular dynamics simulation of mixture PVTX properties. *Geochemica et Cosmochimica Acta,* **60**, 1209-1216.

Dyar, M.D., Guidotti, C.V., Core, D.P., Wearn, K.M., Wise, M.A., Francis, C.A., Johnson, K. & Brady, J.B. (1999). Stable-isotope and crystal chemistry of tourmaline across pegmatite-country rock boundaries at Black Mountain and Mount Mica, south-western Maine, USA: *European Journal of Mineralogy,* **11**, 281-294.

Eby , G. N., Woolley A. R., Krueger, H.L., Ewing, W., Faxon. E.H. & Roden-Tice, M. (1995). Geochronology and history of the northern part of the Chilwa alkaline province, Malawi. *Journal of African Earth Sciences,* **20**, 275-288.

Eby, G. N., Woolley, A. & Collerson, K. (2004). The Chilwa Alkaline Province, Malawi – geochemistry, isotope geology, and petrogenesis. *32nd International Geological Congress Florence 2004 – Scientific Sessions: abstracts* (**part 1**), p.703.

Eby, G.N., Woolley, A.R., Din, V. & Platt, G. (1998). Geochemistry and petrogenesis of nepheline syenites: Kasungu – Chipala, Ilomba, and Ulindi nepheline syenite intrusions, North Nyasa Alkaline Province, Malawi. *Journal of Petrology,* **39**, 1405-1424.

Encyclopedia of Geology, (2004). *Africa/Pan-African Orogeny*, Vol.1, Elsevier, Amsterdam.

Ercit, T.S. (1992). Oxide mineralogy of the Mattawa pegmatite district – extreme Ta fractionation for muscovite class pegmatites: *Geological Association of Canada / Mineralogical Association of Canada, Program with Abstracts*, v**17**, p. A32.

Ercit, T.S. (2005). REE-enriched granitic pegmatites *In*: Linnen, R.L. and Samson, I.M (Eds). Rare-element geochemistry and mineral deposits. *Geological Association of Canada Short Course Notes,* **17**, 175-199.

Evans, R.J., Ashwal, L.D. & Hamilton, M.A. (1999). Mafic, ultramafic and anorthositic rocks of the Tete Complex, Mozambique: petrology, age and significance. *South African Journal of Geology,* **102**, 153-166.

Fagereng, A. (2013). Fault segmentation, deep rift earthquakes and crustal rheology: Insights from 2009 Karonga sequence and seismicity in the Rukwa Malawi rift zone. *Tectono-Physics*, 601, 216-225.

Faure, G. (1997). Principles of isotope geology. Cambridge University Press, Cambridge, 506pp.

Fernandez-Alonso, M. (2007). Geological map of the Mesoproterozoic north-eastern Kibaran Belt. Royal Museum for Central Africa. Tervuren (Belgium): catalogue of maps and digital data, and http://www.africamuseum.be.

Fitches, W.R. (1970). A part of the Ubendian orogenic belt in northern Malawi and Zambia. *Geologische Rundschau*, **59**, 444-457.

Fitches, W. R. (1971). Sedimentation and tectonics at the northeast end of the Irumide Orogenic Belt, N. Malawi and Zambia. *Geologische Rundschau*, **60(2)**, 589-619.

Foord, E.E., Cërny P., Jackson L.L., Sherman, D.M. & Eby, R.K. (1995). Mineralogical and geochemical evolution of micas from miarolitic pegmatites of the anorogenic Pikes Peak batholiths, Colorado. *Mineralogy and Petrology*, v.**55**, p1-26.

Forster, M.D. (1960). Interpretation of the composition of lithium micas. U.S. *Geological. Survey Professional Paper*, **354-E**, 115-47.

Foster, A. (1965). Der Kristallinsockel im oestlichen Nordrhodesien und sein Verband mitanderen Baueinheiten Zentral- and Ostafrikas. *Geotektonische Forschungen,* **20 (I-II),** 115.

Foster, R.P., Leahy, K., Hunns, S.R., Pelham, D.A., Lawrence, S.R. & Harrison, A.E. (2001). Pan-African terranes: realizing the metal potential. *Transactions of the Institute of Mineralogy and Metallurgy (Section B: Applied Earth sciences). Australian Journal of Mining* **110.**

Frei, D. & Gerdes, A. (2009). Precise and accurate in situ U-Pb dating of zircon with high sample throughput by automated LA-SF-ICP-MS. *Chemical Geology*, **261**, 261-270.

Fritz, H., Abdelsalam, A., Ali, K.A., Bingen, B., Collins, A.S., Fowler, A.R., Ghebreab, W., Hauzenberger, C.A., Jackson, P., Kusky, Y., Macey, P., Muhongo, S., Stern, R.J. & Viola, G. (2013). Orogen styles in the East African Orogens: A review of the Neoproterozoic to Cambrian Tectonic evolution. *Journal of African Earth Sciences*, **86**, 65-106.

Gallagher, M. (1959). Classification of beryl pegmatites. *Geological Survey of Great Britain. Atomic Energy Division. Report* No 215.

Gaskell, J.L. (1973). The geology of the Mzimba area. *Bulletin of Geological Survey of Malawi*, **37**.

GEUS, (1999). An integrated approach to mineral exploration and environmental assessment in southern and eastern Africa – a pilot study in Tanzania (*RUFF project number* **90953**).

Gill, R. (2010). Igneous rocks and processes. 1st ed. Chichester, West Sussex, UK: Wiley-Blackwell, pp. Chapter 9 (Alkaline Rocks) p291.

Ginsburg, A.L., Tomofeyev, I.N., & Feldman, L.G. (1979). Principles of Geology of Granitic Pegmatites [in Russian]. Nedra, Moscow (summarized in Cërny, **1982**).

GLITTER - data reduction software for Laser Ablation Microscope. ARC National Key Centre for Geochemical Evolution and Metallogeny of Continents (GEMOC) and CSIRO Exploration and Mining, Access Macquarie Ltd., Australia.

Glodny, J., Kühn, A., & Austrheim, H. (2008). Geochronology of fluid-induced eclogite and amphibolite facies metamorphic reactions in a subduction - collision system, Bergen Arcs, Norway. *Contributions to Mineralogy and Petrology*, ***156***(**1**), 27-48.

Glover, A.S., Rogers, W.Z. & Barton, J.E. (2012). Granitic Pegmatites: storehouses of industrial minerals. *Elements: An International Magazine of Mineralogy, Geochemistry, and Petrology,* **8(4)**, 269-273.

Goscombe, B. & Gray, D. (2003). Granulites of the Malawi Mosaic. *Conference abstract, SGTSG Kalbari.*

Grantham, G.H., Macey, P.H., Horie, K., Kawakami, T., Ishikawa, M., Satish-Kumar M., Tsuchiya, N. Grase P., Azevedo, S. (2013). Comparison of the metamorphic history of Monapo Complex, northern Mozambique and Balchenfjella and Asuthameren areas, Sör Rondane, Antarctica: Implications for the Kuunga Orogeny and the amalgamation of N and S Gondwana. *Precambrian Research,* **243**, 85-135.

Grantham, G.H., Macey, P.H., Ingram, B.A., Roberts, M.P., Amstrong, R.A, Hokada, T., Shiraishi, K., Bisnath, A. & Manhica, V. (2007). Terrane correlation between Antarctica, Mozambique and Sri Lanka; Comparisons of geochronology, lithology, structure and metamorphism. *U.S Geological Survey and the National Academies; USGS 1047. 10th International Symposium on Antarctic Earth Sciences Abstract* **004.**

Grantham, G.H., Macey, P.H., Ingram, B.A., Roberts, M.P., Armstrong, R.A., Hokada, T., Shiraishi, K., Jackson, C., Bisnath, A. & Manhica, V. (2008). *In*: Satish-Kumar, M., Montoyoshi, Y., Osani, Y., Hiroi, Y., Shiraishi, K. (Eds.). Geodynamic evolution of East Antarctica: A key to East-West Gondwana connection. *Geological Society, London, Special Publications,* **308**, 91-119.

Graziani, G., Gubelin, E. & Lucchesi, S. (1983). The genesis of an emerald from the Kitwe District, Zambia. *N Jb. Miner. Mh*., 175-86.

Habgood, F. (1963). The geology of the country west of Shire River between Chikhwawa and Chiromo. *Bulletin of Geological Survey, Nyasaland*, **14**.

Hanson, R.E. (2003). Proterozoic geochronology and tectonic evolution of Southern Africa. *In:* Yoshinda, M., Windley, B. F., Dasgupta, S. (Eds.) Proterozoic East Gondwana: Supercontinent Assembly and Breakup. Vol **2**. *Geological Society of London Special Publication, London*, 427-463.

Harding, A.E. (1982). The geology of Mwanya area: explanation of degree sheet 1232, SW quarter. *Reprint, Geological Survey Zambia,* No. **91**.

Harris, J.F. (1981). Summary of the geology of Tanganyika. *Part IV: Economic geology. Tanganyika, Memoir,* **1**, 143pp.

Haslam, H.W., Brewer, M.S., Davies, A.E. & Darbyshire, D.F.P. (1980). Anatexis and high-grade metamorphism in the Champhira dome, Malawi; petrological and Rb-Sr studies. *Mineralogical Magazine*, **43**, 701-714.

Haslam, H.W., Darbyshire, D.F.P. & Davies, A.E., (1983). Irumide and post-Mozambique plutonism in Malawi. *Geological Magazine,* **120**, 21-35.

Haslam, H.W., Rundle, C.C. & Brewer, M.S. (1986). Rb-Sr studies of metamorphic and igneous events in eastern Zambia. *Journal of African Earth Sciences*. **5(5),** 447-453.

Hickman, A.C.J. (1975). The geology of the Lusukuzi area; explanation of degree sheets 1232 SE quarter and 1233 SW quarter. *Bulletin of Geological Survey, Zambia* No. **50**.

Holloway, J.R. (1987). Igneous fluid. In Thermodynamic Modelling of geological materials: Minerals, Fluids and Melts (eds. Carmichael ISE, Eugster HP). *Reviews in Mineralogy*, **17**, 211-233.

Holmes, A. (1951). The sequence of Pre-Cambrian orogenic belts in south and central Africa. *18th International Geological Congress, London*, **14**, 17-33.

Holt, D.N. (1965). The Kangankunde Hill rare earth prospect. *Bulletin of Geological Survey Malawi*, **20**.

Hopkins, D.A.S. (1973). The geology of the Rumphi-Nkhata Bay area. *Bulletin of Geological Survey Malawi,* **38/39**.

Huizenga, J. M. (2010). Short course in fluid inclusions. Short course handbook, 1-46

Hunter, D.R. (1981). Structural Provinces. Developments in Precambrian Geology Volume II: The Precambrian of the southern hemisphere,. Armsterdam, Elservier, 397-410.

Hutchinson, R. W. & Claus, R.J. (1956). Pegmatite deposits, Alto Ligonha District, Portuguese East Africa. *Economic Geology*, **51**, 757-780

Icenhover, J.P. & London, D. (1995). An experimental study of element partitioning among biotite, muscovite, and co-existing peraluminous silicic melt at 200 MPa (H_2O). *American Mineralogist,* **80**: 1229-1251.

Icenhover, J.P. & London, D. (1996). Experimental partitioning of Rb, Cs, Sr, and Ba between alkali feldspar and peraluminous melt. *American Mineralogist,* **81**: 719-734.

International Monetary Fund, (2005). Malawi, Poverty Reduction Strategy Paper Annual Progress Report, June IMF Country Report No. **05**/209.

Jackson, S., Pearson, N., Griffin. W. & Belousova, E. (2004). The application of laser ablation – inductively coupled plasma - mass spectrometry to in situ U-Pb zircon geochronology. *Chemical Geology*, **211**, 47-69.

Jacobs, J., Bauer, W. & Thomas, R.T. (2006). A Himalayan-type indentor-escape tectonic model for southern part of the Late Neoproterozoic/Early Palaeozoic East African-Antactic Orogen. Colloquium *of African Geology (CAG21), 2006, Maputo, Mozambique. Abstract Volume,* 71-72.

Jacobs, J., Bingen, B., Thomas, R.J., Bauer, W., Wingate, M. & Feito, P. (2008a). Early Palaeozoic orogenic collapse and voluminous late-tectonic magmatism in Dronning Maud Land and Mozambique: insights into the partially delaminated orogenic root of East African-Antarctic Orogen? *In*: Satish-Kumar, M., Montoyoshi, Y., Osani, Y., Hiroi, Y, Shiraishi, K. (Eds.). Geodynamic evolution of East Antarctica: a key to East West Gondwana connection. *Geological Society, London, Special Publications,* **308**, 69-90.

Jahns, R. H. (1982). Internal evolution of granitic pegmatites in P. Cërny (Ed.) Granitic pegmatites in science and industry, Short Course Handbook. *Mineralogical Association of Canada*, Winnipeg **8**, 327-393.

Jahns, R.H. (1955). The study of pegmatites. *Economic Geology Fiftieth Anniversary Volume*, 1025-1130.

Jahns, R.H. & Burnham, C.W. (1969). Experimental studies of pegmatite genesis 1: A model for the derivation and crystallisation of granitic pegmatites. *Economic Geology,* **64**, 843-864.

Jamal, D.L. & De Wit, M. (2004). U-Pb geochronology and Sm-Nd data from Lurio Belt, NE-Mozambique; significance for crustal evolution. *In*: Abstract Volume of the 20th Colloquium of African Geology, BRGM, Orleans, France, pp. **204-205**.

Jamal, D.L., Zartman, R.E. & De Wit, M.J. (1999). U-Pb single zircon dates from the Lurio Belt, northern Mozambique: Kibaran and Pan-African orogenic events highlighted. *Journal of African Earth Science*, **28**, 32.

Johns, C.C., Liyungu, K., Mwale, G., Mabuku, S., Sakungo, F., Tembo D., Vallance, G., & Barr, M.W.C. (1989). The stratigraphic and structural framework of Eastern Zambia; results of a geotraverse. *Journal African Earth Sciences,* **9**, 123-136.

Johnson, S.P., De Waele, B. & Tembo, F. (2006b). The southern Irumide Belt of Zambia. *In*: XXI Colloquium of African Geology, 2006, Maputo, Mozambique, *Abstract Volume*, 75-77.

Johnson, S.P., De Waele, B., Tembo, F., Kitongo, C., Tani, K., Qing, C., Lizuka T, & Dunkley, D. (2007). Geochemistry, geochronology and isotopic evolution of the Chewore-Rufunsa Terrane, southern Irumide Belt: a Mesoproterozoic continental margin arc. *Journal of Petrology,* **48**, 1411-1441.

Johnson, S.P., Rivers, T. & De Waele, B. (2005). A review of the Mesoproterozoic to early Palaeozoic magmatic and tectonothermal history of south-central Africa: Implications for Rodinia and Gondwana. *Journal of the Geological Society of London,* **162**, 433-450.

Jolliff, B.L., Papike, J.J. & Shearer C.K. (1987). Fractionation trends in mica and tourmaline as indicator of pegmatite internal evolution: Bob Ingersoll pegmatite, Black Hills, South Dakota. *Geochimica et Cosmochimica Acta*, **51**, 519-534.

Jonsson, E. & Hogdahl, K. (1999). Alkalin magmatism och mineralforekomster I sodra Malawi. *Geologiskt Forum,* **22**, 8-12.

Kankuzi, C.F., (2009). The distribution and controls of mineralised pegmatites of Mount Malosa West. Unpublished MSc thesis. University of Malawi, pp. 114.

Karmakar, S. & Schenk, V. (2016). Mesoproterozoic UHT metamorphism in Southern Irumide Belt, Chipata, Zambia: petrology and in situ monazite dating. *Precambrian Research*, **275**, 332-356.

Kazimoto, E., Schenk, V. & Appel, P. (2015). Granulite facies metamorphic events in the north-western Ubendian Belt of Tanzania: Implications for the Neoarchean to Palaeoproterozoic crustal evolution. *Precambrian Research*, **256**, 31-47.

Keller, P., Encarnacion, R.R., Alfonso, P.P. & Francois, F. (1999). Chemistry, paragenesis and significance of tourmaline in pegmatites of the Southern Tin Belt, central Namibia. *Chemical Geology*, **158**, 203-225.

Kennedy, W.G. (1964). The structural differentiation of Africa in the Pan African episode. – *Resident Institute of African Geology*. University of Leeds *8th Annual Report*, 48-49.

Keppler, H. (1993). Influence of fluorine on the enrichment of high field strength trace elements in granitic rocks. *Contributions to Mineralogy and Petrology* **114**: 479-488.

Key, R. & Ochieng, J. (1991). The growth of rubies in South-east Kenya. *Journal of Gemmology,* **22(8):** 484-496.

King, A.W. & Dawson, A.L. (1976). The geology of the Mangochi-Makanjira area. *Bulletin of Geological Survey Malawi,* **35**.

Klerkx, J., Theunissen, K. & Delvaux, D. (1998). Persistent fault controlled basin formation since the Proterozoic along the western branch of the East African Rift. *Journal of African Earth Sciences,* **26**, 347-361.

Knorring, O.V., Sahama, T.G. & Siivola, J. (1973). Natural bismuth vanadate from the Mutala pegmatite area, Mozambique. *Contributions to Mineralogy and Petrology* **41**, 325-331.

Kontak, D.J., Dostal, J, Kurt-Kyser T. & Archbald, A. (2002). Isotopic and fluid-inclusion study of 370 Ma pegmatite-aplite sheets, Peggy Cove, Nova Scotia, Canada, *Canadian Mineralogist,* **40,** 51249-1286.

Kröner, A. (1977). The Precambrian geotectonic evolution of Africa: plate accretion versus plate destruction. *Precambrian Research*, **4**, 163-213.

Kröner, A. (2001). The Mozambique Belt of East Africa and Madagascar; significance of zircon and Nd model ages for Rodinia and Gondwana supercontinent formation and dispersal. *South African Journal of Geology,* **104**, 151-166.

Kröner, A., Braun, I. & Jackel, P. (1996). Zircon geochronology of anatectic melts and residues from a high-grade politic assemblage at Ihosy, southern Madagascar: evidence of for Pan-African granulite metamorphism. *Geological Magazine*, **133**, 311-323.

Kröner, A., Dirks, P.H.G.M. & Jamal, D.L. (200b). Archean, Kibaran and Pan-African zircon ages from granitoid rocks in north-western Mozambique. *Abstract Volume*, Geoluanda 2000, Luanda, Angola, 24-25.

Kröner, A., Sacchi, R., Jaeckel, P. & Costa, M. (1997). Kibaran magmatism and Pan-African granulite metamorphism in northern Mozambique: single zircon ages and regional implications. *Journal of African Earth Sciences,* **25**, 467-484.

Kröner, A., Willner, A.P., Hegner, E., Jaeckel, P. & Nemchin, A. (2001). Single zircon ages, PT evolution and Nd isotopic systematic of high grade gneisses in southern Malawi and their bearing on the evolution of the Mozambique Belt into southern Africa. *Precambrian Research*, **109**, 257-291.

Krumgalz, B.S., Pogoresky, R. & Pitzer, K.S. (1996). Volumetric properties of single aqueous electrolytes from zero to saturation concentrations at 298.15 K represented by Pitzer‟s Ion-Interaction Equation. *Journal of Physical Chemistry Reference Data*, **25**, 663-689.

Kullerud, L. (1991). On the calculation of isochrons. *Chemical Geology: Isotope Geoscience section*, ***87*(2)**, 115-124.

Laetsch, T. & Downs, R. (2006). Software for identification and refinement of cell parameters from powder diffraction data of minerals using the RRUFF Project and American Mineralogist Crystal Structure Databases (Crystal Sleuth Software). *Abstracts from the 19th General Meeting of the International Mineralogical Association. Kobe, Japan*, 23-28 July 2006.

Lächelt, S. (2004). The Geology and Mineral Resources of Mozambique. Direccao Natinal de Geoloigia, Mozambique.

Landes, K.K. (1935). Age and distribution of pegmatites. *American Mineralogist,* pp. 81.

Lenharo, S.I.R., Pollard, P.J. & Born, H. (2003). Petrology and textural evolution of granites associated with tin and rare metals mineralisation at the Pitinga mine, Amazonas, Brazil. *Lithos,* **66**, 37-61.

Lenoir, J.L., Liegeois, J.P., Theunissen, K. & Klerkx, J. (1994a). The Palaeoproterozoic Ubendian shear belt in Tanzania: geochronology and structure. *Journal of African Earth Sciences,* **19**, 169-184.

Linnen, R. L. (1998). Depth of emplacement, fluid provenance and metallogeny in granitic terranes: a comparison of western Thailand with other tin belts. *Mineralium Deposita*, **33(5)**, 461-476.

Linnen, R. L., Litchtervelde, M. & Cërny, P. (2012). Granitic pegmatites as sources of strategic metals. *Elements: An International Magazine of Mineralogy, Geochemistry, and Petrology,* **8(4)**, 275-280.

London, D. (1990). Internal differentiation of rare-element pegmatites; a synthesis of recent research *In:* Stein, H.J. and Hannah, J.L. (Eds.) Ore-bearing granite systems; petrogenesis and mineralizing processes. *Geological Society of America, Special Paper,* **246**, 35-50.

London, D. (1992). The application of experimental petrology to the genesis and crystallisation of granitic pegmatites; *The Canadian Mineralogist,* **30**, 499-540.

London, D. (1995). Geochemical features of peraluminous granites, as sources of lithophile metal deposits. *In:* Thomson, J.F.H. (Ed.) Magmas, fluids and ore deposits. *Mineralogical Association of Canada Short Course Handbook* **23**, 175.

London, D. (1996). Granitic pegmatites. *Transactions of the Royal Society Edinburgh, Earth Sciences*, 87, 305-19.

London, D. (1997). Estimating abundances of volatile and other mobile components in evolved silicic melts through mineral-melt equilibria. *Journal of Petrology*, **38**, 1691-1706.

London, D. (2005). Geochemistry of alkalis and alkali earths in ore-forming granites, pegmatites, and rhyolites *In:* Linnen, R. and Samson, I. (Eds). Rare element geochemistry of ore deposits. *Geological Association of Canada, Short Course Handbook* **17**, 17-43.

London, D. (2008). Pegmatites. *Canadian Mineralogist Special Publication,* **10**, p347.

London, D. (2009). The origin of primary textures in granitic pegmatites. *Canadian Mineralogist,* **47**, 697-724.

London, D. (2014). A petrologic assessment of internal zonation in granitic pegmatites. *Lithos,* **184-187**, 74-104.

London, D. & Burt, D. M. (1982). Lithium aluminosilicate occurrences in pegmatites and the lithium aluminosilicate phase diagram. *American Mineralogist,* **67**, 483-493.

London, D. & Evensen, J.M. (2003). Beryllium in silicic magmas and the origin of beryl-bearing pegmatites. In: Grew E.S. (Ed.), Beryllium: mineralogy, petrology and geochemistry. *Mineralogical Society of America Reviews in Mineralogy and Geochemistry,* **50**, 445-486.

London, D. & Kontak, D.J. (2012). Granitic pegmatites: scientific wonders and economic bonanzas. *Elements: An international Magazine of Mineralogy, Geochemistry, and Petrology,* **8(4)**, 257-261.

London, D. & Morgan, G.B. (2012). The pegmatite puzzle. *Elements: An International Magazine of Mineralogy, Geochemistry and Petrology,* **8(4)**, 263-268.

London, D., Hervig, R.L. & Morgan, G.B. VI. (1988). Melt-vapour solubilities and element partitioning in peraluminous granite-pegmatite systems: experimental results with Macusani glass at 200 MPa. *Contributions to Mineralogy and Petrology,* **99**, 360-373.

London, D., Morgan, G.B. VI, & Hervig R.L. (1989). Vapour-undersaturated experiments with Macusani glass + H_2O at 200 MPa, and the internal differentiation of granitic pegmatites. *Contributions to Mineralogy and Petrology,* **102**, 1-7.

London, D., Morgan, G.B. VI & Wolf, M.B. (1996). Boron in granitic rocks and their contact aureoles. *In:* Grew E.S. and Anovitz, L.M. (Eds.) Boron mineralogy, petrology and geochemistry, *Reviews in Mineralogy and Geochemistry*, **33**, ch.7 *Mineralogical Society of America*, Washington, D.C.

Ludwig, K.R., (2003). Isoplot Version/Ex version 3: a Geochronological toolkit for Microsoft Excel. *Geochronology Centre, Berkeley.*

Ludwig, K.R. (2009). Isoplot/Ex ver 3.71: A geochronological toolkit for Microsoft Excel: *Berkeley Geochronology Centre Special Publication,* **4**, p 77.

Lulin, J-M., Jourde, G., Mestraud, J-L. & Mroz, J-P. (1985). Un nouveau gîte â Nb, Ta, U, T.R en Afrique orientale: le complexe alcalin de Meponda (Rêpublic populaire de Mozambique): *Chronique de la Recherche Minière*, **480**, 35-48.

Maboko, M.A.H. & Nakamura, E. (2001). Isotopic dating of juvenile Neoproterozoic crust in the Usambala Mountains of northeastern Tanzania: A link between the Mozambique Belt and the Arabian-Nubian shield? *Precambrian Research,* **113**, 227-242.

Macey, P.H., Miller, J.A., Rowe, C.D., Grantham, G.H., Siegfied, P., Armstrong, R.A., Kemp. J., Becalau, J. (2013). Geology of the Monapo Klipple, NE Mozambique and its significance for assembly of central Gondwana. *Precambrian Research,* **233** (2013) 259-281.

Macey, P.H., Ingram, B.A., Crownwright, M. S., Botha, G.A., Roberts, M.R., Grantham, G.H., Maree, L.P, Botha, P.M.W., Opperman, R., Haddon, I.G., Nolte, J.C., & Rower, M. (2007). Map Explanation Sheets Alto Molocue (1537), Murrupula (1538), Nampula (1539), Mognicual (1540), Errecgo (1637), Gile (1638), and Angoche (1639-40). National Directorate of Geology, Republic of Mozambique.

Macey, P.H., Thomas, R.J. & 21 others (2010). Mesoproterozoic geology of the Nampula Block, northern Mozambique: tracing fragments of the Mesoproterozoic crust in the Gondwana. *Precambrian Research,* **182**, 124-148.

Malisa, E. & Muhongo, S. (1990). Tectonic setting of gemstone mineralisation in the Proterozoic metamorphic terrane of the Mozambique Belt in Tanzania. *Precambrian Research*, **46(1)**, 167-176.

Mapani, B. (1999). Tectonic and metamorphic evolution of the Serenje and adjoining areas. *In*: De Waele. B., Tembo, F., Key, R.M. (Eds.), Abstracts Volume IGCP **418/419** *Geological Society of Zambia, Lusaka*, 16.

Mapani, B.S., Rivers, T., Tembo, F., De Waele, B. & Katongo, C. (2004). Growth of the Irumide terranes and slices of Archean age in eastern Zambia. *Geoscience Africa 2004, Abstract Volume* **2**, University of the Witwatersrand, Johannesburg, South Africa, pp. 14-415.

Martin, R.F. (2007). The importance of tectonic setting in understanding granitic pegmatites. *Granitic Pegmatites: The State of the Art – International Symposium* 06th -12th May 2007, Porto, Portugal.

Martin, R.F. & De Vito, C. (2005). The patterns of enrichment of felsic pegmatites ultimately depend on tectonic setting. *Canadian Mineralogist,* **43**, 2027-2048.

Martin, R.F., De Vito, C. & Sokolov, M. (2009). Pegmatites, just like granites: apples and oranges are not just the same! *Estudos Geologicos,* **19(2)**, 11-14.

Mattinson, J.M. (2010). Analysis of the relative decay constants of ^{235}U and ^{238}U by multi-step CA-TMS measurements of closed-system natural zircon samples. *Chemical Geology,* **275**(186-198).

McCauley, A.D. & Bradley, D.C. (2014). The Global age distribution of granitic pegmatites. *Canadian Mineralogist,* **52(2)**: 183-190.

McConnell, R.B. (1950). Outline of the geology of Ufipa and Ubende. *Geological Survey of Tanganyika. Bulletin* **19**, 62.

McConnell, R.B. (1972). Geological development of the rift system of eastern Africa; *Geological Society of America, Bulletin* **83**, p. 2549-2572.

Meert, J. (2003). A synopsis of events related to the assembly of eastern Gondwana. *Tectonophysics,* **362**, 1-40.

Meert, J. & van der Voo, R. (1997). The assembly of Gondwana 880-550 Ma. *Journal of Geodynamics*, **23**, 223-235.

Meert, J., van der Voo, R. & Ayub, S (1995). Paleomagnetic investigation of the Neoproterozoic Gangwe lavas and Mbozi complex, Tanzania and the assembly of Gondwana. *Precambrian Research*, 104, 123-146.

Melcher, F., Sit, G. Martin, N., Gabler, E., Bahr, A., Gerdes, A., Bratz, H., Davis, H. & Dewaele, S. (2008b). Fingerprinting of Conflict minerals; Columbite tantalite ("coltan") ores. *SGA News*, 23-14 (June 2008).

Melcher, F., Graupner T., Sitnikova M., Henjes-Kunst, F., Orberthur, T., Gabler, E., Bahr, A., Gerdes, A., Bratz, H. & Rantitsch, G. (2009). Ein Herkunftsnachweis für Niob-Tantalerze am Beisspiel afrikanischer Selten-Element-Pegmatite. *Mitt Österr. Mineral. Ges*. **155**, 231-267.

Melcher, F., Graupner, T., Gabler, H., Sitnikova, M., Henjes-Kunst, F., Oberthur, T., Gerdes, A., & Dewaele, S. (2015). Tantalum-(niobium-tin) mineralisation in African pegmatites and rare metal granites: Constraints from Ta-Nb oxide mineralogy, geochemistry and U-Pb geochronology. *Ore Geology Reviews,* **64**, 667-719.

MGDS, (2006). Malawi Government Printer, Zomba.

Möller, A., Mezger, K. & Schenk, V. (2000). U-Pb dating of metamorphic minerals: Pan-African metamorphism prolonged slow cooling of high pressure granulites in Tanzania, East Africa. *Precambrian Research*, **104**, 123-146.

Muhongo, S. (1999). Anatomy of the Mozambique Belt of eastern and southern Africa; Evidence from Tanzania. *Gondwana Research*, **2**, 369-375.

Muhongo, S., Tuisku, P. & Mtoni, Y. (1999). Pan-African pressure-temperature evolution of the Merelani area in the Mozambique Belt in northeast Tanzania. *Journal of African Earth Sciences*, **29(2)**, 353-365.

Nabelek, P.I. & Ternes, K. (1997). Fluid inclusions in the Harney Peak Granite, Black Hills, South Dakota, USA: Implications for solubility and evolution of magmatic volatiles and crystallisation of leucogranite magmas. *Geochemica et Cosmochimica Acta*, 61, 1447-1465.

Nabelek, P.I., Whittington, A.G. & Sibescu, M.L.C. (2010). The role of H_2O in rapid emplacement and crystallisation of granite pegmatites: resolving the paradox of large crystals in highly undercooled melts. *Contributions to Mineralogy and Petrology,* **160**, 313-325.

Nakamura, N. (1974). Determination of REE, Ba, Fe, Mg, Na, and K in carbonaceous and ordinary chondrites. *Geochimica et Cosmochimica Acta*, **38**, 757-775.

Nasdala, L., Hofmeister, W., Norberg, N., Mattinson, J.M., Corfu, F., Dörr, W., Kamo, S.L., Kennedy, A.K., Kronz, A., Reiners, P.W., Frei, D., Kośler, J., Wan, Y., Gotze, J., Hager, T., Kröner, A. & Valley, J.W. (2008). Zircon M257- a homogenous natural reference material for the ion microprobe U-Pb analysis of zircon. *Geostandards and Geoanalytical Research*, **32**, 247-265.

Nash, R.A., (1962). The Geology and Mineralogy of some Northern Rhodesian pegmatites. *PhD Thesis*.

Neiva, A.M.R. (2013). Micas, feldspars and columbite-tantalite minerals from the zoned granitic lepidolite-subtype pegmatite at Namivo, Alto Ligonha, Mozambique. *European Journal of Mineralogy*, **25(6),** 967-985.

Norconsult, (2007a). Mineral Resources Management Capacity Building Project, Republic of Mozambique: Component 2: Geological infrastructure Development Project, Geological Mapping Lot 1: Sheet Explanation: 32 sheets; Scale: 1/250000, Report No. B6.f, National Directorate of Geology, Republic of Mozambique.

Norconsult, (2007b). Mineral Resources Management Capacity Building Project, Republic of Mozambique: Component 2: Geological infrastructure Development Project, Geological Mapping Lot 1; Geophysical Interpretation, Report No. B4, National Directorate of Geology, Republic of Mozambique.

Patney, R.K., & Tether, J. (1988). The gem-bearing pegmatites of Eastern Zambia. *Zambian Journal of Applied Earth Sciences,* **2(2)**: 41-54.

Pearce, N.J.G., Perkins, W.T., Westgate, J.A, Gordon, M.P., Jackson S.E., Neal, C.R. & Chenery, S.P. (1997). A compilation of new and published trace element data for NIST SRM 610 and NIST SRM 612 glass reference material. *Geostandards Newsletter*, **21**: 115-144.

Peters, E.R. (1975). The Geology of the South Viphya area. *Geological Survey Department Bulletin*, **36**, 1-44.

Petersen, O.V. & Grossmann, M. (1994). Some pegmatite minerals from Zomba district, Malawi. *Mineralogical Record*, **25**, 29-38.

Petters, S.W. (1991). Regional Geology of Africa. Springer-Verlag. p722.

Pezzotta, F., & Laurs, B.M. (2011). Tourmaline: The kaleidoscopic gemstone. *Elements: An International Magazine of Mineralogy, Geochemistry and Petrology,* **7**: 333-338.

Pinna, P. (1995). On the dual nature of the Mozambique Belt, Mozambique to Kenya. *Journal of African Earth Sciences*, **21(3)**, 477-48.

Pinna, P., Jourde, G., Calvez. J.Y., Mroz, J.P. & Marques, J.M. (1993). The Mozambique Belt in northern Mozambique: Neoproterozoic (1100-850 Ma) crustal growth and tectogenesis, and superimposed Pan-African (800-550 Ma) tectonism. *Precambrian Research*, **62**, 1-59.

Platt, R. G. & Woolley, A.R. (1986). The mafic mineralogy of the peralkaline syenites and granites of the Mulanje complex, Malawi. *Mineralogical Magazine,* **50**:85-99.

Porada, H. (1989). Pan African rifting and orogenesis in southern to equatorial Africa and Eastern Brazil. *Precambrian Research,* **44**, 103-136.

Potter, R.W. & Brown, D.L. (1977). The volumetric properties of aqueous sodium chloride solutions from 0 to 500^{o}C and pressures up to 2000 bars based regression of available data in the literature. *U.S. Geological Survey Bulletin* 1421-C, 36p.

Ray, G.E. (1974). The structural and metamorphic geology of northern Malawi. *Journal of the Geological Society, London* **130(5)**, 427-440.

Ray, G.E. (1975). The geology of the Chitipa-Karonga area. *Bulletin Geological Survey Malawi* **42.**

Redlich, O. & Kwong, J.N.S. (1949). On the thermodynamics of solutions V: an equation of state. Fugacities of gaseous solutions. *Chemical Reviews* **44**, 233-244.

Reed, B.L. (1986). Descriptive model of Sn greisens deposits, in D. P. Cox and D. A. Singer (Eds.) Characteristics of mineral deposit occurrences. *U.S Geological Survey Bulletin* **1693**.

Ren, M. (2004). Partition of Sr, Ba, Y, and LREE between alkali feldspars and peraluminous silicic magma. *American Mineralogist,* **89**, 1290-1303.

Ring, U. (1993). Aspects of the kinematic history of mechanics of superposition of the Proterozoic mobile belts of eastern central Africa (Northern Malawi and Southern Tanzania). *Precambrian Research,* **62**, 207-226.

Ring, U., Kröner, A. & Toulkeredis, T. (1997). Palaeoproterozoic granulite facies metamorphism and granitoid intrusions in the Ubendian-Usagaran Orogen of northern Malawi, east-central Africa. *Precambrian Research,* **85**, 27-51.

Ring, U., Kröner, A. Buchcraldt, R., Toulkeredis, T. & Layer, P. (2002). Shear-zone patterns and eclogite-facies metamorphism in the Mozambique Belt of northern Malawi, east-central Africa: implications for the assembly of Gondwana. *Precambrian Research,* **116**, 19-56.

Roda-Robles, E., Pesquera, A., Gil-Crespo, P.P., Torres-Ruiz, J. & De-Parseral, P. (2006). Mineralogy and geochemistry of micas from the Pinilla de Fermoselle pegmatite (Zamora Spain). *European Journal of Mineralogy,* **18**, 369-377.

Roedder, E. (1984). Fluid inclusions: *Mineralogical Association of America., Review of. Mineralogy*, no. **12**, 644p.

Rudnick, R. L. & Gao, S., (2003). Composition of the continental crust, *Treaties of Geochemistry*, **3.01**:1-56.

Sacchi, R., Marques, J., Costa, M. & Casati, C. (1984). Kibaran events in the southernmost Mozambique Belt. *Precambrian Research*, **25**, 141-159.

Salvi, S. & Williams-Jones, A.E. (2005). Alkaline granite-syenite deposits. *In*: Linnen, R.L., Samson I.M. (Eds). Rare-elements geochemistry and mineral deposits. *Geochemical Association of Canada Short course Notes,* **17**, 315-341.

Schluter, T. (2006). *Geological atlas of Africa*. New York, NY: Springer.

Schneiderhohn, H. (1961). Die Erzlargerstaetten der Erde II. *Die Pegmatite*. Gustav Fischer Verlag, Stuttgart.

Shackleton, R.M. (1987). Precambrian plate tectonics in Africa. *In*: Coward, M.P. and Ries, A.C. (Eds.). Collision tectonics. *Geological Society Special Publication No*. **19**, 329-349.

Shackleton, R.M. (1994). Review of late Precambrian sutures, ophiolite malanges and tectonics of eastern Egypt and north-east Sudan. *Geologische Rundschau*, **83(3)**, 537-546.

Shackleton, R.M. (1996). The final collision zone between East and West Gondwana; where is it? *Journal of African Earth Science*, **23**, 271-287.

Shaw, R. A., Goodenough, K. M., Roberts, N. M. W., Horstwood, M. S. A., Chenery, S. R. and Gunn, A. G. (2016). Petrogenesis of rare-metal pegmatites in high-grade metamorphic terranes : A case study from the Lewisian Gneiss Complex of north-west Scotland. *Precambrian Research*, 281, 338‑362.

Shepherd, T. J., Ranbin, A.H., & Alderton, D.H.M. (1985). A practical guide to fluid inclusion studies. Blackie, Glasgow, 239 pp.

Shigley, J.E. & Kampf, A.R. (1984). Gem-bearing pegmatites: a review. *Gems and Gemmology*, 64-77.

Simmons, W.B. (2007). Chapter 8: Gem-bearing pegmatites *In:* Groat, L.A. *Geology of Gem Deposits*, Short Course Series **37**, *Mineralogical Association of Canada*, Quebec, 169-206.

Simmons, W.B. & Webber, K.L. (2008). Pegmatite genesis – state of the art: *European Journal of Mineralogy,* **20(4)**, 421-438.

Simmons, W.B., Pezzotta, F., Shigley, J.E., & Beurlen, H. (2012). Granitic pegmatites as sources of coloured gemstones. *Elements: An international Magazine of Mineralogy, Geochemistry, and Petrology,* **8(4)**, 281-287.

Simmons, W.B., Webber, K.L., Falster, A.U. & Nizamoff, J.W. (2003). Pegmatology; Pegmatite Mineralogy, *Petrology and Petrogenesis*, Rubellite Press, New Orleans, LA, **176**.

Simmons, W.B., Laurs, B.M., Falster A.U., Koivula, J.L. & Webber, K.L. (2005). Mount Mica - A renaissance in Maine‟s gem tourmaline production: *Gems and Gemmology*, summer 2005, p150-163.

Simonet, C., Okundi, S. & Masai, P. (2000). General setting of coloured gemstone deposits in the Mozambique Belt of Kenya – Preliminary considerations. In *Proceedings 9th Conference of the Geological Society of Kenya, Nairobi, Kenya*, 123-138.

Sinclair, W.D. (1996). Granitic Pegmatites. *Canadian Mineralogist,* **21**, 503-512.

Sirbescu, M.L.C. & Nabelek, P.I. (2003). Crystallisation conditions and evolution of magmatic conditions and evolutions of magmatic fluids in the Harney Peak Granite and associated pegmatites, Black Hills, South Dakota – Evidence from fluid inclusions. *Geochemica et Cosmochimica Acta*, **67**, 2443-2465.

Skjerlie, K.P. & Johnston, A.D. (1992). Vapour-absent melting at 10 kbar of biotite- and amphibolites-bearing tonalitic gneiss; implications for the generation of A-type granites. *Geology* **20**, 263-266.

Sláma, J., Košler, J., Condon D.J., Crowley, J.L., Gerdes, A., Hanchar, J.M., Horstwood, M.S.A, Morris, G.A., Nasdala, L., Norberg, N., Schaltegger, U., Schoene B, Tubrett M.N. & Whitehouse, M.J. (2008). Plešovice zircon-a new natural reference material for U-Pb and Hf isotopic microanalysis. *Chemical Geology*, **249**:1-35.

Smerekanicz, J.R. and Dudas, F.O. (1999). Reconnaissance fluid inclusion study of Morefield pegmatite, Amelia County, Virginia. *American Mineralogist*, **84**, 746-753.

Smirmov, V., Pentelkov, V., Tolochko, V., Trifan, M. & Zhukov, S. (1973). Geology and minerals of the central part of the western rift. *Geological Survey of Tanzania, Report (USSR) on Geological Mapping,* p333.

Smith, P.E. & Farquhar, R.M. (1989). Direct dating of Phanerozoic sediments by the ^{238}U-^{206}Pb method. *Nature*, **341** , pp. 518-520.

Snelling, N.J. (1963). Age Determination Unit. Overseas Geological Surveys Annual Report (for 1962), 30-39.

Soave, G. (1972). Equilibrium constants from a modified Redlich-Kwong equation of state. *Chemical Engineering Science*, **27**, 1197-1203.

Sommer, H., Hauzenberger, C., Kröner, A., Wingate, M.T.D. & Muhongo, S. (2003). Metamorphic petrology and zircon geochronology of high-grade rocks from the Central Mozambique Belt of Tanzania, crystal recycling of Archean and Palaeoproterozoic material during the Pan-African Orogeny. *Journal of Metamorphic Geology,* **21**, 915-934.

Sowerby, J.R. & Keppler, H. (2002). The effect of fluorine, boron, and excess sodium on the critical curve in the albite-H_2O system. *Contributions to Mineralogy and Petrology,* **143**, 32-37.

Span, R. & Wagner, W. (1996). A new equation of state for carbon dioxide covering the fluid region from triple –point temperature to 1100 K at pressures up to 800 MPa. *Journal of Physical Chemistry Reference Data* **25**, 1509-1596.

Stacey, J.S. & Kramers J.D. (1975). Approximation of terrestrial lead isotope evolution by a two-stage model. *Earth Planetary Sciences Letters*, **26**: 207-227.

Stern, R.J. (1994). Arc assembly and continental collision in the Neoproterozoic East African Orogen: Implications in the consolidation of Gondwanaland. *Annual Reviews of Earth and Planetary Science*, **22**, 319-354.

Sutton, J., Watson, J. & James, T.C. (1954). A study of the metamorphic rocks of Karema and Kungwe Bay, Western Tanganyika. *Geological Survey of Tanganyika, Bulletin* **22,** pp70.

Swanson, S.E. & Fenn, P.M. (1992). The effect of F and Cl in albite crystallisation: a model for granitic pegmatites? *Canadian Mineralogist,* **30**, 549-559.

Tack, L., Wingate, M., De Waele, B., Meert, J., Belousova, E.A., Griffin, B., Tahon, A. & Fernandes, A. (2010). The 1375 Ma „Kibaran event" in Central Africa: Prominent emplacement of bimodal magmatism under extensional regime. *Precambrian Research*, **180**, 63-84.

Taylor, B.E., Foord, E.E. & Friedrichsen, H. (1979). Stable isotope and fluid inclusions studies of gem-bearing granitic pegmatite-aplite dikes, San Diego Co., California. *Contributions to Mineralogy and Petrology,* **68**, 187-205.

Taylor, S.R. & McLennan, S.M. (1995). The geochemical evolution of the continental crust. *Reviews in Geophysics,* **33,** 241-265.

Taylor, S.R., Rudnick R.L., McLennan, S.C. & Ericksson K.A. (1986). Rare-earth element patterns in Archean high-grade metasediments and their tectonic significance. *Geochimica et Acta*, **50**, 2267-2279.

Thatcher, E.C. (1973). Gneisses and granites in the Malawi Province of the Mozambique Belt. *Special Publication of Geological Society of South Africa,* **3**, 149-155.

Thatcher, E.C. (1974). The geology of the Nyika area. *Bulletin of Geological Survey, Malawi,* **40**, 1-90.

Theunissen, K., Klerkx J., Melnikov, A. &, Mruma A. (1996). Mechanisms of inheritance of rift faulting in the western branch of East African Rift, Tanzania. *Tectonic*s **15(4**), 776-790.

Theunissen, K., Lenoir, J.L., Liegeois, J.P., Delvaux, D. & Mruma, A. (1992). Empreinte pan-africane majeure dans la chaine Ubendienne de Tanzanie sud –occidentale; geochronology U-Pb sur zircon et context structural. C.*R. Acadamie Science Paris* **314**, 1355-1362.

Thiery, R., Kerkhof, A.M. van den, & Dubessy, J. (1994a). Phase equilibria modelling applied to fluid inclusions: liquid-vapour equilibria and calculations of molar volume in the CO_2-CH_4-N_2 system. *Geochemica et Cosmochimica Acta* **58**, 1073-1082.

Thiery, R., Kerkhof, A.M. van den, & Dubessy, J. (1994b). vX properties of CH_4-CO_2 and CO_2-N_2 fluid inclusions: Modelling for T<31^{o}C and P<400 bars. *European Journal of Mineralogy*, **6**, 753-771.

Thomas, R.J., Agenbacht, A.L.D., Cornell, D.H., & Moore, J.M. (1994) The Kibaran of southern Africa: tectonic evolution and metallogeny. *Ore Geology Reviews* **9**, 131-160.

Thomas, R. M., Foster, H.J. & Heinrich, W. (2003). The behaviour of boron in a peraluminous granite-pegmatite system and associated hydrothermal solutions: a melt and fluid inclusion study, *Contributions to Mineralogy and Petrology*, **144**: 457-472.

Thomas, R. & Davidson, P. (2012). Water in granite and pegmatite-forming melts. *Ore Geology Reviews,* **46**, 32-46.

Thomas, R., Davidson, P. & Beurlen, H. (2012). The competing models for the origin and internal evolution of granitic pegmatites in the light of melt and fluid inclusion research. *Mineralogy and Petrology,* **106**, 55-73.

Thomas, R., Davidson, P. & Badanina, E. (2009). A melt and fluid inclusions assemblage in beryl from pegmatite in the Orlovka amazonite granite, East Transbaikalia, Russia: implications for pegmatite-forming melt systems. *Mineralogy and Petrology,* **96**, 29-140.

Thomas, R., Webster, J.D. & Davidson, P. (2011). Be-daughter minerals in fluid and melt inclusions: implications for the enrichment of Be in granite-pegmatite systems. *Contributions to Mineralogy and Petrology,* **161**, 483-495.

Thomas, R., Webster, J.D., Rhede, D., Seifert, W., Rickers, K., Forster, H. J, Hendrich, W. & Davidson, P. (2006). The transition from peraluminous to peralkaline granitic melts; Evidence from the melt inclusions and accessory minerals. *Lithos,* **91**, 137-149.

Tischendorf, G., Gottesmam, B., Föster, H. & Trumbull, R.B. (1997). On Li-bearing micas: estimating Li from electron microprobe analyses and an improved diagram for graphical representation. *Mineralogical Magazine,* **61**, 809-834.

Trueman, D.I. & Cërny, P. (1982). Exploration of rare-element granitic pegmatites. *In* Granitic pegmatites in science and industry, (ed.) Cërny, P. *Mineralogical Association of Canada, Short Course Handbook,* **8**, 463-493.

Ueda, K., Jacobs J., Thomas, R.J., Kosler, J., Jourdan, F. & Matola, R. (2012). Delamination-induced late-tectonic deformation and high-grade metamorphism of the Proterozoic Nampula Complex, northern Mozambique. *Precambrian Research,* **196-197**, 275-94.

UNESCO Geotraverse Team, (1983). Structural evolution of the Ubendian Belt; preliminary results of a geotraverse between Karema and Mpanda (Tanzania) Musee Royale I"Afrique Centrale (Tervuren, Belgium). *Departement Geologique Minerale Rapporte Annale,* **1981-1982**, 147-152.

Unrug, R. (1992). The supercontinent cycle and Gondwanaland assembly: Component cratons and the timing of suturing events. *Journal of Geodynamics*, **16**, 215-240.

Unrug, R. (1996). The assembly of Gondwanaland. *Episodes*, **19**, 11-20.

Unrug, R. (1998). The geodynamic map of Gondwana supercontinent assembly. *Journal of Earth Sciences,* **26(2)** ix-x.

Van den Kerkhof, A.M. (1988). CO_2 – CH_4 – N_2 in fluid inclusions: theoretical modelling and geological applications. PhD. Diss. Free Uni., Amsterdam, 206pp.

Van Orman, J.R., Grove T.L., Shimidzu, N. & Layne, G.D. (2001). Rare earth element diffusion in a natural pyrope single crystal at 2.8 GPa. *Contributions of Mineralogy and Petrology,* **142**, 1095-1117.

Varlamoff, N. (1972). Central and West African rare-metal granitic pegmatites, related aplites, quartz veins and mineral deposits. *Mineralium Deposita*, **7(2)**, 202-216.

Vieira, R., Roda-Robles, E., Persquera, A., & Lima, A.M.C. (2011). Chemical variation and significance of micas from Fregenada-Almendra pegmatitic field (Central–Iberian Zone, Spain and Portugal, *American Mineralogist,* **96 (4)**: 637-645.

Villa, I.M., De Bièvre, P., Holden, N.E. & Renne, P.R. (2015). IUPAC-IUGS recommendation on the half-life of ^{87}Rb. *Geochimica et Cosmochimica Acta*, **164**, 382-385.

Villaros, A., Deveaud, S. & Pichavant, M. (2010). Mica crystallisation as a marker of pegmatite composition. 21st Meeting of the International Mineralogical Association, Sep 2014, Johannesburg, South Africa. *gp10-pegmatites, and pegmatites mineralogy* – poster, pp. **270**. http://www.ia2014.co.za/documents/IMA2014%ABSTRACT%20VOLUME_2.pdf

Viola, G., Hendersen, I.H.C., Bingen, B., Thomas, R.J., Smethurst, M.A. & de Azavedo, S. (2008). Growth and collapse of a deeply eroded orogen; insights from structural and geochronological constraints on the Pan-African evolution of NE Mozambique. *Tectonics* **27**, TC5009. http://dx.doi.org/10.1029/2008TC002284.

Vrana, S., Kachlik, V., Kröner, A., Marheine, D., Seifert, A.V., Iaaek, V. & Baburek, J. (2004). Ubendian basement and its late Mesoproterozoic and early Neoproterozoic structural and metamorphic overprint in north-eastern Zambia. *Journal of African Earth Sciences* **38**, 1-21.

Walshaw, R.D. (1965). The geology of the Ntcheu-Balaka Area. *Bulletin of Geological Survey Malawi* **19**.

Walter, M.J. (1972). The geology of the Lilongwe-Dowa area. *Bulletin of Geological Survey Malawi* **26**.

Wang, Z.G., Yu, X.Y. & Zhao, Z, H. (1989). Geochemistry of rare earth elements, Science Press, Beijing, **535**p.

Webber, K.L. & Simmons, W.B. (2007). Crystallisation dynamics in granitic pegmatites: *The State of the art- International Symposium* 06th-12th May 2007, Porto, Portugal.

Webber, K.L., Falster, A.U., Simmons, W.B. & Foord, E.E. (1997). The role of diffusion - controlled oscillatory nucleation in the formation of line rock in pegmatite-aplite dikes. *Journal of Petrology* **38**, 1777-1791.

Westerhof, A.B.P, Lehtonen, M.I., Makitie, H., Manninen, T., Pekkala, Y., Gustafsson, B. & Tahon, A. (2008). The Tete-Chipata Belt: a new multiple terrane element from Western Mozambique and Southern Zambia *In*: Pekkala, Y., Lehto, T., and Makititie, H. (Eds.) GTK Consortium Geological Surveys in Mozambique 2002-2007, *Geological Survey of Finland, Special Paper,* **48**, 145-166.

White, W.M. (2015) Isotope geochemistry. Wiley Blackwell **496**.

Wiedenbeck, M., Allé, P., Corfu, F., Griffin, W.L., Meier, M., Oberli, F., Von Quadt, A., Roddick, J.C. & Spiegel, W. (1995). Three natural zircon standards for analyse. *Geostandards Newsletter*, **19**, 1-23.

Wilson, T.J., Grunow, A. M. & Hanson, R. E. (1997). Gondwana assembly: the view from southern Africa and east Gondwana. *Journal of Geodynamics*, **23**, 263-286.

Wise, M.A., (1999). Characterization and classification of NYF-type pegmatites. *Canadian Mineralogist*, **37**, 802-803.

Wise, M.A. (2009). Mineralogy, petrology, and geochemistry of granitic pegmatites; *a publication of PegCamp 2009*; Washington D.C., Smithsonian Institution, **44**.

WITec Project Data Analysis Software, (2012). WITec GmbH.

Woolley, A.R. (2001). Alkaline rocks and carbonatites of the world. **3**. *Africa*. *The Geological Society of London*, London, U.K.

Woolley, A.R. & Jones, G.C (1987). Lithosphere metasomatism and the petrogenesis of the Chilwa Province of the alkaline igneous rocks and carbonatites, Malawi. *Journal of African Earth Sciences* **6**, 891-898.

World Bank, (2015). New York, USA, accessed September 15, 2017 via URL http://projects.worldbank.org/P120825/mw-mining-governance-growth-support-project?lang=en

World Bank, (2017). New York, USA, accessed August 29, 2017 via URL http://www.worldbank.org/en/country/malawi/overview

Zgambo, N. (1995). The Lundazi aquamarine pegmatites of Eastern Zambia *(1995 International Conference on Industrial Minerals: Investment Opportunities in Southern Africa 7-9 June 1995 Proceedings)*.

Zhang Y.G., & Frantz J.D. (1987). Determination of the homogenisation temperatures and densities of supercritical fluids in the system NaCl-KCl-$CaCl_2$-H_2O using synthetic fluid inclusions. *Chemical Geology,* **64**, 335-350.

APPENDICES

Appendix 1.1: Sample Codes for geochemical, Geochronological and Fluid inclusion studies and mineralogical features of the studied pegmatites from Malawi.

MICA GEOCHEM. CODE	GEOCHRON. CODE	FLINC. (QTZ) CODE	Mineralogical features
CNC1B, 1B2, 1B3			Qtz, Kfs, Ms, Tur, Ab, and Ta, whereas Grt, Ap, Ilm and Sp are accessory minerals.
	GCN1		Two Ms varieties of different grain size (Ms 1 and 2) – Kfs used for Rb-Sr dating
		CNC1B_1	Qtz
		CNC1B2_1	Qtz
CCC			Varying amounts of light grey Ms, Kfs, clear Qtz, Brl, Pl, Tur, and occasional Grt and Ta. Deep blue Brl.
MWC			Ms, Kfs, Qtz, Brl, Tur and occasional Ta.
	GCW 1		Pl and two texturally distinct varieties of Ms used for Rb-Sr dating
		CCC1B_1	Qtz
		MWC _1	Qtz
GM			
GM1			Qtz, Pl, Kfs, greyish Ms, Brl, Mnz, Grt and Sp.
GM3			Qtz, Pl, Kfs, pale brownish Ms, Brl, Mnz, Grt, with occasional Ta.
GM5			Qtz, Pl, Kfs, pale greenish Ms, Brl, Scl, Mnz, Grt, with occasional Ta.
		GM3_1	Qtz
		GM5_1	Qtz
		MEM1B_1	Light to deep purple amethyst from Qtz veins
	GM1		Two Ms varieties, Kfs and Pl were used for Rb-Sr dating
HEM			
HEM2A			Pl, Ep, greyish Ms, Kfs, Brl, Grt, clear Qtz, black Tur
HEM3B			Pl, Ep, greyish Ms, Grt, pale blue Brl, Qtz, black Tur and occasional Ta.
HEM4B			Pl, Ep, greyish to black Bt, Kfs, Grt, clear Qtz and black Tur with striations
		HEM1A_1	Qtz
		HEM2C_1	Qtz
DHD			
DHD1A			Pl, elongated light grayish Ms books, Kfs, Tur, some Qtz showing sugary texture, Grt, Ap and Sp.
DHD1B			Pl, Ms, Kfs, Tur, Qtz, Grt, Ap, and occasional Ta.
DHD1C			Pl, Ms, Tur, Qtz, Grt, Sp and occasional Ta
DHD1E			Pl, Kfs, sporadic Bt, Qtz, Grt, Sp and some Tur.
	GD1		Ms1/2 and Pl
		DHD1C_1	Qtz

Symbols used: Ab: albite, Ap: Apatite, Bt: biotite: Kfs: K-feldspar, Ms: muscovite, Qtz: quartz, Tur: tourmaline: Zrn: zircon, Scl: schorl, Mic: microcline, Ilm: ilmenite, Ta; tantalite, Mnz: monazite, Pl: plagioclase, Grt: garnet, Sp: sphene, Brl: beryl, Aeg: aegerine.

Appendix 1.1 (continued**):** Sample Codes for geochemical, Geochronological and Fluid inclusion studies and mineralogical features of the studied pegmatites from Malawi.

MICA GEOCHEM. CODE	GEOCHRON. CODE	FLINC. (QTZ) CODE	Mineralogical features
GENERAL for GNS1-7			Tur is occasionally in massive form but usually it is subhedral. It varies from black tourmaline to yellowish green to deep green in colour. Tur shows radiating growth on micas. Ms is found in all the zones but in some samples there are two texturally distinct varieties of Ms. Blocky feldspar predominates the intermediate zone.
GNS1-3			
GNS1			Coarse-grained Qtz, greenish Ms often intergrown with Tur, some Tur radiates on greenish muscovite. Kfs, Pl, Mnz, Grt, Sp and occasional Ta.
GNS3			Coarse - grained Qtz, pale greenish to medium brown Ms, Kfs, Pl, Scl, Mnz, Grt, and Sp.
	GNS1		two texturally distinct fractions of Ms, Kfs and Pl were used for Rb-Sr dating.
		GNS1	Qtz
GNS4-7			
GNS4			Pl, Qtz, books of light brown Ms, and Tur
GNS6			Pl, Qtz, Kfs, light colour to pale greenish Ms, Tur, Grt. Mnz, and Sp.
GNS7			Pl, Qtz, whitish Kfs, greenish to amber Ms, Tur, Grt, Mnz, and Sp.
	GNS4		Ms fractions and Pl used for Rb-Sr dating
		GNS4_1	Qtz
MSN			
MSN1B			Qtz, Pl (oligoclase), alkali feldspar, light greyish to greenish Ms, Tur, red Grt, Sp and Mnz.
MSN2B			Qtz, Pl (oligoclase), alkali feldspar, light brownish Ms, and Tur.
MSN3A			Qtz, Pl (oligoclase), alkali feldspar, Tur, light greyish Ms, Mnz, Grt, and Ilm.
MSN3D			Qtz, Pl (oligoclase), alkali feldspar, Tur, light greyish Ms, red Grt, Sp and Mnz.
GN1			Kfs, Ms, Qtz, and Tur.
	GN1		Ms1/2 and Kfs used for Rb-Sr dating.
		MSNB2	Qtz
		MSN7g	Qtz
General for CUB			Pegmatites show amethyst colours of different intensities from light purple (stage 1) to deep purple (stage 4).Occasionally, the amethyst is twinned and it has double terminations. The feldspar has dark grey to pinkish colour.
CUB1B			blackish Bt , Kfs, Qtz, Pl and accessory Grt, Ilm and Mnz. Has stage 4 more deep purple amethyst,
CUB2B			light brownish Bt , Kfs, Qtz, Pl, Ep and accessory Grt, Ilm and Mnz. Has stage 3 deep purple amethyst.
CUB3B			Bt, Kfs, Qtz, Pl and accessory Grt, Ilm and Mnz. Has stage 2 purple amethyst, and brownish Bt

Symbols used: Ab: albite, Ap: Apatite, Bt: biotite: Kfs: K-feldspar, Ms: muscovite, Qtz: quartz, Tur: tourmaline: Zrn: zircon, Scl: schorl, Mic: microcline, Ilm: ilmenite, Ta; tantalite, Mnz: monazite, Pl: plagioclase, Grt: garnet, Sp: sphene, Brl: beryl, Aeg: aegerine.

Appendix 1.1 (continued**):** Sample Codes for geochemical, Geochronological and Fluid inclusion studies and mineralogical features of the studied pegmatites from Malawi.

MICA GEOCHEM. CODE	GEOCHRON. CODE	FLINC. (QTZ) CODE	Mineralogical features
CUB4B			dark brownish Bt, Kfs, Qtz, Pl and accessory Grt, Ilm and Mnz. Has stage 1 light purple amethyst.
	GU1		Kfs, Pl and Bt
		CUB1A_1	Qtz
X	**MNM**	**X**	intergrown coarse-grained Kfs, Bt, Zrn, Qtz and accessory phases of Sp and Mnz. Bt shows iron staining. Zrn reaches up approximately 30mm in size and is generally euhedral, elongated, prismatic with bipyramidal terminations. Zrn was used for U-Pb dating.
X	**NNO**	**X**	coarse crystals of Kfs, Tur, Qtz, fairly abundant books of Ms, and the accessory phases Grt, Zrn and Ilm. Euhedral, prismatic Zrn with bipyramidal terminations, and well defined faces. Zrn was used for U-Pb dating.
X	**ZA**	**X**	intergrown coarse-grained Mic, Aeg, Qtz, Bt and light brownish euhedral and prismatic Zrn that was used for U-Pb dating.
X	**THMB**	**X**	intergrown coarse-grained Kfs, Ap, Zrn, Qtz, Bt and Ilm. Zrn reaches up approximately 3.5cm in size and is euhedral, prismatic with bipyramidal terminations, and well-defined faces. Zrn was used for U-Pb dating.

Symbols used: Ab: albite, Ap: Apatite, Bt: biotite: Kfs: K-feldspar, Ms: muscovite, Qtz: quartz, Tur: tourmaline: Zrn: zircon, Scl: schorl, Mic: microcline, Ilm: ilmenite, Ta; tantalite, Mnz: monazite, Pl: plagioclase, Grt: garnet, Sp: sphene, Brl: beryl, Aeg: aegerine.

Appendix 1.2: LA-SF-ICP-MS U-Th-Pb dating methodology, CAF, Stellenbosch University

Laboratory & Sample Preparation	
Laboratory name	Central Analytical Facility, Stellenbosch University
Sample type / mineral	In-situ thin section analysis of zircon
Sample preparation	Polished thin sections
Laser ablation system	
Make, Model & type	ASI Resolution SE50, ArF Excimer ATL Atlex
Ablation cell & volume	Laurin Technology M50 double Helix cell
Laser wavelength	193 nm
Pulse width	20 ns
Fluence	2 J/cm^{-2} (measured with external energy meter above sample funnel)
Repetition rate	9 Hz
Spot size	25 µm
Sampling mode / pattern	25 µm single spot analyses
Cell carrier gas	100% He, Ar and N_2 make-up gases combined using injectors into double Helix sampling funnel
Pre-ablation laser warm-up (background collection)	3 cleaning shots followed by 15 seconds background collection
Ablation duration	15 seconds
Wash-out delay	15 seconds
Cell carrier gas flows	330 ml/min He
ICP-MS Instrument	
Make, Model & type	Thermo Finnigan Element2 single collector HR-SF-ICP-MS
Sample introduction	Via Nylon 10 tubing
RF power	1350 W
Make-up gas flow	910 ml/min Ar & 0.03 ml/min N_2
Detection system	Single collector secondary electron multiplier
Masses measured	202, 204, 206, 207, 208, 232, 233, 235, 238
Integration time per peak	4 ms
Total integration time per reading	1 sec *(represents the time resolution of the data)*
Sensitvity	30000 cps/ppm Pb
Dead time	6 ns
Data Processing	
Gas blank	15 second on-peak
Calibration strategy	Zircon: GJ-1 used as primary reference material, 91500, Plešovice & M127 used as secondary reference material (Quality Control);
Reference Material info	GJ-1 (Jackson et al., 2004), 91500 (Wiedenbeck et al., 1995), M127 (Nasdala et al., 2008; Mattinson 2010), Plesovice (Slama et al., 2008).
Data processing package used / Correction for LIEF	In-house spreadsheet data processing using intercept method for LIEF correction
Mass discrimination	Standard-sample bracketing with $^{207}Pb/^{206}Pb$ and $^{206}Pb/^{238}U$ normalized to reference material GJ-1
Common-Pb correction, composition and uncertainty	204-method, Stacey & Kramers (1975) composition at the projected age of the mineral, 5% uncertainty assigned
Uncertainty level & propagation	Ages are quoted at 2 sigma absolute, propagation is by quadratic addition. Reproducibility and age uncertainty of reference material and common-Pb composition uncertainty are propagated.
Quality control / Validation	M127: Concordia age = 527±5 Ma (2s, MSWD = 0.88) Plešovice: Concordia age = 339±4 Ma (2s, MSWD = 0.50) 91500: Concordia age = 1065±22 Ma (2s, MSWD = 0.76)
Other information	For detailed method description see Frei & Gerdes (2009)

Appendix 2.1A: Detailed major elements data of micas from the Palaeoproterozoic tourmaline-bearing pegmatite (CNC) from Nthalire, and from the Pan-African beryl- and tourmaline-bearing pegmatites from Chisenga (CCC) and Wenya (MWC) in Chitipa.

Sample	CNC1B_1	CNC1B_2	CNC1B_3	CNC1B_4	CNC1B_5	CNC1B_6	CNC1B_7	CNC1B_8	CNC1B_9	CNC1B_10
SiO_2	45.99	44.83	45.54	45.74	45.65	45.56	45.69	45.39	45.84	45.87
TiO_2	0.20	0.19	0.22	0.24	0.30	0.21	0.32	0.32	0.31	0.31
Al_2O_3	32.76	32.17	32.73	32.73	32.70	32.58	32.64	31.87	32.35	32.45
FeO	4.14	4.25	3.42	3.40	3.69	4.00	3.58	3.76	3.81	3.77
MnO	0.12	0.00	0.08	0.00	0.11	0.04	0.08	0.08	0.09	0.00
MgO	1.01	1.01	0.98	1.00	1.02	1.11	1.00	1.06	1.15	1.05
CaO	0.00	0.01	0.02	0.03	0.00	0.04	0.00	0.00	0.00	0.02
Na_2O	0.71	0.57	0.57	0.56	0.73	0.50	0.59	0.52	0.62	0.47
K_2O	12.24	11.75	11.96	12.40	13.03	12.69	12.73	12.24	12.26	12.49
F	0.00	0.00	0.12	0.00	0.00	0.08	0.00	0.00	0.06	0.09
Cl	0.01	0.03	0.03	0.00	0.02	0.00	0.00	0.04	0.01	0.00
Li_2O*	0.00	0.00	0.00	0.00	0.00	0.00	0.00	0.00	0.00	0.00
H_2O*	4.48	4.35	4.35	4.43	4.45	4.44	4.49	4.37	4.40	4.40
Subtotal	101.67	99.16	100.01	100.54	101.69	100.67	101.11	99.65	100.89	100.92
O=F,Cl	0.00	0.01	0.06	0.00	0.01	0.03	0.00	0.01	0.03	0.04
Total	101.67	99.15	99.95	100.54	101.69	100.64	101.11	99.64	100.86	100.88
Si	6.15	6.17	6.19	6.19	6.15	6.19	6.17	6.21	6.20	6.20
Al^{iv}	1.85	1.83	1.81	1.81	1.85	1.81	1.83	1.79	1.80	1.80
Al^{vi}	3.38	3.38	3.43	3.41	3.34	3.36	3.37	3.36	3.35	3.37
Ti	0.02	0.02	0.02	0.03	0.03	0.02	0.03	0.03	0.03	0.03
Fe	0.46	0.49	0.39	0.39	0.42	0.45	0.40	0.43	0.43	0.43
Mn	0.01	0.00	0.01	0.00	0.01	0.01	0.01	0.01	0.01	0.00
Mg	0.20	0.21	0.20	0.20	0.21	0.22	0.20	0.22	0.23	0.21
Li*	0.00	0.00	0.00	0.00	0.00	0.00	0.00	0.00	0.00	0.00
Ca	0.00	0.00	0.00	0.01	0.00	0.01	0.00	0.00	0.00	0.00
Na	0.18	0.15	0.15	0.15	0.19	0.13	0.15	0.14	0.16	0.12
K	2.09	2.06	2.07	2.14	2.24	2.17	2.23	2.14	2.11	2.15
OH*	4.00	3.99	3.94	4.00	4.00	3.97	4.00	3.99	3.97	3.96
F	0.00	0.00	0.05	0.00	0.00	0.03	0.00	0.00	0.03	0.04
Cl	0.00	0.01	0.01	0.00	0.01	0.00	0.00	0.01	0.00	0.00
TOTAL	18.35	18.31	18.28	18.32	18.44	18.35	18.39	18.32	18.33	18.32
Y total	4.08	4.10	4.05	4.03	4.01	4.05	4.01	4.05	4.06	4.04
X total	2.27	2.22	2.23	2.29	2.43	2.30	2.39	2.27	2.28	2.28

* Calculated.

Appendix 2.1A (continued): Detailed major elements data of micas from the Palaeoproterozoic tourmaline-bearing pegmatite (CNC) from Nthalire, and the Pan-African beryl- and tourmaline-bearing pegmatites from Chisenga (CCC) and Wenya (MWC) in Chitipa.

Sample	CCC1A_1	CCC1A_2	CCC1A_3	CCC1A_4	CCC1A_5	CCC1A_6	CCC1A_7	CCC1A_8	CCC1A_9	CCC1A_10
SiO_2	46.11	46.21	46.42	46.04	46.58	46.33	46.59	46.33	44.52	46.64
TiO_2	0.34	0.33	0.35	0.34	0.36	0.37	0.32	0.36	0.28	0.38
Al_2O_3	32.39	32.02	32.29	32.61	32.57	32.54	32.39	32.26	31.30	32.53
FeO	3.56	3.47	3.63	3.16	3.51	3.52	3.23	3.36	4.90	3.14
MnO	0.11	0.04	0.06	0.07	0.01	0.07	0.07	0.03	0.15	0.04
MgO	0.94	0.93	0.93	0.88	0.88	0.92	0.93	0.99	0.89	0.89
CaO	0.00	0.04	0.00	0.00	0.00	0.01	0.00	0.05	0.03	0.00
Na_2O	0.88	0.49	0.68	0.85	0.75	0.58	0.47	0.63	0.35	0.75
K_2O	12.62	12.92	12.66	12.21	12.28	12.52	10.89	12.84	12.40	12.52
F	0.82	0.95	0.78	0.78	0.83	0.74	0.74	0.70	0.69	0.63
Cl	0.01	0.00	0.04	0.05	0.01	0.00	0.04	0.02	0.02	0.01
Li_2O*	0.18	0.22	0.17	0.17	0.18	0.15	0.15	0.14	0.14	0.12
H_2O*	4.09	4.00	4.10	4.06	4.13	4.12	4.08	4.13	4.00	4.25
Subtotal	102.05	101.60	102.12	101.21	102.09	101.87	99.91	101.84	99.66	101.90
O=F,Cl	0.35	0.40	0.34	0.34	0.35	0.31	0.32	0.30	0.30	0.27
Total	101.70	101.21	101.86	100.87	101.74	101.56	99.59	101.54	99.37	101.64
Si	6.17	6.24	6.23	6.21	6.21	6.22	6.30	6.23	6.16	6.15
Al^{iv}	1.83	1.76	1.77	1.79	1.79	1.79	1.70	1.77	1.84	1.85
Al^{vi}	3.28	3.33	3.34	3.39	3.39	3.36	3.46	3.34	3.27	3.36
Ti	0.04	0.03	0.04	0.03	0.04	0.04	0.03	0.04	0.03	0.04
Fe	0.40	0.39	0.41	0.36	0.39	0.40	0.37	0.38	0.57	0.35
Mn	0.01	0.01	0.01	0.01	0.00	0.01	0.01	0.00	0.02	0.01
Mg	0.19	0.19	0.19	0.18	0.17	0.19	0.19	0.20	0.18	0.18
Li*	0.10	0.12	0.09	0.09	0.10	0.08	0.08	0.08	0.08	0.06
Ca	0.00	0.01	0.00	0.00	0.00	0.00	0.00	0.01	0.00	0.00
Na	0.23	0.13	0.18	0.22	0.19	0.15	0.12	0.17	0.09	0.19
K	2.33	2.22	2.16	2.10	2.07	2.14	1.88	2.20	2.19	2.32
OH*	3.65	3.60	3.66	3.66	3.65	3.69	3.68	3.70	3.69	3.74
F	0.35	0.40	0.33	0.33	0.35	0.31	0.32	0.30	0.30	0.26
Cl	0.00	0.00	0.01	0.01	0.00	0.00	0.01	0.01	0.01	0.00
TOTAL	18.57	18.42	18.39	18.38	18.35	18.36	18.13	18.40	18.43	18.50
Y total	4.01	4.06	4.06	4.05	4.08	4.07	4.13	4.03	4.15	3.98
X total	2.55	2.36	2.34	2.32	2.27	2.30	2.00	2.37	2.29	2.52

* Calculated.

Appendix 2.1A: (continued): Detailed major elements data of micas from the Palaeoproterozoic tourmaline-bearing pegmatite (CNC) from Nthalire, and the Pan-African beryl- and tourmaline-bearing pegmatites from Chisenga (CCC) and Wenya (MWC) in Chitipa.

Sample	MWC1A_1	MWC1A_2	MWC1A_3	MWC1A_4	MWC1A_5	MWC1A_6	MWC1A_7	MWC1A_8	MWC1A_9	MWC1A_10
SiO_2	46.27	46.33	46.59	46.71	47.01	46.60	46.53	46.24	46.32	46.58
TiO_2	0.62	0.59	0.63	0.67	0.61	0.65	0.62	0.61	0.68	0.67
Al_2O_3	32.55	32.81	32.23	32.44	32.64	32.36	32.21	32.30	32.10	32.53
FeO	3.21	3.05	3.67	3.42	3.41	3.58	3.53	3.48	3.70	3.64
MnO	0.06	0.07	0.03	0.05	0.07	0.02	0.02	0.09	0.18	0.15
MgO	1.07	1.01	1.04	1.06	1.01	1.05	1.08	1.09	1.03	1.05
CaO	0.00	0.00	0.01	0.03	0.00	0.00	0.01	0.00	0.00	0.00
Na_2O	0.65	0.71	0.68	0.57	0.64	0.57	0.91	0.63	0.60	0.56
K_2O	11.42	11.71	12.01	12.04	11.12	12.03	11.25	10.87	12.19	11.62
F	1.20	1.09	1.02	0.96	1.01	1.15	0.99	1.01	1.17	1.20
Cl	0.00	0.00	0.00	0.00	0.00	0.02	0.02	0.01	0.00	0.01
Li_2O*	0.30	0.26	0.24	0.22	0.24	0.28	0.23	0.24	0.29	0.30
H_2O*	3.98	4.05	4.09	4.07	4.03	3.95	4.08	4.05	4.11	3.97
Subtotal	101.32	101.67	102.23	102.05	101.78	102.26	101.50	100.61	102.46	102.27
O=F,Cl	0.51	0.46	0.43	0.40	0.43	0.49	0.42	0.43	0.49	0.51
Total	100.81	101.21	101.80	101.64	101.36	101.77	101.08	100.19	101.97	101.76
Si	6.23	6.22	6.14	6.22	6.26	6.22	6.18	6.25	6.21	6.19
Al^{iv}	1.77	1.78	1.86	1.78	1.74	1.78	1.82	1.75	1.79	1.81
Al^{vi}	3.30	3.31	3.27	3.31	3.38	3.31	3.24	3.31	3.28	3.26
Ti	0.08	0.08	0.08	0.09	0.06	0.08	0.08	0.08	0.08	0.09
Fe	0.35	0.34	0.41	0.38	0.38	0.40	0.43	0.39	0.39	0.40
Mn	0.01	0.01	0.00	0.01	0.01	0.00	0.00	0.01	0.02	0.02
Mg	0.21	0.20	0.20	0.21	0.20	0.21	0.21	0.22	0.19	0.21
Li*	0.16	0.14	0.13	0.12	0.13	0.15	0.12	0.13	0.15	0.16
Ca	0.00	0.00	0.00	0.00	0.00	0.00	0.00	0.00	0.00	0.00
Na	0.17	0.18	0.17	0.15	0.17	0.15	0.23	0.16	0.15	0.14
K	2.09	2.13	2.18	2.04	1.89	2.04	2.11	2.00	2.12	2.13
OH*	3.50	3.55	3.58	3.60	3.58	3.51	3.58	3.58	3.53	3.50
F	0.50	0.45	0.42	0.40	0.43	0.48	0.41	0.42	0.47	0.50
Cl	0.00	0.00	0.00	0.00	0.00	0.00	0.01	0.00	0.00	0.00
TOTAL	18.36	18.38	18.45	18.30	18.21	18.33	18.44	18.29	18.38	18.40
Y total	4.11	4.07	4.10	4.11	4.16	4.14	4.10	4.12	4.11	4.13
X total	2.25	2.31	2.35	2.19	2.05	2.19	2.34	2.17	2.26	2.27

* Calculated

Appendix 2.1B: Detailed trace element data of micas from the Palaeoproterozoic tourmaline-bearing pegmatite from Nthalire in Chitipa. All concentrations are given in ppm.

Element	CNC1B1	CNC1B2	CNC1B3	CNC1B4	CNC1B5	CNC1B6	CNC1B7	CNC1B8	CNC1B9	CNC1B10
Li	37.66	35.45	32.46	33.25	36.95	37.36	36.78	33.26	27.54	29.56
Be	2.52	1.71	2.51	3.03	2.24	3.74	2.47	4.74	2.04	7.32
B	42.63	42.96	50.57	59.30	61.17	57.98	52.93	52.93	46.58	66.96
Sc	56.81	36.61	29.69	27.40	21.22	44.44	29.17	19.07	25.88	20.39
Ti	1756.77	1595.10	1478.30	1350.49	1291.83	1648.08	1466.71	1245.57	1369.85	2088.13
V	12.32	15.80	18.42	20.30	28.67	13.66	18.94	28.89	20.02	128.14
Cr	0.16	0.15	0.14	0.14	0.15	0.18	0.18	0.29	0.16	12.56
Mn	270.49	258.88	273.09	262.48	277.25	263.17	262.18	230.65	229.72	241.19
Co	4.09	4.93	4.50	4.12	5.43	8.49	4.81	3.60	4.01	3.53
Ni	2.66	2.57	3.63	4.06	3.46	2.90	3.38	4.41	3.78	4.48
Cu	0.47	0.14	0.15	0.04	0.22	0.09	0.05	0.21	0.22	33.61
Zn	59.42	51.12	58.94	55.52	64.12	62.19	60.66	36.59	37.82	127.62
Ga	139.77	120.37	120.76	112.29	115.85	128.68	122.01	109.51	110.42	85.11
Rb	1636.70	1509.73	1579.15	1510.58	1516.40	1567.25	1531.14	1547.76	1510.02	1075.68
Sr	2.39	2.30	2.64	2.36	2.78	2.95	2.70	2.73	2.85	6.19
Y	0.00	0.00	0.01	0.00	0.00	0.00	0.01	0.03	0.01	0.07
Zr	2.97	2.35	2.50	2.42	2.41	2.93	3.03	2.61	2.29	2.11
Nb	440.90	380.31	381.76	297.04	307.59	386.03	347.73	299.88	353.17	46.43
Mo	5.16	4.46	4.40	3.86	4.66	4.71	4.32	4.17	4.28	4.69
Sn	13.12	9.56	9.30	7.21	7.60	9.98	8.38	6.47	7.90	13.46
Cs	26.71	24.23	25.93	27.39	27.76	26.91	25.17	31.47	26.81	99.30
Ba	72.25	73.96	87.08	78.76	171.17	80.92	81.22	61.45	82.91	335.02
Hf	0.45	0.40	0.44	0.43	0.39	0.55	0.46	0.52	0.34	0.27
Ta	14.78	14.93	16.73	14.74	17.11	15.75	16.28	17.82	16.75	11.47
W	89.03	76.09	83.68	67.71	75.42	84.35	76.36	68.48	77.33	59.28
Pb	3.85	3.12	3.81	3.65	4.16	4.51	4.06	5.09	3.48	8.93
Th	0.0008	0.0008	0.0016	0.0000	0.0018	0.0014	0.0016	0.0022	0.0000	0.0034
U	0.0257	0.0244	0.0224	0.0186	0.0264	0.0148	0.0187	0.0248	0.0163	0.0225

Appendix 2.1B (continued): Detailed trace element data of micas from the Pan-African beryl- and tourmaline-bearing pegmatites from Chisenga (CCC) and Wenya (MWC) in Chitipa. All concentrations are given in ppm.

Element	CCC1A1	CCC1A2	CCC1A3	CCC1A4	CCC1A5	CCC1A6	CCC1A7
Li	787.52	840.97	976.54	998.65	766.49	803.41	739.05
Be	10.13	12.16	9.85	14.81	10.44	10.42	9.01
B	37.65	35.75	44.58	28.86	34.93	30.88	33.80
Sc	35.40	37.07	28.29	27.34	36.55	39.13	37.51
Ti	2328.41	2531.14	2075.42	2182.83	2387.78	2547.51	2492.39
V	39.04	51.06	23.62	33.72	45.78	50.13	54.02
Cr	1.66	3.67	32.17	7.46	0.95	1.31	2.31
Mn	475.97	507.05	481.27	543.28	494.36	529.42	493.02
Co	15.49	12.27	2.77	23.58	3.48	4.98	3.33
Ni	1.70	1.97	2.61	2.94	1.67	1.67	1.78
Cu	0.86	1.10	0.75	0.41	0.36	1.50	1.17
Zn	118.65	123.38	133.26	127.70	130.90	135.90	127.96
Ga	129.15	126.85	117.94	120.43	125.90	133.90	123.37
Rb	1458.32	1410.35	1349.77	1446.79	1431.13	1506.23	1484.93
Sr	1.38	1.43	1.12	1.22	1.54	1.70	1.52
Y	0.00	0.07	0.01	0.00	0.03	0.01	0.00
Zr	2.11	2.44	1.63	1.90	2.09	2.23	2.26
Nb	200.05	205.09	190.37	200.13	210.12	222.10	211.28
Mo	0.10	0.09	0.02	0.12	0.11	0.11	0.13
Sn	25.08	25.73	20.75	22.63	25.42	29.46	26.71
Cs	16.63	16.23	15.36	17.27	16.16	17.09	16.16
Ba	125.20	143.07	98.91	102.76	140.07	153.96	152.37
Hf	0.27	0.21	0.24	0.23	0.22	0.37	0.27
Ta	11.91	12.42	12.22	13.05	12.87	13.89	12.74
W	25.13	24.37	25.89	24.63	26.46	28.94	25.40
Pb	4.28	4.37	3.26	3.51	4.46	5.55	4.55
Th	0.0014	0.0073	0.0031	0.0000	0.0021	0.0000	0.0022
U	0.0044	0.0053	0.0030	0.0038	0.0069	0.0159	0.0015

Appendix 2.1B (continued): Detailed trace element data of micas from the Pan-African beryl- and tourmaline-bearing pegmatites from Chisenga (CCC) and Wenya (MWC) in Chitipa. All concentrations are given in ppm.

Element	MWC1A1	MWC1A2	MWC1A3	MWC1A4	MWC1A5	MWC1A6	MWC1A7	MWC1A8	MWC1A9	MWC1A10
Li	1072.66	1179.77	1101.93	1235.87	1135.84	1233.14	956.18	1032.64	1321.05	1056.03
Be	17.78	20.26	19.50	16.18	20.79	18.82	26.37	17.35	19.98	20.14
B	40.94	40.92	34.43	26.70	29.02	37.47	38.21	34.76	35.68	30.52
Sc	37.11	39.38	30.87	33.20	38.85	33.93	35.01	40.76	44.80	31.83
Ti	4244.80	4353.38	3787.33	4230.51	4516.85	4142.39	4091.33	4411.86	4906.97	3914.39
V	17.63	19.29	7.82	9.39	18.82	10.42	18.18	17.59	26.11	8.44
Cr	0.12	0.18	0.13	0.14	0.15	0.18	0.62	0.59	0.50	0.14
Mn	693.88	783.23	738.37	733.68	882.27	738.41	875.39	724.08	641.13	798.88
Co	2.42	2.73	2.07	2.64	2.38	2.55	3.33	3.24	3.16	2.27
Ni	0.47	0.20	0.06	0.11	0.38	0.06	0.19	0.17	0.47	0.11
Cu	0.08	0.09	0.03	0.03	0.08	0.04	0.03	0.30	0.20	0.03
Zn	101.07	116.58	118.24	105.82	125.53	112.91	142.31	102.21	97.36	112.03
Ga	116.47	120.57	112.74	127.20	119.19	119.15	117.44	119.02	124.38	116.66
Rb	1582.42	1670.60	1643.21	1660.19	1749.80	1736.53	1555.36	1694.86	1699.32	1744.21
Sr	4.36	4.45	3.17	3.30	3.52	3.77	3.55	4.01	5.08	3.39
Y	0.02	0.02	0.00	0.03	0.04	0.04	0.01	0.01	0.01	0.02
Zr	3.18	3.27	2.66	2.99	2.44	3.27	2.45	2.52	3.38	3.14
Nb	188.83	201.15	190.37	210.01	204.97	204.28	180.90	203.41	210.41	198.49
Mo	0.36	0.16	0.41	0.21	0.10	0.28	0.23	0.34	0.35	0.17
Sn	17.38	16.87	14.38	15.82	14.89	17.01	14.05	15.83	16.57	15.53
Cs	20.53	22.60	22.16	24.09	21.38	24.49	21.28	24.59	20.94	23.92
Ba	105.56	108.48	70.07	75.77	98.89	78.52	102.97	110.75	143.17	67.98
Hf	0.36	0.38	0.31	0.29	0.20	0.22	0.26	0.26	0.34	0.31
Ta	20.09	21.57	20.31	21.50	18.66	21.55	18.73	22.79	23.38	21.04
W	31.51	32.60	30.21	30.93	36.16	32.11	31.25	40.66	41.88	31.81
Pb	4.85	4.57	4.17	4.65	3.81	4.60	4.28	4.19	5.22	4.20
Th	0.0021	0.0012	0.0008	0.0009	0.0012	0.0014	0.0020	0.0026	0.0014	0.0017
U	0.0100	0.0119	0.0143	0.0054	0.0132	0.0016	0.0173	0.0157	0.0012	0.0059

Appendix 2.1C: Detailed Upper Continental Crust (UCC- Taylor and McLennan, 1995) normalised rare earth element (REE) data of micas from the Palaeoproterozoic tourmaline-bearing pegmatites (CNC) from Nthalire in Chitipa. All concentrations are given in ppm.

Element	CNC1B1	CNC1B2	CNC1B3	CNC1B4	CNC1B5	CNC1B6	CNC1B7	CNC1B8	CNC1B9	CNC1B10
La	0.0579	0.8970	0.0360	0.0660	0.8370	0.0000	0.0000	3.5730	0.0000	6.4200
Ce	0.1293	0.0000	0.0902	0.0000	0.1382	0.6272	0.9152	0.1664	0.0000	0.2944
Pr	0.0080	0.0178	0.0080	0.0054	0.0000	0.0000	0.0080	0.1306	0.0511	0.2499
Nd	0.0000	0.2418	0.1716	0.0000	0.0000	0.4160	0.2080	1.1960	0.0000	3.6920
Sm	0.0252	0.0437	0.0176	0.0000	0.0000	0.0378	0.0000	0.0108	0.0630	0.0999
Eu	0.0064	0.0013	0.0000	0.0017	0.0056	0.0000	0.0000	0.0040	0.0000	0.0114
Gd	0.0000	0.0380	0.0251	0.0293	0.0342	0.0000	0.0000	0.0308	0.0000	0.0726
Tb	0.0005	0.0000	0.0009	0.0006	0.0000	0.0000	0.0005	0.0006	0.0000	0.0008
Dy	0.0147	0.0000	0.0000	0.0000	0.0210	0.0000	0.0000	0.0252	0.0000	0.0364
Ho	0.0012	0.0000	0.0008	0.0000	0.0008	0.0011	0.0008	0.0008	0.0000	0.0030
Er	0.0048	0.0000	0.0035	0.0045	0.0065	0.0051	0.0000	0.0101	0.0047	0.0083
Tm	0.0008	0.0000	0.0005	0.0004	0.0002	0.0000	0.0000	0.0078	0.0000	0.0003
Yb	0.0103	0.0000	0.0154	0.0233	0.0000	0.0000	0.0000	0.0180	0.0101	0.0224
Lu	0.0011	0.0005	0.0003	0.0008	0.0010	0.0000	0.0004	0.0012	0.0013	0.0009

Appendix 2.1C: (continued) Detailed UCC-normalised (Taylor and McLennan, 1995) rare earth element (REE) data of micas from the Pan-African beryl- and tourmaline-bearing pegmatites from Chisenga (CCC) and Wenya (MWC) in Chitipa. All concentrations are given in ppm.

Element	CCC1A1	CCC1A2	CCC1A3	CCC1A4	CCC1A5	CCC1A6	CCC1A7
La	0.0000	0.3210	0.0345	0.0000	0.0660	0.0000	0.0990
Ce	0.2176	0.6784	0.0672	0.1600	0.4352	0.0890	0.2624
Pr	0.0000	0.0084	0.0000	0.0110	0.0142	0.0110	0.0121
Nd	0.2288	0.0000	0.0000	0.1378	0.2366	0.0000	0.2132
Sm	0.0000	0.0540	0.0522	0.0000	0.0284	0.0000	0.0311
Eu	0.0024	0.0033	0.0000	0.0045	0.0119	0.0107	0.0193
Gd	0.0194	0.0000	0.0000	0.0000	0.0346	0.0346	0.0220
Tb	0.0005	0.0005	0.0000	0.0005	0.0007	0.0000	0.0000
Dy	0.0000	0.0108	0.0214	0.0000	0.0165	0.0000	0.0130
Ho	0.0006	0.0000	0.0006	0.0009	0.0010	0.0000	0.0000
Er	0.0000	0.0085	0.0242	0.0076	0.0076	0.0000	0.0083
Tm	0.0003	0.0002	0.0002	0.0000	0.0004	0.0000	0.0000
Yb	0.0242	0.0462	0.0000	0.0000	0.0282	0.0000	0.0213
Lu	0.0003	0.0000	0.0005	0.0015	0.0018	0.0017	0.0000

Appendix 2.1C: (continued) Detailed UCC-normalised (Taylor and McLennan, 1995) rare earth element (REE) data of micas from the Pan-African beryl- and tourmaline-bearing pegmatites from Chisenga (CCC) and Wenya (MWC) in Chitipa. All concentrations are given in ppm.

Element	MWC1A1	MWC1A2	MWC1A3	MWC1A4	MWC1A5	MWC1A6	MWC1A7	MWC1A8	MWC1A9	MWC1A10
La	0.0798	0.0000	0.0000	0.0000	0.1020	0.0507	0.2160	0.4530	0.0000	0.2430
Ce	0.1933	0.0000	0.1530	0.0000	0.4608	0.3520	0.3008	4.0320	0.0000	0.1702
Pr	0.0135	0.0000	0.0060	0.0000	0.0090	0.0000	0.0185	0.0000	0.0000	0.0000
Nd	0.0000	0.0000	0.1846	0.1352	0.1378	0.0000	0.0000	0.0000	0.0000	0.2860
Sm	0.0266	0.0284	0.0266	0.0279	0.0000	0.0000	0.0000	0.0000	0.0000	0.0383
Eu	0.0077	0.0290	0.0034	0.0246	0.0202	0.0034	0.0071	0.0000	0.0202	0.0299
Gd	0.0327	0.0285	0.1444	0.0000	0.0281	0.0426	0.0186	0.0353	0.0631	0.0274
Tb	0.0000	0.0000	0.0000	0.0000	0.0016	0.0010	0.0000	0.0013	0.0000	0.0000
Dy	0.0193	0.0000	0.0111	0.0000	0.0000	0.0000	0.0266	0.0294	0.0368	0.0000
Ho	0.0000	0.0017	0.0009	0.0000	0.0000	0.0000	0.0000	0.0017	0.0000	0.0000
Er	0.0087	0.0000	0.0000	0.0129	0.0054	0.0051	0.0050	0.0483	0.0085	0.0225
Tm	0.0000	0.0013	0.0039	0.0024	0.0038	0.0002	0.0002	0.0006	0.0008	0.0000
Yb	0.1100	0.0726	0.0077	0.1914	0.1716	0.0770	0.0220	0.1738	0.1188	0.0770
Lu	0.0042	0.0068	0.0076	0.0071	0.0052	0.0082	0.0014	0.0063	0.0086	0.0072

Appendix 2.1D: Detailed chondrite-normalised (Nakamura, 1974) rare earth element (REE) data of micas from the Palaeoproterozoic tourmaline-bearing pegmatites (CNC) from Nthalire in Chitipa. All concentrations are given in ppm.

Element	CNC1B1	CNC1B2	CNC1B3	CNC1B4	CNC1B5	CNC1B6	CNC1B7	CNC1B8	CNC1B9	CNC1B10
La	0.0000	0.1260	0.0051	0.0091	0.1180	0.0000	0.0000	0.5030	0.0000	0.9030
Ce	0.0000	0.0000	0.0000	0.0000	0.0000	0.0000	0.0233	0.0042	0.0000	0.0076
Pr	0.0000	0.0000	0.0120	0.0000	0.0000	0.0000	0.0000	0.1970	0.0780	0.3790
Nd	0.0000	0.0000	0.0000	0.0000	0.0000	0.0350	0.0180	0.1000	0.0000	0.3110
Sm	0.0000	0.0000	0.0270	0.0000	0.0000	0.0000	0.0000	0.0160	0.0900	0.1500
Eu	0.1300	0.0000	0.0000	0.0330	0.1140	0.0000	0.0000	0.0800	0.0000	0.2300
Gd	0.0000	0.0000	0.0000	0.0000	0.0000	0.0000	0.0000	0.0410	0.0000	0.0960
Tb	0.0000	0.0000	0.0000	0.0000	0.0000	0.0000	0.0000	0.0260	0.0000	0.0360
Dy	0.0000	0.0000	0.0000	0.0000	0.0240	0.0000	0.0000	0.0290	0.0000	0.0420
Ho	0.0000	0.0000	0.0000	0.0000	0.0000	0.0000	0.0000	0.0180	0.0000	0.0670
Er	0.0000	0.0000	0.0091	0.0000	0.0000	0.0000	0.0000	0.0270	0.0000	0.0000
Tm	0.0000	0.0000	0.0000	0.0000	0.0000	0.0000	0.0000	0.9600	0.0000	0.0360
Yb	0.0000	0.0000	0.0430	0.0660	0.0000	0.0000	0.0000	0.0000	0.0000	0.0630
Lu	0.1400	0.0690	0.0000	0.1070	0.1310	0.0000	0.0000	0.1470	0.1600	0.1120

Appendix 2.1D: (continued) Detailed chondrite-normalised (Nakamura, 1974) rare earth element (REE) data of micas from the Pan-African beryl- and tourmaline-bearing pegmatites from Chisenga (CCC) and Wenya (MWC) in Chitipa. All concentrations are given in ppm.

Element	CCC1A1	CCC1A2	CCC1A3	CCC1A4	CCC1A5	CCC1A6	CCC1A7
La	0.0000	0.0450	0.0000	0.0000	0.0000	0.0000	0.0140
Ce	0.0055	0.0000	0.0000	0.0000	0.0000	0.0000	0.0000
Pr	0.0000	0.0000	0.0000	0.0000	0.0000	0.0000	0.0000
Nd	0.0000	0.0000	0.0000	0.0000	0.0000	0.0000	0.0000
Sm	0.0000	0.0000	0.0000	0.0000	0.0000	0.0000	0.0000
Eu	0.0000	0.0000	0.0000	0.0910	0.2390	0.2200	0.3900
Gd	0.0000	0.0000	0.0000	0.0000	0.0000	0.0000	0.0000
Tb	0.0000	0.0000	0.0000	0.0230	0.0000	0.0000	0.0000
Dy	0.0000	0.0000	0.0000	0.0000	0.0000	0.0000	0.0000
Ho	0.0000	0.0000	0.0000	0.0000	0.0230	0.0000	0.0000
Er	0.0000	0.0000	0.0660	0.0000	0.0000	0.0000	0.0000
Tm	0.0000	0.0000	0.0000	0.0000	0.0000	0.0000	0.0000
Yb	0.0680	0.1310	0.0000	0.0000	0.0800	0.0000	0.0600
Lu	0.0000	0.0000	0.0000	0.1940	0.2250	0.2200	0.0000

Appendix 2.1D: (continued) Detailed chondrite-normalised (Nakamura, 1974) rare earth element (REE) data of micas from the Pan-African beryl- and tourmaline-bearing pegmatites from Chisenga (CCC) and Wenya (MWC) in Chitipa. All concentrations are given in ppm.

Element	MWC1A1	MWC1A2	MWC1A3	MWC1A4	MWC1A5	MWC1A6	MWC1A7	MWC1A8	MWC1A9	MWC1A10
La	0.0000	0.0000	0.0000	0.0000	0.0140	0.0000	0.0300	0.0000	0.0000	0.0000
Ce	0.0000	0.0000	0.0000	0.0000	0.0000	0.0000	0.0000	0.0000	0.0000	0.0000
Pr	0.0000	0.0000	0.0000	0.0000	0.0000	0.0000	0.0280	0.0000	0.0000	0.0000
Nd	0.0000	0.0000	0.0000	0.0000	0.0000	0.0000	0.0000	0.0000	0.0000	0.0240
Sm	0.0000	0.0000	0.0000	0.0000	0.0000	0.0000	0.0000	0.0000	0.0000	0.0000
Eu	0.1600	0.5900	0.0000	0.4900	0.4200	0.0690	0.1400	0.0000	0.4200	0.6100
Gd	0.0000	0.0000	0.1900	0.0000	0.0000	0.0000	0.0000	0.0000	0.0000	0.0000
Tb	0.0000	0.0000	0.0000	0.0000	0.0690	0.0000	0.0000	0.0000	0.0000	0.0000
Dy	0.0000	0.0000	0.0000	0.0000	0.0000	0.0000	0.0310	0.0000	0.0000	0.0000
Ho	0.0000	0.0380	0.0000	0.0000	0.0000	0.0000	0.0000	0.0000	0.0000	0.0000
Er	0.0000	0.0000	0.0000	0.0350	0.0000	0.0000	0.0000	0.1280	0.0000	0.0610
Tm	0.0000	0.1500	0.4800	0.2900	0.4600	0.0000	0.0000	0.0000	0.0000	0.0000
Yb	0.3100	0.2100	0.0000	0.5400	0.4800	0.2100	0.0590	0.4900	0.3300	0.2200
Lu	0.5400	0.8600	0.9600	0.9000	0.6600	1.0400	0.1700	0.8100	1.0900	0.9200

Appendix 2.2A: Detailed major element data of micas from the Pan-African aquamarine-bearing pegmatites from Kafukule (GM) and Luhomero (HEM) in Mzimba.

Sample	GM1_1	GM1_2	GM1_3	GM1_4	GM1_5	GM1_6	GM1_7	GM1_8	GM1_9	GM1_10
SiO_2	46.60	46.05	44.81	46.80	46.41	46.12	46.31	46.41	45.93	46.55
TiO_2	0.14	0.18	0.12	0.15	0.15	0.17	0.21	0.14	0.17	0.17
Al_2O_3	33.29	33.54	32.96	34.35	34.21	33.81	33.81	33.95	33.22	33.89
FeO	2.81	2.74	2.35	2.19	2.40	2.41	3.04	2.95	2.37	2.55
MnO	0.00	0.00	0.02	0.00	0.00	0.01	0.00	0.05	0.01	0.00
MgO	0.88	0.79	0.80	0.83	0.80	0.78	0.77	0.74	0.81	0.83
CaO	0.00	0.00	0.00	0.00	0.00	0.07	0.03	0.01	0.02	0.00
Na_2O	0.70	0.90	0.64	0.71	0.70	0.83	0.66	0.78	0.58	0.55
K_2O	12.18	12.40	11.97	12.11	12.22	11.80	11.37	11.45	11.01	11.20
Rb_2O	0.00	0.00	0.00	0.00	0.00	0.00	0.00	0.00	0.00	0.00
Cs_2O	0.00	0.00	0.00	0.00	0.00	0.00	0.00	0.00	0.00	0.00
F	0.16	0.17	0.24	0.27	0.11	0.29	0.18	0.20	0.21	0.19
Cl	0.04	0.00	0.00	0.00	0.00	0.00	0.03	0.00	0.01	0.00
Cr_2O_3	0.04	0.00	0.00	0.00	0.01	0.00	0.00	0.00	0.00	0.00
Li_2O*	0.00	0.00	0.00	0.01	0.00	0.02	0.00	0.00	0.00	0.00
H_2O*	4.43	4.38	4.23	4.40	4.45	4.33	4.39	4.40	4.31	4.39
Subtotal	101.78	101.16	98.14	101.81	101.45	100.63	100.80	101.07	98.64	100.32
O=F,Cl	0.08	0.07	0.10	0.11	0.05	0.12	0.08	0.08	0.09	0.08
Total	101.70	101.09	98.04	101.69	101.41	100.51	100.72	100.98	98.55	100.25
Si	6.18	6.18	6.18	6.20	6.18	6.19	6.20	6.20	6.25	6.23
Al^{iv}	1.82	1.82	1.82	1.80	1.82	1.81	1.80	1.80	1.75	1.77
Al^{vi}	3.49	3.49	3.54	3.57	3.55	3.54	3.54	3.54	3.58	3.58
Ti	0.01	0.02	0.01	0.01	0.02	0.02	0.02	0.01	0.02	0.02
Cr	0.00	0.00	0.00	0.00	0.00	0.00	0.00	0.00	0.00	0.00
Fe	0.31	0.31	0.27	0.24	0.27	0.27	0.34	0.33	0.27	0.29
Mn	0.00	0.00	0.00	0.00	0.00	0.00	0.00	0.01	0.00	0.00
Mg	0.17	0.16	0.16	0.16	0.16	0.16	0.15	0.15	0.16	0.17
Li*	0.00	0.00	0.00	0.00	0.00	0.01	0.00	0.00	0.00	0.00
Ca	0.00	0.00	0.00	0.00	0.00	0.01	0.01	0.00	0.00	0.00
Na	0.18	0.23	0.17	0.18	0.18	0.22	0.17	0.20	0.15	0.14
K	2.13	2.12	2.11	2.05	2.08	2.02	1.94	1.95	1.91	1.91
Rb	0.00	0.00	0.00	0.00	0.00	0.00	0.00	0.00	0.00	0.00
Cs	0.00	0.00	0.00	0.00	0.00	0.00	0.00	0.00	0.00	0.00
OH*	3.92	3.93	3.89	3.89	3.96	3.88	3.92	3.92	3.91	3.92
F	0.07	0.07	0.11	0.11	0.05	0.12	0.08	0.08	0.09	0.08
Cl	0.01	0.00	0.00	0.00	0.00	0.00	0.01	0.00	0.00	0.00
TOTAL	18.30	18.33	18.27	18.22	18.25	18.24	18.17	18.19	18.10	18.10
Y total	4.00	3.97	3.99	3.99	3.99	3.99	4.05	4.04	4.03	4.05
X total	2.31	2.36	2.28	2.23	2.26	2.25	2.12	2.15	2.07	2.06
Al total	5.31	5.31	5.36	5.37	5.37	5.35	5.34	5.35	5.33	5.35

* Calculated.

Appendix 2.2A (continued): Detailed major element data of micas from the Pan-African aquamarine-bearing pegmatites from Kafukule (GM) and Luhomero (HEM) in Mzimba.

Sample	GM3_1	GM3_2	GM3_3	GM3_4	GM3_5	GM3_6	GM3_7	GM3_8	GM3_9	GM3_10
SiO_2	45.18	45.58	45.35	45.90	45.51	45.62	45.73	45.55	45.77	45.96
TiO_2	0.26	0.24	0.23	0.21	0.30	0.23	0.22	0.20	0.23	0.26
Al_2O_3	31.76	31.94	31.62	31.95	32.20	32.03	32.33	32.93	32.13	32.87
FeO	3.63	3.78	3.68	3.99	3.63	3.56	3.77	3.80	3.63	3.66
MnO	0.12	0.04	0.07	0.08	0.14	0.04	0.23	0.13	0.12	0.02
MgO	0.62	0.56	0.60	0.54	0.59	0.63	0.66	0.57	0.62	0.62
CaO	0.04	0.00	0.01	0.01	0.00	0.00	0.01	0.00	0.00	0.01
Na_2O	0.81	0.75	0.92	0.18	0.74	0.74	0.73	0.52	0.42	0.26
K_2O	12.12	11.41	12.20	11.89	12.50	12.44	12.91	12.95	12.55	12.68
Rb_2O	0.19	0.11	0.09	0.09	0.17	0.12	0.13	0.12	0.16	0.09
Cs_2O	0.00	0.00	0.00	0.04	0.00	0.01	0.02	0.00	0.00	0.00
F	0.87	0.60	0.80	0.71	0.81	0.76	0.65	0.56	0.68	0.52
Cl	0.01	0.00	0.00	0.00	0.00	0.01	0.00	0.00	0.00	0.01
Cr_2O_3	0.02	0.02	0.05	0.01	0.00	0.00	0.05	0.01	0.01	0.04
Li_2O*	0.19	0.11	0.17	0.15	0.18	0.16	0.13	0.10	0.13	0.08
H_2O*	3.95	4.09	3.98	4.05	4.02	4.03	4.13	4.17	4.08	4.20
Subtotal	99.76	99.21	99.77	99.78	100.79	100.37	101.69	101.60	100.53	101.28
O=F,Cl	0.37	0.25	0.34	0.30	0.34	0.32	0.27	0.24	0.28	0.22
Total	99.39	98.96	99.43	99.48	100.45	100.05	101.42	101.37	100.24	101.06
Si	6.21	6.26	6.23	6.28	6.20	6.23	6.19	6.16	6.24	6.20
Al^{iv}	1.79	1.74	1.77	1.73	1.80	1.77	1.81	1.84	1.76	1.80
Al^{vi}	3.36	3.42	3.35	3.42	3.37	3.38	3.34	3.40	3.40	3.43
Ti	0.03	0.02	0.02	0.02	0.03	0.02	0.02	0.02	0.02	0.03
Cr	0.00	0.00	0.01	0.00	0.00	0.00	0.01	0.00	0.00	0.00
Fe	0.42	0.43	0.42	0.46	0.41	0.41	0.43	0.43	0.41	0.41
Mn	0.01	0.01	0.01	0.01	0.02	0.01	0.03	0.02	0.01	0.00
Mg	0.13	0.12	0.12	0.11	0.12	0.13	0.13	0.11	0.13	0.13
Li*	0.11	0.06	0.10	0.08	0.10	0.09	0.07	0.05	0.07	0.05
Ca	0.01	0.00	0.00	0.00	0.00	0.00	0.00	0.00	0.00	0.00
Na	0.22	0.20	0.25	0.05	0.20	0.20	0.19	0.14	0.11	0.07
K	2.13	2.00	2.14	2.07	2.17	2.17	2.23	2.23	2.18	2.18
Rb	0.02	0.01	0.01	0.01	0.02	0.01	0.01	0.01	0.01	0.01
Cs	0.00	0.00	0.00	0.00	0.00	0.00	0.00	0.00	0.00	0.00
OH*	3.62	3.74	3.65	3.69	3.65	3.67	3.72	3.76	3.71	3.78
F	0.38	0.26	0.35	0.31	0.35	0.33	0.28	0.24	0.29	0.22
Cl	0.00	0.00	0.00	0.00	0.00	0.00	0.00	0.00	0.00	0.00
TOTAL	18.42	18.27	18.43	18.23	18.43	18.40	18.46	18.42	18.35	18.31
Y total	4.06	4.06	4.03	4.10	4.04	4.03	4.03	4.04	4.05	4.05
X total	2.36	2.21	2.39	2.13	2.38	2.37	2.43	2.38	2.30	2.26
Al total	5.15	5.17	5.12	5.15	5.17	5.15	5.16	5.25	5.16	5.23

* Calculated.

Appendix 2.2A (continued): Detailed major element data of micas from the Pan-African aquamarine-bearing pegmatites from Kafukule (GM) and Luhomero (HEM) in Mzimba.

Sample	GM5_1	GM5_2	GM5_3	GM5_4	GM5_5	GM5_6	GM5_7	GM5_8	GM5_9	GM5_10	GM5_11
SiO_2	45.30	45.88	45.96	46.03	46.85	46.43	45.73	46.21	45.81	45.79	46.24
TiO_2	0.05	0.09	0.00	0.06	0.07	0.04	0.06	0.05	0.11	0.06	0.07
Al_2O_3	31.58	31.56	32.05	32.21	31.37	32.19	31.96	31.00	31.56	32.12	32.24
FeO	3.53	3.73	3.56	3.72	3.77	3.71	3.87	3.30	3.86	3.50	3.64
MnO	0.68	0.67	0.63	0.52	0.72	0.73	0.76	0.88	0.71	0.57	0.56
MgO	0.00	0.00	0.01	0.01	0.00	0.00	0.00	0.02	0.00	0.00	0.00
CaO	0.00	0.00	0.03	0.01	0.00	0.00	0.03	0.00	0.00	0.00	0.00
Na_2O	0.59	0.38	0.30	0.43	0.53	0.48	0.59	0.60	0.53	0.48	0.50
K_2O	13.02	12.90	12.40	12.66	12.25	12.79	13.08	13.32	13.42	13.72	12.99
Rb_2O	0.49	0.43	0.33	0.33	0.39	0.35	0.42	0.44	0.46	0.40	0.35
Cs_2O	0.05	0.00	0.00	0.00	0.04	0.01	0.01	0.01	0.00	0.02	0.00
F	2.16	2.42	2.16	2.07	2.37	2.07	2.06	2.37	2.10	1.63	2.02
Cl	0.01	0.00	0.00	0.00	0.00	0.02	0.00	0.01	0.00	0.02	0.00
Cr_2O_3	0.00	0.00	0.04	0.05	0.05	0.01	0.01	0.01	0.04	0.00	0.01
Li_2O*	0.60	0.68	0.60	0.57	0.66	0.57	0.57	0.66	0.58	0.43	0.55
H_2O*	3.36	3.26	3.38	3.45	3.32	3.47	3.45	3.30	3.42	3.65	3.51
Subtotal	101.41	101.98	101.43	102.00	102.40	102.87	102.60	102.80	102.59	102.38	102.77
O=F,Cl	0.91	1.02	0.91	0.87	1.00	0.88	0.87	1.00	0.88	0.69	0.85
Total	100.50	100.96	100.52	101.13	101.40	101.99	101.74	101.80	101.71	101.69	101.92
Si	6.19	6.25	6.25	6.23	6.32	6.24	6.20	6.27	6.22	6.21	6.23
Al^{iv}	1.81	1.75	1.75	1.77	1.68	1.76	1.80	1.73	1.78	1.79	1.77
Al^{vi}	3.27	3.32	3.40	3.38	3.33	3.36	3.31	3.22	3.27	3.36	3.36
Ti	0.01	0.01	0.00	0.01	0.01	0.00	0.01	0.01	0.01	0.01	0.01
Cr	0.00	0.00	0.00	0.01	0.01	0.00	0.00	0.00	0.00	0.00	0.00
Fe	0.40	0.43	0.41	0.42	0.43	0.42	0.44	0.49	0.44	0.40	0.42
Mn	0.08	0.08	0.07	0.06	0.08	0.08	0.09	0.10	0.08	0.07	0.06
Mg	0.00	0.00	0.00	0.00	0.00	0.00	0.00	0.00	0.00	0.00	0.00
Li*	0.33	0.37	0.33	0.31	0.36	0.31	0.31	0.36	0.32	0.24	0.30
Ca	0.00	0.00	0.00	0.00	0.00	0.00	0.01	0.00	0.00	0.00	0.00
Na	0.21	0.10	0.08	0.11	0.14	0.13	0.16	0.16	0.17	0.13	0.13
K	2.44	2.24	2.15	2.19	2.11	2.19	2.27	2.30	2.37	2.37	2.23
Rb	0.04	0.04	0.03	0.03	0.03	0.03	0.04	0.04	0.04	0.03	0.03
Cs	0.00	0.00	0.00	0.00	0.00	0.00	0.00	0.00	0.00	0.00	0.00
OH*	3.07	2.96	3.07	3.12	2.99	3.12	3.12	2.98	3.10	3.30	3.14
F	0.93	1.04	0.93	0.88	1.01	0.88	0.88	1.02	0.90	0.70	0.86
Cl	0.00	0.00	0.00	0.00	0.00	0.00	0.00	0.00	0.00	0.01	0.00
TOTAL	18.78	18.58	18.47	18.51	18.49	18.52	18.62	18.68	18.69	18.60	18.54
Y total	4.08	4.20	4.20	4.18	4.21	4.17	4.16	4.18	4.11	4.06	4.15
X total	2.70	2.38	2.26	2.33	2.28	2.35	2.46	2.51	2.58	2.53	2.39
Al total	5.08	5.07	5.14	5.15	5.00	5.12	5.11	4.95	5.05	5.15	5.14

* Calculated.

Appendix 2.2A (continued): Detailed major element data of micas from the Pan-African aquamarine-bearing pegmatites from Kafukule (GM) and Luhomero (HEM) in Mzimba.

Sample	HEM1B_1	HEM1B_2	HEM1B_3	HEM1B_4	HEM1B_5	HEM1B_6	HEM1B_7	HEM1B_8	HEM1B_9	HEM1B_10
SiO_2	46.17	46.47	46.37	46.35	46.04	46.91	45.69	46.71	46.31	46.86
TiO_2	0.75	0.75	0.78	0.79	0.70	0.53	0.78	0.55	0.51	0.77
Al_2O_3	31.44	31.38	31.33	31.55	31.37	31.76	31.84	31.37	31.32	31.71
FeO	3.71	3.19	3.04	3.69	3.27	3.26	3.12	3.75	3.79	3.83
MnO	0.11	0.12	0.10	0.00	0.11	0.17	0.00	0.04	0.08	0.10
MgO	1.01	1.03	0.99	1.05	1.00	1.01	1.01	1.03	0.95	0.95
CaO	0.01	0.00	0.00	0.00	0.00	0.01	0.01	0.00	0.00	0.01
Na_2O	0.46	0.78	0.59	0.68	0.60	0.58	0.83	0.55	0.81	0.43
K_2O	13.23	13.17	12.62	12.60	12.83	12.88	13.01	12.43	12.43	11.96
F	1.38	1.35	1.18	1.23	1.40	1.00	1.35	1.31	1.18	1.04
Cl	0.03	0.02	0.00	0.01	0.01	0.00	0.00	0.00	0.00	0.01
Cr_2O_3	0.05	0.02	0.00	0.01	0.01	0.00	0.00	0.02	0.02	0.04
Li_2O*	0.35	0.34	0.29	0.31	0.36	0.24	0.35	0.33	0.29	0.25
H_2O*	3.84	3.87	3.92	3.93	3.81	4.08	3.80	3.89	3.92	4.04
Subtotal	102.54	102.49	101.20	102.17	101.50	101.41	101.77	101.98	101.61	101.98
O=F,Cl	0.59	0.57	0.50	0.52	0.59	0.42	0.57	0.55	0.50	0.44
Total	101.95	101.92	100.70	101.65	100.91	100.99	101.20	101.53	101.11	101.54
Si	6.15	6.18	6.21	6.17	6.17	6.18	6.18	6.21	6.19	6.22
Al^{iv}	1.85	1.82	1.79	1.83	1.83	1.82	1.82	1.79	1.81	1.78
Al^{vi}	3.24	3.25	3.31	3.27	3.28	3.27	3.25	3.28	3.29	3.32
Ti	0.08	0.08	0.08	0.08	0.07	0.05	0.08	0.07	0.05	0.08
Cr	0.01	0.00	0.00	0.00	0.00	0.00	0.00	0.00	0.00	0.00
Fe	0.41	0.36	0.34	0.41	0.37	0.47	0.35	0.42	0.42	0.42
Mn	0.01	0.01	0.01	0.00	0.01	0.02	0.00	0.01	0.01	0.01
Mg	0.20	0.21	0.20	0.21	0.20	0.20	0.20	0.20	0.19	0.19
Li*	0.19	0.18	0.16	0.16	0.19	0.13	0.19	0.18	0.16	0.13
Ca	0.00	0.00	0.00	0.00	0.00	0.00	0.00	0.00	0.00	0.00
Na	0.12	0.20	0.15	0.18	0.16	0.15	0.22	0.14	0.21	0.11
K	2.25	2.23	2.15	2.14	2.19	2.17	2.24	2.11	2.12	2.02
OH*	3.41	3.43	3.50	3.48	3.41	3.58	3.42	3.45	3.50	3.56
F	0.58	0.57	0.50	0.52	0.59	0.42	0.58	0.55	0.50	0.43
Cl	0.01	0.00	0.00	0.00	0.00	0.00	0.00	0.00	0.00	0.00
TOTAL	18.51	18.52	18.40	18.44	18.48	18.44	18.53	18.40	18.45	18.28
Y total	4.14	4.08	4.09	4.13	4.13	4.13	4.07	4.15	4.12	4.15
X total	2.37	2.44	2.31	2.31	2.35	2.31	2.46	2.25	2.33	2.13
Al total	5.09	5.07	5.10	5.10	5.11	5.09	5.07	5.07	5.10	5.10

* Calculated

Appendix 2.2A (continued): Detailed major element data of micas from the Pan-African aquamarine-bearing pegmatites from Kafukule (GM) and Luhomero (HEM) in Mzimba.

Sample	HEM2A_1	HEM2A_2	HEM2A_3	HEM2A_4	HEM2A_5	HEM2A_6	HEM2A_7	HEM2A_8	HEM2A_9	HEM2A_10
SiO_2	45.89	45.73	46.30	46.06	46.10	45.71	45.27	44.82	45.33	46.13
TiO_2	0.59	0.63	0.60	0.77	0.80	0.41	1.06	1.04	0.97	1.04
Al_2O_3	31.68	31.60	31.35	31.26	31.22	31.23	31.32	30.77	30.97	30.90
FeO	3.73	3.11	3.16	3.84	3.19	3.26	3.80	4.41	4.44	3.94
MnO	0.07	0.11	0.17	0.01	0.12	0.11	0.15	0.06	0.06	0.06
MgO	0.97	0.95	1.06	1.01	1.02	0.98	1.27	1.24	1.18	1.29
CaO	0.02	0.03	0.00	0.01	0.01	0.00	0.00	0.03	0.00	0.02
Na_2O	0.55	0.51	0.56	0.75	0.74	0.71	0.55	0.67	0.56	0.60
K_2O	12.55	12.82	12.60	12.87	12.74	12.30	12.44	11.95	12.99	12.93
F	1.27	1.25	1.13	1.22	1.17	1.22	0.66	0.63	0.69	0.53
Cl	0.01	0.00	0.00	0.00	0.01	0.02	0.01	0.02	0.00	0.01
Cr_2O_3	0.02	0.00	0.00	0.00	0.00	0.01	0.01	0.01	0.03	0.00
Li_2O*	0.32	0.31	0.27	0.31	0.29	0.30	0.13	0.12	0.14	0.09
H_2O*	3.83	3.81	3.94	3.91	3.92	3.80	4.08	4.05	4.08	4.18
Subtotal	101.48	100.86	101.13	102.01	102.33	100.06	100.73	99.80	101.44	101.71
O=F,Cl	0.54	0.53	0.47	0.52	0.49	0.52	0.28	0.27	0.29	0.23
Total	100.94	100.33	100.66	101.50	101.84	99.54	100.45	99.54	101.15	101.49
Si	6.21	6.22	6.21	6.15	6.18	6.26	6.17	6.17	6.17	6.24
Al^{iv}	1.79	1.78	1.80	1.85	1.82	1.74	1.83	1.83	1.83	1.76
Al^{vi}	3.27	3.29	3.31	3.23	3.27	3.30	3.20	3.17	3.15	3.16
Ti	0.06	0.06	0.06	0.09	0.08	0.04	0.11	0.11	0.10	0.11
Cr	0.00	0.00	0.00	0.00	0.00	0.00	0.00	0.00	0.00	0.00
Fe	0.42	0.35	0.35	0.43	0.36	0.37	0.43	0.51	0.51	0.45
Mn	0.01	0.01	0.02	0.00	0.01	0.01	0.02	0.01	0.01	0.01
Mg	0.20	0.19	0.21	0.20	0.20	0.20	0.26	0.26	0.24	0.26
Li*	0.17	0.17	0.15	0.16	0.16	0.17	0.07	0.07	0.08	0.05
Ca	0.00	0.00	0.00	0.00	0.00	0.00	0.00	0.01	0.00	0.00
Na	0.15	0.14	0.14	0.19	0.19	0.19	0.15	0.18	0.15	0.16
K	2.17	2.23	2.15	2.19	2.18	2.15	2.16	2.10	2.26	2.23
OH*	3.46	3.46	3.52	3.48	3.50	3.47	3.71	3.72	3.70	3.77
F	0.54	0.54	0.48	0.52	0.49	0.53	0.29	0.27	0.30	0.23
Cl	0.00	0.00	0.00	0.00	0.00	0.01	0.00	0.00	0.00	0.00
TOTAL	18.44	18.45	18.40	18.50	18.46	18.43	18.40	18.39	18.48	18.41
Y total	4.13	4.08	4.11	4.11	4.08	4.09	4.09	4.11	4.08	4.03
X total	2.32	2.36	2.30	2.39	2.37	2.34	2.31	2.28	2.41	2.39
Al total	5.06	5.07	5.11	5.08	5.09	5.04	5.03	5.00	4.97	4.92

* Calculated

Appendix 2.2A (continued): Detailed major element data of micas from the Pan-African aquamarine-bearing pegmatites from Kafukule (GM) and Luhomero (HEM) in Mzimba.

Sample	HEM3B_1	HEM3B_2	HEM3B_3	HEM3B_4	HEM3B_5	HEM3B_6	HEM3B_7	HEM3B_8	HEM3B_9	HEM3B_10
SiO_2	46.13	46.28	45.75	45.91	45.72	45.11	44.99	45.71	46.15	45.56
TiO_2	1.04	1.12	1.09	1.22	1.12	1.05	1.00	1.13	1.04	1.08
Al_2O_3	31.04	31.28	30.67	31.05	31.01	31.10	30.51	31.05	31.05	30.66
FeO	4.28	4.11	4.44	4.22	4.02	4.32	3.87	4.07	4.14	3.65
MnO	0.10	0.08	0.00	0.09	0.07	0.18	0.04	0.08	0.05	0.00
MgO	1.27	1.31	1.19	1.35	1.25	1.29	1.37	1.36	1.25	1.20
CaO	0.05	0.00	0.00	0.00	0.00	0.00	0.00	0.06	0.02	0.00
Na_2O	0.52	0.45	0.32	0.55	0.50	0.33	0.59	0.43	0.55	0.46
K_2O	11.61	12.40	13.26	13.01	13.45	13.48	13.10	13.21	12.74	12.67
F	0.66	0.61	0.63	0.43	0.57	0.54	0.64	0.57	0.57	0.52
Cl	0.02	0.00	0.00	0.00	0.00	0.00	0.00	0.00	0.00	0.00
Cr_2O_3	0.01	0.00	0.01	0.00	0.00	0.00	0.01	0.05	0.00	0.01
Li_2O*	0.13	0.12	0.12	0.06	0.10	0.09	0.12	0.10	0.10	0.09
H_2O*	4.11	4.17	4.12	4.26	4.17	4.17	4.06	4.18	4.24	4.13
Subtotal	100.96	101.92	101.62	102.14	102.00	101.67	100.30	102.00	101.80	100.04
O=F,Cl	0.28	0.26	0.27	0.18	0.24	0.23	0.27	0.24	0.24	0.22
Total	100.68	101.67	101.35	101.97	101.76	101.44	100.03	101.75	101.56	99.82
Si	6.25	6.22	6.22	6.16	6.17	6.11	6.19	6.16	6.15	6.24
Al^{iv}	1.75	1.78	1.78	1.84	1.83	1.89	1.81	1.84	1.85	1.76
Al^{vi}	3.20	3.18	3.13	3.08	3.10	3.08	3.14	3.13	3.18	3.20
Ti	0.11	0.11	0.11	0.12	0.11	0.11	0.10	0.12	0.12	0.11
Cr	0.00	0.00	0.00	0.00	0.00	0.00	0.00	0.01	0.00	0.00
Fe	0.48	0.46	0.51	0.47	0.45	0.50	0.45	0.47	0.48	0.42
Mn	0.01	0.01	0.00	0.02	0.01	0.02	0.01	0.01	0.01	0.00
Mg	0.26	0.26	0.24	0.27	0.29	0.26	0.28	0.27	0.25	0.25
Li*	0.07	0.06	0.07	0.03	0.06	0.05	0.07	0.06	0.05	0.05
Ca	0.01	0.00	0.00	0.00	0.00	0.00	0.00	0.01	0.00	0.00
Na	0.14	0.12	0.09	0.14	0.13	0.09	0.16	0.11	0.14	0.12
K	2.01	2.13	2.30	2.40	2.38	2.50	2.30	2.29	2.16	2.22
OH*	3.71	3.74	3.73	3.82	3.76	3.77	3.72	3.76	3.76	3.78
F	0.28	0.26	0.27	0.18	0.24	0.23	0.28	0.24	0.24	0.23
Cl	0.00	0.00	0.00	0.00	0.00	0.00	0.00	0.00	0.00	0.00
TOTAL	18.28	18.34	18.44	18.54	18.54	18.61	18.50	18.47	18.40	18.36
Y total	4.13	4.09	4.06	4.00	4.02	4.02	4.04	4.06	4.09	4.02
X total	2.15	2.24	2.38	2.54	2.52	2.59	2.46	2.41	2.31	2.34
Al total	4.95	4.96	4.91	4.92	4.93	4.97	4.95	4.96	5.03	4.95

* Calculated

Appendix 2.2A (continued): Detailed major element data of micas from the Pan-African aquamarine-bearing pegmatites from Kafukule (GM) and Luhomero (HEM) in Mzimba.

Sample	HEM4B_1	HEM4B_2	HEM4B_3	HEM4B_4	HEM4B_5	HEM4B_6	HEM4B_7	HEM4B_8	HEM4B_9	HEM4B_10
SiO_2	38.86	38.84	38.36	38.54	38.83	38.72	38.06	38.82	39.19	38.58
TiO_2	1.29	1.31	1.32	1.29	1.34	1.33	1.26	1.21	1.26	1.34
Al_2O_3	16.11	16.26	16.14	15.85	15.94	16.04	15.98	16.24	16.19	16.32
FeO	2.37	2.21	2.50	2.73	2.78	2.71	2.62	2.86	2.35	2.67
MnO	0.04	0.04	0.12	0.06	0.08	0.01	0.10	0.04	0.06	0.05
MgO	23.59	23.61	23.32	23.30	23.56	23.36	23.26	23.30	23.29	23.23
CaO	0.00	0.02	0.02	0.01	0.00	0.00	0.00	0.00	0.04	0.00
Na_2O	0.28	0.27	0.02	0.09	0.28	0.07	0.07	0.20	0.15	0.28
K_2O	12.47	12.74	13.00	12.96	13.09	13.09	12.76	12.56	12.57	12.38
F	1.37	1.30	1.46	1.23	1.51	1.47	1.33	1.40	1.59	1.30
Cl	0.02	0.02	0.01	0.06	0.05	0.00	0.02	0.02	0.02	0.03
Cr_2O_3	0.00	0.00	0.00	0.01	0.00	0.01	0.00	0.00	0.06	0.00
Li_2O*	1.60	1.59	1.46	1.51	1.61	1.59	1.37	1.59	1.70	1.52
H_2O*	3.62	3.66	3.54	3.64	3.58	3.59	3.57	3.61	3.53	3.63
Subtotal	101.61	101.87	101.27	101.28	102.00	102.00	100.38	101.84	101.97	101.33
O=F,Cl	0.58	0.55	0.62	0.53	0.65	0.62	0.56	0.59	0.68	0.56
Total	101.03	101.32	100.65	100.74	101.35	101.38	99.82	101.25	101.30	100.77
Si	5.45	5.44	5.43	5.45	5.42	5.43	5.43	5.45	5.48	5.44
Al^{iv}	2.55	2.56	2.57	2.55	2.58	2.57	2.57	2.55	2.52	2.56
Al^{vi}	0.12	0.12	0.12	0.10	0.04	0.10	0.12	0.14	0.15	0.15
Ti	0.14	0.14	0.14	0.14	0.14	0.14	0.14	0.13	0.13	0.14
Cr	0.00	0.00	0.00	0.00	0.00	0.00	0.00	0.00	0.01	0.00
Fe	0.28	0.26	0.30	0.32	0.32	0.33	0.31	0.34	0.28	0.31
Mn	0.01	0.01	0.01	0.01	0.01	0.00	0.01	0.01	0.01	0.01
Mg	4.94	4.93	4.92	4.91	4.96	4.89	4.95	4.87	4.86	4.88
Li*	0.90	0.90	0.83	0.86	0.90	0.90	0.79	0.90	0.95	0.86
Ca	0.00	0.00	0.00	0.00	0.00	0.00	0.00	0.00	0.01	0.00
Na	0.08	0.07	0.01	0.03	0.09	0.02	0.02	0.06	0.04	0.08
K	2.23	2.28	2.35	2.34	2.34	2.33	2.32	2.25	2.24	2.23
OH*	3.39	3.42	3.34	3.44	3.32	3.35	3.40	3.38	3.29	3.41
F	0.61	0.58	0.66	0.55	0.67	0.65	0.60	0.62	0.70	0.58
Cl	0.00	0.01	0.00	0.01	0.01	0.00	0.00	0.00	0.01	0.01
TOTAL	20.69	20.70	20.68	20.70	20.80	20.72	20.65	20.68	20.67	20.65
Y total	6.38	6.35	6.32	6.33	6.37	6.36	6.31	6.38	6.38	6.35
X total	2.31	2.35	2.36	2.37	2.43	2.35	2.34	2.30	2.29	2.30
Al total	2.66	2.69	2.69	2.64	2.62	2.67	2.69	2.69	2.67	2.71

* Calculated

Appendix 2.2B: Detailed trace element data of micas from the Pan- African aquamarine-bearing pegmatites from Kafukule (GM) and Luhomero (HEM) in Mzimba. All concentrations are given in ppm.

Element	GM11	GM12	GM13	GM14	GM15	GM16	GM17	GM18	GM19	GM110	GM31
Li	251.57	252.94	218.64	251.43	259.63	265.80	233.26	230.00	232.30	121.61	839.77
Be	7.36	9.17	8.27	6.42	6.33	11.12	8.34	14.64	18.37	2.76	22.39
B	30.47	45.40	38.55	44.91	35.65	38.67	32.88	36.89	44.56	28.08	64.23
Sc	19.41	22.15	18.25	21.47	21.99	22.11	21.13	20.49	22.90	10.27	3.37
Ti	1136.18	1218.35	998.76	1102.50	1148.86	1179.83	1142.88	1089.54	1174.14	557.09	1572.75
V	10.81	11.69	9.93	11.03	10.56	11.41	11.32	14.32	11.76	8.47	15.65
Cr	2.97	1.33	2.92	1.92	1.82	1.72	1.79	17.67	1.91	45.05	0.09
Mn	275.23	262.56	231.49	270.01	275.37	283.57	269.23	301.48	233.44	296.74	641.48
Co	1.71	2.00	1.51	1.41	1.54	1.73	1.60	5.01	1.85	2869.05	1.87
Ni	1.57	2.17	1.41	2.08	1.13	2.18	1.68	1.86	1.89	4.71	0.74
Cu	0.03	0.08	0.13	0.04	0.26	0.10	0.24	1.25	0.73	1376.60	0.04
Zn	73.66	69.64	68.74	74.63	75.33	103.90	67.92	148.12	98.02	18.50	125.14
Ga	101.53	105.40	93.71	104.66	102.22	105.46	105.86	102.94	108.47	39.93	138.64
Rb	820.05	858.28	717.06	787.59	804.03	844.36	801.07	788.78	864.90	337.50	3472.52
Sr	3.10	3.78	2.77	3.61	3.69	3.57	3.47	3.16	3.48	3.28	0.13
Y	0.00	0.02	0.00	0.01	0.00	0.01	0.00	0.13	0.02	0.05	0.01
Zr	1.89	2.46	1.76	2.12	2.54	2.63	2.10	2.12	2.13	2.38	2.03
Nb	75.34	79.75	64.50	73.23	76.84	77.06	71.99	68.40	76.87	47.86	450.58
Mo	0.09	0.16	0.24	0.16	0.24	0.07	0.07	0.10	0.08	0.00	0.08
Sn	27.87	27.39	22.51	27.19	28.70	29.18	27.55	24.17	27.74	129.28	10.58
Cs	10.19	10.03	7.60	8.56	8.64	11.50	9.78	8.66	13.44	9.08	104.65
Ba	32.19	37.56	34.49	35.49	35.75	37.99	39.47	42.40	40.02	26.17	3.55
Hf	0.27	0.34	0.28	0.31	0.35	0.31	0.31	0.26	0.28	0.15	0.44
Ta	4.71	5.70	4.40	5.27	5.60	5.58	5.08	4.70	5.48	3.26	56.41
W	18.32	19.96	16.72	19.45	20.10	21.14	18.69	20.35	19.93	7.52	19.76
Pb	5.78	7.16	6.07	7.08	6.75	6.78	6.40	6.25	6.18	4.11	2.91
Th	0.0070	0.0000	0.0014	0.0015	0.0015	0.0015	0.0015	0.0166	0.0017	0.0188	0.0014
U	0.0070	0.0022	0.0000	0.0043	0.0013	0.0090	0.0032	0.4200	0.0014	0.0680	0.0016

Appendix 2.2B (continued): Detailed trace element data of micas from the Pan- African aquamarine-bearing pegmatites from Kafukule (GM) and Luhomero (HEM) in Mzimba. All concentrations are given in ppm.

Element	GM32	GM33	GM34	GM35	GM36	GM37	GM38	GM39	GM310
Li	862.21	738.70	925.97	1016.11	782.33	810.62	756.53	835.62	770.23
Be	26.85	17.76	28.30	25.48	22.10	23.70	21.89	27.37	21.95
B	59.50	67.22	74.95	50.64	55.27	63.85	72.67	74.91	70.60
Sc	3.34	3.23	3.62	3.40	3.34	3.21	3.17	3.42	3.19
Ti	1679.76	1491.64	1536.40	1615.03	1630.48	1603.26	1461.10	1612.54	1506.57
V	16.11	15.30	15.10	18.89	19.58	16.73	16.78	17.12	17.01
Cr	0.21	0.15	0.32	0.12	0.39	0.11	0.09	0.23	0.12
Mn	827.21	588.52	759.94	877.36	691.23	741.23	592.52	635.69	613.47
Co	2.00	1.65	2.37	2.22	2.16	2.17	1.95	2.61	1.98
Ni	0.27	0.92	0.62	0.36	0.20	0.26	0.07	0.25	0.28
Cu	0.23	0.03	0.26	0.33	0.05	0.07	0.03	0.11	0.15
Zn	249.14	89.30	217.12	367.48	156.67	225.20	99.38	137.98	140.78
Ga	140.10	131.42	127.68	141.15	140.04	138.57	124.79	127.97	133.27
Rb	3574.38	3186.29	3363.07	3370.72	3372.68	3365.42	2993.27	3298.36	3136.69
Sr	0.10	0.25	0.21	0.10	0.15	0.12	0.12	0.14	0.12
Y	0.03	0.05	0.04	0.00	0.01	0.00	0.01	0.21	0.02
Zr	2.36	1.77	3.61	2.03	1.99	1.91	1.73	1.91	1.77
Nb	485.07	420.66	455.69	446.07	457.49	446.90	409.65	449.46	420.43
Mo	0.04	0.12	0.27	0.05	0.23	0.08	0.11	0.07	0.07
Sn	10.92	11.01	11.25	11.07	10.61	10.51	9.72	10.87	10.17
Cs	113.28	93.13	102.25	97.73	97.34	99.62	89.65	99.99	90.92
Ba	3.19	3.69	4.54	4.39	3.33	3.65	3.44	3.45	3.69
Hf	0.38	0.40	0.45	0.40	0.30	0.43	0.37	0.38	0.43
Ta	64.67	54.01	63.81	54.91	53.03	55.65	48.32	62.58	53.62
W	22.74	19.40	21.45	19.90	18.55	20.23	16.93	21.16	18.89
Pb	2.93	3.26	2.70	2.54	2.86	2.79	2.36	2.95	3.06
Th	0.0017	0.0130	2.7000	0.0008	0.0027	0.0034	0.0023	0.0083	0.0074
U	0.0055	0.0016	0.0032	0.0083	0.0016	0.0053	0.0034	0.0049	0.0041

Appendix 2.2B (continued): Detailed trace element data of micas from the Pan- African aquamarine-bearing pegmatites from Kafukule (GM) and Luhomero (HEM) in Mzimba. All concentrations are given in ppm.

Element	GM51	GM52	GM53	GM54	GM55	GM56	GM57	GM58	GM59	GM510
Li	4560.51	4935.59	4853.62	5000.11	5263.57	5702.67	5966.51	5308.38	5002.51	5104.18
Be	28.21	24.21	29.62	29.60	26.78	21.44	25.24	28.16	23.98	24.18
B	104.57	88.22	77.89	84.28	92.08	83.33	67.39	85.56	75.71	84.26
Sc	0.70	0.71	0.59	0.57	0.47	0.65	0.50	0.70	0.61	0.64
Ti	402.17	430.14	452.72	448.86	437.14	441.16	467.72	460.76	450.69	444.60
V	0.02	0.03	0.02	0.03	0.02	0.02	0.02	0.02	0.05	0.03
Cr	0.22	0.20	0.17	0.21	0.20	0.15	0.22	0.19	0.20	0.21
Mn	5670.67	5935.23	6097.07	6114.23	5347.33	5621.18	7112.05	6593.39	6322.29	5893.39
Co	0.11	0.08	0.09	0.11	0.16	0.25	0.05	0.10	0.04	0.10
Ni	0.09	0.05	0.07	0.06	0.05	0.04	0.06	0.07	0.09	0.07
Cu	0.07	0.03	0.30	0.08	0.03	0.11	0.31	0.10	0.08	0.13
Zn	2690.63	2739.11	2852.31	2780.69	2185.37	2116.04	3165.27	2765.68	2544.81	2125.80
Ga	154.88	158.53	158.52	162.37	162.99	156.36	161.86	161.90	163.62	160.82
Rb	6327.95	6659.61	7061.21	6899.52	6736.70	6752.25	7919.24	7306.06	7378.65	7216.95
Sr	0.07	0.02	0.01	0.03	0.01	0.02	0.01	0.01	0.02	0.02
Y	0.00	0.00	0.00	0.00	0.03	0.00	0.05	0.00	0.01	0.05
Zr	0.68	0.83	0.95	0.88	0.69	0.81	0.94	0.88	0.86	0.80
Nb	172.31	185.67	199.71	189.84	187.34	190.20	198.10	197.97	195.54	195.26
Mo	0.04	0.05	0.07	0.06	0.07	0.04	0.09	0.06	0.02	0.06
Sn	6.68	7.71	8.04	7.87	7.16	7.44	7.71	8.31	7.18	7.45
Cs	225.16	244.54	269.77	250.40	247.28	262.50	323.95	289.35	284.00	268.08
Ba	0.62	0.61	0.64	0.57	0.40	0.96	0.51	0.64	0.56	0.49
Hf	0.18	0.22	0.20	0.25	0.15	0.20	0.34	0.18	0.23	0.21
Ta	35.49	38.37	40.84	38.70	36.28	36.09	45.66	41.71	39.19	39.87
W	6.85	7.16	8.33	7.20	7.41	6.47	8.90	8.35	7.89	7.34
Pb	2.26	2.60	1.85	2.27	2.41	2.85	2.17	1.98	2.21	2.19
Th	0.0017	0.0013	0.0000	0.0009	0.0000	0.0000	0.0023	0.0000	0.0009	0.0014
U	0.0024	0.0022	0.0024	0.0048	0.0018	0.0127	0.0000	0.0015	0.0032	0.0019

Appendix 2.2B (continued): Detailed trace element data of micas from the Pan- African aquamarine-bearing pegmatites from Kafukule (GM) and Luhomero (HEM) in Mzimba. All concentrations are given in ppm.

	HEM1B1	HEM1B2	HEM1B3	HEM1B4	HEM1B5	HEM1B6	HEM1B7	HEM1B8	HEM1B9	HEM1B10	HEM2A1
Li	1151.78	1297.76	1320.72	1348.54	1325.33	1348.54	1281.05	1366.37	1278.04	1126.20	1306.55
Be	16.45	18.76	18.48	20.09	20.41	17.21	15.61	23.31	20.06	20.90	22.32
B	29.86	29.50	20.23	23.70	24.63	22.35	26.64	28.69	24.65	28.06	43.16
Sc	38.87	30.70	28.82	23.34	24.00	41.61	40.00	20.71	24.29	29.26	24.03
Ti	4080.95	3659.11	3665.75	3328.45	3367.63	4574.12	4284.82	3076.11	3258.45	3445.17	3211.87
V	15.86	7.24	7.20	4.51	5.43	24.30	24.29	3.05	4.15	6.92	5.05
Cr	0.15	0.18	0.20	0.14	0.12	0.13	0.15	0.14	0.15	0.18	0.15
Mn	608.84	703.28	725.00	777.13	796.94	628.22	610.79	878.50	758.99	704.88	761.43
Co	3.11	21.16	23.86	10.77	10.07	10.31	5.12	19.09	2.62	19.75	10.78
Ni	0.32	0.15	0.05	0.16	0.06	0.45	0.32	0.17	0.13	0.16	0.13
Cu	0.13	0.49	0.69	0.25	0.36	0.32	0.13	0.68	0.06	0.42	1.83
Zn	97.99	101.40	103.64	110.44	113.88	83.33	95.69	116.63	119.94	116.43	129.61
Ga	119.18	118.02	121.19	114.85	119.90	120.72	117.94	118.41	116.21	114.50	114.60
Rb	1613.19	1699.95	1684.90	1737.66	1815.68	1603.39	1524.78	1861.38	1756.99	1624.66	1693.29
Sr	3.79	2.95	3.11	1.99	2.15	4.33	4.24	1.86	2.15	2.45	2.41
Y	0.05	0.02	0.05	0.02	0.06	0.02	0.03	0.01	0.02	0.01	0.06
Zr	0.21	3.06	4.27	3.73	3.22	3.12	2.87	2.85	2.71	2.84	4.23
Nb	186.90	197.82	193.98	195.18	206.16	196.81	179.76	199.05	202.10	185.33	192.46
Mo	0.37	0.18	0.40	0.28	0.32	0.17	0.18	0.09	0.17	0.23	0.17
Sn	14.69	15.09	14.26	12.41	12.82	17.34	16.48	12.01	13.11	13.46	11.99
Cs	21.46	23.92	23.98	24.69	24.97	19.94	19.27	25.81	25.84	22.69	23.97
Ba	97.93	57.35	57.67	36.95	35.46	121.63	113.05	29.06	34.46	51.03	37.51
Hf	0.30	0.33	0.26	0.31	0.29	0.28	0.26	0.34	0.35	0.26	0.31
Ta	19.68	21.83	22.31	21.92	22.58	20.74	19.26	21.72	22.26	19.91	23.00
W	36.49	31.27	30.15	33.62	35.85	36.40	35.31	32.06	30.89	36.05	34.74
Pb	4.50	6.68	4.78	3.46	5.72	4.12	4.34	3.37	4.17	3.66	5.82
Th	0.0018	0.0018	0.1110	0.0015	0.0740	0.0127	0.0011	0.0013	0.0009	0.0013	0.2630
U	0.0082	0.0269	0.0850	0.0123	0.0157	0.0107	0.0083	0.0056	0.0029	0.0098	0.0409

Appendix 2.2B (continued): Detailed trace element data of micas from the Pan-African aquamarine-bearing pegmatites from Kafukule (GM) and Luhomero (HEM) in Mzimba. All concentrations are given in ppm.

Element	HEM2A2	HEM2A3	HEM2A4	HEM2A5	HEM2A6	HEM2A7	HEM2A8	HEM2A9	HEM2A10
Li	1262.18	1168.19	1339.02	1000.41	959.73	1100.01	969.12	1115.71	1038.97
Be	18.35	20.12	18.53	23.16	20.54	22.66	17.61	23.96	25.08
B	29.36	30.08	22.55	35.36	72.84	66.43	78.42	64.55	69.47
Sc	40.36	32.39	34.98	29.50	71.66	83.89	45.68	54.02	87.58
Ti	4358.29	3891.24	4102.90	3686.68	5271.18	5440.89	4531.83	4970.29	5565.07
V	29.12	8.91	10.46	8.02	182.46	172.18	143.64	149.99	184.79
Cr	0.39	0.15	0.15	0.26	0.12	0.13	1.05	0.29	0.21
Mn	593.31	706.33	708.10	768.30	401.23	578.11	409.38	765.26	600.55
Co	5.12	2.61	2.57	40.23	3.59	3.95	3.22	5.30	8.56
Ni	0.71	0.26	0.14	0.08	2.73	2.76	7.52	6.58	2.42
Cu	0.74	0.42	0.11	1.23	0.27	0.21	0.07	0.10	0.71
Zn	100.82	115.40	108.85	117.59	62.16	83.77	63.19	125.15	70.04
Ga	112.70	116.39	118.79	121.97	86.01	95.19	83.66	91.27	102.28
Rb	1459.41	1634.42	1701.91	1693.21	1178.19	1282.92	1374.73	1499.58	1320.62
Sr	4.82	3.49	3.84	2.86	4.11	4.52	2.78	3.05	5.25
Y	0.04	0.03	0.03	0.07	0.02	0.02	0.01	0.03	0.03
Zr	2.81	3.07	3.24	3.11	1.82	1.78	1.42	1.72	1.92
Nb	178.63	194.86	198.49	191.83	85.86	91.72	99.31	118.23	92.78
Mo	0.21	0.22	0.18	0.24	0.01	0.06	0.07	0.03	0.02
Sn	17.25	14.76	16.16	13.70	19.42	18.52	14.80	15.88	20.30
Cs	19.17	23.07	23.12	22.33	189.71	225.83	237.96	272.75	212.96
Ba	132.12	70.49	81.46	63.92	279.66	564.45	323.88	397.68	609.95
Hf	0.27	0.32	0.32	0.32	0.22	0.26	0.28	0.35	0.29
Ta	19.88	21.73	22.74	21.07	55.48	62.08	93.33	105.51	60.53
W	31.06	31.88	32.00	36.09	18.97	18.77	17.83	19.02	19.86
Pb	4.97	4.72	4.86	4.62	4.59	4.53	4.07	4.04	5.12
Th	0.0202	0.0009	0.0143	0.0470	0.0075	0.0025	0.0006	0.0008	0.0041
U	0.0113	0.0064	0.0162	0.0626	0.0168	0.0119	0.0046	0.0082	0.0174

Appendix 2.2B (continued): Detailed trace element data of micas from the Pan-African aquamarine-bearing pegmatites from Kafukule (GM) and Luhomero (HEM) in Mzimba. All concentrations are given in ppm.

Element	HEM3B1	HEM3B2	HEM3B3	HEM3B4	HEM3B5	HEM3B6	HEM3B7	HEM3B8	HEM4B1	HEM4B2	HEM4B3
Li	1118.93	1121.60	1086.52	1106.70	1101.94	1049.41	1124.26	1114.07	50.04	48.28	49.82
Be	20.73	20.59	22.01	19.44	26.46	21.53	25.68	21.91	0.39	0.20	0.03
B	72.18	78.97	79.52	75.51	93.96	90.40	79.97	83.86	66.06	70.55	54.63
Sc	92.36	90.03	88.07	92.54	81.13	79.25	85.85	85.50	1.58	1.65	1.54
Ti	5955.85	5857.37	5699.77	5857.14	5219.20	5217.51	5465.25	5605.43	6684.01	6561.07	7058.39
V	189.42	190.04	174.27	182.60	168.83	165.08	176.55	173.69	125.67	123.10	134.05
Cr	0.13	0.16	0.14	0.15	0.11	0.19	0.24	0.26	70.63	65.58	65.65
Mn	731.64	669.13	569.98	523.07	606.05	535.02	695.69	594.10	569.67	540.46	628.21
Co	4.44	4.30	4.35	3.49	4.10	3.71	4.45	4.53	16.82	6.86	7.97
Ni	3.14	3.07	4.08	3.92	2.75	3.25	2.45	3.93	4.04	5.05	3.36
Cu	0.10	0.03	0.10	0.04	0.15	0.15	0.21	0.30	1.16	1.04	1.55
Zn	119.82	117.38	116.86	95.20	106.84	94.62	93.64	112.67	143.52	157.66	166.66
Ga	98.13	96.66	97.87	100.86	94.47	94.65	94.76	98.60	64.09	60.49	59.17
Rb	1351.30	1300.40	1363.53	1400.50	1240.88	1231.74	1273.37	1335.57	542.43	541.98	571.98
Sr	5.11	5.00	4.98	5.15	4.65	4.54	4.69	4.64	6.02	5.50	5.91
Y	0.04	0.04	0.03	0.01	0.02	0.03	0.04	0.03	0.01	0.01	0.00
Zr	1.95	1.88	1.83	2.15	1.55	1.67	1.82	1.85	17.64	17.28	18.60
Nb	97.23	93.24	96.27	99.66	86.34	85.26	90.86	94.55	46.26	44.60	47.44
Mo	0.05	0.05	0.05	0.05	0.02	0.06	0.04	0.03	0.01	0.08	0.04
Sn	20.85	20.58	19.09	20.19	18.22	17.13	18.62	18.39	3.39	3.31	3.08
Cs	238.31	230.47	242.34	251.15	227.14	213.45	227.94	240.22	37.18	37.22	38.26
Ba	562.43	505.11	580.15	625.70	530.64	514.58	544.08	567.58	1304.72	1210.48	1313.78
Hf	0.29	0.30	0.26	0.39	0.24	0.23	0.22	0.29	0.29	0.36	0.36
Ta	63.12	60.13	61.17	71.70	58.95	57.84	61.69	61.58	3.25	3.00	3.12
W	18.56	19.00	18.12	19.88	17.37	17.35	18.66	18.49	0.01	0.01	0.02
Pb	4.67	4.65	4.59	5.17	4.24	4.40	4.74	5.09	3.24	2.65	2.56
Th	0.0000	0.0016	0.0054	0.0018	0.0007	0.0016	0.0021	0.1020	0.0014	0.0000	0.0006
U	0.0113	0.0063	0.0076	0.0161	0.0105	0.0152	0.0162	0.0621	0.1006	0.0850	0.0960

Appendix 2.2B (continued): Detailed trace element data of micas from the Pan-African aquamarine-bearing pegmatites from Kafukule (GM) and Luhomero (HEM) in Mzimba. All concentrations are given in ppm.

Element	HEM4B4	HEM4B5	HEM4B6	HEM4B7	HEM4B8	HEM4B9	HEM4B10
Li	52.12	47.25	48.67	50.22	50.52	50.80	45.23
Be	0.08	0.20	0.33	0.25	0.45	0.14	0.28
B	59.86	71.37	67.08	62.34	52.18	48.51	55.21
Sc	1.71	1.66	1.66	1.42	1.33	1.48	1.50
Ti	7679.57	6517.53	6547.43	6333.63	6634.63	6605.64	6504.72
V	137.52	121.59	117.56	120.17	125.30	125.71	123.00
Cr	65.87	61.09	68.11	60.63	62.16	65.26	63.85
Mn	655.75	513.36	579.36	559.19	541.96	560.75	540.51
Co	4.44	7.34	5.85	11.39	8.99	29.86	3.61
Ni	3.08	4.87	3.35	3.57	3.84	4.09	4.82
Cu	0.54	1.77	0.48	1.57	0.58	1.05	0.82
Zn	174.20	147.52	175.45	157.06	154.62	122.01	153.07
Ga	60.10	60.41	64.06	63.79	62.16	59.73	56.75
Rb	560.31	539.96	533.89	548.10	548.46	565.56	530.80
Sr	5.93	9.70	5.29	5.80	5.72	6.48	5.21
Y	0.02	0.00	0.00	0.01	0.01	0.01	0.00
Zr	20.31	17.58	16.29	17.92	16.87	18.23	16.96
Nb	49.68	45.43	44.56	44.94	46.10	47.08	45.52
Mo	0.00	0.04	0.02	0.03	0.02	0.04	0.03
Sn	3.20	3.33	3.40	3.24	3.26	3.62	3.02
Cs	39.85	37.06	35.27	36.50	38.01	37.72	38.09
Ba	1452.52	1283.02	1160.70	1245.56	1203.14	1228.97	1317.35
Hf	0.34	0.29	0.20	0.28	0.22	0.28	0.30
Ta	3.14	2.98	2.91	3.12	3.00	2.99	3.06
W	0.02	0.03	0.04	0.02	0.02	0.01	0.03
Pb	2.44	4.27	2.32	3.06	3.76	3.63	2.84
Th	0.0023	0.0009	0.0000	0.0009	0.0006	0.0014	0.0000
U	0.0950	0.0997	0.1130	0.1331	0.0940	0.1040	0.1030

Appendix 2.2C: Detailed UCC-normalised (Taylor and McLennan, 1995) rare element (REE) data of micas from the Pan-African aquamarine-bearing pegmatites from Kafukule (GM) and Luhomero (HEM) in Mzimba. All concentrations are given in ppm.

Element	GM11	GM12	GM13	GM14	GM15	GM16	GM17	GM18	GM19	GM110
La	0.1710	0.0591	0.0309	0.0771	0.0000	0.0000	0.0000	2.0430	0.0000	0.0000
Ce	0.1562	0.2003	0.0000	0.1069	0.1555	0.0000	0.0000	6.6752	0.1267	10.6240
Pr	0.0123	0.0000	0.0000	0.0094	0.0000	0.0067	0.0000	0.0824	0.0091	0.0824
Nd	0.1300	0.0000	0.2262	0.1404	0.0000	0.0000	0.1430	1.0660	0.1924	7.2800
Sm	0.0000	0.0450	0.0000	0.0000	0.0351	0.0419	0.0000	0.0567	0.0000	0.0000
Eu	0.0054	0.0220	0.0124	0.0361	0.0102	0.0187	0.0273	0.0134	0.0282	0.0263
Gd	0.0000	0.0452	0.0236	0.0209	0.0350	0.0296	0.0000	0.0182	0.0350	0.0000
Tb	0.0045	0.0000	0.0000	0.0005	0.0000	0.0000	0.0008	0.0015	0.0007	0.0000
Dy	0.0112	0.0000	0.0000	0.0000	0.0249	0.0172	0.0000	0.0578	0.0165	0.2135
Ho	0.0009	0.0000	0.0000	0.0000	0.0016	0.0010	0.0000	0.0019	0.0000	0.0000
Er	0.0000	0.0552	0.0000	0.0000	0.0094	0.0000	0.0000	0.0173	0.0108	0.0966
Tm	0.0005	0.0000	0.0004	0.0011	0.0000	0.0000	0.0000	0.0005	0.0000	0.0000
Yb	0.0550	0.0594	0.0000	0.0084	0.0099	0.0000	0.0172	0.0304	0.0117	0.0000
Lu	0.0003	0.0004	0.0004	0.0009	0.0004	0.0006	0.0011	0.0007	0.0024	0.0077

Appendix 2.2C: (continued) Detailed UCC-normalised (Taylor and McLennan, 1995) rare element (REE) data of micas from the Pan-African aquamarine-bearing pegmatites from Kafukule (GM) and Luhomero (HEM) in Mzimba. All concentrations are given in ppm.

Element	GM31	GM32	GM33	GM34	GM35	GM36	GM37	GM38	GM39	GM310
La	0.0000	0.4920	0.6660	1.1100	0.2370	1.1700	0.0456	0.0000	0.0000	0.8040
Ce	0.0666	3.0720	2.7520	11.7760	2.9632	2.4960	0.7680	5.1200	0.8320	2.1760
Pr	0.0083	0.1093	0.0483	0.1988	0.0504	0.0341	0.0000	0.0050	0.0000	0.0348
Nd	0.1768	0.0000	0.6760	0.0000	0.4940	0.1170	0.1456	0.0000	0.0000	0.6370
Sm	0.0365	0.0000	0.0000	0.0000	0.0252	0.0000	0.0342	0.0374	0.1035	0.0374
Eu	0.0023	0.0000	0.0000	0.0031	0.0093	0.0000	0.0018	0.0020	0.0048	0.0025
Gd	0.0182	0.0281	0.0380	0.0760	0.0255	0.0000	0.0300	0.0156	0.0521	0.0133
Tb	0.0007	0.0000	0.0000	0.0000	0.0008	0.0000	0.0006	0.0004	0.0014	0.0006
Dy	0.0000	0.0420	0.0140	0.0000	0.0000	0.0000	0.0140	0.0000	0.0214	0.0154
Ho	0.0037	0.0018	0.0010	0.0027	0.0006	0.0010	0.0000	0.0010	0.0000	0.0009
Er	0.0000	0.0000	0.0064	0.0156	0.0000	0.0000	0.0000	0.0071	0.0173	0.0071
Tm	0.0000	0.0005	0.0002	0.0000	0.0000	0.0002	0.0008	0.0003	0.0010	0.0003
Yb	0.0275	0.0000	0.0154	0.0374	0.0000	0.0070	0.0141	0.0154	0.0220	0.0000
Lu	0.0002	0.0003	0.0003	0.0013	0.0003	0.0006	0.0002	0.0012	0.0006	0.0003

Appendix 2.2C: (continued) Detailed UCC-normalised (Taylor and McLennan, 1995) rare element (REE) data of micas from the Pan-African aquamarine-bearing pegmatites from Kafukule (GM) and Luhomero (HEM) in Mzimba. All concentrations are given in ppm.

Element	GM51	GM52	GM53	GM54	GM55	GM56	GM57	GM58	GM59	GM510
La	0.0390	0.0420	0.0000	0.0000	0.4560	0.0000	0.6300	0.0000	0.2460	1.2660
Ce	0.0000	0.0000	0.1088	0.0800	0.1088	0.1306	4.7360	0.1734	1.6640	2.8928
Pr	0.0067	0.0100	0.0068	0.0000	0.0067	0.0000	0.0195	0.0097	0.0000	0.0966
Nd	0.2002	0.3016	0.1222	0.1508	0.4420	0.2002	1.5340	0.2054	0.4420	0.8346
Sm	0.0509	0.0608	0.0000	0.0450	0.0000	0.0293	0.0000	0.0000	0.0306	0.0342
Eu	0.0015	0.0000	0.0000	0.0016	0.0015	0.0000	0.0028	0.0000	0.0000	0.0194
Gd	0.0209	0.0494	0.0357	0.0000	0.0000	0.0293	0.0000	0.0000	0.0217	0.0494
Tb	0.0005	0.0000	0.0000	0.0008	0.0000	0.0000	0.0000	0.0000	0.0000	0.0011
Dy	0.0168	0.0000	0.0000	0.0179	0.0172	0.0000	0.0158	0.0175	0.0126	0.0469
Ho	0.0000	0.0009	0.0007	0.0000	0.0000	0.0000	0.0015	0.0014	0.0007	0.0013
Er	0.0000	0.0000	0.0124	0.0000	0.0000	0.0078	0.0072	0.0000	0.0000	0.0064
Tm	0.0003	0.0004	0.0003	0.0004	0.0000	0.0000	0.0005	0.0000	0.0000	0.0003
Yb	0.0143	0.0088	0.0000	0.0088	0.0084	0.0117	0.0000	0.0086	0.0000	0.0066
Lu	0.0000	0.0000	0.0000	0.0004	0.0000	0.0000	0.0014	0.0004	0.0005	0.0005

Appendix 2.2C: (continued) Detailed UCC-normalised (Taylor and McLennan, 1995) rare element (REE) data of micas from the Pan-African aquamarine-bearing pegmatites from Kafukule (GM) and Luhomero (HEM) in Mzimba. All concentrations are given in ppm.

Element	HEM1B1	HEM1B2	HEM1B3	HEM1B4	HEM1B5	HEM1B6	HEM1B7	HEM1B8	HEM1B9	HEM1B10
La	0.0369	0.0960	0.4530	0.0480	0.0720	0.1080	0.0000	0.0336	0.0345	0.0474
Ce	0.9984	1.1200	0.0736	0.0659	0.0000	0.3264	0.0896	0.2240	0.0768	0.1344
Pr	0.0000	0.0047	0.0000	0.0327	0.0000	0.0083	0.0084	0.0000	0.0000	0.0057
Nd	0.2990	0.0494	0.0000	0.1742	0.0000	0.0000	0.1794	0.2080	0.1248	0.0000
Sm	0.0284	0.0000	0.0000	0.0000	0.0383	0.0000	0.0000	0.0365	0.0000	0.0257
Eu	0.0031	0.0144	0.0201	0.0289	0.0074	0.0041	0.0177	0.0074	0.0194	0.0273
Gd	0.0494	0.0148	0.0357	0.0000	0.0334	0.0000	0.0000	0.0369	0.0327	0.0000
Tb	0.0007	0.0000	0.0000	0.0000	0.0000	0.0005	0.0000	0.0008	0.0007	0.0000
Dy	0.0116	0.0175	0.0000	0.0000	0.0000	0.0154	0.0112	0.0151	0.0245	0.0256
Ho	0.0007	0.0008	0.0012	0.0009	0.0009	0.0012	0.0000	0.0006	0.0000	0.0000
Er	0.0000	0.0239	0.0265	0.0000	0.0000	0.0000	0.0071	0.0110	0.0055	0.0085
Tm	0.0002	0.0006	0.0009	0.0014	0.0005	0.0015	0.0006	0.0000	0.0007	0.0000
Yb	0.1232	0.1650	0.0946	0.2222	0.0550	0.2684	0.0642	0.1562	0.1276	0.1408
Lu	0.0112	0.0075	0.0073	0.0142	0.0090	0.0072	0.0043	0.0086	0.0090	0.0065

Appendix 2.2C: (continued) Detailed UCC-normalised (Taylor and McLennan, 1995) rare element (REE) data of micas from the Pan-African aquamarine-bearing pegmatites from Kafukule (GM) and Luhomero (HEM) in Mzimba. All concentrations are given in ppm.

Element	HEM2A1	HEM2A2	HEM2A3	HEM2A4	HEM2A5	HEM2A6	HEM2A7	HEM2A8	HEM2A9	HEM2A10
La	0.6000	0.2910	0.0369	0.0675	0.3930	0.1320	0.0525	0.0000	0.0561	0.2340
Ce	0.7104	0.4352	0.1728	0.4416	2.2016	0.2240	0.0262	0.5504	0.1376	0.2816
Pr	0.0348	0.0083	0.0062	0.0048	0.0362	0.0114	0.0045	0.0087	0.0048	0.0031
Nd	0.5304	0.2522	0.0910	0.1430	0.5200	0.2080	0.0000	0.0000	0.0520	0.1326
Sm	0.0266	0.0374	0.0095	0.0423	0.0473	0.0351	0.0360	0.0338	0.0000	0.0135
Eu	0.0093	0.0184	0.0137	0.0129	0.0078	0.0393	0.0226	0.0260	0.0194	0.0241
Gd	0.0471	0.0327	0.0000	0.0000	0.0532	0.0251	0.0000	0.0293	0.0000	0.0194
Tb	0.0015	0.0000	0.0005	0.0002	0.0014	0.0005	0.0008	0.0000	0.0004	0.0005
Dy	0.0273	0.0154	0.0231	0.0046	0.0630	0.0147	0.0042	0.0196	0.0108	0.0000
Ho	0.0013	0.0007	0.0016	0.0008	0.0030	0.0013	0.0012	0.0000	0.0005	0.0013
Er	0.0000	0.0081	0.0219	0.0124	0.0251	0.0179	0.0120	0.0064	0.0184	0.0150
Tm	0.0005	0.0003	0.0011	0.0008	0.0019	0.0008	0.0016	0.0006	0.0008	0.0014
Yb	0.1914	0.0926	0.1214	0.1408	0.1100	0.1782	0.2530	0.0990	0.2002	0.1936
Lu	0.0047	0.0067	0.0083	0.0054	0.0049	0.0121	0.0111	0.0048	0.0078	0.0109

Appendix 2.2C: (continued) Detailed UCC-normalised (Taylor and McLennan, 1995) rare element (REE) data of micas from the Pan-African aquamarine-bearing pegmatites from Kafukule (GM) and Luhomero (HEM) in Mzimba. All concentrations are given in ppm.

Element	HEM3B1	HEM3B2	HEM3B3	HEM3B4	HEM3B5	HEM3B6	HEM3B7	HEM3B8
La	0.000	0.010	0.000	0.000	0.000	0.000	0.005	0.000
Ce	0.002	0.005	0.006	0.000	0.000	0.011	0.009	0.018
Pr	0.000	0.005	0.018	0.000	0.000	0.010	0.000	0.000
Nd	0.000	0.000	0.000	0.000	0.000	0.030	0.000	0.000
Sm	0.000	0.057	0.026	0.000	0.000	0.065	0.041	0.013
Eu	0.820	0.658	0.745	0.620	0.690	0.459	0.543	0.568
Gd	0.039	0.043	0.000	0.000	0.000	0.000	0.000	0.000
Tb	0.017	0.000	0.000	0.000	0.000	0.036	0.000	0.000
Dy	0.030	0.000	0.013	0.000	0.000	0.014	0.000	0.009
Ho	0.000	0.000	0.000	0.000	0.046	0.000	0.030	0.000
Er	0.027	0.105	0.028	0.000	0.077	0.061	0.057	0.000
Tm	0.097	0.162	0.107	0.000	0.093	0.081	0.151	0.112
Yb	0.758	0.656	0.549	0.530	0.590	0.583	0.841	0.481
Lu	1.480	1.510	1.550	2.310	1.110	1.410	1.680	1.200

Appendix 2.2C: (continued) Detailed UCC-normalised (Taylor and McLennan, 1995) rare element (REE) data of micas from the Pan-African aquamarine-bearing pegmatites from Kafukule (GM) and Luhomero (HEM) in Mzimba. All concentrations are given in ppm.

Element	HEM4B1	HEM4B2	HEM4B3	HEM4B4	HEM4B5	HEM4B6	HEM4B7	HEM4B8	HEM4B9	HEM4B10
La	0.0720	0.8520	0.0270	0.3990	0.1320	0.0900	0.0450	0.0261	0.0780	0.3030
Ce	0.1792	0.0749	0.3136	0.0480	0.1005	0.0890	0.1376	0.0000	0.5312	0.1555
Pr	0.0070	0.0639	0.0046	0.0060	0.0000	0.0000	0.0000	0.0000	0.0078	0.0149
Nd	0.0988	0.1742	0.0000	0.1586	0.0000	0.0962	0.1924	0.0000	0.8840	0.0988
Sm	0.0311	0.0207	0.0207	0.0000	0.0000	0.0288	0.0203	0.0000	0.0324	0.0000
Eu	0.0133	0.0052	0.0011	0.0000	0.0143	0.0161	0.0176	0.0075	0.0035	0.0101
Gd	0.0156	0.0000	0.0000	0.0137	0.0000	0.0323	0.0144	0.0000	0.0000	0.0144
Tb	0.0004	0.0010	0.0005	0.0004	0.0000	0.0000	0.0000	0.0004	0.0006	0.0007
Dy	0.0158	0.0151	0.0123	0.0079	0.0000	0.0119	0.0070	0.0119	0.0133	0.0203
Ho	0.0000	0.0000	0.0005	0.0006	0.0000	0.0000	0.0005	0.0000	0.0009	0.0008
Er	0.0042	0.0068	0.0039	0.0000	0.0037	0.0000	0.0000	0.0054	0.0000	0.0069
Tm	0.0002	0.0000	0.0007	0.0000	0.0000	0.0000	0.0002	0.0004	0.0000	0.0003
Yb	0.0180	0.0000	0.0000	0.0000	0.0130	0.0000	0.0139	0.0227	0.0158	0.0000
Lu	0.0009	0.0000	0.0000	0.0000	0.0004	0.0012	0.0006	0.0003	0.0002	0.0002

Appendix 2.2D: Detailed chondrite-normalised (Nakamura, 1974) rare element (REE) data of micas from the Pan-African aquamarine-bearing pegmatites from Kafukule (GM) and Luhomero (HEM) in Mzimba. All concentrations are given in ppm.

Element	GM11	GM12	GM13	GM14	GM15	GM16	GM17	GM18	GM19	GM110
La	0.0240	0.0000	0.0000	0.0000	0.0000	0.0000	0.0000	0.2880	0.0000	0.0000
Ce	0.0000	0.0000	0.0000	0.0000	0.0000	0.0000	0.0000	0.1700	0.0000	0.2700
Pr	0.0000	0.0000	0.0000	0.0000	0.0000	0.0000	0.0000	0.1250	0.0000	0.0000
Nd	0.0000	0.0000	0.0000	0.0000	0.0000	0.0000	0.0000	0.0900	0.0000	0.6200
Sm	0.0000	0.0000	0.0000	0.0000	0.0000	0.0000	0.0000	0.0850	0.0000	0.0000
Eu	0.1090	0.4400	0.2500	0.7300	0.2100	0.3800	0.5500	0.2690	0.5600	0.0000
Gd	0.0000	0.0000	0.0000	0.0000	0.0000	0.0000	0.0000	0.0000	0.0000	0.0000
Tb	0.2000	0.0000	0.0000	0.0000	0.0000	0.0000	0.0000	0.0670	0.0000	0.0000
Dy	0.0000	0.0000	0.0000	0.0000	0.0000	0.0000	0.0000	0.0670	0.0000	0.0000
Ho	0.0000	0.0000	0.0000	0.0000	0.0000	0.0000	0.0000	0.0430	0.0000	0.0000
Er	0.0000	0.1490	0.0000	0.0000	0.0000	0.0000	0.0000	0.0470	0.0000	0.0000
Tm	0.0000	0.0000	0.0000	0.1280	0.0000	0.0000	0.0000	0.0620	0.0000	0.0000
Yb	0.1580	0.1700	0.0000	0.0000	0.0000	0.0000	0.0000	0.0860	0.0000	0.0000
Lu	0.0000	0.0000	0.0540	0.1110	0.0000	0.0740	0.1340	0.0890	0.3100	0.9800

Appendix 2.2D: (continued) Detailed chondrite-normalised (Nakamura, 1974) rare element (REE) data of micas from the Pan-African aquamarine-bearing pegmatites from Kafukule (GM) and Luhomero (HEM) in Mzimba. All concentrations are given in ppm.

Element	GM31	GM32	GM33	GM34	GM35	GM36	GM37	GM38	GM39	GM310
La	0.0000	0.0690	0.0940	0.1550	0.0330	0.1660	0.0000	0.0000	0.0000	0.1130
Ce	0.0000	0.0790	0.0710	0.3010	0.0760	0.0630	0.0196	0.1310	0.0220	0.0555
Pr	0.0000	0.1650	0.0740	0.3000	0.0770	0.0510	0.0000	0.0000	0.0000	0.0530
Nd	0.0000	0.0000	0.0570	0.0000	0.0420	0.0000	0.0120	0.0000	0.0000	0.0540
Sm	0.0000	0.0000	0.0000	0.0000	0.0000	0.0000	0.0000	0.0000	0.0000	0.0560
Eu	0.0000	0.0000	0.0000	0.0000	0.1880	0.0000	0.0000	0.0000	0.0960	0.0490
Gd	0.0000	0.0000	0.0000	0.1000	0.0000	0.0000	0.0000	0.0000	0.0000	0.0180
Tb	0.0000	0.0000	0.0000	0.0000	0.0360	0.0000	0.0000	0.0000	0.0000	0.0000
Dy	0.0000	0.0470	0.0000	0.0000	0.0000	0.0000	0.0000	0.0000	0.0000	0.0180
Ho	0.0840	0.0000	0.0000	0.0000	0.0000	0.0000	0.0000	0.0000	0.0000	0.0200
Er	0.0000	0.0000	0.0000	0.0000	0.0000	0.0000	0.0000	0.0000	0.0470	0.0190
Tm	0.0000	0.0000	0.0000	0.0000	0.0000	0.0000	0.0970	0.0000	0.0000	0.0000
Yb	0.0770	0.0000	0.0000	0.1000	0.0000	0.0000	0.0000	0.0000	0.0610	0.0000
Lu	0.0000	0.0000	0.0000	0.1600	0.0000	0.0750	0.0000	0.1500	0.0000	0.0000

Appendix 2.2D: (continued) Detailed chondrite-normalised (Nakamura, 1974) rare element (REE) data of micas from the Pan-African aquamarine-bearing pegmatites from Kafukule (GM) and Luhomero (HEM) in Mzimba. All concentrations are given in ppm.

Element	GM51	GM52	GM53	GM54	GM55	GM56	GM57	GM58	GM59	GM510
La	0.0056	0.0000	0.0000	0.0000	0.0640	0.0000	0.0880	0.0000	0.0000	0.1780
Ce	0.0000	0.0000	0.0000	0.0000	0.0000	0.0000	0.1200	0.0000	0.0420	0.0738
Pr	0.0000	0.0000	0.0000	0.0000	0.0000	0.0000	0.0000	0.0000	0.0000	0.1460
Nd	0.0000	0.0000	0.0100	0.0000	0.0370	0.0000	0.1290	0.0000	0.0370	0.0700
Sm	0.0000	0.0910	0.0000	0.0670	0.0000	0.0000	0.0000	0.0000	0.0000	0.0520
Eu	0.0000	0.0000	0.0000	0.0000	0.0000	0.0000	0.0000	0.0000	0.0000	0.3930
Gd	0.0000	0.0000	0.0470	0.0000	0.0000	0.0000	0.0000	0.0000	0.0000	0.0650
Tb	0.0000	0.0000	0.0000	0.0000	0.0000	0.0000	0.0000	0.0000	0.0000	0.0460
Dy	0.0000	0.0000	0.0000	0.0000	0.0000	0.0000	0.0000	0.0000	0.0000	0.0540
Ho	0.0000	0.0210	0.0000	0.0000	0.0000	0.0000	0.0000	0.0000	0.0000	0.0300
Er	0.0000	0.0000	0.0000	0.0000	0.0000	0.0000	0.0000	0.0000	0.0000	0.0000
Tm	0.0000	0.0000	0.0000	0.0480	0.0000	0.0000	0.0000	0.0000	0.0000	0.0370
Yb	0.0000	0.0000	0.0000	0.0000	0.0000	0.0000	0.0000	0.0000	0.0000	0.0180
Lu	0.0000	0.0000	0.0000	0.0000	0.0000	0.0000	0.1800	0.0000	0.0000	0.0640

Appendix 2.2D: (continued) Detailed chondrite-normalised (Nakamura, 1974) rare element (REE) data of micas from the Pan-African aquamarine-bearing pegmatites from Kafukule (GM) and Luhomero (HEM) in Mzimba. All concentrations are given in ppm.

Element	HEM1B1	HEM1B2	HEM1B3	HEM1B4	HEM1B5	HEM1B6	HEM1B7	HEM1B8	HEM1B9	HEM1B10
La	0.000	0.014	0.064	0.000	0.010	0.015	0.000	0.000	0.000	0.000
Ce	0.000	0.029	0.000	0.000	0.000	0.000	0.002	0.006	0.002	0.004
Pr	0.000	0.007	0.000	0.050	0.000	0.000	0.000	0.000	0.000	0.000
Nd	0.000	0.004	0.000	0.000	0.000	0.000	0.000	0.017	0.000	0.000
Sm	0.000	0.000	0.000	0.000	0.000	0.000	0.000	0.000	0.000	0.000
Eu	0.062	0.291	0.410	0.580	0.149	0.083	0.357	0.149	0.390	0.550
Gd	0.000	0.020	0.000	0.000	0.000	0.000	0.000	0.000	0.000	0.000
Tb	0.000	0.000	0.000	0.000	0.000	0.000	0.000	0.000	0.000	0.000
Dy	0.000	0.000	0.000	0.000	0.000	0.000	0.013	0.000	0.028	0.030
Ho	0.000	0.018	0.000	0.000	0.000	0.000	0.000	0.000	0.000	0.000
Er	0.000	0.065	0.072	0.000	0.000	0.000	0.000	0.000	0.015	0.000
Tm	0.000	0.069	0.110	0.169	0.059	0.177	0.069	0.000	0.087	0.000
Yb	0.350	0.465	0.270	0.630	0.155	0.760	0.181	0.440	0.359	0.400
Lu	1.430	0.950	0.920	1.800	1.140	0.910	0.550	1.100	1.140	0.830

Appendix 2.2D: (continued) Detailed chondrite-normalised (Nakamura, 1974) rare element (REE) data of micas from the Pan-African aquamarine-bearing pegmatites from Kafukule (GM) and Luhomero (HEM) in Mzimba. All concentrations are given in ppm.

Element	HEM2A1	HEM2A2	HEM2A3	HEM2A4	HEM2A5	HEM2A6	HEM2A7	HEM2A8	HEM2A9	HEM2A10
La	0.084	0.041	0.005	0.000	0.055	0.019	0.007	0.000	0.008	0.033
Ce	0.000	0.011	0.004	0.011	0.056	0.006	0.001	0.014	0.004	0.007
Pr	0.053	0.000	0.000	0.007	0.055	0.017	0.007	0.013	0.007	0.005
Nd	0.045	0.000	0.008	0.000	0.044	0.000	0.000	0.000	0.004	0.011
Sm	0.000	0.000	0.014	0.000	0.000	0.000	0.000	0.000	0.000	0.021
Eu	0.189	0.372	0.277	0.261	0.158	0.790	0.456	0.520	0.391	0.487
Gd	0.062	0.000	0.000	0.000	0.000	0.000	0.000	0.000	0.000	0.026
Tb	0.067	0.000	0.023	0.009	0.062	0.000	0.000	0.000	0.017	0.022
Dy	0.032	0.000	0.000	0.005	0.073	0.000	0.005	0.000	0.000	0.000
Ho	0.030	0.017	0.036	0.017	0.070	0.000	0.000	0.000	0.012	0.030
Er	0.000	0.022	0.059	0.034	0.068	0.049	0.033	0.000	0.050	0.041
Tm	0.000	0.000	0.136	0.099	0.237	0.103	0.193	0.077	0.100	0.165
Yb	0.543	0.262	0.343	0.397	0.312	0.500	0.713	0.280	0.566	0.545
Lu	0.594	0.850	1.060	0.687	0.620	1.530	1.420	0.610	0.990	1.390

Appendix 2.2D: (continued) Detailed chondrite-normalised (Nakamura, 1974) rare element (REE) data of micas from the Pan-African aquamarine-bearing pegmatites from Kafukule (GM) and Luhomero (HEM) in Mzimba. All concentrations are given in ppm.

Element	HEM3B1	HEM3B2	HEM3B3	HEM3B4	HEM3B5	HEM3B6	HEM3B7	HEM3B8
La	0.000	0.010	0.000	0.000	0.000	0.000	0.005	0.000
Ce	0.002	0.005	0.006	0.000	0.000	0.011	0.009	0.018
Pr	0.000	0.005	0.018	0.000	0.000	0.010	0.000	0.000
Nd	0.000	0.000	0.000	0.000	0.000	0.030	0.000	0.000
Sm	0.000	0.057	0.026	0.000	0.000	0.065	0.041	0.013
Eu	0.820	0.658	0.745	0.620	0.690	0.459	0.543	0.568
Gd	0.039	0.043	0.000	0.000	0.000	0.000	0.000	0.000
Tb	0.017	0.000	0.000	0.000	0.000	0.036	0.000	0.000
Dy	0.030	0.000	0.013	0.000	0.000	0.014	0.000	0.009
Ho	0.000	0.000	0.000	0.000	0.046	0.000	0.030	0.000
Er	0.027	0.105	0.028	0.000	0.077	0.061	0.057	0.000
Tm	0.097	0.162	0.107	0.000	0.093	0.081	0.151	0.112
Yb	0.758	0.656	0.549	0.530	0.590	0.583	0.841	0.481
Lu	1.480	1.510	1.550	2.310	1.110	1.410	1.680	1.200

Appendix 2.2D: (continued) Detailed chondrite-normalised (Nakamura, 1974) rare element (REE) data of micas from the Pan-African aquamarine-bearing pegmatites from Kafukule (GM) and Luhomero (HEM) in Mzimba. All concentrations are given in ppm.

Element	HEM4B1	HEM4B2	HEM4B3	HEM4B4	HEM4B5	HEM4B6	HEM4B7	HEM4B8	HEM4B9	HEM4B10
La	0.010	0.120	0.000	0.056	0.019	0.013	0.006	0.000	0.000	0.043
Ce	0.000	0.000	0.008	0.000	0.000	0.000	0.004	0.000	0.000	0.000
Pr	0.000	0.097	0.000	0.000	0.000	0.000	0.000	0.000	0.012	0.023
Nd	0.008	0.000	0.000	0.000	0.000	0.000	0.000	0.000	0.000	0.000
Sm	0.000	0.000	0.000	0.000	0.000	0.000	0.000	0.000	0.000	0.000
Eu	0.269	0.104	0.000	0.000	0.287	0.330	0.355	0.150	0.071	0.200
Gd	0.000	0.000	0.000	0.000	0.000	0.000	0.000	0.000	0.000	0.000
Tb	0.000	0.040	0.000	0.000	0.000	0.000	0.000	0.000	0.000	0.000
Dy	0.000	0.000	0.000	0.000	0.000	0.000	0.008	0.000	0.000	0.024
Ho	0.000	0.000	0.000	0.000	0.000	0.000	0.000	0.000	0.000	0.000
Er	0.000	0.000	0.000	0.000	0.000	0.000	0.000	0.000	0.000	0.019
Tm	0.023	0.000	0.091	0.000	0.000	0.000	0.000	0.000	0.000	0.000
Yb	0.051	0.000	0.000	0.000	0.037	0.000	0.039	0.064	0.045	0.000
Lu	0.113	0.000	0.000	0.000	0.000	0.158	0.074	0.000	0.000	0.000

Appendix 2.3A: Detailed major element data of micas from the Pan- African Dowa pegmatites (DHD) in central Malawi.

	DHD1A_1	DHD1A_2	DHD1A_3	DHD1A_4	DHD1A_5	DHD1A_6	DHD1A_7	DHD1A_8	DHD1A_9	DHD1A_10	DHD1B_1
SiO_2	46.32	46.28	46.50	46.24	46.42	46.91	46.30	46.67	47.04	46.36	46.08
TiO_2	0.24	0.29	0.18	0.33	0.16	0.17	0.17	0.24	0.15	0.17	0.08
Al_2O_3	35.96	35.27	35.98	35.18	35.20	35.75	34.74	35.88	35.13	35.58	33.39
FeO	1.44	1.42	1.32	1.24	1.28	0.98	1.18	1.31	1.55	1.18	3.06
MnO	0.00	0.00	0.00	0.00	0.02	0.00	0.00	0.01	0.02	0.06	0.10
MgO	0.44	0.47	0.45	0.46	0.50	0.61	0.51	0.46	0.60	0.52	0.67
CaO	0.01	0.03	0.03	0.01	0.01	0.00	0.03	0.02	0.01	0.02	0.05
Na_2O	0.94	0.86	1.00	0.75	0.70	0.87	0.82	0.69	0.98	0.85	0.67
K_2O	11.28	11.37	11.66	12.47	12.24	11.79	11.78	11.93	11.87	12.57	12.67
Rb_2O	0.00	0.00	0.00	0.00	0.00	0.00	0.00	0.00	0.00	0.00	0.06
F	0.15	0.21	0.10	0.27	0.00	0.03	0.09	0.00	0.06	0.03	0.33
Cl	0.00	0.00	0.03	0.01	0.03	0.00	0.00	0.00	0.00	0.00	0.06
Cr_2O_3	0.03	0.00	0.02	0.00	0.02	0.00	0.00	0.01	0.00	0.00	0.03
H_2O*	4.47	4.41	4.52	4.38	4.51	4.55	4.44	4.56	4.53	4.53	4.29
Subtotal	101.28	100.60	101.78	101.36	101.09	101.67	100.06	101.76	101.93	101.87	101.55
O=F,Cl	0.07	0.09	0.05	0.12	0.01	0.01	0.04	0.00	0.02	0.01	0.15
Total	101.21	100.51	101.73	101.24	101.08	101.65	100.03	101.76	101.91	101.85	101.40
Si	6.12	6.16	6.10	6.14	6.17	6.17	6.20	6.14	6.19	6.12	6.19
Al ^{iv}	1.88	1.84	1.90	1.86	1.84	1.84	1.80	1.86	1.81	1.88	1.81
Al ^{vi}	3.72	3.69	3.69	3.65	3.67	3.70	3.68	3.70	3.64	3.66	3.47
Ti	0.02	0.03	0.02	0.03	0.02	0.02	0.02	0.02	0.02	0.02	0.01
Cr	0.00	0.00	0.00	0.00	0.00	0.00	0.00	0.00	0.00	0.00	0.00
Fe	0.16	0.16	0.18	0.14	0.14	0.11	0.13	0.14	0.17	0.13	0.34
Mn	0.00	0.00	0.00	0.00	0.00	0.00	0.00	0.00	0.00	0.01	0.01
Mg	0.09	0.09	0.09	0.09	0.10	0.12	0.10	0.09	0.12	0.10	0.14
Li*	0.00	0.00	0.00	0.00	0.00	0.00	0.00	0.00	0.00	0.00	0.02
Ca	0.00	0.00	0.00	0.00	0.00	0.00	0.00	0.00	0.00	0.00	0.01
Na	0.24	0.22	0.28	0.19	0.18	0.22	0.21	0.18	0.25	0.22	0.18
K	1.90	1.93	1.95	2.11	2.07	1.98	2.01	2.00	1.99	2.12	2.17
Rb	0.00	0.00	0.00	0.00	0.00	0.00	0.00	0.00	0.00	0.00	0.01
OH*	3.94	3.91	3.95	3.88	3.99	3.99	3.96	4.00	3.98	3.99	3.85
F	0.06	0.09	0.04	0.12	0.00	0.01	0.04	0.00	0.02	0.01	0.14
Cl	0.00	0.00	0.01	0.00	0.01	0.00	0.00	0.00	0.00	0.00	0.01
TOTAL	18.13	18.13	18.21	18.23	18.19	18.15	18.16	18.14	18.19	18.26	18.34
Y total	3.99	3.97	3.97	3.92	3.94	3.95	3.93	3.96	3.95	3.92	3.99
X total	2.14	2.16	2.23	2.31	2.26	2.20	2.23	2.18	2.24	2.34	2.36
Al total	5.60	5.53	5.59	5.51	5.51	5.54	5.48	5.56	5.45	5.54	5.29

* Calculated.

Appendix 2.3A (continued): Detailed major element data of micas from the Pan- African Dowa pegmatites (DHD) in central Malawi.

Sample	DHD1B_2	DHD1B_3	DHD1B_4	DHD1B_5	DHD1B_6	DHD1B_7	DHD1B_8	DHD1B_9	DHD1B_10	DHD1C_1	DHD1C_2
SiO_2	45.74	45.97	45.81	46.05	45.37	45.89	45.52	45.58	46.15	46.53	46.06
TiO_2	0.06	0.10	0.04	0.05	0.11	0.05	0.06	0.09	0.08	0.24	0.21
Al_2O_3	33.41	32.92	33.36	33.49	33.07	33.50	33.01	33.13	33.92	33.24	32.43
FeO	3.69	3.39	3.24	3.27	3.22	3.34	3.05	3.38	3.36	3.04	2.65
MnO	0.06	0.07	0.00	0.11	0.17	0.06	0.07	0.00	0.10	0.03	0.09
MgO	0.72	0.67	0.69	0.69	0.65	0.65	0.65	0.63	0.68	0.93	0.91
CaO	0.00	0.01	0.00	0.00	0.04	0.00	0.04	0.01	0.01	0.00	0.02
Na_2O	0.75	0.84	0.66	0.58	0.76	0.86	0.57	0.62	0.66	0.76	0.67
K_2O	11.49	11.99	12.87	11.47	12.05	11.79	12.13	11.18	12.08	12.62	13.60
Rb_2O	0.07	0.01	0.12	0.08	0.11	0.08	0.08	0.07	0.10	0.00	0.00
F	0.36	0.34	0.35	0.47	0.38	0.20	0.22	0.38	0.37	0.08	0.28
Cl	0.02	0.04	0.00	0.02	0.01	0.10	0.00	0.03	0.01	0.00	0.00
Cr_2O_3	0.04	0.03	0.03	0.07	0.04	0.00	0.00	0.04	0.04	0.04	0.00
Li_2O*	0.00	0.00	0.00	0.00	0.00	0.00	0.00	0.00	0.00	0.00	0.01
H_2O*	4.27	4.26	4.29	4.23	4.23	4.33	4.30	4.21	4.31	4.48	4.34
Subtotal	100.67	100.65	101.47	100.57	100.19	100.84	99.69	99.34	101.86	101.99	101.27
O=F,Cl	0.16	0.15	0.15	0.20	0.16	0.11	0.09	0.17	0.16	0.03	0.12
Total	100.51	100.50	101.32	100.37	100.03	100.73	99.60	99.17	101.71	101.96	101.15
Si	6.17	6.22	6.17	6.20	6.17	6.18	6.20	6.21	6.16	6.19	6.17
Al^{iv}	1.83	1.79	1.83	1.80	1.83	1.82	1.80	1.79	1.84	1.82	1.83
Al^{vi}	3.49	3.46	3.47	3.52	3.47	3.50	3.51	3.53	3.50	3.41	3.40
Ti	0.01	0.01	0.00	0.01	0.01	0.01	0.01	0.01	0.01	0.02	0.02
Cr	0.00	0.00	0.00	0.00	0.00	0.00	0.00	0.00	0.00	0.00	0.00
Fe	0.42	0.38	0.37	0.37	0.37	0.38	0.35	0.39	0.38	0.38	0.30
Mn	0.01	0.01	0.00	0.01	0.02	0.01	0.01	0.00	0.01	0.00	0.01
Mg	0.14	0.14	0.14	0.14	0.13	0.13	0.13	0.13	0.13	0.18	0.18
Li*	0.02	0.02	0.02	0.04	0.02	0.00	0.00	0.02	0.02	0.00	0.01
Ca	0.00	0.00	0.00	0.00	0.01	0.00	0.01	0.00	0.00	0.00	0.00
Na	0.20	0.22	0.17	0.15	0.20	0.23	0.15	0.16	0.17	0.20	0.17
K	1.98	2.07	2.21	1.97	2.09	2.03	2.11	1.94	2.06	2.14	2.38
Rb	0.01	0.00	0.01	0.01	0.01	0.01	0.01	0.01	0.01		
OH*	3.84	3.85	3.85	3.80	3.84	3.89	3.91	3.83	3.84	3.97	3.88
F	0.15	0.15	0.15	0.20	0.16	0.08	0.10	0.16	0.16	0.03	0.12
Cl	0.00	0.01	0.00	0.00	0.00	0.02	0.00	0.01	0.00	0.00	0.00
TOTAL	18.26	18.31	18.38	18.22	18.33	18.28	18.27	18.19	18.29	18.34	18.47
Y total	4.08	4.01	3.99	4.09	4.02	4.02	4.00	4.08	4.05	4.01	3.92
X total	2.18	2.29	2.39	2.13	2.30	2.26	2.27	2.11	2.24	2.33	2.55
Al total	5.32	5.25	5.30	5.32	5.30	5.32	5.30	5.32	5.339	5.23	5.23

* Calculated.

Appendix 2.3A (continued): Detailed major element data of micas from the Pan- African Dowa pegmatites (DHD) in central Malawi.

	DHD1C_3	DHD1C_4	DHD1C_9	DHD1C_10	DHD1E_1	DHD1E_2	DHD1E_3	DHD1E_4	DHD1E_5	DHD1E_6
SiO_2	46.52	45.76	46.17	46.20	39.00	39.04	39.13	38.73	38.57	38.93
TiO_2	0.20	0.25	0.18	0.26	1.45	1.35	1.37	1.38	1.40	1.24
Al_2O_3	32.45	32.81	33.05	33.30	16.06	16.05	16.04	15.92	15.93	16.23
FeO	3.13	3.07	3.12	3.14	4.13	3.23	3.56	3.74	3.66	3.46
MnO	0.13	0.00	0.00	0.03	0.05	0.02	0.13	0.11	0.02	0.03
MgO	0.90	0.82	0.90	0.90	22.57	22.58	22.63	22.78	22.54	22.06
CaO	0.00	0.00	0.00	0.00	0.00	0.02	0.00	0.05	0.02	0.03
Na_2O	0.72	0.78	0.87	0.64	0.27	0.24	0.06	0.19	0.22	0.22
K_2O	13.34	13.54	12.35	12.78	12.64	12.80	13.14	12.20	12.03	11.72
Rb_2O	0.00	0.00								
F	0.13	0.27	0.15	0.12	1.11	1.35	1.19	1.10	1.16	1.16
Cl	0.00	0.00	0.00	0.00	0.02	0.05	0.05	0.06	0.03	0.11
Cr_2O_3	0.01	0.02	0.00	0.02	0.00	0.03	0.00	0.03	0.03	0.01
Li_2O*	0.00	0.01	0.00	0.02	0.27	0.34	0.29	0.27	0.29	0.29
H_2O*	4.48	4.32	4.50	4.36	3.68	3.55	3.64	3.65	3.60	3.58
Subtotal	102.00	101.64	101.28	101.62	101.26	100.67	101.23	100.20	99.48	99.07
O=F,Cl	0.05	0.11	0.07	0.14	0.47	0.58	0.51	0.48	0.49	0.51
Total	100.94	101.53	101.21	101.49	100.79	100.10	100.71	99.73	98.98	98.55
Si	6.14	6.17	6.18	6.15	5.55	5.58	5.57	5.55	5.56	5.62
Al ^{iv}	1.86	1.83	1.82	1.85	2.45	2.42	2.43	2.45	2.44	2.39
Al ^{vi}	3.41	3.39	3.41	3.37	0.25	0.28	0.26	0.24	0.27	0.37
Ti	0.02	0.03	0.02	0.03	0.16	0.15	0.15	0.15	0.15	0.14
Cr	0.00	0.00	0.00	0.00	0.00	0.00	0.00	0.00	0.00	0.00
Fe	0.35	0.35	0.36	0.38	0.49	0.39	0.42	0.45	0.44	0.42
Mn	0.02	0.00	0.00	0.00	0.01	0.00	0.02	0.01	0.00	0.00
Mg	0.18	0.17	0.18	0.18	4.79	4.81	4.80	4.87	4.84	4.74
Li*	0.00	0.00	0.00	0.01	0.16	0.20	0.17	0.15	0.17	0.17
Ca	0.00	0.00	0.00	0.00	0.00	0.00	0.00	0.01	0.00	0.01
Na	0.21	0.20	0.22	0.17	0.08	0.07	0.02	0.05	0.06	0.06
K	2.25	2.33	2.22	2.34	2.29	2.33	2.39	2.23	2.21	2.16
Rb										
OH*	3.95	3.89	3.94	3.87	3.49	3.38	3.45	3.49	3.47	3.44
F	0.05	0.11	0.06	0.14	0.50	0.61	0.54	0.50	0.53	0.53
Cl	0.00	0.00	0.00	0.00	0.01	0.01	0.01	0.02	0.01	0.03
TOTAL	18.43	18.46	18.41	18.48	20.21	20.23	20.22	20.17	20.15	20.06
Y total	3.97	3.93	3.97	3.97	5.84	5.82	5.82	5.88	5.88	5.84
X total	2.46	2.53	2.44	2.50	2.37	2.41	2.40	2.29	2.28	2.22
Al total	5.27	5.22	5.23	5.22	2.69	2.70	2.69	2.69	2.71	2.76

* Calculated.

Appendix 2.3A (continued): Detailed major element data of micas from the Pan- African Dowa pegmatites (DHD) in central Malawi.

Sample	DHD1E_7	DHD1E_8	DHD1E_9	DHD1E_10
SiO_2	38.41	38.46	38.68	39.03
TiO_2	1.32	1.32	1.29	1.31
Al_2O_3	15.95	15.81	15.87	16.05
FeO	3.69	3.66	3.48	4.14
MnO	0.03	0.03	0.04	0.07
MgO	22.54	22.31	22.23	22.33
CaO	0.02	0.00	0.00	0.00
Na_2O	0.37	0.25	0.19	0.31
K_2O	12.97	13.17	13.55	13.10
F	1.01	1.26	1.11	1.08
Cl	0.08	0.07	0.04	0.01
Cr_2O_3	0.00	0.02	0.00	0.00
Li_2O*	0.24	0.32	0.27	0.26
H_2O	3.67	3.54	3.63	3.75
Sub tot	100.28	100.22	100.37	101.43
O=F,Cl	0.44	0.55	0.48	0.46
Total	99.84	99.68	99.89	100.97
Si	5.53	5.55	5.57	5.51
Al^{iv}	2.47	2.45	2.43	2.49
Al^{vi}	0.23	0.24	0.26	0.21
Ti	0.14	0.14	0.14	0.14
Cr	0.00	0.00	0.00	0.00
Fe	0.44	0.44	0.42	0.52
Mn	0.00	0.00	0.01	0.01
Mg	4.84	4.80	4.77	4.83
Li*	0.14	0.18	0.16	0.15
Ca	0.00	0.00	0.00	0.00
Na	0.10	0.07	0.05	0.08
K	2.38	2.42	2.49	2.35
OH*	3.52	3.41	3.49	3.52
F	0.46	0.58	0.51	0.48
Cl	0.02	0.02	0.01	0.00
TOTAL	20.29	20.30	20.29	20.30
Y total	5.80	5.81	5.75	5.86
X total	2.49	2.50	2.54	2.44
Al total	2.71	2.69	2.69	2.70

* Calculated.

Appendix 2.3B: Detailed trace element data of micas from the Pan- African Dowa pegmatites (DHD) in central Malawi. All concentrations are given in ppm.

	DHD1A1	DHD1A2	DHD1A3	DHD1A4	DHD1A5	DHD1A6	DHD1A7	DHD1A8	DHD1A9	DHD1A10	DHD1B1
Li	382.25	385.29	40.43	41.35	43.79	44.00	41.86	40.03	42.71	41.76	998.07
Be	13.78	13.70	15.08	16.15	16.30	15.11	14.16	19.45	18.80	18.28	23.83
B	32.25	32.87	103.98	120.46	119.23	124.21	106.49	130.12	134.56	108.35	60.74
Sc	14.11	13.62	8.14	7.95	8.64	10.24	8.36	10.14	11.31	13.31	1.00
Ti	1627.67	1587.47	1598.60	1505.21	1380.88	1409.31	1240.50	1479.82	1514.82	1839.88	496.49
V	40.15	39.01	5.15	4.18	2.33	3.03	1.79	3.14	3.44	4.80	10.75
Cr	0.15	0.19	0.56	0.31	0.23	0.16	0.18	0.13	0.20	0.21	0.25
Mn	317.59	240.05	39.06	39.67	42.40	41.94	41.42	38.81	39.35	40.27	572.24
Co	1.55	5.44	1.68	1.66	1.71	1.71	1.60	1.53	1.60	1.99	5.99
Ni	0.14	0.05	2.00	1.82	2.05	2.44	1.75	1.62	1.86	2.04	0.06
Cu	0.03	0.12	0.20	0.03	0.06	0.04	0.08	0.05	0.04	0.06	0.98
Zn	42.47	33.39	43.24	44.07	44.31	43.95	42.23	40.40	43.30	44.37	217.98
Ga	85.40	80.80	85.92	84.43	86.92	93.52	92.29	95.47	98.89	102.54	131.74
Rb	1063.45	1049.52	300.17	302.47	303.78	283.62	287.52	266.15	271.12	267.75	2891.20
Sr	0.63	0.77	26.09	32.63	39.66	37.79	30.54	32.32	35.65	29.46	0.11
Y	0.01	0.01	0.02	0.02	0.01	0.01	0.01	0.02	0.01	0.01	0.00
Zr	2.90	2.59	1.35	1.22	1.26	1.28	1.35	1.22	1.37	1.52	1.55
Nb	84.70	84.87	25.80	25.98	27.14	26.23	25.82	25.18	25.69	27.17	182.74
Mo	0.24	0.22	0.01	0.02	0.02	0.02	0.02	0.02	0.02	0.02	0.14
Sn	13.23	11.61	32.26	33.43	36.45	36.82	28.95	26.79	33.07	33.03	60.99
Cs	18.56	18.12	4.78	4.56	4.69	3.39	3.86	3.12	3.31	3.22	48.92
Ba	5.38	4.75	973.80	1004.60	1130.04	1352.69	1271.79	1275.36	1343.84	1533.21	1.03
Hf	0.30	0.31	0.10	0.14	0.16	0.16	0.12	0.16	0.13	0.14	0.36
Ta	8.82	8.83	2.40	2.51	2.93	2.25	2.02	1.92	2.26	1.83	14.86
W	36.01	33.59	31.03	30.52	31.52	32.65	30.48	32.31	33.90	37.60	18.10
Pb	3.48	3.23	25.43	27.84	30.22	29.98	26.75	25.22	29.59	27.62	2.50
Th	0.0000	0.0000	0.0013	0.0014	0.0000	0.0010	0.0020	0.0013	0.0010	0.0000	0.0000
U	0.0030	0.0030	0.0011	0.0010	0.0021	0.0020	0.0010	0.0008	0.0000	0.0000	0.0050

Appendix 2.3B (continued): Detailed trace element data of micas from the Pan- African Dowa pegmatites (DHD) in central Malawi. All concentrations are given in ppm.

	DHD1B2	DHD1B3	DHD1B4	DHD1B5	DHD1B6	DHD1B7	DHD1B8	DHD1B9	DHD1B10	DHD1C1	DHD1C2
Li	998.05	964.38	1063.45	1034.33	951.91	921.13	1024.61	1021.03	964.25	436.25	389.47
Be	21.38	21.83	23.20	20.62	23.07	22.88	20.88	18.68	22.89	14.22	11.81
B	66.43	67.17	55.45	64.77	65.67	68.83	58.52	74.33	60.73	59.16	62.77
Sc	0.81	0.83	0.85	1.01	0.74	0.84	0.91	0.90	0.96	12.42	12.92
Ti	491.88	469.46	519.57	534.41	483.56	487.00	512.69	499.76	484.98	1611.03	1640.06
V	10.74	10.24	11.13	11.27	10.58	10.70	11.11	10.54	11.88	41.86	43.48
Cr	0.17	0.15	0.18	0.89	0.18	0.16	0.16	0.49	0.30	0.14	0.13
Mn	571.34	535.22	596.59	866.70	573.07	609.62	592.12	611.64	561.48	439.57	312.13
Co	0.60	6.45	1.26	6.46	0.65	0.80	1.46	1.48	0.83	1.29	1.68
Ni	0.06	0.06	0.07	0.05	0.04	0.08	0.06	0.15	0.05	0.15	0.05
Cu	0.03	1.49	0.46	1.23	0.18	0.31	0.44	0.34	0.51	0.07	0.04
Zn	204.02	196.92	207.07	269.61	202.27	211.48	204.68	212.43	184.53	39.00	42.37
Ga	133.10	140.40	135.88	132.36	133.03	135.18	129.51	143.24	132.47	80.46	86.17
Rb	2760.23	2828.51	2874.60	2796.69	2772.03	2864.09	2845.99	3056.19	2748.37	1027.42	1067.35
Sr	0.04	0.18	0.04	0.15	0.06	0.05	0.06	0.02	0.08	0.69	0.62
Y	0.00	0.01	0.00	0.21	0.00	0.00	0.01	0.00	0.01	0.00	0.00
Zr	1.31	1.35	1.58	1.45	1.57	1.48	1.65	1.37	1.33	2.51	2.54
Nb	178.75	173.68	182.68	179.99	177.01	176.00	177.10	183.06	172.25	86.62	88.20
Mo	0.12	0.26	0.12	0.21	0.13	0.15	0.13	0.32	0.18	0.22	0.16
Sn	57.60	58.62	64.05	59.59	58.86	56.78	59.45	57.41	55.55	12.94	13.42
Cs	45.83	46.13	49.68	54.00	46.58	46.84	49.28	47.67	43.33	18.47	19.59
Ba	0.30	0.52	0.25	2.46	0.29	0.20	0.27	0.25	0.39	3.72	4.78
Hf	0.29	0.24	0.30	0.29	0.29	0.23	0.27	0.21	0.23	0.25	0.30
Ta	14.43	14.25	15.19	15.24	14.29	14.33	14.58	13.50	13.79	7.41	9.15
W	18.73	19.51	19.79	19.70	18.98	18.68	18.93	19.35	19.28	27.46	32.12
Pb	2.53	2.86	2.65	3.43	2.64	2.48	2.49	3.05	2.75	2.64	3.23
Th	0.0000	0.0000	0.0020	0.1520	0.0010	0.0008	0.0012	0.0012	0.0000	0.0023	0.0014
U	0.0010	0.0007	0.0040	0.0330	0.0007	0.0040	0.0020	0.0000	0.0030	0.0040	0.0020

Appendix 2.3B (continued): Detailed trace element data of micas from the Pan- African Dowa pegmatites (DHD) in central Malawi. All concentrations are given in ppm.

	DHD1C3	DHD1C4	DHD1C5	DHD1C6	DHD1C7	DHD1C8	DHD1C9	DHD1C10	DHD1E1	DHD1E2	DHD1E3
Li	366.81	351.78	412.57	399.38	394.76	384.71	357.00	377.00	72.93	75.28	72.84
Be	12.21	12.45	17.65	13.73	14.04	14.68	13.87	12.71	0.28	0.25	0.43
B	67.93	59.37	69.12	63.77	61.00	65.37	64.94	57.54	49.04	52.27	43.78
Sc	12.13	12.48	13.04	13.26	11.75	12.91	11.16	12.62	1.42	1.39	1.35
Ti	1460.80	1524.03	1573.83	1560.08	1620.91	1656.74	1571.80	1574.31	6850.73	7108.28	6986.97
V	41.63	38.34	41.81	36.74	43.73	39.88	47.11	39.33	116.79	119.25	117.04
Cr	0.13	0.13	0.32	0.14	0.29	0.16	0.12	0.34	76.64	76.90	78.24
Mn	192.67	238.76	271.74	311.58	326.28	314.16	418.13	397.88	541.98	551.99	555.37
Co	1.85	1.61	1.49	1.57	1.89	1.47	1.44	1.74	12.47	7.62	7.64
Ni	0.23	0.05	0.05	0.09	0.05	0.16	0.14	0.03	8.62	8.11	8.40
Cu	0.03	0.03	0.16	0.03	0.09	0.03	0.13	0.21	8.74	2.51	0.92
Zn	22.95	32.71	45.59	45.38	46.19	34.14	43.96	40.97	188.75	211.81	213.54
Ga	77.66	81.56	84.86	80.94	84.10	84.90	86.35	81.15	65.08	67.51	67.33
Rb	997.99	1040.61	1093.43	1024.94	1078.05	1050.80	1068.89	1027.89	538.54	544.13	544.58
Sr	0.55	0.55	0.97	0.49	0.64	0.56	0.58	0.59	9.87	0.00	9.74
Y	0.01	0.01	0.01	0.02	0.01	0.00	0.01	0.01	0.01	0.01	0.01
Zr	2.51	2.46	2.58	2.55	2.71	2.38	2.52	2.63	15.89	16.36	16.08
Nb	80.20	82.48	85.42	84.16	88.22	85.48	86.61	84.78	46.93	49.20	49.56
Mo	0.09	0.12	0.12	0.17	0.22	0.13	0.14	0.21	0.13	0.12	0.10
Sn	11.47	11.88	13.20	13.21	13.51	13.41	12.36	13.02	3.36	3.19	3.10
Cs	17.68	18.28	21.46	18.67	20.46	18.70	19.80	19.09	39.13	38.71	38.71
Ba	4.60	5.91	4.76	5.05	4.11	4.68	4.62	5.65	1371.76	1433.54	1444.55
Hf	0.28	0.29	0.26	0.24	0.32	0.18	0.27	0.33	0.30	0.34	0.26
Ta	8.38	8.24	8.93	8.13	9.01	9.13	9.27	8.81	3.02	3.28	3.24
W	34.59	35.31	35.91	33.40	33.06	34.82	36.13	35.32	0.09	0.04	0.05
Pb	3.06	3.30	3.10	2.77	3.58	3.11	3.19	3.19	3.15	3.07	2.89
Th	0.0013	0.0000	0.0010	0.0000	0.0020	0.0012	0.0020	0.0014	0.0006	0.0020	0.0009
U	0.0040	0.0050	0.0130	0.0110	0.0010	0.0030	0.0070	0.0030	0.1350	0.1250	0.1400

Appendix 2.3B (continued): Detailed trace element data of micas from the Pan- African Dowa pegmatites (DHD) in central Malawi. All concentrations are given in ppm.

	DHD1E4	DHD1E5	DHD1E6	DHD1E7	DHD1E8	DHD1E9	DHD1E10
Li	75.66	71.13	73.39	69.74	70.06	73.33	73.82
Be	0.09	0.32	0.25	0.30	0.29	0.23	0.25
B	41.94	48.02	51.60	48.59	50.54	48.95	41.94
Sc	1.54	1.51	1.33	1.28	1.32	1.46	1.42
Ti	7453.40	7415.70	6949.75	6843.94	6670.70	7019.58	7282.53
V	120.56	120.98	117.61	115.27	110.96	118.42	120.96
Cr	81.33	79.11	78.38	76.02	76.76	77.40	81.61
Mn	568.49	565.94	556.10	541.67	532.62	547.09	577.84
Co	8.69	13.51	8.40	8.72	7.94	34.94	8.02
Ni	8.78	9.09	8.06	8.20	8.35	7.95	8.71
Cu	2.60	1.99	3.41	1.38	1.53	2.15	1.99
Zn	200.93	189.14	202.94	206.65	199.32	160.42	203.94
Ga	64.11	60.66	62.91	66.14	64.79	64.84	61.28
Rb	560.07	552.99	544.57	526.03	522.07	535.76	563.23
Sr	10.45	10.08	9.89	8.54	9.00	10.15	9.93
Y	0.02	0.03	0.01	0.02	0.01	0.01	0.01
Zr	17.12	16.74	16.40	14.61	15.43	16.91	17.07
Nb	51.19	50.28	50.57	48.08	49.63	47.61	52.19
Mo	0.10	0.09	0.08	0.12	0.09	0.12	0.05
Sn	3.26	3.22	3.18	3.03	2.94	3.81	3.14
Cs	40.00	40.90	38.91	37.40	37.41	39.37	39.57
Ba	1506.68	1464.00	1424.11	1387.01	1367.64	1350.41	1471.54
Hf	0.36	0.28	0.28	0.29	0.27	0.30	0.31
Ta	3.45	3.26	3.24	3.14	3.26	3.14	3.30
W	0.03	0.05	0.05	0.03	0.05	0.03	0.04
Pb	3.13	3.10	2.96	2.82	2.78	3.06	2.94
Th	0.0010	0.0030	0.0030	0.0012	0.0020	0.0020	0.0180
U	0.1030	0.1160	0.1270	0.1220	0.1430	0.1260	0.1290

Appendix 2.3C: Detailed UCC-normalised (Taylor and McLennan, 1995) rare earth element (REE) data of micas from the Pan-African tourmaline-bearing pegmatites (DHD) in Dowa central Malawi. All concentrations are given in ppm.

Element	DHD1A1	DHD1A2	DHD1A3	DHD1A4	DHD1A5	DHD1A6	DHD1A7	DHD1A8	DHD1A9	DHD1A10
La	0.0960	0.0660	0.0600	0.0960	0.0600	0.0450	0.0600	0.0390	0.0900	0.0183
Ce	0.0000	0.0000	0.0755	0.1408	0.1216	0.0390	0.0826	0.0000	0.0352	0.0710
Pr	0.0000	0.0080	0.0000	0.0070	0.0000	0.0000	0.0000	0.0000	0.0106	0.0000
Nd	0.2834	0.4940	0.2236	0.1508	0.0000	0.2262	0.0000	0.1456	0.1976	0.0000
Sm	0.0000	0.0000	0.0419	0.0000	0.0554	0.0302	0.0000	0.0000	0.0410	0.0140
Eu	0.0092	0.0013	0.1989	0.1778	0.2605	0.2103	0.1954	0.1839	0.2367	0.1769
Gd	0.0422	0.0000	0.0000	0.0224	0.0281	0.0338	0.0000	0.0365	0.0198	0.0448
Tb	0.0000	0.0005	0.0017	0.0012	0.0015	0.0000	0.0000	0.0008	0.0013	0.0008
Dy	0.0154	0.0106	0.0214	0.0186	0.0126	0.0242	0.0000	0.0221	0.0200	0.0000
Ho	0.0009	0.0008	0.0022	0.0000	0.0013	0.0000	0.0000	0.0006	0.0007	0.0000
Er	0.0000	0.0000	0.0057	0.0000	0.0131	0.0000	0.0044	0.0000	0.0025	0.0000
Tm	0.0003	0.0000	0.0000	0.0010	0.0003	0.0004	0.0012	0.0009	0.0005	0.0009
Yb	0.0726	0.0227	0.0396	0.0805	0.0917	0.0264	0.0858	0.0858	0.0691	0.0444
Lu	0.0026	0.0031	0.0049	0.0037	0.0066	0.0028	0.0038	0.0023	0.0031	0.0030

Appendix 2.3C: (continued) Detailed UCC-normalised (Taylor and McLennan, 1995) rare earth element (REE) data of micas from the Pan-African tourmaline-bearing pegmatites (DHD) in Dowa central Malawi. All concentrations are given in ppm.

Element	DHD1B1	DHD1B2	DHD1B3	DHD1B4	DHD1B5	DHD1B6	DHD1B7	DHD1B8	DHD1B9	DHD1B10
La	0.5280	0.0480	0.1080	0.0990	9.3600	0.0609	0.0000	0.9570	0.0000	0.0000
Ce	1.0112	0.0666	0.0000	1.1968	17.5360	0.1920	0.0717	0.0000	1.7280	0.1664
Pr	0.0099	0.0000	0.0000	0.0000	0.6127	0.0000	0.0000	0.0000	0.0000	0.0120
Nd	0.0000	0.1768	0.0000	0.0000	10.8680	0.0000	0.1352	0.0000	0.5460	0.2548
Sm	0.0252	0.0446	0.0000	0.0284	0.3825	0.0266	0.0392	0.0554	0.0000	0.0266
Eu	0.0013	0.0000	0.0000	0.0025	0.0112	0.0015	0.0000	0.0020	0.0117	0.0014
Gd	0.0308	0.0000	0.1178	0.0000	0.1292	0.0266	0.0441	0.0000	0.0000	0.0000
Tb	0.0000	0.0000	0.0010	0.0000	0.0044	0.0005	0.0000	0.0000	0.0005	0.0005
Dy	0.0000	0.0000	0.0161	0.0000	0.0550	0.0245	0.0228	0.0525	0.0000	0.0000
Ho	0.0000	0.0008	0.0000	0.0015	0.0062	0.0009	0.0009	0.0013	0.0007	0.0009
Er	0.0000	0.0000	0.0052	0.0092	0.0439	0.0028	0.0052	0.0052	0.0076	0.0000
Tm	0.0004	0.0000	0.0003	0.0004	0.0007	0.0000	0.0000	0.0000	0.0004	0.0000
Yb	0.0000	0.0000	0.0000	0.0081	0.0594	0.0077	0.0084	0.0000	0.0081	0.0075
Lu	0.0003	0.0000	0.0003	0.0002	0.0009	0.0003	0.0000	0.0000	0.0004	0.0003

Appendix 2.3C: (continued) Detailed UCC-normalised (Taylor and McLennan, 1995) rare earth element (REE) data of micas from the Pan-African tourmaline-bearing pegmatites (DHD) in Dowa central Malawi. All concentrations are given in ppm.

Element	DHD1C1	DHD1C2	DHD1C3	DHD1C4	DHD1C5	DHD1C6	DHD1C7	DHD1C8	DHD1C9	DHD1C10
La	0.0000	0.0000	0.0336	0.0336	0.0591	0.0351	0.0000	0.0000	0.0000	0.0000
Ce	0.1018	0.0000	0.0000	0.0915	0.2176	0.0000	0.0000	0.0973	0.8512	0.0922
Pr	0.0000	0.0060	0.0000	0.0000	0.0000	0.0060	0.0121	0.0000	0.0086	0.0107
Nd	0.0000	0.0000	0.1742	0.0000	0.1248	0.1274	0.1300	0.1300	0.1300	0.0000
Sm	0.0000	0.0540	0.0000	0.0000	0.0261	0.0000	0.0387	0.0000	0.0000	0.0000
Eu	0.0045	0.0000	0.0000	0.0000	0.0000	0.0193	0.0064	0.0030	0.0053	0.0013
Gd	0.0448	0.0190	0.0255	0.0255	0.0258	0.0000	0.0000	0.0270	0.0000	0.0258
Tb	0.0007	0.0000	0.0005	0.0000	0.0000	0.0007	0.0000	0.0000	0.0000	0.0005
Dy	0.0000	0.0000	0.0000	0.0000	0.0186	0.0371	0.0000	0.0193	0.0000	0.0151
Ho	0.0000	0.0000	0.0000	0.0000	0.0012	0.0000	0.0000	0.0000	0.0000	0.0000
Er	0.0000	0.0000	0.0299	0.0085	0.0049	0.0000	0.0073	0.0127	0.0000	0.0000
Tm	0.0000	0.0000	0.0000	0.0000	0.0005	0.0003	0.0000	0.0011	0.0000	0.0006
Yb	0.0484	0.0748	0.1144	0.1056	0.0000	0.0572	0.0506	0.0000	0.0330	0.0000
Lu	0.0005	0.0033	0.0069	0.0092	0.0017	0.0036	0.0032	0.0071	0.0034	0.0022

Appendix 2.3C: (continued) Detailed UCC-normalised (Taylor and McLennan, 1995) rare earth element (REE) data of micas from the Pan-African tourmaline-bearing pegmatites (DHD) in Dowa central Malawi. All concentrations are given in ppm.

Element	DHD1E1	DHD1E2	DHD1E3	DHD1E4	DHD1E5	DHD1E6	DHD1E7	DHD1E8	DHD1E9	DHD1E10
La	0.1140	0.3750	0.1590	1.3500	1.4040	0.1590	0.4020	0.8580	0.9120	0.2280
Ce	0.0710	0.4416	0.0224	1.1072	3.8528	0.2432	0.1728	2.4000	0.1856	0.0538
Pr	0.0157	0.0187	0.0045	0.0469	0.0270	0.0015	0.0064	0.0348	0.0053	0.0067
Nd	0.1898	0.4056	0.1690	0.6838	0.8320	0.0650	0.1352	0.4082	0.5616	0.0676
Sm	0.0000	0.0167	0.0086	0.0000	0.0405	0.0068	0.0279	0.0212	0.0410	0.0140
Eu	0.0099	0.0121	0.0171	0.0247	0.0215	0.0118	0.0208	0.0189	0.0142	0.0157
Gd	0.0057	0.0304	0.0061	0.0251	0.0205	0.0201	0.0141	0.0410	0.0251	0.0304
Tb	0.0005	0.0000	0.0003	0.0010	0.0008	0.0007	0.0006	0.0003	0.0000	0.0000
Dy	0.0000	0.0070	0.0084	0.0119	0.0119	0.0088	0.0144	0.0081	0.0298	0.0126
Ho	0.0009	0.0008	0.0007	0.0007	0.0007	0.0003	0.0005	0.0005	0.0006	0.0003
Er	0.0037	0.0000	0.0000	0.0041	0.0030	0.0051	0.0000	0.0027	0.0045	0.0041
Tm	0.0004	0.0001	0.0003	0.0005	0.0000	0.0002	0.0001	0.0002	0.0003	0.0002
Yb	0.0090	0.0063	0.0163	0.0205	0.0088	0.0194	0.0040	0.0205	0.0000	0.0183
Lu	0.0002	0.0007	0.0009	0.0012	0.0006	0.0007	0.0004	0.0006	0.0000	0.0003

Appendix 2.3D: Detailed chondrite-normalised (Nakamura, 1974) rare earth element (REE) data of micas from the Pan-African tourmaline-bearing pegmatites (DHD) in Dowa central Malawi. All concentrations are given in ppm.

Element	DHD1B10	DHD1A1	DHD1A2	DHD1A3	DHD1A4	DHD1A5	DHD1A6	DHD1A7	DHD1A8	DHD1A9	DHD1A10
La	0.0000	0.0134	0.0094	0.0086	0.0135	0.0084	0.0000	0.0084	0.0000	0.0127	0.0026
Ce	0.0042	0.0000	0.0000	0.0000	0.0000	0.0032	0.0010	0.0000	0.0000	0.0009	0.0018
Pr	0.0000	0.0000	0.0000	0.0000	0.0000	0.0000	0.0000	0.0000	0.0000	0.0000	0.0000
Nd	0.0000	0.0000	0.0410	0.0190	0.0000	0.0000	0.0000	0.0000	0.0000	0.0167	0.0000
Sm	0.0000	0.0000	0.0000	0.0000	0.0000	0.0000	0.0450	0.0000	0.0000	0.0620	0.0210
Eu	0.0000	0.1850	0.0000	4.0200	3.6000	5.2500	4.2400	3.9400	3.7100	4.7800	3.5700
Gd	0.0000	0.0000	0.0000	0.0000	0.0000	0.0000	0.0000	0.0000	0.0480	0.0260	0.0000
Tb	0.0000	0.0000	0.0000	0.0750	0.0000	0.0000	0.0000	0.0000	0.0340	0.0000	0.0000
Dy	0.0000	0.0000	0.0000	0.0000	0.0000	0.0150	0.0000	0.0000	0.0000	0.0000	0.0000
Ho	0.0000	0.0000	0.0000	0.0510	0.0000	0.0000	0.0000	0.0000	0.0140	0.0150	0.0000
Er	0.0000	0.0000	0.0000	0.0000	0.0000	0.0000	0.0000	0.0120	0.0000	0.0072	0.0000
Tm	0.0000	0.0000	0.0000	0.0000	0.1220	0.0330	0.0000	0.1510	0.1130	0.0610	0.1080
Yb	0.0000	0.2060	0.0640	0.1140	0.2270	0.2590	0.0750	0.2430	0.2440	0.1950	0.1260
Lu	0.0000	0.3300	0.3900	0.6200	0.4700	0.8400	0.3610	0.4800	0.2870	0.3990	0.3780

Appendix 2.3D: (continued) Detailed chondrite-normalised (Nakamura, 1974) rare earth element (REE) data of micas from the Pan-African tourmaline-bearing pegmatites (DHD) in Dowa central Malawi. All concentrations are given in ppm.

Element	DHD1B1	DHD1B2	DHD1B3	DHD1B4	DHD1B5	DHD1B6	DHD1B7	DHD1B8	DHD1B9	DHD1B10
La	0.0740	0.0000	0.0150	0.0140	1.3160	0.0000	0.0000	0.1340	0.0000	0.0000
Ce	0.0260	0.0000	0.0000	0.0000	0.4470	0.0000	0.0000	0.0000	0.0450	0.0042
Pr	0.0000	0.0000	0.0000	0.0000	0.9270	0.0000	0.0000	0.0000	0.0000	0.0000
Nd	0.0000	0.0000	0.0000	0.0000	0.9150	0.0000	0.0000	0.0000	0.0460	0.0000
Sm	0.0000	0.0000	0.0000	0.0000	0.5800	0.0000	0.0000	0.0000	0.0000	0.0000
Eu	0.0000	0.0000	0.0000	0.0000	0.2250	0.0300	0.0000	0.0000	0.2400	0.0000
Gd	0.0000	0.0000	0.1600	0.0000	0.1720	0.0000	0.0000	0.0000	0.0000	0.0000
Tb	0.0000	0.0000	0.0000	0.0000	0.1870	0.0000	0.0000	0.0000	0.0000	0.0000
Dy	0.0000	0.0000	0.0000	0.0000	0.0640	0.0000	0.0000	0.0630	0.0000	0.0000
Ho	0.0000	0.0000	0.0000	0.0000	0.1420	0.0000	0.0000	0.0000	0.0000	0.0000
Er	0.0000	0.0000	0.0000	0.0000	0.1190	0.0074	0.0000	0.0000	0.0000	0.0000
Tm	0.0000	0.0000	0.0000	0.0000	0.0900	0.0000	0.0000	0.0000	0.0000	0.0000
Yb	0.0000	0.0000	0.0000	0.0000	0.1680	0.0000	0.0230	0.0000	0.0000	0.0000
Lu	0.0000	0.0000	0.0000	0.0000	0.1110	0.0320	0.0000	0.0000	0.0000	0.0000

Appendix 2.3D: (continued) Detailed chondrite-normalised (Nakamura, 1974) rare earth element (REE) data of micas from the Pan-African tourmaline-bearing pegmatites (DHD) in Dowa central Malawi. All concentrations are given in ppm.

Element	DHD1C1	DHD1C2	DHD1C3	DHD1C4	DHD1C5	DHD1C6	DHD1C7	DHD1C8	DHD1C9	DHD1C10
La	0.0000	0.0000	0.0000	0.0000	0.0000	0.0000	0.0000	0.0000	0.0000	0.0000
Ce	0.0000	0.0000	0.0000	0.0000	0.0000	0.0000	0.0000	0.0000	0.0000	0.0000
Pr	0.0000	0.0000	0.0000	0.0000	0.0000	0.0000	0.0000	0.0000	0.0000	0.0160
Nd	0.0000	0.0000	0.0000	0.0000	0.0000	0.0000	0.0000	0.0000	0.0000	0.0000
Sm	0.0000	0.0000	0.0000	0.0000	0.0000	0.0000	0.0000	0.0000	0.0000	0.0000
Eu	0.0910	0.0000	0.0000	0.0000	0.0000	0.3900	0.1300	0.0610	0.1070	0.0000
Gd	0.0000	0.0000	0.0000	0.0000	0.0000	0.0000	0.0000	0.0000	0.0000	0.0000
Tb	0.0000	0.0000	0.0000	0.0000	0.0000	0.0000	0.0000	0.0000	0.0000	0.0000
Dy	0.0000	0.0000	0.0000	0.0000	0.0000	0.0430	0.0000	0.0000	0.0000	0.0000
Ho	0.0000	0.0000	0.0000	0.0000	0.0000	0.0000	0.0000	0.0000	0.0000	0.0000
Er	0.0000	0.0000	0.0810	0.0230	0.0000	0.0000	0.0000	0.0340	0.0000	0.0000
Tm	0.0000	0.0000	0.0000	0.0000	0.0580	0.0000	0.0000	0.1300	0.0000	0.0000
Yb	0.1400	0.2100	0.3200	0.3000	0.0000	0.1610	0.1430	0.0000	0.0910	0.0000
Lu	0.0000	0.4100	0.8800	1.1700	0.2200	0.4600	0.4000	0.9000	0.4300	0.2800

Appendix 2.3D: (continued) Detailed chondrite-normalised (Nakamura, 1974) rare earth element (REE) data of micas from the Pan-African tourmaline-bearing pegmatites (DHD) in Dowa central Malawi. All concentrations are given in ppm.

Element	DHD1E1	DHD1E2	DHD1E3	DHD1E4	DHD1E5	DHD1E6	DHD1E7	DHD1E8	DHD1E9	DHD1E10
La	0.0158	0.0527	0.0224	0.1900	0.1970	0.0223	0.0564	0.1210	0.1280	0.0322
Ce	0	0.0113	0.0006	0.0282	0.0980	0.0062	0.0043	0.0611	0.0047	0.0014
Pr	0.0238	0.0284	0.0000	0.0710	0.0410	0.0023	0.0096	0.0520	0.0080	0.0000
Nd	0	0.034	0.0000	0.0580	0.0700	0.0055	0.0000	0.0340	0.0470	0.0057
Sm	0	0.025	0.0130	0.0000	0.0000	0.0100	0.0000	0.0320	0.0000	0.0210
Eu	0.202	0.246	0.3450	0.4990	0.4340	0.2390	0.4190	0.3820	0.2860	0.3150
Gd	0.0073	0	0.0081	0.0330	0.0000	0.0000	0.0000	0.0540	0.0330	0.0000
Tb	0	0	0.0141	0.0430	0.0000	0.0000	0.0270	0.0114	0.0000	0.0000
Dy	0	0.0081	0.0000	0.0140	0.0000	0.0100	0.0000	0.0000	0.0350	0.0000
Ho	0	0.019	0.0000	0.0000	0.0000	0.0072	0.0000	0.0000	0.0000	0.0075
Er	0	0	0.0000	0.0000	0.0079	0.0139	0.0000	0.0073	0.0000	0.0000
Tm	0.051	0.018	0.0000	0.0580	0.0000	0.0220	0.0074	0.0230	0.0000	0.0230
Yb	0.026	0	0.0460	0.0580	0.0250	0.0550	0.0111	0.0570	0.0000	0.0510
Lu	0	0.086	0.1110	0.1520	0.0830	0.0920	0.0000	0.0730	0.0000	0.0320

Appendix 2.4A: Detailed major element data of micas from tourmaline-bearing and sunstone-bearing pegmatites (GNS, MSN) from Ntcheu and amethyst-bearing pegmatites (CUB) from Balaka.

	GNS1_1	GNS1_2	GNS1_3	GNS1_4	GNS1_5	GNS1_6	GNS1_7	GNS1_8	GNS1_9	GNS1_10	GNS3_1
SiO_2	46.16	46.44	46.10	46.05	45.77	45.23	46.52	46.45	45.99	46.15	46.08
TiO_2	0.07	0.05	0.08	0.10	0.09	0.18	0.16	0.19	0.18	0.05	0.07
Al_2O_3	31.94	31.80	32.11	32.11	31.59	32.68	33.32	33.48	33.44	33.17	35.06
FeO	3.02	3.36	3.33	3.49	3.23	2.41	3.06	2.98	2.74	2.51	1.83
MnO	0.05	0.03	0.00	0.00	0.06	0.07	0.07	0.03	0.10	0.05	0.08
MgO	0.91	0.91	0.89	0.94	0.88	0.40	0.45	0.42	0.37	0.63	0.37
CaO	0.00	0.00	0.01	0.01	0.00	0.01	0.00	0.01	0.03	0.00	0.00
Na_2O	0.28	0.63	0.54	0.49	0.54	0.62	0.37	0.69	0.47	0.43	0.32
K_2O	12.47	12.56	12.55	11.93	12.75	13.05	12.74	13.10	13.02	13.41	13.14
F	0.14	0.00	0.00	0.00	0.14	0.01	0.00	0.08	0.00	0.12	0.19
Cl	0.01	0.00	0.01	0.00	0.01	0.01	0.00	0.00	0.01	0.00	0.01
Cr_2O_3	0.00	0.00	0.00	0.02	0.00	0.00	0.00	0.01	0.01	0.00	0.00
H_2O*	4.32	4.41	4.41	4.40	4.30	4.36	4.47	4.46	4.44	4.39	4.42
Subtotal	99.36	100.19	100.01	99.53	99.35	99.03	101.17	101.89	100.80	100.89	101.58
O=F,Cl	0.06	0.00	0.00	0.00	0.06	0.01	0.00	0.03	0.00	0.05	0.08
Total	99.30	100.19	100.01	99.53	99.29	99.02	101.17	101.86	100.80	100.84	101.49
Si	6.31	6.31	6.27	6.28	6.28	6.21	6.24	6.19	6.20	6.23	6.12
Al^{iv}	1.69	1.69	1.73	1.73	1.72	1.79	1.76	1.81	1.80	1.77	1.88
Al^{vi}	3.45	3.40	3.42	3.43	3.40	3.51	3.51	3.50	3.52	3.50	3.60
Ti	0.01	0.01	0.01	0.01	0.01	0.02	0.02	0.02	0.02	0.01	0.01
Cr	0.00	0.00	0.00	0.00	0.00	0.00	0.00	0.00	0.00	0.00	0.00
Fe	0.35	0.38	0.38	0.40	0.37	0.28	0.34	0.33	0.31	0.28	0.20
Mn	0.01	0.00	0.00	0.00	0.01	0.01	0.01	0.00	0.01	0.01	0.01
Mg	0.19	0.18	0.18	0.19	0.18	0.08	0.09	0.08	0.08	0.13	0.07
Ca	0.00	0.00	0.00	0.00	0.00	0.00	0.00	0.00	0.00	0.00	0.00
Na	0.07	0.17	0.14	0.13	0.14	0.17	0.10	0.18	0.12	0.11	0.08
K	2.17	2.18	2.18	2.07	2.23	2.29	2.18	2.23	2.24	2.31	2.39
OH*	3.94	4.00	4.00	4.00	3.94	3.99	4.00	3.97	4.00	3.95	3.92
F	0.06	0.00	0.00	0.00	0.06	0.01	0.00	0.03	0.00	0.05	0.08
Cl	0.00	0.00	0.00	0.00	0.00	0.00	0.00	0.00	0.00	0.00	0.00
TOTAL	18.24	18.31	18.31	18.24	18.34	18.35	18.25	18.34	18.30	18.34	18.37
Y total	3.99	3.97	3.99	4.03	3.96	3.89	3.97	3.93	3.94	3.92	3.89
X total	2.25	2.34	2.32	2.20	2.38	2.45	2.28	2.41	2.37	2.42	2.48
Al total	5.14	5.09	5.15	5.16	5.11	5.29	5.27	5.31	5.32	5.28	5.49

* Calculated

Appendix 2.4A (continued**):** Detailed major element data of micas from tourmaline-bearing and sunstone-bearing pegmatites (GNS, MSN) from Ntcheu and amethyst-bearing pegmatites (CUB) from Balaka.

	GNS3_2	GNS3_3	GNS3_4	GNS3_5	GNS3_6	GNS3_7	GNS3_8	GNS3_9	GNS3_10	GNS6_1	GNS6_2
SiO_2	46.63	46.51	46.63	46.22	45.86	46.29	46.81	45.91	46.62	46.79	46.72
TiO_2	0.03	0.07	0.07	0.07	0.04	0.08	0.08	0.04	0.07	0.07	0.04
Al_2O_3	34.27	34.84	35.24	34.62	34.43	34.58	34.11	34.74	33.48	32.72	32.88
FeO	2.22	1.82	1.67	2.28	1.79	1.97	1.93	2.10	2.29	2.94	3.82
MnO	0.17	0.00	0.05	0.03	0.02	0.00	0.19	0.09	0.14	0.00	0.10
MgO	0.35	0.33	0.36	0.35	0.33	0.38	0.51	0.28	0.64	0.73	0.83
CaO	0.00	0.00	0.00	0.05	0.04	0.00	0.02	0.03	0.00	0.00	0.00
Na_2O	0.37	0.59	0.51	0.08	0.18	0.51	0.44	0.58	0.33	0.64	0.64
K_2O	13.31	12.61	12.81	11.54	11.77	13.56	12.92	13.05	13.68	12.40	11.54
F	0.03	0.00	0.11	0.00	0.00	0.01	0.03	0.04	0.15	0.00	0.10
Cl	0.00	0.00	0.00	0.00	0.03	0.00	0.00	0.00	0.00	0.00	0.01
Cr_2O_3	0.00	0.02	0.03	0.02	0.00	0.01	0.00	0.00	0.00	0.00	0.01
H_2O*	4.55	4.55	4.48	4.46	4.42	4.52	4.51	4.50	4.41	4.46	4.42
Subtotal	101.93	101.33	101.95	99.72	98.91	101.90	101.54	101.64	101.83	100.75	101.12
O=F,Cl	0.01	0.00	0.05	0.00	0.01	0.00	0.01	0.02	0.07	0.00	0.04
Total	101.92	101.33	101.91	99.72	98.90	101.89	101.52	101.34	101.77	100.75	101.07
Si	6.13	6.13	6.17	6.21	6.21	6.15	6.21	6.10	6.23	6.29	6.26
Al ^{iv}	1.87	1.87	1.83	1.79	1.79	1.86	1.79	1.90	1.77	1.71	1.74
Al ^{vi}	3.56	3.56	3.66	3.69	3.71	3.60	3.54	3.58	3.51	3.48	3.46
Ti	0.00	0.01	0.01	0.01	0.00	0.01	0.01	0.00	0.01	0.01	0.00
Cr	0.00	0.00	0.00	0.00	0.00	0.00	0.00	0.00	0.00	0.00	0.00
Fe	0.24	0.20	0.19	0.26	0.20	0.22	0.21	0.23	0.26	0.33	0.43
Mn	0.02	0.00	0.01	0.00	0.00	0.00	0.02	0.01	0.02	0.00	0.01
Mg	0.07	0.06	0.07	0.07	0.07	0.08	0.10	0.06	0.13	0.15	0.17
Ca	0.00	0.00	0.00	0.01	0.01	0.00	0.00	0.00	0.00	0.00	0.00
Na	0.09	0.15	0.13	0.02	0.05	0.13	0.11	0.15	0.09	0.17	0.17
K	2.43	2.46	2.16	1.98	2.03	2.30	2.35	2.38	2.33	2.13	1.97
OH*	3.99	4.00	3.95	4.00	3.99	4.00	3.99	3.98	3.94	4.00	3.96
F	0.01	0.00	0.05	0.00	0.00	0.00	0.01	0.02	0.07	0.00	0.04
Cl	0.00	0.00	0.00	0.00	0.01	0.00	0.00	0.00	0.00	0.00	0.00
TOTAL	18.42	18.45	18.22	18.04	18.07	18.33	18.35	18.42	18.33	18.26	18.21
Y total	3.89	3.84	3.93	4.03	3.99	3.91	3.88	3.89	3.91	3.96	4.07
X total	2.53	2.61	2.29	2.01	2.09	2.43	2.47	2.53	2.42	2.29	2.14
Al total	5.43	5.43	5.49	5.48	5.50	5.46	5.33	5.49	5.28	5.19	5.20

* Calculated

Appendix 2.4A (continued**):** Detailed major element data of micas from tourmaline-bearing and sunstone-bearing pegmatites (GNS, MSN) from Ntcheu and amethyst-bearing pegmatites (CUB) from Balaka.

	GNS6_3	GNS6_4	GNS6_5	GNS6_6	GNS6_7	GNS6_8	GNS6_9	GNS6_10	GNS7_1	GNS7_2	GNS7_3
SiO_2	45.92	47.10	46.46	45.97	46.95	46.83	46.64	46.46	46.51	46.43	44.93
TiO_2	0.08	0.08	0.01	0.00	0.00	0.08	0.03	0.00	0.16	0.20	0.13
Al_2O_3	32.28	32.61	32.69	32.05	32.93	32.99	32.90	33.02	31.68	31.27	31.23
FeO	3.84	3.31	4.01	3.12	3.33	3.47	3.57	3.01	4.30	4.07	3.92
MnO	0.10	0.12	0.10	0.11	0.06	0.10	0.00	0.00	0.10	0.05	0.00
MgO	0.81	0.79	0.78	0.77	0.79	0.81	0.66	0.75	0.98	1.09	0.94
CaO	0.01	0.01	0.00	0.00	0.01	0.02	0.01	0.05	0.00	0.02	0.02
Na_2O	0.42	0.45	0.58	0.52	0.57	0.23	0.51	0.42	0.49	0.51	0.37
K_2O	11.77	12.21	12.14	12.62	12.01	12.73	13.09	12.68	13.02	13.14	13.96
F	0.05	0.00	0.03	0.12	0.12	0.17	0.11	0.09	0.07	0.06	0.15
Cl	0.03	0.01	0.00	0.00	0.03	0.01	0.00	0.00	0.00	0.00	0.00
Cr_2O_3	0.00	0.01	0.00	0.00	0.00	0.00	0.01	0.01	0.04	0.00	0.00
H_2O*	4.37	4.47	4.44	4.33	4.42	4.41	4.43	4.42	4.42	4.40	4.27
Subtotal	99.68	101.17	101.25	99.61	101.21	101.94	101.95	100.91	101.76	101.22	99.91
O=F,Cl	0.03	0.00	0.01	0.05	0.06	0.08	0.05	0.04	0.03	0.03	0.06
Total	99.65	101.17	101.23	99.56	101.15	101.19	101.91	100.87	101.73	101.20	99.85
Si	6.26	6.31	6.25	6.28	6.29	6.25	6.24	6.25	6.26	6.29	6.21
Al ^{iv}	1.74	1.69	1.75	1.72	1.72	1.75	1.76	1.75	1.74	1.71	1.79
Al ^{vi}	3.44	3.46	3.43	3.44	3.48	3.43	3.44	3.49	3.29	3.28	3.29
Ti	0.01	0.01	0.00	0.00	0.00	0.01	0.00	0.00	0.02	0.02	0.01
Cr	0.00	0.00	0.00	0.00	0.00	0.00	0.00	0.00	0.00	0.00	0.00
Fe	0.44	0.37	0.45	0.36	0.37	0.42	0.40	0.34	0.50	0.46	0.45
Mn	0.01	0.01	0.01	0.01	0.01	0.01	0.00	0.00	0.01	0.01	0.00
Mg	0.16	0.16	0.16	0.16	0.16	0.16	0.13	0.15	0.20	0.22	0.19
Ca	0.00	0.00	0.00	0.00	0.00	0.00	0.00	0.01	0.00	0.00	0.00
Na	0.11	0.12	0.15	0.14	0.15	0.06	0.13	0.11	0.13	0.13	0.10
K	2.05	2.09	2.08	2.20	2.05	2.18	2.24	2.18	2.27	2.27	2.46
OH*	3.97	4.00									
F	0.02	0.00	3.99	3.95	3.94	3.93	3.95	3.96	3.97	3.97	3.94
Cl	0.01	0.00	0.01	0.05	0.05	0.07	0.05	0.04	0.03	0.03	0.06
			0.00	0.00	0.01	0.00	0.00	0.00	0.00	0.00	0.00
TOTAL	18.22	18.21									
			18.28	18.31	18.22	18.27	18.34	18.27	18.41	18.40	18.52
Y total	4.06	4.01									
X total	2.16	2.20	4.05	3.97	4.02	4.03	3.97	3.98	4.01	3.99	3.95
Al total	5.18	5.15	2.23	2.34	2.20	2.25	2.37	2.29	2.40	2.41	2.56
			5.18	5.16	5.20	5.19	5.19	5.24	5.03	4.99	5.09

* Calculated

Appendix 2.4A (continued**):** Detailed major element data of micas from tourmaline-bearing and sunstone-bearing pegmatites (GNS, MSN) from Ntcheu and amethyst-bearing pegmatites (CUB) from Balaka.

	GNS7_4	GNS7_5	GNS7_6	GNS7_7	GNS7_8	GNS7_9	GNS7_10
SiO_2	46.09	46.06	46.35	45.21	46.23	46.34	46.24
TiO_2	0.23	0.23	0.14	0.22	0.22	0.13	0.23
Al_2O_3	31.81	31.14	32.12	31.81	32.20	31.64	31.50
FeO	3.85	3.95	3.59	3.88	3.65	3.45	3.79
MnO	0.10	0.00	0.00	0.02	0.00	0.00	0.02
MgO	1.07	1.07	1.02	0.73	0.96	1.03	0.89
CaO	0.00	0.00	0.01	0.04	0.00	0.02	0.08
Na_2O	0.50	0.34	0.57	0.49	0.33	0.26	0.38
K_2O	13.56	13.30	13.14	13.08	13.13	13.15	12.72
F	0.14	0.09	0.00	0.03	0.00	0.00	0.01
Cl	0.00	0.00	0.00	0.03	0.00	0.00	0.00
Cr_2O_3	0.00	0.00	0.00	0.00	0.00	0.00	0.00
H_2O*	4.43	4.35	4.45	4.35	4.44	4.41	4.48
Subtotal	101.77	100.53	101.38	99.86	101.15	100.43	100.32
O=F,Cl	0.06	0.04	0.00	0.02	0.00	0.00	0.01
Total	101.72	100.49	101.38	99.85	101.15	100.43	100.32
Si	6.28	6.29	6.25	6.21	6.24	6.30	6.25
Al ^{iv}	1.72	1.72	1.75	1.79	1.76	1.70	1.75
Al ^{vi}	3.30	3.29	3.36	3.36	3.37	3.37	3.37
Ti	0.02	0.02	0.01	0.02	0.02	0.01	0.02
Cr	0.00	0.00	0.00	0.00	0.00	0.00	0.00
Fe	0.43	0.45	0.41	0.45	0.41	0.39	0.45
Mn	0.01	0.00	0.00	0.00	0.00	0.00	0.00
Mg	0.21	0.22	0.20	0.15	0.19	0.21	0.18
Ca	0.00	0.00	0.00	0.01	0.00	0.00	0.01
Na	0.13	0.09	0.15	0.13	0.09	0.07	0.10
K	2.31	2.31	2.26	2.29	2.26	2.28	2.17
OH*	3.94	3.96	4.00	3.98	4.00	4.00	4.00
F	0.06	0.04	0.00	0.01	0.00	0.00	0.01
Cl	0.00	0.00	0.00	0.01	0.00	0.00	0.00
TOTAL	18.41	18.39	18.39	18.41	18.34	18.33	18.30
Y total	3.97	3.99	3.98	3.98	4.00	3.98	4.02
X total	2.44	2.41	2.41	2.43	2.35	2.35	2.28
Al total	5.02	5.01	5.11	5.15	5.13	5.07	5.12

* Calculated.

Appendix 2.4A (continued**):** Detailed major element data of micas from tourmaline-bearing and sunstone-bearing pegmatites (GNS, MSN) from Ntcheu and amethyst-bearing pegmatites (CUB) from Balaka.

	MSN1B_1	MSN1B_2	MSN1B_3	MSN1B_4	MSN1B_5	MSN1B_6	MSN1B_7	MSN1B_8	MSN1B_9	MSN1B_10	MSN3A_1
SiO_2	46.59	46.50	46.48	46.62	46.34	46.13	46.56	46.32	46.12	46.90	46.17
TiO_2	0.03	0.04	0.09	0.03	0.05	0.07	0.02	0.02	0.00	0.07	0.06
Al_2O_3	33.03	33.26	33.23	32.85	33.03	33.14	33.04	33.05	32.63	32.63	34.34
FeO	3.72	3.14	3.79	3.76	3.36	3.37	3.30	3.32	2.89	3.77	2.38
MnO	0.02	0.19	0.13	0.05	0.01	0.08	0.12	0.07	0.08	0.15	0.08
MgO	0.83	0.80	0.82	0.80	0.88	0.79	0.75	0.77	0.64	0.81	0.54
CaO	0.06	0.00	0.03	0.00	0.00	0.00	0.00	0.01	0.00	0.00	0.01
Na_2O	0.33	0.59	0.35	0.48	0.36	0.48	0.43	0.50	0.46	0.32	0.46
K_2O	12.65	12.60	12.47	12.44	12.68	12.80	12.46	12.68	13.89	12.16	12.91
F	0.00	0.11	0.08	0.08	0.06	0.01	0.08	0.04	0.04	0.00	0.09
Cl	0.00	0.00	0.00	0.00	0.03	0.00	0.00	0.02	0.00	0.03	0.01
Cr_2O_3	0.05	0.00	0.00	0.02	0.04	0.00	0.00	0.00	0.05	0.02	0.01
H_2O*	4.55	4.49	4.53	4.49	4.48	4.53	4.46	4.46	4.42	4.47	4.45
Subtotal	101.86	101.71	101.97	101.62	101.32	101.40	101.22	101.24	101.21	101.33	101.50
O=F,Cl	0.00	0.05	0.03	0.03	0.03	0.01	0.03	0.02	0.02	0.01	0.04
Total	101.86	101.66	101.94	101.59	101.29	101.39	101.19	101.22	101.20	101.33	101.46
Si	6.30	6.28	6.24	6.31	6.28	6.24	6.24	6.20	6.24	6.29	6.17
Al ^{iv}	1.70	1.72	1.76	1.70	1.72	1.76	1.76	1.80	1.77	1.72	1.83
Al ^{vi}	3.43	3.46	3.43	3.43	3.45	3.40	3.43	3.42	3.43	3.44	3.57
Ti	0.00	0.00	0.01	0.00	0.01	0.01	0.00	0.00	0.00	0.01	0.01
Cr	0.01	0.00	0.00	0.00	0.00	0.00	0.00	0.00	0.01	0.00	0.00
Fe	0.41	0.35	0.42	0.42	0.37	0.37	0.37	0.37	0.33	0.42	0.27
Mn	0.00	0.02	0.01	0.01	0.00	0.01	0.01	0.01	0.01	0.02	0.01
Mg	0.16	0.16	0.16	0.16	0.17	0.16	0.15	0.15	0.13	0.16	0.11
Li*	0.00	0.00	0.00	0.00	0.00	0.00	0.00	0.00	0.00	0.00	0.00
Ca	0.01	0.00	0.00	0.00	0.00	0.00	0.00	0.00	0.00	0.00	0.00
Na	0.09	0.15	0.09	0.12	0.09	0.12	0.11	0.13	0.12	0.08	0.12
K	2.13	2.12	2.16	2.10	2.15	2.33	2.29	2.34	2.40	2.08	2.20
OH*	4.00	3.96	3.97	3.97	3.97	4.00	3.97	3.98	3.98	3.99	3.96
F	0.00	0.05	0.03	0.03	0.03	0.01	0.03	0.02	0.02	0.00	0.04
Cl	0.00	0.00	0.00	0.00	0.01	0.00	0.00	0.00	0.00	0.01	0.00
TOTAL	18.24	18.26	18.28	18.24	18.25	18.40	18.36	18.42	18.42	18.21	18.28
Y total	4.02	3.99	4.03	4.02	4.01	3.95	3.96	3.95	3.91	4.05	3.96
X total	2.22	2.27	2.25	2.23	2.24	2.45	2.40	2.47	2.52	2.16	2.32
Al total	5.13	5.18	5.19	5.13	5.17	5.17	5.19	5.22	5.20	5.15	5.41

* Calculated.

Appendix 2.4A (continued**):** Detailed major element data of micas from tourmaline-bearing and sunstone-bearing pegmatites (GNS, MSN) from Ntcheu and amethyst-bearing pegmatites (CUB) from Balaka.

	MSN3A_2	MSN3A_3	MSN3A_4	MSN3A_5	MSN3A_6	MSN3A_7	MSN3A_8	MSN3A_9	MSN3A_10	MSN3D_1	MSN3D_2
SiO_2	46.64	46.13	46.64	46.48	46.37	46.10	46.01	46.67	46.65	46.61	46.76
TiO_2	0.04	0.14	0.06	0.07	0.01	0.07	0.03	0.10	0.16	0.05	0.04
Al_2O_3	34.29	34.25	34.42	32.78	33.17	32.87	32.42	32.26	32.27	32.77	33.09
FeO	2.40	2.55	2.17	2.95	2.85	2.66	3.69	3.43	3.65	3.38	3.45
MnO	0.00	0.04	0.00	0.01	0.00	0.07	0.00	0.01	0.08	0.00	0.20
MgO	0.49	0.62	0.49	0.78	0.63	0.65	0.79	0.89	0.93	0.77	0.87
CaO	0.04	0.00	0.03	0.00	0.00	0.05	0.00	0.00	0.02	0.00	0.00
Na_2O	0.48	0.57	0.28	0.45	0.64	0.33	0.33	0.30	0.37	0.46	0.60
K_2O	12.91	13.12	13.00	13.82	13.73	12.25	12.49	12.84	12.84	13.07	12.74
F	0.01	0.00	0.00	0.04	0.04	0.07	0.00	0.02	0.02	0.07	0.04
Cl	0.00	0.01	0.02	0.03	0.00	0.01	0.01	0.00	0.02	0.00	0.00
Cr_2O_3	0.05	0.01	0.00	0.00	0.01	0.00	0.00	0.02	0.00	0.01	0.00
H_2O*	4.57	4.57	4.60	4.44	4.48	4.59	4.41	4.52	4.46	4.44	4.56
Subtotal	101.90	101.98	101.70	101.85	101.94	99.70	100.16	101.04	101.46	101.63	101.56
O=F,Cl	0.00	0.00	0.01	0.03	0.02	0.03	0.00	0.01	0.01	0.03	0.02
Total	101.90	101.98	101.70	101.83	101.92	99.67	100.16	101.04	101.45	101.61	101.54
Si	6.15	6.18	6.20	6.24	6.18	6.50	6.25	6.22	6.29	6.25	6.18
Al ^{iv}	1.85	1.82	1.80	1.77	1.82	1.50	1.75	1.78	1.71	1.75	1.82
Al ^{vi}	3.60	3.54	3.63	3.42	3.48	3.83	3.44	3.42	3.38	3.43	3.45
Ti	0.00	0.01	0.01	0.01	0.00	0.01	0.00	0.01	0.02	0.01	0.00
Cr	0.01	0.00	0.00	0.00	0.00	0.00	0.00	0.00	0.00	0.00	0.00
Fe	0.26	0.28	0.24	0.34	0.32	0.29	0.42	0.38	0.41	0.38	0.38
Mn	0.00	0.01	0.00	0.00	0.00	0.01	0.00	0.00	0.01	0.00	0.02
Mg	0.10	0.12	0.10	0.16	0.12	0.13	0.16	0.18	0.19	0.15	0.17
Li*	0.00	0.00	0.00	0.00	0.00	0.00	0.00	0.00	0.00	0.00	0.00
Ca	0.01	0.00	0.00	0.00	0.00	0.01	0.00	0.00	0.00	0.00	0.00
Na	0.12	0.15	0.07	0.12	0.17	0.08	0.09	0.08	0.10	0.12	0.15
K	2.16	2.20	2.16	2.37	2.33	1.03	2.16	2.29	2.19	2.24	2.17
OH*	4.00	4.00	4.00	3.97	3.98	3.97	4.00	3.99	3.99	3.97	3.98
F	0.00	0.00	0.00	0.02	0.02	0.03	0.00	0.01	0.01	0.03	0.02
Cl	0.00	0.00	0.01	0.01	0.00	0.00	0.00	0.00	0.00	0.00	0.00
TOTAL	18.26	18.30	18.19	18.41	18.42	17.39	18.28	18.35	18.29	18.33	18.34
Y total	3.97	3.96	3.96	3.93	3.92	4.26	4.03	3.99	4.00	3.97	4.02
X total	2.29	2.34	2.23	2.48	2.50	1.12	2.25	2.36	2.29	2.36	2.32
Al total	5.46	5.36	5.43	5.18	5.30	5.33	5.19	5.20	5.09	5.18	5.27

* Calculated.

Appendix 2.4A (continued**):** Detailed major element data of micas from tourmaline-bearing and sunstone-bearing pegmatites (GNS, MSN) from Ntcheu and amethyst-bearing pegmatites (CUB) from Balaka.

	MSN3D_3	MSN3D_4	MSN3D_5	MSN3D_6	MSN3D_7	MSN3D_8	MSN3D_9	MSN3D_10
SiO_2	46.62	46.77	46.81	46.58	46.68	46.42	46.99	46.41
TiO_2	0.07	0.04	0.04	0.00	0.00	0.06	0.02	0.02
Al_2O_3	32.76	32.61	33.14	32.95	33.00	32.60	33.20	32.89
FeO	3.40	3.45	3.35	3.38	3.25	3.44	3.17	3.41
MnO	0.10	0.02	0.00	0.01	0.07	0.13	0.02	0.07
MgO	0.81	0.78	0.83	0.79	0.81	0.74	0.79	0.80
CaO	0.03	0.02	0.01	0.00	0.03	0.03	0.07	0.02
Na_2O	0.55	0.50	0.42	0.53	0.53	0.53	0.46	0.65
K_2O	12.84	12.78	12.23	12.17	11.80	11.97	12.04	12.64
F	0.11	0.03	0.07	0.13	0.05	0.02	0.13	0.02
Cl	0.01	0.00	0.03	0.00	0.00	0.01	0.00	0.02
Cr_2O_3	0.00	0.00	0.04	0.00	0.01	0.00	0.01	0.00
H_2O*	4.43	4.52	4.46	4.40	4.44	4.43	4.46	4.48
Subtotal	101.73	101.51	101.44	100.92	100.67	100.38	101.35	101.43
O=F,Cl	0.05	0.01	0.04	0.06	0.02	0.01	0.06	0.01
Total	101.68	101.50	101.41	100.87	100.65	100.37	101.29	101.41
Si	6.23	6.24	6.27	6.26	6.27	6.27	6.28	6.25
Al ^{iv}	1.77	1.76	1.73	1.74	1.73	1.73	1.72	1.75
Al ^{vi}	3.39	3.40	3.48	3.48	3.50	3.46	3.51	3.43
Ti	0.01	0.00	0.00	0.00	0.00	0.01	0.00	0.00
Cr	0.00	0.00	0.00	0.00	0.00	0.00	0.00	0.00
Fe	0.38	0.45	0.37	0.38	0.37	0.39	0.35	0.40
Mn	0.01	0.00	0.00	0.00	0.01	0.02	0.00	0.01
Mg	0.16	0.15	0.17	0.16	0.16	0.15	0.16	0.16
Li*	0.00	0.00	0.00	0.00	0.00	0.00	0.00	0.00
Ca	0.01	0.00	0.00	0.00	0.00	0.00	0.01	0.00
Na	0.20	0.13	0.11	0.14	0.14	0.14	0.12	0.17
K	2.27	2.19	2.08	2.09	2.02	2.06	2.03	2.15
OH*	3.95	3.99	3.96	3.95	3.98	3.99	3.94	3.99
F	0.05	0.01	0.03	0.06	0.02	0.01	0.06	0.01
Cl	0.00	0.00	0.01	0.00	0.00	0.00	0.00	0.00
TOTAL	18.42	18.33	18.21	18.24	18.20	18.23	18.18	18.32
Y total	3.95	4.01	4.02	4.02	4.03	4.02	4.02	4.00
X total	2.47	2.32	2.19	2.22	2.16	2.21	2.16	2.33
Al total	5.16	5.16	5.20	5.22	5.23	5.19	5.23	5.18

* Calculated.

Appendix 2.4A (continued**):** Detailed major element data of micas from tourmaline-bearing and sunstone-bearing pegmatites (GNS, MSN) from Ntcheu and amethyst-bearing pegmatites (CUB) from Balaka.

	CUB1B_1	CUB1B_2	CUB1B_3	CUB1B_4	CUB1B_5	CUB1B_6	CUB1B_7	CUB1B_8	CUB1B_9	CUB1B_10	CUB2B_1
SiO_2	38.93	39.21	37.69	39.21	39.31	39.15	39.03	38.69	38.97	39.22	38.67
TiO_2	1.50	1.63	1.45	1.58	1.56	1.50	1.49	1.52	1.50	1.47	1.65
Al_2O_3	17.01	16.63	15.19	16.53	16.51	16.54	17.01	16.62	17.06	16.99	16.29
FeO	3.39	3.23	3.52	3.55	3.61	3.69	3.81	3.80	4.13	3.45	3.38
MnO	0.05	0.06	0.01	0.00	0.00	0.00	0.07	0.00	0.02	0.01	0.10
MgO	22.29	22.22	20.65	22.09	21.94	22.01	22.33	22.50	22.20	22.43	22.61
CaO	0.05	0.04	0.09	0.07	0.13	0.04	0.05	0.00	0.06	0.04	0.00
Na_2O	0.34	0.43	0.77	0.31	0.07	0.46	0.34	0.52	0.23	0.38	0.29
K_2O	11.28	11.10	11.31	10.92	10.92	10.43	10.54	10.77	10.85	11.09	11.38
F	0.94	1.18	1.19	1.16	1.17	1.11	1.13	1.06	1.24	1.30	1.34
Cl	0.08	0.05	0.10	0.16	0.13	0.07	0.10	0.07	0.09	0.05	0.00
Cr_2O_3	0.03	0.00	0.01	0.00	0.02	0.01	0.05	0.00	0.04	0.02	0.00
Li_2O*	1.62	1.70	1.27	1.70	1.73	1.68	1.65	1.55	1.72	1.70	1.55
H_2O*	3.82	3.71	3.47	3.68	3.68	3.71	3.73	3.74	3.70	3.67	3.67
Subt	101.31	101.19	96.70	100.94	100.78	100.41	101.32	100.83	101.81	101.82	100.64
O=F,Cl	0.41	0.51	0.52	0.52	0.52	0.48	0.50	0.46	0.54	0.56	0.57
Total	100.90	100.68	96.18	100.42	100.26	99.93	100.82	100.37	101.26	101.26	100.07
Si	5.45	5.49	5.57	5.51	5.53	5.51	5.46	5.45	5.46	5.46	5.39
Al ^{iv}	2.55	2.51	2.43	2.49	2.48	2.49	2.54	2.55	2.54	2.54	2.61
Al ^{vi}	0.26	0.24	0.22	0.24	0.26	0.26	0.26	0.21	0.26	0.25	0.06
Ti	0.16	0.17	0.16	0.17	0.17	0.16	0.16	0.16	0.16	0.15	0.17
Cr	0.00	0.00	0.00	0.00	0.00	0.00	0.01	0.00	0.00	0.00	0.00
Fe	0.40	0.38	0.44	0.42	0.42	0.43	0.45	0.45	0.48	0.40	0.44
Mn	0.01	0.01	0.00	0.00	0.00	0.00	0.01	0.00	0.00	0.00	0.01
Mg	4.65	4.64	4.55	4.63	4.60	4.62	4.65	4.72	4.60	4.66	4.76
Li*	0.91	0.96	0.75	0.96	0.98	0.95	0.93	0.88	0.96	0.96	0.87
Ca	0.01	0.01	0.02	0.01	0.02	0.01	0.01	0.00	0.01	0.01	0.00
Na	0.09	0.12	0.22	0.08	0.02	0.13	0.09	0.14	0.06	0.10	0.08
K	2.01	1.98	2.13	1.96	1.96	1.87	1.88	1.93	1.93	1.97	2.38
OH*	3.57	3.47	3.42	3.45	3.45	3.49	3.48	3.51	3.43	3.41	3.41
F	0.42	0.52	0.55	0.51	0.52	0.50	0.50	0.47	0.55	0.57	0.59
Cl	0.02	0.01	0.03	0.04	0.03	0.02	0.02	0.02	0.02	0.01	0.00
TOTAL	20.50	20.49	20.49	20.46	20.42	20.43	20.43	20.49	20.46	20.50	20.77
Y total	6.38	6.39	6.13	6.41	6.42	6.43	6.45	6.41	6.46	6.42	6.31
X total	2.11	2.11	2.37	2.05	2.00	2.00	1.98	2.08	2.00	2.08	2.46
Al total	2.81	2.75	2.65	2.74	2.73	2.75	2.80	2.76	2.80	2.79	2.67

* Calculated.

Appendix 2.4A(continued**):** Detailed major element data of micas from tourmaline-bearing and sunstone-bearing pegmatites (GNS, MSN) from Ntcheu and amethyst-bearing pegmatites (CUB) from Balaka.

	CUB2B_2	CUB2B_3	CUB2B_4	CUB2B_5	CUB2B_6	CUB2B_7	CUB2B_8	CUB2B_9	CUB2B_10	CUB3B_1	CUB3B_2
SiO_2	38.68	38.76	38.77	39.04	38.76	39.02	38.37	39.00	38.91	38.54	38.63
TiO_2	1.65	1.73	1.65	1.70	1.72	1.69	1.77	1.54	1.73	1.51	1.42
Al_2O_3	16.43	16.49	16.39	16.28	16.53	16.47	16.47	16.65	16.45	16.16	16.18
FeO	3.20	3.24	3.20	3.48	3.52	3.08	3.37	3.22	3.30	3.68	3.29
MnO	0.11	0.06	0.03	0.04	0.00	0.04	0.02	0.00	0.01	0.10	0.06
MgO	22.61	22.44	22.58	22.62	22.55	22.41	22.49	22.50	22.46	23.03	23.14
CaO	0.00	0.03	0.01	0.03	0.00	0.00	0.00	0.03	0.03	0.00	0.04
Na_2O	0.23	0.34	0.12	0.41	0.37	0.29	0.31	0.38	0.27	0.40	0.31
K_2O	11.32	11.27	11.48	11.36	11.43	11.75	11.77	11.34	11.62	11.23	11.79
F	1.33	1.09	1.41	1.29	1.32	1.30	1.38	1.38	1.38	1.15	1.18
Cl	0.02	0.05	0.01	0.03	0.00	0.02	0.02	0.04	0.02	0.03	0.06
Cr_2O_3	0.02	0.00	0.00	0.02	0.01	0.02	0.03	0.03	0.02	0.00	0.02
Li_2O*	1.64	1.60	1.57	1.65	1.57	1.73	1.66	1.70	1.62	1.80	1.97
H_2O*	3.68	3.79	3.60	3.69	3.67	3.69	3.61	3.66	3.65	3.83	3.81
Subt	100.89	100.90	100.80	101.64	101.45	101.52	101.24	101.56	101.46	101.46	101.89
O=F,Cl	0.56	0.47	0.60	0.55	0.56	0.55	0.63	0.59	0.59	0.49	0.51
Total	100.33	100.43	100.21	101.09	100.89	100.97	100.61	100.97	100.87	100.97	101.38
Si	5.43	5.39	5.45	5.43	5.41	5.47	5.43	5.44	5.42	5.41	5.49
Al ^{iv}	2.57	2.61	2.55	2.57	2.59	2.53	2.57	2.56	2.58	2.59	2.51
Al ^{vi}	0.12	0.09	0.16	0.10	0.14	0.17	0.12	0.16	0.12	0.15	0.13
Ti	0.17	0.18	0.17	0.18	0.18	0.18	0.19	0.16	0.18	0.16	0.15
Cr	0.00	0.00	0.00	0.00	0.00	0.00	0.00	0.00	0.00	0.00	0.00
Fe	0.37	0.41	0.38	0.45	0.43	0.36	0.39	0.37	0.38	0.42	0.38
Mn	0.01	0.01	0.00	0.01	0.00	0.01	0.00	0.00	0.00	0.01	0.01
Mg	4.69	4.73	4.73	4.69	4.69	4.65	4.70	4.65	4.70	4.72	4.76
Li*	0.92	0.89	0.89	0.93	0.88	0.97	0.93	0.95	0.91	0.99	1.08
Ca	0.00	0.00	0.00	0.01	0.00	0.00	0.00	0.01	0.00	0.00	0.01
Na	0.06	0.15	0.03	0.11	0.10	0.08	0.08	0.10	0.07	0.11	0.08
K	2.38	2.28	2.24	2.19	2.21	2.26	2.26	2.32	2.33	2.10	2.08
OH*	3.41	3.51	3.37	3.43	3.42	3.42	3.34	3.39	3.39	3.49	3.48
F	0.58	0.48	0.63	0.57	0.58	0.57	0.65	0.60	0.61	0.50	0.51
Cl	0.00	0.01	0.00	0.01	0.00	0.01	0.01	0.01	0.01	0.01	0.01
TOTAL	20.73	20.74	20.60	20.67	20.64	20.66	20.68	20.73	20.70	20.66	20.66
Y total	6.29	6.31	6.33	6.36	6.33	6.32	6.33	6.30	6.30	6.45	6.50
X total	2.44	2.43	2.27	2.31	2.31	2.34	2.35	2.43	2.41	2.21	2.16
Al total	2.70	2.70	2.71	2.67	2.72	2.70	2.70	2.72	2.70	2.74	2.64

* Calculated

Appendix 2.4A (continued**):** Detailed major element data of micas from tourmaline-bearing and sunstone-bearing pegmatites (GNS, MSN) from Ntcheu and amethyst-bearing pegmatites (CUB) from Balaka.

	CUB3B_3	CUB3B_4	CUB3B_5	CUB3B_6	CUB3B_7	CUB3B_8	CUB3B_9	CUB3B_10	CUB4B_1	CUB4B_2	CUB4B_3
SiO_2	38.74	38.59	38.53	38.53	38.57	38.57	38.56	38.55	38.96	38.82	38.59
TiO_2	1.59	1.55	1.53	1.45	1.52	1.48	1.56	1.55	1.55	1.64	1.66
Al_2O_3	16.36	16.24	16.49	16.47	16.52	16.57	16.24	16.22	16.53	16.53	16.55
FeO	3.67	3.63	3.33	3.86	3.64	3.83	3.63	3.61	3.34	3.22	3.27
MnO	0.03	0.00	0.04	0.07	0.02	0.05	0.05	0.03	0.12	0.02	0.06
MgO	22.86	23.03	23.04	22.65	22.90	22.68	22.87	22.86	22.58	22.51	22.75
CaO	0.05	0.07	0.01	0.15	0.02	0.03	0.00	0.01	0.01	0.00	0.01
Na_2O	0.24	0.27	0.27	0.30	0.40	0.26	0.43	0.56	0.19	0.25	0.33
K_2O	11.34	11.30	11.54	11.05	11.35	11.35	11.71	11.65	12.05	11.98	11.84
F	1.15	1.44	1.16	1.23	1.30	1.13	1.34	1.20	1.31	1.42	1.24
Cl	0.06	0.06	0.07	0.05	0.13	0.05	0.02	0.04	0.03	0.04	0.06
Cr_2O_3	0.06	0.04	0.00	0.07	0.01	0.05	0.04	0.04	0.00	0.00	0.00
Li_2O*	1.85	1.81	1.79	1.79	1.78	1.86	1.52	1.77	1.69	1.70	1.75
H_2O*	3.81	3.69	3.79	3.74	3.70	3.84	3.62	3.79	3.63	3.63	3.73
Subt	101.81	101.72	101.60	101.43	101.86	101.74	101.57	101.87	102.00	101.76	101.82
O=F,Cl	0.50	0.62	0.50	0.53	0.58	0.49	0.57	0.51	0.60	0.61	0.54
Total	101.31	101.10	101.10	100.90	101.29	101.26	101.00	101.36	101.40	101.15	101.29
Si	5.45	5.41	5.44	5.47	5.45	5.44	5.43	5.42	5.46	5.46	5.45
Al ^{iv}	2.55	2.59	2.56	2.54	2.55	2.56	2.57	2.58	2.55	2.55	2.55
Al ^{vi}	0.16	0.19	0.14	0.20	0.18	0.15	0.12	0.12	0.19	0.17	0.17
Ti	0.16	0.16	0.16	0.15	0.16	0.15	0.17	0.16	0.16	0.17	0.17
Cr	0.01	0.00	0.00	0.01	0.00	0.01	0.00	0.00	0.00	0.00	0.00
Fe	0.46	0.42	0.48	0.45	0.42	0.44	0.43	0.42	0.39	0.38	0.38
Mn	0.00	0.00	0.01	0.01	0.00	0.01	0.01	0.00	0.01	0.00	0.01
Mg	4.68	4.73	4.72	4.67	4.71	4.73	4.80	4.70	4.69	4.73	4.71
Li*	1.02	1.00	0.99	1.00	0.99	1.03	0.86	0.98	0.95	0.95	0.98
Ca	0.01	0.01	0.00	0.02	0.00	0.00	0.00	0.00	0.00	0.00	0.00
Na	0.06	0.07	0.07	0.08	0.11	0.07	0.12	0.15	0.05	0.07	0.09
K	2.02	1.97	2.03	1.95	2.00	2.05	2.10	2.22	2.16	2.13	2.09
OH*	3.49	3.36	3.48	3.45	3.40	3.50	3.40	3.47	3.37	3.37	3.44
F	0.50	0.62	0.50	0.54	0.57	0.49	0.59	0.52	0.62	0.63	0.54
Cl	0.01	0.01	0.02	0.01	0.03	0.01	0.00	0.01	0.01	0.01	0.01
TOTAL	20.58	20.55	20.60	20.53	20.57	20.62	20.60	20.74	20.60	20.59	20.60
Y total	6.49	6.50	6.50	6.48	6.46	6.50	6.38	6.38	6.39	6.40	6.42
X total	2.09	2.05	2.10	2.05	2.11	2.12	2.22	2.37	2.21	2.20	2.18
Al total	2.71	2.78	2.71	2.73	2.74	2.71	2.69	2.70	2.73	2.71	2.72

* Calculated

Appendix 2.4A (continued**):** Detailed major element data of micas from tourmaline-bearing and sunstone-bearing pegmatites (GNS, MSN) from Ntcheu and amethyst-bearing pegmatites (CUB) from Balaka.

	CUB4B_4	CUB4B_5	CUB4B_6	CUB4B_7	CUB4B_8	CUB4B_9	CUB4B_10
SiO_2	38.74	38.57	38.58	38.57	38.58	38.54	38.40
TiO_2	1.68	1.50	1.72	1.70	1.69	1.71	1.55
Al_2O_3	16.34	16.44	16.39	16.50	16.40	16.46	16.11
FeO	2.75	3.02	3.15	3.10	3.33	3.31	3.54
MnO	0.10	0.04	0.08	0.10	0.05	0.07	0.01
MgO	22.91	22.86	22.71	22.73	22.87	22.87	22.73
CaO	0.00	0.01	0.00	0.04	0.00	0.04	0.03
Na_2O	0.15	0.13	0.21	0.24	0.12	0.20	0.31
K_2O	11.67	11.84	11.30	12.09	11.31	11.34	12.09
F	1.34	1.35	1.34	1.44	1.29	1.31	1.26
Cl	0.02	0.03	0.05	0.04	0.03	0.03	0.01
Cr_2O_3	0.04	0.03	0.05	0.01	0.01	0.03	0.04
Li_2O*	1.60	1.75	1.69	1.66	1.63	1.80	1.76
H_2O*	3.64	3.68	3.68	3.64	3.70	3.75	3.74
Subt	100.99	101.24	100.95	101.85	101.02	101.46	101.59
O=F,Cl	0.57	0.58	0.58	0.61	0.55	0.56	0.54
Total	100.42	100.66	100.37	101.33	100.47	100.90	101.05
Si	5.44	5.45	5.43	5.41	5.41	5.42	5.44
Al^{iv}	2.56	2.55	2.57	2.59	2.59	2.58	2.56
Al^{vi}	0.14	0.16	0.11	0.11	0.10	0.08	0.06
Ti	0.18	0.16	0.18	0.18	0.18	0.18	0.16
Cr	0.01	0.00	0.01	0.00	0.00	0.00	0.00
Fe	0.32	0.35	0.37	0.36	0.39	0.38	0.43
Mn	0.01	0.01	0.01	0.01	0.01	0.01	0.00
Mg	4.78	4.72	4.71	4.76	4.75	4.74	4.74
Li*	0.90	0.97	0.94	0.93	0.91	0.99	0.98
Ca	0.00	0.00	0.00	0.01	0.00	0.01	0.01
Na	0.04	0.04	0.06	0.06	0.03	0.05	0.08
K	2.26	2.29	2.35	2.30	2.36	2.32	2.31
OH*	3.40	3.40	3.40	3.36	3.43	3.43	3.45
F	0.59	0.59	0.59	0.63	0.56	0.57	0.55
Cl	0.01	0.01	0.01	0.01	0.01	0.01	0.00
TOT	20.64	20.69	20.73	20.71	20.72	20.75	20.77
Y tot	6.33	6.36	6.32	6.34	6.33	6.38	6.38
X tot	2.31	2.32	2.41	2.37	2.39	2.37	2.39
Al tot	2.70	2.70	2.68	2.70	2.68	2.66	2.62

* Calculated

Appendix 2.4B: Detailed trace element data of micas from tourmaline-bearing and sunstone-bearing pegmatites (GNS, MSN) from Ntcheu and amethyst-bearing pegmatites (CUB) from Balaka. All concentrations are given in ppm.

	GNS11	GNS12	GNS13	GNS14	GNS15	GNS16	GNS17	GNS18	GNS19	GNS110	GNS31
Li	14.67	14.80	14.83	14.18	13.16	7.47	6.87	6.45	4.34	9.34	6.61
Be	1.73	1.83	2.17	1.65	2.43	4.54	4.09	4.90	4.66	3.69	9.98
B	143.99	146.78	152.45	178.05	176.45	288.95	280.17	316.67	297.63	239.57	509.39
Sc	23.53	23.48	22.19	18.40	12.29	15.61	15.81	17.70	14.69	7.38	11.64
Ti	766.77	763.46	737.10	658.34	486.77	1005.82	1095.99	1089.51	1019.28	535.55	456.97
V	18.07	18.20	17.90	6.60	1.52	68.70	75.50	78.11	70.86	1.97	9.12
Cr	0.11	0.17	0.10	0.13	0.09	0.11	0.09	0.50	0.12	0.13	1.36
Mn	284.10	291.69	283.50	287.79	314.50	443.67	473.31	431.08	446.13	306.87	323.51
Co	2.08	2.18	2.05	1.95	1.64	0.59	0.72	0.89	0.75	1.34	57.86
Ni	0.13	0.19	0.19	0.15	0.14	0.04	0.05	0.09	0.09	0.10	0.46
Cu	0.03	0.03	0.03	0.04	0.07	0.03	0.04	0.31	0.02	0.03	2.34
Zn	51.16	49.88	49.33	47.30	51.04	77.74	79.29	77.48	67.45	54.02	22.38
Ga	229.65	232.22	229.38	234.19	218.59	133.62	142.13	142.45	133.61	217.12	161.28
Rb	309.41	310.01	299.90	301.20	294.92	532.19	584.71	575.29	540.37	318.04	560.67
Sr	17.17	17.18	16.22	16.03	16.20	4.05	4.17	7.41	4.37	13.85	8.12
Y	0.05	0.06	0.06	0.05	0.05	0.04	0.06	0.04	0.02	0.04	0.05
Zr	1.23	1.31	1.29	1.14	0.97	1.64	1.75	1.58	1.52	0.94	0.50
Nb	54.11	53.95	51.90	50.14	41.14	118.70	127.73	130.20	115.87	50.77	95.73
Mo	0.42	0.42	0.45	0.39	0.31	0.05	0.10	0.02	0.08	0.27	0.00
Sn	3.25	3.24	3.22	2.84	2.08	4.88	5.04	4.43	4.80	1.80	5.23
Cs	9.78	9.54	9.37	9.24	8.75	24.39	27.32	48.54	26.25	9.96	29.01
Ba	4701.38	4739.86	4608.78	4211.95	3945.67	228.94	229.41	657.85	252.80	3710.41	739.24
Hf	0.23	0.24	0.21	0.25	0.20	0.39	0.51	0.40	0.40	0.21	0.27
Ta	1.24	1.21	1.21	1.22	1.08	3.85	4.20	5.14	3.89	1.34	3.52
W	45.39	43.80	43.13	41.67	31.83	20.50	20.01	26.21	19.51	35.90	7.97
Pb	12.40	12.31	12.56	11.84	13.99	18.97	19.18	23.68	18.72	14.28	27.21
Th	0.0008	0.0021	0.0008	0.0011	0.0007	0.0005	0.0042	0.0023	0.0010	0.0007	0.0027
U	0.0050	0.0019	0.0035	0.0033	0.0048	0.0042	0.0076	0.0000	0.0028	0.0035	0.0013

Appendix 2.4B (continued**):** Detailed trace element data of micas from tourmaline-bearing and sunstone-bearing pegmatites (GNS, MSN) from Ntcheu and amethyst-bearing pegmatites (CUB) from Balaka. All concentrations are given in ppm.

Element	GNS32	GNS33	GNS34	GNS35	GNS36	GNS37	GNS38	GNS39	GNS310	GNS61	GNS62
Li	5.47	6.56	5.57	4.92	4.17	5.69	6.00	5.38	5.72	12.91	10.89
Be	10.83	8.65	8.82	9.85	9.37	8.88	8.96	7.19	8.50	1.82	2.26
B	439.61	496.40	484.94	450.65	453.24	509.43	422.30	415.14	408.67	200.05	216.75
Sc	14.69	11.14	21.38	37.09	30.54	17.20	24.20	23.28	16.30	10.44	9.64
Ti	507.13	464.61	600.63	876.48	770.38	503.04	709.33	703.32	562.13	487.63	440.57
V	11.00	8.66	18.53	31.27	28.96	14.34	13.39	10.49	9.30	2.05	2.08
Cr	0.08	0.13	1.79	0.61	0.98	0.10	0.49	0.17	0.10	0.34	0.37
Mn	351.55	320.80	306.16	318.73	267.67	307.02	317.09	343.91	376.15	347.38	319.52
Co	14.58	1.49	1.41	0.78	8.29	0.70	0.97	1.18	0.98	28.61	21.03
Ni	0.37	0.14	0.37	0.36	0.47	0.19	0.43	0.15	0.17	0.10	0.20
Cu	0.38	0.05	0.23	0.10	0.35	0.03	0.21	4.86	0.09	2.57	1.58
Zn	30.24	31.39	30.08	30.14	28.56	30.16	31.87	33.80	35.65	46.30	44.84
Ga	151.74	155.62	153.57	159.14	154.70	144.19	156.19	150.52	160.56	211.81	213.06
Rb	506.32	575.80	568.63	568.92	526.78	521.07	560.41	546.56	535.56	325.50	297.86
Sr	7.09	8.64	7.92	7.33	7.78	7.89	8.91	7.91	8.04	14.69	12.92
Y	0.03	0.04	0.07	0.04	0.04	0.03	0.09	0.03	0.03	0.06	0.04
Zr	0.55	0.61	0.65	0.63	0.46	0.49	0.68	0.58	0.57	1.06	1.01
Nb	96.89	107.53	113.78	130.82	124.53	104.52	106.93	96.08	98.21	51.66	48.36
Mo	0.02	0.01	0.01	0.01	0.01	0.03	0.02	0.00	0.02	0.39	0.30
Sn	4.86	4.13	5.28	7.60	7.49	4.85	5.35	4.90	4.50	2.63	2.51
Cs	25.31	31.00	32.33	40.18	43.44	28.65	33.00	30.96	27.49	10.64	9.85
Ba	689.25	584.70	640.71	852.85	848.27	590.24	823.14	731.05	944.09	3975.85	3694.15
Hf	0.20	0.18	0.23	0.22	0.25	0.26	0.23	0.27	0.18	0.23	0.20
Ta	3.02	3.36	3.95	7.51	11.18	3.54	5.46	4.39	3.18	1.29	1.31
W	7.91	5.42	5.11	6.71	4.74	5.23	7.78	6.51	9.34	39.41	38.24
Pb	21.16	27.86	26.49	26.25	25.86	23.78	24.29	21.49	22.38	13.31	11.85
Th	0.0010	0.0000	0.0060	0.0010	0.0012	0.0007	0.0111	0.0007	0.0004	0.0011	0.0000
U	0.0011	0.0009	0.1160	0.0017	0.0018	0.0000	0.0015	0.0013	0.0039	0.0042	0.0035

Appendix 2.4B (continued**):** Detailed trace element data of micas from tourmaline-bearing and sunstone-bearing pegmatites (GNS, MSN) from Ntcheu and amethyst-bearing pegmatites (CUB) from Balaka. All concentrations are given in ppm.

	GNS63	GNS64	GNS65	GNS66	GNS67	GNS68	GNS69	GNS610	GNS71	GNS72	GNS73
Li	11.46	12.93	13.91	12.85	12.57	11.15	12.07	9.38	10.12	15.14	15.82
Be	3.15	2.26	2.04	2.40	2.04	3.29	3.69	4.73	6.37	6.44	5.16
B	218.53	206.32	176.27	175.96	210.59	263.90	257.50	295.95	129.53	92.09	86.22
Sc	9.97	11.51	15.19	14.85	10.44	7.27	7.10	7.81	70.05	76.64	78.68
Ti	466.73	511.12	578.90	560.10	482.45	438.10	428.91	437.34	1657.98	1624.92	1661.37
V	1.93	1.54	2.70	2.71	1.66	3.46	2.57	6.97	53.26	54.86	53.59
Cr	0.14	0.21	0.14	0.13	0.18	0.14	0.13	0.40	0.38	0.29	0.13
Mn	369.50	327.21	315.89	354.26	329.12	404.97	414.40	384.71	207.55	247.44	259.37
Co	2.03	3.73	15.46	16.01	5.05	1.24	1.51	1.26	1.83	2.17	2.27
Ni	0.11	0.09	0.19	0.22	0.10	0.05	0.05	0.11	1.45	1.67	1.84
Cu	0.14	0.24	1.53	2.14	0.42	0.10	0.07	0.20	0.26	0.08	0.21
Zn	52.63	55.00	44.85	45.27	48.04	58.95	59.56	54.10	60.81	62.20	62.67
Ga	220.94	225.12	220.86	211.26	207.75	196.27	204.03	173.51	283.87	270.04	252.40
Rb	303.58	315.12	316.02	308.80	313.50	349.56	341.43	371.32	314.09	292.13	301.78
Sr	14.34	15.45	16.92	16.19	14.77	12.22	12.13	10.94	16.54	17.70	18.51
Y	0.06	0.06	0.06	0.05	0.04	0.04	0.04	0.55	0.02	0.02	0.04
Zr	0.93	1.00	1.06	1.11	0.95	1.22	1.09	1.04	1.31	1.71	1.84
Nb	48.58	50.30	51.00	49.66	49.24	57.29	54.45	60.11	58.79	55.99	56.88
Mo	0.34	0.36	0.35	0.33	0.34	0.20	0.23	0.16	0.65	0.60	0.62
Sn	2.03	2.20	2.68	2.73	2.04	1.82	1.74	1.77	7.74	9.21	9.79
Cs	9.99	9.88	10.05	9.58	10.03	12.56	11.43	31.38	9.39	8.79	8.98
Ba	3848.70	4092.69	4485.02	4275.78	3950.47	2987.69	3206.55	2339.26	5654.69	5632.99	5684.55
Hf	0.22	0.24	0.20	0.21	0.16	0.24	0.28	0.19	0.29	0.30	0.26
Ta	1.33	1.31	1.29	1.23	1.26	1.64	1.48	2.75	1.46	1.14	1.12
W	37.69	41.04	42.04	40.02	38.16	35.61	35.08	31.57	58.69	57.92	57.66
Pb	13.40	13.51	12.98	12.80	12.62	15.31	14.96	16.66	14.87	12.56	12.19
Th	0.0003	0.0000	0.0000	0.0008	0.0011	0.0004	0.0010	0.0022	0.0018	0.0013	0.0016
U	0.0015	0.0022	0.0021	0.0020	0.0041	0.0034	0.0044	0.0027	0.0017	0.0076	0.0076

Appendix 2.4B (continued**):** Detailed trace element data of micas from tourmaline-bearing and sunstone-bearing pegmatites (GNS, MSN) from Ntcheu and amethyst-bearing pegmatites (CUB) from Balaka. All concentrations are given in ppm.

	GNS74	GNS75	GNS76	GNS77	GNS78	GNS79	GNS710	GNS711	GNS712	GNS713	GNS714
Li	18.46	14.11	17.25	14.37	16.54	17.75	19.50	17.39	15.22	14.78	15.99
Be	5.13	4.10	5.27	4.23	4.54	5.69	4.22	5.21	4.65	4.77	4.91
B	100.38	102.84	114.73	130.74	122.10	107.70	104.23	113.70	126.66	136.74	132.97
Sc	79.32	54.92	59.67	56.66	61.10	80.87	68.01	52.61	49.43	42.38	51.30
Ti	1716.43	1337.11	1447.16	1456.83	1495.53	1690.74	1856.15	1830.61	1474.04	1351.55	1294.16
V	56.98	33.24	35.88	35.26	36.71	56.69	60.91	49.92	45.24	41.20	50.30
Cr	0.12	0.15	0.19	0.12	0.12	0.27	0.18	0.15	0.32	0.22	0.54
Mn	299.20	192.81	239.52	203.03	230.85	245.63	256.45	219.30	155.71	145.15	159.59
Co	2.45	2.45	2.55	2.08	2.52	2.48	3.05	2.93	2.21	2.88	4.33
Ni	2.11	1.45	1.78	1.68	1.46	2.25	2.05	2.03	1.55	2.09	1.87
Cu	0.15	0.54	0.77	0.14	0.48	0.35	0.26	0.24	0.30	0.17	1.34
Zn	68.41	52.84	55.79	48.20	51.41	55.35	55.71	51.80	54.40	51.72	53.54
Ga	269.67	249.87	271.68	259.60	264.99	267.67	246.26	237.23	253.54	247.94	245.68
Rb	310.27	342.16	296.91	282.73	299.77	307.00	340.13	349.56	330.81	314.25	328.02
Sr	17.88	16.51	16.99	18.41	19.05	17.80	16.65	15.35	13.70	13.47	14.90
Y	0.05	0.08	0.05	0.02	0.02	0.02	0.03	0.02	0.02	0.01	0.12
Zr	1.90	1.06	1.58	1.46	1.60	1.66	1.41	1.32	0.69	0.81	1.71
Nb	56.62	49.82	52.47	52.99	55.50	56.61	60.23	58.70	57.97	52.74	51.02
Mo	0.40	0.69	0.45	0.58	0.61	0.54	0.56	0.46	0.52	0.46	0.43
Sn	9.90	6.75	7.54	7.88	7.63	9.54	8.17	6.70	7.37	6.37	6.51
Cs	9.11	15.00	8.73	9.30	9.71	9.09	10.91	13.56	11.81	11.58	11.70
Ba	5820.02	5009.24	5004.03	5059.66	5358.80	5608.08	5458.97	4876.20	4671.61	4415.92	4554.70
Hf	0.30	0.21	0.27	0.23	0.27	0.31	0.27	0.24	0.16	0.20	0.28
Ta	1.09	1.15	1.08	1.11	1.18	1.11	1.68	1.83	1.83	2.12	2.31
W	60.09	53.89	52.77	51.85	55.04	57.89	58.49	56.63	54.54	53.46	50.85
Pb	12.73	14.93	11.49	14.11	15.29	15.22	14.73	15.02	15.28	14.93	16.04
Th	0.0011	0.0021	0.0007	0.0010	0.0009	0.0011	0.0018	0.0006	0.0015	0.0010	0.0088
U	0.0126	0.0049	0.0109	0.0077	0.0033	0.0041	0.0021	0.0043	0.0052	0.0035	0.0033

Appendix 2.4B (continued**):** Detailed trace element data of micas from tourmaline-bearing and sunstone-bearing pegmatites (GNS, MSN) from Ntcheu and amethyst-bearing pegmatites (CUB) from Balaka. All concentrations are given in ppm.

	MSN1B1	MSN1B2	MSN1B3	MSN1B4	MSN1B5	MSN1B6	MSN1B7	MSN1B8	MSN1B9	MSN1B10	MSN3A1
Li	12.61	14.92	14.33	13.68	14.14	14.12	12.83	13.76	13.55	13.71	5.72
Be	5.93	3.97	2.66	3.12	2.28	4.24	5.61	2.11	5.18	4.51	3.68
B	238.53	219.89	218.41	211.91	196.81	212.99	219.21	218.78	212.60	187.08	275.84
Sc	9.14	9.79	9.50	9.21	9.34	9.38	9.24	9.02	8.86	9.87	15.79
Ti	459.79	470.27	464.87	464.05	463.55	472.45	450.24	448.57	436.39	469.13	699.89
V	2.80	2.29	2.20	2.39	2.36	2.85	2.75	2.20	2.30	2.99	55.13
Cr	0.11	0.13	0.14	0.22	0.32	0.12	0.16	0.12	0.21	0.13	0.12
Mn	284.64	377.20	384.69	385.34	371.81	319.28	264.35	364.83	349.95	366.79	148.78
Co	8.82	1.72	1.73	2.55	22.08	3.68	9.78	1.82	8.56	12.96	1.64
Ni	0.15	0.14	0.08	0.26	0.12	0.09	0.20	0.07	0.19	0.20	0.29
Cu	1.08	0.15	0.06	1.86	1.12	0.35	0.45	0.06	0.62	0.79	0.13
Zn	66.52	73.28	64.56	63.22	51.24	61.89	57.79	58.20	64.42	61.70	42.78
Ga	231.02	233.86	230.84	218.05	216.51	219.66	224.36	228.29	221.76	206.20	148.15
Rb	323.64	327.69	326.42	337.97	337.92	333.76	312.57	310.15	309.12	331.72	441.25
Sr	13.50	14.59	14.50	14.55	14.78	14.99	13.78	13.76	14.22	14.17	12.93
Y	0.05	0.05	0.05	0.06	0.07	0.04	0.08	0.05	0.08	0.08	0.02
Zr	0.95	1.27	0.94	0.97	0.97	1.03	0.90	0.90	0.87	0.73	0.99
Nb	51.85	55.09	55.06	55.11	54.50	54.50	51.67	53.06	50.68	53.48	84.31
Mo	0.24	0.36	0.31	0.29	0.29	0.34	0.28	0.22	0.25	0.18	0.10
Sn	2.00	1.95	1.87	1.90	2.21	1.98	2.06	1.73	2.01	2.21	3.19
Cs	10.75	10.52	10.33	10.77	10.50	10.65	9.89	9.78	9.71	11.01	23.41
Ba	3864.27	4162.08	4173.37	4112.53	4157.25	4236.46	3941.61	4003.95	3905.77	3918.78	1599.97
Hf	0.22	0.26	0.21	0.18	0.18	0.21	0.20	0.21	0.20	0.20	0.24
Ta	1.40	1.44	1.41	1.42	1.36	1.42	1.41	1.38	1.33	1.38	2.79
W	39.18	41.60	39.74	40.23	38.84	38.38	36.37	38.88	35.95	37.98	19.62
Pb	15.16	14.45	13.97	14.40	13.65	14.86	14.75	13.38	13.69	13.51	21.32
Th	0.0014	0.0008	0.0008	0.0004	0.0000	0.0008	0.0011	0.0008	0.0090	0.0011	0.0015

Appendix 2.4B (continued**):** Detailed trace element data of micas from tourmaline-bearing and sunstone-bearing pegmatites (GNS, MSN) from Ntcheu and amethyst-bearing pegmatites (CUB) from Balaka. All concentrations are given in ppm.

	MSN3A2	MSN3A3	MSN3A4	MSN3A5	MSN3A6	MSN3A7	MSN3A8	MSN3A9	MSN3A10	MSN3D1	MSN3D2
Li	8.32	16.06	8.26	7.76	8.61	9.52	6.29	7.15	6.87	16.40	23.60
Be	3.83	2.45	3.68	4.28	4.02	4.02	3.03	3.31	4.05	4.76	4.78
B	303.65	380.14	463.73	388.33	398.72	340.76	272.88	316.19	417.76	0.00	0.00
Sc	10.57	29.09	7.11	8.22	8.66	15.83	14.84	13.92	12.90	9.51	9.65
Ti	560.33	803.12	335.29	473.39	486.53	524.81	915.59	825.90	436.94	443.76	444.99
V	17.00	26.40	9.22	7.26	8.02	30.72	63.61	64.48	19.38	2.65	2.51
Cr	0.28	0.14	0.11	0.19	0.14	0.11	0.27	2.35	0.17	0.16	0.15
Mn	213.16	104.13	118.87	193.11	166.53	166.03	147.88	187.51	153.47	292.85	297.34
Co	3.12	3.56	1.49	1.03	5.13	5.60	2.86	6.90	2.98	1.83	1.67
Ni	0.10	1.02	0.28	0.05	0.08	0.59	0.39	0.46	0.43	0.11	0.12
Cu	0.15	0.32	0.11	0.04	0.30	0.20	0.15	0.76	0.21	0.07	0.24
Zn	58.92	21.26	34.14	58.18	47.76	37.94	43.08	49.70	39.52	68.02	68.69
Ga	171.11	159.11	177.88	164.72	172.55	197.17	114.61	138.44	189.91	232.74	233.74
Rb	474.22	519.57	467.20	463.88	528.88	500.11	518.19	505.16	448.43	303.78	306.37
Sr	14.65	11.17	12.92	12.96	14.93	17.87	9.49	6.34	15.19	13.95	13.94
Y	0.02	0.03	0.02	0.03	0.03	0.04	0.01	0.08	0.03	0.04	0.06
Zr	0.82	0.87	0.59	0.76	0.57	0.77	1.29	1.35	0.61	0.86	0.88
Nb	67.47	117.93	88.57	83.78	96.84	87.97	111.59	102.57	81.85	52.22	52.14
Mo	0.12	0.07	0.05	0.12	0.07	0.18	0.07	0.08	0.10	0.27	0.29
Sn	3.35	4.26	2.23	1.93	2.56	3.49	4.52	4.22	3.05	1.84	1.87
Cs	34.37	51.65	37.55	34.11	45.54	26.95	25.68	25.45	28.13	9.83	9.98
Ba	2315.98	2102.31	1999.89	1750.25	1973.77	3513.10	446.60	456.06	2863.72	3695.15	3767.59
Hf	0.27	0.59	0.21	0.21	0.23	0.23	0.39	0.40	0.19	0.19	0.21
Ta	4.30	19.58	4.44	2.60	3.36	2.79	3.95	3.54	2.73	1.49	1.44
W	26.07	17.06	15.32	23.67	19.29	24.00	19.93	16.79	22.65	37.05	38.16
Pb	24.14	26.94	29.01	22.88	28.45	29.10	23.33	19.90	27.87	15.11	15.31
Th	0.0012	0.0007	0.0007	0.0013	0.0021	0.0011	0.0009	0.0058	0.0021	0.0010	0.0017

Appendix 2.4B (continued**):** Detailed trace element data of micas from tourmaline-bearing and sunstone-bearing pegmatites (GNS, MSN) from Ntcheu and amethyst-bearing pegmatites (CUB) from Balaka. All concentrations are given in ppm.

	MSN3D3	MSN3D4	MSN3D5	MSN3D6	MSN3D7	MSN3D8	MSN3D9	MSN3D10	MSN3D11	MSN3D12	MSN3D13
Li	20.57	21.58	19.14	20.80	18.73	19.47	18.14	19.72	12.48	17.10	16.87
Be	2.70	2.53	2.69	2.28	2.50	2.48	2.77	2.94	5.52	4.55	4.52
B	0.00	7711.98	3789.16	2725.74	2146.47	1690.93	1386.20	1206.45	814.45	715.82	665.02
Sc	10.09	10.27	9.69	9.74	9.28	9.81	9.42	9.01	9.69	9.15	9.29
Ti	450.28	458.68	456.46	458.69	445.53	444.46	448.43	446.83	442.39	428.89	446.24
V	2.27	2.33	2.35	2.40	2.30	2.33	2.31	2.18	2.61	2.22	3.98
Cr	0.19	0.15	0.23	0.16	0.18	0.17	0.21	0.14	0.18	0.15	2.32
Mn	358.10	374.09	338.42	364.78	345.58	365.60	339.48	338.50	282.81	300.39	293.56
Co	1.77	1.81	1.78	1.75	1.73	1.78	1.71	1.80	1.66	1.78	1.89
Ni	0.12	0.13	0.09	0.07	0.08	0.16	0.19	0.14	0.23	0.14	0.20
Cu	0.17	0.11	0.44	0.41	0.37	0.66	0.24	0.62	0.35	0.48	1.34
Zn	66.43	67.20	65.50	67.52	67.79	67.84	69.80	69.78	65.66	65.50	68.94
Ga	221.96	226.00	214.69	217.90	233.48	235.81	238.85	235.55	233.72	237.43	228.82
Rb	306.73	314.31	323.40	316.10	301.92	308.48	315.70	329.25	306.90	301.21	313.50
Sr	13.86	14.01	14.50	13.83	13.69	13.77	14.15	14.60	13.76	13.68	13.73
Y	0.05	0.06	0.05	0.05	0.06	0.05	0.05	0.07	0.05	0.06	0.09
Zr	0.94	0.95	1.00	1.04	0.94	0.94	0.96	1.01	0.94	0.85	1.04
Nb	53.05	55.07	54.93	54.11	52.10	53.33	53.44	54.03	52.10	51.60	53.29
Mo	0.30	0.25	0.26	0.24	0.19	0.27	0.26	0.25	0.17	0.28	0.23
Sn	1.83	1.85	1.90	1.77	1.79	1.86	1.87	1.82	1.83	1.72	1.90
Cs	9.88	10.15	10.27	10.34	10.09	9.95	10.43	10.84	9.94	9.95	10.52
Ba	3832.05	3926.78	3971.85	3838.13	3717.45	3795.30	3947.01	4002.26	3737.36	3792.82	3730.02
Hf	0.20	0.23	0.21	0.22	0.20	0.22	0.17	0.19	0.18	0.19	0.25
Ta	1.35	1.46	1.41	1.42	1.37	1.44	1.38	1.42	1.36	1.37	1.46
W	37.41	38.48	37.69	39.15	37.98	38.10	37.10	37.01	36.77	37.09	39.88
Pb	13.58	13.82	14.10	13.66	13.43	13.77	13.98	14.39	15.61	14.44	15.82
Th	0.0006	0.0010	0.0014	0.0023	0.0017	0.0010	0.0003	0.0003	0.0014	0.0000	0.0072
U	0.0039	0.0052	0.0047	0.0041	0.0051	0.0041	0.0021	0.0035	0.0020	0.0014	0.0041

Appendix 2.4B (continued): Detailed trace element data of micas from tourmaline-bearing and sunstone-bearing pegmatites (GNS, MSN) from Ntcheu and amethyst-bearing pegmatites (CUB) from Balaka. All concentrations are given in ppm.

	MSN3D14	MSN3D15	CUB1B1	CUB1B2	CUB1B3	CUB1B4	CUB1B5	CUB1B6	CUB1B7	CUB1B8	CUB1B9
Li	17.56	17.74	151.79	135.39	111.23	95.78	91.04	93.55	73.67	68.80	76.75
Be	4.67	4.31	0.68	0.19	0.10	0.16	0.12	0.12	0.13	0.03	0.27
B	604.07	529.38	151.25	163.63	167.68	210.98	170.22	101.30	105.91	118.04	128.26
Sc	9.51	9.52	1.62	1.66	1.59	1.57	1.56	1.61	1.52	1.62	1.69
Ti	456.03	451.96	8212.84	8718.75	8288.62	8503.33	8317.84	8769.72	8797.68	8740.94	8460.16
V	2.87	2.53	75.41	77.37	70.97	69.99	70.05	74.06	73.27	72.87	70.82
Cr	0.14	0.16	60.88	64.90	60.36	60.84	61.38	58.52	58.76	61.25	58.75
Mn	288.32	301.46	279.62	279.46	269.51	290.73	287.30	306.52	303.08	299.91	300.43
Co	1.80	1.87	14.91	14.43	13.44	13.69	13.52	13.83	13.75	13.74	13.51
Ni	0.20	0.13	74.84	73.28	69.08	68.72	72.80	73.50	73.61	69.77	72.14
Cu	0.36	0.42	0.75	0.50	0.14	0.15	0.23	0.19	0.05	0.12	0.06
Zn	68.17	66.55	219.13	203.22	190.04	194.22	188.79	183.86	177.29	181.38	186.81
Ga	225.86	226.04	57.87	55.48	54.47	60.75	59.66	57.82	55.30	57.63	62.61
Rb	314.77	315.06	502.65	536.04	498.56	504.79	508.39	511.66	513.77	510.19	499.81
Sr	14.16	14.12	6.08	9.40	10.21	11.95	11.10	13.63	14.17	14.43	13.45
Y	0.06	0.08	6.83	0.33	0.06	0.02	0.07	0.12	0.05	0.02	0.01
Zr	0.91	1.04	3.21	8.63	9.05	16.24	13.23	14.82	16.37	18.26	15.90
Nb	53.67	54.11	48.61	48.45	45.75	47.68	47.87	48.71	48.14	48.22	46.64
Mo	0.24	0.29	0.01	0.01	0.01	0.00	0.02	0.01	0.01	0.00	0.01
Sn	1.83	1.91	2.04	1.79	1.61	1.56	1.58	1.63	1.57	1.50	1.50
Cs	10.33	10.23	24.88	26.77	25.56	24.79	25.09	24.58	24.57	24.40	24.20
Ba	3850.55	3898.46	1129.33	1219.95	1130.75	1166.05	1155.22	1254.62	1248.01	1253.12	1231.47
Hf	0.23	0.22	0.07	0.18	0.20	0.29	0.24	0.25	0.25	0.32	0.27
Ta	1.49	1.39	2.53	2.65	2.50	2.73	2.67	2.58	2.62	2.70	2.63
W	37.43	36.88	0.01	0.01	0.01	0.00	0.02	0.00	0.00	0.00	0.00
Pb	15.62	14.38	1.49	1.68	1.63	1.82	2.03	1.70	1.64	1.63	1.90
Th	0.0014	0.0000	0.0183	0.0032	0.0008	0.0000	0.0018	0.0008	0.0012	0.0008	0.0018
U	0.0034	0.0043	0.0130	0.0264	0.0172	0.0633	0.0432	0.0462	0.0520	0.0618	0.0551

Appendix 2.4B (continued): Detailed trace element data of micas from tourmaline-bearing and sunstone-bearing pegmatites (GNS, MSN) from Ntcheu and amethyst-bearing pegmatites (CUB) from Balaka. All concentrations are given in ppm.

	CUB1B10	CUB1B11	CUB2B1	CUB2B2	CUB2B3	CUB2B4	CUB2B5	CUB2B6	CUB2B7	CUB2B8	CUB2B9
Li	73.28	73.74	43.48	46.35	48.35	49.20	49.91	44.24	62.55	50.82	45.17
Be	0.17	0.12	0.05	0.06	0.00	0.13	0.06	0.08	0.15	0.10	0.04
B	106.22	90.46	54.21	53.13	45.87	41.90	45.27	49.60	55.38	50.75	42.25
Sc	1.54	1.62	1.22	1.28	1.08	1.39	1.22	1.17	1.31	1.23	1.26
Ti	8441.10	8499.91	8611.20	8529.88	8886.33	9256.56	9353.05	8920.46	8855.90	8746.01	8997.78
V	70.49	72.76	67.85	67.84	69.13	72.74	72.23	68.79	70.08	68.61	70.14
Cr	59.05	57.90	63.83	62.64	63.17	68.73	66.69	60.48	60.27	58.04	64.90
Mn	297.11	304.25	267.02	264.67	275.16	282.51	286.69	281.89	287.99	277.04	265.79
Co	13.61	13.75	12.90	13.49	13.16	13.88	13.64	13.22	13.41	13.07	13.89
Ni	71.04	71.78	69.03	68.09	67.09	72.01	70.80	71.04	72.41	68.97	71.45
Cu	0.22	0.57	0.06	0.07	0.06	0.12	0.19	0.10	0.07	36.91	0.09
Zn	183.93	186.48	209.82	209.87	195.77	205.20	200.46	193.77	203.26	202.15	206.84
Ga	62.07	60.60	57.89	60.62	55.34	55.69	55.63	54.60	58.32	59.69	58.44
Rb	500.97	499.88	533.05	518.37	516.37	534.18	535.76	521.33	528.61	514.60	518.41
Sr	13.39	13.53	13.52	13.58	12.61	14.44	14.91	14.42	14.62	12.98	13.14
Y	0.01	0.02	0.07	0.02	0.01	0.01	0.06	0.09	0.02	0.02	0.03
Zr	19.34	16.91	14.23	13.53	15.97	15.55	16.14	15.45	15.10	23.65	33.73
Nb	46.41	46.42	44.31	43.61	43.21	47.33	47.25	46.16	45.90	46.47	44.21
Mo	0.01	0.01	0.01	0.01	0.01	0.01	0.00	0.01	0.00	0.01	0.01
Sn	1.56	1.49	1.80	1.82	1.73	1.68	1.72	1.65	1.58	1.76	1.90
Cs	23.67	24.13	24.67	24.61	24.05	25.43	25.18	24.41	24.40	23.75	24.35
Ba	1209.08	1222.24	1239.31	1262.56	1279.14	1364.31	1380.84	1325.32	1331.92	1287.58	1248.28
Hf	0.32	0.33	0.25	0.26	0.27	0.27	0.28	0.25	0.26	0.35	0.38
Ta	2.57	2.65	2.44	2.58	2.54	2.57	2.69	2.55	2.62	2.58	2.53
W	0.00	0.00	0.00	0.00	0.00	0.00	0.00	0.00	0.00	0.00	0.00
Pb	1.81	1.93	1.81	1.81	1.82	1.89	1.85	1.70	1.86	1.80	1.86
Th	0.0013	0.0011	0.0008	0.0009	0.0000	0.0010	0.0006	0.0007	0.0009	0.0000	0.0011
U	0.0749	0.0757	0.0433	0.0303	0.0564	0.0395	0.0502	0.0542	0.0397	0.1216	0.1950

Appendix 2.4B (continued): Detailed trace element data of micas from tourmaline-bearing and sunstone-bearing pegmatites (GNS, MSN) from Ntcheu and amethyst-bearing pegmatites (CUB) from Balaka.

	CUB2B10	CUB3B1	CUB3B2	CUB3B3	CUB3B4	CUB3B5	CUB3B6	CUB3B7	CUB3B8	CUB3B9	CUB3B10
Li	48.36	66.21	61.69	78.88	64.26	80.85	67.06	71.00	56.23	52.40	56.94
Be	0.10	0.12	0.08	0.10	0.11	0.20	0.14	0.11	0.12	0.10	0.69
B	40.80	83.29	78.12	70.70	90.03	59.04	61.03	51.52	57.66	65.47	60.87
Sc	1.36	1.54	1.67	1.56	1.65	1.47	1.51	1.52	1.60	1.49	1.53
Ti	9344.15	7841.75	8032.08	8285.95	7878.35	7532.77	7780.54	7997.40	8122.82	7659.21	7922.32
V	72.23	72.76	74.53	76.34	73.14	69.90	72.05	74.11	75.45	71.81	70.35
Cr	67.80	55.24	55.51	57.17	56.64	58.45	54.75	56.57	60.58	55.27	57.70
Mn	277.14	290.55	288.57	288.05	286.57	269.45	276.09	286.24	295.98	276.90	271.21
Co	13.94	16.32	14.53	15.42	59.86	14.70	20.12	18.64	17.13	13.82	26.61
Ni	71.16	67.99	69.99	70.86	68.59	71.59	69.80	69.58	69.45	65.27	65.61
Cu	0.10	1.64	0.28	0.33	2.85	1.10	2.22	3.76	0.25	0.07	19.07
Zn	201.49	208.15	206.41	210.75	182.77	189.40	193.91	199.88	197.56	190.25	185.99
Ga	55.55	55.97	56.67	52.82	53.63	52.78	54.15	53.79	53.46	53.00	49.61
Rb	543.54	529.42	544.05	554.43	552.90	458.15	536.01	543.93	554.15	518.30	412.05
Sr	14.45	13.39	13.81	14.25	13.96	12.57	13.29	13.24	13.83	12.98	12.25
Y	0.02	0.07	0.14	1.27	0.38	5.97	0.08	0.36	0.10	0.08	11.87
Zr	16.46	18.52	18.42	17.60	19.36	17.59	17.22	18.64	18.30	17.84	18.78
Nb	47.70	50.75	52.34	52.49	50.42	48.69	50.65	52.37	52.09	49.70	50.59
Mo	0.01	0.00	0.00	0.01	0.00	0.01	0.01	0.01	0.00	0.01	0.01
Sn	2.03	1.65	1.68	1.72	2.91	1.72	1.86	1.88	1.67	1.55	2.82
Cs	25.62	25.63	25.99	26.73	26.96	23.44	25.21	26.66	26.97	24.79	21.49
Ba	1374.30	1139.79	1170.67	1183.83	1142.00	984.43	1128.33	1144.22	1161.22	1110.02	886.81
Hf	0.29	0.29	0.32	0.33	0.33	0.26	0.30	0.29	0.31	0.30	0.30
Ta	2.77	2.55	2.60	2.56	2.42	2.46	2.51	2.52	2.54	2.41	2.53
W	0.00	0.01	0.00	0.00	0.00	0.00	0.00	0.00	0.00	0.00	0.00
Pb	1.90	1.84	1.65	1.89	1.95	1.90	1.77	1.87	1.58	1.52	1.83
Th	0.0012	0.0003	0.0012	0.0012	0.0000	0.0013	0.0043	0.0011	0.0003	0.0008	0.0022
U	0.0390	0.0496	0.0458	0.0390	0.0521	0.0513	0.0626	0.0601	0.0579	0.0527	0.0493

Appendix 2.4B (continued): Detailed trace element data of micas from tourmaline-bearing and sunstone-bearing pegmatites (GNS, MSN) from Ntcheu and amethyst-bearing pegmatites (CUB) from Balaka.

Element	CUB3B11	CUB3B12	CUB3B13	CUB3B14	CUB4B1	CUB4B2	CUB4B3	CUB4B4	CUB4B5
Li	59.35	56.51	56.18	58.09	89.17	107.75	88.30	93.34	94.19
Be	0.26	0.13	0.04	0.18	0.15	0.11	0.05	0.19	0.18
B	62.13	55.41	49.53	47.30	82.67	87.96	105.96	91.87	82.24
Sc	1.53	1.56	1.56	1.51	1.49	1.65	1.63	1.69	1.60
Ti	7817.42	7717.47	7727.60	7853.26	7720.39	7926.87	7550.44	7561.78	8009.04
V	70.51	71.31	72.26	72.93	73.54	74.17	72.82	70.70	75.22
Cr	54.06	53.58	55.48	54.54	56.24	56.16	53.69	55.65	58.00
Mn	278.81	276.46	274.68	277.22	268.41	276.16	273.09	259.42	280.22
Co	14.48	17.27	16.64	14.89	15.05	16.40	16.43	26.82	15.13
Ni	68.41	67.11	66.70	67.96	70.87	70.03	70.86	72.31	68.75
Cu	0.44	1.30	0.83	0.04	0.58	4.10	1.11	2.65	2.20
Zn	210.16	203.42	193.77	207.45	194.46	198.49	200.24	171.77	205.42
Ga	58.80	56.39	55.29	54.96	51.07	53.30	54.36	56.05	56.11
Rb	520.39	520.75	533.42	533.58	563.28	577.91	572.48	552.15	585.75
Sr	12.41	12.96	13.28	13.20	12.45	11.31	13.19	12.78	14.15
Y	0.12	0.18	0.21	0.06	0.03	0.17	0.11	0.92	0.37
Zr	17.41	19.52	17.14	18.13	16.04	13.47	16.45	16.24	16.40
Nb	49.75	49.13	50.56	50.97	51.12	52.29	50.00	49.66	52.69
Mo	0.01	0.01	0.01	0.00	0.01	0.02	0.01	0.01	0.01
Sn	1.85	1.82	1.81	1.75	2.15	2.01	2.06	2.56	2.07
Cs	24.44	25.02	25.28	25.61	27.41	27.30	27.30	26.88	27.90
Ba	1114.00	1098.07	1132.82	1122.39	1123.36	1162.75	1128.41	1080.57	1192.67
Hf	0.31	0.33	0.29	0.31	0.32	0.29	0.26	0.31	0.29
Ta	2.61	2.53	2.49	2.57	2.40	2.46	2.43	2.49	2.57
W	0.00	0.00	0.00	0.00	0.00	0.03	0.01	0.02	0.02
Pb	1.68	1.68	1.66	1.59	2.21	2.42	2.71	3.79	2.88
Th	0.0003	0.0008	0.0012	0.0012	0.0021	0.0021	0.0003	0.0065	0.0014
U	0.0501	0.0693	0.0429	0.0578	0.0445	0.0431	0.0587	0.0520	0.0421

Appendix 2.4B: (continued) Detailed trace element data of micas from tourmaline-bearing and sunstone-bearing pegmatites (GNS, MSN) from Ntcheu and amethyst-bearing pegmatites (CUB) from Balaka. All concentrations are given in ppm.

Element	CUB4B6	CUB4B7	CUB4B8	CUB4B9	CUB4B10
Li	98.67	80.80	90.69	92.40	86.66
Be	0.27	0.16	0.22	0.07	0.14
B	68.69	76.21	81.21	94.31	88.36
Sc	1.64	1.67	1.61	1.63	1.55
Ti	8092.16	8512.90	8070.88	8022.16	7966.38
V	78.73	80.35	75.02	75.10	73.14
Cr	60.34	62.11	57.93	57.39	55.41
Mn	263.68	289.18	277.46	276.56	276.56
Co	15.63	15.32	14.84	18.73	14.89
Ni	74.45	72.04	69.72	68.95	69.28
Cu	1.66	1.59	1.19	0.97	1.21
Zn	217.75	199.17	193.01	190.05	209.06
Ga	51.09	51.88	52.20	57.42	58.23
Rb	536.59	615.38	589.07	584.42	582.30
Sr	11.37	15.30	13.21	15.05	13.76
Y	3.46	0.12	0.47	0.59	0.23
Zr	13.92	17.88	16.31	18.05	17.77
Nb	52.43	56.10	53.01	52.68	52.59
Mo	0.03	0.01	0.01	0.02	0.01
Sn	2.90	2.12	1.85	2.07	2.02
Cs	25.62	28.65	27.42	27.65	26.91
Ba	1039.76	1233.66	1192.90	1209.19	1185.68
Hf	0.30	0.31	0.30	0.32	0.31
Ta	2.60	2.61	2.44	2.60	2.59
W	0.03	0.01	0.00	0.00	0.01
Pb	3.73	2.61	2.27	2.44	2.50
Th	0.0018	0.0012	0.0008	0.0007	0.0002
U	0.0423	0.0574	0.0486	0.0495	0.0645

Appendix 2.4C: Detailed UCC-normalised (Taylor and McLennan, 1995) rare earth element data (REE) of micas from tourmaline-bearing and sunstone-bearing pegmatites (GNS, MSN) from Ntcheu and amethyst-bearing pegmatites (CUB) from Balaka. All concentrations are given in ppm.

Element	GNS11	GNS12	GNS13	GNS14	GNS15	GNS16	GNS17	GNS18	GNS19	GNS110
La	0.0870	0.1590	0.0648	0.1380	0.1230	0.0450	0.0690	0.1320	0.0690	0.0390
Ce	0.1920	0.0902	0.0250	0.0442	0.0608	0.0634	0.1600	0.5184	0.0000	0.0320
Pr	0.0085	0.0057	0.0000	0.0019	0.0076	0.0036	0.0089	0.0165	0.0141	0.0053
Nd	0.2236	0.1716	0.1690	0.0832	0.1144	0.0780	0.1274	0.0000	0.1612	0.0000
Sm	0.0378	0.0113	0.0198	0.0527	0.0239	0.0473	0.0266	0.0423	0.0239	0.0126
Eu	0.0568	0.0636	0.0652	0.0507	0.0662	0.0250	0.0254	0.0099	0.0261	0.0576
Gd	0.0262	0.0410	0.0179	0.0125	0.0201	0.0114	0.0258	0.0608	0.0296	0.0262
Tb	0.0012	0.0002	0.0000	0.0005	0.0004	0.0003	0.0000	0.0008	0.0002	0.0005
Dy	0.0273	0.0000	0.0042	0.0074	0.0172	0.0098	0.0000	0.0249	0.0000	0.0097
Ho	0.0009	0.0024	0.0014	0.0006	0.0003	0.0011	0.0013	0.0000	0.0006	0.0021
Er	0.0209	0.0225	0.0228	0.0363	0.0179	0.0127	0.0062	0.0115	0.0150	0.0219
Tm	0.0014	0.0022	0.0021	0.0023	0.0023	0.0009	0.0005	0.0009	0.0007	0.0008
Yb	0.2860	0.3080	0.2134	0.2266	0.2288	0.1012	0.1430	0.4642	0.0902	0.1980
Lu	0.0123	0.0127	0.0145	0.0132	0.0156	0.0052	0.0068	0.0186	0.0053	0.0133

Appendix 2.4C: (continued) Detailed UCC-normalised (Taylor and McLennan, 1995) rare earth element data (REE) of micas from tourmaline-bearing and sunstone-bearing pegmatites (GNS, MSN) from Ntcheu and amethyst-bearing pegmatites (CUB) from Balaka. All concentrations are given in ppm.

Element	GNS31	GNS32	GNS33	GNS34	GNS35	GNS36	GNS37	GNS38	GNS39	GNS310
La	0.0870	0.0000	0.0450	0.1890	0.0792	0.0630	0.0282	0.2250	0.0750	0.0618
Ce	0.1920	0.0576	0.0608	0.1920	0.1600	0.0691	0.0000	0.4224	0.1984	0.0589
Pr	0.0085	0.0049	0.0000	0.0185	0.0000	0.0097	0.0000	0.0241	0.0000	0.0053
Nd	0.2236	0.1300	0.1170	0.1534	0.1664	0.1326	0.2808	0.3432	0.1404	0.1118
Sm	0.0378	0.0536	0.0342	0.0320	0.0347	0.0000	0.0000	0.0446	0.0212	0.0230
Eu	0.0568	0.0276	0.0209	0.0223	0.0214	0.0205	0.0229	0.0231	0.0197	0.0204
Gd	0.0262	0.0000	0.0175	0.0228	0.0251	0.0350	0.0217	0.0707	0.0000	0.0312
Tb	0.0012	0.0239	0.0008	0.0009	0.0007	0.0002	0.0008	0.0007	0.0006	0.0006
Dy	0.0273	0.0000	0.0203	0.0000	0.0042	0.0091	0.0000	0.0592	0.0151	0.0000
Ho	0.0009	0.0010	0.0004	0.0018	0.0010	0.0000	0.0011	0.0023	0.0000	0.0008
Er	0.0209	0.0207	0.0363	0.0260	0.0219	0.0136	0.0092	0.0271	0.0000	0.0067
Tm	0.0014	0.0015	0.0022	0.0013	0.0014	0.0012	0.0004	0.0013	0.0010	0.0010
Yb	0.2860	0.1892	0.2222	0.1958	0.1760	0.1408	0.1342	0.1685	0.1320	0.2002
Lu	0.0123	0.0073	0.0099	0.0091	0.0090	0.0080	0.0062	0.0095	0.0096	0.0087

Appendix 2.4C: (continued) Detailed UCC-normalised (Taylor and McLennan, 1995) rare earth element data (REE) of micas from tourmaline-bearing and sunstone-bearing pegmatites (GNS, MSN) from Ntcheu and amethyst-bearing pegmatites (CUB) from Balaka. All concentrations are given in ppm.

Element	GNS61	GNS62	GNS63	GNS64	GNS65	GNS66	GNS67	GNS68	GNS69	GNS610
La	0.2100	0.0870	0.1020	0.1020	0.1020	0.2580	0.2070	0.0810	0.1680	0.8340
Ce	0.2816	0.1920	0.3968	0.0000	0.2176	0.2752	0.0000	7.5840	0.0858	0.8320
Pr	0.0097	0.0085	0.0054	0.0000	0.0060	0.0060	0.0100	0.0000	0.0091	0.0660
Nd	0.0000	0.2236	0.2028	0.2028	0.0884	0.1794	0.0936	0.2236	0.0000	1.3520
Sm	0.0297	0.0378	0.0243	0.0000	0.0383	0.0086	0.0257	0.0252	0.0234	0.1229
Eu	0.0543	0.0568	0.0473	0.0600	0.0615	0.0500	0.0441	0.0632	0.0558	0.0707
Gd	0.0182	0.0262	0.0182	0.0407	0.0338	0.0445	0.0000	0.0315	0.0403	0.2014
Tb	0.0007	0.0012	0.0009	0.0002	0.0003	0.0003	0.0006	0.0009	0.0000	0.0096
Dy	0.0235	0.0273	0.0102	0.0081	0.0161	0.0074	0.0109	0.0151	0.0140	0.3080
Ho	0.0011	0.0009	0.0010	0.0008	0.0006	0.0021	0.0014	0.0010	0.0009	0.0146
Er	0.0221	0.0209	0.0147	0.0262	0.0269	0.0311	0.0189	0.0235	0.0242	0.1198
Tm	0.0017	0.0014	0.0013	0.0025	0.0016	0.0012	0.0009	0.0033	0.0021	0.0037
Yb	0.2134	0.2860	0.1958	0.2112	0.3322	0.2464	0.2112	0.1958	0.3410	0.2530
Lu	0.0120	0.0123	0.0129	0.0117	0.0149	0.0146	0.0146	0.0136	0.0172	0.0164

Appendix 2.4C: (continued) Detailed UCC-normalised (Taylor and McLennan, 1995) rare earth element data (REE) of micas from tourmaline-bearing and sunstone-bearing pegmatites (GNS, MSN) from Ntcheu and amethyst-bearing pegmatites (CUB) from Balaka. All concentrations are given in ppm.

Element	GNS71	GNS72	GNS73	GNS74	GNS75	GNS76	GNS77	GNS78	GNS79	GNS710	GNS711	GNS712	GNS713	GNS714
La	0.3150	0.2730	0.2250	0.1530	2.7450	0.1890	0.0723	0.0510	0.1260	0.2220	0.1230	0.2340	0.0930	2.4690
Ce	0.4672	0.0000	0.0000	0.0928	2.2016	0.0928	0.3072	0.0486	0.0486	0.1299	0.1664	0.2624	0.2176	1.4912
Pr	0.0094	0.0082	0.0000	0.0000	0.1037	0.0000	0.0000	0.0043	0.0000	0.0093	0.0000	0.0056	0.0000	0.0930
Nd	0.0754	0.0000	0.1820	0.0000	1.5340	0.0000	0.2860	0.0000	0.1274	0.0468	0.0000	0.1248	0.2132	2.0020
Sm	0.0000	0.0441	0.0518	0.0000	0.1071	0.0000	0.0000	0.0000	0.0455	0.0414	0.0000	0.0351	0.0342	0.0684
Eu	0.0826	0.0730	0.0874	0.1082	0.0730	0.0730	0.0695	0.0749	0.0666	0.0651	0.0715	0.0499	0.0554	0.0489
Gd	0.0000	0.0315	0.0323	0.0479	0.0703	0.0239	0.0243	0.0201	0.0137	0.0346	0.0452	0.0308	0.0000	0.1041
Tb	0.0015	0.0000	0.0005	0.0007	0.0015	0.0004	0.0005	0.0010	0.0010	0.0006	0.0000	0.0007	0.0000	0.0016
Dy	0.0000	0.0546	0.0095	0.0000	0.0844	0.0000	0.0172	0.0000	0.0119	0.0161	0.0077	0.0158	0.0000	0.0641
Ho	0.0010	0.0000	0.0009	0.0000	0.0034	0.0005	0.0016	0.0007	0.0004	0.0007	0.0006	0.0009	0.0000	0.0028
Er	0.0078	0.0083	0.0099	0.0000	0.0085	0.0041	0.0046	0.0071	0.0037	0.0078	0.0035	0.0000	0.0127	0.0196
Tm	0.0000	0.0007	0.0004	0.0000	0.0009	0.0008	0.0004	0.0005	0.0003	0.0012	0.0003	0.0000	0.0000	0.0008
Yb	0.0398	0.0792	0.1206	0.1738	0.0878	0.1305	0.0099	0.1439	0.0312	0.0539	0.0235	0.0101	0.0000	0.0568
Lu	0.0026	0.0085	0.0106	0.0113	0.0041	0.0079	0.0032	0.0064	0.0039	0.0050	0.0033	0.0007	0.0006	0.0022

Appendix 2.4C: (continued) Detailed UCC-normalised (Taylor and McLennan, 1995) rare earth element data (REE) of micas from tourmaline-bearing and sunstone-bearing pegmatites (GNS, MSN) from Ntcheu and amethyst-bearing pegmatites (CUB) from Balaka. All concentrations are given in ppm.

Element	MSN1B1	MSN1B2	MSN1B3	MSN1B4	MSN1B5	MSN1B6	MSN1B7	MSN1B8	MSN1B9	MSN1B10
La	0.3060	0.0960	0.2520	0.1020	0.3360	0.2070	0.1740	0.1080	0.5730	0.7170
Ce	0.3264	0.2112	0.0653	0.3776	0.2240	0.2816	0.2816	0.0653	1.1968	2.0096
Pr	0.0051	0.0031	0.0057	0.0127	0.0067	0.0023	0.0151	0.0057	0.0327	0.0391
Nd	0.1092	0.0000	0.2132	0.1222	0.0962	0.1014	0.1196	0.0000	0.2366	0.6708
Sm	0.0374	0.0140	0.0365	0.0000	0.0000	0.0527	0.0167	0.0248	0.0243	0.0176
Eu	0.0650	0.0497	0.0556	0.0563	0.0463	0.0670	0.0392	0.0554	0.0583	0.0624
Gd	0.0163	0.0000	0.0156	0.0262	0.0296	0.0152	0.0369	0.0407	0.0255	0.0498
Tb	0.0007	0.0003	0.0000	0.0007	0.0000	0.0000	0.0003	0.0000	0.0008	0.0003
Dy	0.0189	0.0056	0.0151	0.0000	0.0084	0.0154	0.0105	0.0034	0.0238	0.0228
Ho	0.0014	0.0009	0.0013	0.0011	0.0012	0.0010	0.0006	0.0008	0.0006	0.0006
Er	0.0115	0.0081	0.0336	0.0242	0.0347	0.0265	0.0324	0.0145	0.0237	0.0156
Tm	0.0008	0.0019	0.0021	0.0013	0.0013	0.0018	0.0013	0.0021	0.0012	0.0020
Yb	0.2552	0.2706	0.2926	0.3124	0.2112	0.1958	0.1914	0.3366	0.2662	0.2288
Lu	0.0138	0.0160	0.0136	0.0142	0.0158	0.0122	0.0122	0.0146	0.0127	0.0154

Appendix 2.4C: (continued) Detailed UCC-normalised (Taylor and McLennan, 1995) rare earth element data (REE) of micas from tourmaline-bearing and sunstone-bearing pegmatites (GNS, MSN) from Ntcheu and amethyst-bearing pegmatites (CUB) from Balaka. All concentrations are given in ppm.

Element	MSN3A1	MSN3A2	MSN3A3	MSN3A4	MSN3A5	MSN3A6	MSN3A7	MSN3A8	MSN3A9	MSN3A10
La	0.1170	0.1350	0.1980	0.1350	0.2010	0.1710	0.2100	0.1500	1.2420	0.4410
Ce	0.1792	0.0781	0.0275	0.1216	0.1344	0.4608	0.2368	0.3392	4.6528	0.3840
Pr	0.0107	0.0046	0.0000	0.1058	0.0067	0.0062	0.0061	0.0060	0.0362	0.0102
Nd	0.0000	0.0988	0.0000	0.0000	0.2106	0.1768	0.0884	0.2054	1.3234	0.3276
Sm	0.0302	0.0216	0.0212	0.0405	0.0302	0.0248	0.0270	0.0212	0.0671	0.0459
Eu	0.0370	0.0781	0.0563	0.0542	0.0572	0.0706	0.0771	0.0356	0.0337	0.0740
Gd	0.0217	0.0308	0.0266	0.0266	0.0000	0.0327	0.0536	0.0213	0.0190	0.1037
Tb	0.0010	0.0006	0.0008	0.0004	0.0008	0.0007	0.0009	0.0004	0.0007	0.0007
Dy	0.0089	0.0126	0.0046	0.0126	0.0091	0.0147	0.0112	0.0112	0.0697	0.0063
Ho	0.0014	0.0010	0.0010	0.0002	0.0005	0.0008	0.0009	0.0009	0.0028	0.0009
Er	0.0334	0.0060	0.0101	0.0131	0.0166	0.0129	0.0055	0.0094	0.0260	0.0246
Tm	0.0004	0.0010	0.0014	0.0007	0.0010	0.0011	0.0014	0.0011	0.0007	0.0004
Yb	0.2090	0.1148	0.1287	0.0957	0.1342	0.1313	0.4334	0.1782	0.1476	0.1848
Lu	0.0059	0.0070	0.0089	0.0116	0.0074	0.0094	0.0117	0.0072	0.0076	0.0098

Appendix 2.4C: (continued) Detailed UCC-normalised (Taylor and McLennan, 1995) rare earth element data (REE) of micas from tourmaline-bearing and sunstone-bearing pegmatites (GNS, MSN) from Ntcheu and amethyst-bearing pegmatites (CUB) from Balaka. All concentrations are given in ppm.

Element	MSN3D1	MSN3D2	MSN3D3	MSN3D4	MSN3D5	MSN3D6	MSN3D7	MSN3D8
La	0.3270	0.5460	0.6300	0.5370	0.6270	0.4530	0.3660	0.3030
Ce	0.6272	0.5952	0.2944	0.6208	1.2480	0.0851	0.6848	0.6976
Pr	0.0025	0.0048	0.0023	0.0148	0.0107	0.0149	0.0046	0.0049
Nd	0.1664	0.0520	0.1560	0.2184	0.2366	0.0000	0.2028	0.1664
Sm	0.0338	0.0644	0.0644	0.0446	0.0342	0.0225	0.0419	0.0329
Eu	0.1681	0.1575	0.1197	0.1364	0.1417	0.1338	0.1382	0.1417
Gd	0.0498	0.0228	0.0536	0.0718	0.0293	0.0410	0.0148	0.0707
Tb	0.0011	0.0000	0.0000	0.0002	0.0000	0.0009	0.0002	0.0006
Dy	0.0046	0.0042	0.0140	0.0196	0.0196	0.0000	0.0214	0.0000
Ho	0.0016	0.0011	0.0012	0.0018	0.0008	0.0010	0.0005	0.0008
Er	0.0212	0.0140	0.0322	0.0416	0.0140	0.0294	0.0292	0.0248
Tm	0.0008	0.0011	0.0012	0.0017	0.0019	0.0020	0.0012	0.0015
Yb	0.1892	0.3014	0.1980	0.3278	0.2332	0.2838	0.2266	0.2618
Lu	0.0130	0.0114	0.0160	0.0160	0.0161	0.0145	0.0162	0.0155

Appendix 2.4C: (continued) Detailed UCC-normalised (Taylor and McLennan, 1995) rare earth element data (REE) of micas from tourmaline-bearing and sunstone-bearing pegmatites (GNS, MSN) from Ntcheu and amethyst-bearing pegmatites (CUB) from Balaka. All concentrations are given in ppm.

Element	MSN3D9	MSN3D10	MSN3D11	MSN3D12	MSN3D13	MSN3D14	MSN3D15
La	0.3570	0.5760	0.2790	0.2880	1.1490	0.2730	0.5280
Ce	0.4352	0.4416	0.1984	0.1120	2.2208	0.4416	1.5488
Pr	0.0000	0.0050	0.0124	0.0025	0.0724	0.0024	0.0170
Nd	0.1118	0.0000	0.2184	0.2964	0.7722	0.1066	0.5902
Sm	0.0342	0.1017	0.0113	0.0554	0.0680	0.0491	0.0441
Eu	0.1311	0.1602	0.1241	0.1214	0.0961	0.1179	0.0978
Gd	0.0342	0.0562	0.0475	0.0707	0.0429	0.0350	0.0350
Tb	0.0006	0.0006	0.0002	0.0000	0.0006	0.0006	0.0002
Dy	0.0000	0.0182	0.0315	0.0000	0.0182	0.0088	0.0133
Ho	0.0018	0.0010	0.0023	0.0016	0.0021	0.0015	0.0018
Er	0.0340	0.0212	0.0191	0.0391	0.0189	0.0163	0.0244
Tm	0.0016	0.0029	0.0010	0.0022	0.0021	0.0015	0.0026
Yb	0.1892	0.2464	0.2398	0.1848	0.3234	0.2178	0.2574
Lu	0.0163	0.0154	0.0131	0.0133	0.0131	0.0148	0.0116

Appendix 2.4C: (continued) Detailed UCC-normalised (Taylor and McLennan, 1995) rare earth element data (REE) of micas from tourmaline-bearing and sunstone-bearing pegmatites (GNS, MSN) from Ntcheu and amethyst-bearing pegmatites (CUB) from Balaka. All concentrations are given in ppm.

Element	CUB1B1	CUB1B2	CUB1B3	CUB1B4	CUB1B5	CUB1B6	CUB1B7	CUB1B8	CUB1B9	CUB1B10	CUB1B11
La	182.1000	14.4300	3.5910	1.3800	2.9910	4.4400	1.7610	0.8070	0.3930	0.8460	0.8070
Ce	61.8240	3.8336	0.9408	0.5888	0.8256	1.6960	0.2432	0.1536	0.1005	0.1408	0.2432
Pr	12.1410	0.9344	0.1385	0.0476	0.1243	0.2350	0.1399	0.0454	0.0168	0.0504	0.0568
Nd	209.0400	14.8980	3.4320	1.0400	3.4580	3.9520	1.6640	0.7020	0.6890	0.7046	0.8554
Sm	5.7330	0.4095	0.0432	0.0500	0.0531	0.0770	0.0774	0.0635	0.0284	0.0396	0.0176
Eu	0.2059	0.0517	0.0315	0.0260	0.0378	0.0399	0.0451	0.0406	0.0295	0.0374	0.0332
Gd	4.2788	0.2318	0.0266	0.0471	0.0570	0.0642	0.0562	0.0194	0.0133	0.0277	0.0619
Tb	0.0825	0.0035	0.0009	0.0000	0.0010	0.0009	0.0005	0.0005	0.0003	0.0002	0.0005
Dy	2.4990	0.1019	0.0417	0.0154	0.0249	0.0403	0.0196	0.0112	0.0112	0.0112	0.0000
Ho	0.1231	0.0070	0.0011	0.0009	0.0010	0.0035	0.0004	0.0003	0.0004	0.0008	0.0009
Er	0.9338	0.0538	0.0069	0.0124	0.0048	0.0216	0.0090	0.0090	0.0035	0.0067	0.0179
Tm	0.0182	0.0010	0.0001	0.0003	0.0005	0.0006	0.0004	0.0010	0.0003	0.0003	0.0010
Yb	0.7612	0.1199	0.0073	0.0282	0.0152	0.0405	0.0202	0.0370	0.0370	0.0713	0.0640
Lu	0.0149	0.0020	0.0003	0.0016	0.0003	0.0014	0.0008	0.0018	0.0018	0.0036	0.0024

Appendix 2.4C: (continued) Detailed UCC-normalised (Taylor and McLennan, 1995) rare earth element data (REE) of micas from tourmaline-bearing and sunstone-bearing pegmatites (GNS, MSN) from Ntcheu and amethyst-bearing pegmatites (CUB) from Balaka. All concentrations are given in ppm.

Element	CUB2B1	CUB2B2	CUB2B3	CUB2B4	CUB2B5	CUB2B6	CUB2B7	CUB2B8	CUB2B9	CUB2B10
La	2.7690	2.2560	0.4350	1.8540	8.8800	6.2400	0.8190	0.2370	1.4280	0.9810
Ce	0.2560	0.4608	0.2624	0.3776	1.5552	1.1584	0.1434	0.0710	0.2496	0.1139
Pr	0.1392	0.0951	0.0000	0.1377	0.4047	0.3358	0.0462	0.0041	0.1022	0.0575
Nd	2.8600	1.9240	0.5460	1.6900	6.3700	4.4460	0.7774	0.2496	1.3000	0.5772
Sm	0.0806	0.0369	0.0000	0.0185	0.0882	0.1044	0.0162	0.0279	0.0279	0.0000
Eu	0.0298	0.0238	0.0024	0.0242	0.0264	0.0172	0.0145	0.0240	0.0287	0.0244
Gd	0.0688	0.0490	0.0000	0.0205	0.0285	0.1087	0.0205	0.0152	0.0866	0.0228
Tb	0.0009	0.0006	0.0000	0.0004	0.0004	0.0010	0.0008	0.0002	0.0003	0.0010
Dy	0.0256	0.0053	0.0480	0.0154	0.0476	0.0175	0.0119	0.0116	0.0060	0.0063
Ho	0.0029	0.0000	0.0008	0.0007	0.0014	0.0010	0.0002	0.0005	0.0005	0.0005
Er	0.0179	0.0048	0.0000	0.0038	0.0101	0.0074	0.0055	0.0244	0.0085	0.0058
Tm	0.0002	0.0003	0.0000	0.0004	0.0003	0.0002	0.0000	0.0006	0.0012	0.0003
Yb	0.0352	0.0057	0.0506	0.0108	0.0279	0.0497	0.0084	0.0876	0.2046	0.0130
Lu	0.0009	0.0003	0.0021	0.0005	0.0021	0.0006	0.0007	0.0037	0.0095	0.0005

Appendix 2.4C: (continued) Detailed UCC-normalised (Taylor and McLennan, 1995) rare earth element data (REE) of micas from tourmaline-bearing and sunstone-bearing pegmatites (GNS, MSN) from Ntcheu and amethyst-bearing pegmatites (CUB) from Balaka. All concentrations are given in ppm.

Element	CUB3B1	CUB3B2	CUB3B3	CUB3B4	CUB3B5	CUB3B6	CUB3B7	CUB3B8	CUB3B9	CUB3B10	CUB3B11	CUB3B12
La	2.2260	2.1330	27.8100	6.6600	138.9000	1.0530	7.2900	1.8120	1.4700	249.6000	3.1860	4.2300
Ce	0.1619	0.0909	0.8064	0.2496	3.9680	0.0998	0.4224	0.0736	0.2048	12.9920	0.1030	0.1606
Pr	0.1221	0.0987	1.5762	0.3720	7.6822	0.0710	0.4317	0.0987	0.0682	14.4130	0.1775	0.2677
Nd	1.7420	1.8200	29.8480	6.0580	134.9400	1.6380	8.2680	1.2454	0.9594	238.9400	3.6920	4.1340
Sm	0.0653	0.1175	0.8595	0.1368	3.6495	0.0288	0.2790	0.0572	0.0716	7.5600	0.1503	0.0729
Eu	0.0422	0.0238	0.0517	0.0389	0.1487	0.0255	0.0457	0.0363	0.0338	0.2561	0.0301	0.0367
Gd	0.0452	0.0703	0.7144	0.2622	3.0134	0.0289	0.1870	0.0543	0.0448	5.8672	0.0635	0.1216
Tb	0.0007	0.0011	0.0161	0.0024	0.0483	0.0007	0.0047	0.0012	0.0005	0.1331	0.0012	0.0016
Dy	0.0662	0.0221	0.3990	0.0896	1.6275	0.0081	0.0707	0.0343	0.0154	4.4485	0.0434	0.0690
Ho	0.0025	0.0018	0.0202	0.0066	0.0847	0.0000	0.0065	0.0022	0.0012	0.2336	0.0030	0.0025
Er	0.0136	0.0267	0.1332	0.0460	0.6969	0.0076	0.0398	0.0225	0.0067	1.8285	0.0184	0.0317
Tm	0.0004	0.0008	0.0020	0.0008	0.0121	0.0003	0.0011	0.0004	0.0005	0.0356	0.0005	0.0010
Yb	0.0284	0.0506	0.0845	0.0695	0.5214	0.0640	0.0939	0.0266	0.0550	1.6676	0.0308	0.1247
Lu	0.0012	0.0006	0.0022	0.0017	0.0139	0.0020	0.0018	0.0005	0.0015	0.0322	0.0012	0.0035

Appendix 2.4C: (continued) Detailed UCC-normalised (Taylor and McLennan, 1995) rare earth element data (REE) of micas from tourmaline-bearing and sunstone-bearing pegmatites (GNS, MSN) from Ntcheu and amethyst-bearing pegmatites (CUB) from Balaka. All concentrations are given in ppm.

Element	CUB3B13	CUB3B14	CUB4B1	CUB4B2	CUB4B3	CUB4B4	CUB4B5	CUB4B6	CUB4B7	CUB4B8	CUB4B9	CUB4B10
La	5.7600	1.4700	2.1720	5.1960	4.6500	22.5300	16.5900	122.4000	5.3400	12.8100	20.2200	7.9200
Ce	0.3264	0.1030	0.3200	5.2224	1.0112	2.3232	1.1328	4.0512	0.4096	0.8128	1.2288	0.6912
Pr	0.3813	0.0845	0.0966	0.2492	0.2528	1.4619	0.9905	6.4681	0.2492	0.8563	1.0373	0.4501
Nd	5.4080	1.1492	1.6120	3.6920	3.5880	24.1540	16.1980	106.0800	4.0560	12.6100	19.1880	8.6060
Sm	0.1485	0.0320	0.0801	0.1377	0.0392	0.8505	0.3735	2.6010	0.1031	0.3600	0.6210	0.2088
Eu	0.0284	0.0341	0.0387	0.0384	0.0304	0.0729	0.0487	0.1111	0.0376	0.0462	0.0482	0.0357
Gd	0.1626	0.0593	0.0574	0.0505	0.1858	0.4826	0.2664	1.9570	0.1121	0.2926	0.4104	0.1402
Tb	0.0036	0.0005	0.0004	0.0015	0.0015	0.0144	0.0055	0.0409	0.0022	0.0069	0.0084	0.0036
Dy	0.0735	0.0123	0.0308	0.1043	0.0413	0.5670	0.1418	1.2460	0.0413	0.1670	0.2230	0.0728
Ho	0.0050	0.0009	0.0011	0.0032	0.0012	0.0252	0.0051	0.0526	0.0030	0.0089	0.0096	0.0021
Er	0.0186	0.0113	0.0038	0.0182	0.0076	0.2309	0.0207	0.4370	0.0131	0.0660	0.0543	0.0430
Tm	0.0005	0.0003	0.0003	0.0003	0.0003	0.0042	0.0005	0.0079	0.0006	0.0010	0.0010	0.0011
Yb	0.0130	0.0315	0.0161	0.0143	0.0200	0.2266	0.0607	0.3850	0.0341	0.0583	0.0546	0.0612
Lu	0.0007	0.0009	0.0004	0.0008	0.0011	0.0051	0.0016	0.0077	0.0010	0.0017	0.0031	0.0034

Appendix 2.4D: Detailed chondrite-normalised (Nakamura, 1974) rare earth element data (REE) of micas from tourmaline-bearing and sunstone-bearing pegmatites (GNS, MSN) from Ntcheu and amethyst-bearing pegmatites (CUB) from Balaka. All concentrations are given in ppm.

Element	GNS11	GNS12	GNS13	GNS14	GNS15	GNS16	GNS17	GNS18	GNS19	GNS110
La	0.0123	0.0225	0.0091	0.0194	0.0173	0.0000	0.0098	0.0190	0.0095	0.0057
Ce	0.0000	0.0000	0.0006	0.0011	0.0000	0.0016	0.0000	0.0132	0.0000	0.0008
Pr	0.0000	0.0000	0.0000	0.0029	0.0000	0.0055	0.0136	0.0000	0.0000	0.0000
Nd	0.0000	0.0000	0.0000	0.0070	0.0095	0.0066	0.0108	0.0000	0.0000	0.0000
Sm	0.0000	0.0170	0.0300	0.0790	0.0000	0.0000	0.0400	0.0000	0.0000	0.0190
Eu	1.1500	1.2800	1.3200	1.0200	1.3400	0.5050	0.5130	0.2000	0.5280	1.1600
Gd	0.0350	0.0540	0.0000	0.0160	0.0260	0.0150	0.0000	0.0000	0.0000	0.0350
Tb	0.0000	0.0093	0.0000	0.0000	0.0190	0.0130	0.0000	0.0000	0.0110	0.0210
Dy	0.0000	0.0000	0.0048	0.0083	0.0000	0.0000	0.0000	0.0000	0.0000	0.0000
Ho	0.0198	0.0000	0.0320	0.0140	0.0063	0.0260	0.0290	0.0000	0.0000	0.0470
Er	0.0570	0.0610	0.0620	0.0990	0.0490	0.0340	0.0170	0.0000	0.0400	0.0590
Tm	0.1730	0.2730	0.2620	0.2770	0.2850	0.1070	0.0590	0.1100	0.0860	0.0980
Yb	0.8090	0.8680	0.6040	0.6410	0.6450	0.2860	0.4050	1.3100	0.2550	0.5570
Lu	1.5600	1.6200	1.8400	1.6800	1.9800	0.6500	0.8600	2.3500	0.6800	1.6900

Appendix 2.4D: (continued) Detailed chondrite-normalised (Nakamura, 1974) rare earth element data (REE) of micas from tourmaline-bearing and sunstone-bearing pegmatites (GNS, MSN) from Ntcheu and amethyst-bearing pegmatites (CUB) from Balaka. All concentrations are given in ppm.

Element	GNS31	GNS32	GNS33	GNS34	GNS35	GNS36	GNS37	GNS38	GNS39	GNS310
La	0.0000	0.0000	0.0000	0.0267	0.0000	0.0088	0.0000	0.0316	0.0104	0.0000
Ce	0.0240	0.0000	0.0000	0.0049	0.0000	0.0000	0.0000	0.0107	0.0000	0.0000
Pr	0.0000	0.0000	0.0000	0.0280	0.0000	0.0148	0.0000	0.0360	0.0000	0.0000
Nd	0.0000	0.0110	0.0000	0.0000	0.0000	0.0000	0.0240	0.0290	0.0120	0.0000
Sm	0.0000	0.0800	0.0000	0.0000	0.0000	0.0000	0.0000	0.0000	0.0000	0.0350
Eu	0.1900	0.5600	0.4240	0.4490	0.4310	0.4140	0.4600	0.4650	0.4000	0.4130
Gd	0.0000	0.0000	0.0000	0.0300	0.0000	0.0460	0.0000	0.0930	0.0000	0.0410
Tb	0.0480	1.0400	0.0360	0.0400	0.0000	0.0089	0.0000	0.0300	0.0000	0.0000
Dy	0.0000	0.0000	0.0000	0.0000	0.0051	0.0106	0.0000	0.0690	0.0000	0.0000
Ho	0.0370	0.0000	0.0094	0.0420	0.0000	0.0000	0.0000	0.0530	0.0000	0.0000
Er	0.0000	0.0560	0.0990	0.0710	0.0590	0.0370	0.0000	0.0740	0.0000	0.0180
Tm	0.2300	0.1780	0.2750	0.1630	0.1640	0.1450	0.0430	0.1660	0.1230	0.1240
Yb	0.3400	0.5400	0.6270	0.5520	0.4960	0.3970	0.3770	0.4760	0.3760	0.5640
Lu	1.4700	0.9300	1.2600	1.1500	1.1400	1.0100	0.7900	1.2000	1.2200	1.1000

Appendix 2.4D: (continued) Detailed chondrite-normalised (Nakamura, 1974) rare earth element data (REE) of micas from tourmaline-bearing and sunstone-bearing pegmatites (GNS, MSN) from Ntcheu and amethyst-bearing pegmatites (CUB) from Balaka. All concentrations are given in ppm.

Element	GNS61	GNS62	GNS63	GNS64	GNS65	GNS66	GNS67	GNS68	GNS69	GNS610
La	0.0297	0.0410	0.0142	0.0143	0.0143	0.0363	0.0290	0.0000	0.0235	0.1170
Ce	0.0072	0.0133	0.0000	0.0000	0.0055	0.0070	0.0000	0.1930	0.0000	0.0212
Pr	0.0000	0.0000	0.0000	0.0000	0.0000	0.0092	0.0000	0.0000	0.0000	0.1000
Nd	0.0000	0.0310	0.0000	0.0000	0.0075	0.0000	0.0079	0.0190	0.0000	0.1130
Sm	0.0450	0.0000	0.0000	0.0000	0.0000	0.0130	0.0000	0.0000	0.0000	0.1850
Eu	1.1000	0.9600	0.9500	1.2100	1.2400	1.0100	0.8900	1.2800	1.1300	1.4300
Gd	0.0000	0.0480	0.0240	0.0540	0.0000	0.0590	0.0000	0.0000	0.0530	0.2650
Tb	0.0000	0.0210	0.0000	0.0076	0.0150	0.0140	0.0250	0.0000	0.0000	0.4160
Dy	0.0000	0.0120	0.0000	0.0092	0.0000	0.0086	0.0000	0.0000	0.0000	0.3560
Ho	0.0250	0.0410	0.0000	0.0000	0.0000	0.0490	0.0320	0.0220	0.0200	0.3330
Er	0.0600	0.1020	0.0400	0.0710	0.0730	0.0840	0.0510	0.0640	0.0650	0.3260
Tm	0.2150	0.1410	0.1620	0.3090	0.2000	0.1490	0.1130	0.4080	0.2550	0.4550
Yb	0.6020	0.6500	0.5530	0.5930	0.9370	0.6960	0.6000	0.5520	0.9600	0.7140
Lu	1.5200	1.9100	1.6400	1.4900	1.8900	1.8500	1.8500	1.7200	2.1800	2.0800

Appendix 2.4D: (continued) Detailed chondrite-normalised (Nakamura, 1974) rare earth element data (REE) of micas from tourmaline-bearing and sunstone-bearing pegmatites (GNS, MSN) from Ntcheu and amethyst-bearing pegmatites (CUB) from Balaka. All concentrations are given in ppm.

Element	GNS71	GNS72	GNS73	GNS74	GNS75	GNS76	GNS77	GNS78	GNS79	GNS710	GNS711	GNS712	GNS713	GNS714
La	0.0440	0.0380	0.0318	0.0210	0.3860	0.0265	0.0000	0.0073	0.0178	0.0310	0.0171	0.0328	0.0130	0.3470
Ce	0.0119	0.0000	0.0000	0.0000	0.0562	0.0024	0.0078	0.0012	0.0012	0.0000	0.0043	0.0066	0.0000	0.0380
Pr	0.0000	0.0000	0.0000	0.0000	0.1570	0.0000	0.0000	0.0065	0.0000	0.0000	0.0000	0.0000	0.0000	0.1410
Nd	0.0063	0.0000	0.0000	0.0000	0.1290	0.0000	0.0240	0.0000	0.0000	0.0040	0.0000	0.0104	0.0180	0.1690
Sm	0.0000	0.0000	0.0780	0.0000	0.1610	0.0000	0.0000	0.0000	0.0000	0.0000	0.0000	0.0000	0.0000	0.1030
Eu	1.6700	1.4700	1.7600	2.1800	1.4800	1.4700	1.4000	1.5100	1.3400	1.3200	1.4400	1.0100	1.1200	0.9900
Gd	0.0000	0.0000	0.0430	0.0000	0.0930	0.0000	0.0000	0.0270	0.0180	0.0460	0.0600	0.0400	0.0000	0.1380
Tb	0.0000	0.0000	0.0000	0.0000	0.0630	0.0000	0.0000	0.0000	0.0000	0.0000	0.0000	0.0000	0.0000	0.0700
Dy	0.0000	0.0000	0.0108	0.0000	0.0980	0.0000	0.0000	0.0000	0.0137	0.0187	0.0088	0.0180	0.0000	0.0740
Ho	0.0000	0.0000	0.0000	0.0000	0.0780	0.0117	0.0360	0.0152	0.0102	0.0000	0.0147	0.0200	0.0000	0.0640
Er	0.0000	0.0000	0.0270	0.0000	0.0000	0.0112	0.0000	0.0195	0.0098	0.0000	0.0094	0.0000	0.0340	0.0530
Tm	0.0000	0.0850	0.0530	0.0000	0.1100	0.0950	0.0000	0.0650	0.0000	0.1490	0.0000	0.0000	0.0000	0.1030
Yb	0.1120	0.2260	0.3400	0.4900	0.2480	0.3680	0.0000	0.4060	0.0880	0.1520	0.0670	0.0000	0.0000	0.1600
Lu	0.3270	1.0800	1.3400	1.4300	0.5140	1.0000	0.4000	0.8200	0.4970	0.6370	0.4240	0.0830	0.0750	0.2810

Appendix 2.4D: (continued) Detailed chondrite-normalised (Nakamura, 1974) rare earth element data (REE) of micas from tourmaline-bearing and sunstone-bearing pegmatites (GNS, MSN) from Ntcheu and amethyst-bearing pegmatites (CUB) from Balaka. All concentrations are given in ppm.

Element	MSN1B1	MSN1B2	MSN1B3	MSN1B4	MSN1B5	MSN1B6	MSN1B7	MSN1B8	MSN1B9	MSN1B10
La	0.0430	0.0134	0.0355	0.0145	0.0474	0.0291	0.0246	0.0150	0.0810	0.1010
Ce	0.0083	0.0054	0.0000	0.0097	0.0057	0.0072	0.0071	0.0000	0.0304	0.0512
Pr	0.0000	0.0046	0.0000	0.0192	0.0101	0.0035	0.0228	0.0000	0.0500	0.0590
Nd	0.0000	0.0000	0.0000	0.0000	0.0081	0.0085	0.0102	0.0000	0.0198	0.0560
Sm	0.0560	0.0210	0.0000	0.0000	0.0000	0.0000	0.0250	0.0370	0.0370	0.0260
Eu	1.3100	1.0000	1.1200	1.1400	0.9300	1.3500	0.7900	1.1200	1.1800	1.2600
Gd	0.0000	0.0000	0.0210	0.0000	0.0390	0.0200	0.0490	0.0000	0.0000	0.0660
Tb	0.0000	0.0110	0.0000	0.0000	0.0000	0.0000	0.0135	0.0000	0.0330	0.0140
Dy	0.0000	0.0066	0.0000	0.0000	0.0097	0.0000	0.0000	0.0040	0.0280	0.0260
Ho	0.0320	0.0000	0.0310	0.0250	0.0270	0.0230	0.0135	0.0000	0.0000	0.0000
Er	0.0310	0.0220	0.0910	0.0660	0.0950	0.0720	0.0880	0.0390	0.0640	0.0430
Tm	0.0980	0.2320	0.2540	0.1620	0.1590	0.2200	0.1580	0.2620	0.1530	0.2490
Yb	0.7230	0.7620	0.8250	0.8850	0.5960	0.5540	0.5380	0.9500	0.7530	0.6460
Lu	1.7500	2.0300	1.7300	1.8000	2.0000	1.5500	1.5400	1.8500	1.6200	1.9600

Appendix 2.4D: (continued) Detailed chondrite-normalised (Nakamura, 1974) rare earth element data (REE) of micas from tourmaline-bearing and sunstone-bearing pegmatites (GNS, MSN) from Ntcheu and amethyst-bearing pegmatites (CUB) from Balaka. All concentrations are given in ppm.

Element	MSN3A1	MSN3A2	MSN3A3	MSN3A4	MSN3A5	MSN3A6	MSN3A7	MSN3A8	MSN3A9	MSN3A10
La	0.0000	0.0191	0.0280	0.0190	0.0280	0.0240	0.0296	0.0209	0.1740	0.0620
Ce	0.0000	0.0000	0.0007	0.0031	0.0000	0.0118	0.0060	0.0086	0.1186	0.0000
Pr	0.0000	0.0070	0.0000	0.1610	0.0000	0.0093	0.0000	0.0092	0.0550	0.0000
Nd	0.0000	0.0084	0.0000	0.0000	0.0180	0.0149	0.0075	0.0000	0.1110	0.0276
Sm	0.0000	0.0000	0.0000	0.0610	0.0450	0.0000	0.0000	0.0000	0.1010	0.0690
Eu	0.7500	1.5800	1.1400	1.0900	1.1500	1.4300	1.5600	0.7190	0.6810	1.4900
Gd	0.0000	0.0000	0.0350	0.0000	0.0000	0.0430	0.0710	0.0000	0.0250	0.1370
Tb	0.0000	0.0000	0.0000	0.0170	0.0000	0.0000	0.0000	0.0000	0.0000	0.0310
Dy	0.0000	0.0000	0.0052	0.0000	0.0100	0.0000	0.0000	0.0130	0.0810	0.0073
Ho	0.0000	0.0220	0.0000	0.0055	0.0120	0.0000	0.0200	0.0000	0.0630	0.0000
Er	0.0910	0.0160	0.0270	0.0360	0.0450	0.0350	0.0150	0.0260	0.0700	0.0670
Tm	0.0000	0.1270	0.1670	0.0860	0.1190	0.1400	0.1650	0.1300	0.0840	0.0520
Yb	0.5900	0.3240	0.3630	0.2700	0.3770	0.3710	1.2200	0.5040	0.4170	0.5190
Lu	0.7400	0.8800	1.1300	1.4700	0.9400	1.2000	1.4800	0.9200	0.9600	1.2400

Appendix 2.4D: (continued) Detailed chondrite-normalised (Nakamura, 1974) rare earth element data (REE) of micas from tourmaline-bearing and sunstone-bearing pegmatites (GNS, MSN) from Ntcheu and amethyst-bearing pegmatites (CUB) from Balaka. All concentrations are given in ppm.

Element	MSN3D1	MSN3D2	MSN3D3	MSN3D4	MSN3D5	MSN3D6	MSN3D7	MSN3D8
La	0.0460	0.0770	0.0890	0.0760	0.0880	0.0640	0.0520	0.0426
Ce	0.0160	0.0152	0.0076	0.0158	0.0319	0.0022	0.0174	0.0177
Pr	0.0038	0.0072	0.0036	0.0224	0.0000	0.0226	0.0070	0.0074
Nd	0.0140	0.0044	0.0132	0.0183	0.0000	0.0000	0.0171	0.0000
Sm	0.0000	0.0960	0.0960	0.0670	0.0000	0.0340	0.0630	0.0500
Eu	3.4000	3.1800	2.4100	2.7500	2.8600	2.6900	2.7900	2.8700
Gd	0.0660	0.0300	0.0710	0.0950	0.0390	0.0540	0.0200	0.0940
Tb	0.0000	0.0000	0.0000	0.0088	0.0000	0.0000	0.0082	0.0000
Dy	0.0053	0.0051	0.0000	0.0000	0.0000	0.0000	0.0250	0.0000
Ho	0.0360	0.0000	0.0280	0.0410	0.0000	0.0240	0.0109	0.0000
Er	0.0580	0.0380	0.0870	0.1130	0.0380	0.0800	0.0800	0.0680
Tm	0.0980	0.1360	0.1470	0.2130	0.2320	0.2490	0.1440	0.1870
Yb	0.5370	0.8510	0.5580	0.9280	0.6610	0.8000	0.6420	0.7410
Lu	1.6500	1.4500	2.0300	2.0300	2.0400	1.8400	2.0600	1.9700

Appendix 2.4D: (continued) Detailed chondrite-normalised (Nakamura, 1974) rare earth element data (REE) of micas from tourmaline-bearing and sunstone-bearing pegmatites (GNS, MSN) from Ntcheu and amethyst-bearing pegmatites (CUB) from Balaka. All concentrations are given in ppm.

Element	MSN3D9	MSN3D10	MSN3D11	MSN3D12	MSN3D13	MSN3D14	MSN3D15
La	0.0500	0.0810	0.0390	0.0406	0.1610	0.0383	0.0740
Ce	0.0111	0.0000	0.0051	0.0028	0.0567	0.0113	0.0395
Pr	0.0000	0.0076	0.0187	0.0037	0.1100	0.0037	0.0258
Nd	0.0093	0.0000	0.0183	0.0000	0.0650	0.0090	0.0500
Sm	0.0000	0.1530	0.0170	0.0830	0.1020	0.0000	0.0660
Eu	2.6500	3.2400	2.5100	2.4600	1.9400	2.3900	1.9700
Gd	0.0000	0.0750	0.0630	0.0940	0.0000	0.0000	0.0000
Tb	0.0000	0.0270	0.0088	0.0000	0.0270	0.0000	0.0086
Dy	0.0000	0.0210	0.0370	0.0000	0.0210	0.0103	0.0154
Ho	0.0420	0.0240	0.0530	0.0000	0.0470	0.0340	0.0400
Er	0.0930	0.0580	0.0520	0.1060	0.0510	0.0440	0.0670
Tm	0.1940	0.3580	0.1180	0.2680	0.2620	0.1860	0.3240
Yb	0.5360	0.6960	0.6780	0.5220	0.9100	0.6130	0.7260
Lu	2.0700	1.9600	1.6600	1.7000	1.6700	1.8800	1.4700

Appendix 2.4D: (continued) Detailed chondrite-normalised (Nakamura, 1974) rare earth element data (REE) of micas from tourmaline-bearing and sunstone-bearing pegmatites (GNS, MSN) from Ntcheu and amethyst-bearing pegmatites (CUB) from Balaka. All concentrations are given in ppm.

Element	CUB1B1	CUB1B2	CUB1B3	CUB1B4	CUB1B5	CUB1B6	CUB1B7	CUB1B8	CUB1B9	CUB1B10	CUB1B11
La	25.6000	2.0300	0.5050	0.1940	0.4210	0.6260	0.2480	0.1140	0.0550	0.1190	0.1130
Ce	1.5760	0.0977	0.0239	0.0149	0.0211	0.0433	0.0062	0.0038	0.0000	0.0035	0.0062
Pr	18.3900	1.4150	0.2100	0.0720	0.1880	0.3550	0.2110	0.0680	0.0253	0.0760	0.0860
Nd	17.6000	1.2530	0.2880	0.0890	0.2920	0.3320	0.1390	0.0590	0.0580	0.0590	0.0720
Sm	8.6100	0.6130	0.0650	0.0750	0.0800	0.1160	0.1160	0.0950	0.0000	0.0000	0.0260
Eu	4.1500	1.0400	0.6360	0.5250	0.7620	0.8050	0.9100	0.8200	0.5960	0.7560	0.6690
Gd	5.6600	0.3060	0.0000	0.0620	0.0750	0.0850	0.0740	0.0000	0.0180	0.0000	0.0820
Tb	3.5700	0.1490	0.0410	0.0000	0.0420	0.0380	0.0230	0.0000	0.0150	0.0070	0.0200
Dy	2.9000	0.1180	0.0490	0.0000	0.0290	0.0470	0.0000	0.0000	0.0000	0.0000	0.0000
Ho	2.8200	0.1610	0.0000	0.0000	0.0230	0.0800	0.0101	0.0062	0.0098	0.0189	0.0000
Er	2.5400	0.1460	0.0000	0.0330	0.0134	0.0590	0.0000	0.0240	0.0095	0.0180	0.0480
Tm	2.2400	0.1240	0.0091	0.0350	0.0650	0.0710	0.0000	0.1200	0.0000	0.0380	0.1190
Yb	2.1500	0.3390	0.0210	0.0790	0.0430	0.1150	0.0570	0.1040	0.1050	0.2010	0.1810
Lu	1.9000	0.2490	0.0000	0.2090	0.0390	0.1790	0.0980	0.2300	0.2270	0.4540	0.3060

Appendix 2.4D: (continued) Detailed chondrite-normalised (Nakamura, 1974) rare earth element data (REE) of micas from tourmaline-bearing and sunstone-bearing pegmatites (GNS, MSN) from Ntcheu and amethyst-bearing pegmatites (CUB) from Balaka. All concentrations are given in ppm.

Element	CUB2B1	CUB2B2	CUB2B3	CUB2B4	CUB2B5	CUB2B6	CUB2B7	CUB2B8	CUB2B9	CUB2B10
La	0.3900	0.3170	0.0610	0.2610	1.2500	0.8770	0.1150	0.0335	0.2010	0.1380
Ce	0.0066	0.0117	0.0067	0.0096	0.0396	0.0295	0.0037	0.0000	0.0064	0.0029
Pr	0.2110	0.1440	0.0000	0.2090	0.6120	0.5090	0.0690	0.0062	0.1540	0.0870
Nd	0.2410	0.1620	0.0470	0.1430	0.5370	0.3740	0.0650	0.0210	0.1090	0.0490
Sm	0.1210	0.0560	0.0000	0.0280	0.1320	0.1570	0.0240	0.0000	0.0420	0.0000
Eu	0.6030	0.4800	0.0480	0.4900	0.5340	0.3480	0.2940	0.4840	0.5790	0.4910
Gd	0.0910	0.0650	0.0000	0.0000	0.0000	0.1440	0.0000	0.0200	0.1150	0.0000
Tb	0.0400	0.0250	0.0000	0.0000	0.0000	0.0420	0.0340	0.0074	0.0110	0.0420
Dy	0.0300	0.0060	0.0550	0.0180	0.0550	0.0200	0.0000	0.0000	0.0068	0.0072
Ho	0.0660	0.0000	0.0000	0.0000	0.0310	0.0220	0.0044	0.0000	0.0120	0.0000
Er	0.0490	0.0129	0.0000	0.0000	0.0270	0.0000	0.0000	0.0660	0.0000	0.0155
Tm	0.0230	0.0000	0.0000	0.0000	0.0330	0.0280	0.0000	0.0700	0.1400	0.0410
Yb	0.0990	0.0000	0.1420	0.0300	0.0790	0.1400	0.0000	0.2470	0.5760	0.0370
Lu	0.1200	0.0420	0.2600	0.0700	0.2710	0.0820	0.0940	0.4680	1.2100	0.0690

Appendix 2.4D: (continued) Detailed chondrite-normalised (Nakamura, 1974) rare earth element data (REE) of micas from tourmaline-bearing and sunstone-bearing pegmatites (GNS, MSN) from Ntcheu and amethyst-bearing pegmatites (CUB) from Balaka. All concentrations are given in ppm.

Element	CUB3B1	CUB3B2	CUB3B3	CUB3B4	CUB3B5	CUB3B6	CUB3B7
La	0.3130	0.3000	3.9100	0.9390	19.5200	0.1480	1.0240
Ce	0.0041	0.0023	0.0205	0.0064	0.1011	0.0025	0.0108
Pr	0.1850	0.1490	2.3800	0.5630	11.6300	0.1070	0.6530
Nd	0.1470	0.1520	2.5100	0.5090	11.3600	0.1380	0.6960
Sm	0.0980	0.1770	1.2900	0.2050	5.4800	0.0000	0.4170
Eu	0.8510	0.4790	1.0400	0.7800	3.0100	0.5150	0.9200
Gd	0.0600	0.0930	0.9500	0.3470	3.9900	0.0000	0.2470
Tb	0.0000	0.0490	0.6950	0.1060	2.0900	0.0000	0.2060
Dy	0.0770	0.0250	0.4630	0.1040	1.8900	0.0092	0.0820
Ho	0.0570	0.0420	0.4620	0.1500	1.9400	0.0000	0.1490
Er	0.0370	0.0730	0.3620	0.1250	1.8900	0.0000	0.1080
Tm	0.0480	0.0950	0.2490	0.1040	1.4900	0.0420	0.1360
Yb	0.0800	0.1430	0.2380	0.1960	1.4700	0.1810	0.2650
Lu	0.1500	0.0790	0.2780	0.2170	1.7600	0.2580	0.2260

Appendix 2.4D: (continued) Detailed chondrite-normalised (Nakamura, 1974) rare earth element data (REE) of micas from tourmaline-bearing and sunstone-bearing pegmatites (GNS, MSN) from Ntcheu and amethyst-bearing pegmatites (CUB) from Balaka. All concentrations are given in ppm.

Element	CUB3B8	CUB3B9	CUB3B10	CUB3B11	CUB3B12	CUB3B13	CUB3B14
La	0.2550	0.2070	35.1200	0.4480	0.5950	0.8110	0.2070
Ce	0.0000	0.0052	0.3310	0.0000	0.0041	0.0083	0.0026
Pr	0.1500	0.1030	21.8300	0.2680	0.4050	0.5770	0.1280
Nd	0.1050	0.0810	20.1200	0.3110	0.3480	0.4560	0.0970
Sm	0.0860	0.1080	11.3500	0.2260	0.1100	0.2230	0.0480
Eu	0.7320	0.6830	5.1600	0.6070	0.7410	0.5740	0.6870
Gd	0.0720	0.0590	7.7600	0.0840	0.1610	0.2150	0.0780
Tb	0.0510	0.0000	5.7700	0.0540	0.0710	0.1570	0.0000
Dy	0.0400	0.0000	5.1700	0.0510	0.0800	0.0850	0.0142
Ho	0.0490	0.0280	5.3500	0.0670	0.0570	0.1150	0.0210
Er	0.0610	0.0179	4.9700	0.0500	0.0860	0.0510	0.0310
Tm	0.0500	0.0560	4.3700	0.0620	0.1240	0.0590	0.0340
Yb	0.0750	0.1550	4.7100	0.0870	0.3520	0.0360	0.0890
Lu	0.0620	0.1940	4.0900	0.1530	0.4440	0.0900	0.1110

Appendix 2.4D: (continued) Detailed chondrite-normalised (Nakamura, 1974) rare earth element data (REE) of micas from tourmaline-bearing and sunstone-bearing pegmatites (GNS, MSN) from Ntcheu and amethyst-bearing pegmatites (CUB) from Balaka. All concentrations are given in ppm.

Element	CUB4B1	CUB4B2	CUB4B3	CUB4B4	CUB4B5	CUB4B6	CUB4B7	CUB4B8	CUB4B9	CUB4B10
La	0.3050	0.7310	0.6540	3.1700	2.3330	17.2300	0.7530	1.8000	2.8500	1.1150
Ce	0.0081	0.1331	0.0259	0.0592	0.0289	0.1032	0.0105	0.0207	0.0313	0.0176
Pr	0.1470	0.3780	0.3830	2.2100	1.5000	9.7900	0.3780	1.2970	1.5700	0.6820
Nd	0.1360	0.3110	0.3030	2.0300	1.3630	8.9200	0.3420	1.0600	1.6160	0.7230
Sm	0.1200	0.2070	0.0590	1.2700	0.5600	3.9000	0.1550	0.5380	0.9300	0.3140
Eu	0.7800	0.7750	0.6130	1.4700	0.9820	2.2400	0.7580	0.9330	0.9740	0.7210
Gd	0.0760	0.0670	0.2460	0.6360	0.3520	2.5900	0.1480	0.3850	0.5410	0.1850
Tb	0.0000	0.0670	0.0640	0.6240	0.2370	1.7700	0.0940	0.2990	0.3640	0.1540
Dy	0.0360	0.1210	0.0480	0.6610	0.1650	1.4480	0.0480	0.1940	0.2590	0.0850
Ho	0.0000	0.0730	0.0260	0.5770	0.1160	1.2040	0.0680	0.2040	0.2200	0.0470
Er	0.0000	0.0490	0.0210	0.6280	0.0570	1.1860	0.0360	0.1800	0.1470	0.1170
Tm	0.0000	0.0000	0.0330	0.5180	0.0630	0.9640	0.0710	0.1180	0.1280	0.1350
Yb	0.0460	0.0410	0.0560	0.6390	0.1720	1.0860	0.0960	0.1650	0.1540	0.1730
Lu	0.0560	0.1020	0.1350	0.6460	0.2080	0.9810	0.1300	0.2160	0.3890	0.4370